Economic spying charges rattle Chinese-born scientists *p. 732*

A bright extragalactic gamma-ray pulsar *p. 801*

Ancient genome informs on African genetics *p. 820*

Science

$10
13 NOVEMBER 2015
sciencemag.org

AAAS

SPECIAL ISSUE

SEA CHANGES

How climate change is transforming the oceans

CONTENTS

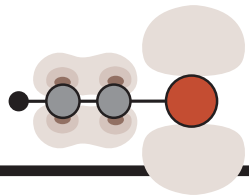

740 & 790
The immediate aftermath of ionization

13 NOVEMBER 2015 • VOLUME 350 • ISSUE 6262

SPECIAL SECTION

Oceans and climate change

ON THE COVER

Melting water streams from an iceberg in Disko Bay on the western coast of Greenland. The iceberg calved from the Ilulissat Glacier (also known as Sermeq Kujalleq or Jakobshavn Glacier), one the world's fastest-moving and most-studied glaciers. Melting polar ice sheets are one consequence of human-induced global warming and could contribute to a substantial increase in global sea levels in the future. See page 750. *Photo: © Paul Souders/Corbis*

SEE ALSO ▸ EDITORIAL P. 721 ▸ NEWS STORY P. 728 ▸ REPORT P. 809 ▸ REPORT BY J. MOUGINOT *ET AL.* 10.1126/science.aac7111

NEWS

IN BRIEF

IN DEPTH

FEATURE

INSIGHTS

PERSPECTIVES

Published by AAAS

CONTENTS

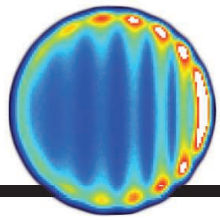

787
Collisions from a slow start

13 NOVEMBER 2015 • VOLUME 350 • ISSUE 6262

SCIENCE (ISSN 0036-8075) is published weekly on Friday, except the last week in December, by the American Association for the Advancement of Science, 1200 New York Avenue, NW, Washington, DC 20005. Periodicals mail postage (publication No. 484460) paid at Washington, DC, and additional mailing offices. Domestic individual membership and subscription (51 issues): $153 ($74 allocated to subscription). Domestic institutional subscription (51 issues): $1282; Foreign postage extra: Mexico, Caribbean (surface mail) $55; other countries (air assist delivery) $85. First class, airmail, student, and emeritus rates on request. Canadian rates with GST available upon request, GST #1254 88122. Publications Mail Agreement Number 1069624. **Printed in the U.S.A.**
Change of address: Allow 4 weeks, giving old and new addresses and 8-digit account number. **Postmaster:** Send change of address to AAAS, P.O. Box 96178, Washington, DC 20090–6178. **Single-copy sales:** $10.00 current issue, $15.00 back issue prepaid includes surface postage; bulk rates on request.

Published by AAAS

Science
AAAS
1200 New York Avenue, NW, Washington, DC 20005
Bateman House, 82-88 Hills Road, Cambridge, UK CB2 1LQ

SUBSCRIPTION SERVICES For change of address, missing issues, new orders and renewals, and payment questions: 866-434-AAAS (2227) or 202-326-6417, FAX 202-842-1065. Mailing addresses: AAAS, P.O. Box 96178, Washington, DC 20090-6178 or AAAS Member Services, 1200 New York Avenue, NW, Washington, DC 20005

INSTITUTIONAL SITE LICENSES 202-326-6730 **REPRINTS:** Author Inquiries 800-635-7181 **COMMERCIAL INQUIRIES** 803-359-4578 **PERMISSIONS** 202-326-6765, permissions@aaas.org **AAAS Member Services** 202-326-6417 or http://membercentral.aaas.org/discounts

INFORMATION FOR AUTHORS See pages 678 and 679 of the 6 February 2015 issue or access www.sciencemag.org/about/authors

Published by AAAS

EDITORIAL

Climate warning, 50 years later

Long before geophysicist Michael Mann's hockey-stick graph became the icon for anthropogenic global warming, the U.S. President's Science Advisory Committee [now known as the President's Council of Advisors on Science and Technology (PCAST)] cautioned President Lyndon B. Johnson that the continued release of CO_2 to the atmosphere from burning fossil fuels would "almost certainly cause significant changes" and "could be deleterious from the point of view of human beings." The committee's report concluded that there could be "marked changes in climate, not controllable through local or even national efforts." In recognition of the 50th anniversary of that first official warning from scientists to policy-makers, the American Association for the Advancement of Science (AAAS), the Carnegie Institution for Science, the American Meteorological Society, and the Linden Trust for Conservation sponsored a 1-day climate symposium on 29 October.

"...policy-makers should be sending thank-you notes—not subpoenas—to express their gratitude to scientists..."

Fifty years ago, the problems of global warming seemed distant and highly uncertain. Today, we are already experiencing impacts from climate change. In the face of mounting urgency, there are signs of hope, though. Within the past few weeks, 10 oil producers, representing 20% of global production, have pledged to reduce greenhouse gas emissions by curbing the flaring of natural gas and investing in carbon capture and storage. The best part of this announcement is the acknowledgment by energy giants BP, Pemex, Statoil, Saudi Aramco, Total, Royal Dutch Shell, BG Group, Eni, Reliance Industries, and Repsol that climate change is a serious problem and that energy companies need to be part of the solution. Unfortunately, the proposed steps are inadequate contributions toward meeting the goal of keeping the increase in average global temperature to below 2°C, a target that would avoid the worst impacts from warming.

Another beacon of hope is the leadership being taken by faith-based groups. Pope Francis has done perhaps the most to raise world awareness of the moral imperative to take action on climate change for the sake of the most disadvantaged members of society, who have done the least to cause the problem. His message resonates far beyond those of Catholic faith. *Laudato Si* joins statements from many other religious leaders, including those of Buddhist, Muslim, Jewish, and other Christian faiths.*

The private sector is also stepping up its responsibility. This past summer, in the ramp-up to the Paris Conference of the Parties to the United Nations Framework Convention on Climate Change, 12 major corporations, including General Motors, Apple, Google, Alcoa, and Bank of America, pledged to invest more than $140 billion in efforts to curtail CO_2 emissions in the next 5 to 10 years.

Although these announcements from diverse sectors are all hopeful signs of a growing awareness of climate-change risk and the need to take action, some leaders are instead distracting scientists from the important work at hand. Last month, the U.S. National Oceanic and Atmospheric Administration (NOAA) received a subpoena from Lamar Smith (R–TX), chairman of the Committee on Science, Space, and Technology in the House of Representatives, for all documents and communications among and between NOAA employees that refer to various global temperature data sets. Ranking member Eddie Bernice Johnson (D–TX) labeled the subpoena "a fishing expedition"† triggered by a NOAA paper published earlier this year in *Science*, "Possible artifacts of data biases in the recent global surface warming hiatus."‡ Senator Edward Markey (D–MA) summed up his opinion at the 50th anniversary event when he suggested that policy-makers should be sending thank-you notes—not subpoenas—to express their gratitude to scientists for sounding the alarm on the perils of greenhouse gas emissions. The senator's remarks remind us that we scientists should thank the many leaders who promote action on climate change.

– Marcia McNutt

Marcia McNutt
Editor-in-Chief
Science *Journals*

*www.interfaithpowerandlight.org/resources/religious-statements-on-climate-change/. †http://democrats.science.house.gov/sites/democrats.science.house.gov/files/Ranking%20Member%20Johnson%20Letter%20to%20Chairman%20Smith%20on%20NOAA%20Subpoena.pdf. ‡T. R. Karl *et al.*, *Science* **348**, 1469 (2015).

10.1126/science.aad7927

PHOTOS: (RIGHT) STACEY PENTLAND PHOTOGRAPHY; (INSET) HHAKIM/ISTOCKPHOTO

NEWS

> “Show us some data that this is ready for prime time.”
>
> **Eric Topol**, director of the Scripps Translational Science Institute in San Diego, California, to STAT on geneticist J. Craig Venter’s Health Nucleus facility, which would charge $25,000 to assess health by sequencing a person’s genome and performing a whole body scan.

IN BRIEF

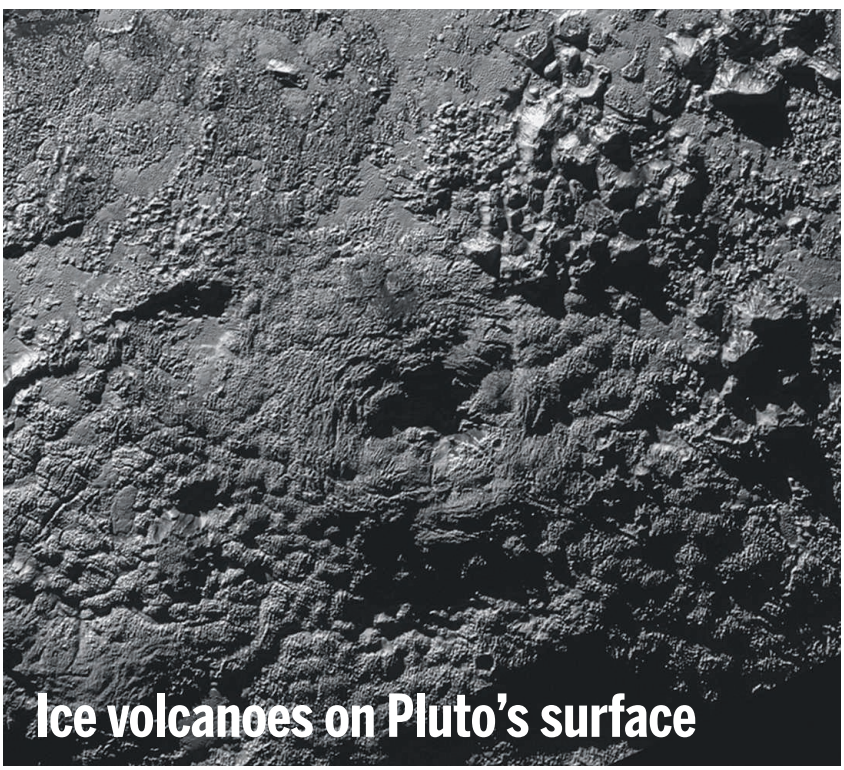

Ice volcanoes on Pluto’s surface

Researchers with NASA’s New Horizons mission have discovered evidence on Pluto for two cryovolcanoes—volcanoes built of frozen ice that once oozed molten ice from the inside of the dwarf planet. The discovery of the two features—provisionally named Wright Mons (pictured, at center) and Piccard Mons—was announced on 9 November at a meeting of the American Astronomical Society in National Harbor, Maryland. It suggests that at some point in Pluto’s past, it had a heat source that melted interior reservoirs of volatile ices, such as nitrogen and methane, which later erupted at the surface. The rims of the cryovolcanoes tower as much as 5 or 6 kilometers high and are more than 150 kilometers across, encircling pits that are nearly as deep as the mountains are tall. “When you see a big mountain with a big hole on the top, it generally points to one thing,” says Oliver White, a New Horizons scientist at Ames Research Center in Mountain View, California. Possible ice volcanoes have been spotted on Triton, a moon of Neptune, and Titan, a moon of Saturn, but Pluto’s cryovolcanoes dwarf them all, White says. http://scim.ag/cryovolcanoes

PHOTO: NASA/JOHNS HOPKINS UNIVERSITY APPLIED PHYSICS LABORATORY/SOUTHWEST RESEARCH INSTITUTE

AROUND THE WORLD

Sierra Leone defeats Ebola

GENEVA, SWITZERLAND | Ebola has infected at least 8794 people in Sierra Leone, 40% of whom have died from the disease, but transmission of the dreaded virus officially came to an end on 7 November. Sierra Leone recorded its first confirmed cases in May 2014. Now, 42 days after two separate blood tests on the last confirmed case of Ebola came back negative, the World Health Organization has declared the epidemic in Sierra Leone over. Liberia was declared Ebola free on 3 September, but in parts of the third affected country, the epidemic continues: Guinea recorded one confirmed case, a newborn, during the week that ended 1 November. The baby’s mother died from the disease, and two of her other children have tested positive, too.

Trudeau fulfills science pledges

OTTAWA | Canada’s Prime Minister Justin Trudeau moved quickly after taking power on 4 November to fulfill his campaign promise to give science and evidence more weight in his government. He appointed two ministers with “science” in their titles: Kirsty Duncan, a medical geographer from the University of Toronto, is minister of science and will focus on supporting basic research. Veteran politico Navdeep Bains is minister of innovation, science, and economic development, and will focus on getting industry to boost applied R&D. Cheering social scientists, Bains immediately reinstated the mandatory long-form census, canceled by the previous government in 2010. He also unmuzzled government scientists, announcing that they were free to speak about their work with the media and the public without prior permission from their communications offices.

Climate change linked to extremes

WASHINGTON, D.C. | A new report by National Oceanic and Atmospheric Administration scientists, published last week in the *Bulletin of the American*

A Qatar-based breeding program aims to return rare Spix's macaws to the Brazilian forest.

Brazilian birds to return home

Believed to be extinct in the wild since 2000, the bright blue Spix's macaws (*Cyanopsitta spixii*) may soon return to the dry "caatinga" forest of northeastern Brazil, thanks to an international effort to return the species to its original habitat. Brazil currently has only 12 specimens in captivity. Now, after years of informal cooperation, the Brazilian government signed an agreement last month to exchange some of its birds with a private collection at the Al Wabra Wildlife Preservation facility in Qatar to aid in both breeding and reintroducing the captive birds. Two older female "ararinhas" from Brazil were sent to Qatar to be artificially inseminated, and a male-female pair was sent to Brazil on 26 October to flock with other youngsters. The aim is to mix bloodlines to improve fertility in the population and produce viable offspring to be released into the wild, possibly as early as 2018. "It's time to send these birds back to nature," says ornithologist Pedro Develey of SAVE Brasil in São Paulo, part of the conservation partnership BirdLife International.

Meteorological Society (*BAMS*), holds climate change accountable for some of 2014's abnormally intense weather events. In an effort to sort out the roles of human-caused climate change and natural fluctuations in last year's global weather, scientists investigated 28 severe climate events. About half were directly linked to human-caused climate change—among them monsoon-triggered flooding in Jakarta, a record heat wave that scorched the Koreas and China in May, and the Himalayan snowstorm in October. The *BAMS* report also provides substantial evidence that climate change is ramping up the likelihood and intensities of heat extremes across the globe, as well as the likelihood of California wildfires, although the report didn't find a specific link to the fires that raged in California in May and September.

Continuous rains left Jakarta flooded in February.

PHOTOS: (TOP TO BOTTOM) © PATRICK PLEUL/DPA/CORBIS; © REYNOLD SUMAYKU/DEMOTIX/CORBIS

Manhattan Project a national park

WASHINGTON, D.C. | Some 70 years after the United States's Manhattan Project produced the first nuclear weapons, the project is slated to become a national park at three related sites. The 2015 National Defense Authorization Act, signed by President Obama in December 2014, authorized a Manhattan Project National Historical Park. This week, Department of Energy Secretary Ernest Moniz and Department of the Interior Secretary Sally Jewell officially established the park with the signing of a Memorandum of Agreement that defines the agencies' respective roles in its creation and management. The park's three locations will be at Oak Ridge, Tennessee, the site of the project's pilot plutonium plant and a uranium enrichment plant; Hanford, Washington, the site of a plutonium production plant; and Los Alamos, New Mexico, where scientists labored to produce the atomic bomb.

Urge to boost science funding

LONDON | With a nervous eye on the United Kingdom's next 4-year funding allocation, to be announced on 25 November, the Science and Technology Committee of the House of Commons this week criticized the government's track record in research funding and called for a strategy to increase it. This summer the government set a goal of cutting ministry budgets by up to 40%. The United Kingdom puts 1.7% of its gross domestic product into R&D, less than the United States (2.8%) and Germany (2.9%), and well below the 2.4% average for developed countries. "The U.K. risks losing its status as a world leader in research," said committee chair Nicola Blackwood in a statement. Meanwhile, on 6 November, the United Kingdom's Department for Business, Innovation & Skills, the main government funder of research, proposed simplifying its system of university grants by eliminating the Higher Education Funding Council. The department also suggested lessening

the administrative burden of its Research Excellence Framework, a massive evaluation of universities for funding purposes. The department will accept comments until 15 January.

Top scientists fill E.U. advice gap

BRUSSELS | Seven scientists, including a Fields medalist and the director of CERN, Europe's premier particle physics lab, were appointed on Tuesday to advise the European commission. This brings an end to a year of suspense since the awkward exit of Scottish biologist Anne Glover, the first and only chief scientific adviser in the commission's history. The group will rely on a team of 25 within the research directorate—up from five staff members on Glover's former team—and will be part of a larger setup to draw advice from other sources across Europe, including learned societies. "I think this format is basically a step up from what existed before in terms of resources," research commissioner Carlos Moedas told *Science*. This new Scientific Advice Mechanism is "a robust solution" that is better suited to the E.U. institutions than a single appointee, he added. **http://scim.ag/ECsciadvisers**

NEWSMAKERS

Potti found guilty of fraud

Perhaps ending a long-running saga, federal officials have declared former Duke University cancer researcher **Anil Potti** guilty of research misconduct. On 9 November, the Office of Research Integrity (ORI) concluded that Potti falsified data in nine papers, a manuscript, and a grant application claiming that certain gene signatures could predict a patient's response to chemotherapy. After Potti published several high-profile papers in 2006, outside biostatisicians raised questions about his work. Duke began formally investigating in 2010. Potti left Duke that year, and Duke later faced a lawsuit from patients in clinical trials based on Potti's studies. As part of a voluntary settlement, Potti "neither admits nor denies ORI's findings of research misconduct." If he seeks federal funding again, his research must be supervised for 5 years. **http://scim.ag/_Potti**

THE *SCIENCE* NEWS QUIZ

This question stumped our online readers this week. Can you outdo them?
When tropical Cyclone Chapala hit Yemen early last week, how much rain fell?

Take the quiz—and find out the answer—here: **http://scim.ag/1MH9WU5**

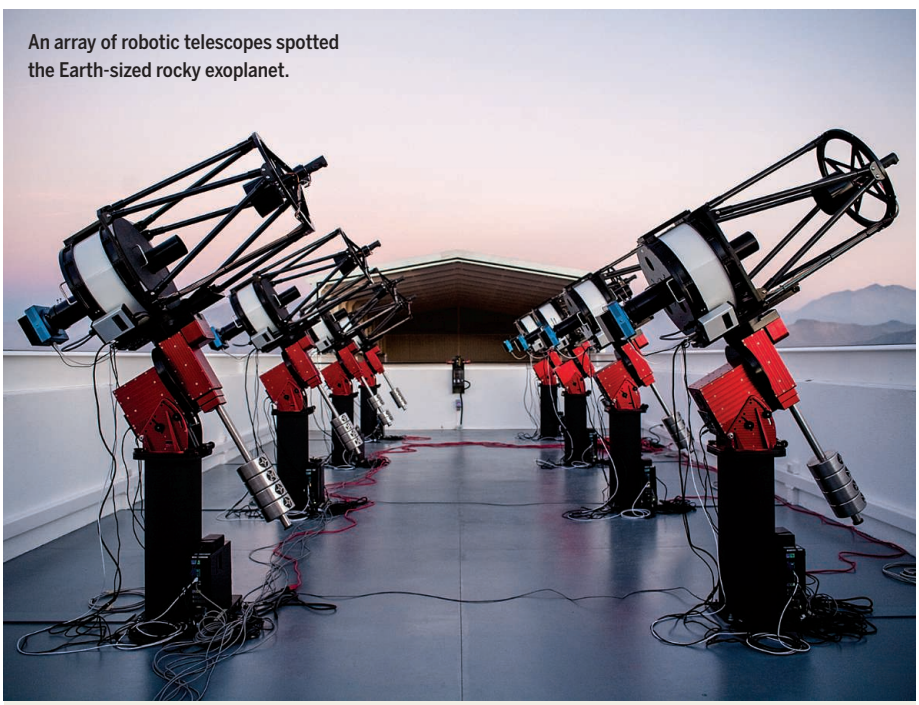

An array of robotic telescopes spotted the Earth-sized rocky exoplanet.

New rocky exoplanet in nearby orbit

Exoplanets may be two a penny these days—nearly 2000 have been confirmed—but one recent discovery is causing a frisson of excitement. GJ 1132b, as it is known, is truly Earth-sized, only 16% bigger in diameter and about the same density as Earth, suggesting a similar rocky crust and iron core. It's orbiting a relatively small, dim star—the most abundant sort in the galaxy. But what makes it particularly noteworthy is its distance, a mere 39 light-years from Earth—a stroll down the street in astronomical terms. Astronomers gather data from exoplanets when they transit in front of their star, revealing their size, and, to an extent, the composition of their atmospheres. Bright stars generate a lot of "noise," drowning out that signal. With the feeble light from its star, its proximity to Earth, and its close-in orbit—providing a transit once every 1.6 days—GJ 1132b could soon be the most-studied exoplanet in the heavens.

BY THE NUMBERS

$1 million

Prize money awarded by the nonprofit forum TED to archaeologist Sarah Parcak (http://scim.ag/TEDgrant) to investigate the looting of ancient Egyptian sites with the help of satellite technology.

$1 billion

Amount of money Toyota will invest in artificial intelligence to create a "guardian angel" for drivers over the next 5 years, via their new Toyota Research Institute.

1377

Number of physicists awarded the Breakthrough Prize in Fundamental Physics this year. Five teams of researchers were recognized for their research on neutrinos, the cosmos's most mysterious subatomic particle.

PHOTO: JONATHAN IRWIN

IN DEPTH

VOLCANOLOGY

Fire down below

New study shows Mount St. Helens may share magma with other volcanoes nearby

Linked magma reservoirs beneath Mount St. Helens could explain the volcano's explosive 1980 eruption.

PHOTO: ROGER WERTH/THE DAILY NEWS

By **Eric Hand**

Geoscientists have revealed the magma plumbing that fed the eruption of Mount St. Helens, the most active volcano in the Pacific Northwest. The emerging picture—one of the most detailed looks yet at the subterranean network beneath a volcano—includes a giant magma chamber between 5 and 12 kilometers below the surface and a second, even larger one, between 12 and 40 kilometers down. The two chambers appear to be connected, which could help explain the sequence of events in the mountain's 1980 eruption and guide volcanologists monitoring the mountain for signs of renewed activity.

So far, the researchers have only a two-dimensional picture of the deep chamber. But if they find it extends far to the north or south, that would imply that the region's volcanoes all draw on the same deep magma supply, says Alan Levander, a geophysicist at Rice University in Houston, Texas, and a leader of the experiment that is doing the subterranean imaging. "It isn't a stretch to say that there's something down there feeding everything," he adds.

Levander unveiled the results on 3 November at a meeting of the Geological Society of America in Baltimore, Maryland—the first detailed images from the largest ever campaign to understand the guts of a volcano with geophysical methods. The campaign, Imaging Magma Under St. Helens (iMUSH), started in 2014 when researchers stuck 2500 seismometers in the ground on trails and logging roads around the volcano. They then detonated 23 explosive shots, each with the force of a small earthquake. "You'd feel this enormous roll in the ground, and everyone would go 'Oh wow,'" Levander says.

The shots sent waves of energy into the crust, and the seismometers picked up reflections. From the travel times of the energy waves—which travel more slowly through magma chambers than through dense rock—the researchers could piece together an image of the crust between depths of 5 and 40 kilometers. To map the crust at shallower depths, they placed 920 seismometers near the volcano summit, where they picked up signals not only from the explosions but also from the background crackle of small earthquakes that occur frequently near Mount St. Helens and even the high-frequency noise produced constantly by Earth itself. Finally, they placed 75 seismometers in wider arcs around the volcano, where they will remain until 2016 to listen for earthquakes that rumble all the way through Earth—so-called "teleseismic earthquakes"—which can reveal features down to 80 kilometers.

The early returns from the project show that the deep magma chamber lies just to the east of the shallow chamber, between Mount St. Helens, the Mount Adams volcano, and a set of dormant volcanoes called the Indian Heaven volcanic field—suggesting that the deep chamber might be supplying magma to all of them. The two magma reservoirs may also explain how the massive 1980 eruption of Mount St. Helens occurred.

In the months before the eruption, a series of small earthquakes was detected, their underground points of origin, or hypocenters, clustering along a particular path. At the time, their location could not be explained. But according to the new picture, those tremors may have taken place as magma was pumped from the lower to the upper chamber, which soon pressurized to the point of eruption. "We can only now understand that those earthquakes are connecting those magma reservoirs," says Eric Kiser, a seismologist at Rice University who works on iMUSH. In the future, he says, volcanologists monitoring Mount St. Helens should sound the alarm if they hear earthquakes along that path. "They could be an indication that you have migration of fluid between the two bodies."

The new picture will please geochemists, who have long favored a stepwise model for eruptions at volcanoes like Mount St. Helens. In a lower chamber, magma can slowly cool, allowing dense crystals to settle to the bottom. That leaves behind a lighter magma that can then rise farther into an upper chamber, ultimately driving an eruption. A similar two-chamber system was imaged this year underneath the supervolcano at Yellowstone National Park in Wyoming.

As the imaging campaign continues, it may clear up several other mysteries. One is a possible sighting of a shallow magma chamber at 2 kilometers' depth, which researchers using a smaller array of seismometers announced in 2009. Brandon Schmandt, a geophysicist at the University of New Mexico, Albuquerque, who is leading the dense 920-seismometer part of iMUSH that is sensitive to such shallow depths, says he sees no sign of the chamber. "If it exists, it

is a minor part of the system," he says.

Another question is how extensive the deepest magma chamber is. Since the 1980s, geoscientists have puzzled over magnetic and electrical measurements suggesting that a layer of rock with unusually high electrical conductivity extends all the way from Mount St. Helens north to Mount Rainier, 75 kilometers away. The layer, called the Southern Washington Cascades Conductor (SWCC), could arise from highly conductive deep ocean sediments that have since turned to rock. But a controversial 2009 study suggested a magma body could also be responsible for the signal—and might be feeding Mount Rainier as well. Levander says the idea that the deep chamber could be the southern end of the SWCC is "tantalizing." The iMUSH team is analyzing data collected by electrodes and magnetometers stuck in more than 100 locations to better understand the SWCC.

Kate Miller, a geophysicist at Texas A&M University in College Station who is not affiliated with iMUSH, says the results at Mount St. Helens will be a boon to volcanologists who want to model the movements of magma through Earth's crust. "You're actually seeing it in action," she says. "Now, you can go in and model the plumbing system." ■

Plumbing a volcano

Last year, researchers set off 23 explosive shots near Mount St. Helens and monitored 3500 seismometers for reflections from under the volcano. The experiment revealed magma chambers, and the deepest one could explain a puzzling underground zone of high electrical conductivity called the Southern Washington Cascades Conductor.

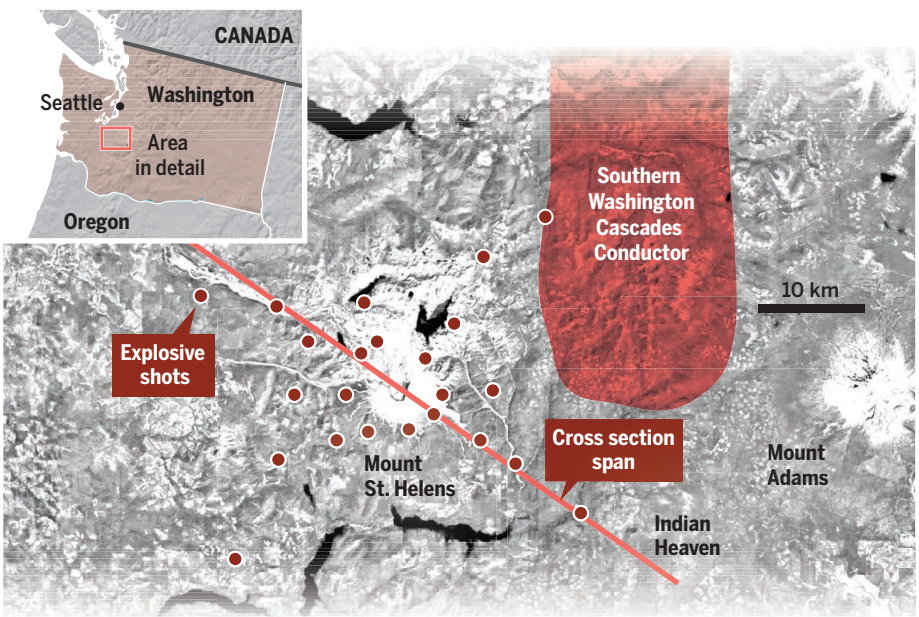

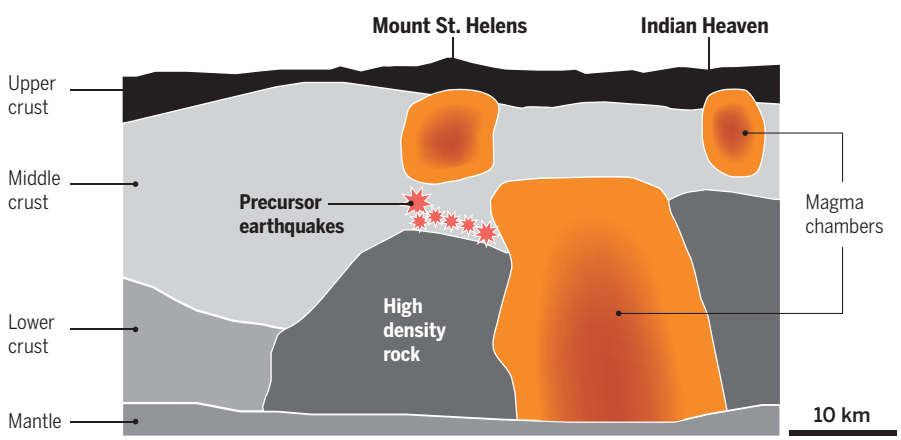

A magma connection

Precursor earthquakes to the volcano's 1980 eruption may have indicated that the lower chamber was filling the upper one with magma.

NUCLEAR POWER

Thorium seen as nuclear's new frontier

Unsung reactor fuel is more abundant than uranium and, proponents say, safer

By **Pallava Bagla**, *in Mumbai, India*

In the 1950s, U.S. nuclear scientists proposed building a fleet of nuclear-powered bombers. That was probably a bad idea. But through decades of technological fits and starts, it has led to what many nuclear experts think could be a very good idea: reactors burning an unheralded radioactive element, thorium.

Compared with uranium, the standard reactor fuel, thorium is more abundant and harder to divert to weapons production, and it yields less radioactive waste. But thorium can't simply be swapped in for uranium in standard reactors. Taking up the engineering gauntlet, several nations are pursuing a complex, largely untested technology that is a distant descendant of that fanciful nuclear powered airplane: thorium reactors in which the fuel is dissolved in a bath of molten salt.

Driving the interest in thorium is the latest in a string of accidents involving uranium-fueled power reactors. The meltdowns at the Fukushima Daiichi Nuclear Power Plant in Japan in March 2011 prompted many countries to take operating reactors offline and to scale back or scuttle plans to build new ones. But after a pause for safety reviews, China and India are gearing up for major nuclear power expansions. They and some other nations are taking a close look at thorium as a nuclear fuel, the theme of a conference here last month that drew participants from 30 countries. India even plans to have a thorium power reactor running within 10 years.

"I'm really excited," says Matthias Krause, a nuclear power expert at the International Atomic Energy Agency in Vienna. In an industry dominated by graying men, Krause says it was refreshing to see "bright young faces and new ideas" at the conference.

Thorium is three to four times more abundant than uranium in Earth's crust. It holds little appeal for would-be bomb-

CREDITS: (GRAPHIC) ADAPTED FROM ERIC KISER AND ALAN LEVANDER; (SATTELITE IMAGE) LANDSAT

makers: Daughter isotopes, born as thorium naturally decays, are highly radioactive, emitting gamma rays that would fry weapon electronics and make thorium-derived bombs cumbersome to store. At the same time, thorium-based fuels yield much less high-level radioactive waste than uranium or plutonium, and molten-salt reactors are touted by their backers as meltdown proof.

The catch is that thorium itself is not fissile. Ratan Kumar Sinha, former chairman of the Atomic Energy Commission (AEC) of India, compares the element to wood that's too soggy for a fire. Thorium must be converted into fissile material much like "wet wood needs to be dried in a furnace," he says. That means bombarding thorium with neutrons to transmute it into fissile uranium-233, either in a conventional solid fuel reactor or in a molten salt reactor (MSR).

India, with the world's largest known thorium reserves, launched a research effort in the mid-1980s. Since 1996, it has been running the Kamini research reactor, the only one in the world that uses uranium-233; that fuel is made by irradiating thorium in another research reactor.

The government plans to open an institute devoted to the element in Visakhapatnam, in southern India, says Sekhar Basu, the new chairman of the AEC of India. Thorium's debut in a commercial reactor may come next year, after India commissions the Prototype Fast Breeder Reactor in Kalpakkam in southern India. The reactor will generate most of its electricity from plutonium, but eventually engineers plan to swaddle its core with a thorium blanket, spawning uranium-233 that will fission to produce small amounts of energy.

Construction of the first reactor to rely largely on thorium is due to start soon at Tarapur, on the Arabian Sea. Slated for completion in the next decade, the 300-megawatt (MW) reactor will burn a mix of thorium, uranium, and plutonium, with about 60% of the power coming from thorium dioxide pellets. That's only the beginning, says Sinha, who calls thorium "the gateway to powering India's economy."

Norway may be the first to follow in India's footsteps with thorium as a solid fuel. Since 2013, it has been testing a mix of thorium and plutonium in a research reactor in Halden as potential fuel stock for Europe's light water power reactors.

China is betting on liquid thorium, a concept first explored at Oak Ridge National Laboratory in Tennessee in the 1950s as a stepchild of the aircraft reactor program. Thorium MSRs remain seductive in part because of their potential safety advantage: In case of an accident, the fluoride salts of thorium and uranium circulating in the core can simply be drained into a storage tank, stopping the fission chain reaction. The Chinese Academy of Sciences's Thorium Molten Salt Reactor Center of Excellence in Shanghai is developing a 10-MW pilot MSR to start running by 2022 and a 100-MW demonstration plant, to be commissioned around 2030, says Hongjie Xu, who is leading the effort.

> ***Thorium is "the gateway to powering India's economy."***
>
> **Ratan Kumar Sinha**, former chair, Atomic Energy Commission of India

The European Commission, too, is taking a hard look at the technology. Last year, it launched a 6-year safety assessment of MSRs. Jiri Krepel, a reactor physicist at the Paul Scherrer Institute in Villigen, Switzerland, predicts that the report will highlight the advantages of thorium, from fuel production to waste management. It "offers a paradigm shift in reactor safety," he says.

Even the United States is getting back in the game—in a small way. A startup called Flibe Energy in Huntsville, Alabama, is developing a liquid-fluoride thorium reactor that hews closely to Oak Ridge's MSR design. Flibe's executive director, Benjamin Soon, envisions small, 10- to 50-MW MSRs being deployed in remote locations for power generation.

Some engineers in Europe and Japan think thorium-fueled MSRs could also be ideal tools for neutering stockpiled plutonium and high-level nuclear waste. The reactors spew high fluxes of neutrons, which could transmute plutonium and waste into radioactive elements with shorter half-lives and potentially generate power as well. The commission has allotted €5 billion to build just such a thorium-fueled test facility in Belgium, called Myrrha, which could be running by 2020.

Yet the disaster-scarred track record of uranium reactors casts a long shadow on thorium, too. Ever since the United States during the Cold War went whole hog into uranium, "the world has been paying a price for the wrong technology choice," argues Jean-Pierre Revol, president of the international Thorium Energy Committee in Geneva, Switzerland. But he and others say that thorium, at long last, is making up for lost time. ■

Pallava Bagla is a science journalist in New Dehli.

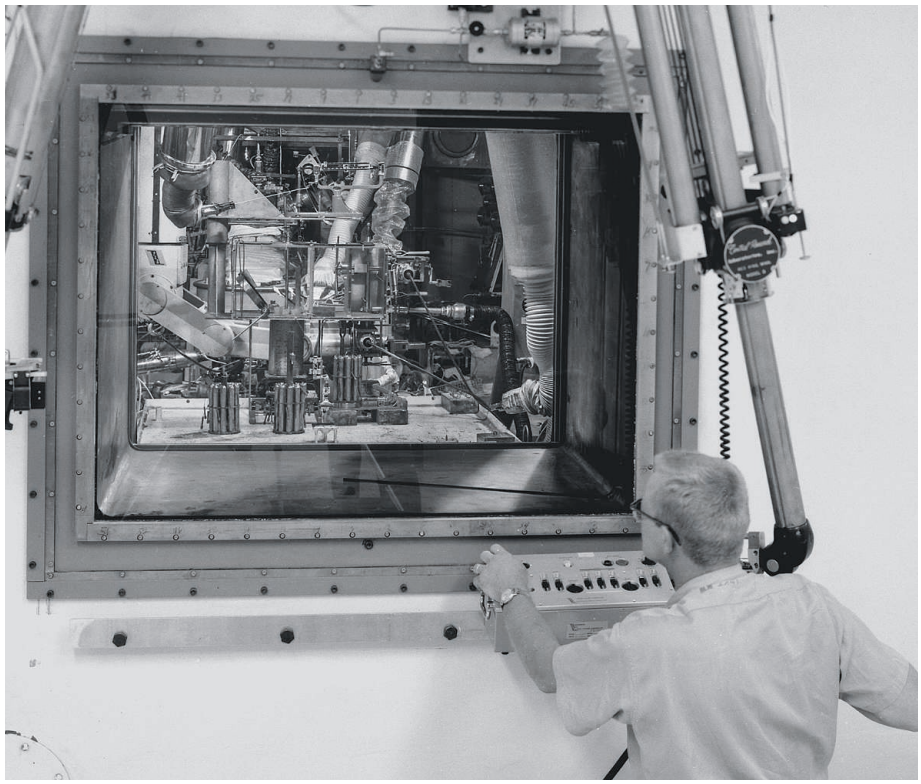

PHOTO: OAK RIDGE NATIONAL LABORATORY

Once written off as a Cold War dead end, Oak Ridge National Laboratory's thorium-powered molten salt reactor, which ran for 5 years in the 1960s, may soon be recast as a trendsetter.

POLAR SCIENCE

How warming oceans unleashed an ice stream

Accelerating retreat of a Greenland glacier could raise sea level for decades to come

By **Carolyn Gramling**

Beneath the calm, white surface of Greenland, rivers of ice are flowing into the ocean—and some are moving very fast indeed. The speedy glaciers on the island's warmer west coast, shedding kilometers of ice into the sea each year as warm ocean waters undermine them, have raised the most alarm about potential sea level rise. But a much bigger glacier is now on the move in Greenland's remote northeast—and a new study suggests it's likely to continue its rush to the sea for decades to come.

The vulnerable glacier, part of a broader flow of ice called the Northeast Greenland Ice Stream, shows that yet another region of Greenland is feeling the effects of warming oceans. "Until fairly recently, we've seen the Northeast Greenland Ice Stream as a cold, remote feature that wasn't likely to do anything interesting," says Ben Smith, a glaciologist at the University of Washington, Seattle, who was not involved in the study. But as Jeremie Mouginot of the University of California (UC), Irvine, lead author of the new paper published online in *Science* today, explains, "It's one more side of Greenland that's starting to lose mass … It's like a boat that is taking on water from all sides."

Hundreds of fjords indent Greenland's coastline, filled with glaciers ending in tongues of floating ice that periodically break off into chunks, or calve. The 600-kilometer-long Northeast Greenland Ice Stream is one of the island's largest, draining 12% of the interior ice sheet. "It's part of the central nervous system of Greenland," says Eric Rignot, also of UC Irvine and a co-author on the paper. "You can see the trace of this ice stream all the way to the summit."

In 2002, a large chunk of one of the ice stream's three terminating glaciers, Zachariæ Isstrøm, broke off. But even then, Smith says, "it wasn't certain that the glacier would respond in any dramatic way." However, in 2012, something appeared to kickstart the giant glacier. "In the last 3 years, it's been going way faster than before," moving at a rate of 2 kilometers per year, Mouginot says. Scientists wanted to know why.

Compiling airborne and satellite data from six different space agencies—NASA, the Japan Aerospace Exploration Agency, the Canadian Space Agency, and three European agencies—the team pieced together ice motions in the region over 40 years. "For the first 25 years, the glacier was stable," Mouginot says. But from 2000 to 2012, it began to move more rapidly; and each year since 2012 it has sped up by about 125 meters per year. Meanwhile, increased melting is whittling away at the leading edge, where the ice meets the ocean, at a rate of about 2 kilometers per year. That's several times slower than the speedy Jakobshavn glacier on the island's west coast—but as Zachariæ Isstrøm continues to flow into the warmer ocean, Mouginot notes, "it has a huge potential" to spur sea level rise.

What is going on under the ice, however, raises the most concern. Using satellite interferometry, the team mapped how the ice bobbed with the tides to infer the point at which the ice floats free of the bedrock. Before 2012, they found, that "grounding line" remained stable, because the glacier was firmly anchored to the sea floor by an underwater rise, or sill. In that year, however, warm ocean waters undermined the glacier far enough to detach it from the sill, they say. "It took a while to push it free of this anchor," Rignot says, which allowed it to flow—and retreat—faster.

The glacier is likely to continue to retreat at its current pace for another 20 to 30 years, he adds, based on the shape of the sea floor. On the inland side of the sill, the sea floor drops and forms a deep basin, into which relatively warm water can easily intrude. Even after the glacier retreats for about another 30 kilometers, reaching the inland end of that basin, a deep channel in the fjord will still let seawater gnaw at the glacier from below.

This work "compellingly" shows the glacier's vulnerability, Smith says—but "figuring out what's going to happen next is the challenge on the table now." The estimate of 20 to 30 years of further grounding line retreat "may be a bit more specific than we can really be at this point," he adds, noting that scientists still have a lot to learn about the warm Atlantic water melting the glacier from below.

Rignot agrees that researchers need a lot more data about both the nearby sea floor and the ocean temperatures next to the glaciers. This summer, NASA began a 6-year project—called the Oceans Melting Greenland (OMG) study—to help close the gap. OMG aims to deploy robot probes to measure seawater temperatures around the coastline while airplanes measure the contours of the glaciers and ships trace the complex bathymetry of its fjords. A sharper picture should emerge of just how warming ocean waters are eating away at the island's fringe of ice—and what the future holds. ■

Draining Greenland

Large regions of the Greenland Ice Sheet drain through speedy Jakobshavn Isbræ and the Northeast Greenland Ice Stream, including the now-accelerating Zachariæ Isstrøm. Fastest flow shown in red.

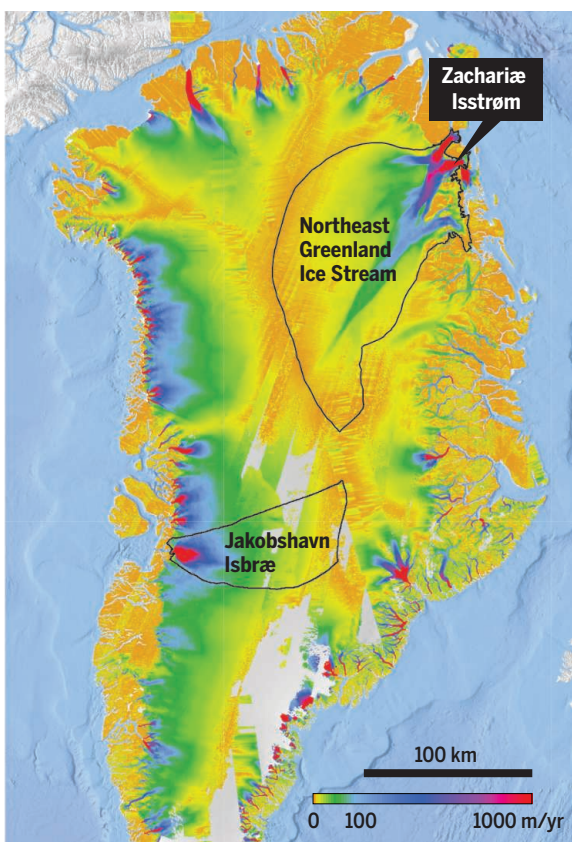

GRAPHIC: ADAPTED FROM KRISTIAN K. KJELDSEN/NATURAL HISTORY MUSEUM OF DENMARK/UNIVERSITY OF COPENHAGEN

The fossilized nervous systems in these 520-million-year-old shrimplike animals suggest how early complex brains arose.

PHOTO: XIAOYA MA, LONDON MUSEUM OF NATURAL HISTORY

EVOLUTION

Fossils, cells point to early appearance of the brain

Nervous systems were well developed by the Cambrian explosion, having evolved in earlier organisms

By **Elizabeth Pennisi**

Hundreds of millions of years ago, animals reached a major milestone: They acquired a brain. Sensation and motor control became centralized in a nervous system with an intricate division of labor, marking the first step along the path to brainy animals like ourselves. But just when and how that happened has been elusive, not least because paleontologists thought that the soft, fragile tissues of the central nervous system would leave few traces in the fossil record.

Now, Nicholas Strausfeld, a neuroscientist at the University of Arizona, Tuscon, and his colleagues have shown that that assumption was wrong—and that modern-looking brains made a startlingly early appearance. Strausfeld won a MacArthur Foundation "genius" award in 1995, and the prize money helped him plunge deep into paleontology and brain evolution. In the 16 November issue of *Current Biology*, his team reports brain structures in multiple fossil arthropods from 520 million years ago. In separate work, they've conducted experiments to confirm that nervous systems really can fossilize.

The bottom line: "The brain and nervous system evolved much earlier than we thought," says Frank Hirth, a neuroscientist at King's College London who teamed up with Strausfeld to edit a special issue of the *Philosophical Transactions of the Royal Society B* on brain evolution, out this week. In that issue, other researchers offer a scenario for how the brain might have evolved in response to the demands of feeding in Precambrian seas and the increasing complexity of early animal body plans.

Until the past decade, the only glimpses of ancient brains came from creatures preserved in amber, which dated to no earlier than 230 million years. In 2008, however, paleontologists reported seeing traces of a central nervous system in 520-million-year-old shrimplike fossils called *Fuxianhuia* unearthed in the Chengjiang Maotianshan Shales in south China. When Xiaoya Ma, a paleontologist at Yunnan University in Kunming, China, showed one of these specimens to Strausfeld, he realized immediately that the "traces" were a complete three-part brain and they teamed up to describe it in a 2012 *Nature* paper. This "brain" was flattened, but was clear enough to show that even that long ago, some creatures had a brain arranged as seen in many arthropods today. Skeptics criticized the work, however, for being based on just one specimen, and argued that the fossil discolorations interpreted as the nervous system could represent other things.

Now, Ma, Strausfeld, and Gregory Edgecombe, a paleontologist at the Natural History Museum in London, describe fossilized nervous systems in seven more *Fuxianhuia* specimens. These brains are preserved as carbon or iron mineral films within the fossils, they report in *Current Biology*.

In a companion paper in the *Philosophical Transactions* special issue, Edgecombe, Ma, and Strausfeld describe lab experiments that may document the earliest stages of such fossilization. They first put the heads of the marine worm *Nereis* on top of fine, seawater-soaked clay similar to the Chengjiang soil in the fossil beds. They covered the heads with a slurry of clay, topped the clay with a glass slide, and compressed it with an 80-gram weight. Over 6 weeks, they increased the weight to 240 grams. When they cracked open the dried, hardened clay a few months later, they found traces of muscle and nerve cell clusters called ganglia, indicating that soft tissue could be preserved in that kind of sediment. Next, the researchers put cockroach brains in a similar setup. After those samples dried, the flattened brains still retained recognizable segments in the right orientation (see images, p. 730).

"More and more studies are demonstrating that under exceptional circumstances, such as quick burial by fine sediments and oxygen-deprived environments, it is possible to practically halt the decomposition of carcasses," says Javier Ortega-Hernández, a paleobiologist at the University of Cambridge in the United Kingdom, who has found traces of nervous systems in fossils from both China and the Burgess Shale Formation in Canada. "I think it is pretty uncontestable that fossilized Cambrian brains are a fact."

> ***"I think it is pretty uncontestable that fossilized Cambrian brains are a fact."***
>
> **Javier Ortega-Hernández**, University of Cambridge

Detlev Arendt, an evolutionary biologist at the European Molecular Biology Laboratory in Heidelberg, Germany, agrees. His team studies brain evolution by comparing development, cells, and molecules in animals from different branches of the tree of life. They also analyze how sponges, worms, sea anemones, and other simple organisms that arose in the early days of animals control their behavior today. From such work, his team has now proposed a series of steps by which simple animals containing cells that could both sense the environment and contract to trigger move-

ment progressed to modern organisms with a brain and a nervous system made up of specialized cell types. "Detlev works in the grand tradition of coming up with a very holistic explanation of many aspects of evolution," says Graham Budd, a paleobiologist at Uppsala University in Sweden.

In the *Philosophical Transactions* special issue, Arendt's team concludes that one trigger for the nervous system's origin was the evolution of cilia and mucus around the oral opening, which enabled feeding on microbes and algae and allowed larger body sizes. In organisms equipped with such a "mouth," it was more efficient for cells to specialize for sensing or for moving and eventually, to connect into a body-wide nerve net, they propose.

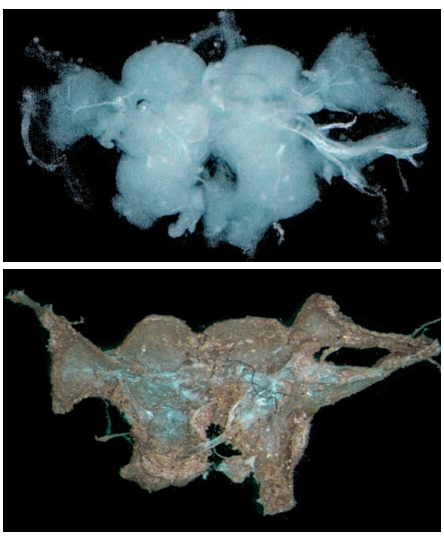

Though a fresh cockroach brain (top) gets compressed and dried out when buried in wet clay (bottom), it retains its basic structure during this analog of fossilization.

As animals developed internal digestive folds that provided more surface area for absorbing nutrients, they enlarged further and developed more elaborate behaviors. In response to the demands of seeking and capturing larger food, and eventually, hunting or eluding capture, different parts of the nerve net took over sensing, integrating, or motor functions, setting these animals on the path to having a real brain. "The brain may have been in place very, very early," Arendt concludes.

Given that there's likely to always be a dearth of fossil evidence about very ancient animals, "the kinds of inferences from comparative developmental studies such as [Arendt's] are, right now, the only speculative route back into time," Strausfeld says. But he is happy to have grounded some of the speculation in the solid rock of fossils. It was MacArthur money well spent, he notes. ■

MEDICINE

Cancer research centers pool tumor genome data

DNA registry could lead to new treatments

By **Jocelyn Kaiser**

It's the latest hope offered to many patients at cancer research centers: Let us sequence your tumor, and maybe we can match it to a drug that will beat back the malignancy. But the reality is that genomic analysis still only helps a small fraction of patients. "More often than not, we don't know what to do with the information," says Charles Sawyers, a researcher at Memorial Sloan Kettering Cancer Center (MSKCC) in New York City.

Now, several large U.S. and European academic medical centers are hoping to change that by pooling data on patients' tumor genomes and their clinical outcomes. The project, announced last week by the American Association for Cancer Research (AACR), has a mouthful of an acronym: GENIE, which stands for Genomics, Evidence, Neoplasia, Information, Exchange. It is spearheaded by Sawyers, who helped develop the leukemia drug Gleevec, one of the most successful gene-targeted therapies.

> ***"It's sort of a sociology experiment for institutional collaboration."***
>
> **Charles Sawyers**, Memorial Sloan Kettering Cancer Center

Sawyers says that GENIE grew out of conversations with colleagues at other cancer centers who are amassing tumor genetic data at a "mind-boggling" rate. "It dawned on us that despite our history of tending to be silos, we could actually benefit from a pooled data sharing operation," he says. So far, seven research centers have signed on, including MSKCC, the Dana-Farber Cancer Institute in Boston, Johns Hopkins University in Baltimore, Maryland, and three organizations in Canada and Europe. AACR has put up $2 million for a 2-year pilot stage to coordinate and store the data.

The centers tend to offer sequencing to late-stage cancer patients whose cancer has spread. Usually they aren't sequencing entire tumor genomes; instead, they sequence a set of known cancer genes, such as *BRAF*, which is often mutated in melanomas, and *EGFR*, which drives the growth of many lung tumors. But although *BRAF* and *EGFR* mutations can be targeted by drugs, often the tumor has only rare, poorly understood mutations.

In other cases, says Sawyer, a seldom-seen mutation suggests a "really interesting, tantalizing hypothesis that is being acted on" at one research center, by giving the patient a drug that had been approved for another cancer. The problem, he explains, is that "the outcomes of those independent single patient decisions aren't captured in an organized way." GENIE will share these rare treatment cases and enable researchers to draw firmer conclusions. The project could also reveal mutations that influence a patient's prognosis. GENIE will "dramatically increase" the amount of publicly available data on tumor mutations and patient outcomes, says lymphoma genomics researcher Louis Staudt of the National Cancer Institute in Bethesda, Maryland, who serves on its advisory board. "It's making use of data that was generated but not milked of all its knowledge."

Working out legal agreements with each center for securely sharing data from medical records wasn't easy, Sawyers says. GENIE's leaders also decided not to develop a standard gene panel; each center will keep using its own, sometimes custom-made set. They vary in size—MSKCC's is one of the biggest with 410 genes—but most lists overlap, Sawyers says.

Another challenge was figuring out how to give researchers who are sharing their hard-earned data a chance to publish any significant discoveries. GENIE members will get 3 months after sequencing a patient's tumor to submit the data to Sage Bionetworks, a nonprofit organization in Seattle, Washington. For the next 6 months, only the contributing institution can see that patient's record within SAGE's database. For the subsequent 6 months, it will be open to the full consortium. Finally, the patient's data will be available to the broader research community.

So far, the registry has data on 17,000 patients and aims to reach 100,000 within 5 years. And Sawyers hopes it will only grow. "It's sort of a sociology experiment for institutional collaboration," he says. ■

PHOTO: SHARON LEES

A little girl is doing well after experimental therapy, but it's too soon to say whether she's been cured.

CANCER IMMUNOTHERAPY

Baby's leukemia recedes after novel cell therapy

Gene editing used to create "off-the-shelf" T cells

By **Jennifer Couzin-Frankel**

A London baby with end-stage leukemia has received a remarkable new cancer treatment with apparent success: off-the-shelf T cells with several gene modifications. The little girl's treatment took place in June; it was announced last week by Great Ormond Street Hospital (GOSH) and is being presented at a meeting early next month. "The follow-up is short," says Carl June, an oncologist at the University of Pennsylvania who wasn't involved in the work. "But what we know is, [it] has given this kid a shot."

The announcement, by a team of physicians at GOSH and University College London, advances a frontier in cancer immunotherapy, in which the body's immune system tackles the disease. For the past several years, June and others have been modifying T cells so they can attack blood cancers, but the cells must be painstakingly isolated from the patients themselves and grown for days in a lab (*Science*, 28 June 2013, p. 1514). Drug companies and doctors dream of using off-the-shelf cells to make the therapy more like a regular drug. Now, by harnessing breakthroughs in genome editing to slice and dice genes in donor T cells, researchers have administered one of what could be many such cancer immunotherapies.

The 11-month-old girl had already run through every treatment. Her immune system was barely functioning, and oncologists couldn't collect T cells from her for personalized therapy. Her parents "were being told, 'We haven't really got anything,'" says Waseem Qasim, a consultant in pediatric immunology at GOSH and cell therapy professor at University College London, who led the work. But GOSH's freezers held a potential solution. The hospital was storing genetically modified T cells belonging to a company in Paris called Cellectis. The cells, from a healthy American donor, had DNA added and two genes erased. Final testing was not complete, but the doctors asked that a vial be given to the child. "This was not even a question," says André Choulika, Cellectis's CEO. The company quickly signed off, as did the parents and the requisite ethicists.

The Cellectis cells had been genetically engineered to avoid two major pitfalls. If transplanted intact, the T cells would act like an invading army, attacking the body while the body attacked them right back. In order to block that reaction, scientists used a gene-editing technique called transcription activatorlike effector nucleases (TALENs) to cut out the T cell receptor gene. Without it, the cells can't recognize the recipient's body as foreign. The cells were also designed to survive the intense therapy the girl was receiving: an antibody called Campath, intended to protect the donor T cells from attack by wiping out the child's own immune system. Campath targets an immune-cell marker called *CD52*, so the company used TALENs to remove *CD52* from its donor cells—ensuring that Campath wouldn't attack them, too. Finally, just as doctors have done with a patient's own T cells, the researchers made DNA modifications to the foreign cells so they would home in on leukemia.

Within a few weeks the child's condition improved. After about 3 months she received a bone marrow transplant, considered a more established long-term treatment, and she's now doing well. Although doctors, including Qasim, agree it's too soon to say she's been cured, they are hopeful. "I'm very enthusiastic about this," says Terry Fry, a pediatric oncologist at the National Cancer Institute in Bethesda, Maryland. He's especially excited because the therapy cleared what he describes as "hurdle one"—the T cells didn't attack the patient, which can cause life-threatening complications.

The next question, Fry says, is how long the cells can survive in the body and fight cancer. "The persistence is hurdle two," he says, and it's something he and others are keen to learn more about. June expects that hurdle will be much harder for the cells to overcome. "I think in the end they will get rejected," he says, but an off-the-shelf therapy could still be transformative. "I'm very bullish that they'll be useful in desperate situations like this, where there isn't time," or it's not possible, to use a patient's own T cells. In a trial slated for next year, June and his colleagues hope to offer cells with three genes sliced out via another editing technology, the popular CRISPR, with the leukemia-busting DNA added in.

"You can totally tune up the genome of the T cells to make it a sharp, cancer-killing machine," Choulika says. But with innovation comes uncertainty. "We're going to need better analysis" of these cells with multiple gene edits, says Michael Jensen, a pediatric oncologist at Seattle Children's hospital in Washington, who has run trials of modified T cell therapy. "As we get into more sophisticated engineering, we have to understand the safety parameters." For now, he and others are hoping that one case will open the door to more, for patients with no other options. ■

NOT GUILTY AS CHARGED

Several cases have unraveled lately against Chinese-born scientists accused of sharing industrial secrets. Critics smell a witch-hunt

By **Mara Hvistendahl**

Just after dawn on 21 May, physicist Xiaoxing Xi awoke to find a dozen or so armed federal agents swarming his home in the Philadelphia, Pennsylvania, suburbs. When he rushed to open the door, they drew their guns and announced that they had a warrant for his arrest. His wife and daughters—one in middle school and the other in college—watched in horror as agents handcuffed Xi, who was still not fully dressed, and escorted him away.

Then interim chair of the physics department at Temple University in Philadelphia, Xi is a naturalized U.S. citizen who has lived and worked in the United States since 1989. He is among the world's leading experts on superconducting thin films, which carry electricity without resistance at very low temperatures. At the time of his arrest, he was in what he calls a "very productive" phase of his career, overseeing nine research projects, including work for Temple's Energy Frontier Research Center, which is funded by the Department of Energy. But now he stood charged with trying to transfer designs for a proprietary technology to China—a device called a pocket heater, produced by Superconductor Technologies Inc. (STI) of Austin, that makes thin films of the superconductor magnesium diboride—and faced 80 years in prison and a $1 million fine.

Xi was released after putting up his home as bail, but his passport was confiscated and his domestic travel restricted to eastern Pennsylvania. For days, his family avoided the windows in their home as television stations broadcast live from their front yard.

PHOTO: MARK MAKELA FOR *THE NEW YORK TIMES*

Superconductor physicist Xiaoxing Xi was accused of attempting to share proprietary technology with China—only to watch the investigation against him unravel.

Over the months that followed, they drained their bank accounts to pay legal fees.

Citing a nondisclosure agreement Xi had signed in 2006 in order to conduct research with a pocket heater, the U.S. attorney's office in Philadelphia, Pennsylvania, had charged him with four counts of wire fraud, for four emails sent to contacts in China about establishing labs and a collaboration involving a thin film deposition device. But on 11 September, before a trial date had been set, the U.S. attorney's office abruptly dropped the charges, noting that "additional information came to the attention of the government." A spokesperson for the office declined to comment further on the case.

At issue, Xi's lawyer and scientists familiar with the case assert: a glaring misinterpretation of the science involved. The devices Xi had discussed with Chinese colleagues were not the pocket heater, they say, and the exchanges posed no threat to U.S. interests. "The whole case against Xiaoxing Xi was just completely misconceived," asserts David Larbalestier, a physicist at Florida State University, Tallahassee, who submitted an affidavit for the defense.

The Obama administration names economic espionage and trade secrets theft as among the primary threats facing the United States. Together with cybercrime, economic espionage is now the Federal Bureau of Investigation's (FBI's) No. 3 priority, after terrorism and counterintelligence. According to testimony by Randall Coleman, assistant director of the FBI counterintelligence division, the number of cases overseen by the bureau's dedicated unit grew by 60% from 2009 to 2013.

Many of those cases involve China. In July, the FBI launched an ambitious public awareness campaign around the issue, releasing a dramatic film depicting a Chinese company attempting to steal trade secrets from a U.S. competitor. In September, economic espionage and cyber espionage were forefront at the meeting between President Obama and Chinese President Xi Jinping, with the two leaders vowing in a landmark agreement not to target each other's companies.

Yet a growing number of scientists have been targeted improperly as Department of Justice (DOJ) attorneys have stepped up prosecutions, advocates say. In the past year alone, charges have been dropped against five Chinese-born scientists accused of crimes related to trade secrets theft or economic spying. A sixth defendant, a New York University (NYU) medical imaging researcher accused of passing confidential information about NYU research into magnetic resonance imaging technology to a company in China, pleaded guilty to a single misdemeanor last March. In several instances, critics say, the U.S. government has charged scientists without understanding the science at the heart of its allegations.

Xi's case is emblematic. Court documents state that "the government seized extensive electronic evidence and searched multiple hard drives" in the process of investigating him. But the prosecutors apparently did not consult technical experts before issuing the indictment, says Nelson Dong, a former DOJ official and an attorney with Dorsey & Whitney in Seattle, Washington, who was not involved in Xi's case. "That suggests to me that people really did rush to judgment," Dong says. "They saw red, so to speak."

The prosecutions have spooked many Chinese-American scientists, who fear that any collaboration with Chinese nationals will invite suspicion. Invoking the botched investigation of Los Alamos National Laboratory physicist Wen Ho Lee more than a decade ago, advocacy groups are lobbying the U.S. government for explanations. Last May, following the sudden dismissal of charges against National Weather Service (NWS) hydrologist Xiafen (Sherry) Chen, who was accused of passing information about the nation's dams to a Chinese official, 22 members of Congress signed a letter to U.S. Attorney General Loretta Lynch requesting an investigation into whether federal employees are being racially targeted. The office responded in a letter that "no policy exists of using race or any other civil rights classification" to single out federal employees for arrest or scrutiny. The attorney general's office did not reply to interview requests.

The targeting of innocent scientists is "a constitutional and civil rights problem," said Representative Ted Lieu (D–CA), one of the letter's signatories, in a statement on 14 September. Xi's crime, according to one legal blog: "Emailing while Chinese-American."

THE THEFT OF SCIENTIFIC SECRETS is nearly as old as science itself. Centuries ago, for example, a young United States depended greatly on know-how spirited out of the United Kingdom, showering accolades on those who swiped designs for U.K. textile machinery. Imperial China was a frequent victim as well, with Western powers stealing its methods of porcelain and tea production. But some argue that the past few decades have marked the dawn of a new era, with everything from sensitive military technology to lucrative agricultural secrets now prized spoils.

> ***"Get the science right before you put these people through the wringer."***
>
> **Brian Sun**, lawyer at Jones Day

"As the world becomes more advanced, technology just becomes worth more," says Peter Toren, a former federal prosecutor and a litigator with Weisbrod Matteis & Copley in Washington, D.C., who specializes in trade secrets cases. "Developing countries and companies in developing countries can save hundreds of millions of dollars in research costs by stealing new technology."

Developing countries are hardly the only perpetrators. In a secret report leaked by Edward Snowden, the U.S. National Security Agency outlined possible scenarios for cyber operations against foreign research centers, with the aim to capture knowledge that "would be useful to U.S. industry." And as late as the 1990s, Toren says, France and Israel were among the world's most prominent industrial spies.

But the U.S. government now sees China as the major foreign threat. Close to half of

the indictments brought under the Economic Espionage Act since its passage in 1996 have involved China, Toren says.

In some cases, U.S. prosecutors have assembled reams of evidence. In 2010, Boeing engineer Dongfan Chung—a naturalized U.S. citizen who was born in China and grew up in Taiwan—was sentenced to 16 years in prison for stealing trade secrets connected to the U.S. Space Shuttle program and Delta IV rocket on behalf of mainland China. When agents raided Chung's home, they found more than 250,000 sensitive documents from defense contractors, some of them hidden in crawl spaces under the house. The FBI alleged that documents in the stash showed Chung was acting at the direction of China's Civil Aviation Administration.

Another successful prosecution came last year, when entrepreneur Walter Lian-Heen Liew was sentenced to 15 years in prison for conspiring to steal trade secrets related to titanium dioxide production from DuPont and sell them to state-owned companies in China. (Former DuPont engineer Robert Maegerle was also convicted in the case.)

But a startling number of cases have unraveled. Last December, the U.S. government dropped charges against two former Eli Lilly and Company scientists in Indiana. The U.S. attorney's office in Indianapolis had alleged that Guoqing Cao and Shuyu Li, both naturalized U.S. citizens and senior biologists at Eli Lilly, passed research on tailored therapies for cancer and drugs to treat diabetes, obesity, and other metabolic disorders to Jiangsu Hengrui Medicine, a company in Lianyungang, China.

The case invited heated rhetoric, with a government prosecutor labeling the defendants traitors in an early bail hearing and the defense in its filings invoking the 1954 anticommunist Senate hearings convened by then-Senator Joseph McCarthy. From October 2013 to November 2014, the two scientists were variously jailed, locked down in a halfway house, and kept in round-the-clock home detention.

Yet case documents submitted by Cao's attorneys claim that the trade secrets he allegedly stole had all appeared in published papers years earlier, and that the information did not include drug molecules, formulae, or data owned by Eli Lilly. In December 2014, several weeks after a judge agreed to release the researchers, the U.S. attorney's office dropped the charges entirely, citing only its "on-going evaluation and assessment of this case." A spokesperson for the U.S. attorney's office in Indianapolis declined to comment further.

Then, last March, the U.S. government dropped charges against Chen, the NWS hydrologist. Peter Zeidenberg, a partner at Arent Fox in Washington, D.C., who represents both Chen and Xi, says that she merely sent a Chinese official—a former classmate whom she contacted as a favor to her nephew—links to publicly available websites, including www.noaa.gov. The official was tasked with planning repairs for China's reservoirs and had asked Chen how such repairs were funded in the United States. Chen then referred the official to a division head at the Army Corps of Engineers with whom she had worked on projects in the past, Zeidenberg says. "Why would she be giving her contact in China the phone number of her boss and say, 'Call her if you have any further questions?' It was absurd," he says. The National Oceanic and Atmospheric Administration declined to comment on the case, citing an ongoing internal review.

XI, NOW 57, was born in Beijing and came of age during the Cultural Revolution. As a teenager, he was sent to the countryside, where he spent several years working in the fields and shoveling pig manure. After the Cultural Revolution ended in 1976, Xi won admission to Peking University in Beijing. He went on to earn a Ph.D. before leaving for the United States in 1989. In 1995 he joined the faculty at Pennsylvania State University, University Park, where his wife, physicist Qi Li, still teaches.

Before the agents pounded on his door and turned his life upside down, Xi oversaw a team of 10 graduate students, one undergraduate, three postdocs, and two non–tenure-track faculty at Temple and received more than a million dollars a year in research funding. The group had just obtained what Xi calls "breakthrough results" on two topics that they planned to submit to *Science* and *Nature*. Xi "is among the best thin-film physicists around," says physicist Paul Chu of the University of Houston in Texas, who sub-

Prosecutors' patchy record

The United States has ramped up prosecutions against Chinese-American scientists for espionage and trade secrets violations. But key cases have fallen apart.

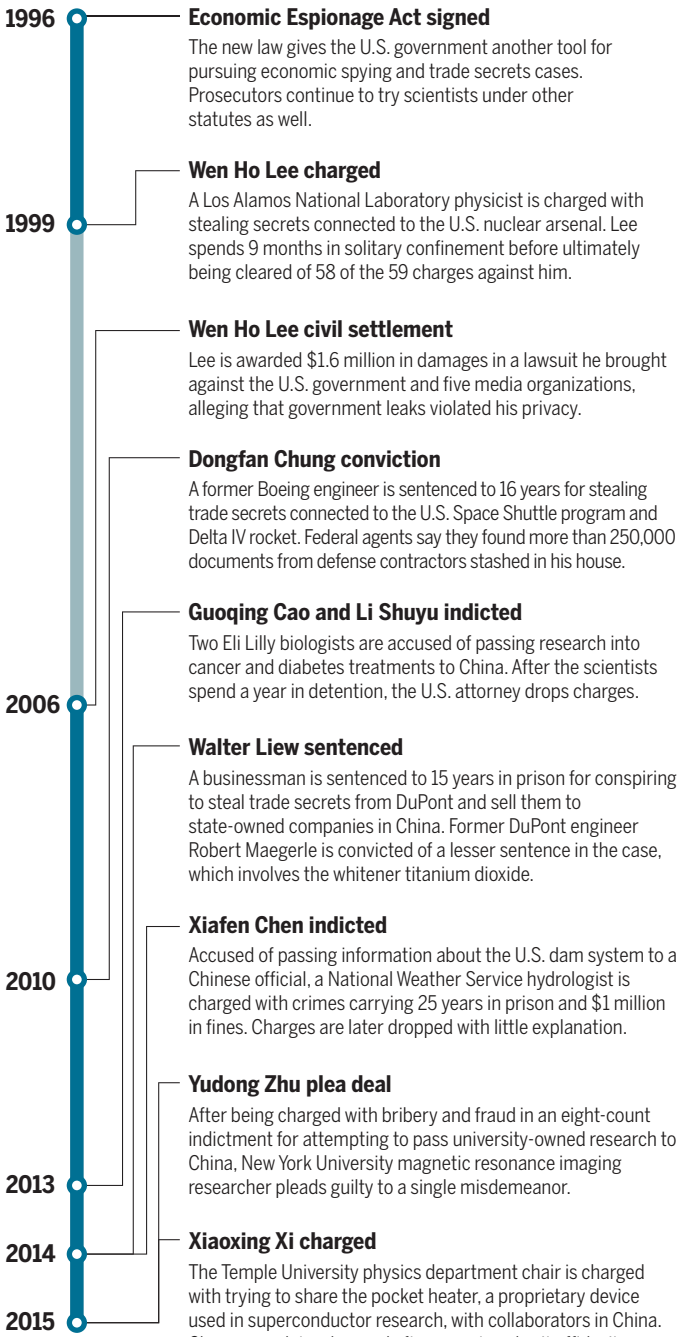

GRAPHIC: A. CUADRA/*SCIENCE*

mitted an affidavit in his defense. After the indictment, Temple placed Xi on administrative leave. Xi says university counsel also advised him not to appear on campus. Temple spokesperson Ray Betzner could not immediately confirm whether this was true.

According to affidavits submitted in the case, the allegations center on Xi's collaboration with two institutes in China, the Shanghai Institute of Applied Physics and Peking University. The indictment alleged that Xi "repeatedly reproduced, sold, transferred, distributed, and otherwise shared" the STI pocket heater with these institutions and then pursued "lucrative and prestigious appointments" in exchange for his assistance. Zeidenberg says Xi never profited financially from the interactions highlighted by the U.S. government.

Rather than the pocket heater, say superconductivity researchers who reviewed emails and other case documents, Xi discussed two distinct magnesium diboride heaters—one of which he invented himself and the other based on his invention—that are fundamentally different from the STI device. The labs he offered to help establish, meanwhile, would have focused on an entirely different line of research—oxide thin films—and thus would not have involved research with the pocket heater or another magnesium diboride heater.

The investigation's premise is off base, Larbalestier told *Science*: "The whole idea that there are huge pots of money that anybody is making out of magnesium diboride is just wrong." The compound, he says, is still in development as a superconducting material, and commercialization is "a decade or 2 decades away." And as John Rowell of Arizona State University, Tempe, wrote in an affidavit, the STI pocket heater, itself a modification of an existing technology invented in Germany in 1993, "is in no sense a revolutionary device."

Others say the case was based on a misreading of the scientific partnerships and teaching exchanges that have flowered since China began aggressively investing in research in the 1990s. Xi's offer to help Chinese colleagues build a world-class lab is a common gesture in international collaborations on superconductivity, which is highly developed in China, Chu says. "Ninety percent of scientists involved in this kind of international exchange" could fit the description of Xi's activities in China, he says.

"I am mystified as to why the case was brought," Larbalestier says.

CRITICS of the Justice Department's prosecutions say the government risks repeating the mistakes made in the case against Wen Ho Lee, who was charged with stealing secrets connected to the U.S. nuclear arsenal in 1999. Lee spent 9 months in solitary confinement as the case against him deteriorated. Though he ultimately pleaded guilty to one felony count of mishandling secrets, the U.S. government was never able to prove that he had conducted espionage. James Parker, the judge in the case, apologized to Lee for the "demeaning, unnecessarily punitive conditions" in which he was detained and denounced cabinet officials for having "embarrassed our entire nation and each of us who is a citizen of it."

Protesters demonstrate against the 1999 detention of physicist Wen Ho Lee, who was charged with stealing secrets connected to the U.S. nuclear arsenal.

"Yes, America has a legitimate concern about cyber hacking and trade secrets theft," says Brian Sun, a trial lawyer with Jones Day in Los Angeles, California, who represented Lee in a successful civil suit against the U.S. government. "But … do your homework. Get the science right before you put these people through the wringer."

Although the charges were dismissed, Xi says that coming in the U.S. government's cross hairs damaged his career. Before his tribulations began, he had been asked to co-author a chapter for a prestigious handbook on superconductors. After the news broke, he says, several co-authors threatened to pull out if he was kept on the project. Although his team continued its research, with other scientists assuming the principal investigator roles he had held, the lab lost critical time on projects funded by grants due for renewal. Eventually, Xi says, his department arranged for him to talk to senior colleagues via teleconferencing, but because he was forbidden to talk to potential witnesses, he did not communicate with his students. Adrift at home for 4 months, he devoted much of his time to his case.

The string of cases has Chinese-American scientists scrambling to understand how they might avoid being targeted. The Committee of 100, a group of influential Chinese-Americans whose membership includes former NASA astronaut Leroy Chiao and David Ho, scientific director of the Aaron Diamond AIDS Research Center in New York City, has held seminars across the country for scientists outlining the laws governing trade secrets theft and export controls on critical technologies and explaining how to avoid inviting suspicion. Scientists involved in collaborations with China or Chinese colleagues "need to assume that their communications are being scrutinized" and "be clear and precise about what they're communicating," Zeidenberg cautions. "There's an assumption that any collaboration is suspect and potentially problematic."

"We need a set of well-defined rules," says Albert Chang, a physicist at Duke University in Durham, North Carolina, and the president of the International Organization of Chinese Physicists and Astronomers. "The indictments have instilled a great deal of uncertainty and anxiety in our community. People are wondering, 'Is this going to happen to me?'" The Committee of 100 and others are pressing the U.S. government for more clarity.

Xi is now back in the lab. On 20 October, Michael Klein, dean of Temple's College of Science and Technology, sent a memo to the physics department welcoming him back as interim chair. But he worries about obtaining research funding, regaining colleagues' trust, and attracting collaborators: "My reputation obviously has been damaged by this," he says. "If this happened to somebody else, I would think that they probably did do some little thing wrong, at least." The ordeal has made him apprehensive about even the most basic of interactions. "I was charged for things that were just normal collaborations," he says. "If all these normal activities could be seen as criminal activities, then the environment is quite frightening." ■

PHOTO: AP PHOTO/BEN MARGOT

INSIGHTS

Snapshots of charge on the move *p. 740*

A gut-vascular barrier *p. 742* ▸

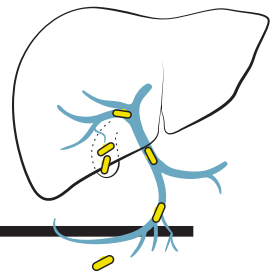

PERSPECTIVES

EVOLUTION

One era you are in—the next you are out

Evolutionary trends in body size changed during a past mass extinction event

By **Peter J. Wagner**

Trends in body size are a rich source of information for evolutionary studies. This is because body size not only has numerous implications for function and life history but also has necessary limits that differ between groups of organisms. Moreover, there are many evolutionary patterns that might underlie trends, and these patterns need not be constant over time. On page 812 of this issue, Sallan and Galimberti (*1*) show that trends in the body sizes of vertebrates during the Devonian and Mississippian (about 420 to 325 million years ago) not only are markedly different at different times but also likely reflect a variety of different evolutionary mechanisms.

The Devonian shows a distinct trend toward larger vertebrates. This sort of trend often reflects a passive trend (*2*) (see the figure, panel A), where clades beginning near some limit (here, nearly as small as they can be) simply add variation in one direction (here, larger animals). However, Sallan and Galimberti present multiple lines of evidence that this reflects an active trend, where the new condition replaces rather than augments the existing condition (see the figure, panels B to D). In particular, their results suggest that driven trends (*3*), where descendants tend to be larger than their ances-

Department of Paleobiology, National Museum of Natural History, Smithsonian Institution, Washington, DC 20560, USA. E-mail: wagnerpj@si.edu

Ancient sealife. Relatives of modern sharks and reef fishes that lived during the Mississippian (about 360 to 325 million years ago) reached sizes of up to 50 cm.

ILLUSTRATION: BOB NICHOLLS

Published by AAAS

tors (see the figure, panel B), predominate. Strong active trends toward increasing size are seen not just for all vertebrates but for five of the seven major taxonomic groups; one of the two exceptions (tetrapods) simply started out large.

Breaking the trends down into finer taxonomic partitions reveals more heterogeneity. The clades showing no real trend tend to be those that begin fairly large, whereas most clades that start small show increases in size. This "subclade test" strongly suggests driven trends among a wide range of different vertebrates (*3*).

The end-Devonian mass extinction (~375 to 360 million years ago) reverses these trends. Three of the five surviving clades show marked decreases in body size. This indicates that selective extinction, at odds with prior selective forces (*4*), induces a new trend (see the figure, panel D). Devonian trends do not just fail to resume in the Mississippian; they are reversed, with a trend toward smaller size. However, whereas the Devonian trends include many groups, the Mississippian trends reflect two vertebrate groups. Chondrichthyans (elasmobranchs and holocephalans, the precursors of extant sharks and rays) are the only major group that shows evidence of driven trends toward smaller-bodied animals. Moreover, chondrichthyans also diversify in the Mississippian. Actinopterygians (bony fish) also increase greatly in diversity, but, unlike chondrichthyans, they begin small and remain small throughout the Mississippian. Thus, the trend is partially caused by small species leaving more (generally small) descendants rather than descendants typically being smaller than their ancestors. This might reflect higher speciation rates for small species (*5*), or small size "hitchhiking" along with elevated diversification happening for other reasons (*6*). Thus, selective extinction and differential diversification of actinopterygians (see the figure, panels C and D) plus driven trends and differential diversification of chondrichthyans (see the figure, panels B and C) drive the overall trend, with other vertebrates being mere onlookers.

As Sallan and Galimberti stress, there are no obvious correlations with extrinsic variables frequently linked to body size. Long-term trends toward cooler global temperature began after the polyphyletic trend toward increasing size but before that trend ceased. Similarly, there is no obvious association between the trends and atmospheric oxygen levels. Sampling controls (*7*) mean that preservational biases against finding small vertebrates in the Late Devonian or large vertebrates in the Mississippian cannot account for the pattern. Instead, Sallan and Galimberti suggest that size trends reflect trends in life-history traits, such as generation time, that are correlated with size. Thus, the distinction between sorting and selection (*8*) becomes important: The trends we see in a fossilizable trait (size) represent sorting of that trait based on selection for an associated unfossilizable trait (life history). Thus, the true role of size might be akin to the "stars" versus "no stars" in panel C in the figure: a trait that is largely (but not entirely) tied to another trait by functional or developmental association (or even simply because of common ancestry) (*7*) and that "hitchhikes" along the main trend.

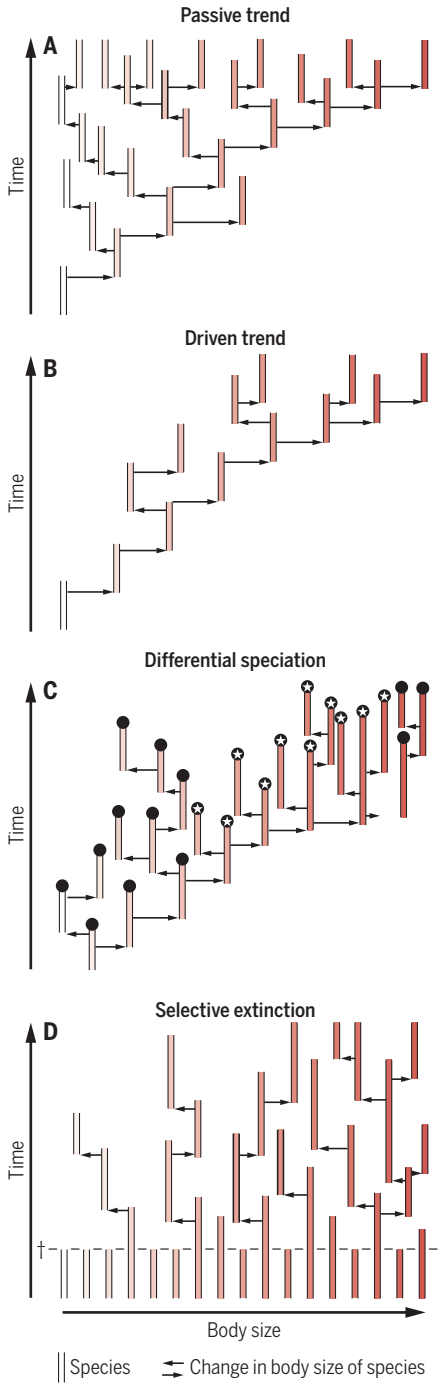

Evolutionary trends. Different trends might underlie Devonian-Mississippian vertebrate evolution. Light colors denote small and dark colors, large body sizes. (**A**) In a passive trend, small species cannot become much smaller, but they can become much bigger (*2*). (B) In a driven trend, size increases are more common than size decreases (*3*). (**C**) Differential speciation means that large species live longer and/or have higher speciation rates (*4*). The stars/not-stars illustrate a hitchhiking trend in which differential speciation/extinction induces trends in other characters (*6*). (**D**) In the case of selective extinction, an extinction event (dashed line) inducing an immediate trend toward smaller taxa despite signs of the opposite trend before the event (*5*). [Figure adapted from (*6*)]

In addition to offering a model for different types of trends, Sallan and Galimberti's work offers two important lessons for research concerning extant taxa. The first is the importance of sampling taxa over time. Suppose a time traveler deposited molecular phylogeneticists in the Mississippian and set them with the task of reconstructing the history of body size among (then) extant vertebrates. Shifting trends make reconstructing ancestral conditions extremely difficult without fossil data (*9*–*11*). Moreover, inferring diversity lost to extinction is generally very difficult given phylogenies of species from just one point in time (*12*). Without fossils, we cannot expect to see indications of when evolutionary parameters themselves changed. Indeed, it goes beyond stating that we need fossils to properly appreciate evolution among extant taxa: We need Devonian fossils to properly appreciate the evolution of subsequent Mississippian taxa.

The second lesson concerns current extinctions. Extinctions in the Late Pleistocene (~126,000 to 12,000 years ago) have preferentially eliminated large mammals (*13*). Large mammals have evolved many times, so it might seem that we should expect them to reevolve in the future. The differences between trends in the Devonian and Mississippian show that we cannot count on the trends of the past being the trends of the future. Thus, if conserving ecological and functional diversity is a priority as well as conserving phylogenetic diversity, then we cannot assume that large animals will quickly reevolve in the future. ■

REFERENCES

1. L. Sallan, A. K. Galimberti, *Science* **350**, 812 (2015).
2. S. J. Gould, *J. Paleont.* **62**, 319 (1988).
3. D. W. McShea, *Evolution* **48**, 1747 (1994).
4. D. Jablonski, *Science* **231**, 129 (1986).
5. S. M. Stanley, *Proc. Natl. Acad. Sci. U.S.A.* **276**, 56 (1975).
6. P. J. Wagner, *Evolution* **50**, 990 (1996).
7. D. J. Bottjer, D. Jablonski, *Palaios* **3**, 540 (1988).
8. E. S. Vrba, S. J. Gould, *Paleobiology* **12**, 217 (1986).
9. J. A. Finarelli, A. Goswami, *Evolution* **67**, 3678 (2013).
10. J. A. Finarelli, J. J. Flynn, *Syst. Biol.* **55**, 301 (2006).
11. G. J. Slater, *Methods Ecol. Evol.* **4**, 734 (2013).
12. L. H. Liow *et al.*, *Syst. Biol.* **59**, 646 (2010).
13. S. K. Lyons *et al.*, *Evol. Ecol. Res.* **6**, 339 (2004).

10.1126/science.aad6283

ILLUSTRATION: P. HUEY/*SCIENCE*

ARTIFICIAL PHOTOSYNTHESIS

More efficient together

Hybrid bioinorganic photosynthesis yields a wide range of chemicals

By **Tian Zhang**

The solar-to-biomass conversion efficiency of natural photosynthesis is between 2.9 and 4.3% for most crops (*1*, *2*). Improving the efficiency of photosynthesis could help increase the appeal of biologically derived fuels and chemicals in comparison with traditional petrochemical processes. One approach to make photosynthesis more efficient is to build hybrid systems that combine inorganic and microbial components to produce specific chemicals. Such hybrid bioinorganic systems lead to improved efficiency and specificity and do not require processed vegetable biomass. They thus prevent harmful competition between biotechnology and the food industry and avoid the environmental perturbation caused by intensive agriculture (*3*).

Durable artificial photosynthetic apparatuses that are completely inorganic have been developed for the production of simple chemicals such as carbon monoxide, methane, and methanol (*4*–*6*). Alternatively, the artificial photosynthesis apparatus can be a bioinorganic hybrid that contains a microbial catalyst (see the figure, panel A). Yang and co-workers have recently reported the use of this type of system for the production not only of simple compounds like methane but also of multicarbon chemicals including acetate, *n*-butanol, polyhydroxybutyrate polymer, and isoprenoids (*7*, *8*). This greater repertoire of products is possible because bioinorganic hybrid artificial photosynthesis can take advantage of the opportunities created by synthetic biology and by the metabolic plasticity of microbial cells.

In a bioinorganic artificial photosynthesis apparatus, an inorganic photoanode and photocathode harvest solar energy to split water into molecular oxygen (O_2), protons, and electrons and generate reducing equivalents that will be used by a microbial catalyst to reduce carbon dioxide (CO_2). In the first of their two studies, Yang and co-workers coupled a TiO_2/Si photoanode with a photocathode in which the acetogen *Sporomusa ovata* was grown directly within a silicone nanowire array (*7*). In this system, *S. ovata* accepts electrons directly from the photocathode (*8*) to reduce CO_2 to acetate. The latter was activated to acetyl–coenzyme A in a second reactor by genetically engineered *Escherichia coli* before being converted into various multicarbon products. In their second study (*9*), they combined a *n*-TiO_2–based photoanode oxidizing water with a *p*-Inp/Pt photocathode to generate H_2 that is then used by the methanogen *Methanosarcina barkerii* for converting CO_2 to methane.

In the apparatus described in (*7*), the conversion efficiency of solar energy to acetate was 0.38% over a period of 200 hours. Because of their relative simplicity compared to natural photosynthesis, artificial photosynthesis systems should be easier to improve. A rational strategy for identifying the best combination of components can readily be established. This would include engineering optimal microbial catalysts, determining the best culture-medium composition and reactor design, and improving photocathode and photoanode for higher conversion efficiency of solar energy into reducing equivalents (*2*).

Bioinorganic artificial photosynthesis can also be achieved by using a photovoltaic (PV) cell to convert solar energy into electricity, which is then used to power a separate microbial electrosynthesis (MES) reactor (*10*) (see the figure, panel B). This approach is different from that described by Yang and co-workers (*7*, *8*) because light harvesting is carried in a compartment separated from the MES reactor where electrons are delivered to the microbial catalyst. This strategy allows the use of PV cells exclusively dedicated to light harvesting, without having to consider their compatibility with living cells.

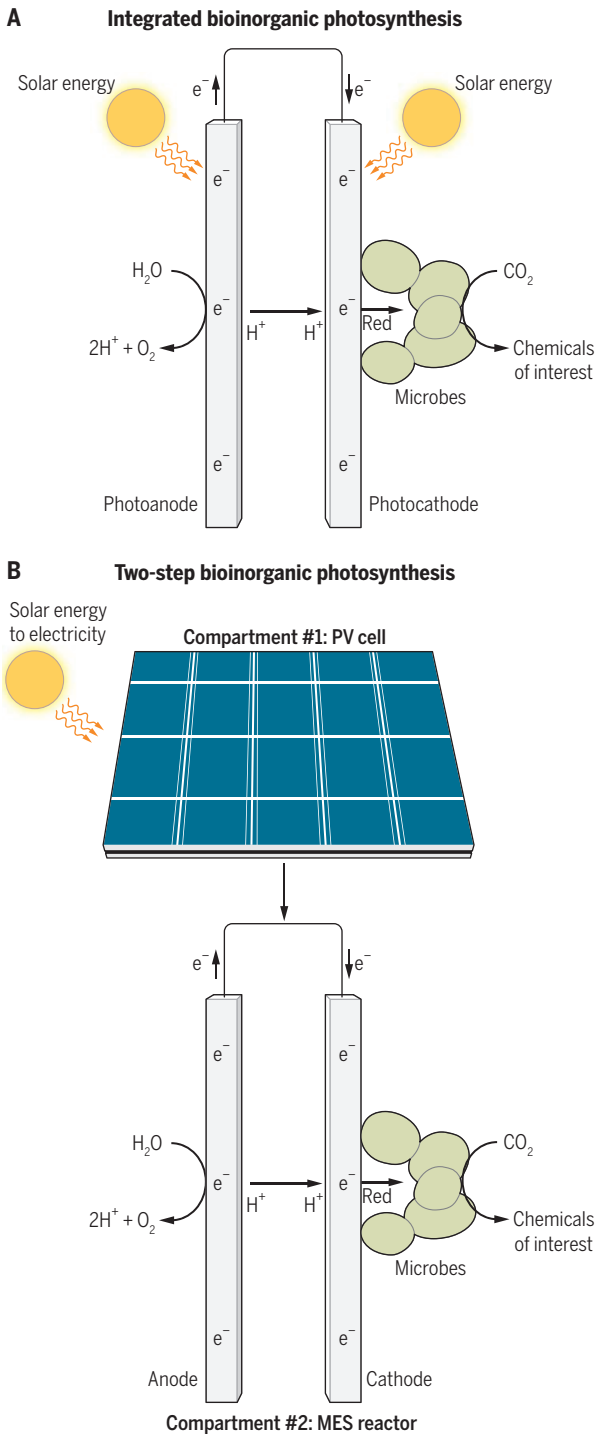

Bioinorganic artificial photosynthesis. (**A**) Integrated bioinorganic artificial photosynthesis apparatus. A photoanode and photocathode are combined in the same reactor to convert solar energy into reducing equivalents (red) that are used by the microbial catalyst to transform the greenhouse gas CO_2 into useful products. (**B**) PV cell coupled with an MES reactor. PV cell can power an MES reactor for the formation of reducing equivalents that are used by the microbial catalyst for CO_2 reduction.

Novo Nordisk Foundation Center for Biosustainability, Technical University of Denmark, 2970 Hørsholm, Denmark. E-mail: zhang@biosustain.dtu.dk

In its most basic form, an MES system consists of an inorganic anode that oxidizes water and a cathode that delivers reducing equivalents to an autotrophic microbial catalyst. MES has been improved in the past 5 years to achieve high electron recovery into chemicals and high production rates from CO_2 (*11*).

Furthermore, MES production is not limited to acetate; MES systems have been used for the electrosynthesis of longer carboxylic acids, acetone, and alcohols (*10*, *12*). With current technology, connecting an acetate-producing MES system to a commercially available PV cell with a solar-to-electrical efficiency of 20% should result in an artificial photosynthesis apparatus capable of converting about 10% of the solar energy into acetate (*13*). More efficient PV cells and MES systems could push the efficiency of artificial photosynthesis into a range where industrial applications become possible.

The efficiency of bioinorganic hybrid artificial photosynthesis for converting solar energy to chemicals has the potential to go well beyond 11 to 12%, the theoretical maximum solar energy–to–biomass conversion efficiency of natural photosynthesis (*14*). Recent advances clearly illustrate that this approach could, in a relatively short time, significantly improve the sustainability of the chemical and energy industries. Hybrid bioinorganic photosynthesis could bring multiple benefits to society by recycling the greenhouse gas CO_2 into useful products with energy from the Sun while avoiding conflicts with food production. ■

"...this approach could... significantly improve the sustainability of the chemical and energy industries."

REFERENCES

1. R. E. Blankenship *et al.*, *Science* **332**, 805 (2011).
2. J. P. Torella *et al.*, *Proc. Natl. Acad. Sci. U.S.A.* **112**, 2337 (2015).
3. D. R. Lovley, K. P. Nevin, *Curr. Opin. Biotechnol.* **24**, 385 (2013).
4. P. G. O'Brien, *Adv. Sci.* **1**, 1400001 (2014).
5. H. Liu *et al.*, *Angew. Chem. Int. Ed.* **54**, 11545 (2015).
6. X. Meng *et al.*, *Angew. Chem. Int. Ed. Engl.* **53**, 11478 (2014).
7. C. Liu *et al.*, *Nano Lett.* **15**, 3634 (2015).
8. K. P. Nevin, T. L. Woodard, A. E. Franks, Z. M. Summers, D. R. Lovley, *mBio*. **1**, e00103-10 (2010).
9. E. M. Nichols *et al.*, *Proc. Natl. Acad. Sci. U.S.A.* **112**, 11461 (2015).
10. P.-L. Tremblay, T. Zhang, *Front. Microbiol.* **6**, 201 (2015).
11. L. Jourdin *et al.*, *J. Mater. Chem. A.* **2**, 13093 (2014).
12. H. Li *et al.*, *Science*. **335**, 1596 (2012).
13. H.-R. Jhonget al., *Curr. Opin. Chem. Eng.* **2**, 191 (2013).
14. D. Parlevliet, N. R. Moheimani, *Aquat. Biosyst.* **10**, 4 (2014).

10.1126/science.aad6452

HISTORY OF SCIENCE

Flow cytometry strikes gold

Flow cytometry remains unparalleled as a high-throughput, high-content single-cell analysis technology

By **J. Paul Robinson**[1] *and* **Mario Roederer**[2]

This month marks the 50th anniversary of the birth of flow cytometry. One would imagine that a technology invented so long ago would be radically different today—yet it has changed remarkably little in its fundamentals. It allows rapid and simultaneous analysis of multiple parameters of live cells in a heterogeneous mix as they flow in a stream through photonic detectors. The data are integrated to give a comprehensive view of the sample. Flow cytometry has become a staple of biological research as well as clinical diagnostics, and its application has been crucial to innumerable advances in immunology and cell biology, and for understanding diseases such as AIDS and cancer. It has spawned the development of dozens of other key technologies and its application continues to expand, ranging from single-cell to cell population analysis.

Flow cytometry was created when an electrical engineer, Mack Fulwyler, disputed the idea that there were two populations of red blood cells. He challenged Clarence Lushbaugh, a pathologist, that using a Coulter Counter—an instrument used to count and size suspended particles—to identify a bimodal population of red blood cells was technically incorrect. However, the only way to disprove the theory was to build an instrument that could physically separate single cells based on population analysis. Thus, the cell sorter and flow cytometry were born. Fulwyler conceived of the idea in 1964 when he wrote to Richard Sweet, the inventor of the technology behind ink jet printers. Within 10 months, the collaborators conceived, designed, built, and successfully tested a cell sorter, leading to the seminal publication in 1965 (*1*) (see the figure). So new was the concept that there was little to cite: The paper had merely five references.

Only 4 years later, the technology would make a major advance. Geneticist Leonard Herzenberg instantly recognized the power of cell sorting (*2*). Combined with Wolfgang Göhde's demonstration of microscope-based flow cytometry to measure cell-associated fluorescence (*3*), the field of cell analysis transformed. Shortly thereafter, Herzenberg was on sabbatical in the laboratory of the biochemist César Milstein at Cambridge University, when Milstein and Georges Köhler invented the Nobel Prize–winning monoclonal antibody technology. Herzenberg understood that these new, specific antibodies could be tagged with fluorescent dyes to selectively label cells in a heterogeneous mix. His laboratory quickly developed dozens of monoclonal antibodies that distinguished subsets of white blood cells, forging a dictionary of immune cell types. Flow cytometry not only allowed multiparameter data to be collected, but cells to be viably sorted into different populations at the same time—and became the so-called "fluorescence-activated cell sorting" (FACS) (*4*).

Flow cytometry entered the field of molecular biology in the mid-1970s when geneticist Joseph Gray developed flow karyotyping techniques that could assess the number and appearance of chromosomes in only 2 min (instead of hours) (*5*), and sort single chromosomes as well. The technology also expanded to the study of DNA and RNA content, and into studies of cell division cycle analysis and programmed cell death (apoptosis), emerging fields at the time.

The continuing drive for higher-content analysis prompted the development of fluorescent dyes such as Texas Red (and later, the Alexa dyes) and cyanine dyes, creating a reagent market that now exceeds $1 billion annually. The advent of inexpensive violet lasers (a byproduct of low-cost Blu-ray discs) led to Brilliant Violet dyes. Quantum dots, which convert light into nearly any color in the visible spectrum with high efficiency, are also now commonly used in flow analysis (*6*). The number of simultaneous measurements possible on each cell has grown from 1 or 2 in the 1970s to more than 30 parameters today (*7*). This makes the next generation of high-parameter flow cytometers competitive with cytometry time-of-flight (CyTOF) technology. In 2011, CyTOF introduced ultrahigh-content flow cytometry based on mass spectrometry (*8*), in which antibodies are labeled with metal-conjugated probes. The procedure is more complicated and not as high-throughput, but like FACS, continues to evolve.

[1]*Department of Basic Medical Sciences and Weldon School of Biomedical Engineering, Purdue University, West Lafayette, IN, USA.* [2]*Vaccine Research Center, National Institute of Allergy and Infectious Diseases, National Institutes of Health, Bethesda, MD, USA. E-mail: jpr@flowcyt.cyto.purdue.edu; roederer@nih.gov*

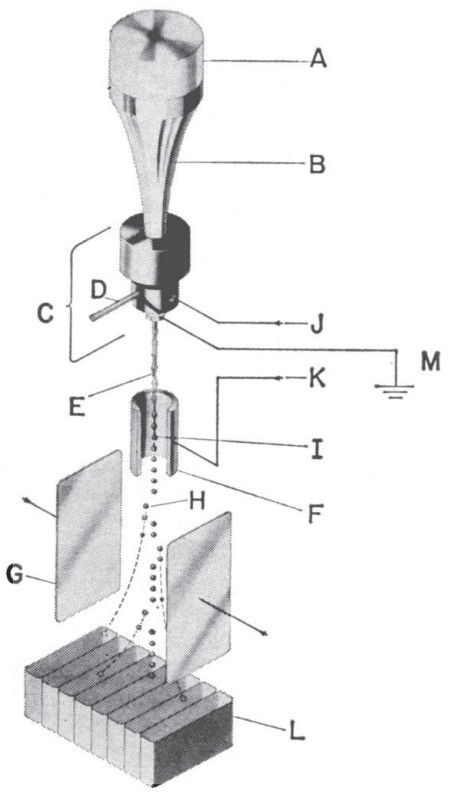

The original flow. M. Fulwyler described the first flow cytometer in 1965 (*1*), proposing that it might be possible to "measure simultaneously two (or more) characteristics of a cell and to make separation dependent on the ratio of such characteristics."

Today, a panoply of assays are used for flow cytometry. The candidates for measurement include biomarkers for stem cells and cancer cells, nucleic acids, reactive oxygen species, microvesicles, and even the functional status of yeast or bacteria. Perhaps the most remarkable growth of the technology is in clinical cytometry. It has recently become standard for some clinical laboratories to operate with 10 or more fluorescent dyes simultaneously, and the clinical market size now exceeds $1 billion.

While cell sorting by flow cytometry has long been a core tool in biomedical research, it quickly has become a standard technology in other biological fields. For example, in the livestock industry, it has been adapted to sort sperm for animal sex selection, spawning an entire commercial enterprise in animal sexing. In environmental sciences, it has been used to separate previously unknown organisms from complex microbial populations. Flow cytometry is also creating new fields of study. Its big data acquisition is opening opportunities for assays based on high-speed robotics (*9*) and advanced analytics that rely on classification techniques for population analysis (*10, 11*). The growing wealth of data is also bolstering a systems biology view of processes, and thereby demanding advanced informatics. Indeed, current challenges with flow cytometry include standardization and the increasing complexity of very high content data analysis.

What lies ahead? New-generation instruments are now capable of very high resolution imaging of cells while they are being sorted (*12*). There is also acoustic-based sorting, which uses ultrasonic radiation pressure to focus cells into the flow—desirable when samples are of low cell concentration. This advance reopens the opportunity for cell cycle analysis under high-speed conditions (*13*). Spectral cytometry, in which the full fluorescence emission spectrum is measured on each cell, presents unique cellular "fingerprints" and enables separation of highly complex mixtures of fluorochrome combinations (*14*). Coherent anti-Stokes Raman scattering flow cytometry may allow sorting of cells based on chemical states in real time (*15*). Substantial efforts at miniaturization and microfluidics are also under way. Here, the goals are high-throughput sorting under sterile conditions for transplantation. Extremely high throughput microfluidic-based cell sorting will likely herald the first major revolution in the fundamental hardware in 50 years.

There are currently over 100 companies in the flow cytometry business, constituting an industry worth more than $3 billion. Ubiquitous in research and clinical medicine, the technology could indeed be argued as having a greater impact on the biomedical field than any other technology. On its 50th anniversary, it truly has struck gold. ■

REFERENCES

1. M. J. Fulwyler, *Science* **150**, 910 (1965).
2. L. A. Herzenberg, L. A. Herzenberg, M. Roederer, *Annu. Rev. Physiol.* **76**, 1 (2014).
3. W. Dittrich, W. Göhde, *Z. Naturforsch.* **24b**, 360 (1969).
4. H. R. Hulett, W. A. Bonner, J. Barrett, L. A. Herzenberg, *Science* **166**, 747 (1969).
5. J. W. Gray *et al.*, *Proc. Natl. Acad. Sci. U.S.A.* **72**, 1231 (1975).
6. A. Watson, X. Wu, M. Bruchez, *BioTechniques* **34**, 296 (2003).
7. P. K. Chattopadhyay, T. M. Gierahn, M. Roederer, J. C. Love, *Nat. Immunol.* **15**, 128 (2014).
8. S. C. Bendall *et al.*, *Science* **332**, 687 (2011).
9. B. S. Edwards, F. Kuckuck, L. A. Sklar, *Cytometry* **37**, 156 (1999).
10. J. P. Robinson, B. Rajwa, V. Patsekin, V. J. Davisson, *Expert. Opin. Drug Deliv.* **7**, 679 (2012).
11. E. Lugli, M. Roederer, A. Cossarizza, *Cytometry A* **77**, 705 (2010).
12. T. C. George *et al.*, *Cytometry A* **59A**, 237 (2004).
13. G. R. Goddard, C. K. Sanders, J. C. Martin, G. Kaduchak, S. W. Graves, *Anal. Chem.* **79**, 8740 (2007).
14. G. Grégori *et al.*, *Cytometry* **81A**, 35 (2012).
15. J.-X. Cheng *et al.*, *Optics Express* **16**, 5782 (2008).

10.1126/science.aad6770

PHYSICS

To catch and smash charge on the hop

High-harmonic spectroscopy can probe charge migration controlled by a laser field

By **Kiyoshi Ueda**

Charge transfer plays a central role in photosynthetic and photocatalytic reactions and has thus been studied extensively in a wide range of systems. Generally, charge transfer is considered to be driven by the nuclear dynamics; nuclear motion in the system couples with electron motion and causes charge transfer. Two decades ago, ultrafast charge transfer was reported in isolated peptide cations (*1*); a theoretical demonstration that charge can migrate from one side to the other in polyatomic molecules without nuclear motion, due solely to electron correlations, soon followed (*2*). To differentiate electron correlation–driven processes from nuclear dynamics–driven ones, the term charge migration was introduced. Electron correlation–driven charge migration is faster than nuclear motion and occurs within femtoseconds, and is one of the most important subjects in attosecond science (*3*). The first report offering evidence of charge migration appeared in 2014 (*4*). On page 790 of this issue, Kraus *et al.* (*5*) describe the most advanced approach to probe attosecond charge migration and how to control it.

To create a wave packet of the charge (that is, a positively charged hole) by removing one electron from a polyatomic molecule, at least two electronic states must be coherently populated by ionization. Kraus *et al.* used laser field ionization of iodoacetylene (HCCI) molecules and created a wave packet that is described by a linear combination of the ground state **G** and the first excited state **E** of the cation. This approach is similar to that used to collect the first evidence of attosecond multielectron dynamics in polyatomic molecules (CO_2) (*6*). The initial wave packet is then given by the relative population of these two states and the relative phase $\Delta\varphi(\tau = 0) = \Delta\varphi_0$

Institute of Multidisciplinary Research for Advanced Materials, Tohoku University, Sendai 980-8577, Japan. E-mail: ueda@tagen.tohoku.ac.jp

CREDIT: IMAGE IS FROM (*1*)

at the time of the ionization. In the field-free condition, the relative phase evolves in time, $\Delta\varphi(\tau) = \Delta\varphi_0 + \Delta E\tau/\hbar$, where ΔE is the energy difference between **G** and **E** and $\hbar$ is Planck's constant divided by 2π. As a result, the charge migrates in the ionized HCCI molecule, from the iodine site (where the ionization occurs) to the two carbons and then back to the iodine site, with a period of 1.85 fs. Kraus *et al.* measured the relative population R for **G** and **E** and the initial relative phase $\Delta\varphi_0$. By extracting the phase information, which is the heart of the work, they have advanced high-harmonic generation (HHG) spectroscopy.

The above description of charge migration is valid only when the system is in the field-free condition. Kraus *et al.* achieved this condition by orienting the HCCI molecules in space impulsively by the laser pulse and ionizing them by another laser pulse whose field is perpendicular to the molecular orientation. Because the direction of the charge migration is perpendicular to the laser field, it is not much influenced by it. When the laser field is parallel to the molecules, population transfer occurs between the **G** and **E** states and the additional relative phase is accumulated. These complications provide a knob to control charge migration. To demonstrate it, however, the relative population $R(\tau)$ and the relative phase $\Delta\varphi(\tau)$ must be monitored as a function of time.

To extract the relative population $R(\tau)$ and the relative phase $\Delta\varphi(\tau)$ from the experiments and to demonstrate that these parameters can indeed be modified by the laser field, Kraus *et al.* performed advanced HHG spectroscopy (see the figure). They measured amplitudes and phases of the high-harmonic emission of the oriented HCCI molecules. They developed a theoretical model that describes the entire process, from laser field ionization generating a free electron wave packet to recombination of the electrons that are driven by the laser field back to the parent molecular ions. The experimental results required for the extraction of $R(\tau)$ and $\Delta\varphi(\tau)$ using this model are the ratio of HHG for parallel and perpendicular orientations of the molecules, the ratio of even and odd HHG for the oriented molecules, and the phase of HHG, ϕ^{HHG}, as a function of molecular orientation. The head-and-tail information about the molecular orientation was essential for spatially resolving charge migration. Another key point of the HHG spectroscopy is that every emitted harmonic order can be mapped to a unique transit time τ of the electron wave packet, as a consequence of the electron trajectories in the laser field. With this mapping, a time resolution of ~100 attoseconds could be achieved.

Kraus *et al.* have made a large step forward in visualizing charge migration and demonstrating that it can be controlled by the laser field. Because charge transfer plays a central role in photosynthetic and photocatalytic reactions, controlling charge migration constitutes a promising approach to the control of such reactions.

Several further remarks are in order. First, Kraus *et al.* extracted only $R(\tau)$ and $\Delta\varphi(\tau)$ from the experiments. They used calculated molecular orbitals to obtain the spatial distribution of the electron densities from $R(\tau)$ and $\Delta\varphi(\tau)$ at each time τ. Direct measurement of the charge density at picometer spatial and attosecond time resolutions is unachievable. Their approach resembles the one used to reconstruct the two-electron wave packet of helium based on the measurement of the relative amplitude and the relative phase of the two doubly excited states coherently populated by the attosecond laser pulse (*7*). In quantum mechanics, any processes can be described by matrix elements that are characterized by amplitudes and phases with the specified basis functions. In this sense, Kraus *et al.* did a complete characterization of charge migration.

Second, they demonstrated that charge migration can be influenced by the laser field. Again this approach is similar to that used to demonstrate that the laser field can modify the relative amplitude and the relative phase (*7*). To fully control charge migration, however, one may need to use coherent control, where tailored light pulses directly shape the wave packet, not just pushing or smashing it, to manipulate the reaction at will (*8*). Recent developments of light sources (*9*, *10*) may open such a pathway in the near future. ■

REFERENCES

1. R. Weinkauf *et al.*, *J. Phys. Chem.* **100**, 18567 (1996).
2. L. S. Cederbaum, J. Zobeley, *Chem. Phys. Lett.* **307**, 205 (1999).
3. S. R. Leone *et al.*, *Nat. Photonics* **8**, 162 (2014).
4. F. Calegari *et al.*, *Science* **346**, 336 (2014).
5. P. M. Kraus *et al.*, *Science* **350**, 790 (2015).
6. O. Smirnova *et al.*, *Nature* **460**, 972 (2009).
7. C. R. Ott *et al.*, *Nature* **516**, 374 (2014).
8. P. Brumer, M. Shapiro, *Principles of the Quantum Control of Molecular Processes* (Wiley-VCH, Berlin, 2003).
9. M. Reduzzi *et al.*, *J. Electron. Spectrosc. Relat. Phenom.* 10.1016/j.elspec.2015.09.002 (2015).
10. E. Allaria *et al.*, *J. Synchrotron Radiat.* **22**, 485 (2015).

10.1126/science.aad3982

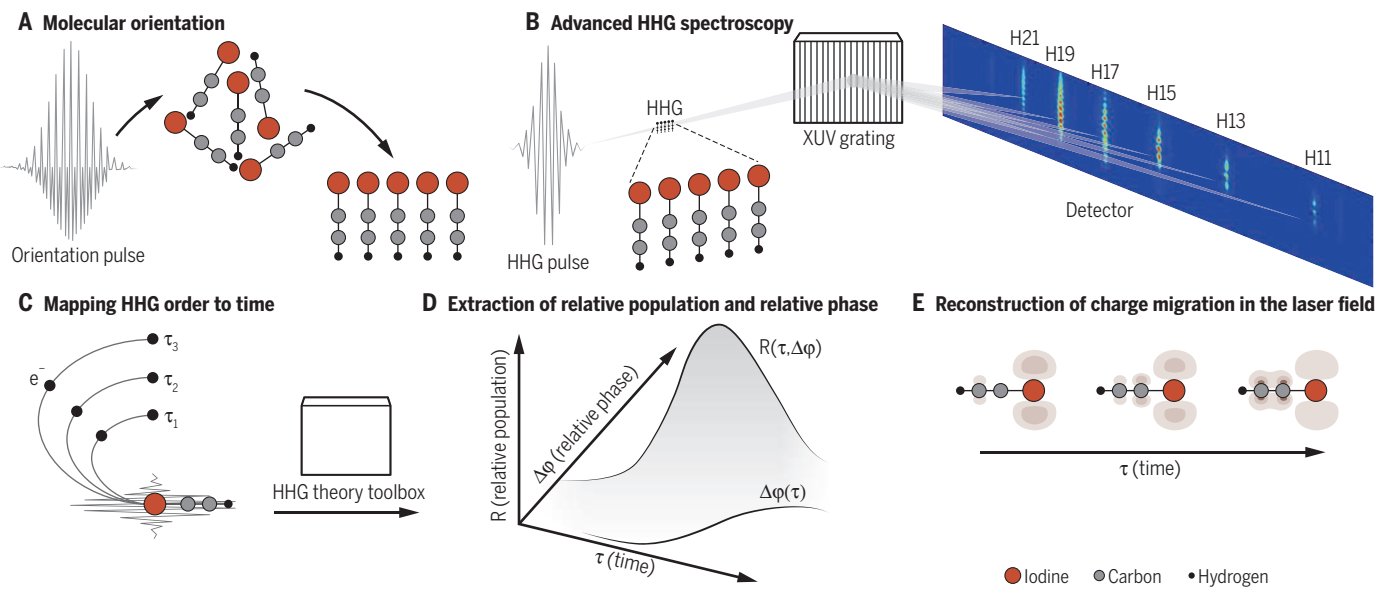

ILLUSTRATION: P. HUEY/*SCIENCE*

Recipe for reconstruction of charge migration. (**A**) The HCCI molecules are impulsively oriented in space by a phase-controlled two-color (800 nm + 400 nm) pulse. (**B**) Amplitudes and phases of the high-harmonic emission of the oriented HCCI molecules are measured. (**C**) Harmonic orders are mapped to the time of probing the wave packet. (**D**) Relative population and relative phase are extracted from the measurement by means of a HHG theory tool. (**E**) Using calculated molecular orbitals, charge migration in the laser field is reconstructed from the relative population and the relative phase.

IMMUNOLOGY

Breaching the gut-vascular barrier

A vascular barrier in the intestinal tract controls pathogen dissemination

By **Romain Bouziat** *and* **Bana Jabri**

The intestinal barrier plays a critical role in health and disease by limiting systemic dissemination of microbes and toxins while allowing nutrients to access the circulation (*1*). The portal venous system ensures that substances absorbed in the intestine transit first through the liver, where they can be further metabolized and detoxified (*2*). Moreover, it is thought that the liver can play a role in tolerance (*3*). On page 830 of this issue, Spadoni *et al.* (*4*) characterize the gut-vascular barrier (GVB) and propose how bacteria can disrupt it, allowing their passage into the bloodstream and spread to the liver and spleen.

Organ-specific barrier mechanisms in mammals must meet different requirements because each organ exerts unique functions and has different levels of exposure to pathogens and exogenous agents. The best-characterized is the blood-brain barrier (BBB), which separates circulating blood from the brain's extracellular fluid. The barrier is formed by vascular endothelial cells, but astroglial cells and pericytes in the brain are in contact with these cells and play an important role in regulating the passage of molecules across the BBB (*5*). Glial cells are also in the gut and help to maintain the intestinal barrier by sending and receiving signals from enteric neurons and intestinal epithelial cells (*6*). Spadoni *et al.* show that enteroglial cells and pericytes are in close contact with intestinal vascular endothelial cells and are an integral part of the GVB, supporting the idea that the BBB and GVB share key features (see the figure). Like the BBB, endothelial cells in the GVB develop tight junctions. However, Spadoni *et al.* show that the GVB allows diffusion of molecules as large as 4 kD, eight times the maximal size observed for the BBB. Whether this plays a physiological role by allowing access of luminal contents of the intestine to the liver to induce tolerance against dietary antigens and commensal microbiota remains to be tested. That the GVB has a size exclusion below 70 kD ensures that bacteria cannot translocate to the bloodstream.

Salmonella typhimurium (*7*) is a Gram-negative bacterial pathogen generally acquired by ingesting contaminated water or food and is the leading cause of human disease among *Salmonella* serotypes. It primarily infects the intestine and can disseminate to the liver, gall bladder, and spleen. The portal venous system also irrigates the gall bladder, a site of chronic persistence for the pathogen. *S. typhimurium* is not only resistant to bile in the gall bladder, but also responds to its presence by expressing resistance genes (*8*). Spadoni *et al.* show that *S. typhimurium* disrupts the GVB, allowing the spread of 70-kD particles to the blood, liver, and spleen in infected mice. Although *S. typhimurium* increases β-catenin signaling in intestinal epithelial cells to promote dissemination (*7*, *9*), the authors observed a surprising decrease in the β-catenin–inducible gene *Axin 2*, suggesting that the pathogen may decrease β-catenin signaling in vascular endothelial cells. Furthermore, the study reveals that overexpression of a degradation-resistant form of β-catenin in mice prevents the spread of *S. typhimurium*, even though an inflammatory response is still induced. These effects depend on the bacterium's pathogenicity island (spi)-2–encoded type III secretion system, which transfers virulence proteins into the host cell (*7*, *10*). This is intriguing because the AvrA virulence protein, encoded by (spi)-1–encoded type III secretion systems, has the opposite effect and prevents β-catenin degradation in intestinal epithelial cells (*7*, *9*). Thus, two type III secretion systems in *S. typhimurium* may exert their functions differentially in epithelial and endothelial cells. β-Catenin stability is controlled by an upstream signaling molecule called Wnt (*11*), and Spadoni *et al.* provide some

Committee on Immunology, Department of Medicine, University of Chicago, Chicago, IL 60637, USA. E-mail: bjabri@bsd.uchicago.edu

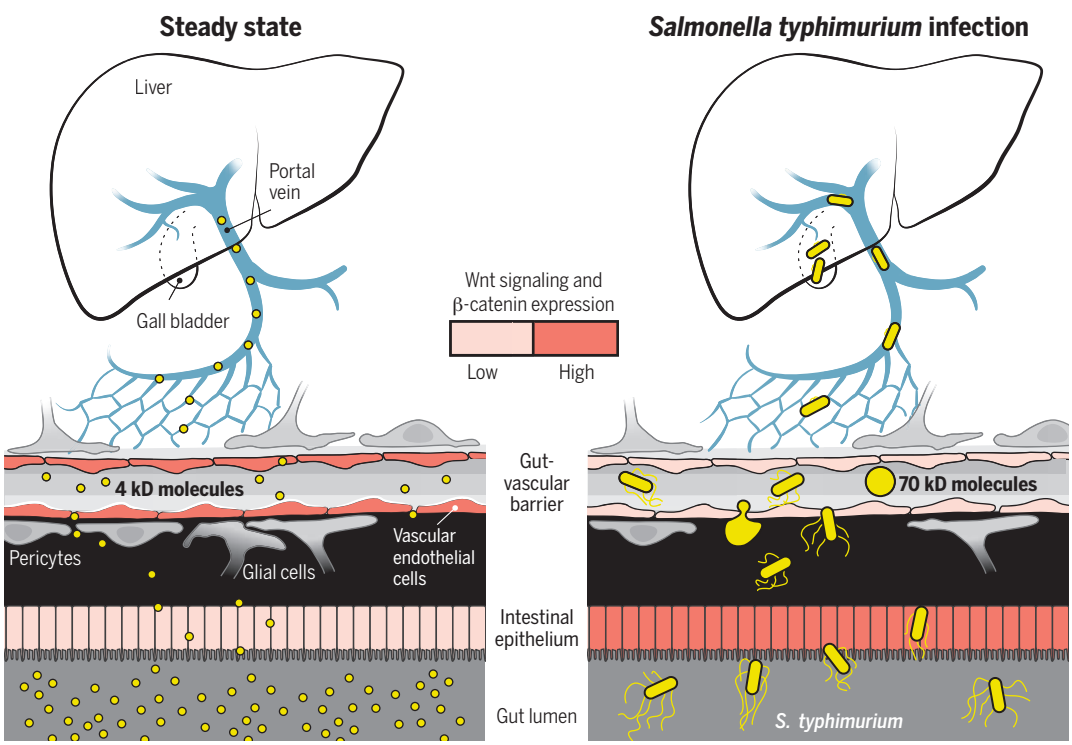

Gut-vascular barrier. Glia and pericytes surround vascular endothelial cells, forming a barrier that allows diffusion of molecules of 4 kD from the intestine to the bloodstream and liver. *S. typhimurium* increases Wnt and β-catenin signaling in intestinal epithelial cells to enhance invasion into the gut. Conversely, *S. typhimurium* blocks Wnt signaling and promotes β-catenin degradation in vascular endothelial cells, altering the barrier and promoting its spread to the gall bladder.

ILLUSTRATION: K. SUTLIFF/*SCIENCE*

indirect evidence that *S. typhimurium* alters β-catenin signaling by inhibiting Wnt signaling. Interestingly, the canonical Wnt pathway also plays a role in the development and integrity of the BBB (*12*).

Spadoni *et al.* report intriguing observations that call for more investigation. In particular, it remains to be determined whether Wnt and β-catenin signaling in intestinal vascular endothelial cells, and the interaction between glial and endothelial cells, play a role in regulating GVB and preventing the translocation of bacteria under homeostatic and pathological conditions. That *Salmonella* discretely regulates β-catenin in host cells is a striking example of how pathogens evolve intricate mechanisms to harness host pathways in a cell-specific manner for their own benefit. Altering GVB makes evolutionary sense for *S. typhimurium* because it could enable it to disseminate and reside in the gall bladder. Dissecting the mechanisms that allow *Salmonella* to block β-catenin signaling in vascular endothelial cells—in particular, determining which effector proteins encoded by the pathogen's (spi)-2 pathogenic island promote β-catenin degradation, and how they do so—may enable therapeutic strategies that prevent the chronic infection and spread of *S. typhimurium* by asymptomatic carriers (*8*).

The findings of Spadoni *et al.* also may lend insight into liver damage in celiac disease. This condition is an enteropathy with an autoimmune component induced by dietary gluten in genetically susceptible individuals (*13*), and it may be linked to disruption of the GVB. Although patients with active celiac disease show an increase in β-catenin protein expression and phosphorylation in intestinal epithelial cells (*14, 15*), studies in intestinal vascular endothelial cells, and specifically in patients with liver disease, have not been performed. More generally, the notion that breaches in the GVB may disrupt systemic immune homeostasis and promote liver damage in patients with autoimmune and intestinal inflammatory disorders warrants investigation in different pathological settings. ■

REFERENCES

1. J. R. Turner, *Nat. Rev. Immunol.* **9**, 799 (2009).
2. M. S. Roberts *et al.*, *Clin. Pharmacokinet.* **41**, 751 (2002).
3. P. A. Knolle, G. Gerken, *Immunol. Rev.* **174**, 21 (2000).
4. I. Spadoni *et al.*, *Science* **350**, 830 (2015).
5. N. J. Abbott *et al.*, *Neurobiol. Dis.* **37**, 13 (2010).
6. B. D. Gulbransen, K. A. Sharkey, *Nat. Rev. Gastroenterol. Hepatol.* **9**, 625 (2012).
7. A. Haraga *et al.*, *Nat. Rev. Microbiol.* **6**, 53 (2008).
8. J. S. Gunn *et al.*, *Trends Microbiol.* **22**, 648 (2014).
9. J. Sun *et al.*, *Am. J. Physiol. Gastrointest. Liver Physiol.* **287**, G220 (2004).
10. R. Figueira, D. W. Holden, *Microbiology* **158**, 1147 (2012).
11. H. Clevers, R. Nusse, *Cell* **149**, 1192 (2012).
12. S. Liebner *et al.*, *J. Cell Biol.* **183**, 409 (2008).
13. P. H. R. Green, B. Jabri, *Lancet* **362**, 383 (2003).
14. K. Juuti-Uusitalo *et al.*, *Clin. Exp. Immunol.* **150**, 294 (2007).
15. R. Ciccocioppo *et al.*, *Am. J. Clin. Pathol.* **125**, 502 (2006).

10.1126/science.aad6768

GLOBAL CHANGE SCIENCE

Stakeholders in climate science: Beyond lip service?

Local knowledge coproduction must be rewarded

By **Nicole L. Klenk,[1]* Katie Meehan,[2] Sandra Lee Pinel,[3] Fabian Mendez,[4] Pablo Torres Lima,[5] Daniel M. Kammen[6]**

Research models are evolving in response to the need for on-the-ground knowledge of climate change impacts on communities. Partnership between researcher and practitioner is vital for adaptive policy efforts (*1*). Transdisciplinary research teams present new opportunities by involving academics and local stakeholders, who actively conceive, enact, and apply research on adaptation and mitigation actions (*2, 3*). In transdisciplinary research, stakeholders are also researchers. But if we want to engage stakeholders in climate research, then we cannot simply pay lip service to the idea while treating them as participants for extractive research.

> ***"...global change science can strengthen its social robustness...when ethical...dilemmas... are... addressed...."***

We categorized a set of 27 climate change research networks (see supplementary materials) that perform various knowledge functions (*4*) and exhibit different forms of stakeholder engagement, from distributing knowledge to users to coproducing it with stakeholders (see the table). These networks represent various investments of time and resources to build the capacity of researchers and stakeholders to coproduce knowledge.

POLICY

Our analysis has three goals: (i) to document and compare examples of climate change research networks and elicit the patterns of knowledge functions; (ii) to demonstrate that many networks are emphasizing knowledge coproduction with stakeholders, with attendant policy implications; and (iii) to build an interactive database of networks so as to ignite broader dialogue on the role of stakeholders in science.

*[1]University of Toronto, Toronto, ON Canada. [2]University of Oregon, Eugene, OR USA. [3]Antioch University New England, Keene, NH USA. [4]University of Valle, Cali, Colombia. [5]Metropolitan Autonomous University, Mexico City, Mexico. [6]University of California, Berkeley CA, USA. *Corresponding author. E-mail: nicole.klenk@utoronto.ca*

Some of the networks reviewed, such as the Climate and Development Knowledge Network (classified as "linking"), are focused on improving how knowledge streams from scientists to relevant stakeholders. Others, such as the Climate Action Network for South Asia ("match-making"), have adopted a more "consultative" approach to knowledge exchange with stakeholders. Transdisciplinarity requires more labor. For example, the Future Earth program ("co-producing") works directly with stakeholders to help script research schemes, frame questions, and collect and analyze data, with the hope that coproduction will result in more policy-relevant knowledge and local empowerment. The key point is not that one model of knowledge production is better than another—nor that all models should be fully "integrative" (*5*)—but that many climate change research networks invite stakeholders to be part of the community of peer experts who assess the validity and relevance of science itself (*6*).

COMPENSATION, INTEGRATION, AND ACCOUNTABILITY. Scholarship on community-engaged research in public health has shown that collaborative research that involves stakeholders as researchers presents a number of ethical and political implications for the governance of science (*7*).

First, at present, transdisciplinary models in climate research assume that stakeholders are rewarded with new knowledge, capacities, and "voice" by taking part in research networks. This assumption only serves to reproduce the power imbalance between scientists and stakeholders, the former remaining in control of the coproduction process. Although stakeholders may be willing to volunteer for the opportunity to engage in research, reliance on self-selected individuals can lead to further marginalization of vulnerable populations whose knowledge and experience is sought, but whose time and resources are limited.

Unlike scientists, stakeholders are not paid for making insights and discoveries.

Collaborative models of climate research

Framework for categorizing the primary knowledge function of research networks

KNOWLEDGE FUNCTION	DESCRIPTION	MODEL OF KNOWLEDGE EXCHANGE	WORK REQUIRED OF STAKEHOLDERS
Linking	Targeted dissemination of knowledge to inform decision-making	From knowledge producers to knowledge users	Together, stakeholders and knowledge producers interpret research evidence for decision-making
Match-making	Connects diverse knowledge producers with users to frame research questions and interpret results	Knowledge producers consult knowledge users	Stakeholders participate in research but do not engage in research themselves
Collaborating	Knowledge users are active throughout the process, including articulation of research questions, design of projects, collection and analysis of data, and production of outputs	Knowledge producers work with knowledge users to produce, understand, and apply knowledge in decision-making	Stakeholder organizations dedicate financial, human, and infrastructure resources to participate in projects; stakeholders and knowledge producers agree on timelines, outputs, and outcomes
Coproducing	Empower and build capacity of stakeholders to critically assess and lead research projects that shape the social order of their communities	Encourages exposure of different and conflicting values, which makes knowledge production more political	Stakeholders and their organizations have institutional structures and processes to enable recursive evaluation of knowledge production and application

Genuine transdisciplinary research requires elevating the role of stakeholders as equal to scientists because of the work they do as coproducers, regardless of the potential instrumental value of the knowledge coproduced. Yet, ethical issues often arise when directly paying research partners, and many institutional review boards (IRBs) flag remuneration as a possible conflict of interest, even for knowledge coproducers. IRBs may need to revisit ethical guidelines and procedures when stakeholders—no longer just participants—are active agents in generating knowledge. IRBs already allow honoraria to incentivize and help defray some costs of stakeholder engagement in research, but this nominal amount is not commensurate with compensating stakeholders as coproducers. A "pay-for-services" model of stakeholder engagement is not the only option, but although equating coproduction with pay may not be appropriate everywhere, neither should it be rejected a priori.

Second, power imbalances between technical expertise and local knowledge point to wider problems of integration and knowledge coproduction in climate science (*8*). The Intergovernmental Panel on Climate Change (IPCC) continues to emphasize quantitative versus qualitative scientific research, expert judgment over local knowledge, and a rather limited understanding of the "human dimensions" of global change (*9, 10*). To effectively scale-up local knowledge coproduction, we need to foster a variety of knowledge-sharing and social-learning platforms, such as the interactive database of research networks to which we invite readers to contribute (rael.berkeley.edu/project/stakeholders-in-science). At the global scale, there is urgent need for the institutionalization of mechanisms of local knowledge mobilization, perhaps within the IPCC, to prevent continued fragmentation of coproduction initiatives. Whereas many networks we examine seek to do this, without a more systematic global means of knowledge integration and dialogue, their efforts will remain local or regional.

Finally, transdisciplinary models of research collaboration have important policy implications, including the need for granting agencies to develop transdisciplinary research governance criteria (*7*) and for universities to revisit their proprietary policies and to develop rights of shared ownership of the knowledge coproduced. Although funding agencies generally require that research partnerships with communities have formal governance structures, such governance agreements are of little use if there are no mechanisms to hold researchers accountable. Granting agencies need to put into place mechanisms for addressing complaints from knowledge coproducers when agreed-upon requirements are not followed through. Drawing on literature on community-based research partnerships, other actions might include a memorandum of understanding outlining goals, principles, and intellectual property rights of partnerships with nonacademic stakeholders; clear roles and responsibilities of knowledge coproducers; and, guidelines for how partnerships will accumulate, store, and mobilize data.

Whether through financial compensation, new modes of recognition, or new governance arrangements, global change science can strengthen its social robustness and relevance when ethical and political dilemmas at the core of knowledge coproduction are openly acknowledged, honestly assessed, and meaningfully addressed. If climate change demands all hands on deck, then it's time to raise the stakes. ■

REFERENCES AND NOTES

1. IPCC, *Working Group I Contribution to the IPCC Fifth Assessment Report (AR5), Climate Change 2013: The Physical Science Basis* (IPCC, Geneva, Switzerland, 2013).
2. D. Hegger *et al.*, *Environ. Sci. Policy* **18**, 52 (2012).
3. S. Serrao-Neumann *et al.*, *Futures* **65**, 97 (2015).
4. N. L. Klenk, S. Wyatt. *For. Pol. Econ.* 10.1016/j.forpol.2015.06.008 (2015).
5. N. L. Klenk, K. Meehan, *Environ. Sci. Policy* **54**, 160 (2015).
6. S. O. Funtowicz, J. R. Ravetz, *Futures* **25**, 739 (1993).
7. J. G. Oetzel *et al.*, *Am. J. Public Health* **105**, 1161 (2015).
8. M. Hulme, *Nat. Clim. Change* **1**, 177 (2011).
9. N. Castree *et al.*, *Nat. Climate Change* **4**, 763 (2014).
10. M. Carey *et al.*, *Nat. Climate Change* **4**, 1038 (2014).

ACKNOWLEDGMENTS

Authors are supported by the Fulbright NEXUS Regional Scholars program, funded by the U.S. Department of State, where D.M.K. is the lead scholar, and the Brazilian Ministry of Education, Agency for Support and Evaluation of Graduate Studies (CAPES). N.L.K. acknowledges funding from the Canadian Social Science and Humanities Research Council Partnership Development Grant: Living with Climate Change. S.L.P. acknowledges funding from SENESYCT, Government of Ecuador, Project Prometeo, and NSF Research Coordination Networks--The Science, Engineering and Education for Sustainability (DEB-1231233). F.M. acknowledges funding from International Development Research Centre, Project Climate Change, Vulnerability, and Health. The views expressed in this publication are those of the authors and do not necessarily reflect the views of supporting agencies.

SUPPLEMENTARY MATERIALS

www.sciencemag.org/content/350/6262/743/suppl/DC1

10.1126/science.aab1495

The 1991 eruption of Mount Pinatubo produced clouds of volcanic ash hundreds of miles across and injected 20 million tons of sulfur dioxide into the stratosphere.

PHOTO: ALBERTO GARCIA/CORBIS

GEOENGINEERING

The Earth experiment

An investigation of the promise and peril of engineered solutions to climate change

By **Eric Oelkers**

The idea of geoengineering, modifying natural processes to derive a perceived benefit, goes back to before recorded civilization, perhaps to the digging of the first drainage ditch. Such ditches allowed us to change a water flow path, making it easier to irrigate farmland or drain an urban area. Over the subsequent millennia, mankind has become far more efficient at diverting the flows of natural substances for the perceived benefit of society. Burning hydrocarbons, for example, has allowed us to achieve unprecedented advances in transportation and the production of goods. In doing so, we have managed to increase the carbon dioxide concentration of the atmosphere by 40% compared with preindustrial times and alter the global climate.

In his new book, *The Planet Remade*, Oliver Morton asks the question: If we can alter global climate in one direction by burning hydrocarbons, can we reverse it by doing something else? The term "geoengineering" has become so synonymous with this notion that many, including Morton, now use it only to describe attempts to control Earth's climate on a global scale.

Geoengineering solutions to climate change tend to fall into two general categories: carbon management and sunlight management. Carbon management involves reducing the carbon dioxide concentration of the atmosphere. In the absence of efforts to curtail the use of hydrocarbons, this means carbon capture and storage. Morton argues against this solution right from the start, quoting a 2009 report from the American Physical Society that states that the cost just to capture 1 ton of carbon dioxide from the atmosphere would be $600 and so would be too expensive. He neglects to discuss more recent studies, which have found that carbon can be captured and stored for no more than a few tens of dollars a ton (*1*).

Morton quickly moves on to his preferred geoengineering solution: the creation of an atmospheric veil made of sulfate aerosols that would limit the solar energy reaching Earth. There is little doubt that this method offers one major advantage. The amount of gas involved, and thus the costs, are far less than carbon capture and storage. No more than a few hundred thousand tons of aerosols might need to be added to the stratosphere annually, compared with the tens of gigatons of carbon dioxide that would need to be removed from our atmosphere. Less appreciated are the limitations and risks associated with sulfate aerosols. Besides the obvious disadvantage that this solution does not address complications such as ocean acidification, much of the support and direction for this solution is predicated on computer climate-prediction models, which are notoriously uncertain.

Even if sulfate aerosols are successful in lowering global temperatures, they may have unintended consequences on our climate. The 1991 eruption of Mount Pinatubo delivered 20 million tons of sulfur dioxide to the stratosphere. Subsequently, Earth experienced warming in some specific regions, as well as a general global cooling. This cooling was associated with less evaporation and a reduction in rainfall over the continents. According to a paper published by Trenberth and Dai of the National Center for Atmospheric Research, a larger proportion of Earth's surface suffered drought conditions in 1992 than at any other time during their 55-year data set (*2*). The 1815 Tambora eruption created a similar atmospheric veil that was sufficiently thick to lower temperatures, alter rainfall patterns, and cause famine in southern China, unprecedented storms in Europe, and July frost in New England (*3*). When considering the potential risks and consequences of managing Earth's climate, I can't help but recall a talk given by the climatologist Wally Broecker, in which he showed a cartoon of a dragon, noting, "The climate system is an angry beast, and we are all poking at it with sticks."

Because it is relatively cheap to add aerosols to the atmosphere, Morton argues that some organization or rogue nation may one day use this technology as a weapon or may attempt to selectively improve one region's climate to the detriment of others. In many ways, this sounds more like the scenario of a science fiction action film than a scientific possibility, but this may indeed be among the challenges that we face over the next century.

The reviewer is affiliated with the Department of Earth Sciences, University College London, London, UK, and the Centre National de la Recherche Scientifique, Toulouse, France. E-mail: e.oelkers@ucl.ac.uk

The Planet Remade
How Geoengineering Could Change the World
Oliver Morton
Princeton University Press, 2015. 438 pp.

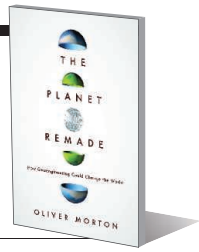

REFERENCES

1. Global CCS Institute, *Economic Assessment of Carbon Capture and Storage Technologies: 2011 Update*; www.globalccsinstitute.com/publications/economic-assessment-carbon-capture-and-storage-technologies-2011-update (2011).
2. K. Trenberth, A. Dai, *Geophys. Res. Lett.* **34**, L15702 (2007).
3. G. D. Wood, *Tambora: The Eruption That Changed the World* (Princeton Univ. Press, Princeton, NJ, 2014).

10.1126/science.aad4340

NEUROENGINEERING

Mind meets machine

High-profile researchers take center stage in a quest to build a brain-machine interface

By **A. Aldo Faisal**

The idea of interfacing humans with machines has been a popular one for more than 40 years, as embodied by the television program *The Six Million Dollar Man*. Whereas the TV show highlighted the feats enabled by the force and speed of the hero's robotic actuators, in real life we appreciate now that the key challenge to developing a useful brain-machine interface (BMI) lies in perfecting a way to seamlessly decode our intentions and translate them into actions.

Malcolm Gay's new book, *The Brain Electric*, captures in an exciting, comprehensible, and dramatic style the race to build the first human-usable "mind"-controlled dexterous robotic arm. Gay uses intuitive explanations of technology and neuroscience that are light on jargon and often told from the perspective of a patient or researcher to make the story accessible to a broad audience. The reader is introduced to a range of important neuroscience concepts, including how the brain controls movement, how it acts as a prediction engine, and the unique role of the mirror neuron system. On the engineering side, the story focuses mainly on invasive neural interfaces, including electrocorticography (ECoG) and electrode arrays, but also introduces clinically newer techniques, including targeted muscle reinnervation (TMR) and deep brain stimulation (DBS).

The scientific "race" is framed as a story of competition between several researchers, including John Donoghue, Miguel Nicolelis, and Andrew Schwartz. Gay is purposely selective in his decision to profile a small group of scientists, and although the narrative is centered on the Americas, this cozy setting makes for good storytelling. The book's chapters are richly illustrated with dialogue, quotes, and anecdotes by and about these protagonists—a testament to the amount of interviews Gay must have undertaken.

The history of the race is presented in a realistic manner, with Gay carefully explaining the scientific ideas behind the different approaches, as well as the realities of how funding promotes scientific advances. The book prominently features large-scale funding initiatives (e.g., DARPA Revolutionizing Prosthetics) and the politics surrounding research as two key factors that act as drivers and milestones of the actual progress (and failure). Gay explains the role of commercializing research, using prominent examples of successes and failures. He also hints at challenges that patents may pose to scientific efforts. From a researcher's perspective, it was also refreshing to see a careful explanation of the challenges that we face in translating basic research concepts in animal systems to solutions that work for humans.

In the book's denouement, Gay finally spells out what he sees as the ultimate goal of the race: a human brain–controlled robotic arm that recapitulates the fluid motion of a natural human arm during eating. In doing so, he is able to declare Schwartz, who developed a robotic prosthetic arm with a full 10 degrees of freedom, as the "winner."

Brain-controlled prosthetic limbs may one day be a reality for the millions of movement-impaired individuals worldwide.

The Brain Electric
The Dramatic High-Tech Race to Merge Minds and Machines
Malcolm Gay
Farrar, Straus and Giroux, 2015.
275 pp.

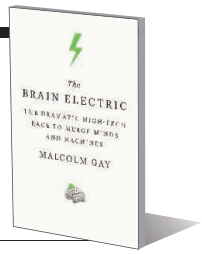

Defining the race in terms of proof-of-concept successes makes for a satisfying read; however, the broader goal of such research is to enable and restore patients' ability to interact with the world. The technologies presented in this book involve seriously invasive approaches and bear considerable risk; in practice, few patients currently qualify for these experimental treatments. The book does little to manage the hopes and expectations of individuals who may one day benefit from such technologies.

The reader is left to imagine where the next book written on this topic will pick up. Such a book could focus, for example, on bidirectional interfaces that can both move and feel. It could also focus on practical challenges, such as reducing the time it takes to learn how to operate these interfaces from months to minutes or how to make these technologies more accessible both in terms of medical intervention and cost.

The race to create a clinically relevant BMI will ultimately be won when the interfacing is such that technology that restores or augments our ability to act feels just like a part of us. To restore function to the planet's 100 million movement-impaired individuals, we will face challenges on many fronts, from technology costs to rehabilitation efforts, and will likely rely on both noninvasive and invasive BMI approaches. We can also envision further races that seek to bring new capabilities such as brain-brain interfacing and human augmentation closer to our wishful grasp.

The Brain Electric is a book that makes the excitement of merging neuroscience and engineering accessible to everyone. I recommend it to young adults to attract them to science and engineering, to graduate students to motivate them, and to the public, who will gain a sense of the challenges and satisfaction associated with doing research.

10.1126/science.aad0787

The reviewer is at the Department of Bioengineering, Imperial College London, London SW7 2AZ, UK. E-mail: a.faisal@imperial.ac.uk

Edited by **Jennifer Sills**

Putting Russia on the genome map

IN THE NEWS story "Who has your DNA—or wants it" (25 September, p. 1475), J. Kaiser listed 17 projects that aim to chart human genetic diversity across the globe in the context of a dozen ongoing national genome sequencing initiatives (*1*). Yet Russia—a country with 1/10th of Earth's landmass, 1/50th of the world's people, and descendants from critical crossroads across human migration history—has a relatively unexplored human genome landscape (*2*). The modern Russian population presents an opportunity to study population history in the wake of the founding of Eurasia, historical relocations throughout the Great Migration Age, the Great Silk Road diaspora, and the forced population displacements of the recent centuries (*3*). The time has come for Russia to build a national genome project of its own.

Genetic admixture occurs when individuals from separate populations interbreed. Mapping Russia's admixture history, and analyzing it in light of the diverse environments faced by the local populations, could create a unique opportunity for disease gene discoveries (*4*). Genome mining of function-altering variants in modern Russian genomes could reveal risk/protective alleles that neither exist nor associate with disease elsewhere. Studies of population ancestry and natural history in Russia would further illuminate the origins of Native Americans, and also provide genomic links to the lost Neandertal and Denisovan cultures discovered in Russia's fossil beds. Russian biomedical research will receive immediate benefit from a database for precision/personalized medicine. Finally, engaging Russian researchers and communities in international projects like this (*1*, *2*) would help integrate its people into the world genomics community.

The Genome Russia Project would close the largest gap in the genome map of the world (*5*). The beginnings of a Genome Russia Project are happening, endorsed by the Russian Academy of Sciences and the Ministry of Education and Science. The Genome Russia Project can and should become an example of open international collaboration and data access with the shared goal of improving human health.

Taras K. Oleksyk,[1,2] Vladimir Brukhin,[1] Stephen J. O'Brien[1]*

[1]Theodosius Dobzhansky Center for Genome Bioinformatics, St. Petersburg State University, St. Petersburg, Russia. [2]University of Puerto Rico, Mayaguez, PR 00680, USA.

*Corresponding author. E-mail: lgdchief@gmail.com

REFERENCES

1. V. Marx, *Nature* **524**, 503 (2015).
2. The 1000 Genomes Project Consortium, *Nature* **526**, 68 (2015).
3. Y. Smirnova, A. Davydova, *Science* **348**, 1068 (2015).
4. M. W. Smith, S. J. O'Brien, *Nat. Genet. Rev.* **6**, 623 (2005).
5. Genome Russia Project (http://genomerussia.bio.spbu.ru) [in Russian].

Tempering threats to temperate forests

C. I. MILLAR and N. L. Stephenson ("Temperate forest health in an era of emerging megadisturbance," Review, 21 August, p. 823) review the increasing susceptibility of temperate forests to stresses such as increasing droughts, insect outbreaks, and more frequent and intense fires ("megadisturbances"). They accurately point out how forests are exceeding critical thresholds and can no longer recover their original composition and ecosystem services. However, they overlook data showing that the opposite is also true: Many temperate forests are suffering from declines in the frequency and intensity of fires (*1*, *2*).

Surprisingly, Millar and Stephenson hold up northern mid-successional oak-hardwood forests of the eastern and central United States as models of "resilient" forests capable of sustaining structure, function, and services. In fact, these forests are undergoing rapid changes in composition and structure, losing diversity and the ability to regenerate key species (*3*–*6*). These changes reflect responses to many drivers, including habitat fragmentation, ungulate browsing, and exotic species invasions, all of which threaten ecosystem services just as observed in western forests (*7*–*9*).

To address these threats and avoid catastrophic collapse, Millar and Stephenson argue that we should anticipate incipient changes and manage forests to facilitate their inevitable transitions, such as by thinning stands and planting species adapted to future conditions. This may be worthwhile, but it presupposes our ability to correctly predict responses to these treatments. Given that we are still learning about the susceptibility of temperate forests to various stresses and the ensuing dynamics, it is premature to assume that we can accurately anticipate and counter these incipient shifts. Cutting trees to save the future forest will also concern those who have seen "forest health" used to justify logging and subvert environmental analysis (*10*). We should instead acknowledge the susceptibility of temperate forests to a spectrum of stresses and admit our uncertainty by treating such interventions as "adaptive management" experiments rather than a mature paradigm to apply widely.

Donald Waller,* Jeremy Ash, Alison Paulson, Grégory Sonnier

Department of Botany, University of Wisconsin–Madison, Madison, WI 53706, USA.

*Corresponding author. E-mail: dmwaller@wisc.edu

Increasing deer populations threaten the health of forests.

PHOTO: © ARTERRA PICTURE LIBRARY/ALAMY STOCK PHOTO

REFERENCES

1. G. J. Nowacki, M. D. Abrams, *Bioscience* **58**, 123 (2008).
2. D. Li, D. M. Waller, *Ecology* **96**, 1030 (2015).
3. T. P. Rooney, S. M. Wiegmann, D. A. Rogers, D. M. Waller, *Conserv. Biol.* **18**, 787 (2004).
4. K. Taverna, R. K. Peet, L. C. Phillips, *J. Ecol.* **93**, 202 (2005).
5. D. A. Rogers, T. P. Rooney, D. M. Waller, *Ecology* **89**, 2482 (2008).
6. T. G. Knoot *et al.*, *For. Ecol. Manage.* **341**, 110 (2015).
7. D. A. Rogers, T. P. Rooney, T. J. Hawbaker, V. C. Radeloff, D. M. Waller, *Conserv. Biol.* **23**, 1497 (2009).
8. A. Davalos, V. Nuzzo, B. Blossey, *J. Ecol.* **102**, 1222 (2014).
9. A. Dobson, B. Blossey, *J. Ecol.* **103**, 153 (2015).
10. W. S. Alverson, W. Kuhlmann, D. M. Waller, *Wild Forests: Conservation Biology and Public Policy* (Island Press, Washington, DC, 1994).

How to measure sustainable progress

IN SEPTEMBER, THE United Nations General Assembly adopted Sustainable Development Goals (SDGs), to be met by the year 2030. These important goals range from poverty eradication and improvements in education and health to the protection of global assets, including the oceans and a stable climate. Unfortunately, neither the SDGs nor their background documents explain how governments should judge whether the development programs they undertake to meet the goals are sustainable.

The system of national accounts (SNA) that is in common use today records resource flows such as consumption, investment, employment, and government expenditure. The SNA is designed to measure gross domestic product (GDP), which is a flow of income (so many international dollars per year). However, because GDP can increase despite the depletion of natural resources, the SNA is ill-equipped to judge the sustainability of the SDGs.

Governments will need a measurement tool that records wealth, comprehensively, including reproducible capital (roads, buildings, and machines), human capital (education and health), and natural capital (land, fisheries, forests, and subsoil resources). GDP does not record the depreciation of capital assets. Although the SNA does account for depreciation of reproducible capital, it arrives at figures for Net Domestic Product (NDP), not wealth. Economic growth should reflect growth in wealth, not growth in GDP or NDP (*1*). If the average wealth per person (adjusted for distribution of wealth) increases as governments attempt to meet the SDGs, the SDGs will be sustainable; if it declines, the SDGs will be unsustainable.

Economic statisticians have begun estimating past movements of wealth over time. The authors of the Inclusive Wealth Report 2014 (IWR2014) (*2*), for example, measured movements in the wealth of 140 nations over the period 1990 to 2010. They used official statistics to arrive at the value of reproducible capital, and they estimated human capital by using data on educational attainment. Owing to severe limitations of data, items of natural capital that were included were limited to agricultural land, forests as stocks of timber, subsoil resources, and fisheries. The national costs of global climate change, although only partially covered, increased during the period. Similarly, the ecological services that are provided routinely by, for example, forests and coastal waters, though incomplete, have decreased. Estimates of wealth changes between 1990 and 2010 were therefore, in all probability, biased upward.

The authors reported that wealth grew at a positive rate in 92% of the countries in the sample, but that the proportion of countries where growth in wealth per person was positive was only 60%. The UN ignored population growth in framing the SDGs, which should be a point of public concern. Moreover, a reliance on growth in world income to finance the SDGs would be a mistake. IWR2014 reported that GDP per capita grew in 90% of the countries in their sample, even as wealth in many of those countries declined.

As nations work to meet the SDGs, their Statistical Offices should begin to prepare wealth accounts and track movements in wealth through time. Just as firms create annual balance sheets, governments should prepare annual wealth accounts. Limiting data to GDP will hinder our ability to evaluate development programs.

P. Dasgupta,[1]* A. Duraiappah,[2] S. Managi,[3] E. Barbier,[4] R. Collins,[5] B. Fraumeni,[6] H. Gundimeda,[7] G. Liu,[8] K. J. Mumford[9]

[1]Professor Emeritus, Department of Economics, University of Cambridge, Cambridge, CB3 9DD, UK. [2]Mahatma Gandhi Institute of Education for Peace and Sustainable Development, New Delhi, 110001, India. [3]Departments of Urban and Environmental Engineering, School of Engineering, Kyushu University, Nishi-ku, Fukuoka, 819-0395, Japan. [4]College of Business Economics and Finance Department, University of Wyoming, East Laramie, WY 82071, USA. [5]MIT Engineering Systems Division, Cambridge, MA 02142, USA. [6]Central University for Finance and Economics, Hunan University, Changsha, Hunan Province, 410006, China. [7]Department of Humanities and Social Sciences, Indian Institute of Technology Bombay, Powai, Mumbai, 400 076, India. [8]Statistics Norway, N-0033, Oslo, Norway. [9]Department of Economics, Purdue University, West Lafayette, IN 47907, USA.

*Corresponding author. E-mail: pd10000@cam.ac.uk

REFERENCES

1. P. Dasgupta, *Human Well-Being and the Natural Environment* (Oxford Univ. Press, Oxford, 2004).
2. UNU-IHDP/UNEP, *Inclusive Wealth Report 2014: Measuring Progress Toward Sustainability* (Cambridge Univ. Press, Cambridge, 2014).

OCEANS OF CHANGE

By **Julia Fahrenkamp-Uppenbrink, David Malakoff, Jesse Smith, Caroline Ash,** *and* **Sacha Vignieri**

In Malé, the capital of the Maldives, more than 120,000 people live just a meter or so above current sea level.

The phrase "climate change" typically evokes thoughts of rising air temperatures or other atmospheric phenomena such as droughts and extreme storms. Much less often do we consider the parallel changes that are occurring in the oceans, despite their extent and importance.

Climate change in the oceans has many facets. One is a rise in sea levels. Scientists are learning about how previous warm periods altered sea levels, and what that past may tell us about the future. To help us cope, so-called green infrastructure, such as planted marshes or oyster reefs, may help protect low-lying shorelines. Climate change is also creating problems for fisheries; for example, commercially valuable stocks move in response to warming seas.

Climate change has caused ocean temperatures to rise, a trend that will continue in the coming centuries even if fossil fuel emissions are curtailed. The uptake of carbon dioxide also makes the oceans more acidic, affecting the ability of organisms to create and maintain calcium-based shells and skeletons. Warm-water corals are particularly susceptible to these effects and may not survive the century unless carbon emissions are greatly reduced. Climate change impacts in the deep ocean are less visible, but the longevity and slow pace of life in the deep makes that ecosystem uniquely sensitive to environmental variability. Marine vertebrates at every depth are being affected, as are humans. Even if international negotiations like those kicking off soon in Paris succeed, we will be coping with the impacts of ocean climate change for centuries.

PHOTO: GEORGE STEINMETZ

INSIDE

RELATED ITEMS

- **EDITORIAL P. 721**
- **REPORT P. 809**
- **REPORT BY J. MOUGINOT *ET AL.* 10.1126/science.aac7111**

GHOSTS OF OCEANS PAST

Ancient reefs and beaches can reveal how high and fast seas rose in the past—and perhaps what the future holds

By **Warren Cornwall**

Andrea Dutton's hunt for ancient coral reefs has taken her from white sand beaches along the Indian Ocean to wave-beaten cliffs beside the Caribbean. But the geologist's strangest field trip may have come last year, when she spent days at a Mexican amusement park carved from the seaside jungle of the Yucatán Peninsula.

Dutton was not there for the water rides and wild animal exhibits. She had made the trek from her lab at the University of Florida in Gainesville to sample the rocks that the park's builders had cut and exposed: the remains of coral reefs more than 100,000 years old. Dutton was stunned by the star and staghorn corals preserved in the outcrops—including a mosaic of fossils in the walls of an underground room next to a jaguar pen. "It was the most amazing exposure to a reef of that period that I have ever seen, or ever will," she recalls.

Dutton seeks out ancient reefs to understand what's in store for Earth's coastlines. She's one of a small cadre of scientists scouring the planet for evidence of how high the oceans rose when polar ice melted during previous global warming spells. The jaguar pen's fossil reefs, for instance, are providing insight into one past episode of sea level rise, driven by the decline of ice sheets in Greenland and Antarctica more than 125,000 years ago.

Accurately measuring ancient sea levels has proven to be difficult work. But by marrying gritty fieldwork with computer models, Dutton and others are showing with increasing certainty that the sea was many meters higher at times when the past climate was only slightly warmer than today. The results are providing important—and sobering—evidence for how high the seas might climb in the future.

"There are a lot of things I'm uncertain about as a scientist," says Dutton, one of the leaders of PALSEA2, an international effort by scientists to nail down the details of ancient sea levels. "But we're certain sea level is going to keep rising" with the extra heat already added to the climate in recent decades. "And not just a little bit. We've got a long way to go."

TO REACH THAT CONCLUSION, sea level researchers have focused on three periods when fossil and chemical evidence indicates that slight wobbles in Earth's orbit, sometimes abetted by elevated levels of atmospheric carbon dioxide (CO_2), triggered global temperatures that were as warm or warmer than today. Some 3 million years ago, global temperatures were 1 to 2 degrees above modern levels and CO_2 levels were about the same as today's 400 parts per million (ppm). In more recent episodes, some 125,000 and 400,000 years ago, the world was close to today's temperatures, but CO_2 levels were likely far lower, at about 250 to 300 ppm (see graphic, p. 755).

In the early 2000s, when Dutton first began trying to gauge past sea levels during

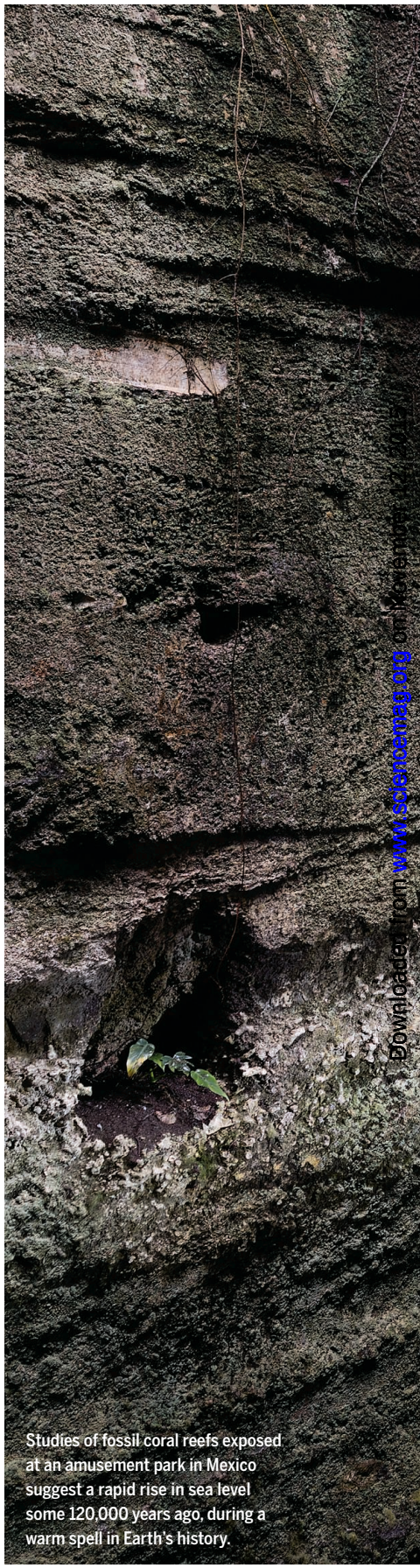

PHOTO: © KEN GARRETT

Studies of fossil coral reefs exposed at an amusement park in Mexico suggest a rapid rise in sea level some 120,000 years ago, during a warm spell in Earth's history.

Geologist Andrea Dutton examines fossil corals, such as these reefs in Florida, as part of her studies of past sea levels.

PHOTO: © MAGGIE STEBER

these periods, some scientists still simply measured how high an ancient shoreline—a beach turned to sandstone, for example, or rocks holding fossils of corals or mollusks—sits above today's sea level. They would date the outcrop, and announce how high the ocean's surface once stood.

The results were sometimes a mess. For instance, when scientists sought to determine what the sea level was 400,000 years ago, shorelines at some sites suggested it was as much as 9 meters higher than today's. But on several islands—Bermuda and the Bahamas—the evidence suggested a difference of as much as 21 meters. The sea could only have risen that high if much of East Antarctica's ice sheet, the world's biggest single mass of ice, had melted. Some scientists doubted that scenario, arguing that the high-standing beaches and corals were a fluke, perhaps created by a giant ancient tsunami.

In fact, a dizzying number of things can cloud efforts to use the past as a crystal ball. The chemical makeup of fossil coral changes over time, making it tricky to calculate its age. There's uncertainty about the depths at which corals grew, complicating efforts to estimate past sea level from an ancient reef's current height above the sea. Ice sheets can be so massive that their sheer gravity drags the ocean's water closer to them; when ice sheets are at their maximum, nearby seas are unusually high, whereas other places are below average, potentially skewing estimates of sea level around the globe. And heavy ice sheets can dimple the crust under them, while nearby land bulges upward. As Jerry Mitrovica, a geophysicist at Harvard University, puts it, Earth "is dynamic, it's evolving. And that's what distorts this lens."

In the last few years, Maureen Raymo, a marine geologist at Columbia University's Lamont-Doherty Earth Observatory in Palisades, New York, has learned just how maddening these complications can be. In 2009, she teamed with scientists from four other universities to figure out how high seas rose during the Pliocene, some 3 million years ago. That's an era scientists are particularly interested in, because CO_2 in the atmosphere then mirrored modern levels. Initially, Raymo expected to gather precise elevation measurements along hundreds of kilometers of ancient shorelines on several continents, adjust for the weight of past glaciers, and then emerge with a fairly precise estimate of sea level.

"That did not happen," Raymo recalls. The measurements were "all over the place."

That's when she learned the importance of one more factor, called dynamic topography. The geologic drama of Earth's tectonic plates is usually associated with earthquakes and fault lines. But massive sections of the planet's crust can also slowly tilt back and forth, rocking like rafts on the ocean. In the United States, for instance, the southern part of the eastern seaboard has been gradually rising relative to the northern part. Ancient shorelines in the southern region may have been uplifted by as much as 60 meters over the past 3 million years, according to one estimate.

For Raymo, that dynamic lift made one of her main research targets—a 900-kilometer-long ancient shoreline running from Georgia to Virginia—nearly unusable. Don't believe "anyone who tells you they know the Pliocene sea level to within 10 meters," she says.

FOR PERIODS more recent than the Pliocene, however, answers are coming into focus with the help of sophisticated computer modeling. In 2012, for example, Raymo and Mitrovica argued that astonishing high-end numbers for sea level rise 400,000 years

ago, from Bermuda and the Bahamas, were largely an illusion created by the weight of ice from an earlier ice age. Bermuda and the Bahamas sat on a spot that had bulged upward during the ice age and sank afterward, they concluded. After adjusting for the effect, they pegged sea level at 6 to 13 meters above today's. Since then, observations in South Africa have pointed to an even narrower range of 8 to 11.5 meters, according to a 2014 study in the *Journal of Climate*.

Along with computer models, studies done in places far from the influence of ice sheets have helped to sharpen the view of the past. Dutton, for example, headed to the Seychelles islands, 1500 kilometers off Africa's eastern coast in the Indian Ocean, to survey shorelines from 125,000 years ago. Besides being geologically quiet, the islands have ancient corals that grew vertically up the sides of rocky outcrops, providing a relatively easy-to-read yardstick of changing sea levels. (Then there are the palm trees and the silky soft beaches. "You have to choose your profession very carefully," Dutton jokes.)

Other researchers are trying to directly measure the major contributor to past sea level rise: losses of polar ice. This month, a team led by John Stone, a geologist at the University of Washington, Seattle, is scouting a place to drill into the bedrock beneath ice sheets in West Antarctica's Pirrit Hills. Their goal is to find radioactive isotopes generated by the rock's exposure to cosmic rays. The presence of the isotopes would indicate that the ice had once vanished there, exposing the bedrock. And because the isotopes decay into other elements at a predictable rate, the researchers hope to use them as a clock that shows when the ice melted. "I really do think we're going to end up knowing something significant once we get these cores," Stone says.

ALREADY, the sea level findings indicate that it may not take much more warming to melt large parts of major ice sheets. Current forecasts suggest a bump of up to 4.8°C by 2100 could lift sea levels by as much as a meter—exposing many coastal communities to serious threats from erosion and flooding. But clues from multiple past warm periods indicate that over time, ice sheets are sensitive to even smaller temperature increases, Dutton says. She was lead author of a study in *Science* this year that noted modern temperatures are close to those 125,000 years ago, when the sea level likely was 6 to 9 meters above today's.

"That suggests … we've warmed [our climate] so rapidly that the ice sheets are out of equilibrium. And they're playing catch-up," she says.

For societies today, though, the biggest question may not be how high the sea ultimately rose during past warmings, but how quickly it happened. In particular, researchers would like to know answers to two questions: Did Antarctic ice melt in sudden surges and, if so, exactly what climate conditions unleashed such an event?

"The biggest question everyone has is, 'How quickly is the West Antarctic Ice Sheet going to collapse?'" Dutton says.

She thinks the fossil reefs in the Yucatán amusement park could help provide answers. A 2009 study of the coral's growth patterns made headlines after it concluded that, some 121,000 years ago, the sea rose as much as 3 meters in less than a century. The surge appears to have drowned one reef, setting the stage for the growth of a second, higher reef, says Paul Blanchon, the study's lead author and a geologist at the National Autonomous University of Mexico's Institute of Marine Sciences & Limnology in Puerto Morelos.

Dutton has doubts about that scenario. She thinks it's possible the estimates were thrown off because the land was sinking as North American glaciers receded.

To get a clearer picture of how fast sea level rose, she would like to return to the Yucatán, as well as to reefs in Australia and Florida. She hopes to drill meters-long reef cores recording past changes in sea levels that can be dated, much as tree rings record past weather. A core where all the coral is close to the same age could indicate that water rose quickly at that time, forcing the coral to grow rapidly upward. A single core with corals spanning thousands of years would indicate a gradual change.

But given the difficulties associated with analyzing fossil corals, don't expect them to produce fine-grained estimates, such as how fast seas rose over a decade or even a century, warns Peter Clark, a geologist at Oregon State University, Corvallis. "We can talk about meters per thousand years, but I don't think we can get it any finer than that," says Clark, one of the two top authors of the Intergovernmental Panel on Climate Change's most recent assessment of sea level science.

Dutton hopes further work in the Yucatán could also help resolve another issue: whether seas rose quickly some 120,000 years ago, after roughly 13,000 years of warmth, as Blanchon has suggested, or soon after the warming began, as she believes. Because the climate varied even during the warm period, knowing the timing could help scientists better decipher what conditions triggered an ice sheet collapse, Dutton says. And understanding those conditions could, in turn, offer clues to the future of today's West Antarctic Ice Sheet, which is already showing signs of an accelerating retreat. "That's why this question—did it happen in the beginning or the end—[is a] first order question now," she says.

Answering it could require studying many more ancient shores, now perched high above seas that are, once again, on the move. ■

Warren Cornwall is a freelance writer in Bellingham, Washington.

Looking back

Studies of past periods when Earth was as warm as today, or warmer, suggest that even a few degrees rise can produce a major increase in sea level.

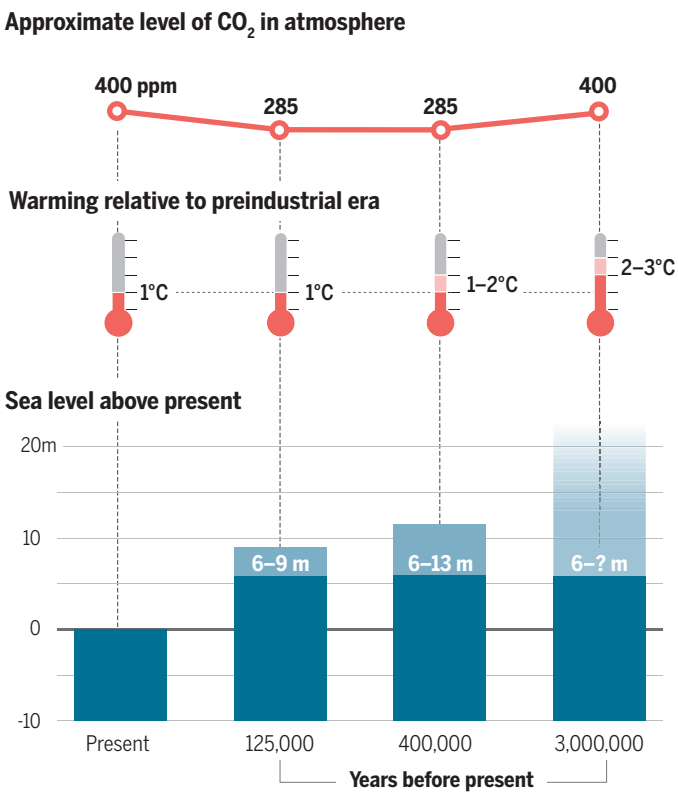

GRAPHIC: A. CUADRA/*SCIENCE*

BREAKING THE WAVES

As a defense against rising seas, shorelines made of marsh grasses and oyster reefs may work better than concrete armor

By **Gabriel Popkin** *Photography by* **Dylan Ray**

When Hurricane Irene hit North Carolina's coast in 2011, waves 2 meters high began pounding the shore. Two properties on Pine Knoll Shores, a community on one of the state's many barrier islands, provided a study in contrasts. One homeowner had installed a concrete bulkhead to protect his yard from the sea. But the churning waves overtopped and ultimately toppled the wall, washing away tons of sediment and leaving a denuded mud flat.

Less than 200 meters away, another owner had installed a "living shoreline"—a planted carpet of marsh grass that gently sloped into the water, held in place by a rock sill placed a few meters offshore. The onrushing water bent the marsh grasses almost flat, but their flexing stalks dampened the waves and their deep roots held the soil. After the hurricane passed, the grasses sprang back; the property weathered the storm largely intact.

The contrast highlights how defenses in-

A marsh constructed on Pivers Island in North Carolina is helping researchers understand the costs and benefits of so-called living shorelines.

spired by nature, rather than concrete armor, can protect coastlines from battering storms, says ecologist Rachel Gittman of Northeastern University's Marine Science Center in Nahant, Massachusetts. In a study of Irene's effects, Gittman found that in hard-hit areas along the North Carolina coast, the storm destroyed or damaged three-quarters of the seawalls and bulkheads and washed away valuable soil. Yet, shores fringed by marsh grasses experienced almost no erosion, and damaged vegetation bounced back within a year. "Plants are really good at handling big storms," Gittman says. "Bulkheads are really not."

Such findings are getting more attention as researchers and coastal planners confront rising seas—and possibly more powerful storms—caused by global warming. That double punch, they say, threatens hundreds of millions of coastal residents around the world and infrastructure worth trillions of dollars.

To be better prepared, many researchers are calling on coastal nations to rethink traditional approaches to shoreline defense, which rely largely on massive earthen dikes, rock barriers, and concrete walls. Such "gray" infrastructure damages coastal ecosystems, researchers argue, and can be difficult and expensive to adapt to changing environmental circumstances. Gittman and others argue that softer, "greener" approaches inspired by marshes, oyster reefs, and other natural features (see graphic, p. 758) can do better. With clever engineering, they say, such features can provide not only cost-effective storm protection, but also healthier ecosystems able to adapt to rising seas. "When you put in a marsh," says environmental scientist Bhaskar Subramanian of the Maryland Department of Natural Resources (DNR) in Annapolis, "you're doing good by nature."

Not everyone is enthusiastic. Many people feel safer behind concrete, and—given the potentially high stakes—policymakers and regulators have been reluctant to shelve time-honored engineering techniques in favor of less familiar approaches. Some researchers also worry that even supposedly green designs could harm marine ecosystems by introducing exotic species and foreign materials into underwater habitats.

Despite the skeptics, the push to green traditionally gray coastal defenses is gaining traction. Prompted by the devastation caused by Hurricanes Katrina and Sandy, the U.S. government is bolstering research into nature-inspired coastal engineering. And a growing number of researchers around the world are evaluating which green techniques might work best—and how gray and green engineering might be combined to create layered defenses.

"There is so much happening on this right now," says ecologist Ariana Sutton-Grier of the University of Maryland (UMD), College Park, and the National Oceanic and Atmospheric Administration (NOAA). "We probably are at a sea change in the way we approach coastal protection."

FOR MILLENNIA, humans have tried to hold back the sea. In China and along the Mediterranean, archaeologists have found evidence of seawalls and other shoreline structures some 2000 years old. And as human populations have grown, so have coastal defenses. In the United States, nearly 23,000 kilometers of shoreline—some 14% of the total—is armored, Gittman and colleagues estimated in August in *Frontiers in Ecology and the Environment*. That proportion could grow to one-third by the end of the century, they add, if coastal development continues at its current pace.

Armoring can have devastating ecological consequences. Rock and concrete barriers reflect rather than dissipate wave energy, causing fast-moving waters to scour the sea floor, destroying marsh and underwater grasses that nurture fish, crabs, and other sea life. Hard structures can also cut off critical flows of sediments from uplands to the coast, starving and obliterating beaches and marshes. And as global sea levels have risen by an estimated 20 cm over the past century, many marshes and beaches have become squeezed between the higher water and unmoving concrete.

The squeeze will worsen if global greenhouse gas emissions continue unabated. Under some scenarios, modelers warn, sea level rise could accelerate to as much as 9 mm per year, driven by melting ice sheets and the expansion of warming seawater. At the same time, warming could catalyze more powerful storms, heightening the threat of wave damage and coastal flooding. Many point to the flooding that occurred in New Orleans, Louisiana, and along the Gulf of Mexico after Hurricane Katrina in 2005, and the devastation wrought by Hurricane Sandy in 2012, as examples of what the future may hold.

The shores of the Chesapeake Bay in Maryland are among the most vulnerable in the United States: Land subsidence there is causing local sea level rise to greatly exceed the global average, making coastal areas more vulnerable to storms. In 2003, a powerful hurricane, Isabel, swept up the coast and across the Chesapeake Bay area, killing 16 people and causing $7 billion worth of damage. It also amplified one of the nation's most prominent efforts to promote living shorelines.

Not long after the storm passed, calls began coming in from distraught landowners, recalls Subramanian of the Maryland DNR, which provides coastal protection assistance to landowners. "All the calls were: 'My bulkhead is floating in the neighbor's property,'" he says.

In contrast, the agency received no complaints from landowners who had installed living shorelines with the agency's help. The constructed marshes had dampened the storm waves and reduced damage, he says, just as they would in North Carolina nearly a decade later. Soon, landowners once wedded to concrete were lining up to get help building their own protective marshes.

Today, Maryland is considered a pioneer in green coastal infrastructure. In 2008, it adopted the nation's first law requiring landowners who want to protect their waterfront to use a living shoreline unless

they can prove that only a hard structure will do the trick. The state has issued permits for more than 1000 living shorelines, almost all around the Chesapeake Bay and its tributaries. Many have not only survived but thrived through storms likely to have overwhelmed traditional gray structures.

Other states, however, have been slow to follow suit, in part because of lingering questions about the environmental impact, effectiveness, and life span of living shorelines and other nature-inspired features.

ONE RESEARCHER trying to answer those questions is ecologist Carolyn Currin of NOAA's Beaufort, North Carolina, laboratory. The lab sits on Pivers Island, a spit of land near Pine Knolls Shore. In 2000, when lab officials had to replace a failed seawall on the island, Currin persuaded them to install a living shoreline, turning an otherwise humdrum construction job into an experiment. NOAA worked with local partners and volunteers to install bags of oyster shells off the island's shore and plant marsh grasses on a graded sand slope.

The new marsh—along with a second one built on the other side of Pivers Island using a rock sill—has allowed researchers to gain new insights into the capabilities and behavior of living shorelines. One finding is that they appear to keep pace with local sea level rise, building up soil that keeps the marsh's surface above the low tide line.

They also have potentially valuable "co-benefits." The artificial marshes pack away relatively large quantities of carbon, Currin and colleagues reported (this month) in *PLOS ONE*. And, as suspected, the rock and oyster-shell sills used to anchor such marshes support more abundant and diverse communities of fish and crustaceans—including economically important species—than do traditional concrete structures, a team led by Gittman concludes in a paper in press at *Ecological Applications*.

Currin, Gittman, and colleagues also are assessing whether shorelines colonized by living oysters can provide an additional layer of defense in shellfish habitat such as North Carolina and the Gulf of Mexico. In one experiment, they have used thousands of bushels of shells to build three artificial oyster reefs off a rapidly eroding beach on Carrot Island in the Rachel Carson Reserve, not far from Pivers Island.

On a visit to the site, ecologist Joel Fodrie waded through quiet water to the reefs. The shell piles, now about 3 years old, were already protecting the beach, trapping sediment and helping it reverse past erosion losses. Better yet, the reef was coming to life, says Fodrie, who works at the University of North Carolina's Institute of Marine Sciences in Morehead City. Tiny crabs scurried across his hands as he examined shells covered with baby oysters. The youngsters should help the reef grow both vertically and horizontally, he noted, improving its protective effects. And properly placed oyster reefs have the capacity to grow in concert with even rapidly rising seas, Fodrie, the institute's Antonio Rodriguez, and colleagues reported last year in *Nature Climate Change*.

The reef project faces challenges, however, Fodrie noted. Waves have pushed some of the oyster sills toward shore and washed away some grasses that researchers had planted. But that's OK, he says. "We planned to have some things fail, so we can see where the boundaries are."

ALTHOUGH SOME SEE living shorelines as a return to nature, others see them as coastal hardening by another name. Retired earth scientist Orrin Pilkey of Duke University in Durham, North Carolina, who has called for limiting coastal development, has criticized many living shoreline projects along the Atlan-

Defending against rising seas, in gray and green

Some researchers are urging a move away from so-called gray coastal defense structures, such as seawalls, flood gates, and rock groins. They say greener structures—including natural or built marshes, oyster and coral reefs, and sandy barrier islands—can provide protection with less ecological damage, and a greater ability to adapt to rising seas. Combining green and gray structures could create hybrid, layered defenses that offer both ecological and economic benefits.

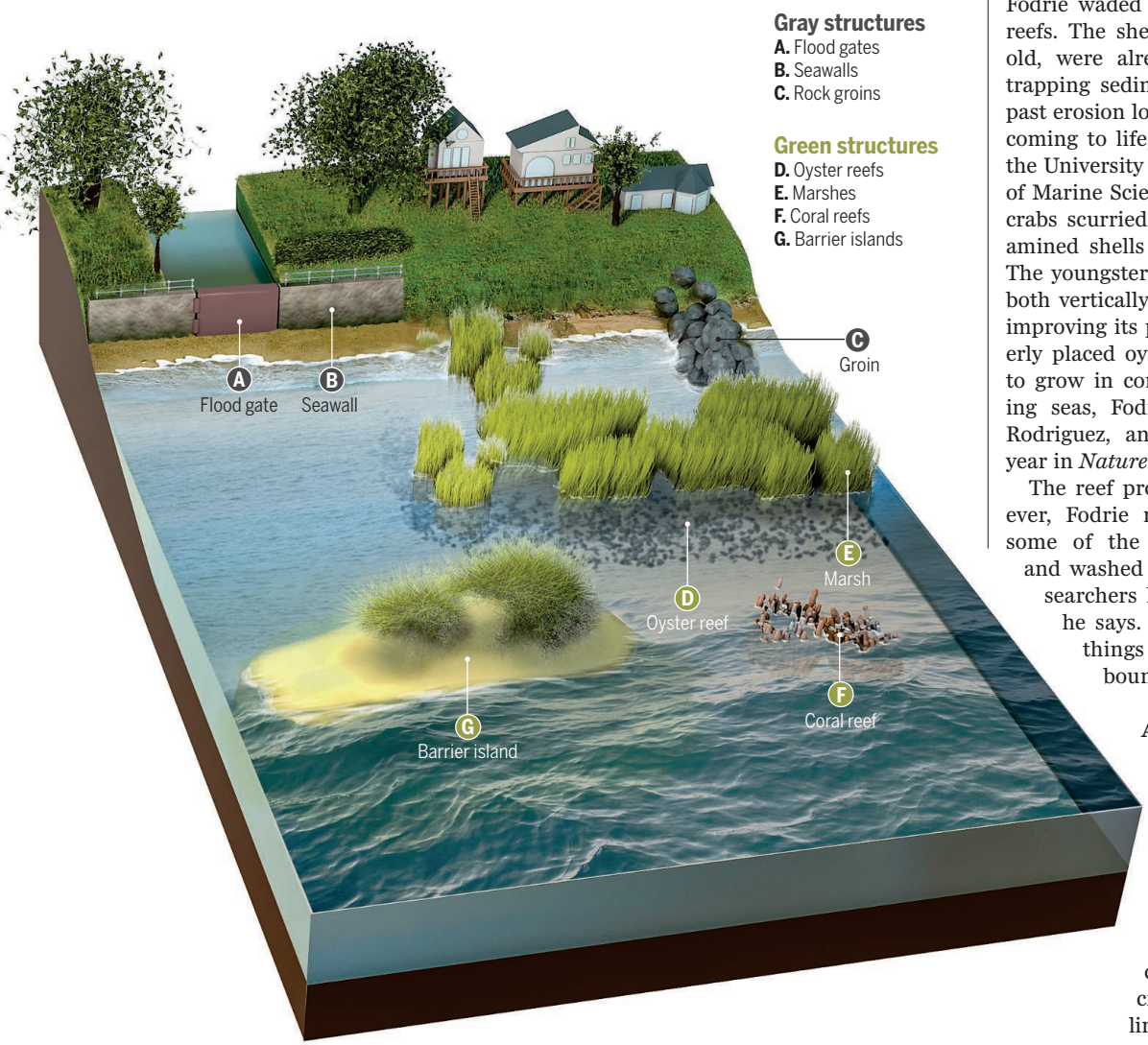

GRAPHIC: V. ALTOUNIAN/*SCIENCE*

Biologist Joel Fodrie inspects an oyster reef that researchers built to protect an eroding beach on North Carolina's Carrot Island. Within 3 years, it was colonized by oyster larvae, creating a living defense that might be able to keep pace with sea level rise.

tic coast because they make heavy use of offshore rock sills to shelter the planted grasses from wave action. The sills, he says, can bury native sea grasses and make it more difficult for fish and crabs to reach intertidal marshes.

Pilkey also complains that a lack of regulatory oversight and scientific monitoring makes it hard to figure out what works and what doesn't. "To me the living shoreline thing is the Wild West," he wrote in an email. "No standards, no enforcement, no real studies especially long term and an aura of environmental holiness."

Even living shoreline promoters acknowledge that projects can come with ecological tradeoffs. Newly constructed marshes in the Chesapeake Bay, for example, can bury sandy, near-shore habitats. "Everyone devalues flat, nonstructural bottoms," says ecologist Donna Bilkovic of the Virginia Institute of Marine Science in Gloucester Point. "But there are lots of animals that live in those sediments."

Green defenses also face substantial regulatory and political hurdles. In the United States, it can often take just a few days to obtain the needed federal and state permits to build a new bulkhead, for instance, but the paperwork for nature-inspired projects can take much longer, in part because they may involve underwater components that bury shallow-water habitats and stretch into shipping lanes. Large projects can also trigger complicated mandatory cost-benefit analyses. For gray projects, economists and engineers have long known how to calculate life span and financial return, but the task can be trickier for green projects, for which the calculus includes cobenefits such as carbon storage or improved fish habitat.

SOME COASTAL EXPERTS have concluded that combining green and gray approaches promises the best payoff, because of their complementary strengths and weaknesses: Green infrastructure is dynamic and adaptable, but can take several years to become fully established, whereas concrete works on day one. Such hybrid defenses might involve building an oyster reef or marsh in front of a concrete seawall or dike, to provide both ecological benefits and multiple layers of storm protection.

> ***"To me, the living shoreline thing is the Wild West. No standards, no enforcement, no real studies ..."***
>
> **Orrin Pilkey**, Duke University

The U.S. Army Corps of Engineers has embraced such "gray-green" thinking, and is promoting it in concert with NOAA and other institutions through an initiative called the Systems Approach to Geomorphic Engineering. The hope, says UMD's Sutton-Grier, is to "capitalize on the strengths of both approaches—you can use gray to protect green as it establishes, or green to protect gray so that [its] lifetime is longer."

The idea is also catching on internationally, with Korea, China, and Australia recently considering or installing combinations of marshes and hard structures. In the Netherlands, where coastal defenses are a matter of national existence, planners are introducing salt marshes and shellfish beds to help lessen storm impacts on seawalls and dikes. (Japan also considered greening its shoreline protection arsenal after the devastating 2011 tsunami, but has so far opted for even larger seawalls.)

The success of green infrastructure, however, may ultimately depend less on governments than on the willingness of millions of individual landowners to try something new, because so much coastline is in private hands. Persuading risk-averse homeowners can be a frustrating process, Gittman says. After Hurricane Irene, she showed the landowner with the toppled bulkhead how much better his neighbor's living shoreline had performed.

But the landowner opted to build a new concrete bulkhead instead, and then put his house up for sale. "People are stubborn," Gittman says. ■

Gabriel Popkin is a freelance writer in Mount Rainier, Maryland. *Reporting support provided by a fellowship from the Institute for Journalism and Natural Resources.*

MOVEABLE FEAST

As fish stocks move in response to warming, regulators struggle to keep pace

By **Marianne Lavelle**

In the early 2000s, trawler crews working the Celtic Sea off Ireland noticed something unusual. Small, spiny, bright orange fish, called boarfish, began appearing in their nets in huge numbers. Previously, the intruders had been a minor nuisance; their sharp spines jammed equipment and damaged the soft flesh of more valuable species, such as cod and hake. Irritated crews tossed them overboard.

As boarfish schools grew, however, the problem became an opportunity. Trawlers retooled to target the fish, which were turned into meal and oil. Boarfish went from trash to treasure, and they now generate more than $10 million annually for Irish fleets.

Scientists aren't exactly sure what is causing the boarfish boom, but there is evidence that a warming ocean is playing a role. And for fishery managers, the boarfish has become one symbol of an emerging global issue: the often surprising disruptions that climate change can create in the world's fisheries, as marine populations move, flourish, and wither as a result of warming seas.

PHOTO: © JEFFREY ROTMAN/CORBIS

Some stocks of Atlantic cod, long a mainstay of commercial fishing, have been hit hard by warming oceans, recent research suggests.

"Climate change is pushing whole [marine] systems to a state we haven't experienced before," says fisheries ecologist William Cheung of the University of British Columbia, Vancouver, in Canada. The reshuffling is creating challenges for scientists seeking to understand a rapidly changing ocean. It is also taxing fishery managers, who tend to view the oceans "as stable, or steady-state," instead of preparing for change, says Richard Merrick, chief scientist of the U.S. National Oceanic and Atmospheric Administration (NOAA) Fisheries in Silver Spring, Maryland. As a result, policymakers are scrambling to build management schemes that can cope with moving fish stocks and shifting ecosystems. The stakes are high, they note, given that ocean fisheries generate $195 billion annually in the United States alone and are a key food source for hundreds of millions of people.

IT HAS LONG BEEN A CHALLENGE to manage marine populations so that the ocean keeps on giving. In the early 1600s, when English explorer John Smith arrived in Jamestown, Virginia, he famously marveled at "more sturgeon than could be devoured by dog or man." Within a few centuries, however, people had severely depleted that species and many others.

Slowly, fishers and scientists learned how to set more sustainable catch limits, by combining a greater knowledge of the reproductive biology of marine species with improved surveying methods and economic data. By the late 20th century, many nations had imposed extensive controls on their fishing fleets, and even struck international agreements to prevent conflicts over stocks that swam across national borders. Such rules have helped many overfished stocks bounce back. Even relatively well-informed policies, however, have often proven difficult to implement, in part because of the ocean's great natural variability. Powerful currents can change course, huge water masses can shift, and fish and shellfish populations are prone to seemingly random booms and busts.

Now, fishery managers say climate change is making their job even more complicated. Oceans have helped moderate the impact of fossil fuel burning by absorbing an estimated one-third of the carbon dioxide that humans have added to the atmosphere, as well as much of the heat generated by greenhouse warming. But marine life is bearing the brunt of living in a giant sink for heat and carbon, which is acidifying as well as warming the waters.

Corals, crustaceans, seagrasses, and phytoplankton are among the many groups of organisms already showing effects from warming seas, researchers say. And fish are on the move, scientists have concluded in numerous studies, including a major survey led by ecologist Malin Pinsky of Rutgers University, New Brunswick, in New Jersey. After studying more than 40 years of census data on some 350 fish species found off North America, his team concluded that some 70% of the species were shifting their ranges, or moving to deeper or shallower waters, in response to changes wrought by warming. The researchers predicted in a 2013 *Science* paper that "rapid range shifts will fundamentally reorganize marine communities" and could "confound traditional management approaches."

AN OLD U.S. COAST GUARD STATION near Tuckerton, New Jersey, now a marine laboratory, holds an eerie record of those changes. More than 1 million translucent fish larvae float in glass vials, cataloged by species and the date they were captured.

Laboratory Director Ken Able, a biologist at the Rutgers University Marine Field Station, started methodically catching the hatchlings 26 years ago in a nearby estuary. Originally, the goal was to learn more about populations of summer flounder (*Paralichthys dentatus*), a much-prized catch. Ultimately, however, Able and his colleagues realized that the estuary is an ideal location for observing the transformation of the North Atlantic. Larvae spawned from Canada to the Caribbean and beyond ride to the region on two great currents—the Labrador Current from the north and the Gulf Stream from the south.

As a result, Able's larvae library has become a record of change. Over time, southern-dwelling species, such as the Atlantic croaker (*Micropogonias undulatus*), have become more abundant. Northern species, including

the Atlantic herring (*Clupea harengus*) and three-spined stickleback (*Gasterosteus aculeatus*), have begun to disappear.

U.S. East Coast fishery managers are still grappling with how their approach should change to address the ebb and flow of these species, some of which is due to fishing practices rather than climate change. But the issue has become urgent for managers in the eastern North Atlantic. Over the past decade, large schools of mackerel (*Scomber scombrus*) began appearing in the waters off Iceland, signaling a northward expansion of the fish's range linked to warmer waters. In 2009, amid a financial crisis, Iceland unilaterally increased its mackerel catch, prompting outrage from competing fleets in the European Union and Norway, which traditionally have had rights to the majority of the catch. They complained that Iceland's expanding fishery (and another in the Faroe Islands) was imperiling their own mackerel stocks.

The science underlying such claims became the focus of fierce debate, with the parties disagreeing over the size of the whole population—a key to setting safe catch limits—and whether the competing fleets were exploiting the same or distinct populations. Opponents even had trouble agreeing on what waters should be included in the mackerel's range, and how best to count the fish.

In a bid to clarify matters, researchers have launched efforts "to make sure that they're discussing the same stocks, using the same methodology … [but] it's quite difficult to maintain a standard that compares apples to apples," says Manuel Barange, director of science at the Plymouth Marine Laboratory in the United Kingdom.

In the meantime, the political impasse has continued, meaning that Iceland has been setting its own catch quotas, instead of working with other nations to establish regionwide catch limits that reflect the changing mackerel distribution.

THE MACKEREL DEADLOCK highlights the difficulty of using traditional fishery surveys to track and predict climate-induced population shifts. Current methods, including the use of dedicated research trawlers to make periodic but limited hauls, may not allow researchers to "adequately capture the future population dynamics in a changing ocean," NOAA officials noted earlier this year in a report. What's more, "a large percentage of the ocean is not being surveyed, let's face it," says Jeff Kaelin of Cape May, New Jersey, a commercial fishing executive and member of regional council that helps set U.S. catch quotas. That means plenty of blind spots where scientists aren't able to see and react to sometimes subtle shifts.

To help fill the gaps, some fishery managers and fishers would like to see more systematic use of commercial fishing vessels to gather information. In the United States, for example, the South Atlantic Fishery Management Council, which sets fishing quotas in federal waters from South Carolina to Florida, is exploring the idea of equipping fishing boats to measure environmental variables, such as temperature. That would allow researchers to study how changes in those conditions affect catches.

The bigger dream, however, is to use such information—combined with real-time data from satellites, buoys, and other platforms—to predict future marine changes, much as weather services now forecast droughts and floods. Such a capability might have enabled fishery managers in New England, for instance, to give fishers advance warning of a record ocean heat wave in 2012 that brought warm-water squid as far north as the Gulf of Maine, and caused lobster catches to rise. Local fishers were unable to take advantage of the squid windfall because there wasn't enough notice to retool their boats with the proper gear, and lobsters rotted in trucks because processors weren't ready.

BETTER OCEAN CLIMATE monitoring systems might also help prevent fishery calamities, a recent study suggests. The collapse of cod (*Gadus morhua*) stocks off New England and Canada's eastern coast has been one of the most studied and debated fishery catastrophes in the world. In both nations, dramatic cod population declines since the 1980s have led officials to essentially shut down once lucrative fisheries. Researchers have long laid much of the blame on overfishing, but have suspected that changing ocean conditions—including warmer waters—also played a role.

That idea got a major boost last month with the publication of a study concluding that rapid ocean warming appears to have catalyzed the decline of one major cod stock living in the Gulf of Maine. Satellite data show that from 2004 to 2013 the ongoing warming of surface waters in the gulf greatly accelerated, a team led by oceanographer Andrew Pershing of the Gulf of Maine Research Institute in Portland, Maine, reported in *Science*. Over the past decade, the Gulf of Maine became the fastest warming spot in the world's oceans, making it hard for young cod to survive. At the time, says Pershing, fishery managers didn't understand what was happening, and so allowed catch quotas to remain too high.

The moral of the story, Pershing says, is

Polar invasion

If greenhouse gas emissions remain high, the Arctic and Southern oceans could see the arrival of up to two new species per half-degree of latitude by 2050 (red areas), according to one study of how more than 800 exploited fish and shellfish stocks might respond to climate change. At the same time, many marine species would disappear from waters closer to the equator.

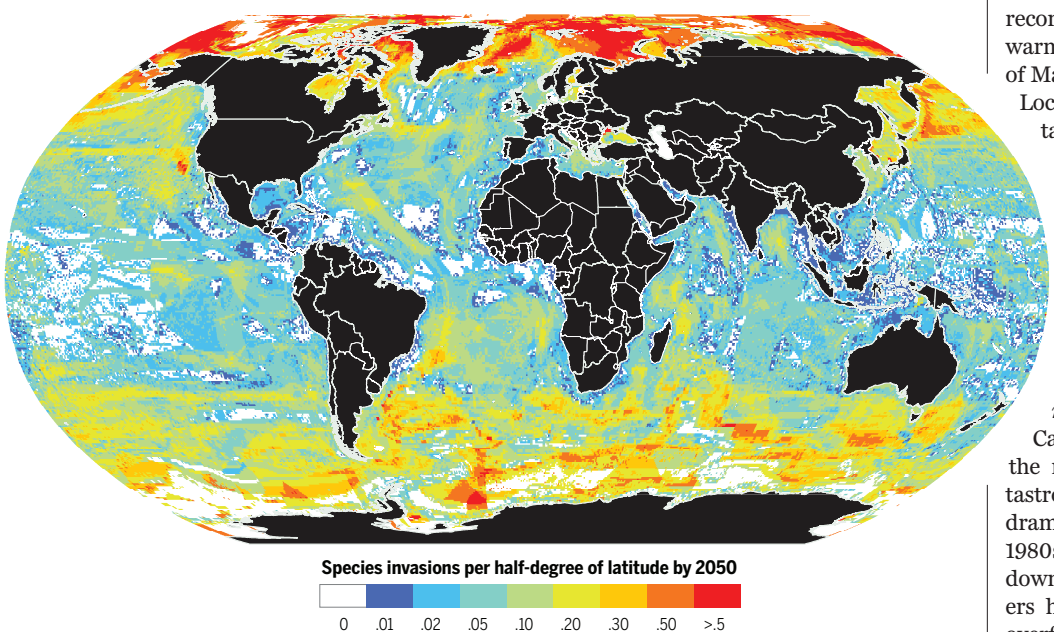

GRAPHIC: WILLIAM CHEUNG, ADAPTED FROM CHEUNG *ET AL.*, *ICES JOURNAL OF MARINE SCIENCES* **72**, (10 OCTOBER 2014) © ACS

For more than 25 years, biologist Kenneth Able has been collecting fish larvae (below) from an estuary in New Jersey, providing clues to a changing ocean.

that "as ecosystems around the world begin to encounter these conditions that are really changing, using history as your guide is not going to be very effective." Gib Brogan, an advocate with the conservation group Oceana in Boston, says the study also underscores the need for fishery regulators to "put a buffer in [management plans] for the uncertainty that comes with climate change."

THAT'S ADVICE that Ireland's emerging boarfish fishery is trying to heed. As catches boomed—reaching 144,000 metric tons in 2010, Ireland's second biggest catch behind mackerel—European fishery managers began to worry. Nobody, they realized, knew much about the little orange fish: how many there were, how quickly they reproduced, or even how long they lived. The managers feared that unregulated fishing could wipe out the stock before the industry even established itself.

Some of the more than 1 million larvae collected by Able's group.

To buy time, the E.U. fisheries commission imposed new rules that reduced catches—and boarfish captains and others began raising money to fund the needed science. In a collaboration that some fishery managers will envy, scientists conducted the first sonar surveys of boarfish schools from commercial fishing boats, with guidance from fishermen on where to find the fish. By analyzing growth rings in fish ear bones, Danish scientists determined boarfish live as long as 30 years. Biologists also calculated how quickly they reproduce, and learned that they have few natural predators. Using old fishing records and new genetic testing methods, they determined that Irish boarfish are homebodies—they didn't migrate from another location to the North Atlantic. And they realized the species has been there a long time, albeit in smaller numbers. That suggests that some change in the environment—an increased food supply, perhaps—boosted boarfish reproduction. And warming waters are a likely catalyst, many scientists believe.

Now, E.U. fishery managers are drawing on that information to devise a long-term management plan for the boarfish. Researchers hope it will acknowledge the possibility of future ocean changes and ecosystem shifts. And the experience could become a model for how other fishing communities can work with scientists to adapt to the changes that climate change will bring, says Kari Stange, a social scientist at Wageningen University in the Netherlands.

Stange recalls one Irish fisherman who was preparing to travel to E.U. headquarters in Belgium to discuss how the new fishery would be managed. He said: "We can't just go to Brussels and say that a lot of fishermen think there's a lot of fish out there," Stange recalls. "They knew they had to come with science." ■

Marianne Lavelle is a freelance journalist in Arlington, Virginia.

PHOTOS: © DREW GURIAN

PERSPECTIVE

The silent services of the world ocean

Thomas F. Stocker

The most recent comprehensive assessment carried out by the Intergovernmental Panel on Climate Change has concluded that "Human influence on the climate system is clear," a headline statement that was approved by all governments in consensus. This influence will have long-lasting consequences for ecosystems, and the resulting impacts will continue to be felt millennia from now. Although the terrestrial impacts of climate change are readily apparent now and have received widespread public attention, the effects of climate change on the oceans have been relatively invisible. However, the world ocean provides a number of crucial services that are of global significance, all of which come with an increasing price caused by human activities. This needs to be taken into account when considering adaptation to and mitigation of anthropogenic climate change.

Earth's oceans are an integral component of the climate system, and as they change and are changed by climate (*1*), so are the services that they provide to people. The ocean service most directly related to human welfare is food production, which is increasingly needed in addition to that from land (*2*). However, there are other, less obvious services that are provided by the ocean, which are associated with some of its key physical properties. The ocean takes up more than 90% of the excess energy in the climate system that results from the altered energy balance at the top of the atmosphere (*3*). The ocean continues to take up energy year after year, and the warming is now detectable on a worldwide scale down to depths of more than 2000 m (*4*). This is unequivocal evidence of recent global warming. Ocean heat uptake continuously and significantly slows atmospheric warming. This physical ocean service is thus an important element in the natural mitigation of climate change, but that heat uptake is only temporary and will be weakening in the future: Excess heat is mixed downward from the sea surface, so the ocean water column will become more stable and capable of less heat uptake as atmospheric warming progresses. Vertical mixing and circulation processes, particularly in the deep-water formation areas of the North Atlantic and the Southern Ocean, may slow down as a consequence of increased water column stability and thus make surface-to-depth transport of heat less efficient in the future. Some indication of a decline has been measured in the North Atlantic (*5*), but continued observation programs there, and in other critical locations in the ocean, are essential to learn more about ocean tipping elements in the Earth system (*6*, *7*).

There is a high price to be paid for this ocean system service, which has the potential to alter a number of parts of a complex and fragile system. Ocean warming will affect large-scale ocean circulation, the distribution of heat and salt in the ocean, the extent of areas of tropical cyclone genesis, and the land-ocean temperature difference, which is the key driver of monsoon systems and determines the statistics of important modes of climate variability (*8*). A warming ocean also affects both the intensity and frequency of extreme events. Recent studies indicate that different rates of heating in the equatorial Pacific Ocean profoundly affect the El Niño–Southern Oscillation by making the positive phase more extreme and thereby causing heavier rainfall in the eastern equatorial Pacific (*9*). El Niño has robust teleconnections to equatorial South America (wetter and warmer in the west and drier in the east), the western equatorial Pacific (drier and warmer), and a southern section of North America (wetter and cooler). Similar increases in extremes are projected for the Indian Ocean Dipole (*10*), with serious implications for the monsoon system, which is crucial for agriculture and food production in many countries in this region. Warming of the surface ocean also enlarges the area over which tropical cyclones pick up energy and thus increases the probability of conditions favorable for the development of these extreme events. Although it remains difficult to provide robust projections of changes in the location, frequency, and intensity of tropical cycles (*1*), a poleward shift of the zone of maximum intensity has already been observed (*11*). This shift will require new efforts of adaptation in regions that were previously less affected by these tropical storms. The altered regional variability and extremity of these storms both exacerbate the impacts on some of the most vulnerable countries. This has to be added to the price tag of the global ocean service of heat uptake, caused by the modification of Earth's energy balance due to the burning of fossil fuels and deforestation.

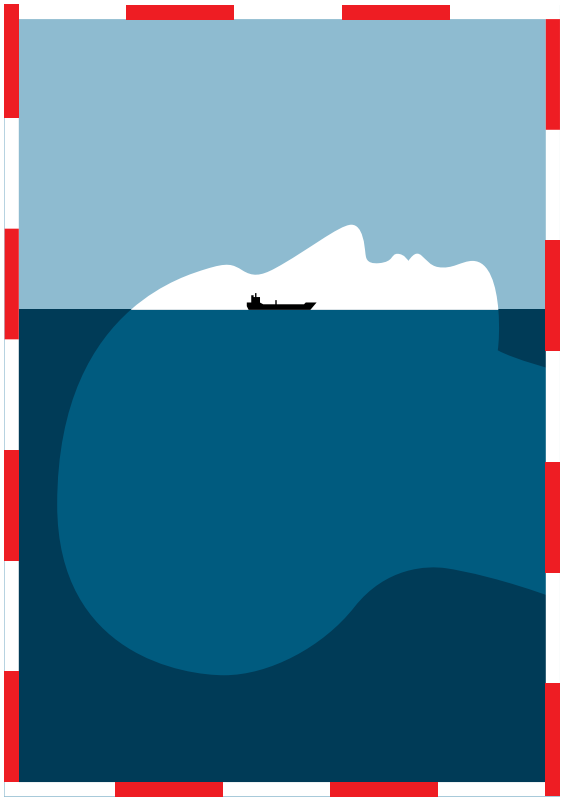

Climate change as seen by Claude Kuhn, a renowned graphics artist from Bern. Sea-level rise is a consequence of climate change, caused by human activities, that will have pervasive and irreversible impacts.

The second key ocean service is the storage and global distribution of excess water from rapidly melting land glaciers (*12*) and the ice sheets of Greenland and Antarctica (*13*), a result of the role of the ocean as the most important reservoir of the global water cycle (*14*). The price of this service is, of course, sea-level rise, which threatens low-lying islands and coastal communities around the world (*15*). Currently, almost 50% of global mean sea-level rise stems from the storage of this excess water. A somewhat smaller fraction is caused by ocean heat uptake, which accounts for about 40% of current sea-level rise. There is growing evidence that the price for this service may rise to much higher levels, possibly even beyond control. Recent model results suggest that critical thresholds for the stability of the West Antarctic Ice Sheet may have been crossed already (*16*). This would mean that sea level could rise by more than 4 m more than the rise projected by calculations based on ocean thermal expansion, glacier melting, and mass loss from polar ice sheets

Climate and Environmental Physics, Physics Institute and Oeschger Centre of Climate Change Research, University of Bern, Bern, Switzerland. E-mail: stocker@climate.unibe.ch

alone (*17*). Although such a scenario would take many centuries to unfold, the challenge associated with adaptation to the loss of coastal land around the world would be beyond imagination. The ocean plays a crucial role in accelerating this process. Although the surface of the Antarctic ice sheet is still quite well shielded from the immediate consequences of atmospheric warming, the fringes of the Antarctic ice sheet are in contact with the ocean water. Global ocean heat uptake now also has warmed the waters circulating around Antarctica (*18*), thus causing very effective and continuous melting of the floating ice shelves from below, the loss of which contributes to a destabilization of vulnerable ice streams through the loss of the buttressing effect that ice shelves provide. Effective management of this risk, by geoengineering for example, seems futile because the extra energy that the ocean has accumulated through our past CO_2 emissions is "safely" stored and will continue to heat the fringes of Antarctica for centuries to come, even though the atmosphere may slowly cool again if global CO_2 emissions are stopped (*19*).

The third key service is the world ocean's uptake of CO_2 emitted by humans. This uptake causes ocean acidification; i.e., an increase in the acidity of seawater. The best estimate for the recent uptake of anthropogenic CO_2 is 2.9 ± 0.5 Gt of carbon in 2013, or nearly 30% of the total global emissions that year (*20*). About 28% of the cumulative anthropogenic CO_2 emissions from 1750 to 2011 is stored in the world ocean (*1*), an amount roughly equivalent to the carbon uptake by the land biosphere since the beginning of the Industrial Revolution. Although the ocean has been a very dependable reservoir of carbon uptake, this service also comes at a price. That price is ocean acidification, a process whose price tag is still largely a blank because we do not know the consequences of large-scale ocean acidification for marine ecosystems, even though they already are recognized as a serious committed risk, particularly in scenarios of high greenhouse gas emissions (*21*). Possible impacts of ocean acidification on marine organisms are changes in growth, body size, feeding, and reproductive success. Impacts such as these have the potential to disrupt the world's largest food webs and ultimately to diminish the fish catch potential in many regions of the world ocean (*22*). For example, one direct impact of warming on ocean food production is that tropical species are increasingly favored, a shift that already has been observed (*23*) and which poses a specific adaptation challenge to those coastal societies, particularly in the tropics, which already have to cope with high levels of vulnerability.

Of all the projections of future climate change, those of ocean acidification on a global scale have the smallest uncertainties (*1*). For a given emission scenario, those small uncertainties enable possibly the only case of robust predictability of an Earth system tipping element: the crossing of the critical threshold of calcium carbonate undersaturation. Model simulations show that this threshold will be first crossed in the Arctic (*24*), even as early as this decade. Progressively larger areas of the ocean will be affected by undersaturation as CO_2 emissions continue. Undersaturation is considered a significant stressor for calcifying organisms and thus will have a serious impact on marine ecosystems worldwide.

Given the prominent role of the ocean in the Earth system as a vital service provider, one wonders why so little attention is still paid to its physical state and the health of its ecosystems in the policy arena. Should we not step up efforts to better measure, understand, and project ocean processes? Many impacts on land due to climate change have been documented, and some irreversible changes have already been identified, such as committed global glacier melting, for instance. Our ignorance of the state of the ocean does not mean that impacts are not happening there; impacts occur whether they are visible to us or not. Perhaps the vastness of the world ocean makes us think that it is safe from our influence and that there still is time to act and avoid the most dangerous and pervasive impacts and consequences of our activities on ocean system services.

We must recognize that Article 2 of the United Nations Framework Convention on Climate Change (UNFCCC), which calls for the prevention of "dangerous anthropogenic interference with the climate system," encompasses much more than the currently agreed-upon maximum warming target of 2°C by the countries that are party to the UNFCCC. The ocean is not explicitly mentioned in Article 2, although there are ample reasons to argue that it should be. Of equal importance to climate warming are the problems of ocean acidification, which is not at all addressed by the warming target; sea-level rise, also not well represented by a target of atmospheric warming; and marine food production, which involves many more drivers than just atmospheric temperature and will suffer impacts due to human activities that are still poorly identified and understood. For each of these issues, we could formulate an additional target.

A combination of such targets must guide our progress toward a sustainable climate future. The challenges of a more holistic approach to Earth system change mitigation will require much more effort by all parties (*25*), in order to keep the door to limiting climate change at a level where most regions and communities will be able to adapt, from closing before our very eyes (*26*). Thorough research, well-designed scientific programs, and international initiatives will provide us with a much better understanding of the ocean and its key influence on all other components of the Earth system. That scientific understanding will be a prerequisite for a responsible stewardship of the world ocean and therefore continued ocean system services and functioning marine ecosystems.

REFERENCES AND NOTES

1. Intergovernmental Panel on Climate Change, Summary for Policymakers, in *Climate Change 2013: The Physical Science Basis. Contribution of Working Group I to the Fifth Assessment Report of the Intergovernmental Panel on Climate Change*, T. F. Stocker *et al.*, Eds. (Cambridge Univ. Press, Cambridge, 2013), pp. 1–30.
2. R. A. Watson *et al.*, *Nat. Commun.* **6**, 7365 (2015).
3. M. Rhein *et al.*, in *Climate Change 2013: The Physical Science Basis. Contribution of Working Group I to the Fifth Assessment Report of the Intergovernmental Panel on Climate Change*, T. F. Stocker *et al.*, Eds. (Cambridge University Press, Cambridge, 2013), pp. 255–316.
4. D. Roemmich *et al.*, *Nat. Clim. Change* **5**, 240–245 (2015).
5. M. A. Srokosz, H. L. Bryden, *Science* **348**, 1255575 (2015).
6. T. F. Stocker, A. Schmittner, *Nature* **388**, 862–865 (1997).
7. T. M. Lenton *et al.*, *Proc. Natl. Acad. Sci. U.S.A.* **105**, 1786–1793 (2008).
8. J. H. Christensen *et al.*, Climate phenomena and their relevance for future regional climate change, in *Climate Change 2013: The Physical Science Basis. Contribution of Working Group I to the Fifth Assessment Report of the Intergovernmental Panel on Climate Change*, T. F. Stocker *et al.*, Eds. (Cambridge Univ. Press, Cambridge, 2013), pp. 1217–1308.
9. W. Cai *et al.*, *Nat. Clim. Change* **5**, 849–859 (2015).
10. B. Ng, W. Cai, K. Walsh, A. Santoso, *Sci. Rep.* **5**, 11697 (2015).
11. J. P. Kossin, K. A. Emanuel, G. A. Vecchi, *Nature* **509**, 349–352 (2014).
12. M. Zemp *et al.*, *J. Glaciol.* **61**, 745–762 (2015).
13. E. Hanna *et al.*, *Nature* **498**, 51–59 (2013).
14. T. F. Stocker, The ocean as a component of the climate system, in *Ocean Circulation and Climate, 2nd Edition. A 21st Century Perspective*, G. Siedler *et al.*, Eds. (Academic Press, Oxford, ed. 2, 2013), pp. 3–30.
15. A. B. A. Slangen *et al.*, *Clim. Change* **124**, 317–332 (2014).
16. I. Joughin, B. E. Smith, B. Medley, *Science* **344**, 735–738 (2014).
17. J. A. Church *et al.*, Sea level change, in *Climate Change 2013: The Physical Science Basis. Contribution of Working Group I to the Fifth Assessment Report of the Intergovernmental Panel on Climate Change*, T. F. Stocker, *et al.*, Eds. (Cambridge Univ. Press, Cambridge, 2013), pp. 1137–1216.
18. S. Schmidtko, K. J. Heywood, A. F. Thompson, S. Aoki, *Science* **346**, 1227–1231 (2014).
19. G.-K. Plattner *et al.*, *J. Clim.* **21**, 2721–2751 (2008).
20. C. Le Quéré *et al.*, *Earth System Sci. Data* **7**, 47–85 (2015).
21. J.-P. Gattuso *et al.*, *Science* **349**, aac4722 (2015).
22. H.-O. Pörtner *et al.*, Ocean systems, in *Climate Change 2014: Impacts, Adaptation, and Vulnerability. Part A: Global and Sectoral Aspects. Contribution of Working Group II to the Fifth Assessment Report of the Intergovernmental Panel on Climate Change*, C. B. Field *et al.*, Eds. (Cambridge Univ. Press, Cambridge, 2014), pp. 411–484.
23. W. W. L. Cheung, R. Watson, D. Pauly, *Nature* **497**, 365–368 (2013).
24. M. Steinacher, F. Joos, T. L. Frölicher, G.-K. Plattner, S. C. Doney, *Biogeoscience* **6**, 515–533 (2009).
25. M. Steinacher, F. Joos, T. F. Stocker, *Nature* **499**, 197–201 (2013).
26. T. F. Stocker, *Science* **339**, 280–282 (2013).

10.1126/science.aac8720

PERSPECTIVE

The deep ocean under climate change

Lisa A. Levin[1]* and Nadine Le Bris[2]

The deep ocean absorbs vast amounts of heat and carbon dioxide, providing a critical buffer to climate change but exposing vulnerable ecosystems to combined stresses of warming, ocean acidification, deoxygenation, and altered food inputs. Resulting changes may threaten biodiversity and compromise key ocean services that maintain a healthy planet and human livelihoods. There exist large gaps in understanding of the physical and ecological feedbacks that will occur. Explicit recognition of deep-ocean climate mitigation and inclusion in adaptation planning by the United Nations Framework Convention on Climate Change (UNFCCC) could help to expand deep-ocean research and observation and to protect the integrity and functions of deep-ocean ecosystems.

Most habitable space for life on Earth is not terrestrial. More than 90% of its livable volume is in the deep ocean, below water depths of 200 m. The diverse ecosystems in this vast realm play a key role in regulating Earth's climate by absorbing excess heat and CO_2 from the atmosphere. The deep ocean thus helps to buffer the greenhouse effect, but in the process it becomes warmer, more acidic, and less oxygenated (*1*) (Fig. 1). Such changes threaten ocean productivity, biodiversity, and provisioning of living resources (*2*). Potential loss of deep-sea biodiversity may suppress adaptation capacity and limit the living library of species, genes, and biomolecules available to future generations (*3*). The regulating capacity of the deep sea slows climate change while recycling nutrients for surface ecosystems, thus supporting food provision and providing economic and societal benefits (*1*, *2*). However, because the deep ocean is vast and expensive to access, most of its species have not yet been described (*4*). Most climate change impacts in the deep ocean will remain unknown unless attention is directed to its vulnerable ecosystems.

Several features of deep-ocean ecosystems set them apart from those of the surface and coastal ocean and shape their response to climate change (*4*). Satellite mapping and robotic studies have shown the seafloor to be highly heterogeneous. Numerous deep-sea habitats, such as seamounts, canyons, hydrothermal vents, and methane seeps, are hotspots of biodiversity and biomass, concentrating photosynthetic or chemosynthetic energy and sometimes providing essential commercial resources.

There are also vast abyssal habitats beneath low-nutrient (oligotrophic) waters. In these habitats, time almost stands still; potato-size Mn nodules form over millions of years, organisms grow slowly, and full recovery from human disturbances might require centuries or more. These ecosystems are all directly connected to climate change through the transport of heat, oxygen, CO_2, and particulate organic carbon (POC) from the ocean surface through ocean circulation and mixing (*1*). In these deep-sea settings, animals can live for hundreds (fish) to thousands (colonial coral) of years. Great longevity and environmental stability may confer limited tolerance to change, limited adaptation ability, and possibly a long time lag between seafloor change and detectable change in fish production or carbon sequestration (*5*). For more than half of the ocean that lies beyond national jurisdictions, different regulators are responsible for the management of living resources in the water column and of the mineral resources on the seafloor, with biodiversity and its climate-change vulnerability existing in a policy vacuum (*6*).

Warming

Few long-term hydrographic or biodiversity data series exist for the deep ocean on climate-relevant time scales (typically several decades). Repeat hydrographic surveys have allowed estimates of decadal warming in deep basins, yielding an average temperature increase of up to 0.1°C per decade in the global ocean (*7*). The situation is, however, heterogeneous among and across deep-sea basins. Much higher warming rates are, for example, documented in the Arctic (*8*) and the southern Ocean (*9*).

Most deep-sea species live in very stable thermal regimes; warming of 1°C or less may exert stress or cause shifts in depth or latitudinal distributions and alter species interactions. In the Palmer Deep near the Antarctic Peninsula, warming above a 1.4°C threshold has allowed invasion of lithodid crabs (Fig. 2A), voracious predators

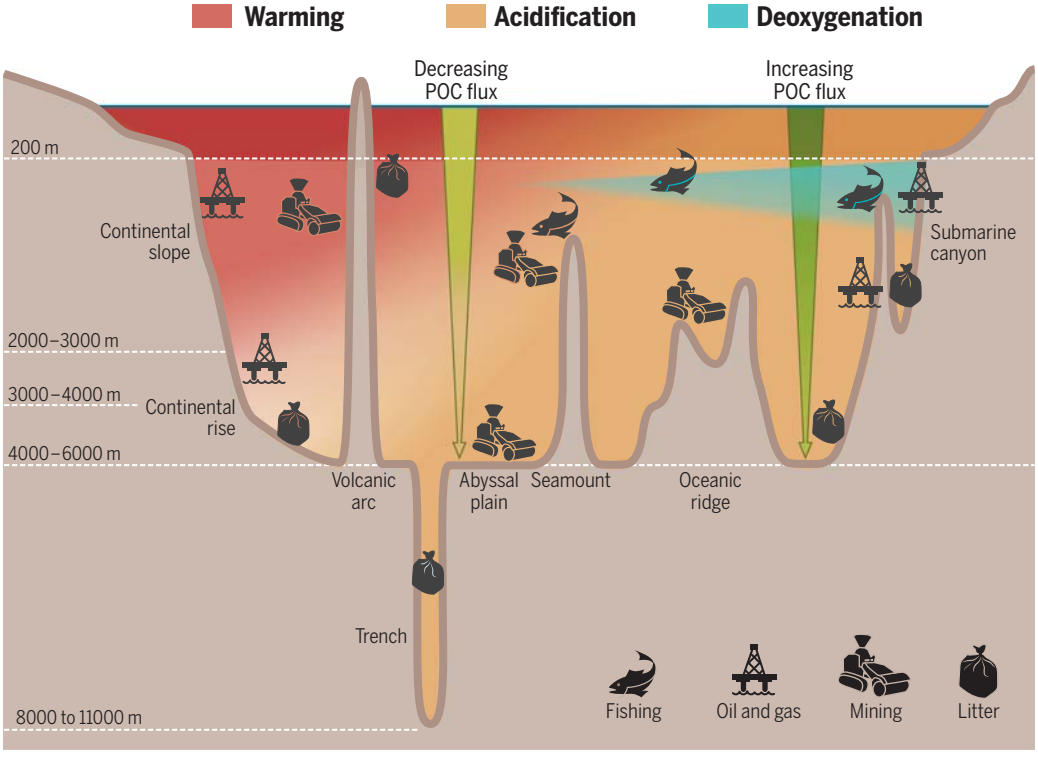

Fig. 1. Humans and climate change in the deep ocean. The schematic illustrates the depth-resolved confluence of current and proposed human exploitation activities and waste disposal with CO_2-induced change in the temperature, pH, and oxygenation of the deep ocean. Overlap of anthropogenic and climate stressors will be greatest along continental margins and at bathyal depths, but changes throughout the deep ocean will compromise ecosystem services globally.

[1]Center for Marine Biodiversity and Conservation, Scripps Institution of Oceanography, University of California San Diego, La Jolla, CA 92093-0218, USA. [2]Sorbonne Universités, UPMC Univ. Paris 6, CNRS, Laboratoire d'Ecogéochimie des Environnements Benthiques, Observatoire Océanologique, 66650 Banyuls-sur-Mer, France.
*Corresponding author. E-mail: llevin@ucsd.edu

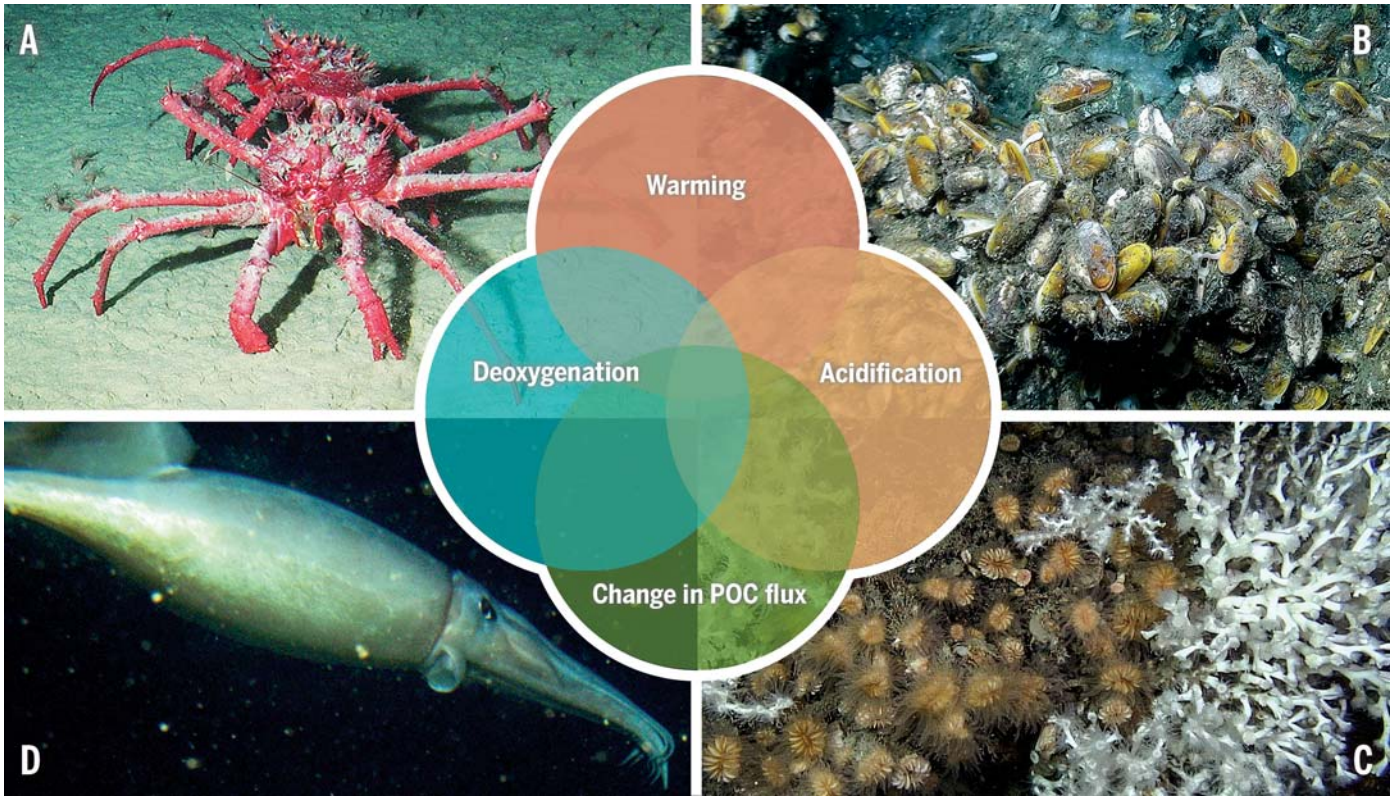

Fig. 2. Winners and losers from exposure to interacting climate stressors. (**A**) King crabs invading Palmer Deep in Antarctica enabled by warming (*9*). (**B**) Cold seep fauna may expand as warming promotes methane release from the seafloor (*12*), such as occurs at sites recently discovered along the Atlantic coast. (**C**) Cold-water coral reefs vulnerable to warming and acidification in Mediterranean canyons. (**D**) Hypoxia-tolerant Humboldt squid (*Dosidicus gigas*) have extended their distribution in concert with expanding oxygen minima along the East Pacific margin (*20*). [Photo credits: (A) Image courtesy of K. Heirman and C. Smith, NSF LARISSA and Ghent University HOLANT projects. (B) Image courtesy of Deepwater Canyons 2013–Pathways to the Abyss, National Oceanic and Atmospheric Administration (NOAA)–Office of Exploration and Research, Bureau of Ocean Energy Management, and U.S. Geological Survey. (C) Image courtesy of N. Le Bris, Laboratoire d'Ecogéochimie des Environnements Benthiques (LECOB), Fondation Total–UPMC. (D) Image courtesy of R. Starr, NOAA–Cordell Bank National Marine Sanctuary]

that appear to have decimated benthic invertebrates (*9*). In the Mediterranean Sea, naturally warm deep waters (13° to 14°C) place deep-water coral species close to their tolerance threshold (*4*). In such semi-enclosed ocean basins, ecosystem responses may be rapid and difficult to predict, because warming is not only faster but also discontinuous as a result of intense deep-water convection events (*10*, *11*).

Warming at upper bathyal depths (200 to 2000 m) also threatens to release more methane from deep continental margins through gas hydrate dissociation. A climate-induced shift in warm currents such as the Gulf Stream may be sufficient to release many gigatons of frozen methane from the seafloor (*12*) (Fig. 2B), surpassing the buffering capacity of the seep microbial and animal biota that routinely oxidize methane (*13*).

Acidification

Both excess atmospheric CO_2 absorption and the oxidation of organic matter in the water column are causing acidification of intermediate-depth waters globally (*14*); subsequent subduction of high-CO_2 waters via thermohaline circulation is contributing to rapid acidification in the North Atlantic (*15*). Direct observation of biological consequences is lacking for the modern deep sea, and laboratory studies on deep-sea organisms are still rare, constrained by the capacity to maintain them alive. Elevated CO_2 is predicted to reduce the suitable habitat range for calcifying species over multiple life stages, because the depth limit at which water becomes corrosive (undersaturated) for aragonite or calcite will move upward. Effects on deep-water corals (Fig. 2C) are of particular concern, because their three-dimensional aragonite structures form vast gardens that support highly diverse communities and provide key nursery habitat to commercial fishes. The limited occurrence of deep-sea corals in waters naturally undersaturated in aragonite suggests that the energetic cost for these foundation species to grow in these conditions is high (*16*).

Deoxygenation

A warming ocean holds less oxygen. A warmer ocean is also more stratified because warm water is less dense than cold water, and strong density gradients reduce vertical mixing. The combined effects of reduced oxygen solubility in warmer water and increased thermal stratification create widespread oxygen reduction, termed deoxygenation (*17*). The effects are greatest at depths of 200 to 700 m and, over the past 50 years, have affected large swaths of naturally hypoxic tropical and subtropical waters in the Eastern Pacific and the Indian Ocean (*18*). Expansion of the world's naturally occurring low oxygen zones (oxygen minimum zones or OMZs) has led to habitat compression for intolerant demersal, mesopelagic, and bill fishes and habitat expansion of hypoxia-tolerant species such as the Humboldt squid (*19*, *20*) (Fig. 2D). Oxygen exerts tremendous control on marine biodiversity through effects on evolution, physiology, reproduction, behavior, and species interactions (*18*, *20*, *21*), as illustrated by El Niño–Southern Oscillation (ENSO)–induced changes in oxygenation. Except for historical core data (*22*), there are few long-term studies that link oxygen reduction to shifts in extant ecosystems on the deep-sea floor.

Organic flux and hydrodynamics

Increased stratification not only limits deep-water ventilation but also reduces nutrient supply to surface waters from the deeper ocean, where organic matter is recycled. Predicted reduction of phytoplankton production will result in lower POC fluxes to the deep ocean, particularly at mid to low latitudes (*23*). Below large oligotrophic areas, already food-poor abyssal plains may be further deprived of organic matter supply, resulting in lower benthic biomass and altered respiration

and bioturbation rates (*5*). Globally, predictions suggest a similar trend affecting 80% of biodiversity hotspots, such as canyons or seamounts, on decadal to century time scales (*23*). But regional variation is evident, and the deep sea beneath some upwelling regions such as the Northeast Pacific is seeing increasing POC fluxes on decadal time scales (*24*). Furthermore, short-term events that accelerate exchange between surface and deep waters are regulated by atmospheric processes (storm-induced convection, mesoscale eddies, and dense water cascading) and, hence, are climate sensitive. These events can affect deep-sea benthos through habitat disturbance and enhanced POC fluxes (*25*), governing the capacity of deep-sea ecosystems to sustain fisheries and provide major regulating services (*26*).

"Reduction and halting of CO_2 emissions are unquestionably the first line of defense; but...the deep ocean will continue to experience the effects of accumulated emissions."

Stressor interactions

As in shallow waters, interactions among climate stressors in deep-sea ecosystems are complex (Fig. 1) (*27*). For example, warming combined with acidification is predicted to deprive deep-water corals now abundant on the South Australia margin of suitable habitat (*28*). In OMZs that are expanding at bathyal depths, acidification from anthropogenic CO_2 is further enhanced, because the same process that draws down the oxygen (respiration) releases carbon dioxide. The combination of expanding midwater deoxygenation from below with surface warming and acidification from above reduces habitability of pelagic waters for species such as vertically migrating fish and krill. They are squeezed into a narrow-depth layer as they migrate to the surface at night to feed and recoup depleted oxygen, increasing their vulnerability to predators (*20*). The likelihood that oxygen stress narrows thermal and pH/CO_2 tolerances or reduces calcification rates has yet to be examined for most deep-water species, but recent studies suggest notable threats for the ecosystem engineer *Lophelia pertusa*, a deep-water coral that forms a habitat for many other species (*29*).

Adaptations to combined climate stressors have occurred in the past over evolutionary time and are exhibited by stress-tolerant organisms in today's ocean (*20*, *22*). For most deep-water species, there are no data on the range shifts, physiological changes, life-history alterations, or rapid evolution necessary to adapt to deep-ocean climate change.

Fueled by a growing demand for food, energy, and raw materials, continental margins and many seamounts are increasingly subject to overfishing and seascape alteration (*30*), oil and gas extraction (*31*), waste disposal (*31*), and proposed minerals mining (*32*). Many areas expected to experience the greatest temperature rise, pH drop, and oxygen loss also experience increasing anthropogenic pressure (Fig. 1). Deep-water coral habitat in the North Atlantic, the Mediterranean Sea, and the sea off southern Australia may be particularly vulnerable, because effects of climate change and direct impact from deep-sea bottom fishing may coincide in these regions (*16*, *28*). As climate and human disturbance converge, the accumulation of impacts may alter the state and functions of deep-ocean ecosystems and reduce the important benefits they provide.

Mitigation and adaptation

How can climate change be mitigated in the deep ocean? Reduction and halting of CO_2 emissions are unquestionably the first line of defense; but in coming years the deep ocean will continue to experience the effects of accumulated emissions. Using the deep ocean for mitigation through geoengineering—for example, by surface fertilization with iron, ocean alkalization (the addition of limestone to surface waters in upwelling regions to reduce CO_2 outgassing), or injection of CO_2 at depth—carries many uncontrolled risks. There can be no changes in deep- or surface-ocean properties without major effects on deep-sea animal densities and trophic guilds (*23*). Geoengineering outcomes would be superimposed on an already changing food supply to the abyss (*24*).

Options to mitigate the effects of climate change in the deep sea are decidedly limited. Spatial planning to restrict direct human disturbance—for example, by creating networks of deep-water marine protected areas—may help to establish refugia for endangered species and habitats and can reduce cumulative stresses. Protections to reduce physical and chemical disturbances from bottom trawling, mine tailings disposal, oil and gas extraction, or even seabed mining in areas subject to the greatest stress of warming, acidification, or deoxygenation will lessen chances of habitat loss and extinction of species and the ecological functions they support.

To address future climate change, the deep ocean must be recognized by the United Nations Framework Convention on Climate Change (UNFCCC). Such recognition should entail greater attention to predicting and reporting the role of the deep ocean in mitigation and the resulting impacts, acknowledgment of the vulnerability and importance of the deep ocean in negotiation text, and the application of adaptation funding to costly deep-ocean observation and ecosystem studies. Investigations of deep-sea processes, functions, and services should inform planetary carbon budgets and feedback modeling, as well as decisions about resource exploitation in the deep ocean. However, 64% of the ocean is beyond national jurisdiction and would thus not automatically be covered by the UNFCCC, which is an agreement among nation states (*33*). Nobody is explicitly responsible for protecting the mitigation potential or resilience of ecosystems in these vast regions. Legal instruments currently being negotiated for climate, biodiversity, and sustainable development could help build global capacity for long-term observation and monitoring of deep-sea ecosystems, both within and beyond national jurisdiction, that are subject to climate-induced change. Such observations will be critical to decision-makers and the health of most of the planet's biosphere in coming decades.

REFERENCES AND NOTES

1. C. Mora *et al.*, *PLOS Biol.* **11**, e1001682 (2013).
2. A. R. Thurber *et al.*, *Biogeosciences* **11**, 3941–3963 (2014).
3. C. W. Armstrong, N. S. Foley, R. Tinch, S. van den Hove, *Ecosyst. Serv.* **2**, 2–13 (2012).
4. E. Ramirez-Llodra *et al.*, *Biogeosciences* **7**, 2851–2899 (2010).
5. C. R. Smith, F. C. De Leo, A. F. Bernardino, A. K. Sweetman, P. M. Arbizu, *Trends Ecol. Evol.* **23**, 518–528 (2008).
6. K. M. Gjerde, D. Currie, K. Wowk, K. Sack, *Mar. Pollut. Bull.* **74**, 540–551 (2013).
7. S. G. Purkey, G. C. Johnson, *J. Clim.* **23**, 6336–6351 (2010).
8. M. Bergmann, T. Soltwedel, M. Klages, *Deep Sea Res. Part 1 Oceanogr. Res. Pap.* **58**, 711–723 (2011).
9. C. R. Smith *et al.*, *Proc. Biol. Sci.* **279**, 1017–1026 (2012).
10. R. Danovaro, A. Dell'Anno, A. Pusceddu, *Ecol. Lett.* **7**, 821–828 (2004).
11. F. Adloff *et al.*, *Clim. Dyn.* (2015).
12. B. J. Phrampus, M. J. Hornbach, *Nature* **490**, 527–530 (2012).
13. J. J. Marlow *et al.*, *Nat. Commun.* **5**, 5094 (2014).
14. R. H. Byrne, S. Mecking, R. A. Feely, X. Liu, *Geophys. Res. Lett.* **37**, L02601 (2010).
15. M. Gehlen *et al.*, *Biogeosciences* **11**, 6955–6967 (2014).
16. C. Yesson *et al.*, *J. Biogeogr.* **39**, 1278–1292 (2012).
17. R. F. Keeling, A. Körtzinger, N. Gruber, *Annu. Rev. Mar. Sci.* **2**, 199–229 (2010).
18. L. Stramma, S. Schmidtko, L. A. Levin, G. C. Johnson, *Deep Sea Res. Part 1 Oceanogr. Res. Pap.* **57**, 587–595 (2010).
19. L. Stramma *et al.*, *Nat. Clim. Change* **2**, 33–37 (2011).
20. W. F. Gilly, J. M. Beman, S. Y. Litvin, B. H. Robison, *Annu. Rev. Mar. Sci.* **5**, 393–420 (2013).
21. A. J. Gooday *et al.*, *Mar. Ecol. (Berl.)* **31**, 125–147 (2010).
22. S. E. Moffitt *et al.*, *PLOS ONE* **10**, e0115246 (2015).
23. D. O. B. Jones *et al.*, *Glob. Change Biol.* **20**, 1861–1872 (2014).
24. K. L. Smith Jr., H. A. Ruhl, M. Kahru, C. L. Huffard, A. D. Sherman, *Proc. Natl. Acad. Sci. U.S.A.* **110**, 19838–19841 (2013).
25. A. Rumín-Caparrós *et al.*, *Biogeosciences* **10**, 3493–3505 (2013).
26. J. B. Company *et al.*, *PLOS ONE* **3**, e1431 (2008).
27. N. Gruber, *Philos. Trans. A Math. Phys. Eng. Sci.* **369**, 1980–1996 (2011).
28. R. E. Thresher, J. M. Guinotte, R. J. Matear, A. J. Hobday, *Nat. Clim. Change* **5**, 635–639 (2015).
29. J. J. Lunden, C. G. McNicholl, C. R. Sears, C. L. Morrison, E. E. Cordes, *Front. Mar. Sci.* **1**, 78 (2014).
30. P. Puig *et al.*, *Nature* **489**, 286–289 (2012).
31. E. Ramirez-Llodra *et al.*, *PLOS ONE* **6**, e22588 (2011).
32. K. J. Mengerink *et al.*, *Science* **344**, 696–698 (2014).
33. UN General Assembly, United Nations Framework Convention on Climate Change. 1771 UNTS 107; S. Treaty Doc No. 102-38; U.N. Doc. A/AC.237/18 (Part II)/Add.1; 31 ILM 849 (1992).

ACKNOWLEDGMENTS

Ideas were developed for Our Common Future Under Climate Change (Paris 2015) and through many discussions with colleagues. Support was provided to L.A.L. by NSF (EAR 1324095) and through the Deep-Ocean Stewardship Initiative by J. M. Kaplan Fund and to N.L.B. by UPMC, CNRS, and Fondation Total (chair "Biodiversity, extreme marine environments and global change"). L.A.L. and N.L.B. are members of the scientific committee of the Ocean and Climate Platform.

10.1126/science.aad0126

PERSPECTIVE

Warm-water coral reefs and climate change

Mark D. Spalding[1]* and Barbara E. Brown[2]

Coral reefs are highly dynamic ecosystems that are regularly exposed to natural perturbations. Human activities have increased the range, intensity, and frequency of disturbance to reefs. Threats such as overfishing and pollution are being compounded by climate change, notably warming and ocean acidification. Elevated temperatures are driving increasingly frequent bleaching events that can lead to the loss of both coral cover and reef structural complexity. There remains considerable variability in the distribution of threats and in the ability of reefs to survive or recover from such disturbances. Without significant emissions reductions, however, the future of coral reefs is increasingly bleak.

Warm-water coral reefs are celebrated for their spectacular diversity (estimates exceed 3 million species) and the critical ecosystem services they provide to many of the 275 million people living close by. Covering 0.07% of the ocean surface and living within 30° latitude of the equator, reef-building corals grow optimally between 23° and 29°C. They support over a quarter of the world's small-scale fishers, generate jobs and foreign exchange through tourism, and provide critical sea defenses against storms, flooding, and land erosion.

Coral reefs are biogenic carbonate structures that accrete over decadal time scales because of the active growth of a living veneer of corals and other calcifying organisms (*1*). Disturbance is a natural part of reef growth and development. Reefs are subject both to local impacts (such as waves, grazing, and bioerosion by coral-boring animals) and to large-scale temporally rare perturbations. The latter include physical impacts (such as storms, tsunamis, and seismic events), ecological imbalances (such as disease and predatory starfish outbreaks), and oceanographic influences (such as altered seawater temperature and pH as well as sediment, nutrient, and freshwater inputs).

Measures of reef state or health such as coral cover, diversity, biomass, surface complexity (rugosity), or key species need to be viewed with an appreciation of this natural dynamism. In healthy systems, losses of key ecosystem components, be they reef-building corals or herbivorous fish, are often transitional. Fish stocks recover, and the net decadal growth of biogenic structure may be maintained even if coral growth is reduced and erosion predominates for a few years. Despite this natural variability, reefs are highly vulnerable to human-induced degradation (*2*). Growing concern for their long-term future has led to urgent calls for action across many public-sector, governmental, and even faith communities.

Human pressures fall into the same broad classes as natural perturbations: physical, ecological, and oceanographic (table S1). The challenge they present is twofold. First, anthropogenic effects act in addition to natural disturbances. Thus, although coral bleaching can be a natural phenomenon, it now occurs more frequently and more severely. Second, many of these pressures are chronic: Although reversible, they are not being reversed. Thus overfishing has left large areas of reefs without key functional groups such as top predators, or with reduced herbivore biomass and diversity, for many years.

In a seminal study of a Caribbean reef, Hughes showed that coral reefs could be taken out of their naturally dynamic equilibrium and shifted toward an alternative state by a combination of natural and anthropogenic perturbations. The observed ecological shift from coral to algal domination (*3*) was later replicated on an Indo-Pacific reef (*4*), and the reality of such phase shifts has now become an established paradigm.

Climate change impacts

Most warm-water corals exhibit a symbiotic relationship with single-celled algae (zooxanthellae) from which they derive much of their nutrition. This relationship breaks down under stress. Algal densities decline and photosynthetic pigments may be reduced. As a result, corals become pale or "bleached" and in some cases die. Mass bleaching events around the world were first noted in 1983 and have been linked to elevated sea temperatures. These events usually last for a few weeks to a few months and are acute threats to the corals, whose presence and structure underpin the entire ecosystem. Severe seawater warming in 1998 affected most coral reef regions and caused widespread coral mortality, particularly in the Indian Ocean.

Most corals live close to their upper thermal maximum, and an increasing frequency of bleaching is projected with warming background temperatures. Even corals surviving bleaching may be affected, with impaired reproduction, susceptibility to disease, and reduced calcification. Within the Caribbean, increases in thermal minima have probably played a role in the spread of disease in acroporid corals (*5*).

Although recovery from the 1998 bleaching has been documented on many reefs, elsewhere it has been linked to phase shifts toward macroalgal dominance (see the case study below). An El Niño–Southern Oscillation event currently beginning has been predicted to match that of 1998 in terms of intensity (*6*) and could drive further

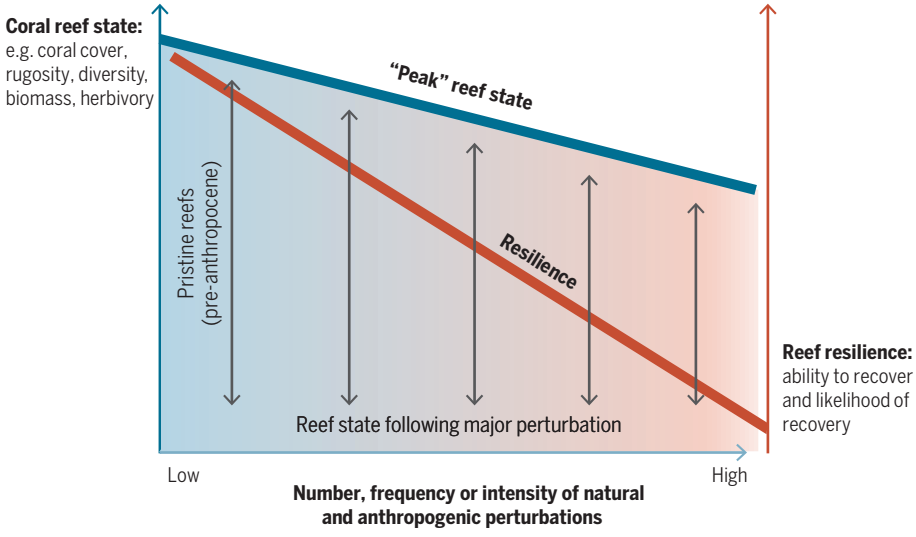

Fig. 1. Reef state varies across a broad spectrum, even in natural conditions, but increasing number, frequency, or intensity of perturbations (*x* axis) will typically affect both the peak state that a reef can attain (blue line) and the resilience of that reef (red line). Double-headed arrows indicate that at any given threat level, reefs may be observed across a broad range of states. For this reason, the large decrease in resilience with increasing threats may not be apparent from simple one-off measures of reef state.

[1]Global Ocean Team, The Nature Conservancy, Department of Physical, Earth and Environmental Sciences, University of Siena, Pian dei Mantellini, 44, 53100 Siena, Italy; and Department of Zoology, University of Cambridge, Cambridge CB2 3EJ, UK. [2]School of Biology, Newcastle University, Newcastle NE1 7RU, UK; and Environmental Research Institute, University of the Highlands and Islands, Thurso KW14 7EE, UK.
*Corresponding author. E-mail: mspalding@tnc.org

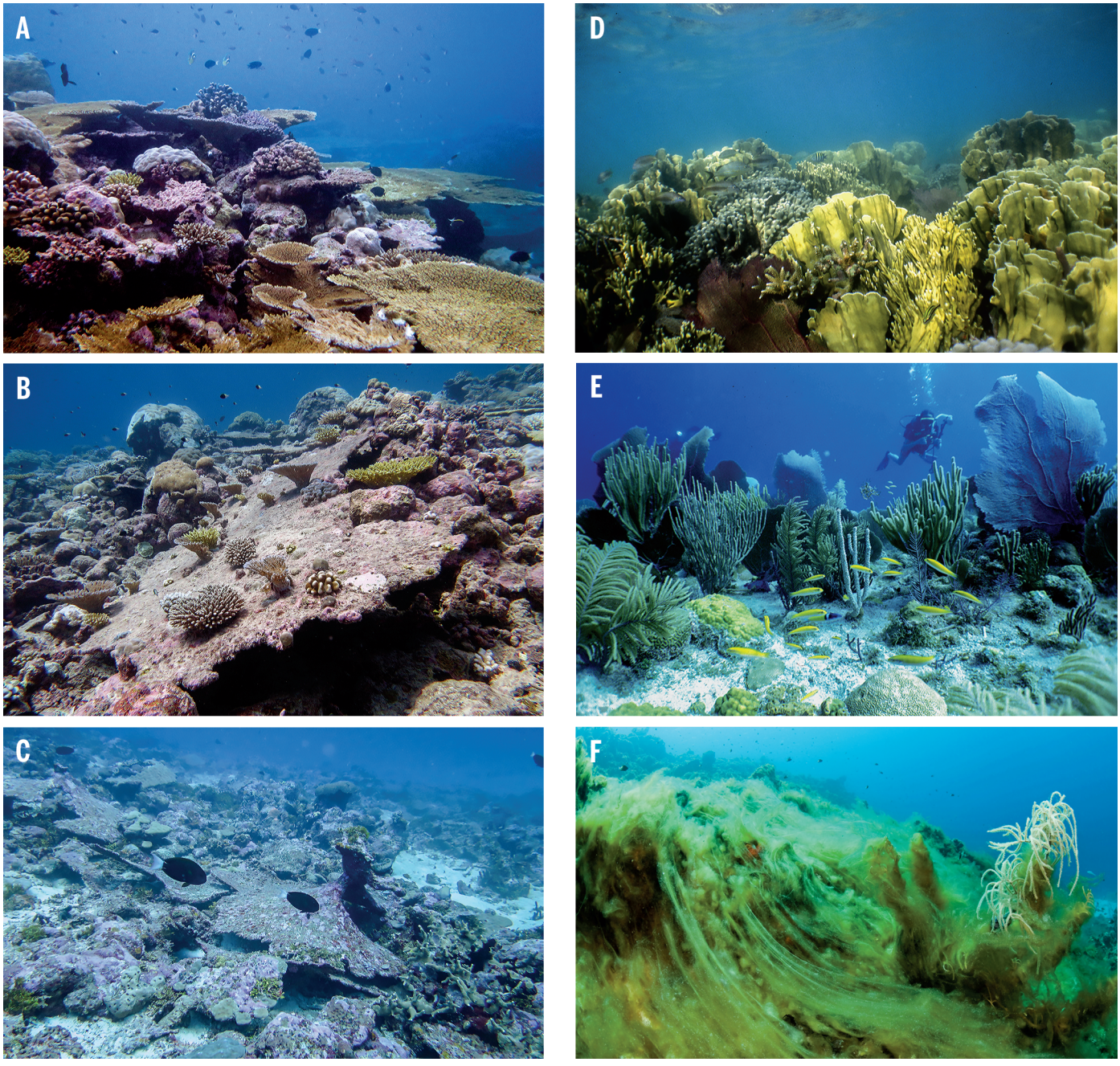

Fig. 2. Indo-Pacific and Caribbean reefs may be observed across a broad spectrum of states. (Left) Reefs of the well-protected Chagos Archipelago (BIOT) were badly damaged by the bleaching event in 1998 (**C**), but most recovered with high recruitment (**B**) over several years to return to high coral cover (**A**). (Right) In the Caribbean, high coral cover (**D**) is now very rare indeed, and "peak" condition for many reefs is a mix of hard corals, soft corals, and macroalgae (**E**). In many places, phase shifts have led to highly altered, algal-dominated "reefs" (**F**), which might no longer meet the definition of a true coral reef.

reef loss. Future trajectories of warming ocean waters present a bleak picture.

Patterns of bleaching, and the responses of corals, are far from homogeneous. McClanahan and others have pointed to considerable variability in bleaching susceptibility between both taxa and locations (*7*, *8*). Bleaching susceptibility appears lower in areas of prior thermal stress and/or in regions subject to natural fluctuations in sea temperature. At finer scales, recent work by Palumbi *et al.* (*9*) in American Samoa showed that at least one widespread species had the ability to acclimatize over a time scale as short as 2 years. Other researchers have demonstrated decade-long memories of acquired tolerance (*10*) and the possibility of transferring thermal tolerance between generations (*11*). Nevertheless, there remains concern about the ability of any species, or indeed the ecosystem as a whole, to adjust sufficiently quickly to match projected rates of temperature rise.

Ocean acidification poses a further chronic threat for coral reefs through reductions in the saturation state of aragonite, which is required to build the coral skeleton. Projected impacts on corals and reef structures include reduced growth, weaker skeletons, increased bioerosion, and potentially dissolution of carbonate substrates and coral skeletons (*12*). As with sea-temperature increases, a rapidly growing research base has added many nuances to original concerns. For

example, some coral species will cope better than others, at least in the early stages of rising CO_2 conditions, and the response among other fauna and flora is highly variable (*13*).

The current state of reefs and resilience

About 75% of the world's reefs are considered threatened by human activities (*2*). Long-term and multisource syntheses reveal dramatic changes to coral reefs in recent decades. The complete physical loss of reefs remains rare, but degradation is now almost ubiquitous. In the Indo-Pacific, coral cover has declined to only 22% of total reef surfaces, after an estimated 2% decline per year from 1997 to 2003 (*14*). On the relatively well-protected Great Barrier Reef, more recent declines are even steeper: An average of 3.4% loss of coral cover per year from 1985 to 2012 has led to a current mean coral cover of only 14% (*15*).

Other metrics for the state of reefs indicate similar patterns. For example, massive declines in rugosity have been reported from the Caribbean (*16*), where over one-third of reefs no longer have sufficient coral to maintain their structure and are now eroding (*17*). Overfishing has affected most of the world's coral reefs: Herbivore biomass is, on average, double on reefs that are not accessible to fishing (*18*), and the abundance of large reef fish species, including sharks, is often 10 times higher around unfished reefs (*19*).

Such changes are influencing the appearance and functional ecology of reefs. The flattening of reef morphology (*16*) is reducing the overall surface area for benthic species and reducing surface complexity associated with niche space for mobile fauna (*20*). The particularly strong declines and phase shifts observed on Caribbean reefs may be regarded as a harbinger for other regions, and indeed some recovery failure has also been noted on Indo-Pacific reefs (case study) (*21*).

Many reefs do, however, have a high capacity for recovery, and after a perturbation they typically return to previous levels of coral cover, rugosity, and biomass. One-off metrics of reef state such as coral cover are therefore of limited use for understanding where a particular reef lies on the threat spectrum (Fig. 1). After severe bleaching, coral cover can return within a decade, although return to the original ecological assembly may take longer and may not occur at all (*22*). The challenge comes when severe perturbations become too frequent to allow full recovery or when multiple perturbations occur at the same time (Fig. 2).

Case study: Coral bleaching impacts in the Indian Ocean

The reefs of the central and western Indian Ocean suffered some of the most extreme impacts from the 1998 bleaching event, with coral mortality often in excess of 90%. Since that event, and despite sublethal bleaching events in some subsequent years, many reefs, such as those in the British Indian Ocean Territory (BIOT; also known as the Chagos Archipelago), have moved toward recovery (*23*). These reefs are protected by the world's largest no-take marine reserve and have few direct anthropogenic pressures. Reefs around the granitic Seychelles islands showed more diverse response trajectories, with some reefs, including most deeper reefs, displaying strong recovery while others moved toward macroalgal–dominated communities with low coral cover (*24*). These were some of the first reefs to show phase shifts outside of the Caribbean. At least two of the five factors associated with these shifts can be linked to anthropogenic disturbance: low herbivore biomass and high nutrient concentrations. Efforts are now under way to improve reef management and undertake restoration in some of these reefs. Such efforts will help, but they may not be sufficient in the face of accelerating climate change. Despite their protection from local threats, some BIOT reefs have shown low recovery and also increasing disease occurrence.

Managing for the future

It is perhaps naïve to try and hold any ecosystem in a pre-Anthropocene state, but equally it is too early to proclaim the end of coral reefs. Reefs are declining in condition globally but not evenly. Furthermore, in many areas, other impacts such as overfishing and pollution are so severe that climate change impacts are at present of secondary importance (*15*). The threat array varies between reefs, but there are also natural differences in resilience, a fact that has led to the concept of building such resilience into reef management. The initial focus has been on identifying and focusing management interventions such as pollution mitigation and overfishing reduction around areas where resilience may already be high (*25*).

Alongside these management approaches are more active interventions such as reef restoration through the use of coral transplants and coral nurseries (*26*). Assisted colonization has been suggested as a strategy, whereby heat-tolerant corals from one region are transferred to another location within their natural range to enhance thermal tolerance in that location (*27*). However, there can be problems with the survival of transplants and risks with possible genetic alteration of subpopulations. There are even calls from some academics within the coral reef research community to consider more radical solutions, ranging from the genetic manipulations of corals or associated symbionts (*28*) to geoengineering through aerosol-based solar radiation management (*29*). Such approaches carry huge risks, from the unintended ecological consequences of genetic modifications to impacts on global hydrological cycles and stratospheric ozone from geoengineering. The fact that they are even being mooted indicates the levels of concern.

Without the stabilization of greenhouse gas concentrations, it seems inevitable that many of the world's coral reefs will become nonaccreting habitats—they will, based on most common definitions, cease to be coral reefs. This will happen more or less rapidly in different locations and will have concomitant and profound impacts on both biodiversity and people. As reefs decline, many of the millions of people who live near reefs will lose critical sources of food, as well as coastal protection and tourism revenues. Ironically, however, the main drivers of current reef decline—pollution, overfishing, sedimentation, and direct destruction—may be just as influential in the near term as climate drivers in the long term. Concerted efforts by governments with jurisdiction over coral reefs may be able to manage these direct threats. This could win critical time both for adaptation and, crucially, for the global community to act on stabilizing and reducing emissions.

REFERENCES AND NOTES

1. M. D. Spalding, C. Ravilious, E. P. Green, *World Atlas of Coral Reefs* (Univ. of California Press, Berkeley, CA, 2001).
2. L. Burke, K. Reytar, M. D. Spalding, A. L. Perry, *Reefs at Risk Revisited* (World Resources Institute, The Nature Conservancy, WorldFish Center, International Coral Reef Action Network, UNEP World Conservation Monitoring Centre, and Global Coral Reef Monitoring Network, Washington, DC, 2011).
3. T. P. Hughes, *Science* **265**, 1547–1551 (1994).
4. T. P. Hughes *et al*., *Curr. Biol.* **17**, 360–365 (2007).
5. C. J. Randall, R. van Woesik, *Nat. Clim. Change* **5**, 375 (2015).
6. M. J. McPhaden, *Nat. Clim. Change* **5**, 791 (2015).
7. T. R. McClanahan, *Mar. Biol.* **144**, 1239–1245 (2004).
8. T. R. McClanahan, M. Ateweberhan, C. A. Muhando, J. Maina, M. S. Mohammed, *Ecol. Monogr.* **77**, 503–525 (2007).
9. S. R. Palumbi, D. J. Barshis, N. Traylor-Knowles, R. A. Bay, *Science* **344**, 895–898 (2014).
10. B. E. Brown, R. P. Dunne, A. J. Edwards, M. J. Sweet, N. Phongsuwan, *Mar. Biol.* **162**, 479–483 (2015).
11. H. M. Putnam, R. D. Gates, *J. Exp. Biol.* **218**, 2365–2372 (2015).
12. J. M. Pandolfi, S. R. Connolly, D. J. Marshall, A. L. Cohen, *Science* **333**, 418–422 (2011).
13. J. Ries, A. Cohen, D. McCorkle, *Geology* **37**, 1131–1134 (2009).
14. J. F. Bruno, E. R. Selig, *PLOS ONE* **2**, e711 (2007).
15. G. De'ath, K. E. Fabricius, H. Sweatman, M. Puotinen, *Proc. Natl. Acad. Sci. U.S.A.* **109**, 17995–17999 (2012).
16. L. Alvarez-Filip, N. K. Dulvy, J. A. Gill, I. M. Côté, A. R. Watkinson, *Proc. R. Soc. London Ser. B* **276**, 3019–3025 (2009).
17. C. T. Perry *et al*., *Nat. Commun.* **4**, 1402 (2013).
18. C. B. Edwards *et al*., *Proc. R. Soc. London Ser. B* **281**, 20131835 (2014).
19. D. Fenner, *Mar. Pollut. Bull.* **84**, 9–16 (2014).
20. J. T. Kerry, D. R. Bellwood, *Coral Reefs* **34**, 41–50 (2015).
21. K. M. Chong-Seng, N. A. J. Graham, M. S. Pratchett, *Coral Reefs* **33**, 449–461 (2014).
22. K. A. Johns, K. O. Osborne, M. Logan, *Coral Reefs* **33**, 553–563 (2014).
23. C. R. C. Sheppard, A. Harris, A. L. S. Sheppard, *Mar. Ecol. Prog. Ser.* **362**, 109–117 (2008).
24. N. A. J. Graham, S. Jennings, M. A. MacNeil, D. Mouillot, S. K. Wilson, *Nature* **518**, 94–97 (2015).
25. P. J. Mumby, N. H. Wolff, Y.-M. Bozec, I. Chollett, P. Halloran, *Cons. Lett.* **7**, 176–187 (2014).
26. B. Rinkevich, *Curr. Opin. Environ. Sustainability* **7**, 28–36 (2014).
27. O. Hoegh-Guldberg *et al*., *Science* **321**, 345–346 (2008).
28. M. J. H. van Oppen, J. K. Oliver, H. M. Putnam, R. D. Gates, *Proc. Natl. Acad. Sci. U.S.A.* **112**, 2307–2313 (2015).
29. L. Kwiatkowski, P. Cox, P. R. Halloran, P. J. Mumby, A. J. Wiltshire, *Nat. Clim. Change* **5**, 777 (2015).

ACKNOWLEDGMENTS

M.D.S. is grateful for the support of the Lyda Hill Foundation and the Anne Ray Charitable Trust. Thanks to P. Kramer, P. zu Ermgassen, and R. Dunne for helpful discussion and assistance.

SUPPLEMENTARY MATERIALS

www.sciencemag.org/content/350/6262/769/suppl/DC1
Table S1

10.1126/science.aad0349

REVIEW

Climate change and marine vertebrates

William J. Sydeman,[1,2]* Elvira Poloczanska,[3,4] Thomas E. Reed,[5] Sarah Ann Thompson[1,6]

Climate change impacts on vertebrates have consequences for marine ecosystem structures and services. We review marine fish, mammal, turtle, and seabird responses to climate change and discuss their potential for adaptation. Direct and indirect responses are demonstrated from every ocean. Because of variation in research foci, observed responses differ among taxonomic groups (redistributions for fish, phenology for seabirds). Mechanisms of change are (i) direct physiological responses and (ii) climate-mediated predator-prey interactions. Regional-scale variation in climate-demographic functions makes range-wide population dynamics challenging to predict. The nexus of metabolism relative to ecosystem productivity and food webs appears key to predicting future effects on marine vertebrates. Integration of climate, oceanographic, ecosystem, and population models that incorporate evolutionary processes is needed to prioritize the climate-related conservation needs for these species.

Marine vertebrates are diverse and charismatic, capturing and impassioning societal interests because of their roles in food, educational, and recreational systems. Largely, this is due to their conspicuousness, a characteristic that makes them ideal for investigating the impacts of climate change on marine ecosystems. Fish provide protein to human populations and support economic and food security, whereas sea turtles, seabirds, and mammals contribute to regional economies (tourism) and cultures, as well as to human subsistence in remote areas. These animals are ecologically relevant, imparting top-down effects on marine food webs that may control community stability (*1*, *2*). Marine vertebrates, particularly seabirds, show great value as ecological indicators and may play pivotal roles in assessments of marine ecosystem health (*3*).

Marine vertebrate–climate relationships have been studied for more than a century. In the early 20th century, when studies of El Niño were in their infancy, clear effects were documented for Peruvian seabirds (*4*). Fish distributional shifts were particularly well documented in extratropical California during the 1957–1959 El Niño event (*5*). Effects of low-frequency climate variability on trophic interactions and marine vertebrate populations were demonstrated in the late 1980s (*6*). It is now well established that fish, birds, and mammals regularly respond to climate phenomena, such as El Niño–Southern Oscillation (ENSO), Pacific Decadal Oscillation (PDO), and Atlantic Multi-Decadal Oscillation (AMO), which fluctuate on a range of temporal scales (*7*, *8*). For example, when the North Atlantic warmed in the early 20th century (~1920s to 1940s) at rates comparable with contemporary warming (*9*), associated ecological changes included widespread northward shifts of fish and increases in fisheries productivity driven by bottom-up processes (*10*, *11*). Thus, changes in marine vertebrate life histories, demographic traits, and distribution have long been a subject of interest. Because marine vertebrates are ecologically important and vulnerable, clearly responsive to climatic factors, and provide extensive economic and aesthetic value to society, it is imperative to better understand the impacts of climate change on these key marine organisms.

[1]Farallon Institute for Advanced Ecosystem Research, Petaluma, CA 94952, USA. [2]Bodega Marine Laboratory/ University of California Davis, Bodega Bay, CA 94923, USA. [3]Commonwealth Scientific and Industrial Research Organisation, Ecosciences Precinct, Brisbane QLD 4102, Australia. [4]Global Change Institute, University of Queensland, St Lucia, Brisbane QLD 4072, Australia. [5]School of Biological, Earth and Environmental Sciences, University College Cork, Cork, Ireland. [6]Climate Impacts Group, University of Washington, Seattle, WA 98195, USA.
*Corresponding author. E-mail: wsydeman@faralloninstitute.org

Taxonomic diversity

Huge challenges to understanding and prediction remain, however, not the least of which concerns the complexity of biological interactions that drive change (Fig. 1). Climate change can affect these animals directly, through physiological functions (*12*), or indirectly, through predator-prey interactions and other trophic mechanisms, or through modification of critical habitats such as coral reefs and seagrass beds. Fish, the dominant marine vertebrate group, demonstrate complex life histories including, for many species, a planktonic life-stage in which habitat occupancy and prey use differs from adult life stages, resulting in different vulnerabilities to environmental change. Most fish are ectothermic and derive oxygen from seawater; thus, their responses to climate change are direct and physiological, with impacts on basic metabolic functions. Furthermore, changes in ocean productivity and prey availability are well demonstrated to drive fluctuations in fish populations. Sea turtles, generally considered ectothermic, are characterized by highly migratory life histories and long age-to-maturity (often decades), and nest on land (sandy beaches), where ambient temperatures determine the sex of embryos. In contrast, marine mammals and seabirds are endothermic; climatic effects on these groups are mostly indirect, influenced primarily by shifts in habitat or prey availability, although coastal inundation of low-lying nesting areas for tropical seabirds (and sea turtles) is also of concern. The high metabolic rate of some species (notably seabirds) necessitates regular access to food resources in order to maintain somatic condition. Thus, the nexus between metabolic shifts and nutritional needs, coupled with variation in ocean productivity and trophic interactions, may be a key predictor of the ability of marine vertebrates to cope with climate change. Moreover, although all marine vertebrates may be considered vagile, some conduct transoceanic or transhemispheric migrations (*13*), whereas others are more sedentary (such as coral reef fish). Reproductive tactics also vary from batch-spawning semelparity (single reproductive episode during life, such as Pacific salmon) to long-term iteroparity (multiple reproductive cycles, such as albatrosses that live upwards of 80 years). Although these fundamental differences result in varying responses among taxonomic groups to climate, a key similarity is that generally, these animals derive sustenance from the oceans.

Observations, mechanisms, and models

Information base

Fisheries, endangered and iconic marine wildlife, seabird monitoring, and society's fascination with marine environments have produced many long-term observational data sets. Fisheries statistics, some exceeding a century, as well as interdecadal monitoring studies at important local habitats—such as nesting or breeding sites for seabirds, sea turtles, and marine mammal populations—are available for global syntheses (*14*). When coupled with environmental data on atmospheric and oceanographic conditions, this provides a rich database with which to examine biophysical relationships and potential climate change impacts on populations. Nonetheless, there remain many gaps in our knowledge; for example, most studies have been conducted in the temperate Northeast Atlantic and the temperate to subarctic North Pacific. Key studies also exist from southern Africa (*15*) and Antarctica (*16*), but many rich areas of the world's oceans remain largely understudied. Additionally, fisheries-dependent data may be compromised by a nonrandom temporal and spatial distribution of fishing effort, and seabird, sea turtle, and marine mammal data sets rarely exceed one period of decadal variability (e.g., the PDO or AMO). This means that for the most part, statistical attribution of changes in marine vertebrate populations to anthropogenic climate change is difficult because few data sets allow one to disentangle unidirectional climate change from low-frequency climate variability. Mechanistic understanding of change has also been elusive.

That said, recent global syntheses provide robust evidence of widespread impacts of climate change on marine vertebrates (*14*, *17*). Contemporaneous changes in coupled ocean variables and processes such as temperature and regional upwelling,

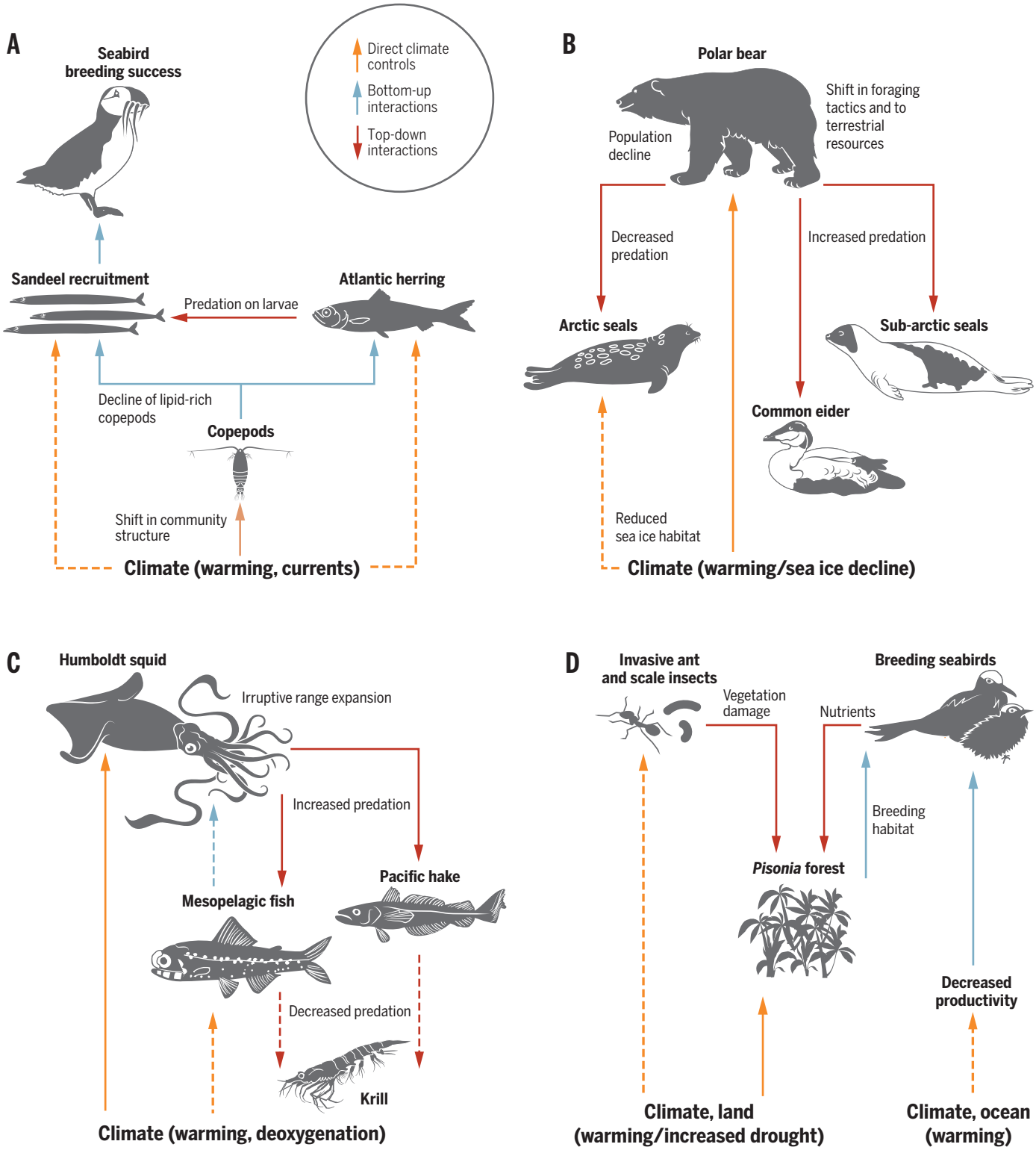

Fig. 1. Four case studies illustrating the complex mechanisms by which climate change can indirectly affect marine vertebrates via trophic interactions. (**A**) Bottom-up effects of climate change in the North Sea. The reduction in lipid-rich copepods results in declines in sandeel recruitment and poor seabird breeding success (*110*). (**B**) Climate-mediated top-down effects of polar bears in the Arctic, with positive impacts (reduced predation) hypothesized for Arctic seals and negative (increased predation) impacts on sub-Arctic seals, nesting eiders, and terrestrial resources (*111*–*113*). (**C**) Potential climate-mediated trophic cascade in the California Current System driven by range expansion of Humboldt squid, with increasing predation on hake and mesopelagic fishes cascading to decreased predation on krill (*63*–*65*). (**D**) Marine-terrestrial coupling and ecological cascade on Coral Sea Islands, southwest Pacific, driven by climate change simultaneously affecting the ocean and land, lessening food availability and reducing nesting habitat quality for seabirds (*114*, *115*). Each case study is a simplified schematic and does not include all potential food web links and interactions. Orange arrows, direct climate controls; blue arrows, bottom-up interactions; red arrows, top-down interactions; solid lines, well supported; dashed lines, hypothesized.

nutrient supplies and primary production, and ocean acidification and deoxygenation (*18*) indicate the potential for causal relationships and the inherent complexities of a three-dimensional (3D) habitat. For example, discontinuities in physical and chemical components of the ocean are observed in vertical and horizontal domains. Potential pathways of marine vertebrate response are also complex and include classic climate-to-predator bottom-up food web dynamics (Fig. 1A), climatically driven shifts in predation pressure on mesopredators (Fig. 1B), as well as other potential mechanisms, including trophic cascades and terrestrial-marine coupling (Fig. 1, C and D). Thus, understanding climate change impacts on marine ecosystem primary and secondary productivity and availability of prey to consumers is vital to predicting future responses to climate change. Responses in terms of phenology, distribution, and demography will also be mediated by climate change impacts on critical habitats, such as coral reefs and seagrass beds used by fish as adult foraging grounds or juvenile nurseries, sandy nesting beaches for sea turtles and seabirds, and sea ice, which provides foraging and breeding habitats for polar bears (Arctic) and penguin species (Antarctic).

Phenology

Phenology is the study of the timing of recurring biological events and how these are influenced by climate, such as the seasonal phasing of phytoplankton blooming in marine ecosystems or timing of egg-laying in seabirds. Climate change is causing variation in the peak and seasonality of both temperature and primary production in the oceans (*19*, *20*). Generally, warm seasons are arriving earlier and ending later (*21*) and are expected to advance the timing of spring migrations and breeding, delay autumn migrations, and alter the seasonal peak abundances of marine organisms (*22*). Phenological responses have been well demonstrated in many species of seabirds and zooplankton, including larval fish (*23*). Globally, spring phenologies of all marine species (including planktonic and nektonic species) have advanced by 4.4 ± 1.1 days per decade since the mid–20th century (*14*); responses are variable among taxonomic groups. For example, seabirds were not significantly different from zero owing to regional advances and delays in breeding dates. Delayed breeding for emperor penguins (*Aptenodytes forsteri*) and other seabird species in the western Antarctic was linked to a delay in sea ice breakup, which has been hypothesized to influence prey availability and limit access to prey resources (*24*). Similar delays were reported for northern gannets (*Sula bassana*) in the northeast Atlantic and linked to warmer temperatures, also presumably related to prey resources (*25*). No unidirectional trends in phenology were observed for several seabird species in the North Pacific (*26*, *27*), although the timing of breeding of seabirds in this region tracks phase shifts of the PDO. In contrast, earlier breeding for little penguins (*Eudyptula minor*) in Australia has been linked to ocean warming and improved prey availability (*28*). Similarly, nesting phenology in sea turtles has been linked to ocean temperature; however, evidence of climate change responses is weak and overshadowed by regional variations (*29*, *30*). The initiation of breeding migrations is likely driven by environmental conditions on distant feeding grounds (turtles deposit fat reserves that are mobilized later for breeding) (*31*), although to date, remote climate effects have yet to be investigated.

Fish phenologies show similar complexities, although studies are rare. The phenology of adult salmon (*Oncorhynchus* spp.) migration in Alaska shows population-specific advances and delays (*32*); delays for sockeye (*O. nerka*) run timing may be related to warm river conditions and low summer stream flows. In the North Sea, advanced spawning of sole (*Solea solea*) corresponded to warmer winter temperatures, which likely accelerated gonadal development (*33*). Off California, both earlier and later seasonal peaks in larval fish abundance (n = 43 species) were observed, corresponding to the preferred habitat of each species (*34*); neritic species that reside near upwelling centers showed delays in peak abundance, whereas timing for peak abundance has advanced for more pelagic, offshore-dwelling species.

Although research clearly shows a range of phenological responses to recent climate change, in general we lack clear "yardsticks" for how marine vertebrates should change their phenology to avoid loss of fitness (for example, phenological responses of food species or predators against which to compare focal species responses) (*35*). Few models project anticipated changes in phenology (*36*); however, a rare study (*37*) presents an individual-based modeling framework for characterizing climate change effects on phenology, and there is scope for adapting such models to other species and contexts (*38*). Phenological shifts can maintain alignment of predator and prey or other resources in time or space as climate changes (*39*), but there is no reason to assume perfect tracking across trophic levels (*40*); indeed, some phenological responses may disadvantage individuals. Most studies, including those showing both advances and delays in breeding date and peak abundance, hypothesize phenological responses via metabolic shifts or prey resources, but few have demonstrated matching of vertebrate needs with prey availability relative to climate change (*41*–*43*).

"Marine vertebrates, particularly seabirds, show great value as ecological indicators and may play pivotal roles in assessments of marine ecosystem health."

Distribution

Climate change and ocean warming are predicted to cause shifts in marine vertebrate distributions, and thus diversity (patterns in the richness of communities) (*22*, *44*). Anticipated impacts include increases in species richness in temperate-subarctic biomes, local species extinctions in tropical biomes, and the emergence of no-analog communities (*44*–*46*). Small-ranged species, which dominate in the tropics, and polar communities may be at highest risk from warming (*44*). Climate-related redistributions are best studied in fish. Recent decadal increases in fish community diversity and productivity observed in the high-latitude northeast Atlantic (*47*) and Bering Sea (*48*) have been linked to regional warming. Whether or not boreal/subpolar fish production will continue to increase as a function of climate change is a key question. Latitudinal shifts will induce changes in photoperiodic responses (day length differs in newly colonized areas). In some cases, enhancing growth because of longer day lengths for feeding (*49*), and in others, disrupting trophic synchronies or, particularly in polar oceans, resulting in shorter windows of food availability (*50*).

Across the globe, distribution shifts of, on average, 30.6 ± 5.2 km per decade have been reported, and the fastest responses are for fish and zooplankton, including larval fish (*14*). Differences in the speed and direction of shifts among fish and invertebrate populations may be explained by local rates of isotherm shifts (*51*). Shifts in depths occupied have also been documented as cold-water species take refuge in cooler, deeper waters, particularly where latitudinal shifts are blocked (*52*, *53*). For example, in the northern Gulf of Mexico, where the coastline prohibits poleward distributional shifts, demersal fish assemblages instead shifted deeper (*51*). Fishing complicates interpretations of climate-driven redistributions (*54*) and can amplify or obscure responses to climate change (*55*, *56*). As an example, cod distribution in the North Sea has shifted northward, eastward, and deeper over the past century; the northward shift and deepening have been linked to warming; however, the shift eastward was linked to fishing pressure, complicating interpretations and attribution to climate change (*57*).

Warming combines with other oceanographic processes to influence species redistributions. Numerous range extensions have been observed in fish of temperate waters of southeast Australia and linked to regional warming as well as a strengthening of the East Australian Current; the mechanism includes enhanced transport of larvae and juveniles (*58*). In the northwest Atlantic, changes in silver hake (*Merluccius bilinearis*) distribution were correlated with the position of the Gulf Stream, although the hake respond to changes in bottom temperatures arising from the same changes in circulation patterns that influence the Gulf Stream (*59*).

Ocean acidification, in addition to changes in temperature, presents risks to larval fish in particular, whereas oxygen availability is an important determinant of fish metabolic rates and their ability to cope with warming, ultimately affecting growth and body size (*12*). Oxygen declines also are projected to result in poleward and

vertical contractions of habitats and a reduction in fish body size (*60*–*62*). Humboldt squid off California, however, appear to have responded to warming and deoxygenation with a recent range expansion, increasing predation pressure on commercial fish species (Fig. 1C) (*63*–*65*).

Distribution shifts of air-breathing marine vertebrates are also expected as a consequence of warming temperatures, primarily through modification of prey availability or critical habitats. Declining sea ice has forced polar bears to use terrestrial food resources as sea ice foraging habitats decline and denning is driven into coastal areas (Fig. 1B) (*66*, *67*). Seabird redistributions have been documented for South African and Australian breeding colonies in relation to changes in prey availability (*68*, *69*). One climate model analysis suggests shifts in North Pacific albatrosses corresponding to a poleward shift of the Transition Zone Chlorophyll Front (*46*); albatross observations in Alaska corroborate these results by showing a northward shift in the center of distribution and increased albatross density in the subarctic Bering Sea (*70*).

Demography

Numerous demographic responses (for example, vital rate statistics such as reproductive success and survival) have been shown for seabirds, sea turtles, and fish, and contrasting responses to environmental measurements are apparent. For example, Antarctic sea ice extent (SIE) has a positive effect on adult survival and a negative effect on egg hatching rates in emperor penguins (*Aptenodytes forsteri*) (*71*, *72*) and negative or statistically nonsignificant relationships with snow petrel survival (*Pagodroma nivea*) (*73*, *74*). Additionally, there is evidence that "moderate is better," with intermediate SIE related to the highest survival rates for Adélie penguins (*Pygoscelis adeliae*) (*75*, *76*); moderate ice cover promotes primary productivity and facilitates access to prey resources by foraging seabirds.

In general, ocean warming correlates negatively with seabird breeding success and survival; examples include puffins from Norway (*77*) and shags and auks in the UK (*78*), but this is not always the case. Positive relationships have been demonstrated between breeding success and temperature for little penguins off Australia (*79*), as well as two Antarctic albatross species (*80*) and puffins off Russia (*81*). An example highlighting the link between foraging success and breeding success is the recent poleward shift in wandering albatross (*Diomedea exulans*) distributions as westerly wind fields in the Southern Ocean have strengthened and moved poleward (*82*). As a result, albatross foraging trips have shortened in duration, and breeding success has improved. Variation in survival may also relate to sea surface temperature (SST); for example, Waugh *et al*. (*83*) documented a negative relationship between the survival of rare Westland petrels (*Procellaria westlandia*) and SST anomalies in areas frequented by the birds during the breeding season, but a positive relationship between those two factors in foraging areas used in the nonbreeding season. In sea turtles, the sex of hatchlings is determined by incubation temperatures of eggs in nests dug above sandy beaches (female biases arise above ~29°C). Air temperatures on many beaches worldwide have already warmed to, or are close to, all female-producing temperatures, and temperature projections indicate further biases (*84*). However, population units may span many beaches in a region, and temperatures fluctuate during nesting seasons (for example, reduced with rainfall), so the necessary males may still be produced.

Owing to the availability of excellent data on seabirds, a number of climate-dependent population models have been implemented by coupling demographic data with climate system models. These studies assume that climatic-demographic relationships will remain the same into the future—a bold assumption given developing novel climate states (*85*) and well-documented breakdowns in climate-demographic relationships for fish (*86*). Nonetheless, population viability studies have been revealing. For example, population declines of 11 to 45% by 2100 have been projected for Cassin's auklet (*Ptychoramphus aleuticus*), a planktivorous seabird; this model was based on established relationships between demographic rates (breeding success and adult survival) and upwelling intensity and ocean temperatures (*87*). In the Antarctic, continent-wide declines of emperor penguins have been projected based on local SIE in relation to breeding success and survival estimates (*76*). At the continental scale, interannual variability in SIE promotes population stability because of opposing functions between SIE and breeding success and survival. Climate-dependent models also highlight the complexity of responses in fish. For example, for south Pacific albacore tuna (*Thunnus alalunga*), application of a 2D coupled physical-biological-fisheries model at the ocean basin scale predicts an initial population decline followed by an increase in biomass as a new spawning ground is established toward the end of the 21st century (*88*). However, population dynamics are also sensitive to simulated changes in optimal spawning temperatures; accounting for potential evolutionary processes favoring albacore with preferences for higher optimal ambient spawning temperature suppresses the emergence of a new spawning ground, and stock abundance remains low.

"Changing climate creates systemic effects that ripple through marine food webs, affecting all trophic levels."

Capacity for adaptation

The albacore example underscores a crucial yet relatively understudied issue: the potential for evolutionary adaptation and/or phenotypic plasticity to modulate population responses to climate change. The former involves genetic change across generations driven by natural selection on heritable phenotypes, whereas the latter occurs when individuals use current genes to express different phenotypes in changing environments. Plasticity typically occurs more rapidly than does evolution and thus represents the "first line of defense" in a changing environment. Indeed, a large body of work demonstrates that marine vertebrates have a broad capacity to adjust their behaviors, physiology, and morphology in response to short-term changes in environmental conditions via plasticity in labile (in which phenotype changes at least as fast as the environment) and nonlabile traits (*89*–*91*). Tagging studies of seabirds, marine mammals, and pelagic fish offer opportunities for measuring individual reaction norms—the range of phenotypes produced across environments because of phenotypic plasticity—and fitness correlates and relating these to population-level trends. For example, individual common murres (*Uria aalge*) adjust egg-laying dates in response to climate-related cues, allowing them to track interannual changes in the seasonal peak in forage, with benefits for breeding success (*92*). The need for plasticity in some traits, however, is balanced by selection for relative constancy ("canalization") in others that are more closely correlated with fitness (*91*). Many long-lived pinnipeds and seabirds, for example, maximize fitness by minimizing interannual variance in adult survival and breeding propensity, which in turn dampens the demographic consequences of changing climate (*93*). Antarctic fur seals (*Arctocephalus gazella*) breeding on South Georgia have lost some of this capacity for life history buffering, however, likely because of a lack of plasticity in breeding schedules in the face of reduced food predictability (*93*).

More generally, plasticity has its limits, and evolutionary adaptation of reaction norms themselves may be required for populations to persist in rapidly changing (or increasingly variable) climates. Empirical evidence for evolutionary responses to contemporary climate change in marine vertebrates (indeed, most taxa) is almost completely lacking, but this may reflect detection problems rather than a lack of evolutionary potential (*90*, *91*). Most populations harbor substantial genetic variation for traits affecting fitness, but the key unknown is whether evolution can unfold rapidly enough to prevent extinction (*94*). Phenological traits in particular may experience strong selection; for example, timing of peak nesting of adjacent genetic stocks of the flatback sea turtle *Chelonia depressa* in northern Australia have diverged to coincide with local temperature regimes compatible with high incubation success and suitable hatchling sex ratios, but this likely occurred over thousands of years (*95*). Whether marine vertebrates can keep evolutionary pace with unprecedented (at least in their recent evolutionary history) rates of environmental change is of great concern, and "space-for-time" substitutions may be a poor guide in this respect. In theory, transgenerational adaptation to climate

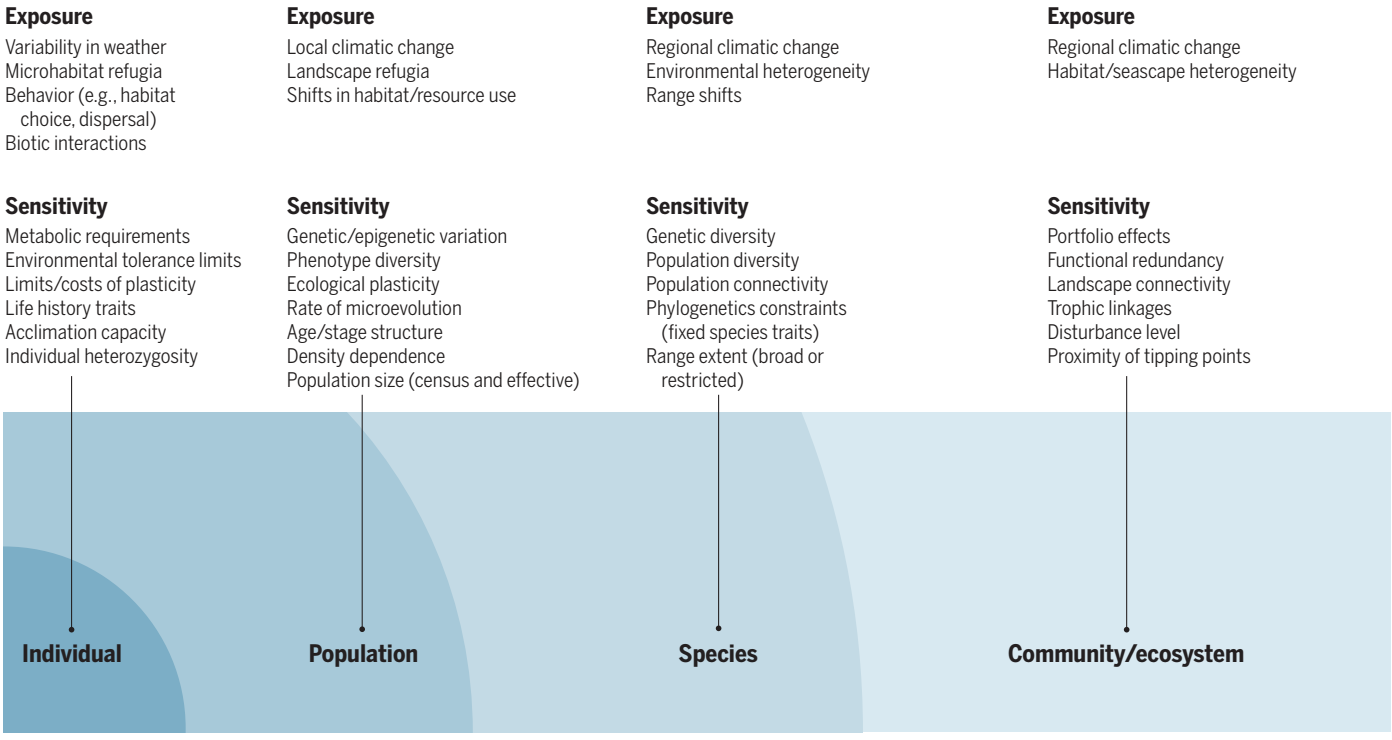

Fig. 2. Intrinsic properties of individuals, populations, species, and communities, together with extrinsic properties of the environments they inhabit, shape their exposure and sensitivity to climate change. Exposure is a function of climatic change and the degree of buffering due to habitat heterogeneity (such as refugia) and behavioral adjustments. Sensitivity is affected by intrinsic factors such as physiological tolerances and (relatively) fixed population/species traits and will be mediated by evolutionary changes, plastic ecological responses, and resilience (the capacity of systems to persist and recover from disturbance). Vulnerability and emergent dynamics at each level of biological organization depend on processes operating at lower levels. For example, phenotypic plasticity and evolutionary adaptation (or lack thereof) propagate up from individuals and populations to affect the resilience of species and communities, and thereby ecosystem function. Additional human stressors and conservation management will further affect ecological and evolutionary resilience by modifying these and other factors. [Adapted from (*101*, *116*)]

change can also occur via epigenetic mechanisms or inherited environmental effects (*96*), but the importance of these mechanisms is uncertain. Laboratory experiments for the few vertebrate species that lend themselves to captive breeding (*97*), or observations of fine-grained population responses (*98*), can be used to infer the potential for phenotypic plasticity and microevolution.

Clearly, marine vertebrate species do not have equal scope for adaptive responses. For example, species that evolved in relatively stable climates are expected to have narrow thermal tolerances (such as stenothermal Antarctic fishes) (*99*) and less capacity for thermal or other types of plasticity than that of populations inhabiting more variable environments. Similarly, historically large, widespread, or well-connected populations may possess greater evolutionary potential than those of small, localized, or isolated populations (*100*). Aside from these general rules of thumb, it is difficult to predict a priori which marine vertebrates will be most capable of adapting to climate change. The strongest generalizations that can be made are that (i) all else being equal, species with shorter generation times will evolve faster than those with longer generation times, at least initially (at evolutionary equilibrium, both are predicted to track a moving optimum at the same annual rate), and (ii) species capable of rapid population growth are more likely to be rescued by evolution (*94*). Marine vertebrates with slow life histories and low annual fecundity—most seabirds, sea turtles, and marine mammals, as well as many sharks—are thus expected to be less evolutionarily resilient to rapid climate change, despite the fact that they have substantial capacity for adaptive plasticity. However, life histories themselves may evolve because of climate-induced selection, although again the pace of such changes will be critical.

Thus, a major challenge remains to understand how the resilience of species, communities, and ecosystems is affected by the plasticity of individuals and microevolution (or a lack thereof) of populations. It is useful in this respect to distinguish among factors affecting exposure to changing environments and those affecting sensitivity to given changes, which together determine vulnerability at each level of biological organization (Fig. 2) (*101*). It is also important to realize that plasticity and evolutionary adaptation by no means guarantee population persistence and can even lead to declines in abundance (*102*). On the other hand, populations and species may respond to climate change idiosyncratically, and such diversity can enhance the resilience of species and communities via portfolio effects (in which the dynamics of biological systems are less variable than their individual components) (*103*). For example, the overall numbers of sockeye salmon *O. nerka* returning to Bristol Bay, Alaska, annually are much less volatile than the numbers returning to individual rivers within the bay, owing to asynchronous dynamics among local populations (*104*). Given the limitations on our forecasting abilities, adaptable conservation strategies that spread risk and maintain genetic and ecological heterogeneity and connectivity are most prudent (*103*, *105*).

Concluding remarks

Changing climate creates systemic effects that ripple through marine food webs, affecting all trophic levels. Most climatic effects on seabird and mammalian consumers, being mid- to upper-trophic-level species, will be indirect, operating via changes in ocean productivity and food webs. In contrast, ectothermic fish may respond immediately and substantially to relatively small changes in temperature and oxygen concentrations and potentially ocean acidification, factors that may affect their metabolism. Endothermic organisms, such as birds and mammals, may not respond directly to physical changes and only to changes in food supplies over time, but once they respond, changes are likely to be substantial and difficult to reverse. Thus, indirect responses, although perhaps delayed, are powerful and potentially long-lasting, hence a challenge for management and conservation. Some impacts may be mediated by phenotypic plasticity or evolutionary change, but the capacity for marine vertebrates to respond

in this manner is variable and unpredictable based on the information at hand. Anthropogenic global warming is anticipated to increase physical and ecosystem variability and bring ecological surprises as novel species interactions and communities form, which further confounds assessment of risks to marine vertebrates.

A variety of new modeling approaches are emerging, from species distribution models (SDMs) and population models to complex ecosystem models operating across varying temporal and spatial scales, all of which involve balancing trade-offs in realism against uncertainties in model parameters and structures (*106*). The latest wave of SDMs better account for interactions between evolution and dispersal (as well as biotic interactions), but their parameterizations are limited by data availability, and increases in model complexity can come at the expense of tractability (*107*). International coordination of modeling efforts (for example, fisheries under the framework of the Inter-sectoral Impact Model Intercomparison Project) (*108*) may provide consistent estimates of uncertainties (*109*). The availability of high-quality data on marine vertebrates, however, facilitates comparative studies of similar species between ecosystems, as well as coupling climate and ecosystems models with genetic and population models, which are feasible approaches to improve understanding and forecasting the future for these key marine animals.

REFERENCES AND NOTES

1. J. A. Estes *et al*., *Science* **333**, 301–306 (2011).
2. D. J. McCauley *et al*., *Science* **347**, 1255641 (2015).
3. B. S. Halpern *et al*., *Nature* **488**, 615–620 (2012).
4. R. C. Murphy, *Oceanic Birds of South America* (American Museum of Natural History, New York, 1936).
5. J. Radovich, *Fish. Bull.* **112**, 1 (1961).
6. N. J. Aebischer, J. C. Coulson, J. M. Colebrookl, *Nature* **347**, 753–755 (1990).
7. R. C. Francis, S. R. Hare, A. B. Hollowed, W. S. Wooster, *Fish. Oceanogr.* **7**, 1–21 (1998).
8. S. Sundby, O. Nakken, *ICES J. Mar. Sci.* **65**, 953–962 (2008).
9. K. R. Wood, J. E. Overland, *Int. J. Climatol.* **30**, 1269–1279 (2010).
10. A. V. Tåning, in *International Commission for the Northwest Atlantic Fisheries: Annual Proceedings, Vol. 3, for the year 1952–53* (Headquarters of the Commission, Imperial Press, Halifax, Canada, 1953), pp. 69–78.
11. K. F. Drinkwater, *Prog. Oceanogr.* **68**, 134–151 (2006).
12. H. O. Pörtner, R. Knust, *Science* **315**, 95–97 (2007).
13. B. A. Block *et al*., *Nature* **475**, 86–90 (2011).
14. E. S. Poloczanska *et al*., *Nat. Clim. Change* **3**, 919–925 (2013).
15. D. Yemane *et al*., *Rev. Fish Biol. Fish.* **24**, 463–483 (2014).
16. J. P. Croxall, P. N. Trathan, E. J. Murphy, *Science* **297**, 1510–1514 (2002).
17. O. Hoegh-Guldberg *et al*., in *Climate Change 2014: Impacts, Adaptation, and Vulnerability. Part B: Regional Aspects. Contribution of Working Group II to the Fifth Assessment Report of the Intergovernmental Panel on Climate Change*, V. R. Barros *et al*., Eds. (Cambridge Univ. Press, Cambridge, 2014), pp. 1655–1731.
18. IPCC, *Climate Change 2013: The Physical Science Basis. Contribution of Working Group I to the Fifth Assessment Report of the Intergovernmental Panel on Climate Change*, T. F. Stocker *et al*., Eds. (Cambridge Univ. Press, Cambridge, 2013).
19. A. R. Stine, P. Huybers, I. Y. Fung, *Nature* **457**, 435–440 (2009).
20. P. W. Boyd, S. Sundby, H.-O. Pörtner, in *Climate Change 2014: Impacts, Adaptation, and Vulnerability. Part A: Global and sectoral aspects. Contribution of Working Group II to the Fifth Assessment Report of the Intergovernmental Panel on Climate Change*, C. B. Field *et al*., Eds. (Cambridge Univ. Press, Cambridge, 2014), pp. 133–136.
21. M. T. Burrows *et al*., *Science* **334**, 652–655 (2011).
22. C. Parmesan, *Annu. Rev. Ecol. Evol. Syst.* **37**, 637–669 (2006).
23. M. Edwards, A. J. Richardson, *Nature* **430**, 881–884 (2004).
24. C. Barbraud, H. Weimerskirch, *Proc. Natl. Acad. Sci. U.S.A.* **103**, 6248–6251 (2006).
25. S. Wanless, M. P. Harris, S. Lewis, M. Frederiksen, S. Murray, *Mar. Ecol. Prog. Ser.* **370**, 263–269 (2008).
26. L. Slater, G. V. Byrd, *J. Biogeogr.* **36**, 465–475 (2009).
27. Y. Watanuki, M. Ito, *Mar. Ecol. Prog. Ser.* **454**, 183–196 (2012).
28. L. E. Chambers, P. Dann, B. Cannell, E. J. Woehler, *Int. J. Biometeorol.* **58**, 603–612 (2014).
29. M. Dalleau *et al*., *PLOS ONE* **7**, e46920 (2012).
30. N. Neeman, N. J. Robinson, F. V. Paladino, J. R. Spotila, M. P. O'Connor, *J. Exp. Mar. Biol. Ecol.* **462**, 113–120 (2015).
31. M. Hamann, C. J. Limpus, D. W. Owens, in *The Biology of Sea Turtles*, P. L. Lutz, J. A. Musick, Eds. (CRC Press, Boca Raton, FL, 2003), vol. 2, pp. 135–161.
32. R. P. Kovach, S. C. Ellison, S. Pyare, D. A. Tallmon, *Glob. Change Biol.* **21**, 1821–1833 (2015).
33. J. I. Fincham, A. D. Rijnsdorp, G. H. Engelhard, *J. Sea Res.* **75**, 69–76 (2013).
34. R. G. Asch, *Proc. Natl. Acad. Sci. U.S.A.* **112**, E4065–E4074 (2015).
35. M. E. Visser, C. Both, *Proc. Biol. Sci.* **272**, 2561–2569 (2005).
36. T. E. Reed *et al*., *PLOS ONE* **6**, e20380 (2011).
37. J. J. Anderson, E. Gurarie, C. Bracis, B. J. Burke, K. L. Laidre, *Ecol. Modell.* **264**, 83–97 (2013).
38. F. Bailleul, V. Grimm, C. Chion, M. Hammill, *Ecol. Evol.* **3**, 2535–2546 (2013).
39. D. H. Cushing, *Adv. Mar. Biol.* **26**, 249–293 (1990).
40. S. Burthe *et al*., *Mar. Ecol. Prog. Ser.* **454**, 119–133 (2012).
41. W. J. Sydeman, S. J. Bograd, *Mar. Ecol. Prog. Ser.* **393**, 185–188 (2009).
42. S. J. Thackeray *et al*., *Glob. Change Biol.* **16**, 3304–3313 (2010).
43. A. Donnelly, A. Caffarra, B. F. O'Neill, *Int. J. Biometeorol.* **55**, 805–817 (2011).
44. J. García Molinos *et al*., *Nat. Clim. Change* 10.1038/nclimate2769 (2015).
45. K. Kaschner, D. P. Tittensor, J. Ready, T. Gerrodette, B. Worm, *PLOS ONE* **6**, e19653 (2011).
46. E. L. Hazen *et al*., *Nat. Clim. Change* **3**, 234–238 (2013).
47. J. G. Hiddink, R. ter Hofstede, *Glob. Change Biol.* **14**, 453–460 (2008).
48. F. J. Mueter, M. A. Litzow, *Ecol. Appl.* **18**, 309–320 (2008).
49. J. Shoji *et al*., *ICES J. Mar. Sci.* **68**, 1165–1169 (2011).
50. K. Saikkonen *et al*., *Nat. Clim. Change* **2**, 239–242 (2012).
51. M. L. Pinsky, B. Worm, M. J. Fogarty, J. L. Sarmiento, S. A. Levin, *Science* **341**, 1239–1242 (2013).
52. A. L. Perry, P. J. Low, J. R. Ellis, J. D. Reynolds, *Science* **308**, 1912–1915 (2005).
53. J. A. Nye, J. S. Link, J. A. Hare, W. J. Overholtz, *Mar. Ecol. Prog. Ser.* **393**, 111–129 (2009).
54. K. Brander, *J. Marine Syst.* **79**, 389–402 (2010).
55. C. H. Hsieh, C. S. Reiss, R. P. Hewitt, G. Sugihara, *Can. J. Fish. Aquat. Sci.* **65**, 947–961 (2008).
56. A. D. Rijnsdorp, M. A. Peck, G. H. Engelhard, C. Mollmann, J. K. Pinnegar, *ICES J. Mar. Sci.* **66**, 1570–1583 (2009).
57. G. H. Engelhard, D. A. Righton, J. K. Pinnegar, *Glob. Change Biol.* **20**, 2473–2483 (2014).
58. P. R. Last *et al*., *Glob. Ecol. Biogeogr.* **20**, 58–72 (2011).
59. J. A. Nye, T. M. Joyce, Y. O. Kwon, J. S. Link, *Nat. Commun.* **2**, 412 (2011).
60. L. Stramma *et al*., *Nat. Clim. Change* **2**, 33–37 (2012).
61. W. W. L. Cheung *et al*., *Nat. Clim. Change* **3**, 254–258 (2013).
62. C. Deutsch, A. Ferrel, B. Seibel, H.-O. Pörtner, R. B. Huey, *Science* **348**, 1132–1135 (2015).
63. L. D. Zeidberg, B. H. Robison, *Proc. Natl. Acad. Sci. U.S.A.* **104**, 12948–12950 (2007).
64. J. C. Field *et al*., *Deep Sea Res. Part II Top. Stud. Oceanogr.* **95**, 37–51 (2013).
65. J. S. Stewart *et al*., *Glob. Change Biol.* **20**, 1832–1843 (2014).
66. A. S. Fischbach, S. C. Amstrup, D. C. Douglas, *Polar Biol.* **30**, 1395–1405 (2007).
67. J. S. Gleason, K. D. Rode, *Arctic* **62**, 405–417 (2009).
68. R. J. M. Crawford *et al*., *Afr. J. Mar. Sci.* **30**, 189–193 (2008).
69. J. N. Dunlop, R. D. Wooller, *Rec. West. Aust. Mus.* **12**, 389–394 (1986).
70. K. J. Kuletz, M. Renner, E. A. Labunski, G. L. Hunt Jr., *Deep Sea Res. Part II Top. Stud. Oceanogr.* **109**, 282–292 (2014).
71. C. Barbraud, H. Weimerskirch, *Nature* **411**, 183–186 (2001).
72. S. Jenouvrier *et al*., *Proc. Natl. Acad. Sci. U.S.A.* **106**, 1844–1847 (2009).
73. C. Barbraud, H. Weimerskirch, *J. Avian Biol.* **32**, 297–302 (2001).
74. S. Jenouvrier, C. Barbraud, H. Weimerskirch, *Ecology* **86**, 2889–2903 (2005).
75. T. Ballerini, G. Tavecchia, S. Olmastroni, F. Pezzo, S. Focardi, *Oecologia* **161**, 253–265 (2009).
76. S. Jenouvrier *et al*., *Nat. Clim. Change* **4**, 715–718 (2014).
77. H. Sandvik, K. E. Erikstad, R. T. Barrett, N. G. Yoccoz, *J. Anim. Ecol.* **74**, 817–831 (2005).
78. S. J. Burthe, S. Wanless, M. A. Newell, A. Butler, F. Daunt, *Mar. Ecol. Prog. Ser.* **507**, 277–295 (2014).
79. J. M. Cullen, L. E. Chambers, P. C. Coutin, P. Dann, *Mar. Ecol. Prog. Ser.* **378**, 269–278 (2009).
80. P. Inchausti *et al*., *J. Avian Biol.* **34**, 170–176 (2003).
81. A. Kitaysky, E. G. Golubova, *J. Anim. Ecol.* **69**, 248–262 (2000).
82. H. Weimerskirch, M. Louzao, S. de Grissac, K. Delord, *Science* **335**, 211–214 (2012).
83. S. M. Waugh *et al*., *Condor* **117**, 147–164 (2015).
84. L. A. Hawkes, A. C. Broderick, M. H. Godfrey, B. J. Godley, *Glob. Change Biol.* **13**, 923–932 (2007).
85. W. J. Sydeman, J. A. Santora, S. A. Thompson, B. Marinovic, E. Di Lorenzo, *Glob. Change Biol.* **19**, 1662–1675 (2013).
86. R. A. Myers, *Rev. Fish Biol. Fish.* **8**, 285–305 (1998).
87. S. G. Wolf, M. A. Snyder, W. J. Sydeman, D. F. Doak, D. A. Croll, *Glob. Change Biol.* **16**, 1923–1935 (2010).
88. P. Lehodey, I. Senina, S. Nicol, J. Hampton, *Deep Sea Res. Part II Top. Stud. Oceanogr.* **113**, 246–259 (2015).
89. P. L. Munday, R. R. Warner, K. Monro, J. M. Pandolfi, D. J. Marshall, *Ecol. Lett.* **16**, 1488–1500 (2013).
90. L. G. Crozier, J. A. Hutchings, *Evol. Appl.* **7**, 68–87 (2014).
91. T. B. Reusch, *Evol. Appl.* **7**, 104–122 (2014).
92. T. E. Reed *et al*., *J. Anim. Ecol.* **78**, 376–387 (2009).
93. J. Forcada, P. N. Trathan, E. J. Murphy, *Glob. Change Biol.* **14**, 2473–2488 (2008).
94. M. Kopp, S. Matuszewski, *Evol. Appl.* **7**, 169–191 (2014).
95. E. S. Poloczanska, C. J. Limpus, G. C. Hays, *Adv. Mar. Biol.* **56**, 151–211 (2009).
96. R. Bonduriansky, A. J. Crean, T. Day, *Evol. Appl.* **5**, 192–201 (2012).
97. J. M. Donelson, P. L. Munday, M. I. McCormick, C. R. Pitcher, *Nat. Clim. Change* **2**, 30–32 (2012).
98. L. G. Crozier, M. D. Scheuerell, R. W. Zabel, *Am. Nat.* **178**, 755–773 (2011).
99. G. N. Somero, *J. Exp. Biol.* **213**, 912–920 (2010).
100. C. M. Sgrò, A. J. Lowe, A. A. Hoffmann, *Evol. Appl.* **4**, 326–337 (2011).
101. S. E. Williams, L. P. Shoo, J. L. Isaac, A. A. Hoffmann, G. Langham, *PLOS Biol.* **6**, 2621–2626 (2008).
102. A. Lopez-Sepulcre, H. Kokko, in *Behavioural Responses to a Changing World. Mechanisms and Consequences*, U. Candolin, B. M. Wong, Eds. (Oxford Univ. Press, Oxford, 2012), pp. 3–15.
103. D. E. Schindler, J. B. Armstrong, T. E. Reed, *Front. Ecol. Environ* **13**, 257–263 (2015).
104. L. A. Rogers, D. E. Schindler, *Oikos* **117**, 1578–1586 (2008).
105. M. M. P. B. Fuentes *et al*., *Mitig. Adapt. Strateg. Glob. Change* 10.1007/s11027-014-9590-3 (2014).
106. A. B. Hollowed *et al*., *ICES J. Mar. Sci.* **70**, 1023–1037 (2013).
107. W. Thuiller *et al*., *Ecol. Lett.* **16** (suppl. 1), 94–105 (2013).
108. www.pik-potsdam.de/research/climate-impacts-and-vulnerabilities/research/rd2-cross-cutting-activities/isi-mip/about.
109. V. Huber *et al*., *Earth Syst. Dynam.* **5**, 399–408 (2014).
110. M. Frederiksen, T. Anker-Nilssen, G. Beaugrand, S. Wanless, *Glob. Change Biol.* **19**, 364–372 (2013).
111. C. Hoover, T. J. Pitcher, V. Christensen, *Ecol. Model.* **264**, 143–156 (2013).
112. M. A. McKinney *et al*., *Glob. Change Biol.* **19**, 2360–2372 (2013).
113. S. A. Iverson, H. G. Gilchrist, P. A. Smith, A. J. Gaston, M. R. Forbes, *Proc. Biol. Sci.* **281**, 20133128 (2014).
114. P. Greenslade, *J. Insect Conserv.* **12**, 333–342 (2008).
115. G. N. Batianoff, G. C. Naylor, J. A. Olds, N. A. Fechner, V. J. Neldner, *Pac. Sci.* **64**, 73–92 (2010).
116. M. I. O'Connor, E. R. Selig, M. L. Pinsky, F. Altermatt, *Glob. Ecol. Biogeogr.* **21**, 693–703 (2012).

ACKNOWLEDGMENTS

We thank J. Piatt, E. Hazen, and B. Black for reviewing earlier versions of the manuscript, and K. Kuletz and P. Gienapp for clarifying statements. W.J.S. and S.A.T. were supported under NSF award OCE-1434732. T.E.R. was supported by the European Research Council (ERC-STG-2014-639192-ALH) and the Irish Government's Beaufort Marine Research Award in Fish Population Genetics.

10.1126/science.aac9874

REVIEW

Climate change in the oceans: Human impacts and responses

Edward H. Allison* and Hannah R. Bassett

Although it has far-reaching consequences for humanity, attention to climate change impacts on the ocean lags behind concern for impacts on the atmosphere and land. Understanding these impacts, as well as society's diverse perspectives and multiscale responses to the changing oceans, requires a correspondingly diverse body of scholarship in the physical, biological, and social sciences and humanities. This can ensure that a plurality of values and viewpoints is reflected in the research that informs climate policy and may enable the concerns of maritime societies and economic sectors to be heard in key adaptation and mitigation discussions.

On 1 September 2015, U.S. President Barack Obama, walking on the moraine below the receding Exit Glacier in Alaska, pointed to the distant ice and said, "This is as good of a signpost of what we're dealing with when it comes to climate change as just about anything" (*1*).

We can see retreating glaciers and shrinking lakes or experience heat waves, crop failures, and extended wildfire seasons. By comparison, the ocean appears unchanging to a public that gives greater credence to climate change science when they have seen or directly experienced changes consistent with its predictions (*2*). Unlike the shrinking Exit Glacier, the oceanic components of climate change remain largely hidden beneath the waves. Similarly, the diverse sectors that make up the global ocean economy, such as energy, transport, fisheries, and tourism, have not been the subject of integrated analysis and are thus subsumed within sectoral analyses that fail to highlight their collective value. The "out of sight, out of mind" nature of ocean change is reflected in the ocean's lack of visibility in global climate change policy debates, including the annual Conference of the Parties to the UN Framework Convention on Climate Change (UNFCCC) (*3*), even though the impacts of climate change on the ocean are well documented (*4*, *5*) and have far-reaching implications for society.

The latest Intergovernmental Panel on Climate Change (IPCC) global assessment identifies the main oceanic elements of observed global environmental change as follows: rising sea surface temperature; thermal expansion of the oceans and melting sea ice, leading to sea-level rise; changes to ocean thermal structure and currents; changes in the periodicity and amplitude of ocean climate cycles such as El Niño; changes in the frequency and severity of hurricanes and typhoons; ocean acidification; and deoxygenation of areas of the sea where thermal stratification is strengthening and nutrients and productivity are rising (oceanic "dead zones") (*4*).

Climate change research in the humanities and social sciences is furthering our understanding of the socially differentiated impacts of climate change, the range of adaptation options being pursued or considered, and the support for and challenges to ongoing technical and political responses to climate change. Much of this insight is missing from most "human dimensions" research in major Earth (and ocean) system science programs; such research is typically limited to attempts to quantify potential vulnerabilities to physical and biochemical changes, economic analyses of the monetary value of threatened ecosystem goods and services, and analyses of the costs and benefits of various options for adaptation and mitigation action (*6*).

> ***"The 'out of sight, out of mind' nature of ocean change is reflected in the ocean's lack of visibility in global climate change policy debates..."***

Near and distant impacts

Ocean-related climate change impacts on human society and institutions will necessitate responses at scales from the individual to the global. Oceanic influences on the global climate system mean that populations and economic activities that are far removed from the sea can be influenced by ocean change. For example, predicted changes in the intensity and frequency of El Niño–Southern Oscillation (ENSO) events, driven by ocean warming (*7*), may alter previously experienced patterns of ENSO-driven variability in Peruvian fish catches (*8*), Indonesian rice harvests (*9*), cholera epidemics in Bangladesh (*10*), crop and livestock production in sub-Saharan Africa (*11*), forest fire risks in the western United States (*12*), and the profitability of winter sports tourism in Arizona (*13*)—all with consequences for societies and economies in these areas. More proximally, maritime and coastal societies will also be affected by climate variability and change that are not specifically or exclusively ocean-related—such as glacial melting, summer heat waves, and changes in precipitation frequency, intensity, and timing—as a result of the many teleconnections between global environmental change, the oceans, and human societies (*14*). These often interacting and indirect pathways complicate our understanding of climate change impacts and challenge our ability to plan adaptive responses.

Probably the greatest adaptation challenges are those faced by people who either live close enough to the coast to be directly affected by a combination of sea-level rise and extreme weather events, have a livelihood and way of life closely linked to the health of the marine environment, or are nutritionally dependent on access to marine resources.

Where there is uncertainty regarding climate change impacts, as with projected increases in the severity or frequency of oceanic storms (*15*), improvements in short- and medium-term forecasts, evacuation plans, shelter provision, and knowledge of the social conditions that lead to vulnerability are helping to reduce loss of life: In Bangladesh, Cyclone Gorka killed an estimated 140,000 people in 1991, whereas Cyclone Sidr, in 2007, claimed between 3500 and 10,000 lives (*16*). Extensive social analysis of the aftermath of Hurricane Katrina has shown that a history of systemic inequality led to disproportionate impacts on the city of New Orleans's African American population, which were still evident years later (*17*).

Climate change impacts on the "blue economy"

As terrestrial sources of energy, minerals, and food come under greater strain from growing demand, governments and the private sector have increasingly looked to the oceans for new resource extraction and business opportunities (Fig. 1) (*18*). The framing of much recent research on climate change impacts on the ocean reflects this shift: A key concern is documenting the potential impacts on established and emergent maritime industries and their ability to generate "blue wealth" (*19*). Environmental valuation approaches are used to estimate the market-equivalent value of ecosystem services, such as the contribution of coral reefs to fisheries, tourism, and coastal protection (*20*).

The future of fisheries in a changing climate, for example, is one important issue. Another is the marine renewable energy sector (offshore wind, tidal, and wave power), which could benefit from increased investment and accelerated technological development if there

School of Marine and Environmental Affairs, University of Washington, Seattle, WA 98195, USA.
*Corresponding author. E-mail: eha1@uw.edu

is substantial policy support for reducing fossil fuel energy use (*21*). A paradoxical short-term benefit of climate change is that melting Arctic sea ice is making new areas accessible to oil exploration and potentially viable for exploitation (*22*, *23*), thereby contributing to emissions that would accelerate warming and acidification. Without adaptive action, some of the largest economic impacts will be on coastal cities, where sea-level rise is expected to make weathering storms more challenging, irrespective of whether they increase in frequency or severity (*24*).

Not all individuals and societies see their relationship with the sea as primarily an economic one, however, and there is widespread concern among both traditional users of the sea (small-scale fisherfolk and coastal indigenous groups) and environmentalists over the race to extract wealth from the oceans (*25*). An understanding of climate change's effects on other, nonmonetary systems of value is needed if we are to develop a fuller understanding of its potential impact on the human relationship with the sea.

Climate change and fisheries

One of the clearest demonstrations that anthropogenic warming has altered ecosystems is the poleward shift in the ranges of exploited fish species since the mid-20th century (*26*).

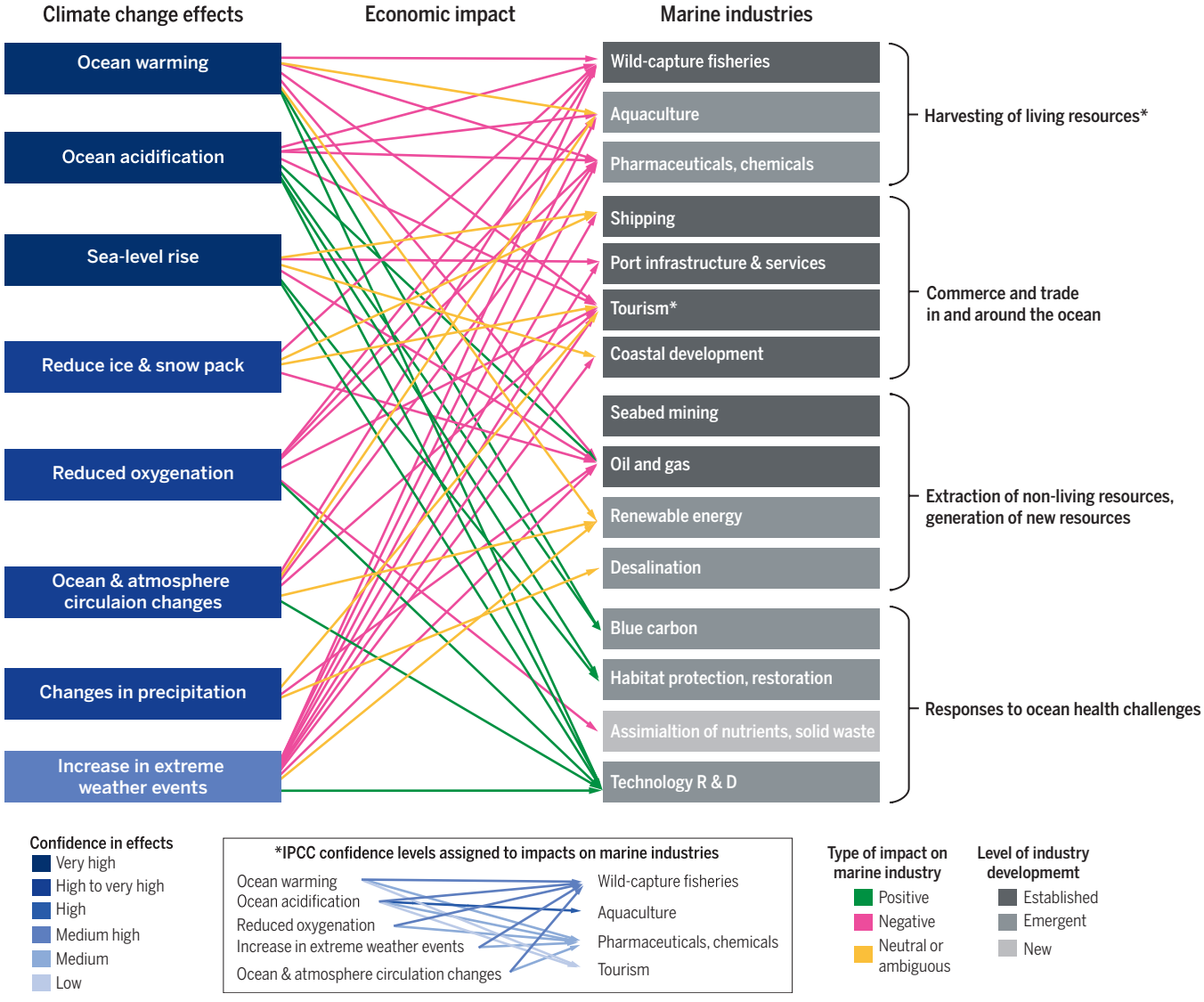

Fig. 1. Established, emerging, and new ocean industries, as identified by the Economist Intelligence Unit (*19*), are listed in the right column; (shades of gray reflect levels of development) and organized by type. Climate change effects are listed in the left column, with shades of blue reflecting the IPCC level of confidence that these changes are taking place and are linked to increased anthropogenic greenhouse gas emissions. The arrows indicate the type of net economic impact (green, positive; pink, negative; yellow, neutral or ambiguous) that these climate change effects are hypothesized to have on the indicated industry. Except where the IPCC has already done so (inset), no level of confidence is ascribed to the hypothesized economic impacts. An IPCC-type systematic review and consensus process would be required to assess all estimates of costs and benefits and add confidence bounds to each potential impact. The IPCC so far has not considered the ocean economy in this way. Globally, negative impacts will be experienced predominantly by industries involved with living-resource harvest, coastal and marine tourism, and ocean commerce and trade. Impacts on nonliving-resource extraction and the generation of new resources are either unstudied, neutral, or negative. Activities involved with responding to ocean health challenges could see high demand and a net positive economic impact. This diagram simplifies what is likely to be a mosaic of regionally differentiated impacts and of multiple interacting pathways of impact. Studies that propose these economic impact pathways and identify their causal mechanisms are given in the supplementary materials (*18*).

Based on relationships between sea surface temperature, ocean circulation, and primary production, two different models have independently predicted slight increases in global ocean fish production capacity by the mid-21st century, with a consistent pattern of decreased production in the tropics and increases at temperate latitudes (*27*, *28*). However, these model-based studies do not consider the range of potentially disruptive factors that could mediate the relationships between climate change, primary production, and fish production. These include the impacts of ocean acidification, which could have severe effects on calcifying organisms in food chains and on commercially harvested shellfish (*29*).

Climate change and ocean acidification impacts on marine ecological dynamics will disproportionately affect people (including indigenous people) living near climate-sensitive environments, such as reef- or ice-dominated coasts, and coastal populations in low-income countries in the tropics, where populations are more nutritionally and economically dependent on marine resources (*30*–*32*).

How is society responding to climate change impacts on oceans and coasts?

Societal responses to climate change range from individual adaptive decisions to attempts by representatives of sovereign states to reach a global consensus on reducing emissions. Although global impact and indicator-based vulnerability studies and global mitigation scenarios are useful starting points for raising awareness of climate change issues and for informing high-level policy, they provide little guidance for action at more local levels. Differences in the way people respond to climate change itself or to policy proposals to address it play out within households and communities and between wealthier and poorer nations. Understanding these social and political dynamics requires different kinds of research than the large-scale, comparative, quantitative, and model-based work that dominates climate science's input to major studies of global environmental change (*6*, *32*).

Efforts to engage citizens in actions to address local and regional effects of climate change in coastal areas have included initiatives such as replanting mangroves, which, if done appropriately (*33*), has benefits for coastal protection, fisheries, and carbon sequestration (*34*). Communications research has shown that nonthreatening images that engage everyday emotions, such as a picture of a community mobilizing to protect their local environment, are more likely to inspire wider citizen action to address climate change impacts than are fear-inducing representations of climate catastrophe (*35*). Citizens engaged in local climate action are in turn more likely to support higher-level policy responses to global change (*36*).

Understanding public perceptions of climate change and the oceans

When asked about climate change, people express a spectrum of views that includes concern, skepticism, belief, denial, and fatalism. Positing a simplistic dichotomy between climate change advocates and deniers is inadequate as a basis for understanding how society is responding, because there is a wide variety of voices in social movements with an interest in climate change (*37*). In the United States, where numerous studies have been conducted, differences in the acceptance of anthropogenic climate change are rooted in conflicting sociopolitical identities rather than in disparities in education or knowledge about climate change (*38*). People's climate change views are thus unlikely to respond to the rationality of more certain and/or more clearly communicated climate science.

Marine- and coastal-focused surveys of public perception are not common and have tended to address climate change in the context of multiple risks. In a large European survey, pollution and the state of fish stocks were the two major environmental issues that came to mind when the oceans were mentioned, with coastal erosion, sea-level rise, and climate change less commonly identified as key concerns (*39*). More than half of the 10,000 people questioned also felt that a change in the frequency of extreme weather was already apparent, although this is among the least certain of climate change effects, according to the IPCC consensus (*4*). Mixed farming-fishing households in coastal East Africa perceived erratic rainfall and rising temperatures to be key risks to their livelihoods, compounded by factors such as wars, unfavorable economic policies, and population increases that have pushed people into living in marginal areas where their livelihoods are more exposed to impacts of climate change (*40*).

Responding to climate change impacts on the ocean: Adaptation

Adaptation responses can be made autonomously by individuals or through planned actions at various scales, from "climate-proofing" coastal urban infrastructure in cities to national and regional agreements. At the local level, for example, coral bleaching often has negative effects on reef fish biomass and therefore on fishers' catches; adaptive responses may include switching to off-reef fisheries or diversifying out of fishing (*38*, *41*).

Climate change adaptation plans formulated by governments and development agencies

Table 1. Some potential contributions of social sciences and humanities to understanding people's responses to ocean climate change.

Themes for social science and humanities research	Potential applications
Understand people's knowledge and perceptions of ocean-related environmental change, including acidification and sea-level rise.	Develop strategies to build support for policies addressing emissions reductions; design effective adaptation measures.
Understand people's moral, political, and emotional responses to climate variability and change.	Influence individual and collective behavior; communicate climate science more effectively; provide targeted material and emotional support to affected communities; articulate moral and ethical positions as well as economic rationales for action.
Identify technological, political, economic, and social trends and forces influencing the climate system.	Identify the best opportunities and processes for transformational change to address climate change drivers.
Understand historical adaptation of societies to variability and change; understand how contemporary adaptation plans and action decisions are made at different scales, from individual to global.	Improve governance, planning, and resource allocation; provide scenarios and visions for future societal adaptation.
Identify social differences and their links to climate vulnerability and resilience.	Target adaptation support; enable marginalized people's voices to be heard in policy; support the agency of those most affected by climate change.
Understand how power is exercised through networks of influence; reveal vested interests; identify people's incentives to undertake or resist climate action.	Challenge power; build coalitions to secure support for climate justice.

tend to focus on material dimensions of life, with adaptive capacity often measured in terms of the asset status of individuals and households. It is less often appreciated that climate change can threaten identity, community cohesion, and sense of place; also, culture shapes how societies respond and adapt to climate-related risks, offering a range of opportunities that may not be apparent to external agents. Many coastal communities that are closely tied to the sea have distinct cultures and ethnicities, with strong attachments to occupation and place. Diversifying and relocating may make sense from an economic rationality or human security perspective, but it may cause irrevocable loss of cultural identity and social well-being (*42*).

Being identified as "vulnerable" may give some leverage to groups in policy negotiations and helps to target financing for adaptation, but there is concern that such labeling also carries risks. Ethnographic analysis of Arctic populations argues that vulnerability analysis can lead to misguided actions based on external perceptions of people's capabilities, and it can shape how people view themselves and undermine their efforts to gain greater autonomy over their own affairs (*43*). Similarly, portraying women in the Global South as being passive victims of climate change undermines their political and social agency (*44*); nevertheless, climate change impacts can reflect, expose, and exacerbate existing gender inequalities, so there are strong arguments for ensuring that adaptation policies are not gender-blind (*45*).

At a more global scale, small-island developing states have exercised moral power in their attempts to secure international, legally binding agreements on emissions and an adaptation fund to assist countries affected by climate change but not responsible for causing it (*46*). Ahead of the December 2009 UNFCCC meeting in Copenhagen, then-President of the Maldives Mohammed Nasheed held an underwater meeting with his ministers to highlight the threat of sea-level rise to his atoll nation. The notion of climate justice provides a moral compass that helps to navigate the complexities of adaptation policy. Small-island states, indigenous coastal people, and the coastal poor in developing countries are among those who have contributed least to anthropogenic climate change, yet they are among the most exposed to its effects. Climate justice is based on a demand that this be recognized. This moral authority is exercised in international climate negotiations and has helped to secure an adaptation fund for which countries preparing national plans of adaptation can apply, though the amount pledged falls short of what was deemed necessary and fair (*47*). The marine fisheries and aquaculture sectors appear in a number of national adaptation plans but may be underrepresented because of the late recognition of the importance of climate change to these sectors (*48*).

One adaptive response that causes particular concern for geopolitical stability is the possibility of people fleeing areas that have become uninhabitable as a result of changes in climate. In the case of coastal zones, sea-level rise in a world in which temperatures have risen by 4°C could displace 187 million people by 2100, unless major investments in coastal defenses are made (*49*).

The potential role of oceans in climate change mitigation

Although the oceans are a major component of global carbon cycles, their ability to contribute to mitigation of climate change though increased carbon sequestration is limited and may decline as the ocean acidifies (*50*). The ocean system can make contributions to mitigation in three ways: (i) conservation and enhancement of "blue carbon" (carbon stored by coastal and marine ecosystems), (ii) improved energy efficiency of ocean-related industries, and (iii) geoengineering. Opportunities to sequester more blue carbon though ecosystem management are largely limited to coastal areas. Although mangroves occupy only 0.5% of the global coastal area, they contribute 10 to 15% (24 Tg of carbon per year) to coastal sediment carbon storage and export 10 to 11% of particulate terrestrial carbon to the ocean (*51*). Along with seagrass meadows and salt marshes, mangroves are being lost or degraded by coastal development, with the resulting release of stored carbon currently negating their contribution to sequestration (*52*). This makes protecting and restoring the ocean's fringing vegetation a high priority. Doing so yields the triple advantages of contributing to mitigation; conferring adaptive benefits to coastal zones through enhanced protection from wave, storm, and tidal erosion; and providing immediate ecological, economic, and social benefits in the form of biodiverse nursery grounds for fish and shellfish that support fisheries and tourism. Conserving and restoring the more hidden but no less important subtidal seagrass beds could confer similar benefits (*53*).

"Ocean-related climate change impacts on human society and institutions will necessitate responses at scales from the individual to the global."

The main maritime industries are currently oil and gas exploration, shipping, fishing and aquaculture, and coastal tourism (Fig. 1). All could benefit from improved environmental governance resulting in reduced energy consumption and emissions. For the offshore oil and gas industry, the largest gains could be made by switching investments from continued extraction and exploration of fossil fuels to harnessing the potential of the oceans to generate renewable energy from tidal and wave power. This is unlikely in the next half-century (*53*). Environmental governance of shipping lags behind that of other transportation sectors and requires concerted pressure from the International Maritime Organization to address (*54*). Fisheries and aquaculture are both relatively energy-efficient ways of supplying humanity with nutritious animal-source foods, more so than most terrestrial animal production systems (*55*); thus, expansion of carbon- and energy-efficient shellfish aquaculture, increased energy efficiency in capture fisheries (including the reduction of fishing overcapacity), and reduced terrestrial livestock production have potential benefits for fishery management, marine conservation, sectoral economic efficiency, healthy human diets, and terrestrial land and water issues. As people get wealthier, they generally want to eat more meat (*56*) rather than seaweed and oysters, but dietary habits and food cultures do change. There are conflicts between the growth of coastal tourism and increasing emissions due to international travel, but energy efficiency measures in destination hotels and behavior changes among visitors are reducing the resource-consumption footprint of the sector, and ecotourism is raising awareness (*57*).

Ocean-based geoengineering solutions to mitigation challenges remain conceptual or experimental. They include modifying atmospheric albedo by cloud brightening, using a fine mist of seawater droplets sprayed by ships; increasing carbon sequestration through ocean fertilization to enhance primary production; adding materials such as carbonate or silicate, mined from the land, that help remove carbon dioxide from the atmosphere (known as "enhanced weathering"); or artificially inducing upwelling of nutrient-rich deep water to increase primary productivity in surface waters. The effects of all these geoengineering solutions on atmospheric temperature and the carbon cycle are uncertain, and their costs are currently prohibitive. There are also ethical concerns and legal obstacles to such permissible pollution (*53*).

Engaging with policy

Millions of people around the world's coasts are taking actions to influence policy, whether kayaking to protest Arctic oil drilling, marching to demonstrate their support for emissions reduction policies, resisting forced relocation, defending their access to fisheries, choosing their own adaptation pathways, or lobbying for an increase in global adaptation funds. Coastal cities are not waiting for globally binding agreements on emissions reductions before taking their own actions to reduce their energy

use and undertaking adaptive actions such as redesigning waterfront areas and coastal defenses (*58*). Documenting and explaining this range of political responses to climate change and reflecting on its implications is a task that the ocean science community has barely begun. Understanding people's interest in climate policy and how they choose to exercise it in terms of their values, means, and ends (*6*) enables an appreciation of the plurality of perspectives that exist outside the ocean science and climate science epistemic communities. Increased attention to people's beliefs and actions, as an integral component of interdisciplinary climate science, could be instrumental in crafting societal responses to the challenges posed by climate change in the oceans (Table 1).

Conclusions

Climate change impacts on the oceans are harder to see than receding glaciers, but they have profound implications for all human societies, not just coastal ones. Increasing societal concern over the fate of the oceans and growing economic interest in generating blue wealth make the oceans pivotal to achieving sustainable development goals. Ocean climate change research, as on land, is dominated by human-natural systems assessments that make good use of economics but limited use of those research disciplines that overlap least with the natural sciences (*59*). Insights from maritime history, ethnographies of coastal cultures, and the political geography of the oceans would strengthen future IPCC assessments of oceanic and coastal change. Including other, non-academic ways of perceiving and knowing, from indigenous knowledge (*60*) to the moral positions of major world religions (*61*), would allow a wide-ranging dialogue about possible responses to a changing climate in different social, cultural, and political settings. A richer understanding of the human dimensions of ocean climate change would assist in making the oceans more visible in climate change policy.

REFERENCES AND NOTES

1. "President Obama visits fading Exit Glacier," *MSNBC*, 1 September 2015; www.msnbc.com/msnbc/watch/president-obama-visits-fading-exit-glacier-517634115589.
2. E. U. Weber, *Nat. Clim. Change* **3**, 312–313 (2013).
3. G. Galland, E. Harrould-Kolieb, D. Herr, *Clim. Policy* **12**, 764–771 (2012).
4. IPCC, *Climate Change 2013: The Physical Science Basis. Contribution of Working Group I to the Fifth Assessment Report of the Intergovernmental Panel on Climate Change*, T. F. Stocker *et al.*, Eds. (Cambridge Univ. Press, Cambridge, 2013).
5. IPCC, *Climate Change 2014: Impacts, Adaptation, and Vulnerability. Part A: Global and Sectoral Aspects. Contribution of Working Group II to the Fifth Assessment Report of the Intergovernmental Panel on Climate Change*, C. B. Field *et al.*, Eds. (Cambridge Univ. Press, Cambridge, 2014).
6. N. Castree *et al.*, *Nat. Clim. Change* **4**, 763–768 (2014).
7. W. Cai *et al.*, *Nat. Clim. Change* **4**, 111–116 (2014).
8. F. P. Chavez, J. Ryan, S. E. Lluch-Cota, M. Niquen C, *Science* **299**, 217–221 (2003).
9. R. L. Naylor, D. S. Battisti, D. J. Vimont, W. P. Falcon, M. B. Burke, *Proc. Natl. Acad. Sci. U.S.A.* **104**, 7752–7757 (2007).
10. M. Pascual, X. Rodó, S. P. Ellner, R. Colwell, M. J. Bouma, *Science* **289**, 1766–1769 (2000).
11. L. C. Stige *et al.*, *Proc. Natl. Acad. Sci. U.S.A.* **103**, 3049–3053 (2006).
12. A. L. Westerling, H. G. Hidalgo, D. R. Cayan, T. W. Swetnam, *Science* **313**, 940–943 (2006).
13. R. H. Bark, B. G. Colby, F. Dominguez, *Clim. Change* **102**, 467–491 (2010).
14. W. N. Adger, H. Eakin, A. Winkels, *Front. Ecol. Environ* **7**, 150–157 (2009).
15. K. E. Trenberth, J. T. Fasullo, T. G. Shepherd, *Nat. Clim. Change* **5**, 725–730 (2015).
16. B. K. Paul, *Nat. Hazards* **50**, 289–304 (2009).
17. R. D. Bullard, B. Wright, in *Race, Place and Environmental Justice After Hurricane Katrina: Struggles to Reclaim, Rebuild and Revitalize New Orleans and the Gulf Coast*, R. D. Bullard, B. Wright, Eds. (Westview Press, Philadelphia, 2009), pp. 19–47.
18. Materials and methods are available as supplementary materials on *Science* Online.
19. *The Blue Economy: Growth, Opportunity and a Sustainable Ocean Economy. An Economist Intelligence Unit Briefing Paper for the World Ocean Summit 2015* (The Economist Intelligence Unit, London, 2015).
20. E. B. Barbier *et al.*, *Ecol. Monogr.* **81**, 169–193 (2011).
21. M. Esteban, D. Leary, *Appl. Energy* **90**, 128–136 (2012).
22. Ø. Harsem, K. Heen, J. M. P. Rodrigues, T. Vassdal, *Polar Rec. (Gr. Brit.)* **51**, 91–106 (2015).
23. W. N. Meier *et al.*, *Rev. Geophys.* **52**, 185–217 (2014).
24. Urban Climate Change Research Network, *Climate Change and Cities: First Assessment Report of the Urban Climate Change Research Network*, C. Rosenzweig, W. D. Solecki, S. A. Hammer, S. Mehrotra, Eds. (Cambridge Univ. Press, Cambridge, 2011).
25. N. J. Bennett, H. Govan, T. Satterfield, *Mar. Policy* **57**, 61–68 (2015).
26. A. L. Perry, P. J. Low, J. R. Ellis, J. D. Reynolds, *Science* **308**, 1912–1915 (2005).
27. W. W. Cheung *et al.*, *Glob. Change Biol.* **16**, 24–35 (2010).
28. M. Barange *et al.*, *Nat. Clim. Change* **4**, 211–216 (2014).
29. J. P. Gattuso *et al.*, *Science* **349**, aac4722 (2015).
30. K. Lynn *et al.*, *Clim. Change* **120**, 545–556 (2013).
31. E. H. Allison *et al.*, *Fish Fish.* **10**, 173–196 (2009).
32. C. Leyshon, *Contemp. Soc. Sci.* **9**, 359–373 (2014).
33. R. R. Lewis III, in *Coastal Wetlands: An Integrated Ecosystem Approach*, G. M. E. Perillo, E. Wolanski, D. R. Cahoon, M. M. Brinson, Eds. (Elsevier, Amsterdam, 2009), pp. 787–800.
34. S. Temmerman *et al.*, *Nature* **504**, 79–83 (2013).
35. S. O'Neill, S. Nicholson-Cole, *Sci. Commun.* **30**, 355–379 (2009).
36. J. Wolf, S. C. Moser, *Wiley Interdiscip. Rev. Clim. Chang.* **2**, 547–569 (2011).
37. B. Shaefer Caniglia, R. J. Brulle, A. Szasz, in *Climate Change and Society: Sociological Perspectives*, R. E. Dunlap, R. J. Brulle, Eds. (Oxford Univ. Press, Oxford, 2015), pp. 235–268.
38. A. M. Bliuc *et al.*, *Nat. Clim. Change* **5**, 226–229 (2015).
39. S. Gelcich *et al.*, *Proc. Natl. Acad. Sci. U.S.A.* **111**, 15042–15047 (2014).
40. M. Bunce, S. Rosendo, K. Brown, *Environ. Dev. Sustain.* **12**, 407–440 (2010).
41. J. E. Cinner *et al.*, *Glob. Environ. Change* **22**, 12–20 (2012).
42. W. N. Adger, J. Barnett, K. Brown, N. Marshall, K. O'Brien, *Nat. Clim. Change* **3**, 112–117 (2013).
43. B. Haalboom, D. C. Natcher, *Arctic* **65**, 319–327 (2012).
44. S. Arora-Jonsson, *Glob. Environ. Change* **21**, 744–751 (2011).
45. G. Terry, *Gend. Dev.* **17**, 5–18 (2009).
46. I. de Águeda Corneloup, A. P. Mol, *Int. Environ. Agreement Polit. Law Econ.* **14**, 281–297 (2014).
47. D. Ciplet, J. T. Roberts, M. Khan, *Glob. Environ. Polit.* **13**, 49–68 (2013).
48. L. Vadacchino, C. De Young, D. Brown, *The Fisheries and Aquaculture Sector in National Adaptation Programmes of Action: Importance, Vulnerabilities and Priorities* (FAO Fisheries and Aquaculture Circular No. 1064, Food and Agriculture Organization of the United Nations, Rome, 2011).
49. R. J. Nicholls *et al.*, *Wiley Interdiscip. Rev. Clim. Chang.* **5**, 129–150 (2014).
50. C. Le Quéré *et al.*, *Nat. Geosci.* **2**, 831–836 (2009).
51. D. M. Alongi, *Ann. Rev. Mar. Sci.* **6**, 195–219 (2014).
52. L. Pendleton *et al.*, *PLOS ONE* **7**, e43542 (2012).
53. L. Clarke *et al.*, in *Climate Change 2014: Mitigation of Climate Change. Contribution of Working Group III to the Fifth Assessment Report of the Intergovernmental Panel on Climate Change*, O. R. Edenhofer *et al.*, Eds. (Cambridge Univ. Press, Cambridge, 2014), pp. 413–510.
54. T. Bruckner *et al.*, in *Climate Change 2014: Mitigation of Climate Change. Contribution of Working Group III to the Fifth Assessment Report of the Intergovernmental Panel on Climate Change*, O. R. Edenhofer *et al.*, Eds. (Cambridge Univ. Press, Cambridge, 2014), pp. 511–597.
55. S. J. Hall, *Blue Frontiers: Managing the Environmental Costs of Aquaculture* (WorldFish, Batu Maung, Malaysia, 2011).
56. C. L. Delgado, *J. Nutr.* **133**, 3907S–3910S (2003).
57. S. Gössling *et al.*, *Ecol. Econ.* **54**, 417–434 (2005).
58. H. Bulkeley, *Annu. Rev. Environ. Resour.* **35**, 229–253 (2010).
59. D. G. Victor, *Nature* **520**, 27–29 (2015).
60. P. Cochran *et al.*, *Clim. Change* **120**, 557–567 (2013).
61. Editorial, *Nat. Clim. Change* **5**, 899 (2015); www.nature.com/nclimate/journal/v5/n10/full/nclimate2821.html.

ACKNOWLEDGMENTS

This Review is based on a plenary presentation given by the first author to the 3rd International Symposium on the Effects of Climate Change on the World's Oceans, Santos, Brazil, 23 to 27 March 2015. We thank the International Council for the Exploration of the Sea and the North Pacific Marine Science Organization for supporting his attendance. We also thank two reviewers for insightful comments and suggestions.

SUPPLEMENTARY MATERIALS

www.sciencemag.org/content/350/6262/778/suppl/DC1
Materials and Methods
Supplementary Text
Tables S1 and S2
References (*62*–*91*)

10.1126/science.aac8721

RESEARCH

Mammoth mandibles reveal migration routes

Lister and Sher, p. 805

IN *SCIENCE* JOURNALS

Edited by **Stella Hurtley**

Basalt lavas at Cape Mercy, Baffin Island

GEOCHEMISTRY

Shaking out water's dusty origin

Where did Earth's water come from? Lavas erupting on Baffin Island, Canada, tap a part of Earth's mantle isolated from convective mixing. Hallis *et al*. studied hydrogen isotopes in the lavas that help to "fingerprint" the origin of water from what could be a primordial reservoir. The isotope ratios for the Baffin Island basalt lavas suggest a pre-solar origin of water in Earth, probably delivered by adsorption onto dust grains. — BG

Science, this issue p. 795

GENOME EDITING

Genome editing with a Cas9 scalpel

The Cas9 nuclease forms the heart of the CRISPR-Cas genome editing system. Cas9 binds small guide RNAs that direct it to its target sites, where the nuclease either cleaves or binds to genomic DNA. Knight *et al*. used single-molecule imaging to track Cas9 in living cells. Cas9 searches the genome for its target sites using rapid three-dimensional diffusion. It spends very little time binding to off-target sites, which explains the high accuracy of the CRISPR-Cas9 editing machine. — GR

Science, this issue p. 823

ATTOSECOND DYNAMICS

Electronic movement flashing into view

Numerous chemical processes begin with ionization: the ejection of an electron from a molecule. What happens in the immediate aftermath of that event? Kraus *et al*. explored this question in iodoacetylene by detecting and analyzing the spectrum of emitted high harmonics (see the Perspective by Ueda). They traced the migration of the residual positively charged hole along the molecular axis on a time scale faster than a quadrillionth of a second. They thereby characterized the capacity of a laser field to steer the hole's motion in appropriately oriented molecules. — JSY

Science, this issue p. 790; see also p. 740

GAMMA-RAY ASTRONOMY

LMC pulsar's bright gamma-ray flashes

Pulsars are rapidly rotating neutron stars that are seen as pulsating sources of radio waves. Some, such as the Crab pulsar, also emit pulses of gamma rays. The Fermi LAT collaboration observed pulsed gamma rays from a pulsar outside our galaxy, the Milky Way. The pulsar, known as PSR J0540–6919, is located in the Large Magellanic Cloud (LMC). This is the most powerful gamma-ray pulsar yet known, with luminosity 20 times that of the Crab. The findings should help to explain how pulsars convert the energy stored in their rotation into detectable electromagnetic emission. — KTS

Science, this issue p. 801

MUCOSAL IMMUNITY

A gut bacterial containment system

Trillions of bacteria selectively inhabit our guts, but how do our bodies keep them contained? Spadoni *et al*. describe

The pulsar was found in the 30 Doradus region of the Large Magellanic Cloud

PHOTOS: (FROM TOP) GM PHOTO IMAGES/ALAMY; TRAPPIST/E. JEHIN/ESO

Published by AAAS

a "gut-vascular barrier" that prevents intestinal microbes from accessing the liver and the bloodstream in mice (see the Perspective by Bouziat and Jabri). Studies with human samples and in mice revealed that the cell biology of the gut-vascular barrier shares similarities with the blood-brain barrier of the central nervous system. Pathogenic bacteria such as *Salmonella typhimurium* could penetrate the gut-vascular barrier in mice, gaining access to the liver and bloodstream, in a manner dependent on the *Salmonella* pathogenicity island 2–type III secretion system. — KLM

Science, this issue p. 830; see also p. 742

HUMAN EVOLUTION

Ancient African helps to explain the present

Tracing the migrations of anatomically modern humans has been complicated by human movements both out of and into Africa, especially in relatively recent history. Gallego Llorente *et al*. sequenced an Ethiopian individual, "Mota," who lived approximately 4500 years ago, predating one such wave of individuals into Africa from Eurasia. The genetic information from Mota suggests that present-day Sardinians were the likely source of the Eurasian backflow. Furthermore, 4 to 7% of most African genomes, including Yoruba and Mbuti Pygmies, originated from this Eurasian gene flow. — LMZ

Science, this issue p. 820

GPCR SIGNALING

Receptor methylation controls behavior

D2 dopamine receptors are targeted by antipsychotic agents to regulate behavior. Likhite *et al*. found putative arginine methylation motifs in some human G protein–coupled receptors (GPCRs), including the D2 dopamine receptor, and in homologs in the worm *Caenorhabditis elegans*. Methylation of the D2 dopamine receptor by the arginine methyltransferase PRMT5 enhanced D2 receptor signaling in cultured cells. *C. elegans* lacking *prmt-5* had behavioral problems similar to those in worms deficient in the D2-like receptor DOP-3. Thus, methylation of GPCRs may be important for clinically relevant targets such as the D2 receptor. — JFF

Sci. Signal. **8**, ra115 (2015).

NEUROTECHNOLOGY

Tireless typing with the brain

It's already a technological feat that the brain can be hooked up to a computer to allow paralyzed individuals to type. But these so-called brain-computer interface (BCI) technologies can be tiring and burdensome for users, requiring frequent breaks and recalibration while mentally typing short texts. Jarosiewicz *et al.* combined three calibration methods—retrospective target interference, velocity bias correction, and adaptive tracking of neural features—in the optimal configuration for seamless typing and stable neural control. The combination allowed four individuals with tetraplegia to compose longer texts at their own pace, with no need to pause for recalibration. — MLF

Sci. Transl. Med. **7**, 313ra179 (2015).

CLIMATE CHANGE

Double jeopardy

In the best of worlds, exploited fish stocks are monitored so that harvest quotas protect the reproductive ability of the population. Climate change is likely to complicate this process substantially. Pershing *et al*. found that cod stocks declined continuously during intense warming in the North Atlantic. Fisheries quotas, even though they were responsibly set and followed by fishers, decreased the reproductive rate. Thus, managing fisheries in a warming world is going to be increasingly problematic. — SNV

Science, this issue p. 809

IN OTHER JOURNALS

Edited by **Sacha Vignieri** *and* **Jesse Smith**

Intestinal worms, aided by a microbiome-rich gut, reduce allergies

IMMUNOLOGY

Worming your way out of allergies

Accumulating evidence suggests that infection with intestinal parasitic worms can protect against allergy. Zaiss et al. investigated how worms reduce allergic reactions, using mice chronically infected with the parasitic worm *Heligmosomoides polygyrus*. They found that worms could reduce the incidence of allergy in mice harboring an intestinal microbiota but not in mice treated with oral antibiotics. The intestinal microbiota of mice infected with *H. polygyrus* produced larger amounts of short-chain fatty acids (SCFAs) than did uninfected mice. Moreover, mice had to express the protein receptor for SCFA in order for worms to protect them from developing allergies. Worm-infected pigs and people also had elevated amounts of SCFAs, suggesting that these metabolites may play a similar role in other organisms. — KLM

Immunity 10.1016/j.immuni.2015.09.012 (2015).

PHOTO: DR JANICE MURRAY, UNIVERSITY OF EDINBURGH/WELLCOME IMAGES

ALSO IN *SCIENCE* JOURNALS

Edited by **Stella Hurtley**

GROWTH CONTROL

Brain keeps body size and shape in check

Animal systems show amazing left-right symmetry—think of how our legs or arms, or the legs or wings of an insect, are matched in size and shape. Environmental insults and growth defects can challenge these developmental programs. In order to limit the resultant variation, juvenile organisms buffer variability through homeostatic mechanisms, so that the correct final size is attained. Vallejo *et al*. report that the *Drosophila* brain mediates such homeostatic control via an insulin-like peptide Dilp8 binding to the relaxin hormone receptor Lgr3. Lgr3 neurons distribute this information to other neuronal populations to adjust the hormones ecdysone, insulin, and juvenile hormone in a manner that stabilizes body and organ size. — BAP

Science, this issue p. 786

MAGNETIC RESONANCE

Mechanically detected spin resonances

The interaction of spins in a sample with a magnetic field can generate forces that can be sensed with cantilever probes. Losby *et al*. measured the resonance signals at room temperature with a micromechanical torque magnetometer. The difference between two applied radio-frequency signals corresponded to the mechanical frequency of the resonator. This approach revealed the vortex core dynamics of the ferri-to-ferro–magnetic transition in a micrometer-sized yttrium-iron-garnet single-crystal disk. — PDS

Science, this issue p. 798

SCATTERING DYNAMICS

Watching collisions in the slow lane

Quantum mechanics aims to "micromanage" the details of collisions between atoms and molecules. However, it's hard to discern all the subtleties under high-energy conditions. Vogels *et al*. slowed down two intersecting beams of helium atoms and nitric oxide (NO) molecules to a relative crawl in order to characterize the collisions precisely. The data revealed short-lived resonances that matched theoretical predictions remarkably well—a striking feat on both sides, given the challenge of accurately modeling NO's unpaired electron. The study highlights chemists' increasingly sophisticated understanding of collision dynamics. — JSY

Science, this issue p. 787

EXTINCTION EVENTS

The small will inherit the Earth...

Understanding how communities and ecosystems recovered from the previous five global extinction events sheds light on how extinctions shape broad patterns of biodiversity. Sallan *et al*. looked across vertebrate species during and after the Devonian extinction (see the Perspective by Wagner). Small-bodied species, with rapid reproductive rates, dominated post-extinction communities, despite the presence of many successful large-bodied species before the extinction. This pattern mimics, to some degree, current patterns of extinction, suggesting that we might expect similar loss of large-bodied species if we continue along our current path. — SNV

Science, this issue p. 812; see also p. 736

MAMMALIAN EVOLUTION

Moving mammoths

Mammoths are a particularly charismatic example of our Pleistocene megafuana. Lister and Sher took a detailed look at mammoth fossils globally and suggest that the North American Columbian mammoth, thought to have arisen from a European species, probably evolved from a more advanced Asian species. Similar dispersal events of Asian mammoths led to later colonization events in Europe and North America. — SNV

Science, this issue p. 805

ANTIVIRAL IMMUNITY

Nlrp6 keeps gut infections in check

Most viruses infect only certain cells of the body. Enteric viruses, such as norovirus and rotavirus, specifically infect the gut. Wang *et al*. now show that the response to such viruses is tissue-specific, too. Antiviral immunity to enteric but not systemic viral infections in mice required Nlrp6, a member of the NOD-like receptor family of proteins that play important roles in host defense. Together with the RNA helicase protein Dhx15, Nlrp6 bound viral RNA and elicited downstream antiviral immune responses necessary for viral clearance. These included the production of type I and type III interferons and the expression of interferon-stimulated genes. — KLM

Science, this issue p. 826

SMALL RNAS

MicroRNAs that control behavior

MicroRNAs (miRNAs) are small noncoding RNAs that regulate gene activity. They repress expression through complementary base pairing interactions with target messenger RNAs. MiRNAs are involved in regulating many cell and developmental processes. Picao-Osorio *et al.* find that miRNAs can also control behavior in the fruit fly *Drosophila*. A specific miRNA locus regulates the self-righting response in larva that ate tipped over onto their backs. The miRNA locus targets a gene required for the normal activity of two neurons involved in the self-righting response. — GR

Science, this issue p. 815

a "gut-vascular barrier" that prevents intestinal microbes from accessing the liver and the bloodstream in mice (see the Perspective by Bouziat and Jabri). Studies with human samples and in mice revealed that the cell biology of the gut-vascular barrier shares similarities with the blood-brain barrier of the central nervous system. Pathogenic bacteria such as *Salmonella typhimurium* could penetrate the gut-vascular barrier in mice, gaining access to the liver and bloodstream, in a manner dependent on the *Salmonella* pathogenicity island 2–type III secretion system. — KLM

Science, this issue p. 830; see also p. 742

HUMAN EVOLUTION

Ancient African helps to explain the present

Tracing the migrations of anatomically modern humans has been complicated by human movements both out of and into Africa, especially in relatively recent history. Gallego Llorente *et al*. sequenced an Ethiopian individual, "Mota," who lived approximately 4500 years ago, predating one such wave of individuals into Africa from Eurasia. The genetic information from Mota suggests that present-day Sardinians were the likely source of the Eurasian backflow. Furthermore, 4 to 7% of most African genomes, including Yoruba and Mbuti Pygmies, originated from this Eurasian gene flow. — LMZ

Science, this issue p. 820

GPCR SIGNALING

Receptor methylation controls behavior

D2 dopamine receptors are targeted by antipsychotic agents to regulate behavior. Likhite *et al*. found putative arginine methylation motifs in some human G protein–coupled receptors (GPCRs), including the D2 dopamine receptor, and in homologs in the worm *Caenorhabditis elegans*. Methylation of the D2 dopamine receptor by the arginine methyltransferase PRMT5 enhanced D2 receptor signaling in cultured cells. *C. elegans* lacking *prmt-5* had behavioral problems similar to those in worms deficient in the D2-like receptor DOP-3. Thus, methylation of GPCRs may be important for clinically relevant targets such as the D2 receptor. — JFF

Sci. Signal. **8**, ra115 (2015).

NEUROTECHNOLOGY

Tireless typing with the brain

It's already a technological feat that the brain can be hooked up to a computer to allow paralyzed individuals to type. But these so-called brain-computer interface (BCI) technologies can be tiring and burdensome for users, requiring frequent breaks and recalibration while mentally typing short texts. Jarosiewicz *et al.* combined three calibration methods—retrospective target interference, velocity bias correction, and adaptive tracking of neural features—in the optimal configuration for seamless typing and stable neural control. The combination allowed four individuals with tetraplegia to compose longer texts at their own pace, with no need to pause for recalibration. — MLF

Sci. Transl. Med. **7**, 313ra179 (2015).

CLIMATE CHANGE

Double jeopardy

In the best of worlds, exploited fish stocks are monitored so that harvest quotas protect the reproductive ability of the population. Climate change is likely to complicate this process substantially. Pershing *et al*. found that cod stocks declined continuously during intense warming in the North Atlantic. Fisheries quotas, even though they were responsibly set and followed by fishers, decreased the reproductive rate. Thus, managing fisheries in a warming world is going to be increasingly problematic. — SNV

Science, this issue p. 809

IN OTHER JOURNALS

Edited by **Sacha Vignieri** *and* **Jesse Smith**

Intestinal worms, aided by a microbiome-rich gut, reduce allergies

IMMUNOLOGY

Worming your way out of allergies

Accumulating evidence suggests that infection with intestinal parasitic worms can protect against allergy. Zaiss et al. investigated how worms reduce allergic reactions, using mice chronically infected with the parasitic worm *Heligmosomoides polygyrus*. They found that worms could reduce the incidence of allergy in mice harboring an intestinal microbiota but not in mice treated with oral antibiotics. The intestinal microbiota of mice infected with *H. polygyrus* produced larger amounts of short-chain fatty acids (SCFAs) than did uninfected mice. Moreover, mice had to express the protein receptor for SCFA in order for worms to protect them from developing allergies. Worm-infected pigs and people also had elevated amounts of SCFAs, suggesting that these metabolites may play a similar role in other organisms. — KLM

Immunity 10.1016/j.immuni.2015.09.012 (2015).

PHOTO: DR JANICE MURRAY, UNIVERSITY OF EDINBURGH/WELLCOME IMAGES

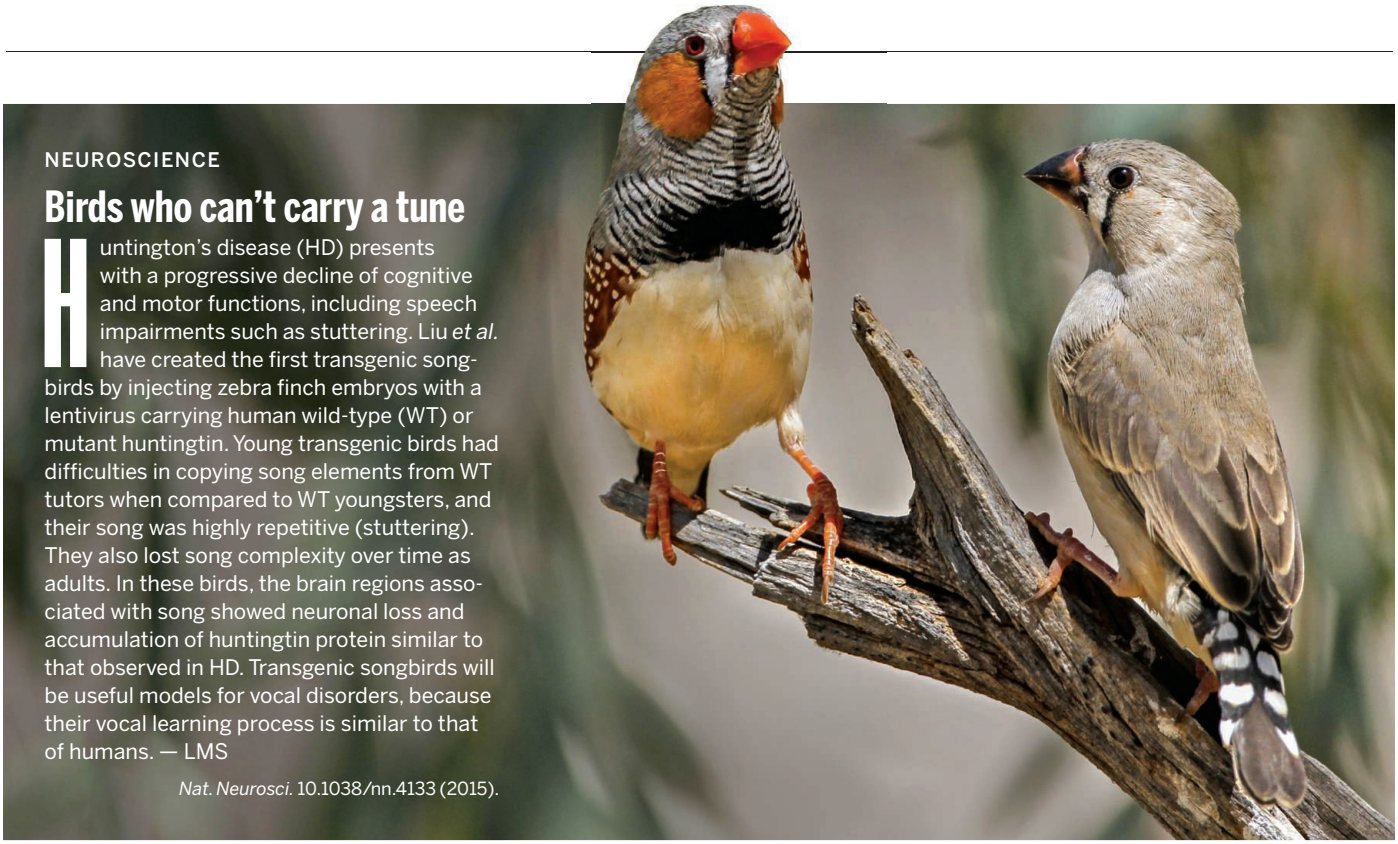

NEUROSCIENCE

Birds who can't carry a tune

Huntington's disease (HD) presents with a progressive decline of cognitive and motor functions, including speech impairments such as stuttering. Liu *et al.* have created the first transgenic songbirds by injecting zebra finch embryos with a lentivirus carrying human wild-type (WT) or mutant huntingtin. Young transgenic birds had difficulties in copying song elements from WT tutors when compared to WT youngsters, and their song was highly repetitive (stuttering). They also lost song complexity over time as adults. In these birds, the brain regions associated with song showed neuronal loss and accumulation of huntingtin protein similar to that observed in HD. Transgenic songbirds will be useful models for vocal disorders, because their vocal learning process is similar to that of humans. — LMS

Nat. Neurosci. 10.1038/nn.4133 (2015).

NEUROSCIENCE

Cannabinoids provide the runner's reward

The "runner's high"—beneficial effects of prolonged exercise that reduce anxiety and pain perception—in mice appears to depend on the production of endogenous cannabinoids rather than endorphins. Mice allowed to do their normal running on a wheel (about 5 km per day) had increased circulating concentrations of β-endorphin (an opioid) and anandamide (an endocannabinoid). Fuss *et al.* found that the depletion of cannabinoid receptor 1 in neurons of the forebrain reduced the beneficial effects of running on anxiety-like behavior and tolerance to a painful stimulus. — LBR

Proc. Natl. Acad. Sci. U.S.A. 10.1073/pnas.1514996112 (2015).

CANCER BIOLOGY

The perils of stress reduction

In today's health-conscious world, it is not unusual for a food item to achieve "superfood" status simply because it contains high levels of "cancer-fighting" antioxidants. This view may be simplistic, because cancer develops and progresses in multiple steps that potentially respond differently to antioxidants. Two new studies converge on the theme that, in the setting of metastasis, antioxidants help the cancer cell and hurt the host. Piskounova *et al.* show that melanoma cells that successfully metastasized in mice were those that had undergone certain metabolic changes that allowed them to withstand oxidative stress. Le Gal *et al.* show that the administration of antioxidants to mice that were predisposed to melanoma had no effect on primary tumor development, but enhanced lymph node metastases. — PAK

Nature 10.1038/nature15726 (2015); *Science Transl. Med.* **7**, 308re8 (2015).

SOLAR CELLS

Getting around solar cell loss

The overall performance of a solar cell depends on many parameters, but harnessing as much light as possible and converting it into electricity are fundamental. Losses in that conversion process, however, are inevitable, either from electrical losses in the material or the connecting circuitry, or "shadow loss" from the contact circuitry itself as it blocks out the sun. Schumann *et al.* show that the principle of optical cloaking could be used to reduce shadow loss. They designed a cloak that is placed over the shadowing contact circuits, effectively rendering the contacts invisible. With more light reaching the cell, it should be able to squeeze out a little more performance. — ISO

Optica **2**, 850 (2015).

INDUCED SEISMICITY

Loading up concern for a triggered quake

Earthquakes of magnitude 4.0, 4.3, and 4.5 have hit the oil and gas hub of Cushing, Oklahoma, over the past 2 years. By considering the two smaller earthquakes, McNamara *et al.* suggest that a much larger earthquake could occur directly below the Cushing oil facility. Earthquakes can redistribute stress, and in this case it appears that this has occurred on the Wilzetta-Whitetail fault just south of Cushing. The most recent, larger earthquake adds to the concern that a more damaging quake is in the region's future. — BG

Geophys. Res. Lett. 10.1002/2015GL064669 (2015).

NANOMATERIALS

From nanoparticle to supercage

Copper (II) hydroxide [$Cu(OH)_2$] can serve as mimic for peroxidase enzymes, provided that internal spaces can be created for substrate molecules. Cai *et al*. show that hollow nanoribbon cages form by adding a copper-ammonia complex to a mixture of amorphous $Cu(OH)_2$ nanoparticles and polyvinylpyrrolidone. Copper ions from the nanoparticle surface reform into arrays of nanoribbons held together by hydrogen bonding to create a box-shaped cage with edge lengths of ~200 nm. These cages showed high activity for the reaction of peroxide with organic substrates such as 3,3′,5,5′-tetramethylbenzidine. — PDS

J. Am. Chem. Soc. 10.1021/jacs.5b09337 (2015).

PHOTO: FLPA/GIANPIERO FERRARI/CORBIS

RESEARCH ARTICLE SUMMARY

GROWTH CONTROL

A brain circuit that synchronizes growth and maturation revealed through Dilp8 binding to Lgr3

Diana M. Vallejo,* Sergio Juarez-Carreño,* Jorge Bolivar, Javier Morante,† Maria Dominguez†

INTRODUCTION: Animals have a remarkable capacity to maintain a constant size, even in the face of genetic and environmental perturbations. Size imperfections and asymmetries have an effect on fitness, potentially decreasing competitiveness, survival, and reproductive success. Therefore, immature animals must employ homeostatic mechanisms to counteract substantial size variations and withstand developmental growth perturbations caused by genetic errors, disease, environmental factors, or injury. Such mechanisms ensure that, despite inevitable variations, the appropriate final body size is attained. A better understanding of homeostatic size maintenance will afford insights into normal organ and organismal size control, as well as the developmental origin of anomalous random left-right asymmetries.

RATIONALE: The *Drosophila* insulin-like peptide Dilp8 has been shown to mediate homeostatic regulation. When growth is disturbed, Dilp8 is strongly activated and sexual maturation is postponed until the affected elements are recomposed; simultaneously, the growth of other organs is retarded during this process. This compensatory mechanism allows the growth of the affected tissues to catch up. It maintains the synchrony between organs so that the animals achieve the correct size, preserving proportionality and bilateral symmetry. However, the Dilp8 receptor and its site of action remain uncharacterized.

RESULTS: We found that Dilp8 binds to and activates the relaxin leucine-rich repeat–containing G protein–coupled receptor Lgr3 to mediate homeostatic control through a pathway dependent on adenosine 3′,5′-monophosphate. Larvae that lack *lgr3* in neurons alone do not respond to Dilp8, indicating that the homeostatic system is centered in the brain. Dilp8 delays reproductive maturation by suppressing the neurons releasing the prothoracicotropic hormone (PTTH), which projects to the prothoracic gland and regulates ecdysone production for growth termination. However, this modulation alone is insufficient to adjust growth and stabilize body size. We show that Dilp8-Lgr3 balances growth against the extended growth period by dampening the production of *dilp3* and *dilp5* by insulin-producing cells (IPCs) in the brain and inhibiting synthesis of the juvenile hormone (JH). We also identify two pairs of dorsomedial neurons in the pars intercerebralis that are necessary and sufficient to mediate the effects of Dilp8. Simultaneous detection of pre- and postsynaptic markers revealed that the Lgr3 neurons mediating this homeostatic control have extensive axonal arborizations. Genetic and GRASP (GFP reconstitution across synaptic partners) analyses demonstrate that these neurons are connected to both the IPCs and PTTH neurons critical for adjusting growth and maturation rate, respectively. Thus, through their extensive axonal arborizations, Lgr3 neurons function like a "neuronal hub": They route peripheral information about growth status to other neuronal populations, thereby synchronizing damaged tissues and other (undamaged) ones and allocating additional development time so that each organ attains the correct size and maintains proportionality and symmetry.

ON OUR WEB SITE

Read the full article at http://dx.doi.org/10.1126/science.aac6767

CONCLUSION: We identified the relaxin receptor Lgr3 as a Dilp8 receptor and defined a brain circuit for homeostatic control of organismal and organ size in the face of perturbations. Lgr3 neurons that respond to Dilp8 signals directly input on the insulin-producing cells and the PTTH-producing neurons. As Lgr3 outputs, the modulation of these neuronal populations according to Dilp8 levels is critical to delay maturation and promote growth compensation in a manner that stabilizes body size. Without adequate Dilp8-Lgr3 signaling, the brain is incapable of stabilizing size between the distinct body parts, and we see left-right asymmetries and size variations that are greater than usual, reflecting developmental instability. ■

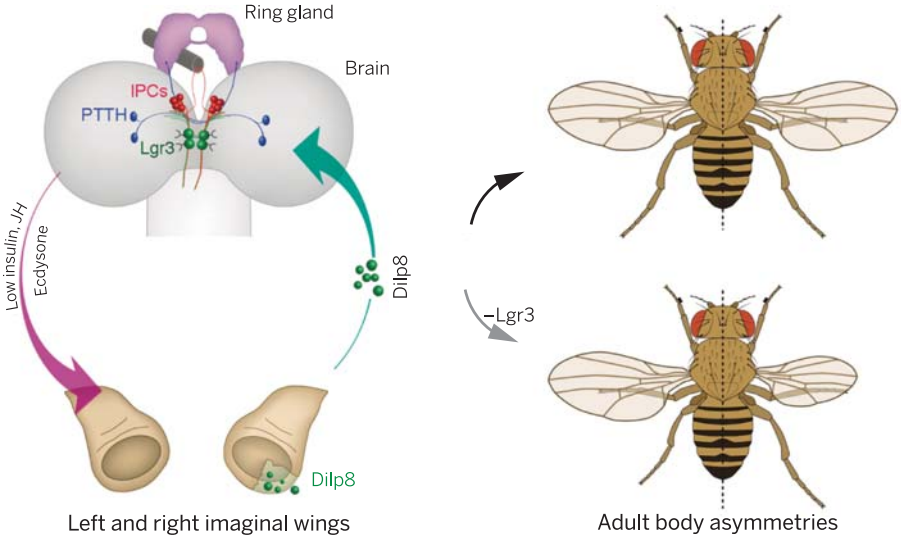

Dilp8-Lgr3 neural circuit and outputs for body-size homeostasis. The brain detects growth status and anomalies via Dilp8 activation of the Lgr3 receptor in two pairs of symmetric neurons. These neurons distribute this information to IPCs and PTTH neurons, which then trigger the hormonal responses that stabilize size. Without Dilp8-Lgr3 homeostasis, the brain cannot correct variation, and identical body parts can display imperfect symmetry and size.

The list of author affiliations is available in the full article online.
*These authors contributed equally to this work.
†Corresponding author. E-mail: m.dominguez@umh.es (M.D.); j.morante@umh.es (J.M.)
Cite this article as D. M. Vallejo *et al.*, *Science* 350, aac6767 (2015). DOI: 10.1126/science.aac6767

RESEARCH ARTICLE

GROWTH CONTROL

A brain circuit that synchronizes growth and maturation revealed through Dilp8 binding to Lgr3

Diana M. Vallejo,[1]* Sergio Juarez-Carreño,[1]* Jorge Bolivar,[2] Javier Morante,[1]† Maria Dominguez[1]†

Body-size constancy and symmetry are signs of developmental stability. Yet, it is unclear exactly how developing animals buffer size variation. *Drosophila* insulin-like peptide Dilp8 is responsive to growth perturbations and controls homeostatic mechanisms that coordinately adjust growth and maturation to maintain size within the normal range. Here we show that Lgr3 is a Dilp8 receptor. Through the use of functional and adenosine 3′,5′-monophosphate assays, we defined a pair of Lgr3 neurons that mediate homeostatic regulation. These neurons have extensive axonal arborizations, and genetic and green fluorescent protein reconstitution across synaptic partners show that these neurons connect with the insulin-producing cells and prothoracicotropic hormone–producing neurons to attenuate growth and maturation. This previously unrecognized circuit suggests how growth and maturation rate are matched and co-regulated according to Dilp8 signals to stabilize organismal size.

The impressive consistency and fidelity in the size of developing organisms (*1*–*3*) reflect both the robustness of genetic programs and the developmental plasticity necessary to counteract the variations in size arising from genetic noise, erroneous morphogenesis, disease, or injury (*4*, *5*). To counterbalance growth abnormalities, systemic homeostatic mechanisms are implemented that delay the onset of the reproductive stage of adulthood until the correct size of the individual and its body parts has been reached (*6*–*9*). Most animals initiate a pubertal transition only after the critical size and body mass have been achieved and, generally, in the absence of tissue damage or growth abnormalities (*5*, *8*–*11*). However, the mechanisms underlying such homeostatic regulation have yet to be fully defined.

Recently, the secreted peptide Dilp8, a member of the insulin/relaxin-like family, has been identified as a factor that mediates homeostatic control in *Drosophila melanogaster*. During the larval (growth) stage, the expression of *dilp8* declines as maturation proceeds, whereas its expression is activated when growth is disturbed (*12*, *13*). Hence, fluctuating Dilp8 levels provide a reliable read-out of overall growth status (e.g., deficit) and the time needed to complete growth. In addition, Dilp8 orchestrates hormonal responses that stabilize body size. This includes (i) inhibiting the production of the steroid hormone ecdysone by the prothoracic gland (PG) until the elements or organs affected are recomposed and also (ii) slowing down growth rates of undamaged tissues to ensure that affected organs catch up with normal tissues so that the adult flies reach a normal body size and maintain body proportions and symmetry. Accordingly, in the absence of *dilp8*, mutant flies are incapable of maintaining such strict control over their size, as reflected by the exaggerated variation in terms of overall proportionality and imperfect bilateral symmetry (*12*). However, the receptor that transduces Dilp8 signals and its site of action remained unknown.

Two models can be envisioned to establish such homeostatic regulation: (i) a central mechanism that dictates coordinated adjustments in both the duration and rate of growth and (ii) an endocrine mechanism that involves sensing and processing Dilp8 signals directly by hormone-producing cells (Fig. 1A) (*14*). In *Drosophila*, several anatomically separate neural populations regulate growth and maturation time by impinging directly on the ring gland [which is made up of the PG and the juvenile hormone-producing corpus allatum (CA)] (*1*, *2*, *4*). Thus, the receptors that transduce the Dilp8 signals of growth status may act directly or may communicate with neurons that produce the prothoracicotropic hormone (PTTH) (*15*) and/or the neurons of the pars intercerebralis, including the insulin-producing cells (IPCs), which synthesize and release insulin-like peptides Dilp2, Dilp3, and Dilp5 (*9*, *16*). Insect PTTH neurons, which are analogous to the gonadotropin-releasing hormone (GnRH) neurons in mammals (*5*, *10*), signal the commitment to sexual reproduction by stimulating the production of ecdysone in the PG to terminate growth (*14*). The IPCs in the pars intercerebralis, a functional equivalent of the mammalian hypothalamus (*10*, *15*), integrate nutritional signals and modulate tissue growth accordingly (*16*–*20*). Manipulation of IPCs by genetic ablation, starvation, or mutations in the single insulin receptor (*17*, *18*, *20*–*22*) leads to the generation of animals with smaller size. Similarly, manipulations of the PTTH neuropeptide and neurons result in adult fly size variations, leading to flies that are larger or smaller than normal due to an extension or acceleration of the larval period (*15*). The insulin receptor also directly activates synthesis of the juvenile hormone (JH) (a hormone that promotes growth and juvenile development) in the CA (*23*) and production of the steroid prohormone ecdysone in the PG (*14*), again augmenting the variation in normal adult size. These observations may explain how environmental and internal influences operate through individual IPCs or PTTH neurons to enable body-size variation and plasticity in developmental timing that can be vital for survival in changing environments. However, the origin of developmental stability and invariant body size may require different or more complex neural mechanisms from those involved in adaptive size regulation.

By employing a candidate approach and biochemical assays, we demonstrate that the orphan relaxin receptor Lgr3 acts as a Dilp8 receptor. We identify the neuronal population molecularly defined by the *lgr3* enhancer fragment *R19B09* (*24*) and show that it is necessary and sufficient to mediate such homeostatic regulation. Using tools for circuit mapping and an adenosine 3′,5′-monophosphate (cAMP) sensor as an indicator of Lgr3 receptor activation in vivo, we determined that a pair of these Lgr3 neurons is highly sensitive to Dilp8. These neurons display extensive axonal arborizations and appear to connect with IPCs and PTTH neurons to form a brain circuit for homeostatic body-size regulation. Our data identify the insulin genes, *dilp3* and *dilp5*, the JH, and the ecdysone hormone as central for developmental size stability. Collectively, these findings unveil a homeostatic circuit that forms a framework for studying how the brain stabilizes body size without constraining the adaptability of the system to reset body size in response to changing needs.

Results

The relaxin receptor Lgr3 mediates Dilp8-induced homeostatic control

Dilp8 bears homology to the human relaxin peptides (*12*, *25*). Therefore, we investigated the role for the two fly relaxin receptors encoded by the orphan leucine-rich repeat–containing

[1]Instituto de Neurociencias, Consejo Superior de Investigaciones Científicas and Universidad Miguel Hernández, Campus de Sant Joan, Apartado 18, 03550 Sant Joan, Alicante, Spain. [2]Departamento de Biomedicina, Biotecnología y Salud Pública, Facultad de Ciencias, Universidad de Cadiz, Polígono Rio San Pedro s/n, 11510 Puerto Real, Spain.
*These authors contributed equally to this work. †Corresponding author. E-mail: m.dominguez@umh.es (M.D.); j.morante@umh.es (J.M.)

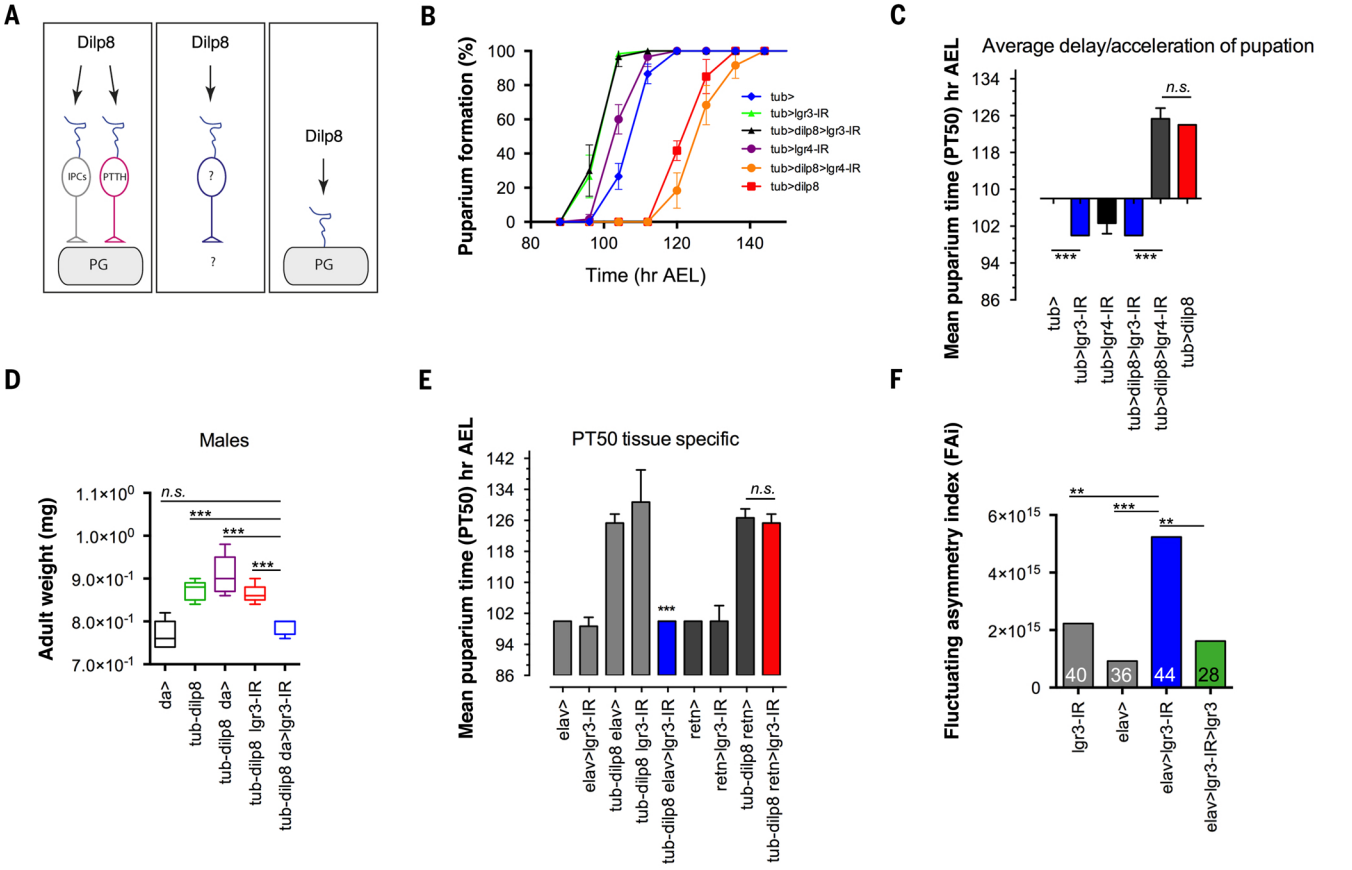

Fig. 1. Orphan relaxin Lgr3 mediates Dilp8 behavior and functions in neurons. (**A**) Model of Dilp8 sensing and homeostatic size regulation. The insulin-like Dilp8 elicits diverse yet coordinated responses that prolong the larval stage (by inhibiting ecdysone production in the PG) and slow down the growth rate (by dampening insulin signaling in the imaginal discs and/or other as-yet-uncharacterized signals). The underlying mechanism may involve direct Dilp8 sensing in neurons expressing PTTH or IPCs, the two prominent yet separate neural circuits that regulate ecdysone production in the PG and/or overall growth rates during larval development. Alternatively, the receptor may transduce Dilp8 signals in a novel neuronal population or directly in endocrine cells. (**B**) Knockdown of *lgr3*, but not of *lgr4*, prevents the pupariation delay induced by *dilp8* overexpression. *tub>* indicates *tubulin-Gal4*. Error bars indicate SD. (**C**) Average puparion time of the indicated genotypes, exposing acceleration or delay relative to their controls. Error bars (SD) are invisible when the three replicates coincide. Approximately 60 pupae per genotype were scored, and the graph shows data pooled from three independent experiments. ***$P < 0.001$ (two-tailed unpaired *t* test). n.s., not significant. (**D**) Knockdown of *lgr3* prevents excess body weight induced by *dilp8* (*tub-dilp8 da>lgr3-IR*). ***$P < 0.001$; significant difference from all controls (two-tailed unpaired *t* test). Data are mean ± SD. $n = 25$ age-synchronized adult males in each genotype. (**E**) Tissue-specific knockdown of *lgr3*, using *UAS-lgr3-IR* and the indicated *Gal4* lines. The graph shows data pooled from three independent experiments, and each data point is mean ± SD. A total of 60 pupae were scored per genotype. ***$P < 0.001$ (two-tailed unpaired *t* test). (**F**) Fluctuating asymmetry index of left-right wings of males of the indicated genotypes and rescued animals. Numbers indicate pairs of wings scored. **$P < 0.01$; ***$P < 0.001$ (*F* test).

G protein–coupled receptors (LGRs) Lgr3 (*CG31096*) and Lgr4 (*CG34411*) (*26*, *27*). We used RNA interference (RNAi) transgene expression (*28*) in animals overexpressing a *UAS-dilp8* transgene under the control of the yeast transcription factor *Gal4* that is driven by the ubiquitous *tubulin-Gal4* promoter (*tub-Gal4 UAS-dilp8 UAS-receptor-RNAi*) (Fig. 1B). Ubiquitous expression of *UAS-RNAi* transgenes (several lines were tested) against each of the fly relaxin receptors reveals whether they are required for developmental delay resulting from *dilp8* overexpression. When the *lgr3*, but not *lgr4*, gene was silenced (*tub-Gal4 UAS-dilp8 UAS-lgr3-RNAi*, hereafter *tub>dilp8>lgr3-IR*), Dilp8-induced developmental delay was fully suppressed (Fig. 1, B and C). Depletion of *lgr3* accelerated pupariation by ~8 hours (Fig. 1C), as in *dilp8* mutants (*13*). We verified the efficiency of the *lgr3*-RNAi transgene by quantitative real-time polymerase chain reaction (qRT-PCR) (fig. S1A).

To investigate the tissue- and cell-specific requirement for Lgr3, we constructed transgenic lines in which the coding sequence of *dilp8* was under the direct control of the ubiquitous *tubulinα1* promoter (*tub-dilp8*) (see materials and methods), and we used a *Gal4/UAS* system to drive tissue-specific expression of the *UAS-lgr3-RNAi* transgene. The delay in pupariation induced by Dilp8 resulted in normal-sized adults, owing to Dilp8-induced growth compensation. Yet, the extra time the *tub-dilp8* larvae spent in the feeding period led to overweight adults (*12*, *13*). Knockdown of *lgr3* also prevented the *dilp8*-overexpressing animals [*tub-dilp8*, *daughterless (da)-Gal4 UAS-lgr3-RNAi*] from being overweight (Fig. 1D).

Tissue-specific knockdown of *lgr3* further showed that Lgr3 is required in the nervous system (*tub-dilp8 elav>lgr3-IR*) (Fig. 1E) and not in the ring gland (using $retn^{R9F04}$-*Gal4*) (fig. S1, B to E). Knockdown of *lgr3* in neurons, but not in the ring gland, also prevented the Dilp8-induced reduction of growth rate (fig. S1, F and G). Further, neuronal depletion of *lgr3* using *elav-Gal4* (*elav>lgr3-IR*) produced adults that displayed greater fluctuations in asymmetry, as evidenced by significantly larger left-right variations in the size of adult wings (Fig. 1F). Expression of a transgenic Lgr3 cDNA (*UAS-lgr3*) (materials and methods) prevented this defect by the RNAi against *lgr3* (*elav>lgr3-IR>lgr3*) (Fig. 1F), excluding potential off-target effects of the RNAi (*28*). Thus, similarities in the phenotypes of *dilp8* (*12*) and *lgr3* loss—as well as the prevention of Dilp8-induced developmental delay, growth-rate reduction, and excess body weight through the loss of *lgr3*—strongly suggest that Lgr3 acts as a Dilp8 receptor. These data also suggest a central mechanism for systemic homeostatic size regulation although other

lgr3-expressing peripheral tissues, such as the larval fat body (*27*), could also contribute.

Lgr3 is a Dilp8 receptor

Next, we used biochemical assays to investigate the interaction of Dilp8 and Lgr3. Human relaxin receptors largely activate cytosolic cAMP (*25*); thus, we tested whether the response of *Drosophila* Kc cells transiently expressing *lgr3* to synthetic *Drosophila* Dilp8 peptides (materials and methods) was coupled to cAMP. To control for specificity, we also transfected Kc cells with constructs encoding the structurally related Lgr4 (*26*, *27*), as well as Lgr2, which is known to provoke a well-characterized cAMP-mediated response upon binding its respective cognate ligand (*29*). Only cells transfected with the *lgr3*-expressing plasmid responded to a 30-min exposure to Dilp8 (50 nM) with an increase in cAMP levels, from 213.8 ± 67.94 fmol/5 × 10^4 cells to 1.612.36 ± 302.6 fmol/5 × 10^4 cells (Fig. 2A and materials and methods). As a reference, the cAMP levels in Kc cells transfected with the empty vector alone were 132.69 ± 66.71 fmol/5 × 10^4 cells and 127.73 ± 77.19 fmol/5 × 10^4 cells in the presence and absence of synthetic Dilp8 (50 nM), respectively (Fig. 2A). This response to Dilp8 is highly specific, because we did not detect comparable changes in cAMP when cells expressing the Lgr4 and Lgr2 receptors were exposed to Dilp8 (Fig. 2A).

A dose-response curve indicated that Dilp8 peptides activate Lgr3 to produce a median effective concentration (EC_{50}) of 6.31 ± 0.12 nM, whereas Lgr4 and Lgr2 did not stimulate cAMP production in response to Dilp8 at any of the doses assayed (Fig. 2B). As the full receptor could not be solubilized, we used a strategy previously employed for the identification of LGR7 and LGR8 as receptors of human relaxin (*30*) and LGR4 and LGR5 of R-spondins (*31*). We cloned the ectodomain of Lgr3, fused it to the epitope 3x hemagglutinin (3xHA), and designated this as Lgr3-ECD::3xHA. On the basis of structural homology of LGRs to glycoprotein hormone receptors (*25*, *31*), the extracellular domain of the Lgr3 is expected to be soluble and to bind cognate ligands. Indeed, we detected a strong colocalization of Dilp8 at the surface of Lgr3-expressing cells (Fig. 2C and fig. S2). Furthermore, we coimmunoprecipitated a Myc-tagged Dilp8 with the extracellular domain of Lgr3 (Lgr3-ECD::3xHA) (Fig. 2D, materials and methods, and fig. S2). Collectively, these data suggest that Lgr3 encodes a functionally relevant Dilp8 receptor that is coupled to cAMP signaling like the human relaxin receptors RXPF1-2 (*25*).

The Lgr3 receptor acts in a small set of central brain neurons

When the endogenous expression of the *lgr3* gene was quantified (fig. S1A) (*27*), it appeared to be expressed only very weakly. Not surprisingly, attempts to map *lgr3*-expressing neurons by conventional immunological approaches using antibodies against the Lgr3 protein (materials and methods) were unsuccessful. For example, the $Lgr3^{719-733}$ antiserum readily detected the Lgr3 protein ectopically expressed using the *GAL4/UAS* system (fig. S2, G to G″), confirming the specificity of our antisera, yet it could not detect endogenous *lgr3* expression, supporting the weak expression of the Lgr3 protein.

Using the *Gal4/UAS* system to coarsely map functionally relevant neurons, we found that Lgr3 is not required within the IPCs themselves (*dilp3-Gal4*), the neuropeptide F-expressing cells (*npf*-Gal4), the circadian clock neurons (*pdf-Gal4* and *per-Gal4*), the PTTH neurons (*ptth*-Gal4), or the ventral nerve cord (VNC) [*teashirt (tsh)-Gal4*], all of which have been previously established to regulate the larval-pupal transition and/or body size in response to nutrition, sensory inputs, and developmental cues (*14*, *15*, *17*, *20*, *32*, *33*). When *UAS-lgr3-RNAi* was expressed in these specific brain regions using these *Gal4* lines in *tub-dilp8* animals, the animals entered pupation at times similar to those of *tub-dilp8* animals carrying *Gal4* or *UAS-lgr3-RNAi* alone (Fig. 3A).

We next took advantage of the available lines expressing *Gal4* under control of genomic fragments from the *lgr3* locus (*24*) (Fig. 3B). We found that using the *R19B09-Gal4* enhancer to deplete *lgr3* (Fig. 3B) fully suppressed the Dilp8-induced delay and did so with the same magnitude as when *lgr3* was ubiquitously depleted by *tub-Gal4* (Fig. 1B). No other *Gal4* enhancer lines prevented the Dilp8-induced delay (Fig. 3B). Depleting *lgr3* in neurons labeled by *R19B09-Gal4* also prevented the slow growth rate of imaginal discs induced by Dilp8, as reflected by the restoration of almost-normal transcript levels for the *Thor/4E-BP* gene, a direct target of the growth inhibitor FoxO, and a diagnosis for imaginal disc growth rates (*12*, *18*) (Fig. 3C). Thus, Dilp8 influences growth and maturation through Lgr3 activation in neurons molecularly defined by the *R19B09* enhancer.

We also found that overexpression of the *UAS-lgr3* transgene in *R19B09*-labeled neurons was sufficient to evoke a ~12-hour delay in pupariation (Fig. 3D), but this process was not delayed when expressed under control of the other *lgr3* genomic fragments (fig. S3). Because most G protein–coupled receptors (GPCRs) display some level of constitutive activity [two-state model of GPCR function (*34*)] in the absence of agonist

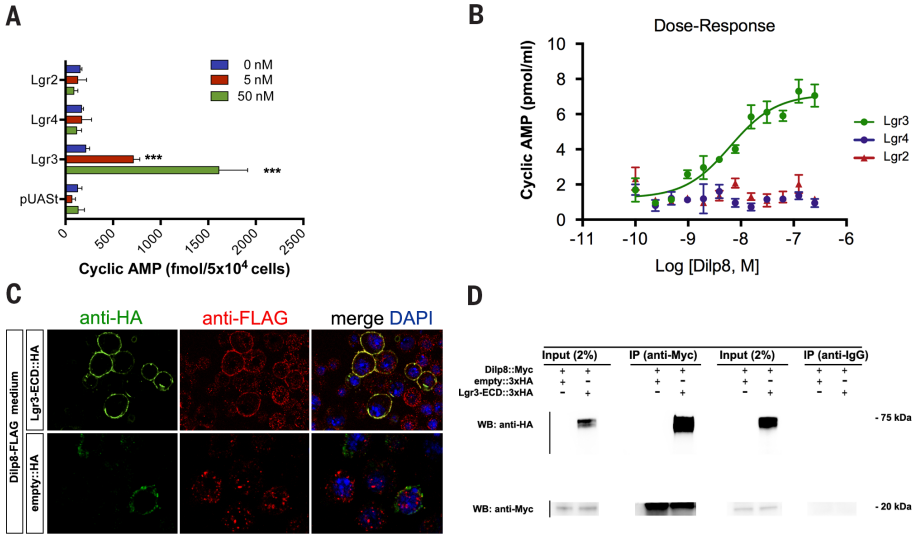

Fig. 2. Lgr3 is a Dilp8 receptor. (**A**) cAMP measurement in untreated *Drosophila* Kc cells (5 × 10^4 cells per culture) transiently transfected with the indicated Lgr plasmids and the empty plasmid or treated with either 5 or 50 nM Dilp8 peptide for 30 min. Data are shown as mean ± SD (n = 3 independent repeats), and the asterisks indicate that the cAMP level was statistically different from untreated controls, ***P < 0.001 (t test). (**B**) Dilp8-stimulated dose-dependent cAMP production by Kc cells expressing Lgr3. The concentration of Dilp8 ranged from 0 to 250 nM. Kc cells were transiently transfected with the *lgr3*, *lgr4*, or *lgr2* plasmids, and an EC_{50} value of 6.31 ± 0.1277 nM was obtained for Lgr3. Exposure of the Kc cells expressing the related receptors Lgr4 or Lgr2 to Dilp8 did not affect cAMP production. A sigmoid fit to the *lgr3* data is shown. Total cAMP production was measured in triplicate (materials and methods). Each data point is mean ± SEM (n = 3 independent repeats). (**C**) Dilp8 and Lgr3 colocalization assessed by confocal immunofluorescence. Kc cells expressing the extracellular domain of Lgr3-ECD::3xHA were incubated with medium containing Dilp8-Flag (materials and methods). The cells were fixed without permeabilizing and were then stained with anti-FLAG (red) and anti-HA (green) antibodies. The nuclei were counterstained with 4′,6-diamidino-2-phenylindole (DAPI). Images are also presented for Kc cells transiently transfected with the empty::3xHA vector and exposed to Dilp8-Flag. Representative images of three repeats are shown. (**D**) Binding of Dilp8 to Lgr3 assessed by coimmunoprecipitation. Rabbit anti-Myc or rabbit anti-IgG antibodies were used to pull down Lgr3-ECD::3xHA complexed to Dilp8-Myc. Input controls are also shown. IP, immunoprecipitation; WB, western blot.

ligands, delayed pupariation due to increased levels of endogenous *lgr3* via overexpression in *R19B09*-labeled neurons might reflect an increased response to a low concentration of endogenous Dilp8 or constitutive activity. However, Lgr3 displays high levels of constitutive activity only when expressed in a heterologous system [human embryonic kidney 293 cells (*27*)]; this high constitutive activity is not observed in *Drosophila* cells (Fig. 2A) or in vivo in neurons (see below). Moreover, Lgr3 activity is greatly increased in the presence of Dilp8 (Fig. 2, A and B, and below). Activation of *R19B09* neurons by expressing the *UAS-NaChBac* ion channel transgene (*35*) was sufficient to trigger a delay of ~18 hours (*R19B09>NaChBac*) (Fig. 3E), which suggests that Dilp8-stimulated Lgr3 activation excites these neurons electrically.

R19B09-Gal4 labels cells in the central brain (CB) and the VNC (Fig. 4A; see figs. S4 and S5A for expression of other *lgr3* enhancer fragments). Together with the observations made for the *tsh-Gal4* line (Fig. 3A), which typically labels all neurons in the VNC (*33*), we conclude that a set of ~12 central neurons per hemisphere, molecularly defined by *R19B09-Gal4*, reflects the Lgr3 neurons that are necessary and sufficient to control size and developmental timing in response to Dilp8. These include neuronal clusters in the dorsomedial region and in the supraesophageous ganglion (SOG) region, as well as individual cells in the dorsal and ventral protocerebrum (Fig. 4, A and B).

A pair of dorsomedial neurons acutely responds to Dilp8

The Lgr3 receptor response to Dilp8 is strongly coupled to cAMP stimulation (Fig. 2, A and B), enabling us to precisely determine the Lgr3-responding neurons via a cAMP biosensor. We used the *CRE-F-luciferase (luc)* construct (CRE, cAMP response element) (Fig. 4B) that has already been characterized in vivo (*36*). Thus, by combining the *CRE-F-luc* construct with *UAS-Flp* and *R19B09-Gal4*, we could assay specific cAMP responses in a physiological context (*R19B09* neurons and *tub-dilp8* background) (Fig. 4, C and D). To test whether the depletion of *lgr3* via *UAS-lgr3-RNAi* rendered the sensor insensitive to Dilp8, we used *elav-Gal4* on the X chromosome.

Typically, two neurons with their soma in the dorsomedial region of the pars intercerebralis were bilaterally and strongly labeled in all *tub-dilp8* brains (Fig. 4, C and C′, cells designated as type 1) but not in wild-type (WT) brains (Fig. 4D) or in *tub-dilp8 elav-Gal4>lgr3-RNAi* brains (Fig. 4E). Two to three weakly labeled cells in the dorsolateral region of the CB (designated as type 2) (Fig. 4, B, C′, and G) were also consistently labeled in *tub-dilp8* brains (Fig. 4, C, C′, and F). Moreover, unilaterally labeled dorsal cells (type 3) were occasionally seen in the three genotypes, and these luciferase-positive cells were identified as neuroblasts and not neurons by simultaneously colabeling with the Miranda (Mira) protein (Fig. 4C).

Other *lgr3* genomic fragments (e.g., *R17G11-Gal4*) (fig. S5) that did not suppress the Dilp8-induced delay failed to produce levels of Dilp8-induced cAMP comparable to those found in *R19B09*-labeled neurons (fig. S5, A and B), in agreement with

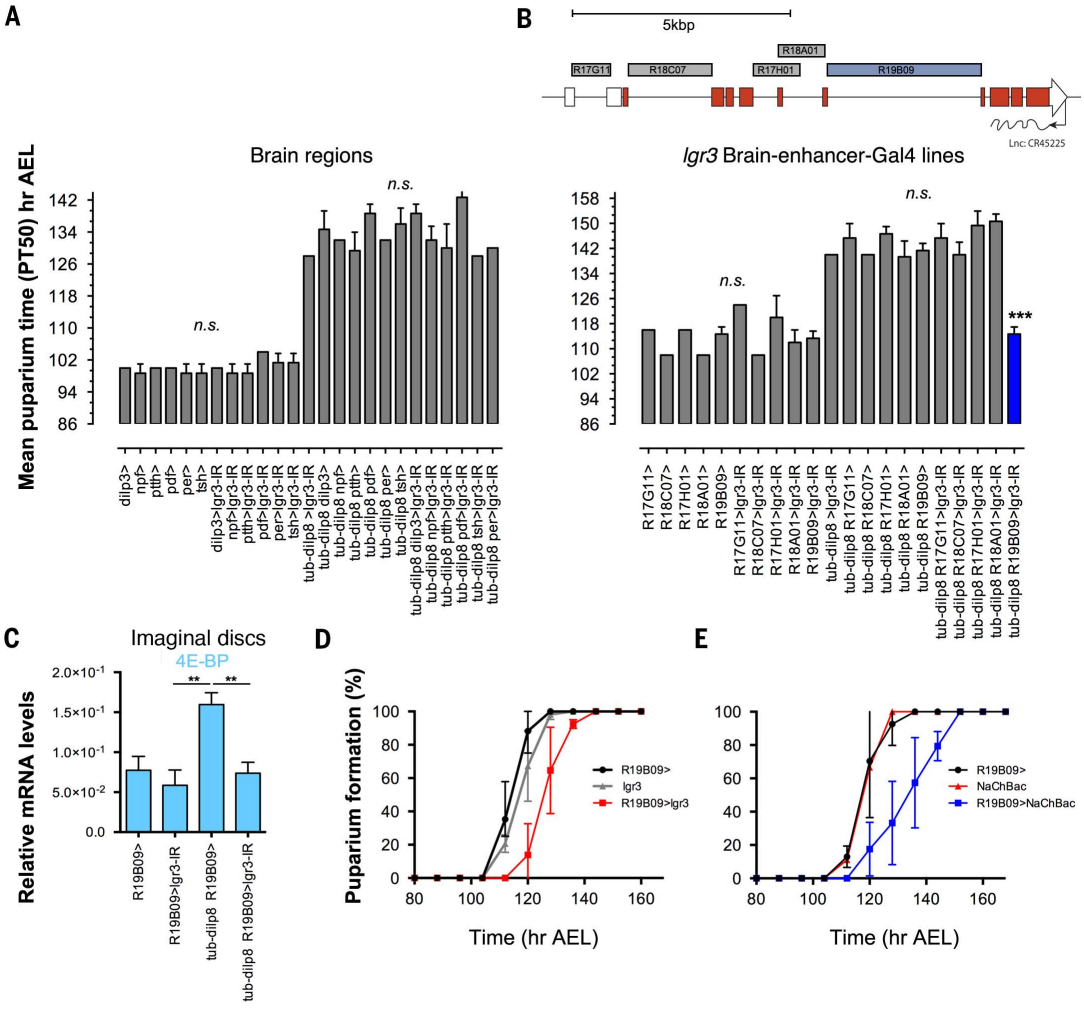

Fig. 3. Lgr3 acts in a set of central neurons molecularly defined by *R19B09-Gal4*. (**A**) Puparion time of animals with brain-region–specific knockdown of *lgr3*, using RNAi and the indicated *Gal4*. (**B**) Puparion time of animals with knockdown of *lgr3*, using *lgr3* brain-enhancer fragment-*Gal4* lines. Organization of the *lgr3* genomic region and the intervals of each of the Lgr3 enhancers (*24*) are presented in the top image. In (A) and (B), data are mean ± SD and are pooled from three independent experiments; 60 pupae were scored per genotype. Error bars are invisible when the three replicates coincide. ***$P < 0.001$ (two-tailed unpaired *t* test). (**C**) Imaginal disc growth rate in the indicated genotypes assayed by expression of the FoxO target gene, *Thor/4E-BP*, analyzed by qRT-PCR. mRNA was isolated from imaginal discs from 15 age-synchronized larvae (100 hours AEL) for each genotype ($n = 3$ biological repeats, mean ± SD). **$P < 0.01$ (two-tailed unpaired *t* test). (**D** and **E**) Cumulative puparion time of animals overexpressing *UAS-lgr3*, using *R19B09-Gal4* (D), or with electrical hyperexcitation of neurons labeled by *R19B09-Gal4*, using the *UAS-NaChBac* ion channel (E). Approximately 60 pupae were scored per genotype. Each data point is mean ± SD ($n = 3$ independent repeats).

their inability to prevent Dilp8-induced delay (Fig. 3B). The number and position of cells that activated de novo luciferase in response to *tub-dilp8* in *CRE-F-luc* brains expressing the *UAS-Flp* panneuronally (Fig. 4F) matched the cells identified using the *R19B09-Gal4* line, which suggests that the neurons labeled by this intronic *lgr3* enhancer represent the majority of cells sensitive to Dilp8 signals. The intensity of luciferase in other Lgr3-independent cells in the *elav-Gal4* brains was not generally altered (fig. S5D), indicating that the loss of *CRE-F-luc* signal in the dorsomedial and dorsolateral neurons was not due to nonspecific effects of the *lgr3-RNAi*.

Lgr3 neurons are connected to PTTH neurons and IPCs

We used *R19B09-Gal4* and *-LexA* constructs (Fig. 5, A to G), presynaptic (syt::GFP; GFP, green fluorescent protein) and postsynaptic (DenMark, dendritic marker) markers (*37*) (Fig. 5, B and C), and brainbow tools (Fig. 5, D to D″) (*38*) to more precisely define the connectivity of possible synaptic interactions of the distinct Lgr3 neuronal populations defined by *R19B09-Gal4*. Lgr3 neurons with their soma in the dorsomedial region and with a prominent response to Dilp8 (Fig. 4C) display extensive axonal arborizations reminiscent of hub neurons (*39*). These axonal arborizations of the dorsomedial Lgr3 neurons cover the dendritic fields and axons of PTTH neurons extensively [Fig. 5, A and B, blue denotes antibody to PTTH (anti-PTTH); and movie S1]. Note that the dendrites of PTTH neurons extend in the same direction as their axons (*15*). Lgr3 axons and dendritic fields (revealed by Syt::GFP and DenMark) (Fig. 5C) are also in close apposition to the IPCs revealed by anti-Dilp2 (Fig. 5, A and C) and by *dilp3-Gal4* (movie S2).

Brainbow-assisted analysis and the pre- and postsynaptic markers revealed that Lgr3 neurons in the dorsomedial region extend both ipsilateral and contralateral axon projections (Fig. 5, D to D″), with thin dendrites descending into the VNC (Fig. 5, B and C, and movie S3). Brainbow analysis also suggests that a dialogue is maintained between the distinct cell subpopulations defined by *R19B09-Gal4* and that this converges on the synaptic sites of the Lgr3 dorsomedial neurons (green neurons in brainbow image; Fig. 5, D and D″).

Spatial overlap between axonal and dendritic arborization is a prerequisite for potential connectivity between defined neurons and their potential targets. In this sense, the dense presynaptic sites of Lgr3 neurons indicate strong connectivity between these neurons and the PTTH neurons and IPCs. Thus, to detect direct connections, we used GRASP (GFP reconstitution across synaptic partners) analysis, which

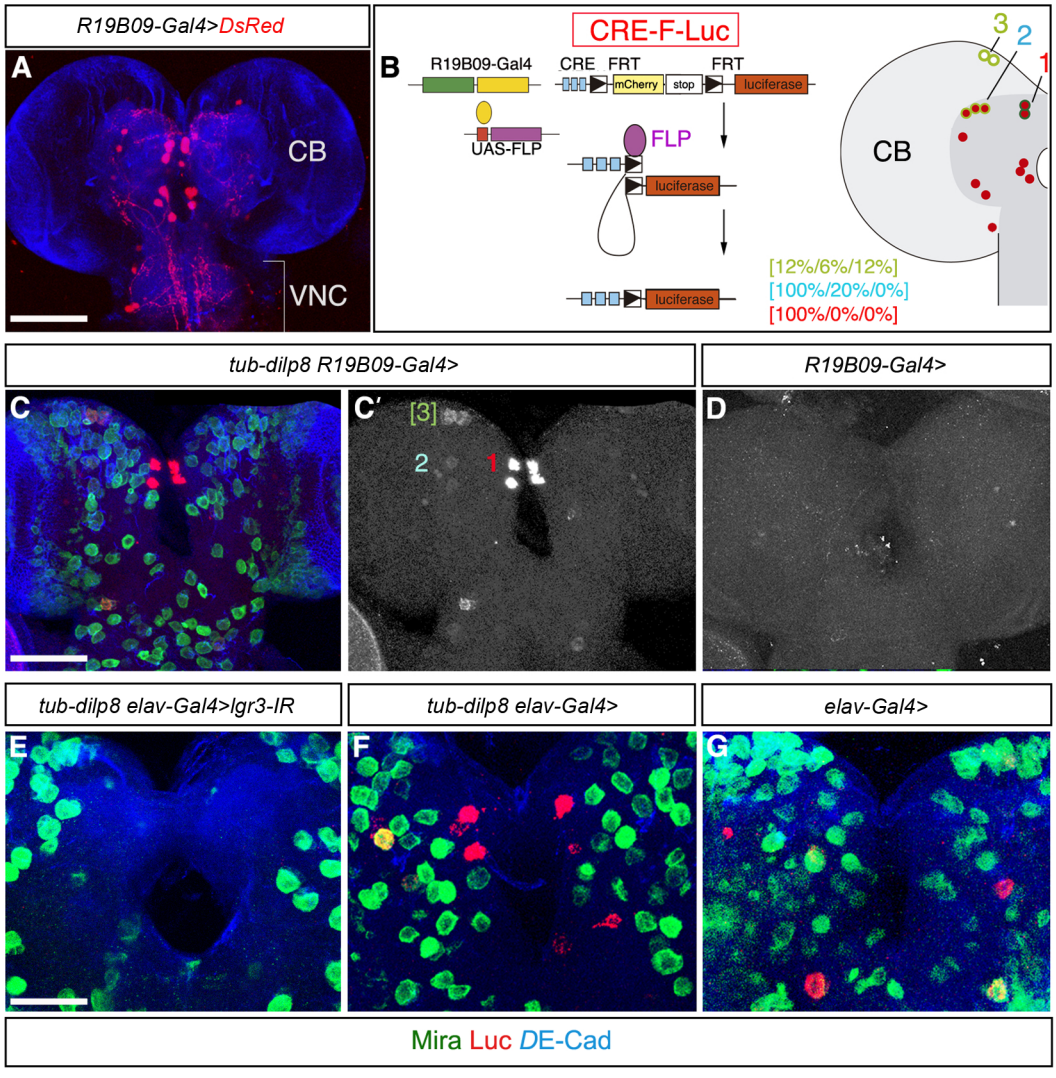

Fig. 4. A targeted cAMP biosensor reveals a pair of neurons responding acutely to Dilp8. (**A**) Expression of *UAS-DsRed* in neurons defined by the *R19B09-Gal4* enhancer (see fig. S4 for the expression of the other *lgr3-Gal4*). (**B**) CRE-F-luc reporter activity is Flp-dependent. (Left) The transgene contains stop sequences flanked by a pair of FRTs (FRT-cassette) inserted between the CREs and the *luciferase* construct. *R19B09-Gal4* activates the *UAS-Flp* transgene, and the FLP protein (purple) excises the FRT cassette in the CRE-F-luc transgene, only in *R19B09* cells. (Right) Central neurons (red dots) labeled by *R19B09-Gal4* and cells that respond to Dilp8 signals (outlined in green). The color code denotes the intensity of the signal; the numbers indicate the quantification in *tub-dilp8/wt/tub-dilp8 lgr3-IR* brains ($n > 10$ brains scored for each genotype). (**C** and **C′**) Higher-magnification views of central neurons in the dorsomedial region stained with anti-Luc (red) and the neuroblast marker anti-Mira (green). The brain is counterstained with anti-DE-Cad (blue). The *luciferase* response in neuroblasts (Mira-positive cells) in the dorsal region (designated as [3]) is not reproducible and can occur unilaterally. (C′) Single-channel confocal image of anti-Luc staining. Genotype: *UAS-Flp/+; tub-dilp8/+; CRE-F-luc/R19B09*. (**D**) Brain of WT control (*UAS-Flp/+; +/+; CRE-F-luc/R19B09*). (**E**) Knockdown of *lgr3* (*elav-Gal4/UAS-Flp; tub-dilp8/+; CRE-F-luc/UAS-lgr3-IR*) inhibits the Dilp8-induced cAMP response detected by luciferase driven by the *CRE-F-luc* construct, reflecting Lgr3 activation and probing specificity of the *UAS-lgr3-IR* transgene. (**F** and **G**) Confocal sections of the control brains (F) *elav-Gal4/UAS-Flp; tub-dilp8/+; CRE-F-luc/+* and (G) *elav-Gal4/UAS-Flp; +/+; CRE-F-luc/+*. Scale bars, 75 μm in (A) and (C) [also applies to (C′) and (D)]; 40 μm in (E) [also applies to (F) and (G)].

is based on the expression of two nonfluorescent split-GFP fragments ($spGFP_{1-10}$ and $spGFP_{11}$) tethered to the membrane in two neuronal populations (*40*). We used *R19B09-LexA* (*24*) to drive expression of *LexAop-spGFP$_{11}$* and *dilp3-Gal4* or *ptth-Gal4* to drive expression of *UAS-spGFP$_{1-10}$* in IPCs and PTTH neurons, respectively (Fig. 5, E and F). When paired with *R19B09-LexA*, strong, specific GRASP signals were observed for IPCs (Fig. 5E and fig. S6, A and B). GRASP signals also suggest possible connections between Lgr3 and PTTH neurons, as detected by immunofluorescence (anti-GFP, Invitrogen) (Fig. 5F) as in (*40*). This punctate staining was lacking in control brains (fig. S6C). We detected unreconstituted GFP, using immunofluorescence resulting from expression of the $spGFP_{1-10}$ fragment at the PTTH soma and axons (compare panels C and F in fig. S6). Immunofluorescence staining of PTTH neurons and signals of GRASP between IPCs and Lgr3 revealed probable synaptic contact sites in the circuit (Fig. 5G, asterisks, and fig. S6, D to H). These data suggest that Lgr3 neurons link Dilp8 input to IPCs and/or PTTH neurons to form a homeostatic circuit for synchronizing growth with maturation timing for body-size regulation.

Inhibition of PTTH neurons and mechanism for puparium delay

We reasoned that activation of Lgr3 neurons would delay pupariation by suppressing PTTH synaptic targets, so we used electrical silencing and genetic tools to investigate functional communication between Lgr3 and PTTH neurons. A PTTH receptor mutation (*torso^{RL3}*) that produces a constitutively active receptor has previously been shown to accelerate puparion formation in heterozygosis by 9.2 hours (*41*). Introducing the *tor^{RL3}* allelic mutation in *tub-dilp8* animals prevented pupariation delay (Fig. 5H) to the same extent as depleting *lgr3* (Fig. 1B) or feeding larvae with the active form of ecdysone, 20E ecdysone (*12*). These observations, coupled with the anatomical and genetic data, establish that the Dilp8-Lgr3 axis acts upstream of the PTTH-torso network, probably by suppressing PTTH neuron activity.

We wanted to probe the sufficiency of electrically silencing the PTTH neurons to delay the timing of the larval-pupal transition. Thus, we tested the effect of hyperpolarization of the membrane of PTTH neurons by expressing the potassium channel mKir2.1, which has proven to be a highly effective approach for shunting neuronal activity in excitable neurons (*42*). Expression of *UAS-mKir2.1* in the PTTH neurons using *ptth-Gal4* produced a larval-pupal transition delay of 12 hours compared with WT controls (Fig. 5I and see Fig. 5K for measurement of ecdysone signaling). This is similar to the effect of genetic ablation of PTTH neurons or genetic inactivation of the *Ptth* gene by RNAi reported previously (*14*). Hence, and as predicted (*14*), the release of PTTH that triggers the larval-pupal transition is related to PTTH neuron activity. However, electrical hyperexcitation by expressing the *UAS-NaChBac* ion channel by *ptth-Gal4* could neither accelerate pupariation nor prevent Dilp8-induced delay (fig. S7). It is possible that the release of PTTH at the larval-pupal transition might additionally require disinhibition of inhibitory input(s), as proposed for the secretion of GnRH from hypothalamic neurons at the onset of puberty (*5*, *10*). Electrical silencing of PTTH neurons did not trigger a compensatory growth response (Fig. 5J), and therefore, the animals bred after the extended larval period were larger than normal. Thus, the coupled control of the growth rate probably involves the other branch (the IPCs) of the Lgr3 neuronal circuit.

The IPCs as an Lgr3 output pathway and the role of JH in growth compensation

Our previous study showed that *dilp8* overexpression reduces the growth rate associated with a reduction in insulin-like peptide *dilp3* (*12*). Hence, we tested the possibility that this transcriptional modulation in the postsynaptic target (IPCs) may be a consequence of the inhibitory input to IPCs from the Lgr3 neurons. Ablation or electrical silencing of IPCs produces adults that are much smaller than normal (*9*, *16*), suggesting that size compensation via Dilp8 is unlikely to affect insulin signaling globally or completely. IPCs modulate growth systemically via circulating insulin-like peptides (such as Dilp2, -3, and -5) and via endocrine mechanisms, such as direct regulation of JH synthesis in the CA (*23*, *43*), which was also recently shown to instructively regulate larval growth in *Drosophila* (*44*, *45*). We therefore examined the expression of candidate output pathways as a read-out of the physiological dialogue between Lgr3 neurons that directly contact the IPCs and the regulation of JH.

Because JH titer is normally determined by its rate of biosynthesis by the larval CA gland, as well as its rate of degradation, we used qRT-PCR to measure the expression of a gene encoding a key biosynthetic enzyme [*juvenile hormone acid methyltransferase* (*JHAMT*)] (*43*) and the direct target of JH that encodes a transcription factor that transduces the actions of JH [*kruppel-homolog-1* (*kr-h1*)] (*46*, *47*). Together, these elements should allow us to detect the effective JH signaling in *tub-dilp8* animals compared with age-synchronized and population-controlled WT animals, as well as *tub-dilp8* animals with depleted *lgr3* in the neurons labeled by *R19B09-Gal4*. We also measured the transcriptional levels of Eip75B, a direct target of the ecdysone receptor, as a read-out for ecdysone signaling (*14*).

Control larvae experience a steep increase in *Eip75B* level at 100 hours after egg laying (AEL), which reflects the surge of ecdysone levels at the time of pupariation in our experimental conditions. As expected, no such accumulation was observed in *tub-dilp8* larvae at 100 hours AEL, but expression of *Eip75B* was restored to almost normal levels in *tub-dilp8* in which the *lgr3* receptor was knocked down in neurons labeled by *R19B09-Gal4* (Fig. 6A). The levels of *dilp3* and *dilp5*, which are known to respond to nutrition and stress (*16*) (Fig. 6B), and of *JHAMT* and *kr-h1* in JH biosynthesis and signaling (Fig. 6C) were also significantly down-regulated in *tub-dilp8* larvae, and their expression was restored to almost-normal levels by specific knockdown of *lgr3* in *R19B09* neurons. This non–cell-autonomous effect was specific because the expression of *dilp2* was not altered (fig. S8).

Although the exact mechanism by which Lgr3 neurons influence JH synthesis and signaling is not known, we attempted to establish a causal role for the observed reduction in JH signaling by pharmacological means. To control for the genetic background, we used *UAS-dilp8* and *tub-Gal4* (*tub>dilp8*) to treat animals overexpressing dilp8; the biologically inactive *UAS-dilp8^{C150A}* peptide hormone served as a control (*12*). The *tub>dilp8* larvae reach the correct pupal size and adult size [as assessed by measuring pupal volume and adult wing size and shape (*12*)]. In contrast, *tub>dilp8* larvae fed with the JH analog (JHA) methoprene produced significantly larger pupae (~25%) than did control animals (Fig. 6D). The onset of pupariation was slightly delayed (~6 hours) and resulted in 100% lethality, which consequently prevented us from measuring adult size. Treatment of control *tub>dilp8^{C150A}* animals that display normal pupation time (*12*) did not increase their size above that of their untreated siblings (Fig. 6D, right) (*44*). Thus, we conclude that reduced JH signaling diminishes larval growth, contributing to ensuing normal-sized tub>*dilp8* animals (Fig. 6E).

Discussion

Our data provide strong evidence that Dilp8 signals for organismal and organ homeostatic size regulation are transduced via the orphan relaxin receptor Lgr3 and that activation of Lgr3 in molecularly defined neurons mediates the necessary hormonal adjustments for such homeostasis. Human insulin/relaxin-like peptides are transduced through four GPCRs: RXFP1 to -4. RXFP1 and -2 are characterized by large extracellular domains containing leucine-rich repeats, similar to fly Lgr3 and Lgr4 receptors (*25*, *26*). Additionally, as for Lgr3 (this study), activation of RXFP1 and -2 by their cognate ligand binding stimulates increased cAMP production (*25*). RXFP3 is distinctly different in structure from fly Lgr3 (*25*), and its biochemical properties are also distinct, but RXPF3 is analogous to fly Lgr3 in the sense that it is found in highest abundance in the brain, suggesting important central functions for relaxin 3/RXFP3 (*48*, *49*). However, a function in pubertal development and/or growth control for vertebrate relaxin receptors is presently unknown.

The neuronal populations that regulate body size and, in particular, the mechanisms by which their regulation generates size variations (plasticity) in response to internal and environmental cues (such as nutrition) have been investigated thoroughly (*4*, *9*, *14*, *16*, *45*, *46*). Less is known about how the brain stabilizes body size to ensure that developing organisms reach the correct, genetically determined size. We also do not know how limbs grow to precisely match the size of

their contralateral limbs, nor do we understand how limbs maintain proportion with other body parts, even when faced with perturbations (this statement is also applicable to other bilaterally symmetric traits). Paired organs are controlled by an identical genetic program and grow in the same hormonal environment, yet small deviations in size can occur as a result of developmental stress, genetic noise, or injury. Imperfections in symmetry thus reflect the inability of an individual to counterbalance variations and growth abnormalities.

Our study shows that without *lgr3*, the brain is unable to detect growth disturbances and, more importantly, cannot adjust the internal hormonal

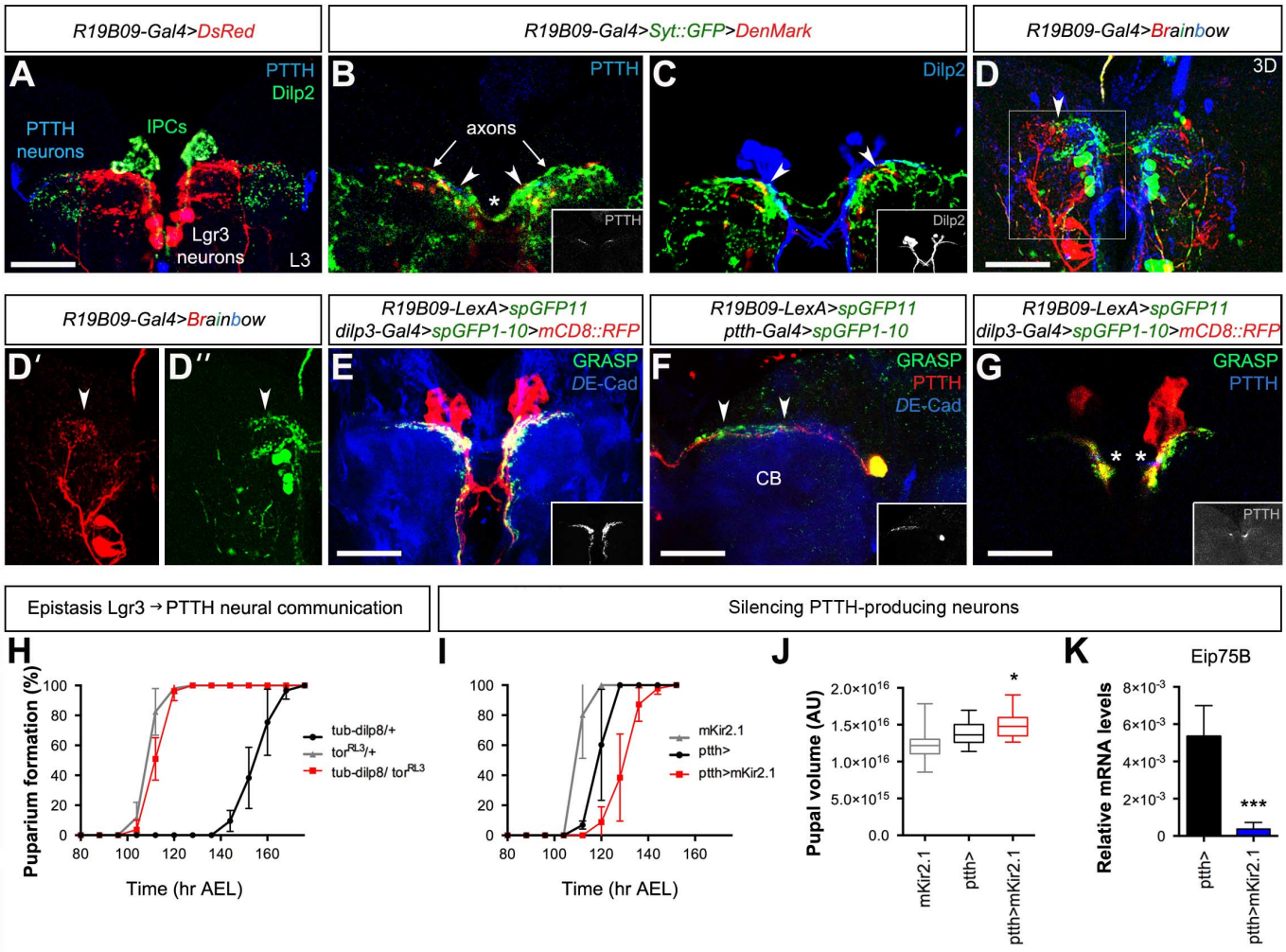

Fig. 5. Lgr3-responding neurons acts as hubs connecting distinct neuron subpopulations. (**A**) Lgr3 neurons with soma in the dorsomedial region and a prominent response to Dilp8 detected by *DsRed* (*R19B09-Gal4>DsRed*) ensheathed PTTH dendritic fields and axons (anti-PTTH, blue) and densely innervated IPCs (anti-Dilp2, green). Image represents a z-projection of confocal optical sections (29 μm thick) from the brain of a larva in the late third-instar (L3) stage. (**B** and **C**) Single confocal optical sections of larval brains of *R19B09-Gal4* driven presynaptic (*UAS-syt::GFP*, green) and post-synaptic (*UAS-DenMark*, red) markers. PTTH-producing neurons are labeled by anti-PTTH [blue (B)] and IPCs by anti-Dilp2 [blue (C)]. Arrowheads point to Lgr3 axonal projections close to PTTH (B) and IPC neural projections (C). Lgr3 axons also project contralaterally (asterisk). Insets show single channels of PTTH (B) and Dilp2 (C). (**D** to **D″**) *UAS-dBrainbow* reveals that projections from distinct neural subpopulations labeled by *R19B09-Gal4* converge on the dorsomedial Lgr3 neurons (green neurons, arrowheads). Single-channel images of Lgr3 neurons in the SOG (red) and dorsomedial (green) regions are shown in (D′) and (D″). Image is a 52-μm-thickness reconstruction of confocal sections. (**E**) Positive, robust signals of GRASP revealed extensive connections between Lgr3 (*R19B09-LexA>spGFP*$_{11}$) and IPCs (*dilp3-Gal4>spGFP*$_{1\text{-}10}$*>mCD8::RFP*). Brains were counterstained with anti-*DE*-Cad (blue). A 21-μm-thick reconstruction is shown. The inset shows GRASP signals (gray). (**F**) GRASP signals (arrowheads) between Lgr3 neurons (*R19B09-LexA>spGFP*$_{11}$) and PTTH-producing neurons (*ptth-Gal4>spGFP*$_{1\text{-}10}$) are detected with immunofluorescence (green) (fig. S6, C and D). Brains were costained with anti-PTTH (red) and anti-*DE*-Cad (blue). The image represents a 26-μm-thick reconstruction. The inset shows GRASP signals (gray). (**G**) Brains stained with anti-PTTH (blue) could detect potential contact sites (asterisks) of the circuit. GRASP signals (green) were contributed by connections between Lgr3 (*R19B09-LexA>spGFP*$_{11}$) and IPCs (red) (*dilp3-Gal4>spGFP*$_{1\text{-}10}$*>mCD8::RFP*). The inset shows single-channel staining (anti-PTTH, gray). The image is a single confocal section (1 μm thick). (**H**) Dilp8-induced delay in puparion formation is prevented by the constitutive active PTTH receptor *torso*^{RL3} mutation. (**I**) Electrical silencing of PTTH neurons (*ptth-Gal4 UAS-mKir2.1*) delays pupariation, as compared with controls. Data in (H) and (I) are pooled from three independent experiments, and each data point is mean ± SD. Approximately 60 pupae were scored per genotype. (**J**) PTTH neuronal silencing does not evoke growth compensation and results in larger pupae, as compared with controls. Data are mean ± SD (n = 3 independent repeats), and a total of 35 pupae were measured per genotype. *P < 0.05 (unpaired t test). AU, arbitrary units. (**K**) Expression of *Eip75B* at 100 hours AEL in control larvae (*ptth-Gal4*) and larvae with electrically silenced PTTH neurons (*ptth>mKir2.1*). ***P < 0.001 (unpaired t test). mRNA was obtained from seven larvae per genotype, and the experiment was repeated three times. Scale bars, 50 μm in (A) [also applies to (C)]; 60 μm in (D) [also applies to (D′) and (D″)]; 40 μm in (E) and (G); and 30 μm in (F).

environment to allocate additional developmental time for restoring affected parts or catching up on growth. Without *lgr3*, the brain is also not capable of retarding the growth rate to compensate for the extra time so that unaffected and affected tissues can develop with normal size, proportionality, and symmetry. Our study also identifies the Lgr3-expressing neurons necessary and sufficient to respond to Dilp8. Moreover, using a cAMP sensor, we have identified a pair of neurons that are highly sensitive to Dilp8.

Communication in neuronal networks is essential for synchronization and efficient performance. Notably, although most neurons have only one axon, Lgr3-responding neurons display extensive axonal arborizations reminiscent of hub neurons (*39*). GRASP analyses show that Lgr3 neurons are broadly connected with the IPCs and, to a lesser extent, with PTTH neurons, linking (Dilp8) inputs to the neuronal populations that regulate the key hormonal outputs modulating larval and imaginal disc growth. Furthermore, the information flow from Lgr3 neurons to IPCs and PTTH may explain how the brain matches growth with maturation in response to Dilp8 (Fig. 6F). This brain circuit provides the basis for studying how the brain copes with genetic and environmental perturbations to stabilize body size, proportions, and symmetry, all of which are vital for survival.

Materials and methods

Drosophila *husbandry*

The five *lgr3* enhancer *Gal4* lines (*R17G11-Gal4*, *R17H01-Gal4*, *R18A01-Gal4*, *R18C07-Gal4*, and *R19B09-Gal4*); the *R17G11-LexA*, *R19B09-LexA*, and *13xLexAop2-IVS-myr::GFP* lines; and the *retn*^{R9F04}*-Gal4* line are from the Janelia Farm Collection (Howard Hughes Medical Institute, Ashburn, VA). The *da-Gal4*, *dilp3-Gal4*, *dpp-Gal4*, *elav-Gal4*, *tub-Gal4*, *P0206-Gal4*, *NPF-Gal4*, *pdf-Gal4*, *per-Gal4*, *ptth-Gal4*, *tsh-Gal4*, *LexAop-CD4::spGFP*$_{11}$, *UAS-CD4::spGFP*$_{1\text{-}10}$, *UAS-dcr2*, *UAS-Denmark*, *UAS-DsRed*, *UAS-Flp*, *UAS-lgr3-TRiP.GL01056-RNAi*, *UAS-mCD8::GFP*, *UAS-mCD8::RFP*, *UAS-mKir2.1*, *UAS-NaChBac*, and *UAS-Syt::GFP* lines are from the Bloomington Stock Center at Indiana University (Bloomington, IN). *UAS-dilp8* and *UAS-dilp8*^{C150A} are described in (*12*). *CRE-F-luc* and *tor*^{RL3} were gifts from J. C. P. Yin and J. Casanova, respectively (*36*, *50*).

Flies were reared in standard "Iberian" fly food at 25°C (except when indicated) on a 14:10-hour light: dark cycle (surrogate of laboratory summer time). Standard Iberian fly food consisted of 15 liters of water, 0.75 kg of wheat flour, 1 kg of brown sugar, 0.5 kg of yeast, 0.17 kg of agar, 130 ml of a 5% nipagin solution in ethanol, and 130 ml of propionic acid.

G-TRACE analysis

G-TRACE (Gal4 technique for real-time and clonal expression) analysis was performed by crossing *UAS-Flp*, *UAS-RedStinger*, and *ubip63-FRT-stop-FRT-StingerGFP* stocks (*51*) with *R19B09-Gal4*, *retn*^{R9F04}*-Gal4*, and *P0206-Gal4* lines.

Brainbow clones

We built *hs-Cre; R19B09-Gal4* stocks and crossed them with *UAS-dBrainbow* (*38*) virgin females.

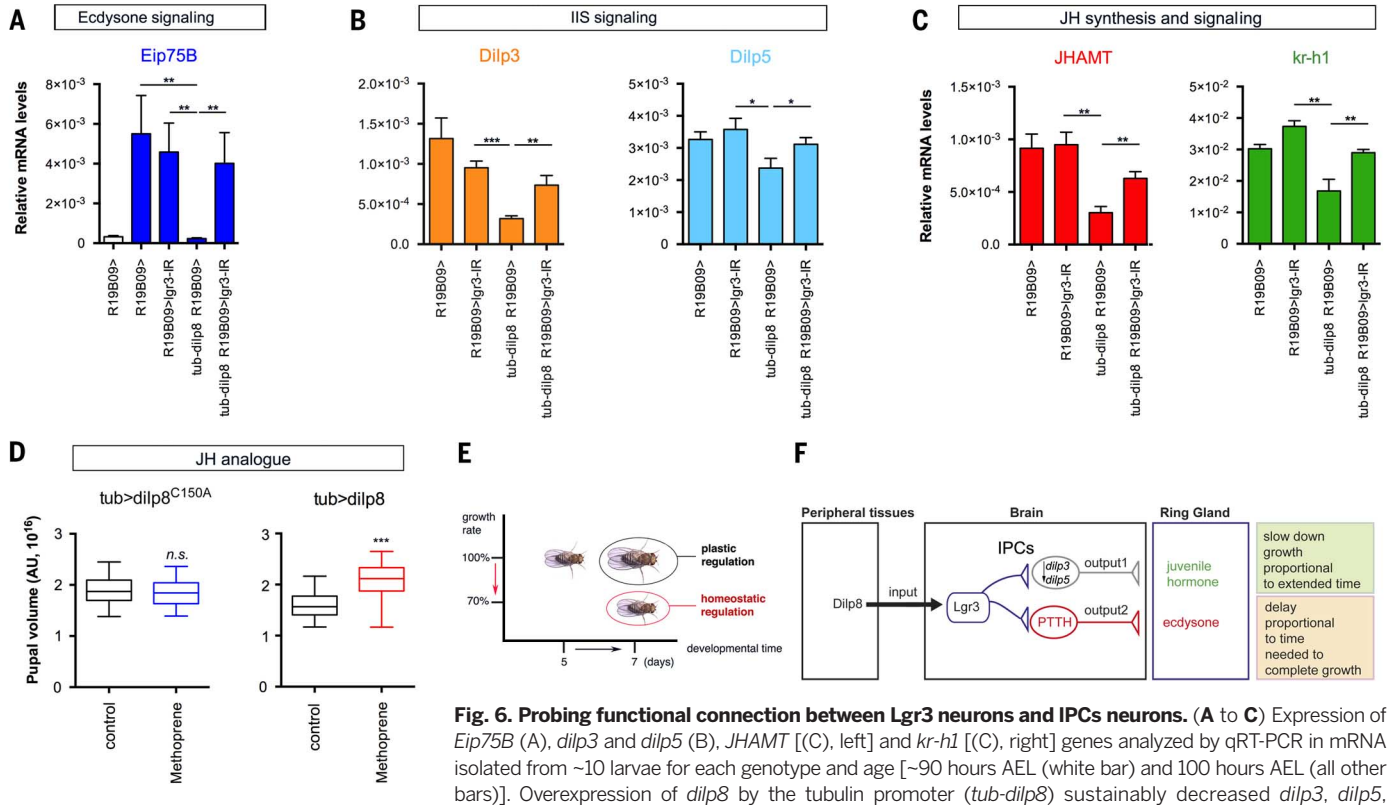

Fig. 6. Probing functional connection between Lgr3 neurons and IPCs neurons. (**A** to **C**) Expression of *Eip75B* (A), *dilp3* and *dilp5* (B), *JHAMT* [(C), left] and *kr-h1* [(C), right] genes analyzed by qRT-PCR in mRNA isolated from ~10 larvae for each genotype and age [~90 hours AEL (white bar) and 100 hours AEL (all other bars)]. Overexpression of *dilp8* by the tubulin promoter (*tub-dilp8*) sustainably decreased *dilp3*, *dilp5*, *JHAMT*, and *kr-h1* transcripts in the extended third-instar larval period, and this regulation was abrogated by specific knockdown of *lgr3* in *R19B09* neurons. Data are mean ± SD (n = 3 repeats). *P < 0.05; **P < 0.01; ***P < 0.001 (two-tailed unpaired t test). IIS, insulin/IGF-like signaling. (**D**) Treatment of JHA abrogates the compensatory growth response of *tub-dilp8* animals. Box-and-whisker plots of the pupal volume of control animals (*tub>dilp8*^{C150A}) (left) and animals overexpressing *dilp8* (*tub>dilp8*) (right). Any differences between *tub>dilp8*^{C150A} animals fed with methoprene [Met] or without (control) are not significant. Met-fed *tub>dilp8* animals produced noticeably larger pupae. Plotted data are pooled from three biological repeats (50 pupae per genotype and treatment). ***P < 0.001 (two-tailed unpaired t test). (**E**) Model for plastic and homeostatic regulation of body size. If the growth rate is fixed, an extension of the developmental time results in larger adults (plastic regulation). If developmentally delayed animals also experience a proportional decrease in growth rate, they will reach a normal adult size (homeostatic regulation). Developmental time (days) represents age at the larval-pupal transition. (**F**) Model of Lgr3 circuit and output pathways. Dilp8 produced by peripheral tissues conveys information about overall growth status. Circulating Dilp8 enters the brain through the blood-brain barrier, in an unknown manner, and binds and activates Lgr3 in a dose-dependent manner. With their high connectivity, Lgr3-responding neurons distribute this growth-status information to IPCs (gray) and PTTH neurons (red), which ensures that rates of growth and maturation are matched and co-regulated according to the intensity of the Dilp8 signals.

We reared fly crosses at 25°C and did not heat-shock them. The following primary antibodies were used: rabbit anti-HA (1/500; Abcam) and mouse anti-V5 (1/500, Invitrogen).

GRASP analysis

We built *R19B09-LexA; LexAop-CD4::spGFP$_{11}$, UAS-CD4::spGFP$_{1-10}$*/TM6B stocks and crossed them with *dilp3-Gal4/CyO-GFP; UAS-mCD8::RFP* (n = 14 larval brains were analyzed) or *ptth-Gal4/CyO-GFP* (n = 43 larval brains were analyzed). Control experiments were performed by staining larval brains of the following genotypes (n = 10 larval brains per genotype were analyzed): *R19B09-LexA; LexAop-CD4::spGFP$_{11}$, UAS-CD4::spGFP$_{1-10}$*/TM6B, *dilp3-Gal4/+; LexAop-CD4::spGFP$_{11}$, UAS-CD4::spGFP$_{1-10}$*/+, or *ptth-Gal4/+; LexAop-CD4::spGFP$_{11}$, UAS-CD4::spGFP$_{1-10}$*/+. The following primary antibodies were used: rabbit anti-GFP (1/2000; Invitrogen) to detect GRASP signal between PTTH and Lgr3 neurons, guinea pig anti-PTTH [1/500 (*52*)], and rat anti–*Drosophila* E-Cadherin (anti-*D*E-Cad) [1/50, Developmental Studies Hybridoma Bank (DSHB)] to counterstain larval brains.

Confocal imaging and immunohistochemistry in brains

Brains were dissected in cold phosphate-buffered saline (PBS), fixed in 4% paraformaldehyde (PFA) for 20 min (*53*), and stained with the following primary antibodies: guinea pig anti-PTTH [1/500 (*52*)], mouse anti-luciferase (1/200, Thermo Fisher Scientific), rabbit anti-Dilp2 [1/500 (*54*)], rabbit anti-Mira [1/2000 (*55*)], rabbit anti-Pdp1 [1/1000 (*56*)], and rat anti-*D*E-Cad (1/50, DSHB). Secondary antibodies were purchased from Invitrogen and Jackson ImmunoResearch. The brains were mounted in Vectashield (Vector Labs), maintaining their three-dimensional (3D) configuration (*53*), and images were obtained on a Leica TCS SP2 confocal microscope. Z stacks were recorded at 1-μm intervals. 3D reconstructions of individual WT *Drosophila* larval brains were created using Imaris software (Bitplane, Zurich, Switzerland). To assess changes in cAMP levels in the larval brain, we used the in vivo CRE-F-luc reporter system (*36*). Dissected brains were stained using mouse anti-luciferase (1/200, Thermo Fisher Scientific).

Generation of DNA constructs and transgenic lines

For the *tub-dilp8::FLAG* construct, *dilp8* cDNA was C-terminally fused in frame to the 3xFLAG coding sequence (*12*) and cloned into the pCaspertubulin promoter plasmid at the KpnI/NotI sites.

The *lgr3* WT cDNA sequence was based on the WT amino acid sequence corresponding to GenBank accession number AAF56490, codon-optimized using GeneOptimizer (GENEART), and cloned into the pMK-RQ plasmid (SfiI/SfiI sites) (GENEART). The obtained construct was verified by sequencing and then cloned into the pUASt plasmid at the EcoRI/NotI sites.

Constructs were injected in w^{1118} embryos following standard P-element–mediated transformation procedures (BestGene).

The entire open reading frame (ORF) sequence of *lgr4* was PCR-amplified from total mRNA obtained from w^{1118} larvae using primers containing attB1 and attB2 Gateway recombination sites whose sequences were as follows:

lgr4 forward primer: 5′-ATGTGTATAGCTCACCTGCCTATCAC-3′

lgr4 reverse primer: 5′-CTACAGATAGCTCATCTGCCGGTGTG-3′

The amplified product was cloned into a pDON/Zeo entry vector (Life Technologies), according to the Gateway technology manual (Life Technologies), and verified by sequencing. Verified entry clones were used to introduce full-length ORFs into the pUASt Gateway plasmid [Drosophila Genomics Resource Center (DGRC), stock no. 1129] by LR recombination (Gateway technology, Life Technologies).

The Lgr3 extracellular domain (hereafter Lrg3-ECD) (amino acid residues 1 to 433) was PCR amplified from the pUASt-*lgr3* full-length plasmid described above using primers containing attB1 and attB2 Gateway recombination sites with the following sequences:

lgr3-ECD forward primer: 5′-ATGGTGTACGGCCGCAGTATCGCCGTG-3′

lgr3-ECD reverse primer: 5′-CAGCACGGGCTTGCTCAGCAGGTC-3′

The PCR product was cloned into pDON/Zeo entry vector (Life Technologies) following the Gateway technology manual instructions (Life Technologies) and verified by sequencing. Entry *Lrg3-ECD* construct was used to introduce the insert into the pUASt-C-terminal 3xHA Gateway plasmid (DGRC, stock no. 1100) by LR recombination (Gateway technology, Life Technologies).

Cell culture

Drosophila S2 and Kc cells (Invitrogen) were cultured in Schneider's *Drosophila* medium (Invitrogen) supplemented with 10% fetal bovine serum (Gibco, Thermo Fisher Scientific) at 25°C in a nonhumidified, ambient-air–regulated incubator.

cAMP measurement

Concentrations of cAMP were measured using the cAMP Enzymeimmunoassay (EIA) System (Amersham, catalog no. RPN2251). *Drosophila* Kc cells (Invitrogen) were seeded (50.000 per well) in a 96-well plate and transfected with the plasmid DNA indicated, using Fugene-HD (Promega). After 36 hours of transfection, cells were exposed for 30 min to the Dilp8 peptide (at 0, 5, or 50 nM; Phoenix Pharmaceuticals, catalog no. 035-79) and 3-isobutyl-1-methylxanthine (IBMX) (100 μM; Sigma, catalog no. I5879). After treatment, the cells were processed according to the manufacturer's protocol, and the cAMP concentrations are presented as femtomoles per well.

EC_{50} determination

The cAMP concentrations were determined using the Direct cAMP ELISA Kit (Enzo Lifescience, catalog no. ADI-900-066) according to the manufacturer's protocol. 50.000 *Drosophila* Kc cells (Invitrogen) were seeded per well in a 96-well plate and transfected with the indicated plasmid DNA, using Fugene-HD (Promega). After 36 hours of transfection, cells were exposed for 30 min to IBMX (100 μM) and Dilp8 peptide (12 serial dilutions of Dilp8 starting from 250 nM to 0 nM). Total intracellular cAMP concentration was determined using the nonacetylation cAMP enzyme immunoassay from 100 μl of 0.1 M HCl in all experiments. cAMP levels were calculated using the 4 Parameter Logistic Curve (4PL) online data analysis tool (MyAssays). Results are expressed in picomoles per milliliter of cAMP. The EC_{50} analysis was calculated with GraphPad Prism software (version 6, for Mac), using a sigmoidal dose-response (variable slope) equation.

Coimmunoprecipitation assays

Drosophila S2 cells (3×10^6 cells per 10-cm dish) were transiently cotransfected with *pActin-Gal4* and either *UAS-lgr3-ECD::3XHA* or empty vector *UAS::3XHA*, using Fugene-HD (Promega). To obtain secreted tagged Dilp8, 6×10^6 S2 cells per 10-cm dish were transiently transfected using the *pActin-Gal4* and *UAS-dilp8::Myc* plasmid. Thirty-six hours after transfection, supernatant containing Dilp8::Myc was collected, filtered, and used to replace the medium of *UAS-lgr3-ECD::3XHA* and *UAS::3XHA* dishes. After 2 hours of incubation, cells were PBS-washed and cross-linked for 30 min using DTSSP [3,3′-dithiobis(sulfosuccinimidyl propionate)] (Thermo Fisher Scientific). Cells were PBS-washed and then lysed using modified RIPA buffer containing proteinase inhibitors. Precleared extracts were incubated at 4°C with 1 μg of rabbit anti-Myc (Abcam, ab9606) or rabbit anti–immunoglobulin G (anti-IgG) (Sigma, I8140). After 2 hours, 25 μl of equilibrated protein A magnetic beads (Millipore, catalog no. 16-661) was added to each extract and incubated over night at 4°C. After three washes using the modified RIPA buffer containing proteinase inhibitors, proteins bound to beads were recovered by boiling for 10 min in 25 μl of 3x sample buffer and were separated by SDS–polyacrylamide gel electrophoresis. After blotting, membranes were incubated in rat anti-HA–horseradish peroxidase (clone 3F10, Roche) and analyzed.

Immunostaining of Drosophila cultured cells

Drosophila Kc cells (8×10^5 cells per well) were cotransfected in six-well plates with *pActin-Gal4* and either *UAS-lgr3-ECD::3XHA* or empty vector *UAS::3XHA* and, in parallel, were cotransfected with *tub-dilp8::FLAG* using Fugene-HD (Promega). Thirty-six hours after transfection, supernatant containing Dilp8::FLAG was collected, filtered, and used to replace medium from *UAS-lgr3-ECD::3XHA* and *UAS::3XHA*. After a 2-hour incubation period, cells were washed twice with PBS, fixed using 4% PFA, and immunostained (cells were not permeabilized). Antibodies used: rabbit anti-HA (1/200, Abcam ab9110) and mouse anti-FLAG-M2 (1/200, Sigma).

Lgr3 antibody

To generate specific antiserum for Lgr3, two peptides corresponding to amino acids 719 to 733 (C+ GWKKITSRKRAEAGN) and 487 to 501

(C+ GVQDYRYRNEYYKVV) (*57*) were synthesized by Eurogentec (Seraing, Belgium) and used to immunize rabbits according to an 87-day polyclonal antibody program.

Quantitative RT-PCR

To assess mRNA levels, total RNA was extracted from *Drosophila* larvae using the RNeasy-Mini Kit (Qiagen). To remove contaminating DNA, RNA was treated with Turbo DNA-free (Ambion, Life Technologies). cDNA was synthesized with SuperScript III First-Strand Synthesis System for RT-PCR (Life Technologies) using oligo-dT primers. qRT-PCR was performed using SYBR Green PCR Master Mix (Applied Biosystems), with gene-specific primers, on an ABI7500 apparatus (Applied Biosystems). *Rp49* primers were used for mRNA normalization. Comparative qRT-PCRs were performed in triplicates, and relative expression was calculated using the comparative Ct method.

Primer sequences:
lgr3:
Forward 5′-GGCAAAGGAGCATACATTTGA-3′
Reverse 5′-TTAAGTGCCAGGATTACACAGC-3′
Thor/4E-BP:
Forward 5′-GAAGGTTGTCATCTCGGATCC-3′
Reverse 5′-ATGAAAGCCCGCTCGTAG-3′
E75B:
Forward 5′-CAACAGCAACAACACCCAGA-3′
Reverse 5′-CAGATCGGCACATGGCTTT-3′
JHAMT:
Forward 5′-ATTCGCATCGACCATGCAGT-3′
Reverse 5′-GAAGTCCATGAGCACGTTACC-3′
Kr-h1:
Forward 5′-ACAATTTTATGATTCAGCCACAACC-3′
Reverse 5′-GTTAGTGGAGGCGGAACCTG-3′
dilp2:
Forward 5′-ATCCCGTGATTCCACACAAG-3′
Reverse 5′-GCGGTTCCGATATCGAGTTA-3′
dilp3:
Forward 5′-ATCCCGTGATTCCACACAAG-3′
Reverse 5′-GCGGTTCCGATATCGAGTTA-3′
dilp5:
Forward 5′-GCCTTGATGGACATGCTGA-3′
Reverse 5′-CATAATCGAATAGGCCCAAGG-3′
rp49:
Forward 5′-TGTCCTTCCAGCTTCAAGATGAC-CATC-3′
Reverse 5′-CTTGGGCTTGCGCCATTTGTG- 3′

Measurement of the developmental timing of pupariation

Females and males (20 to 30 of each) were crossed and, after 24 to 48 hours, flies were transferred to grape juice agar plates with yeast paste and left 4 hours for egg deposition. Parental flies were removed, and laid eggs were incubated 48 hours at 26.5°C. Second-instar larvae were transferred onto 5 ml of *Drosophila* standard Iberian food (20 larvae per tube) and reared at 26.5°C. A survey of the pupae was performed at 8-hour intervals, with "time 0" designated as 4 hours after the initiation of egg laying.

Weight and size measurements

For weighing adult flies, 20 to 30 females and 20 to 30 males were crossed and left 24 hours for egg deposition. Parental flies were transferred every 24 hours to fresh tubes, and laid eggs were reared at 26.5°C. Eclosed adult males of each genotype were collected (five groups of five individuals) and weighed after 12 to 24 hours, using a precision scale.

For pupae volume determination, 20 to 30 females and 20 to 30 males were crossed and left 24 hours for egg deposition. Parental flies were transferred every 24 hours to fresh tubes, and laid eggs were reared at 26.5°C. Pupae were collected and photographed with their dorsal side up. Length and width were measured using ImageJ; volume was calculated according to the following formula: $v = 4/3\pi(L/2)(l/2)^2$ (L, length; l, width).

For adult wing measurements, 20 to 30 females and 20 to 30 males were crossed and left 24 hours for egg deposition. Parental flies were transferred every 24 hours to fresh tubes, and laid eggs were reared at 26.5°C. Adults were collected and left, and the right wings of each individual were excised and rinsed thoroughly with ethanol and mounted in a glycerol-ethanol solution. Wing areas were measured using ImageJ. Intra-individual variation of wing areas was calculated using fluctuating asymmetry index (FAi) as in (*12*), employing the formula $FAi = Var(Ai)$, where Ai are the differences between left and right wing areas of each individual.

Juvenile hormone analog (methoprene) treatment

Males and females (20 to 30 of each) were crossed, and after 24 to 48 hours, flies were transferred to grape juice agar plates with yeast paste and left 4 hours for egg deposition. Parental flies were removed, and laid eggs were incubated 48 hours at 26.5°C. Second-instar larvae were transferred onto 5 ml of *Drosophila* standard Iberian food (20 larvae per tube) and incubated at 26.5°C. Larvae were transferred 24 hours later (72 hours AEL) to 3 ml of *Drosophila* standard Iberian food supplemented with a liquid solution of pure methoprene (Sigma, catalog no. 33375) at a Met:food ratio of 1 μm:1000 μm. An equivalent volume of water was added to the control.

REFERENCES AND NOTES

1. B. A. Edgar, How flies get their size: Genetics meets physiology. *Nat. Rev. Genet.* **7**, 907–916 (2006). doi: 10.1038/nrg1989; pmid: 17139322
2. A. W. Shingleton, The regulation of organ size in *Drosophila*: Physiology, plasticity, patterning and physical force. *Organogenesis* **6**, 76–87 (2010). doi: 10.4161/org.6.2.10375; pmid: 20885854
3. L. Wolpert, Arms and the man: The problem of symmetric growth. *PLOS Biol.* **8**, e1000477 (2010). doi: 10.1371/journal.pbio.1000477; pmid: 20838659
4. J. M. Tennessen, C. S. Thummel, Coordinating growth and maturation - insights from *Drosophila*. *Curr. Biol.* **21**, R750–R757 (2011). doi: 10.1016/j.cub.2011.06.033; pmid: 21959165
5. K. P. Tolson, P. E. Chappell, The changes they are a-timed: Metabolism, endogenous clocks, and the timing of puberty. *Front. Endocrinol.* **3**, 45 (2012). doi: 10.3389/fendo.2012.00045; pmid: 22645521
6. N. F. Parker, A. W. Shingleton, The coordination of growth among *Drosophila* organs in response to localized growth-perturbation. *Dev. Biol.* **357**, 318–325 (2011). doi: 10.1016/j.ydbio.2011.07.002; pmid: 21777576
7. J. F. Hackney, O. Zolali-Meybodi, P. Cherbas, Tissue damage disrupts developmental progression and ecdysteroid biosynthesis in *Drosophila*. *PLOS ONE* **7**, e49105 (2012). doi: 10.1371/journal.pone.0049105; pmid: 23166607
8. I. K. Hariharan, How growth abnormalities delay "puberty" in *Drosophila*. *Sci. Signal.* **5**, pe27 (2012). doi: 10.1126/scisignal.2003238; pmid: 22715466
9. D. S. Andersen, J. Colombani, P. Léopold, Coordination of organ growth: Principles and outstanding questions from the world of insects. *Trends Cell Biol.* **23**, 336–344 (2013). doi: 10.1016/j.tcb.2013.03.005; pmid: 23587490
10. C. L. Sisk, D. L. Foster, The neural basis of puberty and adolescence. *Nat. Neurosci.* **7**, 1040–1047 (2004). doi: 10.1038/nn1326; pmid: 15452575
11. O. Karapanou, A. Papadimitriou, Determinants of menarche. *Reprod. Biol. Endocrinol.* **8**, 115 (2010). doi: 10.1186/1477-7827-8-115; pmid: 20920296
12. A. Garelli, A. M. Gontijo, V. Miguela, E. Caparros, M. Dominguez, Imaginal discs secrete insulin-like peptide 8 to mediate plasticity of growth and maturation. *Science* **336**, 579–582 (2012). doi: 10.1126/science.1216735; pmid: 22556250
13. J. Colombani, D. S. Andersen, P. Léopold, Secreted peptide Dilp8 coordinates *Drosophila* tissue growth with developmental timing. *Science* **336**, 582–585 (2012). doi: 10.1126/science.1216689; pmid: 22556251
14. K. F. Rewitz, N. Yamanaka, M. B. O'Connor, Developmental checkpoints and feedback circuits time insect maturation. *Curr. Top. Dev. Biol.* **103**, 1–33 (2013). doi: 10.1016/B978-0-12-385979-2.00001-0; pmid: 23347514
15. Z. McBrayer *et al.*, Prothoracicotropic hormone regulates developmental timing and body size in *Drosophila*. *Dev. Cell* **13**, 857–871 (2007). doi: 10.1016/j.devcel.2007.11.003; pmid: 18061567
16. D. R. Nässel, O. I. Kubrak, Y. Liu, J. Luo, O. V. Lushchak, Factors that regulate insulin producing cells and their output in *Drosophila*. *Front. Physiol.* **4**, 252 (2013). doi: 10.3389/fphys.2013.00252; pmid: 24062693
17. W. Brogiolo *et al.*, An evolutionarily conserved function of the *Drosophila* insulin receptor and insulin-like peptides in growth control. *Curr. Biol.* **11**, 213–221 (2001). doi: 10.1016/S0960-9822(01)00068-9; pmid: 11250149
18. T. Ikeya, M. Galic, P. Belawat, K. Nairz, E. Hafen, Nutrient-dependent expression of insulin-like peptides from neuroendocrine cells in the CNS contributes to growth regulation in *Drosophila*. *Curr. Biol.* **12**, 1293–1300 (2002). doi: 10.1016/S0960-9822(02)01043-6; pmid: 12176357
19. S. Grönke, D. F. Clarke, S. Broughton, T. D. Andrews, L. Partridge, Molecular evolution and functional characterization of *Drosophila* insulin-like peptides. *PLOS Genet.* **6**, e1000857 (2010). doi: 10.1371/journal.pgen.1000857; pmid: 20195512
20. J. S. Britton, W. K. Lockwood, L. Li, S. M. Cohen, B. A. Edgar, *Drosophila*'s insulin/PI3-kinase pathway coordinates cellular metabolism with nutritional conditions. *Dev. Cell* **2**, 239–249 (2002). doi: 10.1016/S1534-5807(02)00117-X; pmid: 11832249
21. H. Zhang *et al.*, Deletion of *Drosophila* insulin-like peptides causes growth defects and metabolic abnormalities. *Proc. Natl. Acad. Sci. U.S.A.* **106**, 19617–19622 (2009). doi: 10.1073/pnas.0905083106; pmid: 19887630
22. C. Chen, J. Jack, R. S. Garofalo, The *Drosophila* insulin receptor is required for normal growth. *Endocrinology* **137**, 846–856 (1996). pmid: 8603594
23. Y. H. Belgacem, J. R. Martin, Hmgcr in the corpus allatum controls sexual dimorphism of locomotor activity and body size via the insulin pathway in *Drosophila*. *PLOS ONE* **2**, e187 (2007). doi: 10.1371/journal.pone.0000187; pmid: 17264888
24. A. Jenett *et al.*, A GAL4-driver line resource for *Drosophila* neurobiology. *Cell Reports* **2**, 991–1001 (2012). doi: 10.1016/j.celrep.2012.09.011; pmid: 23063364
25. R. A. Bathgate *et al.*, Relaxin family peptides and their receptors. *Physiol. Rev.* **93**, 405–480 (2013). doi: 10.1152/physrev.00001.2012; pmid: 23303914
26. M. B. Van Hiel, H. P. Vandersmissen, T. Van Loy, J. Vanden Broeck, An evolutionary comparison of leucine-rich repeat containing G protein-coupled receptors reveals a novel LGR subtype. *Peptides* **34**, 193–200 (2012). doi: 10.1016/j.peptides.2011.11.004; pmid: 22100731
27. M. B. Van Hiel, H. P. Vandersmissen, P. Proost, J. Vanden Broeck, Cloning, constitutive activity and expression profiling of two receptors related to relaxin receptors in *Drosophila melanogaster*. *Peptides* **68**, 83–90 (2015). doi: 10.1016/j.peptides.2014.07.014; pmid: 25064813

28. J. Q. Ni *et al*., A *Drosophila* resource of transgenic RNAi lines for neurogenetics. *Genetics* **182**, 1089–1100 (2009). doi: 10.1534/genetics.109.103630; pmid: 19487563
29. A. Scopelliti *et al*., Local control of intestinal stem cell homeostasis by enteroendocrine cells in the adult *Drosophila* midgut. *Curr. Biol.* **24**, 1199–1211 (2014). doi: 10.1016/j.cub.2014.04.007; pmid: 24814146
30. S. Y. Hsu *et al*., Activation of orphan receptors by the hormone relaxin. *Science* **295**, 671–674 (2002). doi: 10.1126/science.1065654; pmid: 11809971
31. K. S. Carmon, X. Gong, Q. Lin, A. Thomas, Q. Liu, R-spondins function as ligands of the orphan receptors LGR4 and LGR5 to regulate Wnt/β-catenin signaling. *Proc. Natl. Acad. Sci. U.S.A.* **108**, 11452–11457 (2011). doi: 10.1073/pnas.1106083108; pmid: 21693646
32. Q. Wu *et al*., Developmental control of foraging and social behavior by the *Drosophila* neuropeptide Y-like system. *Neuron* **39**, 147–161 (2003). doi: 10.1016/S0896-6273(03)00396-9; pmid: 12848939
33. J. Berni, S. R. Pulver, L. C. Griffith, M. Bate, Autonomous circuitry for substrate exploration in freely moving *Drosophila* larvae. *Curr. Biol.* **22**, 1861–1870 (2012). doi: 10.1016/j.cub.2012.07.048; pmid: 22940472
34. G. Milligan, Constitutive activity and inverse agonists of G protein-coupled receptors: A current perspective. *Mol. Pharmacol.* **64**, 1271–1276 (2003). doi: 10.1124/mol.64.6.1271; pmid: 14645655
35. M. N. Nitabach *et al*., Electrical hyperexcitation of lateral ventral pacemaker neurons desynchronizes downstream circadian oscillators in the fly circadian circuit and induces multiple behavioral periods. *J. Neurosci.* **26**, 479–489 (2006). doi: 10.1523/JNEUROSCI.3915-05.2006; pmid: 16407545
36. A. K. Tanenhaus, J. Zhang, J. C. P. Yin, In vivo circadian oscillation of dCREB2 and NF-κB activity in the *Drosophila* nervous system. *PLOS ONE* **7**, e45130 (2012). doi: 10.1371/journal.pone.0045130; pmid: 23077489
37. L. J. Nicolaï *et al*., Genetically encoded dendritic marker sheds light on neuronal connectivity in *Drosophila*. *Proc. Natl. Acad. Sci. U.S.A.* **107**, 20553–20558 (2010). doi: 10.1073/pnas.1010198107; pmid: 21059961
38. S. Hampel *et al*., *Drosophila* Brainbow: A recombinase-based fluorescence labeling technique to subdivide neural expression patterns. *Nat. Methods* **8**, 253–259 (2011). doi: 10.1038/nmeth.1566; pmid: 21297621
39. P. Bonifazi *et al*., GABAergic hub neurons orchestrate synchrony in developing hippocampal networks. *Science* **326**, 1419–1424 (2009). doi: 10.1126/science.1175509; pmid: 19965761
40. M. D. Gordon, K. Scott, Motor control in a *Drosophila* taste circuit. *Neuron* **61**, 373–384 (2009). doi: 10.1016/j.neuron.2008.12.033; pmid: 19217375
41. K. F. Rewitz, N. Yamanaka, L. I. Gilbert, M. B. O'Connor, The insect neuropeptide PTTH activates receptor tyrosine kinase torso to initiate metamorphosis. *Science* **326**, 1403–1405 (2009). doi: 10.1126/science.1176450; pmid: 19965758
42. J. J. Hodge, Ion channels to inactivate neurons in *Drosophila*. *Front. Mol. Neurosci.* **2**, 13 (2009). doi: 10.3389/neuro.02.013.2009; pmid: 19750193
43. T. Flatt, M. P. Tu, M. Tatar, Hormonal pleiotropy and the juvenile hormone regulation of *Drosophila* development and life history. *BioEssays* **27**, 999–1010 (2005). doi: 10.1002/bies.20290; pmid: 16163709
44. C. K. Mirth *et al*., Juvenile hormone regulates body size and perturbs insulin signaling in *Drosophila*. *Proc. Natl. Acad. Sci. U.S.A.* **111**, 7018–7023 (2014). doi: 10.1073/pnas.1313058111; pmid: 24778227
45. L. M. Riddiford, J. W. Truman, C. K. Mirth, Y. C. Shen, A role for juvenile hormone in the prepupal development of *Drosophila melanogaster*. *Development* **137**, 1117–1126 (2010). doi: 10.1242/dev.037218; pmid: 20181742
46. M. Jindra, S. R. Palli, L. M. Riddiford, The juvenile hormone signaling pathway in insect development. *Annu. Rev. Entomol.* **58**, 181–204 (2013). doi: 10.1146/annurev-ento-120811-153700; pmid: 22994547
47. C. Minakuchi, X. Zhou, L. M. Riddiford, *Krüppel homolog 1* (*Kr-h1*) mediates juvenile hormone action during metamorphosis of *Drosophila melanogaster*. *Mech. Dev.* **125**, 91–105 (2008). doi: 10.1016/j.mod.2007.10.002; pmid: 18036785
48. R. J. Summers, R. A. Bathgate, J. D. Wade, E. T. van der Westhuizen, M. L. Halls, Roles of the receptor, the ligand, and the cell in the signal transduction pathways utilized by the relaxin family peptide receptors 1-3. *Ann. N. Y. Acad. Sci.* **1160**, 99–104 (2009). doi: 10.1111/j.1749-6632.2009.03828.x; pmid: 19416167
49. C. M. Smith, I. T. Hosken, S. W. Sutton, A. J. Lawrence, A. L. Gundlach, Relaxin-3 null mutation mice display a circadian hypoactivity phenotype. *Genes Brain Behav.* **11**, 94–104 (2012). doi: 10.1111/j.1601-183X.2011.00730.x; pmid: 21899720
50. J. Casanova, G. Struhl, The torso receptor localizes as well as transduces the spatial signal specifying terminal body pattern in *Drosophila*. *Nature* **362**, 152–155 (1993). doi: 10.1038/362152a0; pmid: 8450886
51. C. J. Evans *et al*., G-TRACE: Rapid Gal4-based cell lineage analysis in *Drosophila*. *Nat. Methods* **6**, 603–605 (2009). pmid: 19633663
52. N. Yamanaka *et al*., Neuroendocrine control of *Drosophila* larval light preference. *Science* **341**, 1113–1116 (2013). doi: 10.1126/science.1241210; pmid: 24009394
53. J. Morante, C. Desplan, Dissection and staining of *Drosophila* optic lobes at different stages of development. *Cold Spring Harbor Protoc.* **2011**, 652–656 (2011). doi: 10.1101/pdb.prot5629; pmid: 21632779
54. R. Bader *et al*., The IGFBP7 homolog Imp-L2 promotes insulin signaling in distinct neurons of the *Drosophila* brain. *J. Cell Sci.* **126**, 2571–2576 (2013). doi: 10.1242/jcs.120261; pmid: 23591813
55. H. Ikeshima-Kataoka, J. B. Skeath, Y. Nabeshima, C. Q. Doe, F. Matsuzaki, Miranda directs Prospero to a daughter cell during *Drosophila* asymmetric divisions. *Nature* **390**, 625–629 (1997). doi: 10.1038/37641; pmid: 9403694
56. S. A. Cyran *et al*., *vrille*, *Pdp1*, and *dClock* form a second feedback loop in the *Drosophila* circadian clock. *Cell* **112**, 329–341 (2003). doi: 10.1016/S0092-8674(03)00074-6; pmid: 12581523
57. Single-letter abbreviations for the amino acid residues are as follows: A, Ala; C, Cys; D, Asp; E, Glu; F, Phe; G, Gly; H, His; I, Ile; K, Lys; L, Leu; M, Met; N, Asn; P, Pro; Q, Gln; R, Arg; S, Ser; T, Thr; V, Val; W, Trp; and Y, Tyr.

ACKNOWLEDGMENTS

We thank P. Leopold for reagents and the PTTH antibody; M. Vidal for the *lgr2* plasmid; E. Hafen and H. Stocker for Dilp antibodies; A. Garelli for stock construct and initial work on this project; A. Gontijo for plasmid design; and J. Casanova, J. C. P. Yin, B. J. Dickson, J. Blau, B. Hassan, and F. Matsuzaki for fly stocks or antibodies. We also thank the Bloomington Stock Center (NIH grant P40OD018537), the DGRC (NIH grant OD010949-10), and the Transgenic RNAi Project at Harvard Medical School (NIH National Institute of General Medical Sciences grant R01-GM084947) for providing the fly stocks and plasmids used in this study and the Developmental Studies Hybridoma Bank at the University of Iowa for antibodies. This work was supported by a Ramon y Cajal grant (RyC-2010-07155) and a Ministerio de Economia y Competitividad grant (SAF2012-31467) to J.M.; a Junta de Andalucia PAIDI group CTS-569 to J.B.; and Spanish national grants (SAF2012-35181 and SEV-2013-0317) and a Generalitat Valenciana grant (PROMETEO II/2013/001) to M.D. M.D. was also supported by the Botin Foundation. S.J.-C. is a fellow from Formación del Personal Investigador (grant BES-2013-064947) from the Spanish Ministerio de Economia y Competitividad.

SUPPLEMENTARY MATERIALS

www.sciencemag.org/content/350/6262/aac6767/suppl/DC1
Figs. S1 to S8
Movies S1 to S3

29 May 2015; accepted 24 September 2015
Published online 1 October 2015
10.1126/science.aac6767

REPORTS

SCATTERING DYNAMICS

Imaging resonances in low-energy NO-He inelastic collisions

Sjoerd N. Vogels,* Jolijn Onvlee,* Simon Chefdeville, Ad van der Avoird, Gerrit C. Groenenboom,† Sebastiaan Y. T. van de Meerakker†

In molecular collisions, resonances occur at specific energies at which the colliding particles temporarily form quasibound complexes, resulting in rapid variations in the energy dependence of scattering cross sections. Experimentally, it has proven challenging to observe such scattering resonances, especially in differential cross sections. We report the observation of resonance fingerprints in the state-to-state differential cross sections for inelastic NO-He collisions in the 13 to 19 centimeter^{-1} energy range with 0.3 centimeter^{-1} resolution. The observed structures were in excellent agreement with quantum scattering calculations. They were analyzed by separating the resonance contributions to the differential cross sections from the background through a partitioning of the multichannel scattering matrix. This revealed the partial-wave composition of the resonances and their evolution during the collision.

Acquiring a detailed understanding of interactions between individual molecules is of fundamental importance to physics and chemistry and has a long and rich tradition. Historically, two distinct types of experiments have been conducted to unravel the precise nature of inter- and intramolecular forces. On the one hand, spectroscopic studies yield information on the binding forces that hold the molecule together, as well as on the noncovalent interactions between the molecules. They mainly probe the shape of the interaction potential in the region of the well. Collision experiments, on the other hand, are typically more sensitive to the short-range repulsive part of the potential.

Certainly, the interactions between submicroscopic objects such as atoms and molecules require a full quantum mechanical description. In contrast with molecular spectra, in which the discrete lines and bands directly reveal the quantized energy levels of the molecule, the quantum nature of molecular collisions is more subtle. In addition to the internal states of the molecule, the angular momentum associated with the relative motion of the particles is also quantized. This relative motion is described by a set of partial waves with integer quantum number ℓ (*1*).

Unraveling the contribution of each individual partial wave to a collision cross section would provide the ultimate information that can be retrieved from any collision event. Experimentally, however, it is impossible to select a single partial wave from the pre-collision conditions and to study how the interaction transforms it into post-collision properties. The number of contributing partial waves depends on the de Broglie wavelengths of the particles; observable quantities such as scattering cross sections therefore necessarily represent the quantum mechanical superposition of many partial waves (*2*). Classically, this can be compared with the unavoidable averaging over all possible impact parameters of the two colliding particles (*1*).

At low temperatures, special conditions exist in which a single partial wave can dominate the scattering process, mitigating this fundamental obstacle. When the collision energy is resonant with a quasibound state supported by the interaction potential, the incident particles can temporarily form a long-lived complex. At these energies, a resonant partial wave ℓ_{res} may dominate over all other partial waves, and there will be a strong enhancement of the scattering cross section. For atom-molecule collisions, these so-called scattering resonances may be regarded—in a simplified picture—either as the orbiting of the atom around the molecule (a shape or orbiting resonance), or as the transient excitation of the molecule to a state of higher energy (a Feshbach resonance). After some time, however, the complex falls apart and decays back into a separate atom and molecule (*3*).

Scattering resonances are the most global and sensitive probes of molecular interaction potentials. They depend on both the long-range attractive and the short-range repulsive part of the potential, as well as on the van der Waals well; they are not only sensitive to the shape of the well—as are the spectra of molecular complexes—but also to the depth of the well relative to the dissociation limit. Measurements of the resonance position and width in the integral cross section (ICS) probe the energy and lifetime of the quasibound state from which the resonance originates. Such observations may thus be regarded as a type of collision spectroscopy. Still, they do not yield information on the partial-wave composition of the resonance. More information on the collision dynamics is inferred from the differential cross section (DCS) at the resonance energy. The structured DCS represents the partial-wave fingerprint of the collision process and offers at the resonance the opportunity to experimentally probe the relation between incoming, resonant, and outgoing partial waves. This gives detailed insights into the most fundamental question in molecular collision dynamics: How does the interaction potential transform the reagents into the collision products?

Whereas scattering resonances are well known in electron, neutron, and ultracold atom scattering, the observation of scattering resonances in molecular systems has been a quest for decades. Experimentally, it has proven extremely challenging to reach the required low collision energies and high energy resolution to observe and characterize partial-wave resonances. In crossed-beam experiments, signatures of scattering resonances have been observed in reactive systems with a low excitation barrier, such as the benchmark F + H_2 and F + HD reactions, by using the powerful Rydberg tagging technique to record the angular distribution of the H or D products (*4*–*10*).

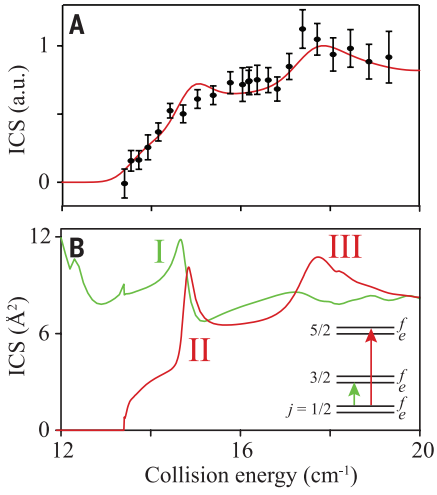

Fig. 1. Collision-energy dependence of the integral cross section for rotational excitation of NO radicals by He atoms. (**A**) Comparison between measured (data points with error bars) and calculated (solid curve) state-to-state inelastic scattering cross sections for excitation into the (5/2*f*) state. Experimental data are in arbitrary units (a.u.). Each data point is averaged over 1000 laser shots with the He and NO beams overlapping (collision signal) and 1000 laser shots with the NO beam only (reference signal). Vertical error bars represent statistical uncertainties at 95% of the confidence interval. The calculated cross section was convoluted with the experimental energy resolution of 0.3 cm^{-1}. (**B**) Calculated state-to-state integral cross sections for excitation into the (3/2*e*) state (green curve) and (5/2*f*) state (red curve). (Inset) Schematic energy-level diagram and inelastic excitation scheme of NO.

Radboud University, Institute for Molecules and Materials, Heijendaalseweg 135, 6525 AJ Nijmegen, Netherlands.
*These authors contributed equally to this work. †Corresponding author. E-mail: basvdm@science.ru.nl (S.Y.T.v.d.M.); gerritg@theochem.ru.nl (G.C.G.)

In these systems, the resonance is associated with the formation of transiently stable transition-state structures. High-resolution anion photodetachment spectroscopy in combination with accurate calculations has recently allowed the observation and characterization of previously unresolved reactive scattering resonances in this system (*11*). Using a merged beam approach, resonances have recently also been observed in ICSs for Penning ionization processes at collision temperatures in the millikelvin regime (*12*, *13*). Even more recently, resonances were observed in inelastic scattering processes at energies near the thermodynamic threshold for rotational excitation of the molecule. Using cryogenically cooled molecular species such as CO and O_2, partial-wave resonances were observed in the state-to-state ICSs for inelastic collisions with He and H_2 target beams at energies down to 4 K (*14*–*16*).

The measurement of DCSs at scattering resonances remains a largely unexplored frontier, in particular for species other than H and D atoms. At low collision energies, the recoil velocities of the scattered molecules are extremely small, and it has proven a daunting task to obtain the angular resolution required to resolve any deflection structure. Here, we report the measurement of DCSs at partial-wave resonances for inelastic collisions between fully state-selected NO radicals [$X^2\Pi_{1/2}$, $v = 0$, $j = 1/2$, f (*17*), referred to hereafter as (1/2*f*)] and He atoms in a crossed-beam experiment. We combined Stark deceleration and velocity-map imaging to probe scattering resonances in the state-to-state and parity-resolved DCSs at energies between 13 and 19 cm^{-1}, with a spectroscopic energy resolution of 0.3 cm^{-1}. The high resolution afforded by the Stark decelerator allowed us to observe structure in the very small velocity-mapped scattering images, directly reflecting the DCSs. Distinct variations in the DCSs were observed as the collision energy was tuned over the resonances. At off-resonance energies, the DCSs were dominated by quantum diffraction oscillations, whereas additional strong forward and backward scattering was found at the resonance energies. We developed a theoretical approach similar to Feshbach-Fano partitioning (*18*, *19*) to disentangle the resonance and background contributions to the DCSs, and we directly revealed the incoming and outgoing waves that characterize the resonances and the background.

Collisions between NO and rare gas atoms represent a seminal class of systems in rotational energy transfer because scattering of open-shell radical species such as NO and OH plays an important role in gas-phase chemical kinetics, combustion, and astrochemistry. Collisions involving these radicals are governed by multiple potential energy surfaces (PESs), parity selection, and propensity rules that are foreign to molecules such as CO and O_2 (*20*). We found excellent agreement with the DCSs predicted with ab initio quantum mechanical close-coupling (QM CC) scattering calculations based on accurate NO-He PESs.

We used a crossed-molecular-beam apparatus with a 45° crossing angle (*21*). A packet of velocity-controlled NO (1/2*f*) radicals, with a velocity spread of 2.1 m/s (*22*) and an angular spread of 1.5 mrad, was produced by using a 2.6-m long Stark decelerator. The beam of He atoms with a mean velocity between 400 and 480 m/s, a velocity spread of 4.3 m/s, and an angular spread of 4.8 mrad was produced by cooling an Even-Lavie valve to cryogenic temperatures. By tuning the NO velocity between 350 and 460 m/s with the Stark decelerator, the collision energy was varied between 13 and 19 cm^{-1}, with an energy resolution of 0.3 cm^{-1}. The scattered NO radicals were state-selectively detected by using a two-color laser ionization scheme and velocity-mapped on a two-dimensional detector.

We studied inelastic collisions that excite the NO (1/2*f*) radicals into either the (3/2*e*) or the (5/2*f*) state. The (5/2 *f*) channel opens within the experimentally accessible energy range

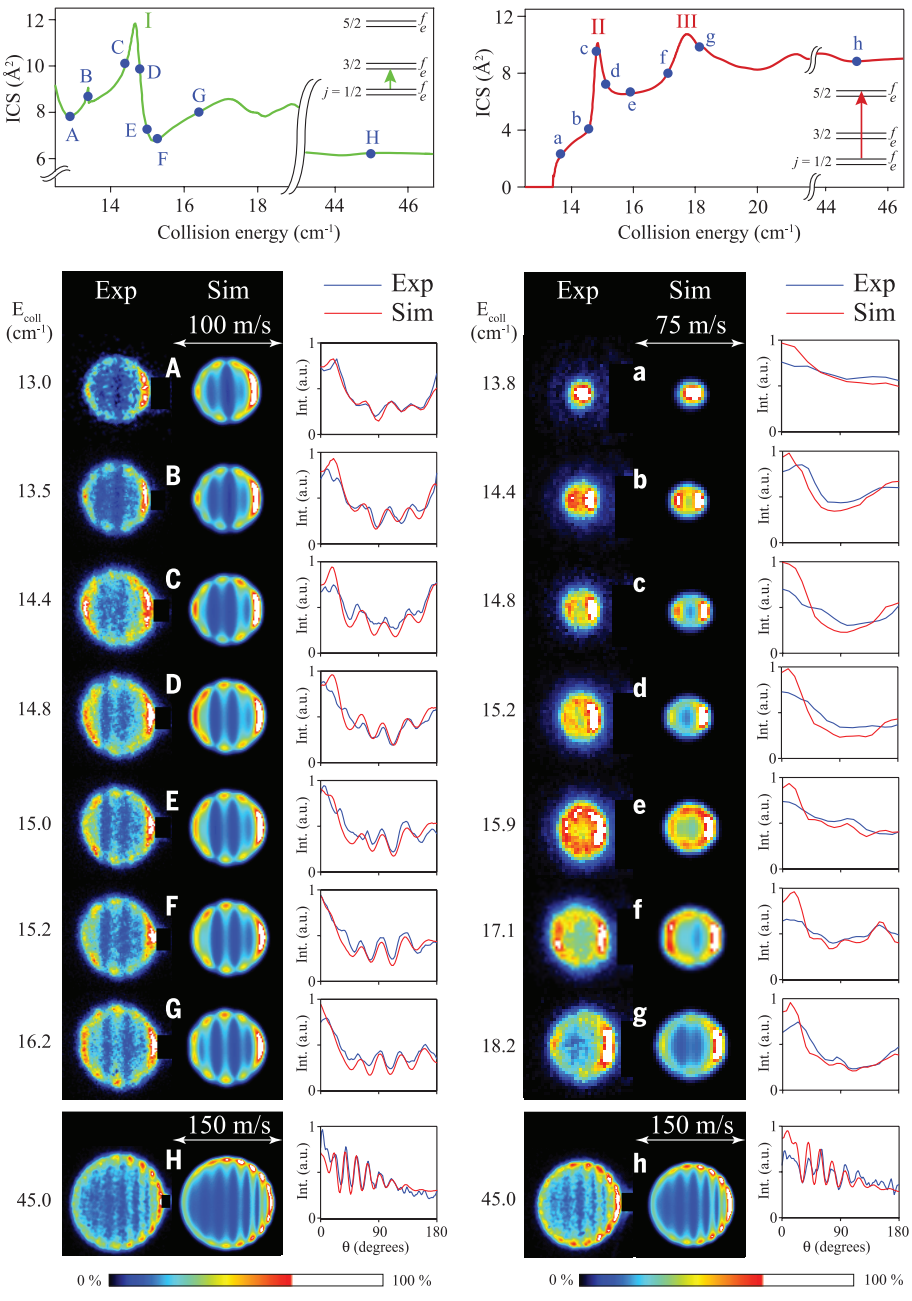

Fig. 2. Experimental and simulated ion images at selected collision energies as indicated at the top. Exp, experimental; Sim, simulated. (**Left**) (1/2*f*) → (3/2*e*) inelastic collisions. (**Right**) (1/2*f*) → (5/2*f*) inelastic collisions. The images are presented so that the relative velocity vector is oriented horizontally, with the forward direction on the right side of the image. Small segments of the images around forward scattering are masked because of imperfect state selection of the NO packet. The angular scattering distributions as derived from the experimental (blue curves) and simulated (red curves) images are shown for each channel and collision energy.

at 13.4 cm^{-1}, and we measured the threshold behavior in the ICS for this channel so as to calibrate both the collision energy and energy resolution (Fig. 1A). We observed a plateau just above threshold and a clear peak around 18 cm^{-1}, which were well reproduced by the theoretical ICS convoluted with the experimental resolution of 0.3 cm^{-1} (*21*). These features were attributed to a narrow (labeled II) and a broader resonance (labeled III) in the theoretical ICS. The theoretical ICS for the (3/2*e*) state (Fig. 1B) showed a clear resonance (labeled I) at a slightly lower energy than that of resonance II.

For both inelastic channels, scattering images were measured at selected energies (Fig. 2). Depending on the energy and the final state probed, the diameter of the low-collision-energy images ranged from only a few to ~60 m/s. The diameter of the (5/2*f*) image approached zero as the energy approached the thermodynamic threshold of the channel, effectively imaging the center-of-mass velocity of the NO-He pair. Despite their small sizes, distinct structure in the images could clearly be discerned. At higher energies, as illustrated by the additional images probed at 45.0 cm^{-1}, the DCSs of both channels feature a rich diffraction pattern that extends from forward to backward scattering. Each diffraction peak in the DCS transformed into a stripe in the image because of the detection method used in the experiment. At low collision energies, the number of diffraction peaks was reduced, and an additional pattern arose in the vicinity of the resonances. As the energy was varied in small energy steps over the resonances, a strong variation in the angular distribution featuring pronounced forward and backward scattering was observed.

To compare our findings with theoretical predictions, we simulated for each energy the image expected from the kinematics of the experiment and the DCS predicted with high-level QM CC calculations (*21*). Both the experimental and simulated images were then analyzed in order to yield the angular scattering distribution, reflecting the DCS convoluted with the experimental energy and angular resolution (*21*). In general, excellent agreement was found between the experimental and simulated scattering distributions, although at some energies, the relative intensities of the observed features differed from the simulated intensities (*23*).

To interpret our results, we first analyzed the partial-wave composition of the scattering cross sections, as well as the scattering wave functions (*21*). We found that for the energies probed, the entrance channel is governed by partial waves up to ℓ_{in} = 8. At the resonance energies, however, a single resonant partial wave ℓ_{res} becomes involved in a quasibound state, which causes the ICS to rise considerably above the background. We found that resonances I and II are associated with a quasibound state of the He-NO(5/2*f*) complex at 14.7 cm^{-1} dominated by ℓ_{res} = 5, whereas resonance III originates from a He-NO(5/2*f*) quasibound state at 17.9 cm^{-1} governed by ℓ_{res} = 6 (*21*).

For an inelastic process, the partial-wave quantum number ℓ is not conserved throughout the collision. The anisotropic interaction potential couples rotational states of the NO molecule with different quantum numbers j and waves with different values of ℓ and determines how the incoming waves ℓ_{in} are transformed into the outgoing waves ℓ_{out} during the collision. At the resonance energies, the quasibound He-NO(5/2*f*) complexes with the well-defined values of ℓ_{res} = 5 (resonances I and II) or 6 (resonance III) decomposed to form a NO radical in either the (3/2*e*) state (resonance I) or the (5/2*f*) state (resonances II and III). When the resonant (5/2*f*) state decays into the lower (3/2*e*) state, such as for resonance I, not only j but also ℓ changes, and ℓ_{out} ranges from 3 to 7 (*21*). When the final NO state is the same as the resonant state, such as for resonances II and III, the dominant value of ℓ_{out} = 5 or 6 is the same as ℓ_{res}. At energies just above the threshold of the (5/2*f*) inelastic channel, at which almost all kinetic energy has been transferred into rotational energy of the NO molecule, the (5/2*f*) state can only decay with ℓ_{out} = 0 (s-wave), ℓ_{out} = 1 (p-wave), and ℓ_{out} = 2 (d-wave). The observed DCS at 13.8 cm^{-1} was dominated by p-wave scattering with small contributions from s- and d-waves (*21*).

At the resonance energies, the DCSs contain specific information on the partial-wave dynamics of the collision process—the relation between ℓ_{in}, ℓ_{res}, and ℓ_{out}. If the scattering were purely determined by a resonance without any background, the scattering matrix **S** would be given by the Breit-Wigner formula, which was originally developed for neutron scattering in 1936 and nowadays is frequently used to describe scattering processes in high-energy particle physics (*24*, *25*). However, in most cases and also in our experiments, the observed ICSs and DCSs result from an interference between resonance and background contributions. We disentangled these contributions for each of the resonances I, II, and III by applying a theoretical analysis similar to Feshbach-Fano partitioning (*18*, *19*). We wrote the energy-dependent multichannel scattering matrix as

$$\mathbf{S}(E) = \mathbf{S}^{bg}(E)\mathbf{U}^{res}(E) \quad (1)$$

where the background contribution $\mathbf{S}^{bg}(E)$ is a slowly varying function of the collision energy E, and the resonance contribution is given by the Breit-Wigner formula

$$\mathbf{U}^{res}(E) = \mathbf{I} - \frac{2i\mathbf{A}}{E - E_{res} + i\Gamma} \quad (2)$$

where **I** is the unit matrix, E_{res} is the energy of the resonance, Γ is its width (or inverse lifetime), and the complex-valued matrix elements $A_{\alpha\beta} = a_\alpha a_\beta^*$ contain the partial widths a_α obeying the relation $\sum_\alpha |a_\alpha|^2 = \Gamma$ (*26*). The idea associated with the Breit-Wigner formula is that in the complex energy plane, where the bound states correspond to poles of the *S*-matrix on the negative real-energy axis, resonances are represented by poles below the positive real axis at positions $E_{res} - i\Gamma$. By analyzing the energy dependence of the *S*-matrix elements in the range of each resonance with an algorithm described in (*21*), we could determine the parameters E_{res}, Γ, and a_α. Then, we separated the resonance contributions to the scattering matrix **S**(*E*) from the background and applied the usual expressions (*27*) to

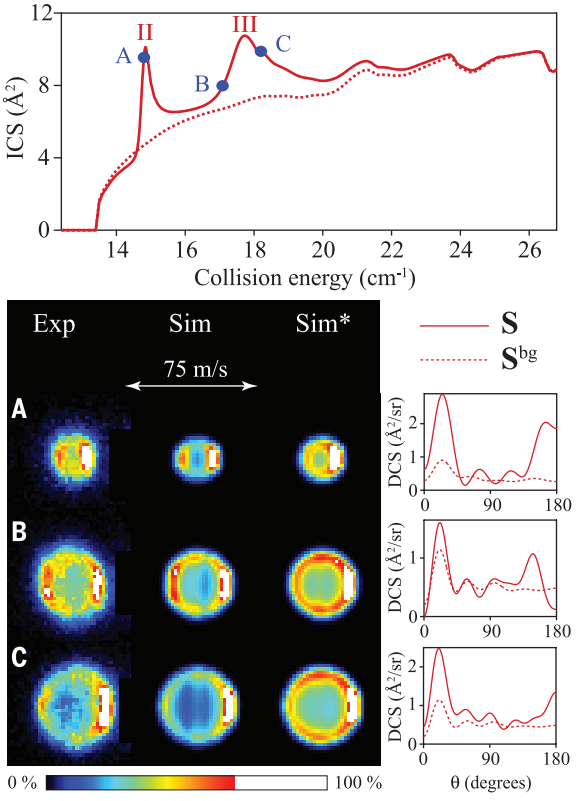

Fig. 3. Effect of resonances II and III on the cross sections for inelastic (1/2*f*) → (5/2*f*) NO-He scattering. Integral cross sections are shown above, and differential cross sections are shown below. Solid lines represent the complete theoretical ICSs and DCSs, and dashed lines indicate the cross sections obtained when only the scattering matrix $\mathbf{S}^{bg}$ in Eq. 1 is included for resonances I, II, and III. (Bottom) The measured (Exp) and simulated images based on either the complete DCSs (Sim) or the DCSs computed with the scattering matrix $\mathbf{S}^{bg}$ only (Sim*) for collision energies of (**A**) 14.8 cm^{-1}, (**B**) 17.1 cm^{-1}, and (**C**) 18.2 cm^{-1}. Resonance I in the (1/2*f*) → (3/2*e*) cross sections is shown in fig. S10.

compute the ICS and DCS from the *S*-matrix, with or without resonance contributions. The results for the final $(5/2f)$ state of NO, where the effects are most pronounced, are shown in Fig. 3. The peaks in the ICS corresponding to both resonances II and III vanish when we only included the background contribution (Fig. 3, top). The effect of the resonances on the DCS at energies close to these resonances is illustrated in Fig. 3, bottom. The background contributions (Fig. 3, dashed lines) show the usual pattern of diffraction oscillations, which are most pronounced for small scattering angles and decrease in amplitude for larger angles. The effect of the resonance contributions is substantial; they lead to additional strong scattering near the forward and backward directions. Also shown in Fig. 3 is a comparison of measured and simulated images at 14.8, 17.1, and 18.2 cm^{-1}. The simulated images were based on DCSs calculated in this energy range, with or without resonance contributions, by taking into account the experimental energy resolution of 0.3 cm^{-1}. Clearly, the experimental images show much better agreement with the simulations when the full DCS is taken into account.

Our theoretical analysis demonstrated that the resonances strongly affect the nature of the DCSs and allowed us to disentangle normal diffraction oscillations from the resonance fingerprints in the DCSs. The DCSs measured for collision energies in the range of the resonances agreed very well with the DCSs obtained from the ab initio calculations, but only when the contributions from the resonances were fully included. This directly confirmed that our experiment indeed images the resonance fingerprints in the DCS.

Our joint experimental and theoretical study showed that scattering resonances in state-to-state cross sections can now be probed with spectroscopic resolution, even for benchmark and chemically relevant systems that involve open-shell species such as NO. DCSs measured at the resonance energies, combined with a theoretical analysis, provided detailed information on the multichannel scattering process and explicitly revealed the effects of the resonances. The theoretical method developed to separate the resonant contributions to the ICSs and DCSs from the background will also be applicable to other systems in which scattering resonances occur.

REFERENCES AND NOTES

1. The partial-wave quantum number ℓ is the quantum mechanical analog of the classical angular momentum $L = \mu v b$, where μ is the reduced mass, v is the relative velocity of the colliding particles, and b is the impact parameter defined as the distance of closest approach in the absence of any interaction.
2. Single partial-wave collisions are only found at temperatures approaching 0 K, at which the scattering is governed by the wave with the lowest possible value for ℓ. Collisions between ultracold atoms and molecules near quantum degeneracy, for instance, are exclusively governed by partial waves with $\ell = 0$ (s-wave) or $\ell = 1$ (p-wave).
3. D. W. Chandler, *J. Chem. Phys.* **132**, 110901 (2010).
4. R. T. Skodje *et al.*, *Phys. Rev. Lett.* **85**, 1206–1209 (2000).
5. W. Shiu, J. J. Lin, K. Liu, *Phys. Rev. Lett.* **92**, 103201 (2004).
6. M. Qiu *et al.*, *Science* **311**, 1440–1443 (2006).
7. Z. Ren *et al.*, *Proc. Natl. Acad. Sci. U.S.A.* **105**, 12662–12666 (2008).
8. W. Dong *et al.*, *Science* **327**, 1501–1502 (2010).
9. T. Wang *et al.*, *Science* **342**, 1499–1502 (2013).
10. T. Yang *et al.*, *Science* **347**, 60–63 (2015).
11. J. B. Kim *et al.*, *Science* **349**, 510–513 (2015).
12. A. B. Henson, S. Gersten, Y. Shagam, J. Narevicius, E. Narevicius, *Science* **338**, 234–238 (2012).
13. E. Lavert-Ofir *et al.*, *Nat. Chem.* **6**, 332–335 (2014).
14. S. Chefdeville *et al.*, *Phys. Rev. Lett.* **109**, 023201 (2012).
15. S. Chefdeville *et al.*, *Science* **341**, 1094–1096 (2013).
16. A. Bergeat, J. Onvlee, C. Naulin, A. van der Avoird, M. Costes, *Nat. Chem.* **7**, 349–353 (2015).
17. The labels $X^2\Pi_{1/2}$, v, and j indicate the electronic state, the vibrational state, and rotational state of the NO radical, respectively. Each rotational state of NO possesses two near-degenerate Λ-doublet components, with symmetry labels e (lower component) and f (upper component), that refer to the total parity of the electronic wave function, exclusive of rotation.
18. U. Fano, *Phys. Rev.* **124**, 1866–1878 (1961).
19. V. Brems, T. Beyer, B. M. Nestmann, H.-D. Meyer, L. S. Cederbaum, *J. Chem. Phys.* **117**, 10635–10647 (2002).
20. M. Kirste *et al.*, *Science* **338**, 1060–1063 (2012).
21. Materials and methods are available as supplementary materials on *Science* Online.
22. All spreads in this manuscript refer to widths (1σ) of a fitted Gaussian distribution.
23. The calibration of the mean experimental collision energy has an uncertainty of ±0.15 cm^{-1}. Small differences between experimental and simulated images are found in particular at energies at which the DCS varies rapidly as a function of collision energy. In addition, the experiment seemed to systematically underestimate the scattering intensity at forward scattering.
24. W. Erlewein, M. von Seggern, J. P. Toennies, *Z. Phys.* **211**, 35–50 (1968).
25. S. H. Sheen, J. G. Skofronick, C. R. Mueller, *Int. J. Quantum Chem.* **9**, 817–824 (1975).
26. J. R. Taylor, *Scattering Theory: The Quantum Theory of Nonrelativistic Collisions* (Wiley, New York, 1972), chap. 20.
27. W. A. Lester Jr., *The $\mathcal{N}$ Coupled-Channel Problem* (Plenum Press, New York, 1976), pp. 1–32.

ACKNOWLEDGMENTS

This work is part of the research program of the Foundation for Fundamental Research on Matter (FOM), which is supported financially by the Netherlands Organization for Scientific Research (NWO). S.Y.T.v.d.M. acknowledges further support from NWO via a VIDI and a TOP grant and from the European Research Council via a Starting Grant. We thank A. van Roij, C. Berkhout, N. Janssen, and P. Claus for expert technical support. We thank J. Kłos for providing us with his NO-He PESs. The authors declare no competing financial interests.

SUPPLEMENTARY MATERIALS

www.sciencemag.org/content/350/6262/787/suppl/DC1
Materials and Methods
Figs. S1 to S10
Table S1
References (*28*–*36*)
Movies S1 and S2

12 August 2015; accepted 6 October 2015
10.1126/science.aad2356

ATTOSECOND DYNAMICS

Measurement and laser control of attosecond charge migration in ionized iodoacetylene

P. M. Kraus,[1] B. Mignolet,[2,3] D. Baykusheva,[1] A. Rupenyan,[1] L. Horný,[1] E. F. Penka,[4] G. Grassi,[1] O. I. Tolstikhin,[5] J. Schneider,[1] F. Jensen,[6] L. B. Madsen,[7] A. D. Bandrauk,[4] F. Remacle,[2] H. J. Wörner[1]*

The ultrafast motion of electrons and holes after light-matter interaction is fundamental to a broad range of chemical and biophysical processes. We advanced high-harmonic spectroscopy to resolve spatially and temporally the migration of an electron hole immediately after ionization of iodoacetylene while simultaneously demonstrating extensive control over the process. A multidimensional approach, based on the measurement and accurate theoretical description of both even and odd harmonic orders, enabled us to reconstruct both quantum amplitudes and phases of the electronic states with a resolution of ~100 attoseconds. We separately reconstructed quasi–field-free and laser-controlled charge migration as a function of the spatial orientation of the molecule and determined the shape of the hole created by ionization. Our technique opens the prospect of laser control over electronic primary processes.

Ultrafast charge transfer plays a key role in chemical reactions, biological processes, and technical applications. For example, charge transfer after photoexcitation on the femtosecond time scale and the associated long-lived coherences observed in photosynthetic systems (*1*) or photovoltaic blends (*2*) have been invoked to explain the high efficiencies of energy conversion in these systems. These charge transfer phenomena are driven by nuclear motion but typically involve a much faster, purely electronic response. This phenomenon was predicted theoretically and called charge migration to distinguish it from the nuclear dynamics–driven charge transfer (*3*–*6*). Charge migration arises whenever multiple electronic states are

[1]Laboratorium für Physikalische Chemie, ETH Zürich, 8093 Zürich, Switzerland. [2]Department of Chemistry, Université de Liège, B4000 Liège, Belgium. [3]PULSE Institute and Department of Chemistry, Stanford University, Stanford, CA 94305, USA. [4]Laboratoire de Chimie Théorique, Université de Sherbrooke, Sherbrooke, Quebec J1K 2R1, Canada. [5]Moscow Institute of Physics and Technology, Dolgoprudny 141700, Russia. [6]Department of Chemistry, Aarhus University, 8000 Aarhus C, Denmark. [7]Department of Physics and Astronomy, Aarhus University, 8000 Aarhus C, Denmark.
***Corresponding author. E-mail: hwoerner@ethz.ch**

coherently populated. Charge migration is likely to be responsible for the unexpected selectivity in photofragmentation of ionized peptides (*7*), leading to the concept of charge-directed chemistry (*8*). Moreover, it offers approaches to probing electron correlation and orbital relaxation phenomena (*3*, *5*, *6*). These prospects make the measurement of charge migration a key goal of attosecond science (*9*). Even more promising is the prospect of controlling charge migration. Steering electrons inside molecules is expected to yield control over reactivity, thereby providing access to regions of potential energy surfaces and consequent reaction pathways that usually remain unexplored (*10*).

Previously described techniques for measuring electronic dynamics include transient absorption (*11*), sequential double ionization (*12*), and photofragmentation spectroscopy (*13*). Although pioneering work on phenylalanine recently reported a resolution of better than 4.5 fs (*13*), such measurements of intramolecular dynamics are inherently limited in temporal resolution by the use of an infrared pulse. Electronic dynamics after strong-field ionization (SFI) have also been inferred from high-harmonic spectra. This approach has been established in seminal studies (*14*, *15*), but a direct reconstruction of the dynamics has remained out of reach, either because no reconstruction approach was established or because experimental data were lacking. Another pioneering approach demonstrated the tomographic reconstruction of time-dependent orbitals at the expense of temporal resolution (*16*).

We advanced high-harmonic spectroscopy (HHS) to reconstruct, at a resolution of ~100 attoseconds (as), the full quantum dynamics of charge migration in spatially oriented polar molecules. We measured both amplitudes and phases of high-harmonic emission from oriented molecules at multiple wavelengths of the driving field. Scaling the wavelength is equivalent to tuning the excursion time of the photoelectron wave packet on the attosecond time scale (*17*). We show that this set of experimental data is sufficient to reconstruct the amplitudes and phases of the transiently occupied electronic states of the cation and to determine the initial shape of the hole created by SFI.

We demonstrated our technique on iodoacetylene (HCCI) because it encompasses several general characteristics of polar polyatomic molecules. These include (i) the simultaneous population of multiple electronic states of the cation by SFI, (ii) strong laser-induced coupling between these states, and (iii) a strong alignment dependence of their coupling. An energy level diagram of $HCCI^+$ is shown in Fig. 1. The $\tilde{X}^+\,^2\Pi$ ground state and $\tilde{A}^+\,^2\Pi$ first excited state [with vertical ionization potentials $I_p^{\tilde{X}^+} = 9.71$ eV and $I_p^{\tilde{A}^+} = 11.94$ eV (*18*)] are both appreciably populated by strong-field ionization [supplementary materials (SM) section 4] and are coupled by a large transition dipole moment (1.35 atomic units, which is equivalent to 3.43 Debye) lying parallel to the molecular axis. This large value originates from the charge-transfer nature of this $\pi \rightarrow \pi^*$ transition (*19*).

We use control over the spatial orientation of the molecule to separately reconstruct quasi–field-free and laser-driven charge migration. For molecules aligned perpendicular to the laser polarization (Fig. 1B), the effect of the laser field on charge migration is negligible. For parallel molecules (Fig. 1C), the laser field induces substantial population transfer between the $\tilde{X}^+$ and $\tilde{A}^+$ states, which depends on the head-to-tail orientation of the molecule.

The concept of the experiment is presented in Fig. 2A. Control over the spatial orientation of the molecules is achieved by impulsively orienting the molecules (*20*). The fixed-in-space ensemble of molecules is then interrogated by a high-harmonic generation (HHG) pulse one rotational period (157.0 ps) later under otherwise field-free conditions. The time resolution in our experiment arises from the subcycle nature of the HHG process: Every emitted harmonic order can be associated with a unique transit time of the electron wave packet in the continuum by experimentally selecting the short electron trajectories (*21*, *22*).

The reconstruction of charge migration in the cation requires several observables. The ratios of emission intensity between molecules aligned parallel or perpendicular to the polarization of the probe pulse (Fig. 2B) exhibit minima located at markedly different photon energies: 23.2 eV for 800 nm (laser field period 2.67 fs) and 35.3 eV for 1300 nm (laser field period 4.33 fs). Such a strong wavelength dependence of the observed

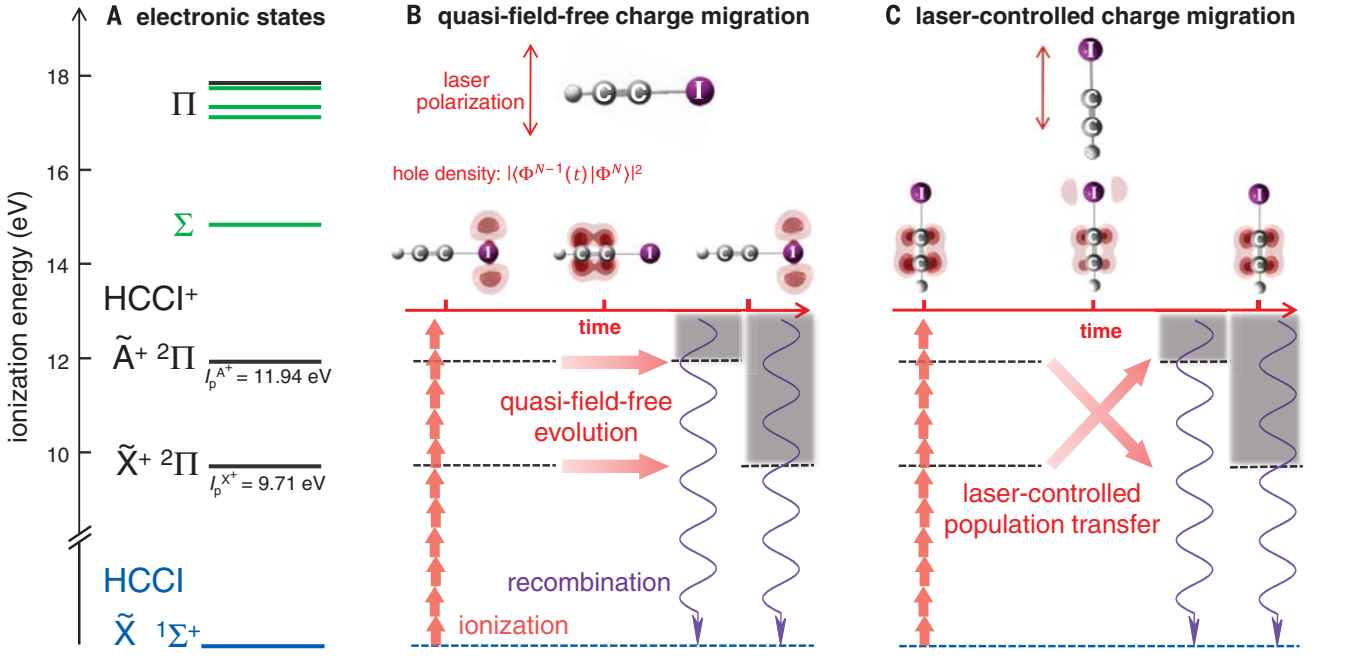

Fig. 1. Electronic energy levels and orientation dependence of charge migration in the iodoacetylene cation. (**A**) Energy level diagram. (**B** and **C**) Illustration of quasi–field-free charge migration (B) and laser-controlled charge migration (C). The energies are computed at the EOM-IP-CCSD/cc-pVTZ level of theory. Strong-field ionization by infrared photons (red arrows) prepares the electron hole. Its evolution is encoded in the high-harmonic emission (violet arrows) at the instant of recombination. For molecules aligned perpendicular to the laser field as shown in (B), the populations of the $\tilde{X}^+$ and $\tilde{A}^+$ states are time-independent. Charge migration takes place as under field-free conditions. The laser field induces strong population transfer between the $\tilde{X}^+$ and $\tilde{A}^+$ states for molecules aligned parallel to the laser field, as depicted in (C). The evolution of the hole density is represented by $|\langle\Phi^{N-1}(t)|\Phi^N\rangle|^2$, where Φ^N and $\Phi^{N-1}(t)$ are the N and $N-1$ electron wave functions of the neutral and ionized molecule, respectively.

minimum cannot be contained in the photorecombination matrix elements and indicates attosecond electronic dynamics in the cation (*23*, *24*). Purely structural minima contained in the photorecombination matrix elements do not shift in photon energy when the driving wavelength is changed (*25*).

Spatially resolving charge migration in the general class of polar molecules additionally requires orientation (i.e., a head-to-tail order), resulting in even-harmonic emission. This was achieved using one phase-controlled two-color (800 nm + 400 nm) laser pulse for impulsive orientation (*26*). Figure 2C shows the intensity ratio of the even harmonics to the averaged intensity of the two adjacent odd harmonic orders (the even-to-odd ratio) observed using a HHG driving wavelength of 800 nm.

A full characterization of electronic quantum dynamics becomes possible through the additional measurement of the phase of high-harmonic emission. We measured the phase ϕ^{HHG} as a function of the alignment angle of the molecules by generating high harmonics in two spatially separated sources in the gas jet (*27*). Here, we extended this technique to a broad range of wavelengths by working with a liquid crystal mask that introduces a voltage-tunable phase shift in one-half of the unfocused probe-beam wave front (SM section 1). Phase measurements for driving wavelengths of 800 nm and 1300 nm are shown in Fig. 2, D and E, for selected harmonic orders. The phase variation as a function of the alignment angle strongly depends on the harmonic order and driving wavelength, not just the emitted photon energy, again suggesting a pronounced charge migration on the attosecond time scale. The phase differences for molecules aligned parallel or perpendicular to the polarization of the laser field for all harmonic orders are summarized in the SM, section 1.

The reconstruction of charge migration in terms of initial (as prepared by ionization at t') and final (at t, the instant of photorecombination) populations and phases of the states of the cation is a numerical inversion problem employing a generalized theory of HHG (SM section 2) that describes all experimental intensity ratios and phase differences between molecules aligned parallel or perpendicular to the laser field. The initial and final populations and phases were retrieved in a global nonlinear least-squares optimization using a Levenberg-Marquardt algorithm with multiple starting values. Our theory includes all relevant electronic states, the continuum structure through the use of scattering-wave matrix elements (*28*), nuclear motion through autocorrelation functions derived from photoelectron spectra (SM section 2), and the molecular axis distribution. The photorecombination dipole matrix elements and the angular variation of the ionization rates were calculated theoretically. These quantities are experimentally accessible using narrowband extreme ultraviolet sources and/or charged-particle detection, which were not available in this study. Because the emission from several channels adds coherently, our experiment is sensitive to both the amplitudes and the phases of the involved electronic states. The mapping from photon energy to transit time ($\tau = t - t'$) was performed using quantum electron trajectories obtained by the saddle-point method (*29*–*31*).

We first reconstructed charge migration for molecules aligned perpendicular to the 800 nm driving field. The reconstructed initial populations are given in Fig. 3B. These results compare well both with time-dependent density functional theory (TDDFT) (SM section 4) (*32*) and with weak-field asymptotic theory (WFAT) (SM section 2) (*33*). Combined with the experimentally retrieved initial phase $\Delta\varphi = \varphi_{\tilde{A}^+}(\tau = 0) - \varphi_{\tilde{X}^+}(\tau = 0)$ (Fig. 3C) between the ground state

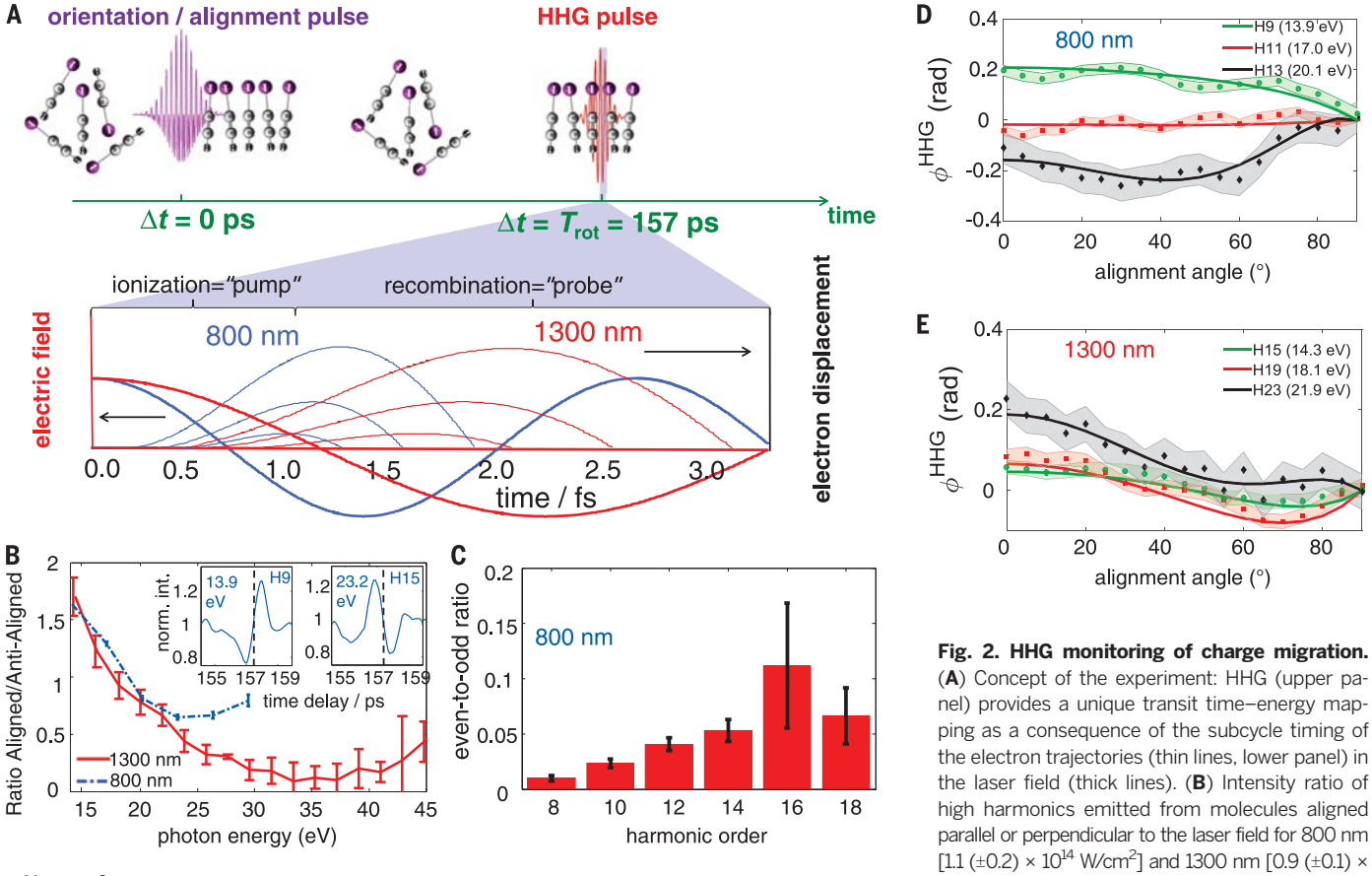

Fig. 2. HHG monitoring of charge migration. (**A**) Concept of the experiment: HHG (upper panel) provides a unique transit time–energy mapping as a consequence of the subcycle timing of the electron trajectories (thin lines, lower panel) in the laser field (thick lines). (**B**) Intensity ratio of high harmonics emitted from molecules aligned parallel or perpendicular to the laser field for 800 nm [1.1 (±0.2) × 10^{14} W/cm^2] and 1300 nm [0.9 (±0.1) × 10^{14} W/cm^2]. The insets show the variation of the intensities of selected harmonic orders of 800 nm. (**C**) Even-to-odd ratio for oriented molecules (800 nm). (**D** and **E**) Alignment dependence of the high-harmonic phase ϕ^{HHG} using 800-nm and 1300-nm pulses, respectively. A sum of the four lowest even-order Legendre polynomials was fitted to the experimental data. The error bars (shaded areas) in all figures correspond to the standard deviation of the measured signal fluctuations. All data were obtained by averaging the signals from at least 1500 laser shots.

and the first excited electronic state of the cation, charge migration is reconstructed as shown in Fig. 3A. The spatial representation of the electron densities further requires the computation of molecular orbitals, which must be chosen to be consistent with those used in the calculation of the photorecombination matrix elements (SM section 2). It also requires the knowledge of the difference of the vertical ionization potentials of the field-free eigenstates, which determines the oscillation period of 1.85 fs and is known from photoelectron spectroscopy (*18*).

Strong-field ionization was found to create a one-electron hole localized at the iodine side of the molecule (Fig. 3D), compatible with the low ionization potential and high polarizability of the I atom. Subsequently, the hole delocalizes over the molecule and then localizes at the acetylene side after 930 as. Because the differential Stark shift of the $\tilde{X}^+$ and $\tilde{A}^+$ levels at the maximal applied field amounted to only 18 meV (SM, section 3, and fig. S11) or 0.8% of the energy level separation, and population transfer is absent by symmetry, the reconstructed dynamics correspond to quasi–field-free charge migration.

We found a ~π difference in the relative initial phase of the $\tilde{X}^+$ and $\tilde{A}^+$ states for parallel alignment (Fig. 3C), which implies that the hole is created on the acetylene side (Fig. 3E). This means that the electron hole is created on the opposite side from where the electron tunneled because ionization via the iodine atom is dominant (fig. S5). Although this result appears counterintuitive at first sight, the reconstructed hole is consistent with ionization to the lowest-lying multielectron eigenstate of the cation in a static field (fig. S12).

The subsequent charge migration for parallel alignment is controlled by the laser field (Fig. 4) and differs substantially from the field-free evolution (Fig. 3A). We first discuss the results obtained with 800-nm pulses. Figure 4A shows the fractional population of the $\tilde{X}^+$ ground state (solid blue line) and the relative phase $\Delta\varphi(\tau) = \varphi_{\tilde{A}^+}(\tau) - \varphi_{\tilde{X}^+}(\tau)$ between the $\tilde{X}^+$ and $\tilde{A}^+$ states (dashed cyan line) for all reconstructed delays. The first striking feature is the strong depletion of the $\tilde{X}^+$ state for early transit times. The population of the $\tilde{X}^+$ state reaches a minimum at 1.02 fs before increasing again. The relative phase between the two eigenstates shows a pronounced jump around the time of maximal depopulation of the ground state. Figure 4A also shows the reconstructed hole density at selected transit times for electron tunneling via the iodine atom. For electron tunneling via the hydrogen atom (Fig. 4B), the population transfer is markedly different from tunneling via iodine (Fig. 4A). Again, the ground state is strongly depopulated at the first reconstructed delay, but its repopulation begins earlier than in Fig. 4A. One of the crucial observables for the reconstruction of side-dependent charge migration is the relative intensity of the even harmonics. Our reconstruction procedure additionally includes the sign dependence of the transition dipole moment on the molecular orientation (SM section 2). The temporal uncertainty in the reconstruction is harmonic order–dependent and amounts to ±110 as on average. The temporal accuracy is limited by the uncertainty in the peak intensity needed to connect the electron transit time to the emitted photon energy (*22*, *29*) and the different transit times associated with the electronic states of the cation involved in the dynamics. The shaded area represents the combined error from all experimental uncertainties.

Turning to the results obtained at 1300 nm, we again find strong population transfer in the laser field, as shown by the reconstructed populations in Fig. 4C for tunneling via the iodine atom. The fractional ground-state population gradually increases until 1.53 fs and then decreases again. Our reconstruction shows a second minimum of the $\tilde{X}^+$ population at 1.71 fs and a subsequent rise for longer delays. For tunneling via the hydrogen atom (Fig. 4D), the behavior is similar, with the maximal population shifted to earlier delays. The electron hole densities reconstructed from the populations and relative phases demonstrate the strong laser control over the dynamics. This fact is further illustrated by movies S1 to S4, which show very rapid changes in the hole density associated with the reconstructed phase jumps. These results clearly show that both the site of electron tunneling and the laser wavelength offer extensive control over charge migration. They also highlight the highly nonadiabatic nature of the strongly driven electronic dynamics (fig. S10).

Our experimental reconstruction of the time-dependent populations and phases is supported by independent calculations (Fig. 4E). The population transfer was calculated by solving the time-dependent Schrödinger equation for the two

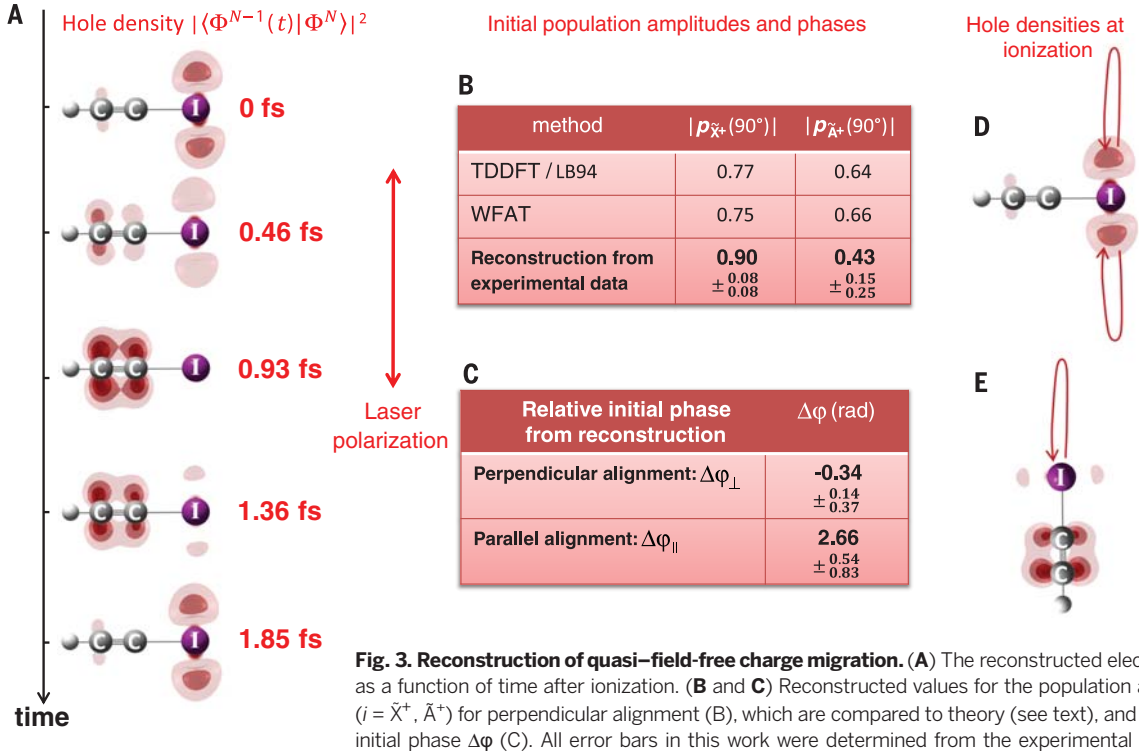

method	$\lvert p_{\tilde{X}^+}(90°)\rvert$	$\lvert p_{\tilde{A}^+}(90°)\rvert$
TDDFT / LB94	0.77	0.64
WFAT	0.75	0.66
Reconstruction from experimental data	**0.90** $\pm^{0.08}_{0.08}$	**0.43** $\pm^{0.15}_{0.25}$

Relative initial phase from reconstruction	Δφ (rad)
Perpendicular alignment: $\Delta\varphi_\perp$	**-0.34** $\pm^{0.14}_{0.37}$
Parallel alignment: $\Delta\varphi_\parallel$	**2.66** $\pm^{0.54}_{0.83}$

Fig. 3. Reconstruction of quasi–field-free charge migration. (**A**) The reconstructed electron dynamics as a function of time after ionization. (**B** and **C**) Reconstructed values for the population amplitudes $|p_i|$ ($i = \tilde{X}^+, \tilde{A}^+$) for perpendicular alignment (B), which are compared to theory (see text), and for the relative initial phase Δφ (C). All error bars in this work were determined from the experimental errors and the uncertainties in the intensity and alignment axis distribution (SM section 2). (**D** and **E**) Reconstructed hole density at the time of ionization for perpendicular (D) and parallel alignment (E). The arrows illustrate the direction of excursion of the continuum electron wave packet.

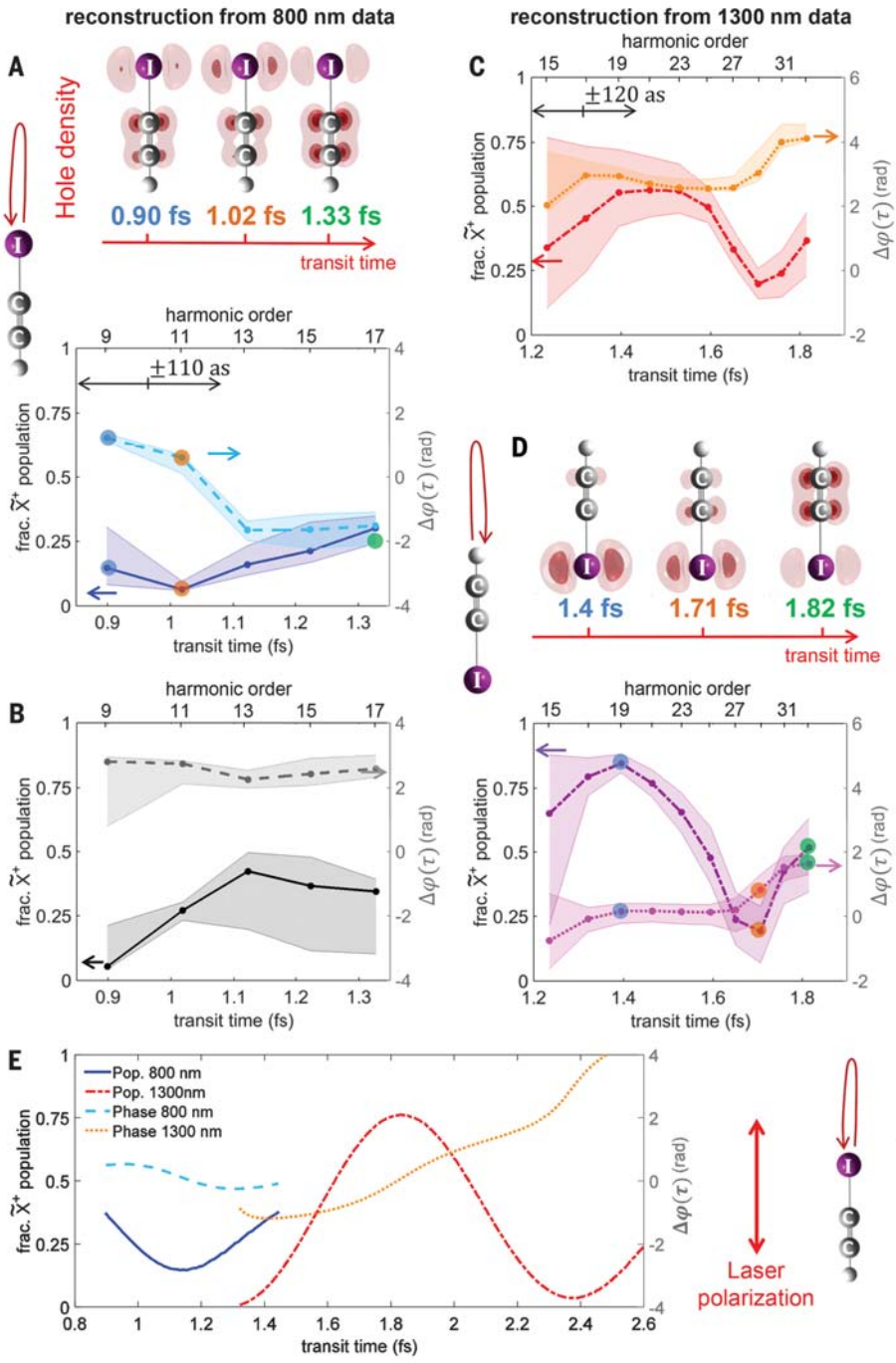

Fig. 4. Laser control over attosecond charge migration. (**A**) Reconstructed hole densities at selected transit times, reconstructed population of the $\tilde{X}^+$ state (blue line; the time-dependent population of the $\tilde{A}^+$ state is given by normalization), and relative phase between the $\tilde{X}^+$ and $\tilde{A}^+$ states (dashed cyan line) for a driving wavelength of 800 nm and electron tunneling via the iodine atom. (**B**) Reconstructed populations and relative phases for tunneling via the hydrogen atom in an 800-nm driving field. (**C**) Same as (B) for electron tunneling via the iodine atom and wavelength of 1300 nm. (**D**) Same as (A) for tunneling via the hydrogen atom and a wavelength of 1300 nm. (**E**) Independently calculated populations and relative phases for tunneling via the iodine atom using the two experimental wavelengths and peak intensities. Calculations for tunneling via the hydrogen atom and complementary hole densities are given in fig. S6.

lowest-lying electronic states of the cation, with all input taken from high-level ab initio calculations (SM sections 3 and 5) and the relative initial phase $\Delta\varphi$ taken from the experimental reconstruction. We have validated the two-state approach in our reconstruction by comparing time-dependent calculations containing between 2 and 10 electronic states of $HCCI^+$ and found that the dynamics are accurately predicted when only the $\tilde{X}^+$ and $\tilde{A}^+$ states of the cation are included (fig. S8).

The theoretical population transfer for 800 nm and tunneling via the I side (blue line in Fig. 4E) correctly predicts the near-complete depletion and repopulation of the ionic ground state, including the associated phase jump. The theoretical depopulation of the ground state is weaker than the reconstructed one (Fig. 4A), and the phase jump is consistently less pronounced. Such jumps are most pronounced for complete depopulations and repopulations of states (see fig. S6, which also shows calculations for tunneling via the H atom). For 1300 nm, the calculations qualitatively agree with the reconstructed dynamics, but the population maximum occurs later than in the experimental results by ~300 as. Given the complexity of the nonadiabatic electronic dynamics (fig. S10), the agreement between experiment (Fig. 4, A and C) and calculations (Fig. 4E) is highly encouraging. The nonadiabatic electronic dynamics introduces a strong dependence of the population transfer on the exact parameters of the laser pulse. The remaining discrepancies may result from electron correlation between the continuum wave packet and the bound electrons beyond that taken into account in the present mean-field description of photorecombination.

Our work outlines several general aspects of the preparation and control of charge migration by intense laser pulses. First, the initial phase of the hole wave packet strongly depends on the orientation of the molecule with respect to the ionizing laser field (Fig. 3, D and E). This suggests molecular alignment and orientation both as necessary for a well-characterized measurement and as an attractive control parameter. Second, the laser field can be used to achieve extensive control over charge migration, especially when the relevant transition dipole moments are large and the level separations are small, resulting in strongly nonadiabatic electronic dynamics. The demonstrated laser control can be further refined by using laser pulses with subcycle-controlled waveforms (*34*)—for example, to steer the electron hole to a particular position within the molecule where it can trigger a desired chemical reaction.

REFERENCES AND NOTES

1. G. S. Engel *et al.*, *Nature* **446**, 782–786 (2007).
2. S. M. Falke *et al.*, *Science* **344**, 1001–1005 (2014).
3. L. Cederbaum, J. Zobeley, *Chem. Phys. Lett.* **307**, 205–210 (1999).
4. A. D. Bandrauk, S. Chelkowski, H. S. Nguyen, *Int. J. Quantum Chem.* **100**, 834–844 (2004).
5. F. Remacle, R. D. Levine, *Proc. Natl. Acad. Sci. U.S.A.* **103**, 6793–6798 (2006).
6. B. Mignolet, R. D. Levine, F. Remacle, *J. Phys. B* **47**, 124011 (2014).
7. R. Weinkauf *et al.*, *J. Phys. Chem.* **100**, 18567–18585 (1996).
8. R. Weinkauf, E. W. Schlag, T. J. Martinez, R. D. Levine, *J. Phys. Chem. A* **101**, 7702–7710 (1997).
9. S. R. Leone *et al.*, *Nat. Photonics* **8**, 162–166 (2014).
10. M. F. Kling, P. von den Hoff, I. Znakovskaya, R. de Vivie-Riedle, *Phys. Chem. Chem. Phys.* **15**, 9448–9467 (2013).
11. E. Goulielmakis *et al.*, *Nature* **466**, 739–743 (2010).

12. A. Fleischer *et al.*, *Phys. Rev. Lett.* **107**, 113003 (2011).
13. F. Calegari *et al.*, *Science* **346**, 336–339 (2014).
14. O. Smirnova *et al.*, *Nature* **460**, 972–977 (2009).
15. Y. Mairesse *et al.*, *Phys. Rev. Lett.* **104**, 213601 (2010).
16. S. Haessler *et al.*, *Nat. Phys.* **6**, 200–206 (2010).
17. H. Niikura *et al.*, *Nature* **421**, 826–829 (2003).
18. M. Allan, E. Kloster-Jensen, J. P. Maier, *J. Chem. Soc. Faraday Trans. II* **73**, 1406–1416 (1977).
19. R. S. Mulliken, *J. Chem. Phys.* **7**, 20 (1939).
20. H. Stapelfeldt, T. Seideman, *Rev. Mod. Phys.* **75**, 543–557 (2003).
21. M. Lein, *Phys. Rev. Lett.* **94**, 053004 (2005).
22. S. Baker *et al.*, *Science* **312**, 424–427 (2006).
23. H. J. Wörner, J. B. Bertrand, P. Hockett, P. B. Corkum, D. M. Villeneuve, *Phys. Rev. Lett.* **104**, 233904 (2010).
24. R. Torres *et al.*, *Phys. Rev. A* **81**, 051802 (2010).
25. C. Vozzi *et al.*, *Nat. Phys.* **7**, 822–826 (2011).
26. S. De *et al.*, *Phys. Rev. Lett.* **103**, 153002 (2009).
27. X. Zhou *et al.*, *Phys. Rev. Lett.* **100**, 073902 (2008).
28. A.-T. Le, R. R. Lucchese, S. Tonzani, T. Morishita, C. D. Lin, *Phys. Rev. A* **80**, 013401 (2009).
29. M. Lewenstein, P. Balcou, M. Y. Ivanov, A. L'Huillier, P. B. Corkum, *Phys. Rev. A* **49**, 2117–2132 (1994).
30. M. V. Frolov, N. L. Manakov, T. S. Sarantseva, A. F. Starace, *J. Phys. B* **42**, 035601 (2009).
31. D. Shafir *et al.*, *Nature* **485**, 343–346 (2012).
32. E. F. Penka, E. Couture-Bienvenue, A. D. Bandrauk, *Phys. Rev. A* **89**, 023414 (2014).
33. O. I. Tolstikhin, T. Morishita, L. B. Madsen, *Phys. Rev. A* **84**, 053423 (2011).
34. A. Wirth *et al.*, *Science* **334**, 195–200 (2011).

ACKNOWLEDGMENTS

We thank M. Lein for valuable discussions and F. Lépine, V. Despré, P. Lopez, and U. Röthlisberger for performing supporting calculations. Supported by ERC starting grant (project no. 307270-ATTOSCOPE) and the Swiss National Science Foundation via the National Centre of Competence in Research Molecular Ultrafast Science and Technology (P.M.K. and H.J.W.), the Fonds National de la Recherche Scientifique of Belgium and Fonds de la Recherche Fondamentale Collective grant 2.4545.12 (B.M. and F.R.), the Belgian American Education Foundation and Wallonie-Bruxelles International (B.M.), Compute Canada through access to high-performance computers (E.F.P. and A.D.B.), the Ministry of Education and Science of Russia state assignment no. 3.679.2014/K (O.I.T.), VKR Centre of Excellence QUSCOPE and ERC starting grant (project no. 277767-TDMET) (L.B.M.).

SUPPLEMENTARY MATERIALS

www.sciencemag.org/content/350/6262/790/suppl/DC1
Materials and Methods
Supplementary Text
Figs. S1 to S14
Tables S1 to S9
Movies S1 to S4
References (*35*–*101*)

29 June 2015; accepted 25 September 2015
Published online 22 October 2015
10.1126/science.aab2160

GEOCHEMISTRY

Evidence for primordial water in Earth's deep mantle

Lydia J. Hallis,[1,2]*† Gary R. Huss,[1,2] Kazuhide Nagashima,[2] G. Jeffrey Taylor,[1,2] Sæmundur A. Halldórsson,[3]‡ David R. Hilton,[3] Michael J. Mottl,[4] Karen J. Meech[1,5]

The hydrogen-isotope [deuterium/hydrogen (D/H)] ratio of Earth can be used to constrain the origin of its water. However, the most accessible reservoir, Earth's oceans, may no longer represent the original (primordial) D/H ratio, owing to changes caused by water cycling between the surface and the interior. Thus, a reservoir completely isolated from surface processes is required to define Earth's original D/H signature. Here we present data for Baffin Island and Icelandic lavas, which suggest that the deep mantle has a low D/H ratio (δD more negative than −218 per mil). Such strongly negative values indicate the existence of a component within Earth's interior that inherited its D/H ratio directly from the protosolar nebula.

Establishing Earth's initial D/H ratio is important for understanding the origin of our planet's water, as well as the dynamical processes that operated during planet formation in the solar system. However, evolution of this ratio occurs over time as a result of surface and mantle processing. Collisions with hydrogen-bearing planetesimals or cometary material after Earth's accretion should have altered the D/H ratio of the planet's surface and upper mantle (*1*). In addition, experimentally based chemical models suggest an increase in the atmospheric D/H value by a factor of 2 to 9 since Earth's formation (*2*). Preferential loss of the lighter hydrogen isotope from the upper atmosphere causes this increase, driven by thermal atmospheric escape or plasma interactions with the atmosphere. As atmospheric D/H is linked with that of ocean water and sediments, the D/H ratio of the mantle also increases with time via subduction and convective mixing. Only areas of the deep Earth that have not participated in this mixing process are likely to preserve Earth's initial D/H ratio.

Studies of the trace-element, radiogenic-isotope, and noble gas isotope characteristics of mid-ocean ridge basalts (MORBs) and ocean-island basalts (OIBs) reveal the existence of domains within Earth's mantle that have experienced distinct evolutionary histories (*3*, *4*). Although alternative theories exist [e.g., (*5*)], most studies suggest that high $^3He/^4He$ ratios in some OIBs indicate the existence of relatively undegassed regions in the deep mantle compared to the upper mantle, which retain a greater proportion of their primordial He (*6*, *7*). Helium-isotope ($^3He/^4He$) ratios more than 30 times the present-day ratio of Earth's atmosphere ($R_A = 1.38 \times 10^{-6}$) (*8*) can be found in volcanic rocks from oceanic islands, including Iceland and Hawaii (*9*–*12*). Early Tertiary (60-million-year-old) lavas from Baffin Island and west Greenland, which represent volcanic rocks from the proto/early Iceland mantle plume, contain the highest recorded terrestrial $^3He/^4He$ ratios of up to 50 R_A (*6*, *7*). These lavas also have Pb and Nd isotopic ratios consistent with primordial mantle ages [4.45 to 4.55 billion years (Ga)] (*13*), indicating the persistence of an ancient, isolated reservoir in the mantle. The undegassed and primitive nature (*14*) of this reservoir means that it could preserve Earth's initial D/H ratio. This study targets mineral-hosted melt inclusions in these rocks in search of this primordial signal.

A range of D/H ratios are found on Earth. We compare the ratio of deuterium (^2H or D) to hydrogen (^1H) relative to Vienna Standard Mean Ocean Water (VSMOW, D/H = 1.5576×10^{-4}) using $\delta D = \{[(D/H)_{unknown}/(D/H)_{VSMOW}] - 1\} \times 1000$, in units of parts per thousand [per mil (‰)]. The hydrological cycle fractionates hydrogen, creating glacial ice [standard Greenland Ice Sheet Precipitation δD = −190‰ (*15*)], ocean water (VSMOW δD = 0‰), and fresh water [δD = 0 to −300‰ (*16*)] reservoirs. Subduction provides a means to mix water back into the mantle, producing a variation in δD from −126 to +46‰ from slab dehydration and sediment recycling (*17*, *18*). The MORB source appears to be better mixed, with a uniform δD of −60 ± 5‰ (*19*).

We measured the D/H ratios of olivine-hosted glassy melt inclusions in two depleted picrite samples (basaltic rocks with abundant Mg-rich olivine) from Padloping Island, northwest Baffin Island (*20*), and in three picrite samples from Iceland's western and northern rift zones (*9*–*11*). The high forsterite (Fo) contents of these olivines (Fo_{87-91}) suggest crystallization from primitive melts (*21*). We monitored possible contamination from crustal materials, or meteoric water due to weathering, by measuring the oxygen-isotope ratios of the samples (*21*). One Icelandic sample shows slightly raised $\delta^{18}O$, indicative of crustal contamination. All other samples fall within the range expected for uncontaminated mantle-derived samples.

Baffin Island melt inclusions are characterized by extremely low D/H ratios, from δD −97 to −218‰

[1]NASA Astrobiology Institute, Institute for Astronomy, University of Hawai'i, 2680 Woodlawn Drive, Honolulu, HI 96822-1839, USA. [2]Hawai'i Institute of Geophysics and Planetology, Pacific Ocean Science and Technology (POST) Building, University of Hawai'i, 1680 East-West Road, Honolulu, HI 96822, USA. [3]Scripps Institution of Oceanography, University California San Diego, 9500 Gilman Drive, La Jolla, CA 92093-0244, USA. [4]Department of Oceanography, University of Hawai'i, Marine Sciences Building 304, 1000 Pope Road, Honolulu, HI 96822, USA. [5]Institute for Astronomy, University of Hawai'i, 2680 Woodlawn Drive, Honolulu, HI 96822, USA.
*Present address: School of Geographical and Earth Sciences, University of Glasgow, Gregory Building, Lillybank Gardens, Glasgow G12 8QQ, UK. **†Corresponding author. E-mail: lydia.hallis@glasgow.ac.uk** ‡Present address: Nordic Volcanological Center, Institute of Earth Sciences, University of Iceland, Askja, Sturlugata 7, 101 Reykjavík, Iceland.

Table 1. Water content, D/H ratio (δD), and $^{18}O/^{16}O$ ratio ($\delta^{18}O$) of Baffin Island and Icelandic samples. Owing to the small size of melt inclusions in the samples, it was mostly not possible to collect hydrogen- and oxygen-isotope data from the same inclusions. Therefore, oxygen-isotope data are calculated on the basis of the average value of melt inclusions (n = 2 to 4) within the same olivine grain as that measured for D/H. Olivine oxygen data are also presented as an average (n = 2 to 6). Scanning electron microscope images showing the location of each data point on the sample surfaces are available (*21*).

Sample and phase	H_2O (ppm)	δD (‰)	2σ (‰)	$\delta^{18}O$ (‰)	2σ (‰)
Baffin Island picrites					
PI-16_area 4_melt inclusion 1	709	–115	38	5.18	0.25
PI-16_area 6_melt inclusion 1	926	–107	39	5.18	0.25
PI-16_area 7_melt inclusion 1	1189	–108	35	5.18	0.25
PI-16_area 8_melt inclusion 1	1039	–122	36	5.18	0.25
PI-16_area 9_melt inclusion 1	1175	–158	51	5.18	0.25
PI-16_area 9_melt inclusion 2	576	–114	40	5.18	0.25
PI-16_area 4_olivine 1	194			4.53	0.34
PI-16_area 6_olivine 1	413			4.53	0.34
PI-16_area 7_olivine 1	153			4.53	0.34
PI-16_area 8_olivine 1	200			4.53	0.34
PI-16_area 9_olivine 1	187			4.53	0.34
PI-19_area 1_melt inclusion 1	1337	–137	35	4.73	0.16
PI-19_area 1_melt inclusion 2	1465	–177	37	4.73	0.16
PI-19_area 2_melt inclusion 1	1719	–173	34	4.73	0.16
PI-19_area 2_melt inclusion 2	1964	–218	34	4.73	0.16
PI-19_area 3_melt inclusion 1	1779	–197	34	4.73	0.16
PI-19_area 6_melt inclusion 1	997	–137	32		
PI-19_area 7_melt inclusion 1	868	–97	34		
PI-19_area 8_melt inclusion 1	901	–126	32		
PI-19_area 1_olivine 1	557			4.38	0.25
PI-19_area 2_olivine 1	641			4.38	0.25
PI-19_area 2_olivine 2	712			4.38	0.25
PI-19_area 3_olivine 1	781			4.38	0.25
PI-19_area 8_olivine 1	187				
PI-19_area 8_olivine 2	190				
Icelandic picrites					
MID-1_bullet 2_melt inclusion 1	946	–88	51	4.83	0.40
MID-1_bullet 2_melt inclusion 2	964	–90	50	4.83	0.40
MID-1_bullet 3_melt inclusion 1	474	–34	53	4.83	0.40
MID-1_bullet 2_olivine 1	157			2.43	0.46
MID-1_bullet 3_olivine 1	85			2.43	0.46
NAL828_bullet 5_melt inclusion 1	600	–34	53	6.54	0.48
NAL828_bullet 5_melt inclusion 2	510	–29	53	6.54	0.48
NAL828_bullet 5_olivine 1	100			5.36	0.46
NAL 688_bullet 13_melt inclusion 1	587	–25	28	5.89	0.35
NAL 688_bullet 13_olivine 1	36			5.72	0.56

(Table 1). Melt-inclusion dehydration, where H_2O preferentially diffuses faster than HDO through encapsulating olivine, accounts for the inverse correlation between δD and water content (Fig. 1A). The longer olivine grains are resident in hot melt before eruption, the stronger the effect of dehydration (*22*). In addition to dehydration, melt-inclusion degassing can also raise D/H ratios and lower water contents. Melt inclusions may undergo degassing due to depressurization during eruption. We selected rapidly quenched subglacially (Iceland) and subaqueously (Baffin Island) erupted samples to mitigate the effects of degassing. However, two of the three Icelandic samples exhibit the high δD and low water contents indicative of this process. Revealingly, sample MID-1 is known to be one of the least degassed Icelandic basalts (*10*) and contains melt inclusions with the lowest δD (–88 to –90‰) and highest H_2O contents [946 to 964 parts per million (ppm)] of the three Icelandic samples.

The wide spread in $\delta^{18}O$ values between samples (Table 1 and Fig. 1B) supports a heterogeneous Baffin Island and Iceland plume with respect to $\delta^{18}O$ (*11*, *23*, *24*). The Baffin Island melt inclusion $\delta^{18}O$ values (4.73 to 5.18‰) are similar to those of Baffin Island picrite matrix glasses (4.84 to 5.22‰) (*25*). These values are lower than typical MORB $\delta^{18}O$ [5.5 ± 0.2‰ (*26*)], indicating a possible correlation between low D/H, low $^{18}O/^{16}O$, and high $^3He/^4He$ as an intrinsic property of the undegassed mantle.

Lithospheric slab dehydration during subduction and deep recycling can produce low D/H ratios in glasses from plume-related localities (*17*, *27*). Basaltic glasses from the Hawaiian Koolau volcano contain low δD values and water contents similar to those of the Baffin Island picrites (*27*) (Fig. 1A). However, the Koolau mantle source is thought to contain a substantial fraction of recycled upper oceanic crust and sediment (*27*), and its distinct $\delta^{18}O$ (Fig. 1B) is attributed to an EM2 signature (sedimentary recycling). The Baffin Island samples do not contain any evidence of a recycled slab component (*21*); hence, their low δD values must be attributed to a different origin. The correlation between low D/H and high $^3He/^4He$ ratios in the Baffin Island and Iceland samples suggests that they originate from a region isolated from mixing. Thus, our data support a heterogeneous mantle, which contains deep, primitive, undegassed regions that have never been involved in subduction-related mixing or recycling (*13*).

Magma-ocean crystallization models (*28*), and Nd isotopic evidence from some of Earth's oldest rocks (*29*), indicate a small volume of late-solidifying dense cumulates developed during the first 30 to 75 million years of Earth history. High pressures near the base of Earth's magma ocean would cause magma to become denser than coexisting minerals; thus, crystallization would proceed from the top downward (*30*). Top-down crystallization would trap volatile elements in cumulates at the deepest section of the mantle. Nd-isotope data suggest that such cumulates still exist, representing a hidden incompatible-element–enriched reservoir complementary to the depleted nature of most of Earth's mantle (*29*, *31*). The depth of this enriched reservoir explains its absence in modern-day upper-mantle melts. However, deep plume melting can transfer melt from the core-mantle boundary to the surface (*32*). The olivine compositions of Baffin Island picrites, as well as other samples with high $^3He/^4He$ (e.g., basalts from western Greenland and the Galapagos), suggest that these lavas originated from a peridotite source ~20% higher in Ni content than the modern depleted mantle source, apparently as a result of interaction with the Ni-rich core (*5*). The noble gas composition of many OIBs, including high proportions of solar Ne, suggests that these plumes sample a volatile-rich reservoir (*33*, *34*).

The lowest measured D/H value (δD = –218‰) provides an upper limit on the D/H of early Earth if the Baffin Island picrite melt inclusions sample a deep mantle reservoir with preserved primitive volatiles. One possibility is that this strongly negative δD was added to the Earth during initial accretion, via dust grains with adsorbed H_2O inherited directly from the protosolar nebula (–870‰) (*35*). The temperature was high at Earth's orbital distance during the early solar system, but 1000 to 500 K would still allow adsorption of 25 to 300% of Earth's ocean water onto fractal grains during Earth's accretion (*36*). Solar wind hydrogen and additional accreting objects from the outer

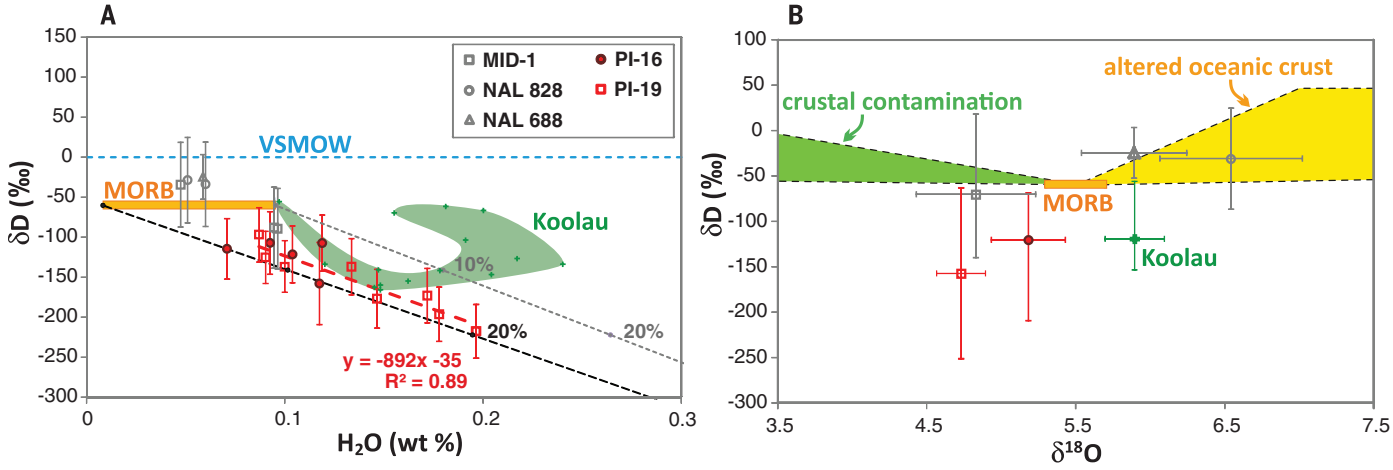

Fig. 1. Hydrogen- and oxygen-isotope ratios. The hydrogen-isotope ratios (δD) of Baffin Island and Icelandic basaltic melt inclusions versus water content (**A**) and oxygen-isotope ratios (**B**). Uncertainties are 2σ, except for (B) δD, where error bars represent the full range of the data set. The δD versus H_2O (A) data trendline gradient for sample PI-19 is shown by the red dashed line. Mixing lines between a protosolar-like deep mantle source [δD = −870‰, H_2O = 0.94 wt %] (*35*) and MORB (*19*, *37*) are shown by the black and gray dashed lines, which assume minimum and maximum MORB source region H_2O contents of 0.008 and 0.095 wt %, respectively (*37*). Melt inclusion data from the Hawaiian Koolau volcano, which contains the lowest δD values of the Hawaiian plume (*27*), are represented by the green crosses and envelope in (A) and green cross in (B). Average melt inclusion δD values are shown on the δD versus $\delta^{18}O$ plot (B). The colored envelopes (B) indicate regions of crustal contamination, based on the $\delta^{18}O$ variation of possible contaminants from the Icelandic crust (−7.5 to +1.65‰, green envelope) (*24*), and hydrothermally altered oceanic crust (+7 to +15‰, yellow envelope) (*26*). The δD variation of the envelopes is as reported for hydrothermally altered oceanic crust (−34 to 46‰) (*17*, *18*).

part of the inner solar system may also have mixed into the accreting planet (*34*). Experimentally based atmospheric chemical models support protosolar nebula adsorption, as they suggest an initial δD between −500 and −889‰ for Earth (*2*).

The δD versus H_2O [weight percent (wt %)] correlation for Baffin Island sample PI-19 (Fig. 1A) suggests that a deep mantle source with a protosolar δD value of −870‰ would have a water content of 0.94 wt %. This value is higher than that calculated for typical bridgmanite (<220 ppm H_2O) (*37*), although post-bridgmanite can contain more hydrogen (*38*). In addition, isotopic ratios show that plume material is not typical of ambient mantle (*4*–*7*), and primary Hawaiian magmas have been shown to contain 0.36 to 0.6 wt % water (*27*). A 20/80% mixture of a protosolar-like deep mantle source (δD = −870‰, H_2O = 0.94 wt %) (*35*) and MORB (*19*, *37*) reproduces the lowest measured Baffin Island δD values. This proportion is consistent with mantle Xe-isotope anomalies, also estimated to reflect admixture with about 20% of a solar Xe component (*33*).

The similarity between the bulk chemical composition of Earth and carbonaceous chondrites indicates that Earth accreted from building blocks similar to these meteorites (*39*). An initial Earth δD value more negative than −218‰ is at the very lower end of the δD range for bulk-rock CM and CI chondrites (+338 to −227‰) (*40*), whereas other carbonaceous chondrite groups have more positive bulk-rock δD (−48 to +763‰) (*40*). However, the δD range for water in CI and CM chondrites is low (−383 to −587‰) (*40*), hinting that their parent bodies may have gained water via protosolar nebula adsorption. Recent reports of Earth-like δD in the martian interior (*41*) also suggest protosolar nebula adsorption as a source for martian water. Therefore, the adsorption mechanism could provide an important source of water in inner solar system terrestrial bodies.

REFERENCES AND NOTES

1. O. Abramov, S. J. Mojzsis, *Nature* **459**, 419–422 (2009).
2. H. Genda, M. Ikoma, *Icarus* **194**, 42–52 (2008).
3. A. W. Hofmann, *Nature* **385**, 219–229 (1997).
4. C. Herzberg *et al.*, *Nature* **493**, 393–397 (2013).
5. H. M. Gonnermann, S. Mukhopadhyay, *Nature* **459**, 560–563 (2009).
6. F. M. Stuart, S. Lass-Evans, J. G. Fitton, R. M. Ellam, *Nature* **424**, 57–59 (2003).
7. N. A. Starkey *et al.*, *Earth Planet. Sci. Lett.* **277**, 91–100 (2009).
8. J. Geiss *et al.*, *Space Sci. Rev.* **110**, 307–335 (2004).
9. D. R. Hilton, K. Grönvold, C. G. Macpherson, P. R. Castillo, *Earth Planet. Sci. Lett.* **173**, 53–60 (1999).
10. E. Füri *et al.*, *Geochim. Cosmochim. Acta* **74**, 3307–3332 (2010).
11. C. G. Macpherson, D. R. Hilton, J. M. D. Day, D. Lowry, K. Grönvold, *Earth Planet. Sci. Lett.* **233**, 411–427 (2005).
12. M. D. Kurz, W. J. Jenkins, S. R. Hart, *Nature* **297**, 43–47 (1982).
13. M. G. Jackson *et al.*, *Nature* **466**, 853–856 (2010).
14. I. Robillard, D. Francis, J. N. Ludden, *Contrib. Mineral. Petrol.* **112**, 230–241 (1992).
15. J. Hoefs, *Stable Isotope Geochemistry*. (Springer, Berlin, ed. 6, 2009).
16. C. Lécuyer, P. Gillet, F. Robert, *Chem. Geol.* **145**, 249–261 (1998).
17. A. M. Shaw *et al.*, *Nat. Geosci.* **5**, 224–228 (2012).
18. Q.-K. Xia *et al.*, *Geophys. Res. Lett.* **29**, 4-1–4-4 (2008).
19. M. Clog, C. Aubaud, P. Cartigny, L. Dosso, *Earth Planet. Sci. Lett.* **381**, 156–165 (2013).
20. D. Francis, *Contrib. Mineral. Petrol.* **89**, 144–154 (1985).
21. Materials and methods are available as supplementary materials on *Science* Online.
22. G. A. Gaetani, J. A. O'Leary, N. Shimizu, C. E. Bucholz, M. Newville, *Geology* **40**, 915–918 (2012).
23. A. A. Gurenko, M. Chaussidon, *Earth Planet. Sci. Lett.* **205**, 63–79 (2002).
24. M. E. Hartley, T. Thordarson, J. G. Fitton, EIMF, *Geochim. Cosmochim. Acta* **123**, 55–73 (2013).
25. A. J. R. Kent *et al.*, *Geochem. Geophys. Geosyst.* **5**, Q11015 (2004).
26. J. M. Eiler, *Rev. Mineral. Geochem.* **43**, 319–364 (2001).
27. E. Hauri, *Chem. Geol.* **183**, 115–141 (2002).
28. L. T. Elkins-Tanton, *Earth Planet. Sci. Lett.* **271**, 181–191 (2008).
29. M. Boyet, R. W. Carlson, *Science* **309**, 576–581 (2005).
30. L. T. Elkins-Tanton, *Astrophys. Space Sci.* **332**, 359–364 (2011).
31. S. Labrosse, J. W. Hernlund, N. Coltice, *Nature* **450**, 866–869 (2007).
32. D. V. Helmberger, L. Wen, X. Ding, *Nature* **396**, 251–255 (1998).
33. G. Holland, C. J. Ballentine, *Nature* **441**, 186–191 (2006).
34. M. Trieloff, J. Kunz, D. A. Clague, D. Harrison, C. J. Allègre, *Science* **288**, 1036–1038 (2000).
35. K. D. McKeegan, L. A. Leshin, *Rev. Mineral. Geochem.* **43**, 279–318 (2001).
36. M. J. Drake, *Meteorit. Planet. Sci.* **40**, 519–527 (2005).
37. W. R. Panero, J. S. Pigott, D. M. Reaman, J. E. Kabbes, Z. Liu, *J. Geophys. Res. Solid Earth* **120**, 894–908 (2015).
38. S. Akber-Knutson, G. Steinle-Neumann, P. D. Asimow, *Geophys. Res. Lett.* **32**, L14303 (2005).
39. B. Marty, *Earth Planet. Sci. Lett.* **313-314**, 56–66 (2012).
40. C. M. Alexander *et al.*, *Science* **337**, 721–723 (2012).
41. L. J. Hallis, G. J. Taylor, K. Nagashima, G. R. Huss, *Earth Planet. Sci. Lett.* **359-360**, 84–92 (2012).

ACKNOWLEDGMENTS

This material is based on work supported by the National Aeronautics and Space Administration through the NASA Astrobiology Institute under Cooperative Agreement no. NNA09-DA77A, issued through the Office of Space Science. We thank D. Francis for allocation of the Baffin Island picrite samples and K. Grönvold for invaluable help in the field in Iceland. The data reported in this paper are tabulated in the supplementary materials. L.J.H. prepared samples, collected and processed data, and was the primary author of this manuscript. G.R.H. and K.N. managed the ion-microprobe, perfected hydrogen- and oxygen-isotope analytical methods, and assisted with data processing. S.A.H. and D.R.H. collected the Icelandic samples and provided Icelandic geological background. G.J.T. assisted with the development of hydrogen-isotope analytical methods and provided solar system disk model chemistry information. K.J.M. initiated this study and provided solar system disk model chemistry information. All authors discussed the results and commented on the manuscript. Correspondence and requests for materials should be addressed to L. J. Hallis (lydia.hallis@glasgow.ac.uk).

SUPPLEMENTARY MATERIALS

www.sciencemag.org/content/350/6262/795/suppl/DC1
Materials and Methods
Supplementary Text
Figs. S1 to S9
Tables S1 to S3
References (*42*–*72*)

3 May 2015; accepted 9 October 2015
10.1126/science.aac4834

MAGNETIC RESONANCE

Torque-mixing magnetic resonance spectroscopy

J. E. Losby,[1,2] F. Fani Sani,[1,2] D. T. Grandmont,[1] Z. Diao,[1,2] M. Belov,[2] J. A. J. Burgess,[1,2] S. R. Compton,[1,2] W. K. Hiebert,[1,2] D. Vick,[2] K. Mohammad,[3] E. Salimi,[3] G. E. Bridges,[3] D. J. Thomson,[3] M. R. Freeman[1,2]*

A universal, torque-mixing method for magnetic resonance spectroscopy is presented. In analogy to resonance detection by magnetic induction, the transverse component of a precessing dipole moment can be measured in sensitive broadband spectroscopy, here using a resonant mechanical torque sensor. Unlike induction, the torque amplitude allows equilibrium magnetic properties to be monitored simultaneously with the spin dynamics. Comprehensive electron spin resonance spectra of a single-crystal, mesoscopic yttrium iron garnet disk at room temperature reveal assisted switching between magnetization states and mode-dependent spin resonance interactions with nanoscale surface imperfections. The rich detail allows analysis of even complex three-dimensional spin textures. The flexibility of microelectromechanical and optomechanical devices combined with broad generality and capabilities of torque-mixing magnetic resonance spectroscopy offers great opportunities for development of integrated devices.

Many complementary methods have emerged for performing magnetic resonance spectroscopy, including nonuniversal but extraordinarily sensitive electron spin (ESR) and nuclear magnetic resonance (NMR) spectroscopies of specific materials via optical or spin-electronic detection. Magnetic resonance force microscopy (MRFM) (*1*) and scanned diamond nitrogen-vacancy center probes (*2*) have measured signals from very small numbers of nuclear spins near surfaces. In MRFM (*3*–*5*), a gradient-dipole interaction between the spin system and a magnetic probe causes a deflection of a micromechanical cantilever, with strong local field gradients leading to very high spin sensitivity and spatial resolution.

The pioneering demonstration of pure mechanical torque detection of spin resonance was reported in 1967 with direct observation of the angular momentum change from resonant radio-frequency (RF) absorption-induced spin-flips (*6*). In this approach, also revisited by Ascoli, Alzetta, and co-workers in a micromechanical implementation (*7*) in 1996 after the early reports of MRFM, a dc magnetic field is applied parallel to the torsion axis of the torque sensor, and signal transduction arises from the reduction of the longitudinal net moment under magnetic resonance conditions. We report on a complementary broadband mechanical approach with greater generality, torque-mixing magnetic resonance spectroscopy (TMRS). TMRS enables direct readout of the transverse RF components of precessing magnetization, directly analogous to how inductive detection of spin resonance is usually implemented and much more versatile for applications (previous works of torque or force detection probe the longitudinal moment change). Below, we apply TMRS to resolve an outstanding experimental challenge: sensitive, simultaneous observations of spin resonance and net magnetic moment for a single micromagnetic specimen, independent measurements prerequisite to complete understanding of the system.

A schematic of the applied RF excitation and demodulation field geometry (Fig. 1A) is shown in the context of a nanotorsional resonator-supported magnetic specimen. A net moment $\mathbf{m}_0$ is induced by a dc magnetic field $\mathbf{H}_0$, applied perpendicular to the torsion axis (z direction). The magnetic resonance is driven by an RF magnetic field with amplitude H_1 at frequency f_1 applied parallel to the torsion axis (y direction). In this arrangement, an RF magnetic moment, orthogonal to both $\mathbf{H}_0$ and $\mathbf{H}_1$, arises from spin precession at magnetic resonances.

It is convenient to describe the transverse moment amplitude $m_x(f_1)$, via an experimental transverse susceptibility $\chi_t(f_1)$, such that the amplitude of the RF driven response is

$$m_x(f_1) = V\chi_t(f_1)H_1 = V\frac{\chi_0 f_{\mathrm{res}}}{\left[(f_{\mathrm{res}} - f_1)^2 + \left(\frac{\Delta f}{2}\right)^2\right]^{1/2}}H_1 \quad (1)$$

where V is the volume of the specimen, f_{res} is the magnetic resonance frequency, Δf is the resonance linewidth, and χ_0 is the baseline low-frequency susceptibility [more details can be found in the supplementary materials (*8*)]. This RF transverse moment is ideally suited to nominally background-free mechanical torque detection because it mimics the original crossed-coil concept for inductive detection (*9*). The key is exposing the sinusoidally varying moment to a second, orthogonal RF tone $\mathbf{H}_2$ at frequency f_2. The two sinusoids then cooperatively generate RF magnetic torques at sum and difference frequencies, $f_1 \pm f_2$, as described by the cross-product in the torque expression, $\boldsymbol{\tau} = \mathbf{m} \times \mu_0\mathbf{H}$. Setting $f_2 = f_1 + f_{\mathrm{mech}}$, where the frequency offset f_{mech} corresponds to a torsion resonance of the mechanical sensor, enables sensitive detection of

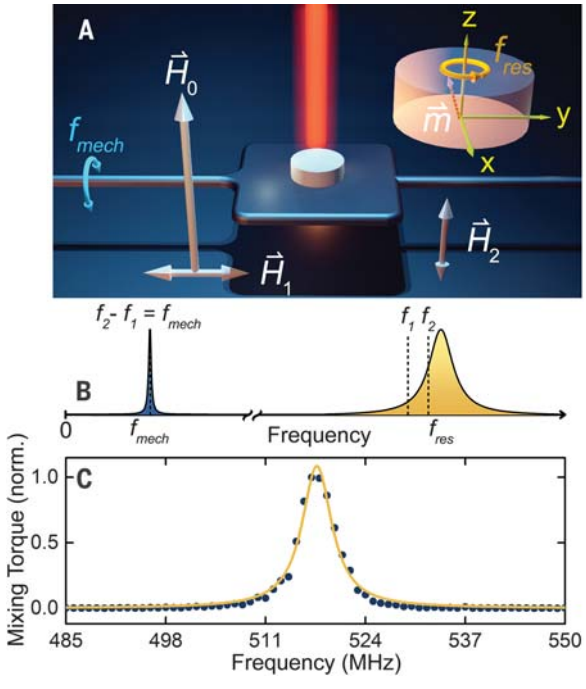

Fig. 1. Torque-mixing magnetic resonance spectroscopy. (**A**) Applied field and torque sensor geometry for TMRS. A spin system (illustrated as a micromagnetic disk), supported by the sensor with mechanical resonance at f_{mech}, is biased in an applied field $\mathbf{H}_0$ (direction arrows not to scale). $\mathbf{H}_1$ (at f_1) is applied to drive the transverse component of magnetic resonance, f_{res} (inset), accompanied by $\mathbf{H}_2$ (at f_2) such that $f_2 - f_1 = f_{\mathrm{mech}}$. (**B**) Frequency-space representation of the down-conversion scheme. (**C**) Torque detection of magnetic resonance at $\mathbf{H}_0$ = 70.5 kA/m. $\mathbf{H}_1$ and $\mathbf{H}_2$ were driven with peak-to-peak field amplitudes of 78 A/m and 190 A/m, respectively. The full resonance linewidth at half maximum, 4.76 MHz, is obtained by fitting the Lorentzian presented in Eq. 1 to the normalized data.

[1]Department of Physics, University of Alberta, 4-181 Centennial Center for Interdisciplinary Science Edmonton, Alberta T6G 2E1, Canada. [2]National Institute for Nanotechnology, 11421 Saskatchewan Drive, Edmonton, Alberta T6G 2M9, Canada. [3]Electrical and Computer Engineering, University of Manitoba, 75 Chancellor's Circle, Winnipeg, Manitoba R3T 5V6, Canada. *Corresponding author. E-mail: mark.freeman@ualberta.ca

a "mixing torque" proportional to the susceptibility in Eq. 1 (*8*).

$$\tau_y(f_{\mathrm{mech}}) = \frac{\mu_0 V H_1 H_2}{2}\chi_t(f_1) \qquad (2)$$

This simple analysis assumes that the spin-lattice relaxation time of the specimen is shorter than the oscillation period of the torque sensor (allowing for magnetic-to-mechanical torque conversion), but otherwise the choice of f_{mech} is unconstrained by sample properties ($f_{\mathrm{res}}, \Delta f$). Higher-order effects will arise when the effective magnetic fields caused by mechanical rotation become non-negligible, at much larger peak angular speeds of the torque sensor (*8*).

The amplitude of the resulting mechanical oscillation is measured by optical interferometry with lock-in amplification at f_{mech}. Spectroscopy is performed by sweeping f_1 through f_{res} while keeping the frequency offset of f_2 constant at f_{mech}, as illustrated by Fig. 1B. There is no requirement for f_1 and f_2 to be separated by more than the resonance linewidth or, in other words, for f_{mech} to be greater than Δf. In situations where $\mathbf{H_2}$ also drives spin resonances, the mixing torque remains zero because $\mathbf{H}_1$ is parallel to the torsion axis. RF fields are applied using transmission lines on a custom, multilayer circuit board. All RF tones are generated using an ultrahigh multifrequency lock-in amplifier (*10*). The measurement scheme and field profiles of the transmission lines are described further in the supplementary materials, figs. S1 to S3 (*8*).

The ferrimagnetic insulator yttrium iron garnet (YIG) is an ideal test material for TMRS. YIG has the narrowest known ferro/ferri-magnetic resonance line (FMR is the common expression for ESR in materials with spontaneous magnetic order yielding a net moment) (*11*, *12*). Mesoscopic YIG structures have a rich resonance spectrum. The magnetic hysteresis exhibited by YIG permits demonstration of the simultaneous capability to measure the net moment of the sample while performing resonance spectroscopy in a microfabricated device. This is of immediate interest in the context of the resurgence of YIG for spin-based device applications (*13*–*17*). Figure 1C shows the mixing torque signal from an f_{res} = 517 MHz FMR mode of a microscopic disk of YIG in an applied field $\mathbf{H}_0$ = 70.5 kA/m. The field geometry for the resonance mode in Fig. 1C (shown in Fig. 1A) is the same as for NMR and electron paramagnetic resonance, but the $f(H)$ dependence is nonlinear, modified by the strong dipolar fields in the ferrimagnet (*8*, *18*).

The monocrystalline YIG disk was sculpted from a thick-film epitaxial starting crystal (*19*) by using a focused ion beam milling procedure designed to minimize ion beam modification of the magnetism of the material. The final structure was 450 ± 10 nm thick and had a radius of 550 ± 30 nm on account of the slightly tapered sidewalls imprinted by the intensity profile of the ion beam. An electron micrograph (Fig. 2A) was taken at the penultimate step of disk fabrication. Details of the fabrication procedure are included in the supplementary materials, fig. S4 (*8*). The monocrystalline nature of the focused ion beam (FIB)–sculpted mesoscopic YIG was confirmed by 300-kV electron diffraction from a YIG reference lamella FIB-milled from the same bulk substrate (Fig. 2B). The hexagonal Laue pattern represents a cubic structure in the (111) crystal orientation. After mounting to the mechanical resonator, the crystal (110) orientation was along $\hat{x}$, perpendicular to the torsion bar axis.

The configuration of magnetization within a mesoscopic magnet is spatially nonuniform but has a well-defined spin texture. The mesoscopic disk has a fully demagnetized ground state at $\mathbf{H}_0 = 0$, a circularly symmetric magnetic vortex texture (*20*, *21*). As a function of the magnetic

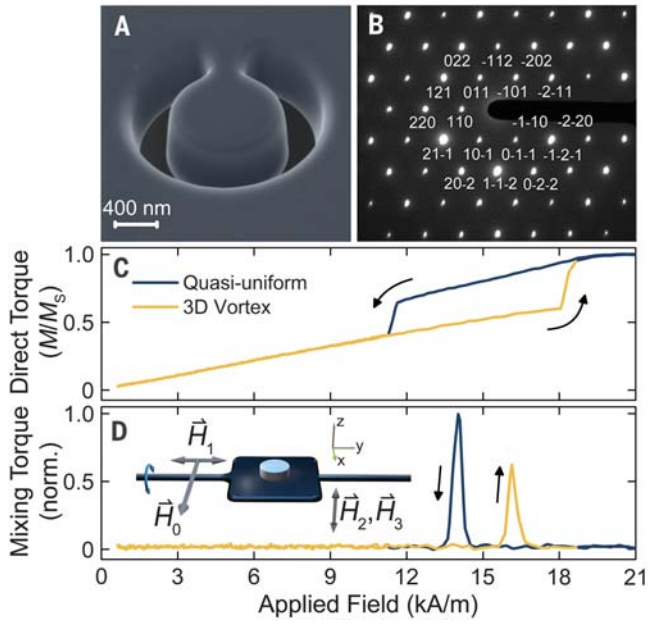

Fig. 2. Simultaneous acquisition of net moment and dynamic response hysteresis loops. (**A**) Focused ion beam–defined microdisk in a bulk YIG crystal before nanomanipulation onto a torsional mechanical resonator [see (*8*) for fabrication procedure]. (**B**) Electron diffraction pattern of a reference YIG lamella milled from the same crystal. The (*h*, *k*, *l*) crystal plane indices are indicated, consistent with the (111) orientation (the zone axis normal to the disk surface). (**C** and **D**) The net moment signal (C) was captured by supplying and lock-in demodulating a small RF drive ($\mathbf{H}_3$ = 23 A/m peak-to-peak) off the mechanical resonance peak, f_3 = 1.8031 MHz, in the *z* direction, whereas $\mathbf{H}_0$ was swept in the *x* direction. The field configuration is shown schematically in the inset of (D). The sweep in (D) is demodulated at f_{mech} = 1.8037 MHz , whereas $\mathbf{H}_1$ was driven at f_1 = 100.1000 MHz with a peak-to-peak amplitude of 78 A/m, and $\mathbf{H}_2$ = 190 A/m at f_2 = 101.9037 MHz. The two colors represent different spin textures, quasi-uniform (dark blue) and 3D vortex (gold).

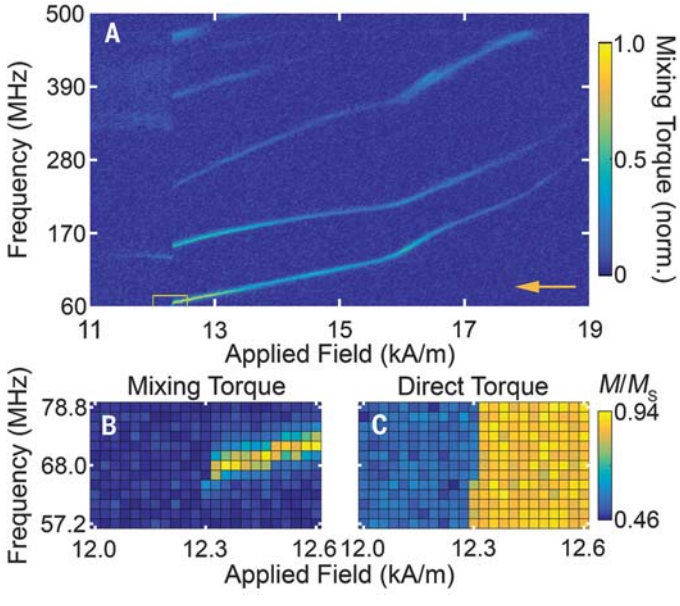

Fig. 3. Torque-mixing magnetic resonance spectroscopy of the YIG microdisk. (**A**) The spectrum is acquired while sweeping the field from high to low, with $\mathbf{H}_1$ = 78 A/m and $\mathbf{H}_2$ = 190 A/m, as in Fig. 2. The field and frequency step sizes are 26.5 A/m and 1.8 MHz, respectively. The arrow represents the direction of the field sweep. (**B**) Enlargement of region outlined in (A). Each pixel represents a data point. (**C**) The simultaneously acquired net magnetic moment measured with $\mathbf{H}_3$ = 23 A/m. The abrupt transitions in both the mixing torque (B) and direct torque (C) signals between the fifth and sixth frequency steps from the bottom at field $\mathbf{H}_0$ = 12.3 kA/m represents the resonantly assisted vortex nucleation event.

field $\mathbf{H}_0$, there are abrupt, hysteretic (irreversible) transitions between vortex textures and quasi-uniform states as one or the other configuration becomes favored energetically. The spin textures are discussed further in (*8*).

The magnetizing-demagnetizing behavior of the YIG disk as a function of $\mathbf{H}_0$ along $\hat{x}$ is shown in Fig. 2C. Because $\mathbf{H}_0$ was not parallel to the torsion axis, the net moment could be recorded simultaneously through torque generated by an additional magnetic tone along $\hat{z}$: $\mathbf{H}_3$ (see Fig. 2D), at a frequency f_3 slightly detuned from f_{mech} but still intersecting the mechanical resonance peak. The two steep transitions in the measured net moment of the disk are magnetic vortex state nucleation at 11.5 kA/m during the field sweep-down and vortex annihilation at 18 kA/m during the field-increasing half of the measurement [reminiscent of the two-dimensional (2D) vortex behavior of thin permalloy disks (*20*, *21*)]. The YIG disk was always in a 3D vortex state below the nucleation field.

Magnetic resonance spectroscopy often is performed at fixed frequency, sweeping the strength of $\mathbf{H}_0$. An example of fixed-frequency TMRS is shown in Fig. 2D, where the frequency f_1 = 100.1000 MHz of the RF drive field $\mathbf{H}_1$ is chosen such that the vortex and quasi-uniform textures both exhibit a resonance (at different values of $\mathbf{H}_0$). The simultaneous dc moment acquisition distinguished unambiguously the magnetic resonances of the two different spin textures.

A spectroscopic map of spin resonances is presented in Fig. 3 for $\mathbf{H}_0$ along $\hat{x}$, corresponding to the upper branch of Fig. 2C (sweeping the field from high to low). A ladder of modal oscillations was observed (*22*), akin to a standing-wave resonance hierarchy wherein each new mode adds a node. The field strength was stepped down in 26.5 A/m increments during this measurement, and at each field step the frequency was swept from low to high. The data of Fig. 3A exhibit decreasing mode amplitudes toward higher field and higher mode number. Two factors contributed to this trend: As the texture became more uniform, a smaller effective volume from each mode contributed to the torque, and higher-order modes had less net coupling to a spatially uniform $\mathbf{H}_1$ drive field. The rich experimental phase diagram provides many features that may be exploited with complementary numerical simulation. For instance, the slope changes common to all ladder modes in Fig. 3A near 16 kA/m indicate a metastable intermediate spin texture involved in the vortex nucleation process. In simulations, all modes show a similar, although more abrupt (hysteretic), pair of jumps where the texture transitions from the quasi-uniform state to a metastable two-vortex state before the creation of the single-vortex state (*8*).

The complex nature of nucleation processes presented an experimental challenge. However, simultaneous monitoring of the net magnetic moment of the sample is a powerful advantage of the TMRS method. Fig. 3, B and C, show individual pixels of the field versus frequency map in the vicinity of the vortex nucleation transition from both torque amplitude channels: the mixing (from $\mathbf{H}_1$ and $\mathbf{H}_2$, the transverse RF susceptibility) torque and the direct (from $\mathbf{H}_3$, net moment) torque. Upon the transition to the 3D vortex state (12.3 kA/m), the quasi-uniform spin texture resonances abruptly ended and those corresponding to the new configuration appeared. Vortex state nucleation was triggered as f_1 stepped up onto the first resonance mode, in this instance. This manipulation was reproducible (the measurement was repeated 36 times), showing that the method is a natural tool for the study of resonantly assisted transitions in mesoscopic magnets (*23*, *24*). Beyond the use of the exquisite mode fingerprint and the simultaneous dynamic and static capabilities of TMRS to study coarse transitions, the sensitivity of the technique also lends itself to study of extremely small effects.

Nanostructures display distinctive magnetizing-demagnetizing fingerprints on account of unavoidable imperfections arising during their fabrication. The spin-dynamical modes are excitations in the presence of this imperfect backdrop. TMRS can probe this connection directly. In a 3D vortex (*25*), the core diameter increased toward the middle of the disk (fig. S6E), lowering the core's energy density. The high-energy density ends of the 3D core interacted with small-scale fabrication-induced imperfections near the disk surfaces, resulting in frequency and amplitude variations of the so-called gyrotropic modes (*26*), the principal excitations of the vortex state in which the core orbits its equilibrium position.

A TMRS map of the 3D vortex state of the YIG disk (Fig. 4A) shows the gyrotropic frequency variability on the order of 10% as the field changed by a few kiloamperes per meter, an effect we attribute to imperfections. An even larger relative variation of modal amplitude supports this interpretation. At the same time, the YIG magnetizing curve exhibited only subtle slope (differential susceptibility) variations, near the resolution of the present measurements. Figure 4B shows a rendering of the simultaneously measured information, with the mixing torque from Fig. 4A averaged within a 9-MHz window around the peak and plotted together with net moment versus field (averaged over the full frequency range). The underfill color represents the frequency of the peak signal. The same qualitative variations in mode amplitude, frequency, and differential susceptibility are reproduced in simulation through the introduction of very shallow grooves at one surface (*8*). The other trend, the red shift of resonance frequency as the annihilation field is approached from below, is a separate effect, not related to disorder (*27*). The

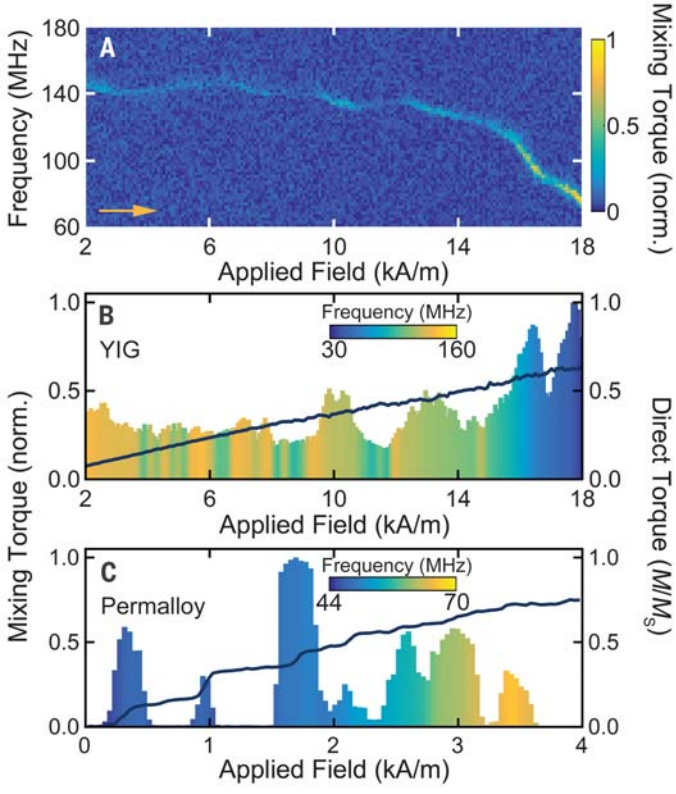

Fig. 4. Low field TMRS for the YIG and permalloy disks in the vortex state. (**A**) The resonances correspond to the first-order vortex core gyration [the core ends at the top and bottom surfaces precess out of phase (*8*)]. The frequency step size is 1.8 MHz, and the field steps are 45 A/m. The arrow indicates the field sweep direction. The RF drive amplitudes are $\mathbf{H}_1$ = 78 A/m and $\mathbf{H}_2$ = 190 A/m. (**B**) Averaged mixing torque (left axis) of the YIG disk from (A), plotted with the simultaneously acquired net magnetic moment (right axis). (**C**) Averaged mixing torque (left axis) and simultaneously acquired net magnetic moment (right axis) for a polycrystalline permalloy disk deposited onto a torque sensor. The 2D vortex gyrotropic mode vanishes at numerous field values, corresponding to where the core is strongly pinned along the pathway it follows as it is pushed from the center toward the edge of the disk with increasing applied field. The colors of the underfills represent the peak frequencies of the signals [see inset color bars in (B) and (C)].

quasi-uniform spin modes, in contrast, are more "internal" to their respective textures and were not appreciably affected by roughness because they did not exhibit energy densities highly localized at the surface, as shown in fig. S8 (*8*).

The direct correlation of spin dynamics with complementary information in the magnetization hysteresis curves typically has been an experimental challenge; most techniques yield high-quality, interpretable observations of one or the other. Thin-film polycrystalline permalloy provides another dramatic example of the capability of TMRS to report both on the equilibrium landscape and on the nonequilibrium response. Averaged torque spectra of the vortex gyrotropic mode in a 15-nm-thick, 2-μm-diameter permalloy disk [deposited onto a torque sensor, as described in (*28*)] are shown in Fig. 4C. The drop-outs of the resonance signal correlated with plateaux of reduced differential susceptibility and correspond to applied field ranges where the vortex core is strongly pinned by grain boundary–dominated magnetic disorder (*29*, *30*). Between these regions, the core could be driven to large amplitude gyration, generating strong resonance signals (*31*).

TMRS provides excellent coupling to small specimens, resulting in high spin sensitivities (*8*). The simplicity of the technique is owed to the recent development of multi-ultrahigh frequency lock-in instrumentation (*10*) and to the natural compatibility of RF transmission line actuators (*8*) with on-chip nanomechanical torque sensors. Straightforward processing to integrate samples onto sensors (*28*, *32*) opens TMRS to a wide variety of materials. The approach is fully broadband, is massively scalable through microfabrication, and has intriguing potential for low-frequency work where induction signals become very small, per Faraday's law. The amplitude of the TMRS torque is frequency-independent.

In addition to the capabilities of simultaneous monitoring of equilibrium net magnetization, detection of the transverse RF moment in TMRS opens the door to porting methods of pulse magnetic resonance to torque-detection platforms. Torque spectroscopy will find utility as a vehicle to explore phenomena in emerging spin-mechanical physics (*33*, *34*). Broadband TMRS forms a foundation for nanomagnetism lab-on-a-chip applications for highly sensitive, noninvasive, and rapid prototyping of individual mesoscopic elements, and it presents another functional method to create and read out dynamic spin-based devices.

REFERENCES AND NOTES

1. H. J. Mamin *et al.*, *Nano Lett.* **9**, 3020–3024 (2009).
2. D. Rugar *et al.*, *Nat. Nanotechnol.* **10**, 120–124 (2015).
3. J. A. Sidles *et al.*, *Rev. Mod. Phys.* **67**, 249–265 (1995).
4. D. Rugar *et al.*, *Science* **264**, 1560–1563 (1994).
5. Z. Zhang, P. C. Hammel, M. Midzor, M. L. Roukes, J. R. Childress, *Appl. Phys. Lett.* **73**, 2036 (1998).
6. G. Alzetta, E. Arimondo, C. Ascoli, A. Gozzini, *Nuovo Cim.* **52**, 392–402 (1967).
7. C. Ascoli *et al.*, *Appl. Phys. Lett.* **69**, 3920 (1996).
8. Supplementary materials are available on *Science* Online.
9. F. Bloch, W. W. Hansen, W. Packard, *Phys. Rev.* **70**, 474–485 (1946).
10. Zurich Instruments, Zurich, Switzerland; model UHF lock-in amplifier with MF and MOD options (www.zhinst.com).
11. L. D. Landau, E. M. Lifshitz, . *Phys. Zeitschr. Sow.* **8**, 153 (1935).
12. J. Griffiths, *Nature* **158**, 670–671 (1946).
13. T. Kikkawa *et al.*, *Phys. Rev. Lett.* **110**, 067207 (2013).
14. B. Heinrich *et al.*, *Phys. Rev. Lett.* **107**, 066604 (2011).
15. J. Flipse, F. L. Bakker, A. Slachter, F. K. Dejene, B. J. van Wees, *Nat. Nanotechnol.* **7**, 166–168 (2012).
16. C. Hahn *et al.*, *Phys. Rev. Lett.* **111**, 217204 (2013).
17. A. A. Serga, A. V. Chumak, B. Hillebrands, *J. Phys. D Appl. Phys.* **43**, 264002 (2010).
18. C. Kittel, *Phys. Rev.* **71**, 270–271 (1947).
19. Shin Etsu Chemical Corporation, Tokyo, Lot Number SEW-3571 (www.rare-earth.jp).
20. R. P. Cowburn, D. K. Koltsov, A. O. Adeyeye, M. E. Welland, D. M. Tricker, *Phys. Rev. Lett.* **83**, 1042–1045 (1999).
21. M. Rahm *et al.*, *Appl. Phys. Lett.* **82**, 4110 (2003).
22. F. Guo, L. M. Belova, R. D. McMichael, *Phys. Rev. Lett.* **110**, 017601 (2013).
23. G. Woltersdorf, C. H. Back, *Phys. Rev. Lett.* **99**, 227207 (2007).
24. Y. Nozaki *et al.*, *Appl. Phys. Lett.* **91**, 082510 (2007).
25. S. Wintz *et al.*, *Phys. Rev. Lett.* **110**, 177201 (2013).
26. J. P. Park, P. Eames, D. M. Engebretson, J. Berezovsky, P. A. Crowell, *Phys. Rev. B* **67**, 020403 (2003).
27. O. V. Sukhostavets *et al.*, *Phys. Rev. Lett.* **111**, 247601 (2013).
28. Z. Diao *et al.*, *J. Vac. Sci. Technol. B* **31**, 051805 (2013).
29. T. Uhlig *et al.*, *Phys. Rev. Lett.* **95**, 237205 (2005).
30. J. A. J. Burgess *et al.*, *Science* **339**, 1051–1054 (2013).
31. T. Y. Chen, Magnetic vortex dynamics: Non-linear dynamics, pinning mechanisms, and dimensionality crossover, Ph.D. thesis, University of Minnesota (2012).
32. J. E. Losby *et al.*, *J. Appl. Phys.* **111**, 07D305 (2012).
33. S.-H. Lim *et al.*, *Europhys. Lett.* **105**, 37009 (2014).
34. S. T. B. Goennenwein, G. E. W. Bauer, S. Maekawa, Eds., *Solid State Commun.* **198** (2014). Special Issue: Spin Mechanics.

ACKNOWLEDGMENTS

The authors very gratefully acknowledge support from Natural Sciences and Engineering Research Council Canada (RGPIN 170827-2010, RGPIN 04239, and RGPIN 2014-04796), Canada Research Chairs (950206567), Alberta Innovates Technology Futures (iCiNano), National Institute for Nanotechnology (NINT A1-004906), Canada Foundation for Innovation (20314), Manitoba Research and Innovation Fund, and Canadian Microelectronics Corp. The nanomechanical torque sensors were fabricated at the University of Alberta NanoFab and NINT. Electron diffraction was performed by P. Li at the NINT microscopy center. D. Fortin assisted in the design and rendering of Fig. 1A. We thank J. P. Davis and R. Lockwood for critical reading of the manuscript, R. E. Wasilyshen for useful conversations, and anonymous referees for constructive suggestions. The data described in the paper are available upon request.

SUPPLEMENTARY MATERIALS

www.sciencemag.org/content/350/6262/798/suppl/DC1
Materials and Methods
Supplementary Text
Figs. S1 to S8
References (*35*–*50*)

16 August 2015; accepted 9 October 2015
10.1126/science.aad2449

GAMMA-RAY ASTRONOMY

An extremely bright gamma-ray pulsar in the Large Magellanic Cloud

The Fermi LAT Collaboration*†

Pulsars are rapidly spinning, highly magnetized neutron stars, created in the gravitational collapse of massive stars. We report the detection of pulsed giga–electron volt gamma rays from the young pulsar PSR J0540–6919 in the Large Magellanic Cloud, a satellite galaxy of the Milky Way. This is the first gamma-ray pulsar detected in another galaxy. It has the most luminous pulsed gamma-ray emission yet observed, exceeding the Crab pulsar's by a factor of 20. PSR J0540–6919 presents an extreme test case for understanding the structure and evolution of neutron star magnetospheres.

The first pulsar was discovered in 1967 as a puzzling celestial source of periodic radio pulses. Nearly 2500 pulsars have since been detected, mostly in the Milky Way but also in other nearby galaxies, and their characteristic pulsed emission has been observed across the electromagnetic spectrum. The energy source for emission from pulsars is the rotation of a magnetized neutron star. The mechanism is radiation by particles accelerated by intense electric fields in the neutron star magnetosphere. The pulsar spins with period P, and the observed rate at which it slows down, $\frac{dP}{dt} = \dot{P}$, sets the scale of the power reservoir for particle acceleration and emission processes. Spin-down power is $\dot{E} = 4\pi^2 I\dot{P}/P^3$, where I denotes the neutron star moment of inertia, taken to be 10^{45} g cm^2 (*1*), which roughly corresponds to a solid sphere of 10 km radius and the mass of the Sun.

The Large Area Telescope (LAT), an imaging instrument on the Fermi satellite sensitive to gamma rays with energies of 20 MeV to 300 GeV (*2*), has detected gamma-ray pulsations from more than 160 pulsars (*3*, *4*). Gamma-ray pulsars have $\dot{E} > 10^{33}$ erg s^{-1}, and a large fraction (>30% in many cases) of their spin-down power is converted into gamma-ray luminosity L_γ. In contrast, radio emission represents a negligible fraction of the total energy output (*3*). Gamma-ray observations thus probe the sites and processes of particle acceleration and radiation in pulsars. Candidate emission regions range across the magnetosphere out to the "light cylinder," where corotation with the neutron star would reach the speed of light (*5*–*7*). In these regions, curvature or synchrotron radiation from accelerated electrons initiates electromagnetic cascades by interacting with the strong magnetic field or with ambient photons; the electron-positron pairs

*All authors with their affiliations appear at the end of this paper.
†Corresponding author. E-mail: pierrick.martin@irap.omp.eu (P.M.); lucas.guillemot@cnrs-orleans.fr (L.G.); francis.e.marshall@nasa.gov (F.M.)

produced are accelerated and radiate in turn, giving rise to further pairs. Emission may also originate in the pulsar's plasma wind, beyond the light cylinder (*8*).

Discriminating between emission scenarios requires spectra and light curves in various wavebands for pulsars with different ages, magnetic field strengths, and viewing geometries. Few pulsars younger than several thousand years are known. The pulsar in the Crab supernova remnant is the best studied and was the most powerful known in pulsed gamma rays (*9*). The Crab pulsar has $\dot{E} = 4.5 \times 10^{38}$ erg s^{-1}. Only one known pulsar has a larger spin-down power—PSR J0537–6910, with $\dot{E} = 4.9 \times 10^{38}$ erg s^{-1}—whereas PSR J0540–6919, only 16 arc min away, has the third highest, $\dot{E} = 1.5 \times 10^{38}$ erg s^{-1}. Both of the latter are located in the Large Magellanic Cloud (LMC), a satellite galaxy of the Milky Way at a distance $d \sim 50$ kpc (*10*). PSR J0537–6910 is a 16-ms pulsar associated with the ~5000-year-old supernova remnant LHA 120-N 157B (*11*, *12*), whereas PSR J0540–6919 is a 50-ms pulsar associated with the ~1140-year-old supernova remnant SNR 0540-69.3 (*13*–*15*). Although these two pulsars are of comparable age and energetics, their gamma-ray behavior appears to be markedly different. This paper reports the detection of gamma-ray pulsations from PSR J0540–6919 and an upper limit on gamma-ray pulsations from PSR J0537–6910.

Fermi-LAT predominantly operates in all-sky survey mode; hence, the LMC has been observed regularly since launch. Gamma-ray emission from the LMC is particularly prominent near the Tarantula nebula (30 Doradus) (*16*), a very active star-forming region that hosts extremely massive stars (*17*, *18*). PSR J0537–6910 and PSR J0540–6919 lie in this area, but until now, neither could be identified as discrete gamma-ray sources. Now, more than six times more data are available as compared with the earlier Fermi-LAT study (*16*), and the recent revision of LAT event reconstruction, called Pass 8, substantially enhanced the sensitivity of LAT data analyses (*19*). We thus revisited the gamma-ray emission from the LMC, and the 30 Doradus region in particular.

We analyzed Pass 8 events from 75 months of Fermi-LAT all-sky survey observations (*20*). The gamma-ray emission from the LMC is shown in Fig. 1, after subtracting fitted models of the Galactic foreground emission, an isotropic background, and pointlike sources outside the LMC. The improved angular resolution with increasing gamma-ray energy makes two pointlike sources coincident with the pulsars stand out above 2 GeV.

The source coincident with PSR J0540–6919 is detected with a statistical significance of 17σ. Its photon spectrum is well described by a power law with exponential cutoff, which is typical of gamma-ray pulsars (*3*). To search for pulsations, we built a rotation ephemeris using Rossi X-ray Timing Explorer (RXTE) (*21*) observations recorded between modified Julian day 54602 (16 May 2008) and 55898 (3 December 2011), shortly before the end of the RXTE mission (table S1). We phase-folded the gamma-ray data from the first 3.5 years of the *Fermi* mission corresponding to the ephemeris. We used the LMC emission model to assign each photon the probability that it originated from PSR J0540–6919, on the basis of reconstructed positions and energies and the instrument response functions (*22*). The probability-weighted $E > 100$ MeV gamma-ray pulse profile for probabilities >0.1 is shown in Fig. 2. The weighted H test parameter (*22*, *23*) is 63.5, corresponding to a significance of 6.8σ, making this the first extragalactic gamma-ray pulsar.

Time-averaged gamma-ray emission from the source coincident with PSR J0537–6910 is detected with significance 11σ. Its spectrum is consistent with a simple power law with photon index 2.1 ± 0.1 extending to >50 GeV without evidence for a cutoff. A weighted phase-fold of the LAT data-based on an RXTE ephemeris limited any pulsed emission to significance <1σ (table S2). The 95% confidence level upper limit on the 0.1 to 10 GeV pulsed luminosity for this pulsar is 1.9×10^{35} erg s^{-1}. This and the lack of a spectral cutoff suggest that strongly pulsed emission is at most a small fraction of the total signal from the source. The gamma-ray signal may instead result from the superposition of weakly modulated pulsar emission and radiation from the pulsar wind nebula and the supernova remnant, in unknown proportions.

The x-ray pulse profile for PSR J0540–6919 is also shown in Fig. 2, obtained by integrating all the RXTE data used to build the timing solution. The profile matches previous results (*24*). We evaluated the optical light curve using the RXTE ephemeris to fold data from the Iqueye photometer mounted on the European Southern Observatory 3.6-m New Technology Telescope (NTT) in January and December 2009 (*25*). We also show a radio profile formed from the sum of 18 bright giant pulses recorded at the Parkes telescope at 1.4 GHz in August 2003 (*26*). Emission components from radio to gamma rays are aligned, but the shape of the pulse varies over the different

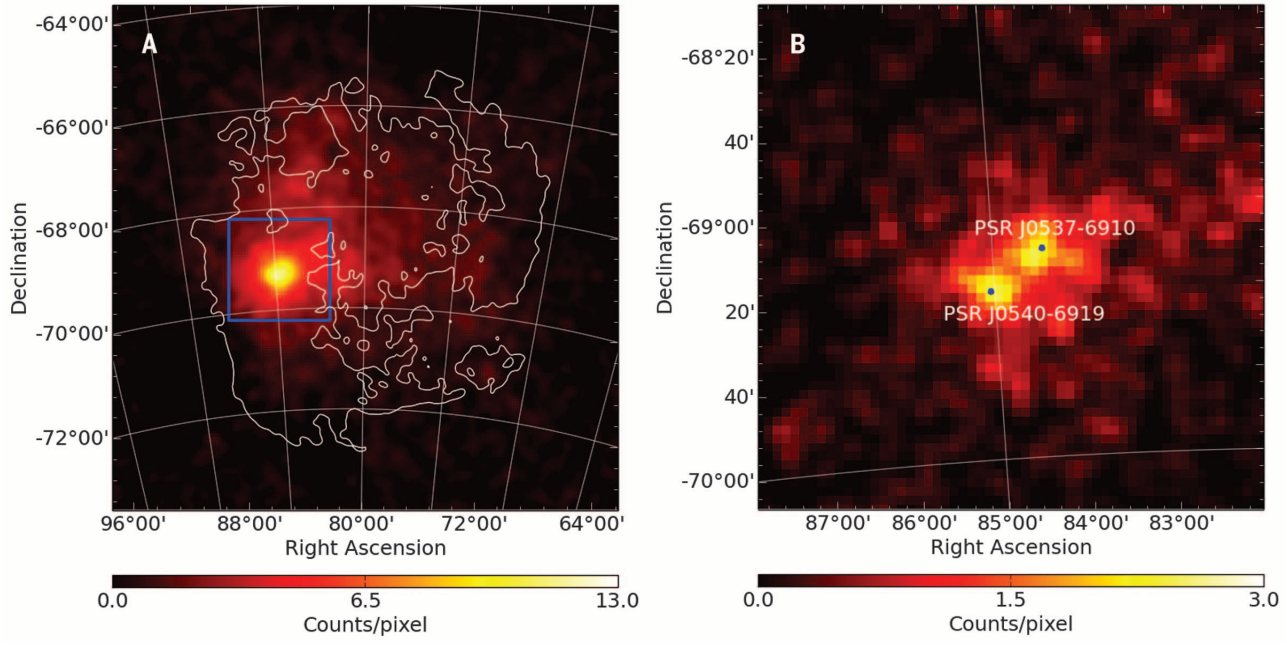

Fig. 1. Sky maps of the LMC. (**A**) 0.2 to 200 GeV gamma-ray emission in a 10° by 10° region encompassing the LMC. The map was smoothed by using a Gaussian kernel with σ = 0.2°. Emission is strongest around 30 Doradus (approximately delimited by the blue box) but also fills much of the galaxy. Contours show the atomic gas distribution. (**B**) 2 to 200 GeV gamma-ray emission in a 2° by 2° region around 30 Doradus. The map was smoothed by using a Gaussian kernel with σ = 0.1°. Better angular resolution at higher energies resolves two components coincident with PSR J0540–6919 and PSR J0537–6910, whose locations are indicated as blue dots. Both maps are given in J2000 equatorial coordinates.

bands. The radio profile exhibits two narrow peaks separated by $\Delta \sim 0.25$ in pulse phase. This double-peak pattern is still visible on top of a broader component in the optical profile. Structures in the x-ray and perhaps gamma-ray profiles are reminiscent of the double radio peaks separated by $\Delta \sim 0.25$, but both profiles are consistent with a single bump spanning the interval between the radio peaks. In outer-magnetosphere models, the pulse peak profiles are sensitive to the magnetic geometry. In the classical vacuum "outer gap" model (*5*), pulse separations as small as $\Delta = 0.25$ occur for high-$\dot{E}$, narrow-gap pulsars when the spin-axis viewing angle ζ is >80° and the magnetic inclination α is <30° (*27*). Models with partly resistive magnetospheres and emission extending beyond the light cylinder point to $\zeta \approx 60°$ and $\alpha \approx 30°$, but differing resistivity prescriptions may allow larger ζ (*7*). For such geometry, the low-altitude classical radio emission would not be observable, leaving only the high-altitude giant pulse component.

The signal above the background estimate in Fig. 2 suggests a steady component of the gamma-ray emission from the direction of PSR J0540–6919. Likelihood analysis of the data in the off-pulse phase interval 0.3 to 0.8 shows a significant (~5σ) point source at the position of PSR J0540–6919. The spectrum is consistent with that of the full phase interval but may be almost as well described by a single power law (fig. S1). We cannot currently distinguish whether this represents an unpulsed magnetospheric component, emission from the associated pulsar wind nebula LHA 120-N 158A or from the surrounding supernova remnant SNR 0540–69.3, or residual emission from the LMC itself. Comparing with the flux in the on-pulse phase interval, we estimate that the pulsed component is ≈75% of the total. The choice of the off-pulse phase interval, hence the unpulsed flux estimate, is conservative because it clearly includes pulsed optical and x-ray emission (Fig. 2).

The phase-averaged spectrum of PSR J0540–6919 is shown in Fig. 3. The photon spectrum is well described by a power law with photon index 2.2 ± 0.1 and exponential cutoff at $E_{cut} = 7.5 \pm 2.6$ GeV. This photon index follows the trend of increasing index with $\dot{E}$ described in (*3*). This correlation can be explained by stronger pair formation activity in high-$\dot{E}$ pulsars, reprocessing the radiation to lower energies and leading to steep radiating particle spectra. PSR J0540–6919 has the second largest magnetic field at the light cylinder of any gamma-ray pulsar known, after the Crab pulsar, with $B_{LC} = 4\pi^2 (I\dot{P})^{1/2} (c^3 P^5)^{-1/2} = 3.62 \times 10^5$ G. Our E_{cut} measurement favors the trend of increasing cutoff energy as a function of B_{LC}, also noted in (*3*), suggesting emission originating from the outer magnetosphere of the neutron star.

The total phase-averaged luminosity of PSR J0540–6919 above 100 MeV is $L\gamma = 4\pi f_\Omega h d^2 = 7.6 \times 10^{36} (d/50\ \text{kpc})^2$ erg s^{-1}, where $h = (2.6 \pm 0.3) \times 10^{-11}$ erg cm^{-2} s^{-1} is the energy flux, and the geometry-dependent beaming correction factor is $f_\Omega \sim 1$ for young pulsars with the most probable viewing angle of ~90° (*27*), which is consistent with the geometrical setting derived above. As stated above, ≈75% of the total luminosity is pulsed and may be safely attributed to the pulsar, 5.7×10^{36} erg s^{-1}. The systematic uncertainties in the spectrum and luminosity of the source due to the complete LMC emission model were found to be smaller than the statistical uncertainties (*28*). And whereas other pulsars' luminosities can be severely affected by distance uncertainties (for example, 25% for the Crab pulsar), for PSR J0540–6919, the distance to the LMC is known to 2% accuracy (*10*).

PSR J0540–6919 is often called the "Crab's twin" because they have similar magnetic field strengths, rotation rates, and ages, so a comparison is in order. The Crab pulse profile has two peaks, phase-aligned from the radio to the gamma-ray band, whereas PSR J0540–6919 has a broad gamma-ray pulse straddling the phase-range of the two narrow radio peaks, with structures in

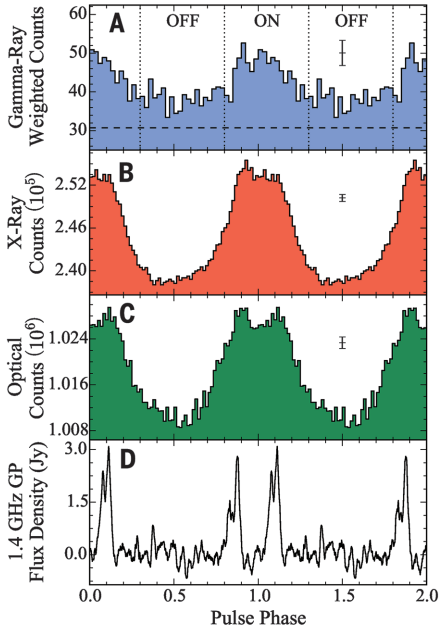

Fig. 2. Pulse profiles for PSR J0540–6919. (**A**) Probability-weighted LAT count profile. The horizontal dashed line approximates the background level. Vertical lines indicate the on- and off-pulse regions used for the LAT spectral analysis. (**B**) RXTE x-ray integrated count profile. (**C**) NTT optical count profile. (**D**) Parkes radio flux profile from summing 18 bright giant radio pulses at 1.4 GHz. Two complete cycles are shown. The error bars in the top three panels represent the median phase bin errors.

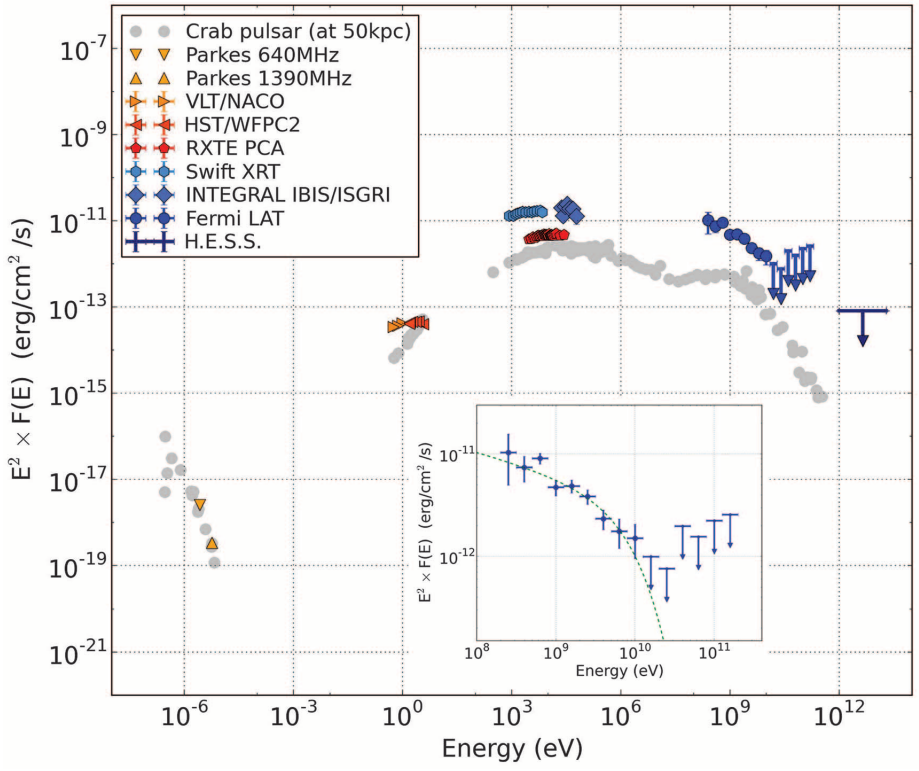

Fig. 3. Spectral energy distribution of PSR J0540–6919. Pulsed radio data are from (*26*, *39*). Extinction-corrected phase-averaged near-infrared and optical fluxes are from (*40*, *41*). X-ray fluxes are from (*24*), including pulsed RXTE data and total spectra for the pulsar and its nebula from Swift and INTEGRAL. Tera–electron volt upper limit is from (*33*). The LAT data points correspond to the phase-averaged emission, which includes an estimated 25% of unpulsed emission. Crab pulsar phase-averaged data rescaled to a 50 kpc distance are shown for comparison in light gray (*9*). (Inset) LAT data fit to a power law with an exponential cutoff.

the optical and x-ray reminiscent of the radio peaks. The similarity in their radio behavior is particularly meaningful because for both pulsars, the radio emission is dominated by so-called "giant pulses," sporadic radio bursts with submicrosecond durations and fluxes with a power-law distribution extending to $>10^3$ times the average value (*29*). In (*26*), it is suggested that the colocation of the giant pulses with high-energy emission occurs in pulsars with high magnetic fields at the light cylinder and very robust and extensive outer-magnetosphere pair production. Before this work, only six other pulsars showed giant pulse emission associated with strong optical, x-ray, or gamma-ray components (*30*). The discovery of gamma-ray emission from PSR J0540–6919 provides a new look at these rare sources.

PSR J0540–6919 and the Crab also share many spectral similarities, as illustrated in the radio-to–gamma ray spectral energy distribution (Fig. 3). With large powers in both pulsed x-rays and gamma rays and the absence of a strong high-energy cutoff, PSR J0540–6919 is similar to the Crab and unlike most middle-aged pulsars, where giga–electron volt gamma-ray power dominates. Both characteristics may originate from the higher pair densities that allow synchrotron self-Compton emission to dominate and produce higher-energy pulsations. It remains to be seen whether PSR J0540–6919 follows the Crab in exhibiting a high-energy tail of pulsed emission, extending far above E_{cut} and likely attributable to inverse Compton scattering (*31*, *32*). The source is currently undetected in tera–electron volt gamma rays (*33*) but may be in reach of future instruments, such as the Cherenkov Telescope Array.

Yet whereas the radio, optical, and x-ray luminosities of PSR J0540–6919 and the Crab are within a factor of ~2, PSR J0540–6919 is much brighter in gamma rays. Its isotropic pulsed gamma-ray luminosity is ~20 times more than the Crab pulsar's, $L_\gamma = 3.2 \times 10^{35}(d/2\ \mathrm{kpc})^2$ erg s^{-1} (*3*). PSR J0540–6919's pulsed luminosity remains larger than that of the Crab pulsar even when including their intense x-ray emission: Combining the 2 to 10 keV and 20 to 100 keV pulsed flux measurements from (*24*) gives an integrated luminosity for PSR J0540–6919 of $L_{X+\gamma} \sim 9.7 \times 10^{36}(d/50\ \mathrm{kpc})^2$ erg s^{-1}, whereas it becomes $L_{X+\gamma} \sim 2.4 \times 10^{36}$ $(d/2\ kpc)$ erg s^{-1} for the Crab (*34*).

The contrast with PSR J0537–6910 is even more striking: It has more than three times greater spin-down power, but its pulsed gamma-ray luminosity may be at least 30 times less than that of PSR J0540–6919. This confirms that L_γ values can vary by more than an order of magnitude for a given $\dot{E}$ range (*3*). Misestimated distances and deviations from $f_\Omega = 1$ can account for only part of this difference. The magnetic inclination may play a considerable role, beyond its effect on the beaming (*35*, *36*).

As mentioned above, the pulse profile of PSR J0540–6919 suggests a high viewing angle of $\zeta > 80°$ and a low magnetic inclination of $\alpha < 30°$. Fits to *Chandra* observations of the pulsar wind nebulae shapes of PSR J0540–6919 and PSR J0537–6910 indicate that both pulsars have similar viewing angles of $\zeta \sim 90°$ (*37*). In such conditions, the nondetection of radio emission from PSR J0537–6910 implies either a high magnetic inclination and a radio luminosity at most half that of PSR J0540–6919, or a misaligned radio beam, hence a low magnetic inclination similar to PSR J0540–6919 (*38*). The former case would confirm the role of the magnetic inclination in the observed dispersion of L_γ; the latter case would mean that the large difference in pulsed luminosity between both pulsars does not stem from different geometries. Alternatively, the nondetection of pulsations from PSR J0537–6910 may imply a weakly modulated gamma-ray light curve. The "outer gap" model predicts such flat pulse profiles for $\zeta = 90°$, $\alpha = 15°$, and a narrow gap (*27*), a geometry quite similar to that inferred for PSR J0540–6919. Very similar ages, energetics, and geometries for PSR J0540–6919 and PSR J0537–6910 would therefore result in remarkable emission differences.

Our gamma-ray measurements of PSR J0540–6919 and PSR J0537–6910 offer a new look at the high-altitude accelerators in the magnetospheres of rare very young pulsars. They also have profound implications for our understanding of the high-energy emission from the LMC: ≈60% of the GeV flux density previously attributed to the 30 Doradus nebula (*16*) is now seen to be emission from PSR J0540–6919. With an additional ≈25% attributable to the source coincident with PSR J0537–6910, only a small fraction of the signal may originate in cosmic rays in 30 Doradus. This calls for further investigation of the relation between star-forming regions and the origin and transport of cosmic rays.

REFERENCES AND NOTES

1. D. R. Lorimer, M. Kramer, *Handbook of Pulsar Astronomy* (Cambridge Univ. Press, Cambridge, 2004).
2. W. B. Atwood *et al.*, *Astrophys. J.* **697**, 1071–1102 (2009).
3. A. A. Abdo *et al.*, *Astrophys. J.* **208** (suppl.), 17 (2013).
4. The Fermi/LAT Collaboration, https://confluence.slac.stanford.edu/display/GLAMCOG/Public+List+of+LAT-Detected+Gamma-Ray+Pulsars (2015).
5. K. S. Cheng, C. Ho, M. Ruderman, *Astrophys. J.* **300**, 500 (1986).
6. A. G. Muslimov, A. K. Harding, *Astrophys. J.* **606**, 1143–1153 (2004).
7. C. Kalapotharakos, A. K. Harding, D. Kazanas, *Astrophys. J.* **793**, 97 (2014).
8. J. Pétri, *Mon. Not. R. Astron. Soc.* **412**, 1870–1880 (2011).
9. R. Bühler, R. Blandford, *Rep. Prog. Phys.* **77**, 066901 (2014).
10. G. Pietrzyński *et al.*, *Nature* **495**, 76–79 (2013).
11. F. E. Marshall, E. V. Gotthelf, W. Zhang, J. Middleditch, Q. D. Wang, *Astrophys. J.* **499**, L179–L182 (1998).
12. Y. Chen *et al.*, *Astrophys. J.* **651**, 237–249 (2006).
13. F. D. Seward, F. R. Harnden Jr., D. J. Helfand, *Astrophys. J.* **287**, L19 (1984).
14. B. J. Williams *et al.*, *Astrophys. J.* **687**, 1054–1069 (2008).
15. T. Brantseg, R. L. McEntaffer, L. M. Bozzetto, M. Filipovic, N. Grieves, *Astrophys. J.* **780**, 50 (2014).
16. A. A. Abdo *et al.*, *Astron. Astrophys.* **512**, A7 (2010).
17. P. A. Crowther *et al.*, *Mon. Not. R. Astron. Soc.* **408**, 731–751 (2010).
18. N. R. Walborn *et al.*, *Astron. Astrophys.* **564**, A40 (2014).
19. W. Atwood *et al.*, 2012 Fermi Symposium proceedings—eConf C121028, http://arxiv.org/abs/1303.3514 (2013).
20. Materials and methods are available as supplementary materials on *Science* Online.
21. H. V. Bradt, R. E. Rothschild, J. H. Swank, *Astron. Astrophys.* **97** (Supp.), 355 (1993).
22. M. Kerr, *Astrophys. J.* **732**, 38 (2011).
23. O. C. de Jager, B. C. Raubenheimer, J. W. H. Swanepoel, *Astron. Astrophys.* **221**, 180 (1989).
24. R. Campana *et al.*, *Mon. Not. R. Astron. Soc.* **389**, 691–700 (2008).
25. S. Gradari *et al.*, *Mon. Not. R. Astron. Soc.* **412**, 2689–2694 (2011).
26. S. Johnston, R. W. Romani, F. E. Marshall, W. Zhang, *Mon. Not. R. Astron. Soc.* **355**, 31–36 (2004).
27. R. W. Romani, K. P. Watters, *Astrophys. J.* **714**, 810–824 (2010).
28. Fermi-LAT collaboration, http://arxiv.org/abs/1509.06903 (2015).
29. J. M. Cordes, N. D. R. Bhat, T. H. Hankins, M. A. McLaughlin, J. Kern, *Astrophys. J.* **612**, 375–388 (2004).
30. A. V. Bilous, T. T. Pennucci, P. Demorest, S. M. Ransom, *Astrophys. J.* **803**, 83 (2015).
31. VERITAS Collaboration *et al.*, *Science* **334**, 69–72 (2011).
32. M. Lyutikov, N. Otte, A. McCann, *Astrophys. J.* **754**, 33 (2012).
33. H.E.S.S. Collaboration, *Science* **347**, 406–412 (2015).
34. R. Willingale *et al.*, *Astron. Astrophys.* **365**, L212–L217 (2001).
35. L. Zhang, K. S. Cheng, Z. J. Jiang, P. Leung, *Astrophys. J.* **604**, 317–327 (2004).
36. G. Brambilla, C. Kalapotharakos, A. K. Harding, D. Kazanas, *Astrophys. J.* **804**, 84 (2015).
37. C.-Y. Ng, R. W. Romani, *Astrophys. J.* **673**, 411–417 (2008).
38. F. Crawford, M. McLaughlin, S. Johnston, R. Romani, E. Sorrelgreen, *Adv. Space Res.* **35**, 1181–1184 (2005).
39. R. N. Manchester, D. P. Mar, A. G. Lyne, V. M. Kaspi, S. Johnston, *Astrophys. J.* **403**, L29 (1993).
40. R. P. Mignani *et al.*, *Astron. Astrophys.* **515**, A110 (2010).
41. R. P. Mignani *et al.*, *Astron. Astrophys.* **544**, A100 (2012).

ACKNOWLEDGMENTS

The Fermi-LAT Collaboration acknowledges support for LAT development, operation, and data analysis from NASA and the U.S. Department of Energy (DOE) (United States); Commissariat à l'Énergie Atomique (CEA)–Institut de Recherche sur les lois Fondamentales de l'Univers (IRFU) and Institut National de Physique Nucléaire et de Physique des Particules/Centre National de la Recherche Scientifique (France); Agenzia Spaziale Italiana (ASI) and Istituto Nazionale di Fisica Nucleare (Italy); Ministry of Education, Culture, Sports, Science and Technology, KEK, and Japan Aerospace Exploration Agency (Japan); and the K. A. Wallenberg Foundation, the Swedish Research Council, and the National Space Board (Sweden). Science analysis support in the operations phase from the Istituto Nazionale di Astrofisica (INAF) (Italy) and Centre National d'Études Spatiales (France) is also gratefully acknowledged. Fermi-LAT data and analysis tools are publicly available from the Fermi Science Support Center at http://fermi.gsfc.nasa.gov/ssc. M.R. was funded by contract FIRB-2012-RBFR12PM1F from the Italian Ministry of Education, University and Research (MIUR).

M. Ackermann,[1] A. Albert,[2] L. Baldini,[2,3] J. Ballet,[4] G. Barbiellini,[5,6] C. Barbieri,[7] D. Bastieri,[8,9] R. Bellazzini,[10] E. Bissaldi,[11] R. Bonino,[12,13] E. Bottacini,[2] T. J. Brandt,[14] J. Bregeon,[15] P. Bruel,[16] R. Buehler,[1] G. A. Caliandro,[2,17] R. A. Cameron,[2] P. A. Caraveo,[18] C. Cecchi,[19,20] E. Charles,[2] A. Chekhtman,[21] C. C. Cheung,[22] J. Chiang,[2] G. Chiaro,[9] S. Ciprini,[19,23,24] J. Cohen-Tanugi,[15] A. Cuoco,[12,13] S. Cutini,[19,23,24] F. D'Ammando,[25,26] F. de Palma[11,27] R. Desiante,[5,28] S. W. Digel,[2] L. Di Venere,[29] P. S. Drell,[2] C. Favuzzi,[11,29] S. J. Fegan,[16] E. C. Ferrara,[14] A. Franckowiak,[2] S. Funk,[30] P. Fusco,[11,29] F. Gargano,[11] D. Gasparrini,[19,23,24] N. Giglietto,[11,29] F. Giordano,[11,29] G. Godfrey,[2] I. A. Grenier,[4] M.-H. Grondin,[31] J. E. Grove,[22] L. Guillemot,[32,33] S. Guiriec,[14,34] K. Hagiwara,[35] A. K. Harding,[14] E. Hays,[14] J. W. Hewitt,[36,37] A. B. Hill,[2,38,] D. Horan,[16] T. J. Johnson,[21] J. Knödlseder,[39,40] M. Kuss,[10] S. Larsson,[41,42] L. Latronico,[12] M. Lemoine-Goumard,[31] J. Li,[43] L. Li,[41,42] F. Longo,[5,6] F. Loparco,[11,29] M. N. Lovellette,[22] P. Lubrano,[19,20] S. Maldera,[12] A. Manfreda,[10] F. Marshall,[14] P. Martin,[39,40] M. Mayer,[1] M. N. Mazziotta,[11] P. F. Michelson,[2] N. Mirabal,[14,34] T. Mizuno,[44] M. E. Monzani,[2] A. Morselli,[45] I. V. Moskalenko,[2] S. Murgia,[46] G. Naletto,[47,48] E. Nuss,[15] T. Ohsugi,[44] M. Orienti,[25] E. Orlando,[2] D. Paneque,[2,49] M. Pesce-Rollins,[2,10] F. Piron,[15] G. Pivato,[10] T. A. Porter,[2] S. Rainò,[11,29] R. Rando,[8,9] M. Razzano,[10] A. Reimer,[2,50] O. Reimer,[2,50] T. Reposeur,[31] R. W. Romani,[2] P. M. Saz Parkinson,[51,52] A. Schulz,[1] C. Sgrò,[10] E. J. Siskind,[53] D. A. Smith,[31] F. Spada,[10] G. Spandre,[10] P. Spinelli,[11,29] D. J. Suson,[54] H. Takahashi,[55] J. B. Thayer,[2] D. J. Thompson,[14] L. Tibaldo,[2] D. F. Torres,[43,56] Y. Uchiyama,[35] G. Vianello,[2] K. S. Wood,[22] M. Wood,[2] L. Zampieri[58]

[1]Deutsches Elektronen Synchrotron DESY, D-15738 Zeuthen, Germany. [2]W. W. Hansen Experimental Physics Laboratory, Kavli Institute for Particle Astrophysics and Cosmology, Department of Physics and SLAC National Accelerator Laboratory, Stanford

University, Stanford, CA 94305, USA. [3]Università di Pisa and Istituto Nazionale di Fisica Nucleare, Sezione di Pisa I-56127 Pisa, Italy. [4]Laboratoire Astrophysique Interactions Multi-échelles, CEA-IRFU/CNRS/Université Paris Diderot, Service d'Astrophysique, CEA Saclay, F-91191 Gif sur Yvette, France. [5]Istituto Nazionale di Fisica Nucleare, Sezione di Trieste, I-34127 Trieste, Italy. [6]Dipartimento di Fisica, Università di Trieste, I-34127 Trieste, Italy. [7]Department of Physics and Astronomy, University of Padova, Vicolo Osservatorio 3, I-35122 Padova, Italy. [8]Istituto Nazionale di Fisica Nucleare, Sezione di Padova, I-35131 Padova, Italy. [9]Dipartimento di Fisica e Astronomia "G. Galilei", Università di Padova, I-35131 Padova, Italy. [10]Istituto Nazionale di Fisica Nucleare, Sezione di Pisa, I-56127 Pisa, Italy. [11]Istituto Nazionale di Fisica Nucleare, Sezione di Bari, I-70126 Bari, Italy. [12]Istituto Nazionale di Fisica Nucleare, Sezione di Torino, I-10125 Torino, Italy. [13]Dipartimento di Fisica Generale "Amadeo Avogadro," Università degli Studi di Torino, I-10125 Torino, Italy. [14]NASA Goddard Space Flight Center, Greenbelt, MD 20771, USA. [15]Laboratoire Univers et Particules de Montpellier, Université Montpellier, CNRS/IN2P3, Montpellier, France. [16]Laboratoire Leprince-Ringuet, École polytechnique, CNRS/IN2P3, Palaiseau, France. [17]Consorzio Interuniversitario per la Fisica Spaziale, I-10133 Torino, Italy. [18]INAF-Istituto di Astrofisica Spaziale e Fisica Cosmica, I-20133 Milano, Italy. [19]Istituto Nazionale di Fisica Nucleare, Sezione di Perugia, I-06123 Perugia, Italy. [20]Dipartimento di Fisica, Università degli Studi di Perugia, I-06123 Perugia, Italy. [21]College of Science, George Mason University, Fairfax, VA 22030, resident at Naval Research Laboratory, Washington, DC 20375, USA. [22]Space Science Division, Naval Research Laboratory, Washington, DC 20375-5352, USA. [23]Agenzia Spaziale Italiana (ASI) Science Data Center, I-00133 Roma, Italy. [24]INAF Osservatorio Astronomico di Roma, I-00040 Monte Porzio Catone (Roma), Italy. [25]INAF Istituto di Radioastronomia, I-40129 Bologna, Italy. [26]Dipartimento di Astronomia, Università di Bologna, I-40127 Bologna, Italy. [27]Università Telematica Pegaso, Piazza Trieste e Trento, 48, I-80132 Napoli, Italy. [28]Università di Udine, I-33100 Udine, Italy. [29]Dipartimento di Fisica "M. Merlin" dell'Università e del Politecnico di Bari, I-70126 Bari, Italy. [30]Erlangen Centre for Astroparticle Physics, D-91058 Erlangen, Germany. [31]Centre d'Études Nucléaires de Bordeaux Gradignan, IN2P3/CNRS, Université Bordeaux 1, BP120, F-33175 Gradignan Cedex, France. [32]Laboratoire de Physique et Chimie de l'Environnement et de l'Espace–Université d'Orléans/CNRS, F-45071 Orléans Cedex 02, France. [33]Station de Radioastronomie de Nançay, Observatoire de Paris, CNRS/INSU, F-18330 Nançay, France. [34]NASA Postdoctoral Program Fellow, USA. [35]3-34-1 Nishi-Ikebukuro, Toshima-ku, Tokyo 171-8501, Japan. [36]Department of Physics and Center for Space Sciences and Technology, University of Maryland Baltimore County, Baltimore, MD 21250, USA. [37]Center for Research and Exploration in Space Science and Technology and NASA Goddard Space Flight Center, Greenbelt, MD 20771, USA. [38]School of Physics and Astronomy, University of Southampton, Highfield, Southampton, SO17 1BJ, UK. [39]CNRS, Institut de Recherche en Astrophysique et Planétologie (IRAP), F-31028 Toulouse cedex 4, France. [40]Université de Toulouse, Université Toulouse III–Paul Sabatier–Observatoire Midi-Pyrénées, IRAP, Toulouse, France. [41]Department of Physics, KTH Royal Institute of Technology, AlbaNova, SE-106 91 Stockholm, Sweden. [42]The Oskar Klein Centre for Cosmoparticle Physics, AlbaNova, SE-106 91 Stockholm, Sweden. [43]Institute of Space Sciences (Institut d'Estudis Espacials de Catalunya–Consejo Superior de Investigaciones Científicas), Campus UAB, E-08193 Barcelona, Spain. [44]Hiroshima Astrophysical Science Center, Hiroshima University, Higashi-Hiroshima, Hiroshima 739-8526, Japan. [45]Istituto Nazionale di Fisica Nucleare, Sezione di Roma "Tor Vergata," I-00133 Roma, Italy. [46]Center for Cosmology, Physics and Astronomy Department, University of California, Irvine, CA 92697-2575, USA. [47]Consiglio Nazionale delle Ricerche–Istituto Di Fotonica E Nanotecnologie UOS Padova LUXOR, via Trasea 7, I-35131 Padova, Italy. [48]Department of Information Engineering, University of Padova, Via G. Gradenigo 6/B, I-35131 Padova, Italy. [49]Max-Planck-Institut für Physik, D-80805 München, Germany. [50]Institut für Astro- und Teilchenphysik and Institut für Theoretische Physik, Leopold-Franzens-Universität Innsbruck, A-6020 Innsbruck, Austria. [51]Santa Cruz Institute for Particle Physics, Department of Physics and Department of Astronomy and Astrophysics, University of California at Santa Cruz, Santa Cruz, CA 95064, USA. [52]Department of Physics, The University of Hong Kong, Pokfulam Road, Hong Kong, China. [53]NYCB Real-Time Computing, Lattingtown, NY 11560-1025, USA. [54]Department of Chemistry and Physics, Purdue University Calumet, Hammond, IN 46323-2094, USA. [55]Department of Physical Sciences, Hiroshima University, Higashi-Hiroshima, Hiroshima 739-8526, Japan. [56]Institució Catalana de Recerca i Estudis Avançats, Barcelona, Spain. [57]INAF–Astronomical Observatory of Padova, Vicolo dell'Osservatorio 5, I-35122 Padova, Italy.

SUPPLEMENTARY MATERIALS

www.sciencemag.org/content/350/6262/801/suppl/DC1
Materials and Methods
Fig. S1
Tables S1 and S2
References (*42*, *43*)

5 June 2015; accepted 7 October 2015
10.1126/science.aac7400

MAMMALIAN EVOLUTION

Evolution and dispersal of mammoths across the Northern Hemisphere

A. M. Lister[1]* and A. V. Sher[2]†

Mammoths provide a detailed example of species origins and dispersal, but understanding has been impeded by taxonomic confusion, especially in North America. The Columbian mammoth *Mammuthus columbi* was thought to have evolved in North America from a more primitive Eurasian immigrant. The earliest American mammoths (1.5 million years ago), however, resemble the advanced Eurasian *M. trogontherii* that crossed the Bering land bridge around that time, giving rise directly to *M. columbi*. Woolly mammoth *M. primigenius* later evolved in Beringia and spread into Europe and North America, leading to a diversity of morphologies as it encountered endemic *M. trogontherii* and *M. columbi*, respectively. In North America, this included intermediates ("*M. jeffersonii*"), suggesting introgression of *M. primigenius* with *M. columbi*. The lineage illustrates the dynamic interplay of local adaptation, dispersal, and gene flow in the evolution of a widely distributed species complex.

Mammoths arrived in Eurasia from Africa around 3 million years ago (Ma) and underwent remarkable adaptive evolution through species *Mammuthus meridionalis* and *M. trogontherii* to *M. primigenius* (the woolly mammoth), with changes in molar and skull structure adaptive to grazing in the increasingly open habitats of the Pleistocene (*1*). Although the pattern is well documented for Eurasia, our understanding of the origin and evolution of North American mammoths is much less clear (Fig. 1).

Our study focused on upper and lower last molars (M^3 and M_3), which show most clearly the lineage transformations (Fig. 2) (*2*). In Europe, the average number of enamel lamellae increases from 13 (*M. meridionalis*) to 19 (*M. trogontherii*) to 24 (*M. primigenius*), while hypsodonty (crown height) almost doubles between the first two species, which also show the most profound changes in skull morphology (*3*–*5*).

The earliest mammoths in North America, and hence their likely time of arrival, date to ~ 1.5 to 1.3 Ma (*6*, *7*). The prevailing view is that early American mammoths were of "primitive" morphology, indicating a close relationship to *M. meridionalis*, the contemporary species in Europe. Early North American fossils have been referred either to that form or to the supposedly related *M. hayi* or *M. haroldcooki (8–13)*. From here, an evolutionary sequence is posited, leading to the late Pleistocene Columbian mammoth *M. columbi*. The transformations would have paralleled those from *M. meridionalis* to *M. trogontherii* in Eurasia, and the species *M. imperator* is frequently cited as an "intermediate" stage (*10*, *14*) (Fig. 1A).

We focused on dated samples but included undated North American specimens that have been referred to "primitive" taxa such as *M. meridionalis* and *M. hayi* (*2*). We found no specimen comparable to Eurasian *M. meridionalis*. Past identifications were often based on worn molars and failed to take into account the mode of eruption and wear among elephants (*2*). Molars replace each other from behind and move slowly forward through the jaw, suffering anterior attrition as they reach the front, progressively reducing molar length and number of lamellae and giving an artificially primitive appearance (Fig. 3). We used the configuration of the anterior roots (*15*), plus the crown length/width ratio expected from complete teeth, to recognize anterior loss, and found that all supposedly primitive molars with 11 to 15 lamellae were incomplete, and the original count was higher or unknown (Fig. 3, supplementary text, and data sets S1 and S2). Conversely, where early and middle Pleistocene molars are complete, they invariably show lamellar counts of 18 to 21, like typical *M. columbi* (Figs. 2C and 4, B and D; figs. S33 and S35 to S40; and data sets S1 and S2). In crown height, the most critical evolutionary index in the lineage, all measurable

[1]Department of Earth Sciences, Natural History Museum, London SW7 5BD, UK. [2]Severtsov Institute of Ecology and Evolution, Moscow 119071, Russia.
***Corresponding author. E-mail: a.lister@nhm.ac.uk** †Deceased.

North American molars are substantially higher-crowned than European *M. meridionalis* specimens (Figs. 2 and 4A and figs. S32 and S40 to S42).

Also considered to support primitive status are high enamel thickness (ET) and low lamellar frequency [LF, the number of lamellae in 10 cm of crown length; here linearized as its reciprocal, lamella length, LL (supplementary methods)]. In many cases, primitive appearance has resulted from deep wear, especially in M_3s where lamellae diverge toward the base (Fig. 3). In some cases also, LF is reduced because of large tooth size (*16*). We compared like with like by standardizing LL and ET for tooth size and, for M_3s, comparing basal rather than mid-crown LFs. Almost all dated North American early and middle Pleistocene specimens plot in the range of late Pleistocene *M. columbi*, as do the undated type and neotype specimens of *M. hayi*, *M. haroldcooki*, and *M. imperator* (Fig. 4, A and C, and figs. S32 to S46). "Primitive" values are seen in individuals from the Ocotillo Formation (~1.1 Ma) and West Victorville [~375 thousand years ago (ka)], California, and from Sonora, Mexico (*12*), but other characters in these specimens do not corroborate *M. meridionalis* grade (supplementary text and figures), and their LLs are approached or exceeded by unquestioned late Pleistocene *M. columbi*, such as an M_3 from La Villa, Mexico (*17*), radiocarbon-dated to ~11.3 ka and with 21 lamellae despite wide lamellar spacing (Fig. 4C, rightmost pink icon).

Although North American material is distinct from European *M. meridionalis* material, its morphology is closely similar to that of *M. trogontherii*, especially in the key variables of lamella number and hypsodonty index (HI) (Figs. 2 and 4). This includes the earliest dated sample preserving these features, from Leisey Shell Pit 1A, Florida [1.3 to 1.1 Ma (*13*)] (figs. S32 to S46). Molars from the Ocotillo Formation (1.1 Ma), previously referred to *M. meridionalis* (*18*), have an estimated M_3 lamellar count of ≥17 (fig. S37) and M^3 HI >165 (Fig. 4A and fig. S32), both of which are above *M. meridionalis* range but within that of *M. trogontherii*.

Mandible shape also changed significantly between *M. meridionalis* and *M. trogontherii*, and most North American specimens, from the early Pleistocene onward, are similar to *M. trogontherii*, with relatively short, high horizontal ramus and symphysis, and wide upright coronoid (figs. S17 and S21). Mandibles of apparently more primitive morphology include one from the Ocotillo Formation (1.1 Ma) assigned to *M. meridionalis* (*11*), but these invariably show M_3 in late wear, and similar morphology can be seen in old individuals of late Pleistocene age (figs. S16 and S24). More work is needed on the ontogeny and evolution of elephantid skulls, but at present, these features do not unequivocally demonstrate the presence of *M. meridionalis* in North America.

The concept of *M. meridionalis* as the first mammoth to enter North America and the progenitor of *M. columbi* was based not only on the supposed primitive morphology of some North American fossils but also on the evolutionary chronology in Eurasia, with the *meridionalis*-to-*trogontherii* transition believed to have occurred around 0.8 to 0.7 Ma (*10*, *14*). *M. meridionalis* was hence the only available ancestor for the earliest North American mammoths ~1.5 Ma. However, advanced mammoths referable to *M. trogontherii* are now known as early as 1.7 Ma in northeast China and 1.2 to 0.8 Ma in northeast Siberia (the earliest available material from that region) (*5*, *19*). Apart from rather small molar size, their morphology is similar to that of both European *M. trogontherii* and North American mammoths (Fig. 4 and figs. S32 to S46). The origin of the more cold- and open-habitat–tolerant

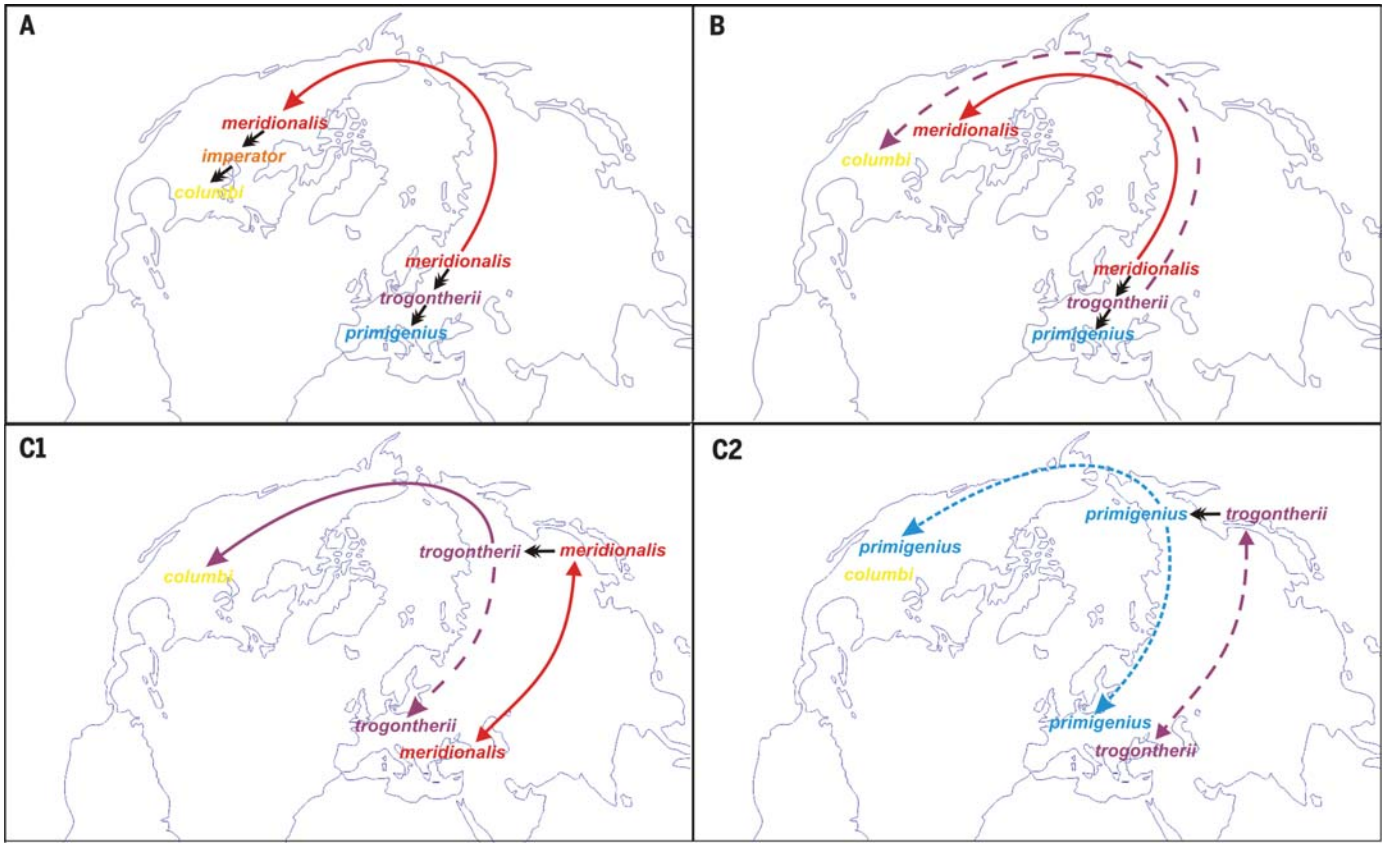

Fig. 1. Models of mammoth dispersal and evolution. (**A**) Parallel evolution from *M. meridionalis* (*3*, *10*, *14*, *30*). (**B**) Sequential entry of *M. meridionalis* and *M. trogontherii* into the New World (*11*, *12*, *29*). (**C**) The model proposed here: (C1) *M. trogontherii* speciates from *M. meridionalis* and enters the New World, producing *M. columbi* and also dispersing to Europe. (C2) *M. primigenius* speciates from *M. trogontherii* and disperses into North America and Europe, where it encounters *M. columbi* and relict *M. trogontherii*, respectively (*5*, *23*, *31*). Black arrows indicate evolutionary transformations; solid, long-dashed, and short-dashed lines indicate successively later dispersals within (A) to (C). Double-ended arrows indicate the Eurasian range. The position of species names is significant only at continental scale.

M. trogontherii from a population of *M. meridionalis* in eastern Asia ≥1.7 Ma puts it in the appropriate time and place to be the source of migration into North America (Fig. 1C1).

Moreover, verifiable remains of *M. meridionalis* have been found neither in northeast Siberia nor in Alaska/Yukon, suggesting that this temperate-adapted species never dispersed as far north as the Beringian transit route. A molar from the Vilui River region (Yakutia) was described as *M. meridionalis* (*20*), but it is a worn fragment of ambiguous attribution. Molars from the Yukon, described as *M. meridionalis* (*21*), are obliquely or deeply worn fragments whose morphology matches that of *M. trogontherii,* as do specimens from Old Crow dated to ~1.1 Ma (*22*) (supplementary text and figs. S32 to S46).

The model that emerges is the dispersal of early *M. trogontherii* into North America ~2.0 to 1.5 Ma, where its descendants persisted, little changed, through to late Pleistocene material identified as *M. columbi* (Fig. 1C1). This is supported by the morphological consistency between samples of early and middle Pleistocene North American mammoths (Fig. 4, A to C), undermining the concept of an intermediate middle Pleistocene stage. The earliest known *M. trogontherii* molars, from Majuangou, China (~1.7 Ma), already have an HI equivalent to that of these samples (Figs. 2 and 4A); their lamella number of 17 is at the low end of *trogontherii* and North American variation, which may suggest an increase to the 18 to 21 range seen in the latter, although sample sizes are small.

Late Pleistocene material from North America includes specimens indistinguishable from earlier ones, but others showing advancement (that is, with lamellar counts of 22 to 24; Fig. 4, B and D, and figs. S33 and S36 to S40). This could simply represent evolution from *M. columbi* (*10*, *14*). However, early in the late Pleistocene, the woolly mammoth *M. primigenius* crossed the Bering land connection. This species (*5*) had high lamella number (typically 24 to 28) and thin lamellae and enamel (Fig. 4 and figs. S32 to S46). Like *M. trogontherii* before it, the woolly mammoth spread both west (into Europe) and east (into North America). Its range in America was largely to the north of that of *M. columbi*, the species meeting around southern Canada and the northern continental United States (*23*). A broad range of morphologies in the late Pleistocene of this region (and some points south) includes intermediate or supposedly unique forms, some of them termed *M. jeffersonii*. This "species" has been variously described in terms of large size, unusual crown shape, and lamellar count

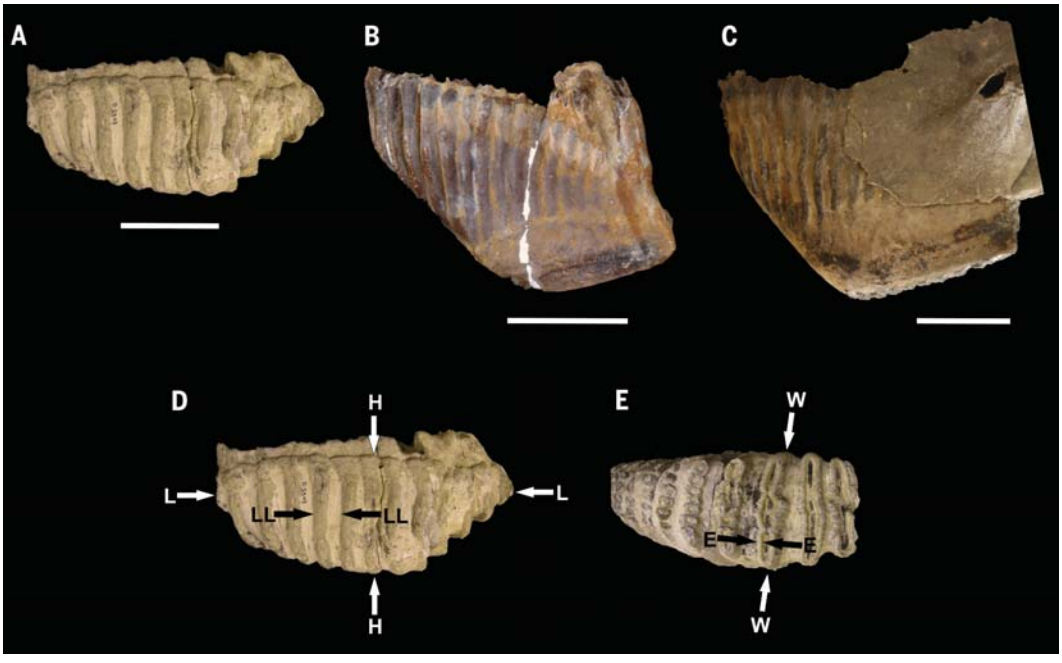

Fig. 2. Mammoth molars showing primitive versus advanced morphologies (A to C) and measurements taken (D and E). Upper third molars (M^3) at equivalent wear stage and adjusted to the same crown length are shown; anterior to right, scale bars 10 cm. (A) M^3 of *M. meridionalis*, Yukarısöğütönü, Turkey (specimen MTA 2306), with low crown and 12 lamellae. (B) M^3 of *M. trogontherii*, Majuangou, China (IVPP V13610 reflected horizontally), high crown and 17 lamellae. (C) M^3, early Pleistocene, Leisey Shell Pit 1A, Florida (UF 85324), high crown and 18 lamellae. (D) and (E) Molar in lateral and occlusal views. L, crown length; H, crown height; LL, lamella length (length of one lamella plus cement interval); W, crown width; E, enamel thickness.

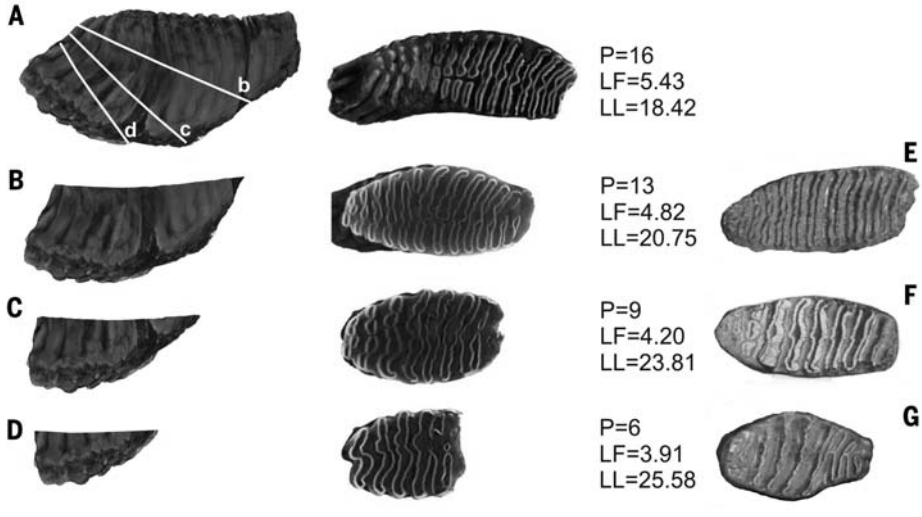

Fig. 3. The effect of wear on mammoth molar morphology. (**A**) M_3 of *M. columbi* (San Felipe de Austin, Texas, NHM 20702, lacking a few lamellae anteriorly) in lateral (left) and occlusal (center) views; white lines b to d show the typical progress of wear. (**B** to **D**) (Left) As (A), sliced and rotated to life position and wear at stages b to d; (center) micro–computed tomography sections of NHM 20702 at lines b to d, representing the occlusal surface and showing a more primitive appearance at the base of the crown. Lamellar number remaining (P), lamellar frequency (LF), and average lamellar length (LL) measured on the upper surface of each slice are shown. (**E** to **G**) Worn *M. columbi* M_3s similar to those in (B) to (D), respectively (supplementary text). (E) Wilber, Nebraska, formerly referred to *M. hayi* (*10*). (F) Frederick, Oklahoma, type of *M. haroldooki*, subsequently referred to *M. meridionalis* (*3*). (G) Staplehurst, Nebraska, type of *M. scotti*, subsequently referred to *M. hayi* (*10*, *13*).

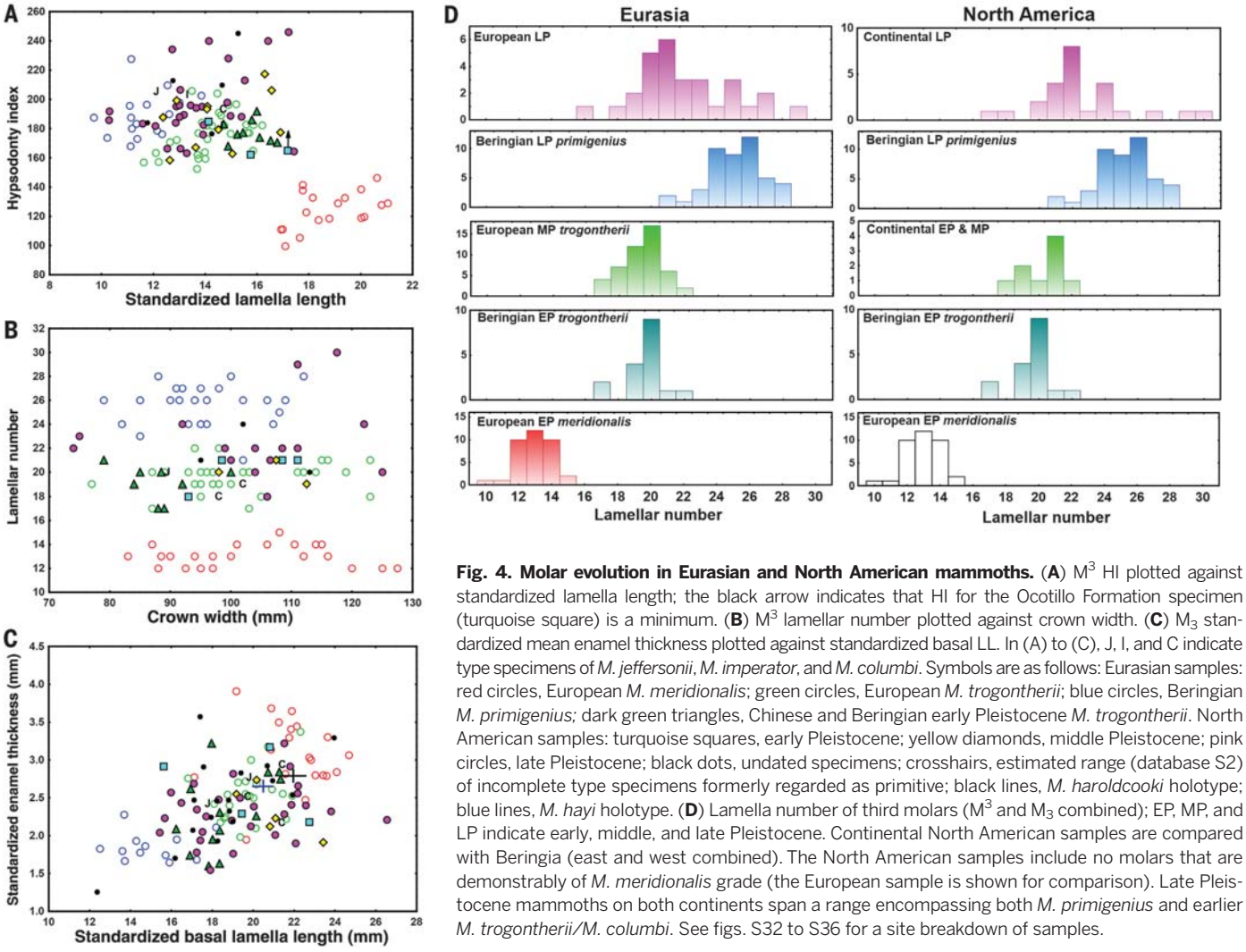

Fig. 4. Molar evolution in Eurasian and North American mammoths. (**A**) M^3 HI plotted against standardized lamella length; the black arrow indicates that HI for the Ocotillo Formation specimen (turquoise square) is a minimum. (**B**) M^3 lamellar number plotted against crown width. (**C**) M_3 standardized mean enamel thickness plotted against standardized basal LL. In (A) to (C), J, I, and C indicate type specimens of *M. jeffersonii*, *M. imperator*, and *M. columbi*. Symbols are as follows: Eurasian samples: red circles, European *M. meridionalis*; green circles, European *M. trogontherii*; blue circles, Beringian *M. primigenius;* dark green triangles, Chinese and Beringian early Pleistocene *M. trogontherii*. North American samples: turquoise squares, early Pleistocene; yellow diamonds, middle Pleistocene; pink circles, late Pleistocene; black dots, undated specimens; crosshairs, estimated range (database S2) of incomplete type specimens formerly regarded as primitive; black lines, *M. haroldcooki* holotype; blue lines, *M. hayi* holotype. (**D**) Lamella number of third molars (M^3 and M_3 combined); EP, MP, and LP indicate early, middle, and late Pleistocene. Continental North American samples are compared with Beringia (east and west combined). The North American samples include no molars that are demonstrably of *M. meridionalis* grade (the European sample is shown for comparison). Late Pleistocene mammoths on both continents span a range encompassing both *M. primigenius* and earlier *M. trogontherii/M. columbi*. See figs. S32 to S36 for a site breakdown of samples.

either intermediate between *M. columbi* and *M. primigenius* or exceeding the latter. Sometimes considered an advanced derivative of *M. columbi*, an alternative hypothesis is that it is a hybrid between *M. columbi* and *M. primigenius.* This interpretation is supported by evidence that mammoths identified morphologically as *M. columbi* and *M. jeffersonii* from this region share a mitochondrial haplogroup most similar to that of North American *M. primigenius* (*24*, *25*). The entire complex of late Pleistocene North American morphologies may therefore reflect a series of populations with variable gene flow among them (a metapopulation). Some are of *primigenius* or *columbi* morphology, whereas others are of intermediate form, accounting in particular for *jeffersonii* morphologies; e.g., specimens from Missouri (*26*) and Osborn's (*12*) "paratype" of *M. jeffersonii* from Kansas (Fig. 4, A to C, and figs. S32 to S34 and S37 to S48). There is no evidence that the range extends outside the spread of typical *primigenius, columbi*, or plausible intermediates.

Parallel variation appears to have arisen in Europe (Fig. 4D). Last-glacial samples span a range of variation encompassing that of both Siberian *M. primigenius* and earlier European material attributed to *M. trogontherii*. This variation occurs both between and within populations (*27*, *28*) and may likewise reflect a complex metapopulation forming as the two species met (*5*) (Fig. 1C2). The potential of hybridization to expand the phenotypic variation available to natural selection is notable.

On this evidence, the source of *M. columbi* lies in *M. trogontherii* of Eurasia, its appearance in North America representing a dispersal and the distinction between the two species largely a matter of usage. The later evolutionary advancement of mammoths, both there and in Europe, results neither from purely lineal change in the incumbent species, nor from simple replacement by *M. primigenius*, but from a dynamic interplay of the two. Taxonomy is difficult to impose on a complex evolutionary process, but the only North American mammoth species that can be validated on current evidence are *M. columbi* and *M. primigenius,* plus possible identification of early Pleistocene specimens from Alaska/Yukon as *M. trogontherii*. An earlier invasion of *M. meridionalis* is still conceivable as a separate, presumably dead-end incursion (*11*, *29*) (Fig. 1B), but until a complete *meridionalis*-like mammoth fossil is discovered in North America, definitive evidence is lacking. This model is also ecologically coherent, in that high-latitude dispersal to North America occurred only after the adaptive shift to the more cold- and grazing-tolerant *M. trogontherii*.

REFERENCES AND NOTES

1. A. M. Lister, A. V. Sher, H. van Essen, G. Wei, *Quat. Int.* **126-128**, 49–64 (2005).
2. Methods, data, specimen descriptions, and acknowledgements are available as supplementary materials on *Science* Online.
3. V. J. Maglio, *Trans. Am. Philos. Soc. New Ser.* **63**, 1–149 (1973).
4. A. M. Lister, in *The Proboscidea: Evolution and Palaeoecology of Elephants and their Relatives*, J. Shoshani, P. Tassy, Eds. (Oxford Univ. Press, Oxford, 1996), pp. 203–213.
5. A. M. Lister, A. V. Sher, *Science* **294**, 1094–1097 (2001).
6. C. J. Bell *et al.*, in *Late Cretaceous and Cenozoic Mammals of North America*, M. O. Woodburne, Ed. (Columbia Univ. Press, New York, 2004), pp. 232–314.
7. L. D. Agenbroad, *Quat. Int.* **126-128**, 73–92 (2005).

8. J. Arroyo-Cabrales, O. J. Polaco, F. Aguilar-Arellano, *Deinsea* **9**, 17–25 (2003).
9. S. G. Lucas *et al.*, *N. M. Geol.* **36**, 48–58 (2014).
10. C. T. Madden, thesis, University of Colorado, Boulder, CO (1981).
11. G. E. McDaniel, G. T. Jefferson, *Deinsea* **9**, 239–252 (2003).
12. H. F. Osborn, *Proboscidea* (American Museum of Natural History, New York, 1942), vol. 2.
13. S. D. Webb, J. P. Dudley, *Bull. Florida Mus. Nat. Hist* **37**, 645–660 (1995).
14. A. M. Lister, in *Morphological Change in Quaternary Mammals of North America*, R. A. Martin, A. D. Barnosky, Eds. (Cambridge Univ. Press, Cambridge, 1993), pp. 178–204.
15. A. V. Sher, V. E. Garutt, *Trans. Acad. Sci. USSR Earth Sci. Sect.* **285**, 195–199 (1987).
16. A. M. Lister, K. A. Joysey, in *Structure, Function and Evolution of Teeth*, P. Smith, E. Tchernov, Eds. (Freund, Jerusalem, 1992), pp. 185–213.
17. S. Gonzalez *et al.*, *J. Hum. Evol.* **44**, 379–387 (2003).
18. G. E. McDaniel Jr., G. T. Jefferson, *Quat. Int.* **142-143**, 124–129 (2006).
19. G. Wei, T. Hiroyuki, C. Jin, X. Fei, *Chikyu Kagaku (Earth Sci.)* **57**, 289–298 (2003).
20. I. A. Dubrovo, *Byull. Comissii po Izuch. Chetvert. Perioda* **17**, 76–79 (1953).
21. C. S. Churcher, *Curr. Res. Pleist.* **3**, 61–64 (1986).
22. A. V. Sher, A. M. Lister, R. E. Morlan, in *The World of Elephants*, L. D. Agenbroad, R. L. Symington, Eds. (Mammoth Site Hot Springs, SD, 2005), pp. 153–157.
23. A. Lister, P. Bahn, *Mammoths: Ice Age Giants* (Frances Lincoln, London, 2007).
24. J. Enk, thesis, McMaster University, Hamilton, Ontario, Canada (2014).
25. J. Enk *et al.*, *Genome Biol.* **12**, R51 (2011).
26. J. J. Saunders *et al.*, *Quat. Int.* **217**, 175–187 (2010).
27. I. V. Foronova, *Quat. Int.* **169-170**, 95–104 (2007).
28. A. M. Lister, R. Grün, *Geol. J.* **50**, 306–320 (2015).
29. C. R. Harington, in *Quaternary Dating Methods*, W. C. Mahaney, Ed. (Elsevier, Amsterdam, 1984), pp. 299–309.

ACKNOWLEDGMENTS

A.L. thanks the Natural Environment Research Council and the Royal Society for funding and colleagues who provided access to collections and helped in various ways (*2*). Raw data are in the supplementary materials (data sets S1 and S2).

SUPPLEMENTARY MATERIALS

www.sciencemag.org/content/350/6262/805/suppl/DC1
Materials and Methods
Supplementary Text
Figs. S1 to S48
Tables S1 to S3
Captions for Data Sets S1 and S2
Acknowledgments
References (*30*–*173*)
Data Sets S1 and S2

13 May 2015; accepted 24 September 2015
10.1126/science.aac5660

CLIMATE CHANGE

Slow adaptation in the face of rapid warming leads to collapse of the Gulf of Maine cod fishery

Andrew J. Pershing,[1]* Michael A. Alexander,[2] Christina M. Hernandez,[1]† Lisa A. Kerr,[1] Arnault Le Bris,[1] Katherine E. Mills,[1] Janet A. Nye,[3] Nicholas R. Record,[4] Hillary A. Scannell,[1,5]‡ James D. Scott,[2,6] Graham D. Sherwood,[1] Andrew C. Thomas[5]

Several studies have documented fish populations changing in response to long-term warming. Over the past decade, sea surface temperatures in the Gulf of Maine increased faster than 99% of the global ocean. The warming, which was related to a northward shift in the Gulf Stream and to changes in the Atlantic Multidecadal Oscillation and Pacific Decadal Oscillation, led to reduced recruitment and increased mortality in the region's Atlantic cod (*Gadus morhua*) stock. Failure to recognize the impact of warming on cod contributed to overfishing. Recovery of this fishery depends on sound management, but the size of the stock depends on future temperature conditions. The experience in the Gulf of Maine highlights the need to incorporate environmental factors into resource management.

Climate change is reshaping ecosystems in ways that affect resources and ecosystem services (*1*). Fisheries, with their tight coupling between ecosystem status and economic productivity, are a prime example of interacting social-ecological systems. The social and ecological value of a fishery depends first and foremost on the biomass of fish, and fishing has often been the dominant driver of the status of the resources and economics of the fishing community. Modern fisheries management is designed to reduce harvesting levels in response to low stock biomass (and vice versa), creating a negative feedback that, in theory, will maintain steady long-term productivity (*2*).

A failure to detect changes in the environment, or to act appropriately when changes are detected, can jeopardize social-ecological systems (*3*). As climate change brings conditions that are increasingly outside the envelope of past experiences, the risks increase. The Gulf of Maine has warmed steadily, and the record warm conditions in 2012 affected the American lobster fishery (*4*). Here, we consider how ocean warming factored into the rapid decline of the Gulf of Maine cod stock (*5*).

We used sea surface temperature (SST) data to characterize temperature trends in the Gulf of Maine since 1982 and over the decade 2004–2013. We compared the Gulf of Maine SST trends to trends around the globe. Variability in Gulf of Maine SST was related to an index of Gulf Stream position as well as the Pacific Decadal Oscillation (PDO) and Atlantic Multidecadal Oscillation (AMO). We then examined the impact of temperature conditions in the Gulf of Maine on the recruitment and survival of Atlantic cod. The resulting temperature-dependent population dynamics model was used to project the rebuilding potential of this stock under future temperature scenarios.

From 1982 to 2013, daily satellite-derived SSTs in the Gulf of Maine rose at a rate of 0.03°C year^{-1} (R^2 = 0.12, P < 0.01, n = 11,688; Fig. 1A). This rate is higher than the global mean rate of 0.01°C year^{-1} and led to gradual shifts in the distribution and abundance of fish populations (*6*–*8*). Beginning in 2004, the warming rate in the Gulf of Maine increased by a factor of ~7, to 0.23°C year^{-1} (R^2 = 0.42, P < 0.01, n = 3653). This period began with relatively cold conditions in 2004 and concluded with the two warmest years in the time series. The peak temperature in 2012 was part of a large "ocean heat wave" in the northwestern Atlantic that persisted for nearly 18 months (*4*).

The recent 10-year warming trend is remarkable, even for a highly variable part of the ocean such as the northwestern Atlantic. Over this period, substantial warming also occurred off western Australia, in the western Pacific, and in the Barents Sea, and cooling was observed in the eastern Pacific and Bering Sea (Fig. 1B). The global ocean has a total area of 3.6 × 10^8 km^2, yet only 3.1 × 10^5 km^2 of the global ocean had warming rates greater than that in the Gulf of Maine over this time period. Thus, the Gulf of Maine has warmed faster than 99.9% of the global ocean between 2004 and 2013 (Fig. 1C). Using SSTs from 1900 to 2013, the likelihood of any 2° × 2° segment of the ocean exceeding this 10-year warming rate is less than 0.3%. According to this analysis, the Gulf of Maine experienced decadal warming that few marine ecosystems have encountered.

As a first step toward diagnosing the potential drivers of the recent warming trend, we correlated the quarterly temperatures in the Gulf of Maine with large-scale climate indicators (table S1). An index of Gulf Stream position (*9*) has the strongest and most consistent relationship with Gulf of Maine temperatures. The correlations with the Gulf Stream Index (GSI) are positive and significant in all quarters, with the

[1]Gulf of Maine Research Institute, 350 Commercial Street, Portland, ME 04101, USA. [2]NOAA Earth System Research Laboratory, Boulder, CO 80305, USA. [3]School of Marine and Atmospheric Sciences, Stony Brook University, Stony Brook, NY 11794, USA. [4]Bigelow Laboratory for Ocean Sciences, 60 Bigelow Drive, East Boothbay, ME 04544, USA. [5]School of Marine Sciences, University of Maine, Orono, ME 04469, USA. [6]Cooperative Institute for Research in Environmental Sciences, University of Colorado, Boulder, CO 80309, USA. ***Corresponding author. E-mail: apershing@gmri.org** †Present address: Woods Hole Oceanographic Institution, Woods Hole, MA 02543, USA. ‡Present address: University of Washington School of Oceanography, Seattle, WA 98105, USA.

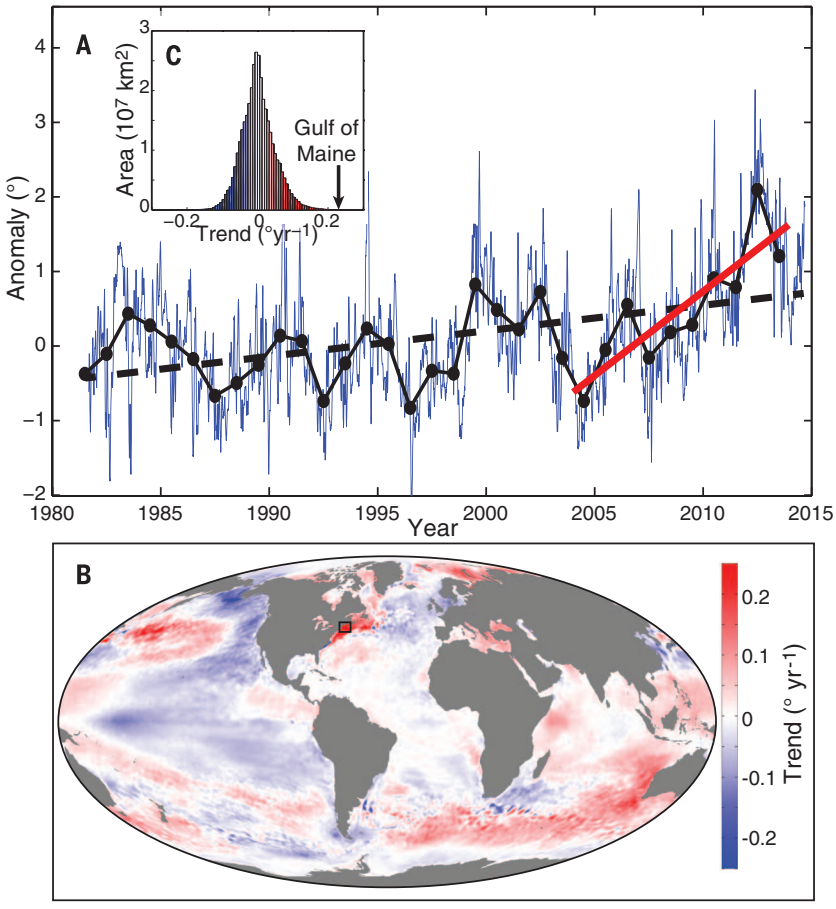

Fig. 1. Sea surface temperature trends from the Gulf of Maine and the global ocean. (**A**) Daily (blue, 15-day smoothed) and annual (black dots) SST anomalies from 1982 to 2013, showing the long-term trend (black dashed line) and trend over the decade 2004–2013 (red solid line). (**B**) Global SST trends, 2004–2013. The Gulf of Maine is outlined in black. (**C**) Histogram of global 2004–2013 SST trends, with the trend from the Gulf of Maine indicated at the right extreme of the distribution.

Table 1. Linear models relating Gulf of Maine summer temperature to climate indicators. GSI, Gulf Stream Index; PDO, Pacific Decadal Oscillation Index; AMO, Atlantic Multidecadal Oscillation Index. The final model uses all three indices. The first set of statistics refers to the models fit to the entire 1982–2013 record. The models were also fit to the 1982–2003 period, then projected onto the 2004–2013 period. The rightmost two columns summarize the out-of-sample performance of the models.

Time series 1	Time series 2	1982–2013			2004–2013 (out of sample)	
		R^2	P	AIC	r^2	P
GSI	—	0.39	0.00	63.92	0.50	0.00
	PDO	0.58	0.00	54.41	0.54	0.00
	AMO	0.66	0.00	48.15	0.64	0.00
PDO	—	0.45	0.00	60.77	0.28	0.01
	AMO	0.50	0.00	59.78	0.32	0.01
AMO	—	0.23	0.01	71.06	0.11	0.13
All		0.70	0.00	45.99	0.65	0.00

strongest correlation occurring in summer (r = 0.63, P < 0.01, n = 31). The PDO (*10*) is negatively correlated with the Gulf of Maine temperatures during spring (r = −0.50) and summer (r = −0.67). Summer temperatures are also positively correlated with the AMO (*11*) (r = 0.48, P < 0.01, n = 31).

Building on the strong correlations with summer temperatures, we developed multiple regression models for summer Gulf of Maine temperatures using combinations of the three indices (Table 1). As judged by Akaike information criterion (AIC) score, the best model used all three indices, and this model explained 70% of the variance in Gulf of Maine summer temperature (R^2 = 0.70, P < 0.01, AIC = 46.0, n = 31). This model was slightly better than one using GSI and the AMO (R^2 = 0.66, P < 0.01, AIC = 48.2, n = 31). We refit each model using data from 1982 to 2003 and then applied the model to the 2004–2012 period. The three-index and GSI-AMO models had nearly identical out-of-sample performance, explaining 65% and 64% of the variance, respectively.

A long-term poleward shift in the Gulf Stream occurred during the 20th century and has been linked to increasing greenhouse gases (*12*). Previous studies have reported an association between Gulf Stream position and temperatures in the northwestern Atlantic (*7*, *13*), and an extreme northward shift in the Gulf Stream was documented during the record warm year of 2012 (*14*). Although the Gulf Stream does not directly enter the Gulf of Maine, northward shifts in the Gulf Stream are associated with reduced transport of cold waters southward on the continental shelf (*15*, *16*). The association between Gulf of Maine temperature and the PDO suggests an atmospheric component to the recent trend. A detailed heat budget calculation for the 2012 event (*17*) found that the warming was due to increased heat flux associated with anomalously warm weather in 2011–2012. These results suggest that atmospheric teleconnections from the Pacific, changes in circulation in the Atlantic Ocean, and background warming have contributed to the rapid warming in the Gulf of Maine.

The Gulf of Maine cod stock has been chronically overfished, prompting progressively stronger management, including the implementation of a quota-based management system in 2010. Despite these efforts, including a 73% cut in quotas in 2013, spawning stock biomass (*SSB*) continued to decline (Fig. 2A). The most recent assessment found that *SSB* in this stock is now less than 3000 metric tons (mt; 1 mt = 1000 kg), which is only 4% of the *SSB* value that gives the maximum sustainable yield (SSB_{msy}) (*5*). This has prompted severe restrictions on the commercial cod fishery and the closure of the recreational fishery.

The Gulf of Maine is near the southern limit of cod, and previous studies have suggested that warming will lead to lower recruitment, suboptimal growth conditions, and reduced fishery productivity in the future (*18*–*20*). Using population estimates from the recent Gulf of Maine cod stock assessment (*5*), we fit a series of stock-recruit models with and without a temperature effect (table S2). The best models exhibited negative relationships between age-1 recruitment and summer temperatures (table S3). Gulf of Maine cod spawn in the winter and spring, so the link with summer temperatures suggests a decrease in the survival of late-stage larvae and settling juveniles. Although the relationship with temperature is statistically robust, the exact mechanism for this is uncertain but may include changes in prey availability and/or predator risk. For example, the abundance of some zooplankton taxa that are prey for larval cod has declined in the Gulf of Maine cod habitat (*21*). Warmer temperatures could cause juvenile cod to move away

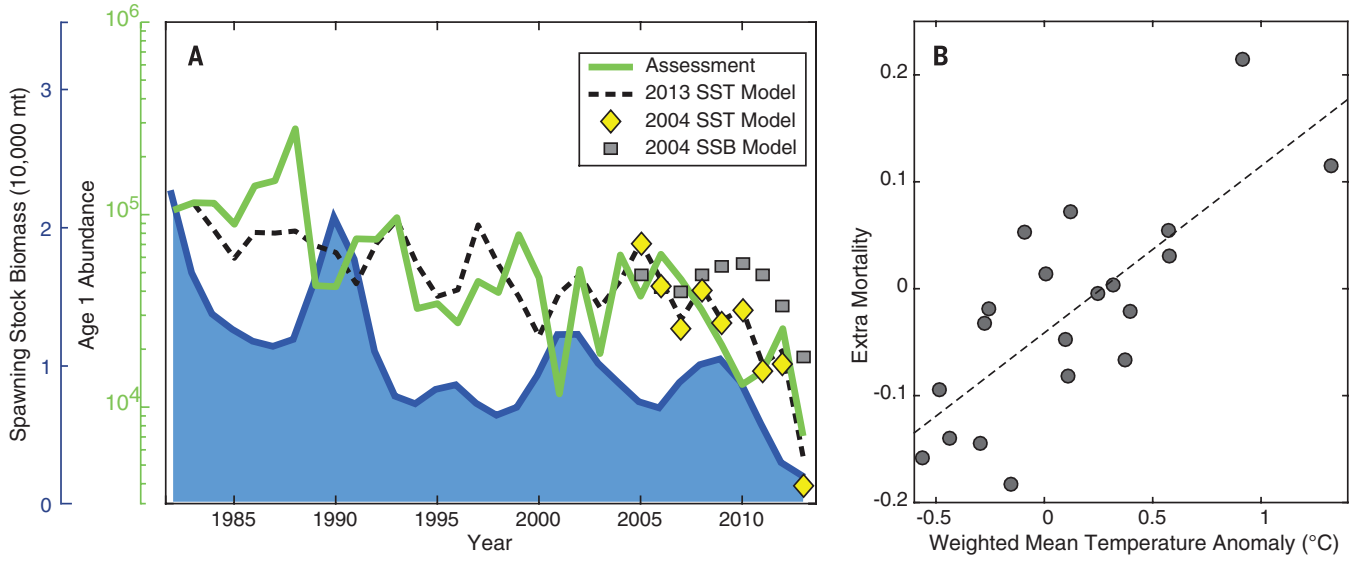

Fig. 2. Relationships between Gulf of Maine cod and temperature. (**A**) Time series of Gulf of Maine cod spawning stock biomass (blue) and age-1 recruitment (green) from the 2014 assessment. Cod age-1 recruitment was modeled using adult biomass and summer temperatures (dashed line). The gray squares are recruitment estimated using a model without a temperature effect fit to data prior to 2004. The yellow diamonds are a temperature-dependent model fit to this earlier period. (**B**) Mortality of age-4 cod as a function of temperature (R^2 = 0.57, P < 0.01, n = 21). The temperature is composed of the fall values from the current year and 3 years prior, weighted using the coefficients from the linear model.

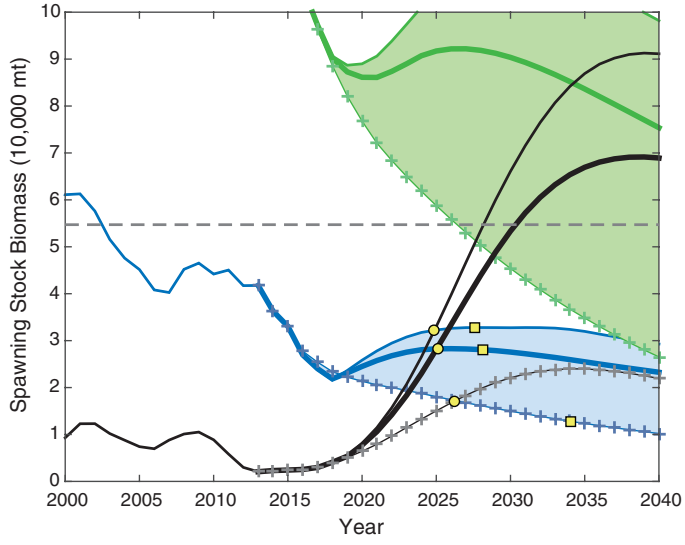

Fig. 3. Temperature-dependent rebuilding potential of Gulf of Maine cod. We simulated a population growing from the 2013 biomass (black curves) without fishing under three temperature scenarios: a cool scenario (solid line) represented by the 10% lower bound of the CMIP-5 ensemble of climate model projections, a warm scenario (heavy line) represented by the climate model ensemble mean, and a hot scenario (plus signs) with warming at the 0.07° year^{-1} rate observed in the summer in the Gulf of Maine since 1982. This population is contrasted against an estimate of the temperature-dependent SSB_{msy} (blue lines and shading), an estimate of SSB_{msy} without accounting for temperature (gray dashed line), and the carrying capacity of the population (green lines and shading). The yellow circles mark where the rebuilding population reaches the temperature-dependent SSB_{msy}; squares denote when a population fished at F = 0.1 would be rebuilt.

from their preferred shallow habitat into deeper water, where risks of predation are higher (*22*).

We also looked for other signatures of temperature within the population dynamics of cod. We found a strong association between the mortality of age-4 fish and fall temperatures from the current year and the second year of life (Fig. 2B, R^2 = 0.57, P < 0.01, n = 21). Age 4 represents an energetic bottleneck for cod because of the onset of reproduction and reduced feeding efficiency as fish transition from benthic to pelagic prey (*23*). Elevated temperatures increase metabolic costs in cod (*24*), exacerbating the energetic challenges at this age. The average weight-at-age of cod in the Gulf of Maine region has been below the long-term mean since 2002 (*25*), and these poorly conditioned fish will have a lower probability of survival (*26*).

The age-4 mortality relationship improves significantly with the addition of temperatures from the second year of life (table S6). This suggests that a portion of the estimated age-4 mortality reflects mortality over the juvenile period that is not explicitly captured in the assessment. Temperature may directly influence mortality in younger fish through metabolic processes described above; however, we hypothesize that predation mortality may also be higher during warm years. Many important cod predators migrate into the Gulf of Maine or have feeding behaviors that are strongly seasonal. During a warm year, spring-like conditions occur earlier in the year, and fall-like conditions occur later. During the 2012 heat wave, the spring warming occurred 21 days ahead of schedule, and fall cooling was delayed by a comparable amount (*4*). This change in phenology could result in an increase in natural mortality of 44% on its own, without any increase in predator biomass (see supplementary text).

If fishing pressure had been effectively reduced, the population should have rebuilt more during the cool years and then declined less rapidly during the warming period. Instead, fishing mortality rates consistently exceeded target levels, even though fishermen did not exceed their quotas. The quota-setting process that is at the heart of fisheries management is highly sensitive to the number of fish aging into the fishery in each year. For Gulf of Maine cod, age classes 4 and 5 dominate the biomass of the stock and the catch (*5*). The temperature-mortality relationship in Fig. 2B means that during warm years, fewer fish are available for the fishery. Not accounting for this effect leads to quotas that are too high. The resulting fishing mortality rate was thus above the intended levels, contributing to overfishing even though catches were within prescribed limits. Socioeconomic pressures further compounded the overfishing. To minimize the impact of the quota cuts on fishing communities,

the New England Fishery Management Council elected to defer most of the cuts indicated for 2012 and 2013 until the second half of 2013. The socioeconomic adjustment coupled with the two warmest years on record led to fishing mortality rates that were far above the levels needed to rebuild this stock.

The impact of temperature on Gulf of Maine cod recruitment was known at the start of the warming period (*20*), and stock-recruitment model fit to data up to 2003 and incorporating temperature produces recruitment estimates (Fig. 2A, yellow diamonds) that are similar to the assessment time series. Ignoring the influence of temperature produces recruitment estimates that are on average 100% and up to 360% higher than if temperature is included (Fig. 2A, gray squares). According to a simple population dynamics model that incorporates temperature, the spawning stock biomass that produces the maximum sustainable yield (SSB_{msy}) has been declining steadily since 2002 (Fig. 3) rather than remaining constant, as currently assumed. The failure to consider temperature impacts on Gulf of Maine cod recruitment created unrealistic expectations for how large this stock can be and how quickly it can rebuild.

We estimated the potential for rebuilding the Gulf of Maine cod stock under three different temperature scenarios: a "cool" scenario that warms at a rate of 0.02° year^{-1}; a "warm" scenario that warms at 0.03° year^{-1}, the mean rate from climate model projections; and a "hot" scenario that follows the 0.07°C year^{-1} trend present in the summer temperature time series. If fishing mortality is completely eliminated, populations in the cool and warm scenarios could rebuild to the temperature-dependent SSB_{msy} in 2025, slightly longer than the 10-year rebuilding timeline established by U.S. law, and the hot scenario would reach its target 1 year later (Fig. 3). Allowing a small amount of fishing (F = 0.1) would delay rebuilding by 3 years in the cool and warm scenarios and 8 years in the hot scenario. Note that estimating SSB_{msy} without temperature produces a management target that may soon be unachievable. By 2030, a rebuilt fishery could produce more than 5000 mt year^{-1} under the warm scenario, a catch rate close to the average for the fishery for the previous decade. Under the hot scenario, the fishery would be 1800 tons year^{-1}—small, but potentially valuable. Thus, how quickly this fishery rebuilds now depends arguably as much on temperature as it does on fishing. Future management of Gulf of Maine cod would benefit from a reevaluation of harvest control rules and thorough management strategy evaluation of the application of temperature-dependent reference points and projections such as these.

As climate change pushes species poleward and reduces the productivity of some stocks, resource managers will be increasingly faced with trade-offs between the persistence of a species or population and the economic value of a fishery. Navigating decisions in this context requires both accurate projections of ecosystem status and stronger guidance from society in the form of new policies. Social-ecological systems that depend on a steady state or are slow to recognize and adapt to environmental change are unlikely to meet their ecological and economic goals in a rapidly changing world.

REFERENCES AND NOTES

1. E. J. Nelson *et al.*, *Front. Ecol. Environ.* **11**, 483–493 (2013).
2. R. Mahon, P. McConney, R. N. Roy, *Mar. Policy* **32**, 104–112 (2008).
3. C. S. Holling, *Ecosystems* **4**, 390–405 (2001).
4. K. E. Mills *et al.*, *Oceanography* **26**, 191–195 (2013).
5. M. C. Palmer, *2014 Assessment Update Report of the Gulf of Maine Atlantic Cod Stock* (U.S. Department of Commerce, 2014).
6. J. A. Nye, J. S. Link, J. A. Hare, W. J. Overholtz, *Mar. Ecol. Prog. Ser.* **393**, 111–129 (2009).
7. J. A. Nye, T. M. Joyce, Y.-O. Kwon, J. S. Link, *Nat. Commun.* **2**, 412 (2011).
8. M. L. Pinsky, B. Worm, M. J. Fogarty, J. L. Sarmiento, S. A. Levin, *Science* **341**, 1239–1242 (2013).
9. T. J. Joyce, C. Deser, M. A. Spall, *J. Clim.* **13**, 2550–2569 (2000).
10. N. J. Mantua, S. R. Hare, *J. Oceanogr.* **58**, 35–44 (2002).
11. R. A. Kerr, *Science* **288**, 1984–1985 (2000).
12. L. Wu *et al.*, *Nat. Clim. Change* **2**, 161–166 (2012).
13. D. G. Mountain, J. Kane, *Mar. Ecol. Prog. Ser.* **398**, 81–91 (2010).
14. G. G. Gawarkiewicz, R. E. Todd, A. J. Plueddemann, M. Andres, J. P. Manning. *Sci. Rep.* **2**, 553 (2012).
15. T. Rossby, R. L. Benway, *Geophys. Res. Lett.* **27**, 117–120 (2000).
16. A. J. Pershing *et al.*, *Oceanography* **14**, 76–82 (2001).
17. K. Chen, G. G. Gawarkiewicz, S. J. Lentz, J. M. Bane, *J. Geophys. Res.* **119**, 218–227 (2014).
18. B. Planque, T. Frédou, *Can. J. Fish. Aquat. Sci.* **56**, 2069–2077 (1999).
19. K. F. Drinkwater, *ICES J. Mar. Sci.* **62**, 1327–1337 (2005).
20. M. Fogarty, L. Incze, K. Hayhoe, D. Mountain, J. Manning, *Mitig. Adapt. Strategies Glob. Change* **13**, 453–466 (2008).
21. K. D. Friedland *et al.*, *Prog. Oceanogr.* **116**, 1–13 (2013).
22. J. E. Linehan, R. S. Gregory, D. C. Schneider, *J. Exp. Biol. Ecol.* **263**, 25–44 (2001).
23. G. D. Sherwood, R. M. Rideout, S. B. Fudge, G. A. Rose, *Deep Sea Res. II* **54**, 2794–2809 (2007).
24. C. Deutsch, A. Ferrel, B. Seibel, H.-O. Pörtner, R. B. Huey, *Science* **348**, 1132–1135 (2015).
25. Northeast Fisheries Science Center, *55th Northeast Regional Stock Assessment Workshop (55th SAW) Assessment Report* (U.S. Department of Commerce, 2013).
26. J. D. Dutil, Y. Lambert, *Can. J. Fish. Aquat. Sci.* **57**, 826–836 (2000).

ACKNOWLEDGMENTS

Supported by the NSF's Coastal SEES Program (OCE-1325484; A.J.P., M.A.A., C.M.H., A.L.B., K.E.M., J.A.N., H.A.S., J.D.S., and A.C.T.), the Lenfest Ocean Program (A.J.P., A.L.B., K.E.M., and G.D.S.), and institutional funds from the Gulf of Maine Research Institute (L.A.K.) and the Bigelow Laboratory for Ocean Sciences (N.R.R.). A.J.P.'s knowledge of fishery management was greatly enhanced by discussions with P. Sullivan, S. Cadrin, J. Kritzer, and other members of the New England Fishery Management Council Scientific and Statistical Committee. M. Palmer provided helpful comments on earlier drafts of the manuscript and facilitated access to the recent stock assessment. The manuscript also benefited from helpful feedback from J. Hare and two anonymous reviewers. The data reported in this paper are tabulated in the supplementary materials and are available from the referenced technical reports and from the National Climate Data Center.

SUPPLEMENTARY MATERIALS

www.sciencemag.org/content/350/6262/809/suppl/DC1
Materials and Methods
Figs. S1 to S6
Tables S1 to S5
References (*27*–*35*)

9 July 2015; accepted 23 September 2015
Published online 29 October 2015
10.1126/science.aac9819

EXTINCTION EVENTS

Body-size reduction in vertebrates following the end-Devonian mass extinction

Lauren Sallan[1]* and Andrew K. Galimberti[2]†

Following the end-Devonian mass extinction (359 million years ago), vertebrates experienced persistent reductions in body size for at least 36 million years. Global shrinkage was not related to oxygen or temperature, which suggests that ecological drivers played a key role in determining the length and direction of size trends. Small, fast-breeding ray-finned fishes, sharks, and tetrapods, most under 1 meter in length from snout to tail, radiated to dominate postextinction ecosystems and vertebrae biodiversity. The few large-bodied, slow-breeding survivors failed to diversify, facing extinction despite earlier evolutionary success. Thus, the recovery interval resembled modern ecological successions in terms of active selection on size and related life histories. Disruption of global vertebrate, and particularly fish, biotas may commonly lead to widespread, long-term reduction in body size, structuring future biodiversity.

Body size plays a crucial role in life histories, affecting generation times, energy demands, and population sizes (*1*, *2*). Size increases (Cope's rule) are thought to define Phanerozoic biodiversity, resultant from coordinated active trends, preferential survival of larger-bodied forms (lineage sorting), or passive diffusion (*2*–*4*). In contrast, the Lilliput effect—that is, temporary size reduction after mass extinction—is supported by few observations and remains under dispute (*4*, *5*). This effect is widely considered a passive result of extinction

[1]Department of Earth and Environmental Science, University of Pennsylvania, Philadelphia, PA 19104, USA. [2]Department of Biology, Kalamazoo College, Kalamazoo, MI 49006, USA. *Corresponding author. E-mail: lsallan@sas.upenn.edu †Present address: School of Biology and Ecology, University of Maine, Orono, ME 04469, USA.

selectivity or taphonomic bias (*4*, *5*). Global, long-term size reduction has not been proposed or reported following mass extinction (*4*). Persistent shrinkage has been restricted to specialized groups—such as birds, plankton, or island faunas (*6*–*9*)—in normal times.

Devonian-Mississippian [419 to 323 million years ago (Ma)] vertebrates were the first to exhibit modern ranges of body size (*10*–*12*), jaw and body forms (*5*, *13*), diet (*5*, *14*), and biodiversity (*5*, *15*). Their diversification was coincident with dramatic temperature and atmospheric oxygen changes (*11*, *16*, *17*). The mid-Paleozoic vertebrate record is thus an ideal test case for body-size phenomena. Limited samples of Paleozoic marine fishes have been used to link size increases with atmospheric oxygen rises (*2*, *10*, *11*), despite the lack of a physiological mechanism (*5*). Yet, Phanerozoic (especially Paleozoic) vertebrate size data remain poorly sampled (*2*, *5*, *10*–*12*, *18*).

The Paleozoic vertebrate record is divided by the Hangenberg event (359 Ma), arguably the most severe mass extinction for this group (*5*, *13*–*15*) (fig. S1). This event involved the loss of 11 of 22 major jawed vertebrate clades (corresponding to orders) and >96% of species (*19*) and also entailed ecosystem restructuring (*5*, *13*–*15*). The end-Devonian event should have affected size distributions as a correlate of other ecological traits (*1*). Yet, there are no hypotheses or comprehensive data sets for vertebrate size change across the event, just as these are lacking for other extinctions (*5*). This is a glaring oversight, considering the current declines in fish populations, especially larger-bodied forms (*18*), and the need for predictions of long-term effects.

We assembled a database of 1120 body lengths (in centimeters) for Devonian-Mississippian vertebrates (*20*) (tables S1 and S2); our database contains the vast majority of named species from all biomes (fig. S1). Using log-transformed sizes binned by stage (1326 points) (table S3), we found that Devonian vertebrates exhibited persistent stepwise size increases [ordinary least squares (OLS) and reduced major axis (RMA) regressions $P = 0.0001$, $r = 0.45$] (Fig. 1A, figs. S2 to S8, and tables S4 and S5) in line with Cope's rule predictions (*2*–*4*). In contrast, vertebrates exhibited persistent body-size reduction over the Mississippian (OLS and RMA $P = 0.0001$, $r = -0.25$) (tables S2 to S5; Fig. 1A; and figs. S3, S4, and S6), with significant differences between distributions in subsequent stages (Mann-Whitney *U* test; Tournaisian versus Visean: $P = 0.0041$; Visean versus Serpukhovian: $P = 0.018$) (table S6). This finding supports the notion of global shrinkage in vertebrates after the end-Devonian extinction, a prolonged Lilliput effect or reverse Cope's rule (*4*).

Prolonged shrinkage could result from cumulative short-term Lilliput effects after repeated abiotic events (*4*). However, although glacial aftershocks occurred during the early recovery interval, the Mississippian was more abiotically stable than the later Devonian (*17*, *18*, *21*). There is no evidence for further vertebrate turnover linked with perturbations (*5*, *13*–*15*). We fit multiple conflicting temperature and oxygen models to determine whether our data supported climate-based hypotheses for size change (tables S7 to S12). Contrary to energetics-based assumptions (*2*, *10*, *11*), vertebrate sizes were negatively correlated with one oxygen model (GEOCARBSULFvolc; $P = 0.0001$, $r = -0.33$) (*18*) yet showed no relationship with the others (tables S9 to S11). Contrary to Bergmann's rule that size is negatively influenced by temperature (*4*), vertebrate sizes were positively correlated with one sea surface temperature proxy (δO_{18} sea surface; $P = 0.0001$; $r = 0.020$) (*16*) yet showed no relationship with other estimates (tables S7 to S9).

To determine the exact drivers of our divergent size patterns, we fit active trend (directional change), random walk, and stasis models alongside the best-fit oxygen and temperature estimates (*16*, *17*). An active trend with a shift centered on the end-Devonian event was overwhelmingly supported [359 Ma; Akaike weight (AW): 0.93] (table S13). Thus, vertebrate size change was driven by active selection stemming from biotic factors and/or long-term conditions, which suggests that relationships with climatic change and smaller abiotic events were incidental (*11*).

To determine whether preservational biases affected overall patterns, we analyzed size structure for well-sampled faunas (Fig. 2A and table S14). Large vertebrates (>80 cm in body length) were overrepresented in Late Devonian ecosystems (Figs. 2A and 3A and tables S12 to S16). Thus, global patterns mirrored local trends. Faunas from after the extinction, particularly those during "Romer's Gap" (359 to 331 Ma) (*5*, *16*), showed

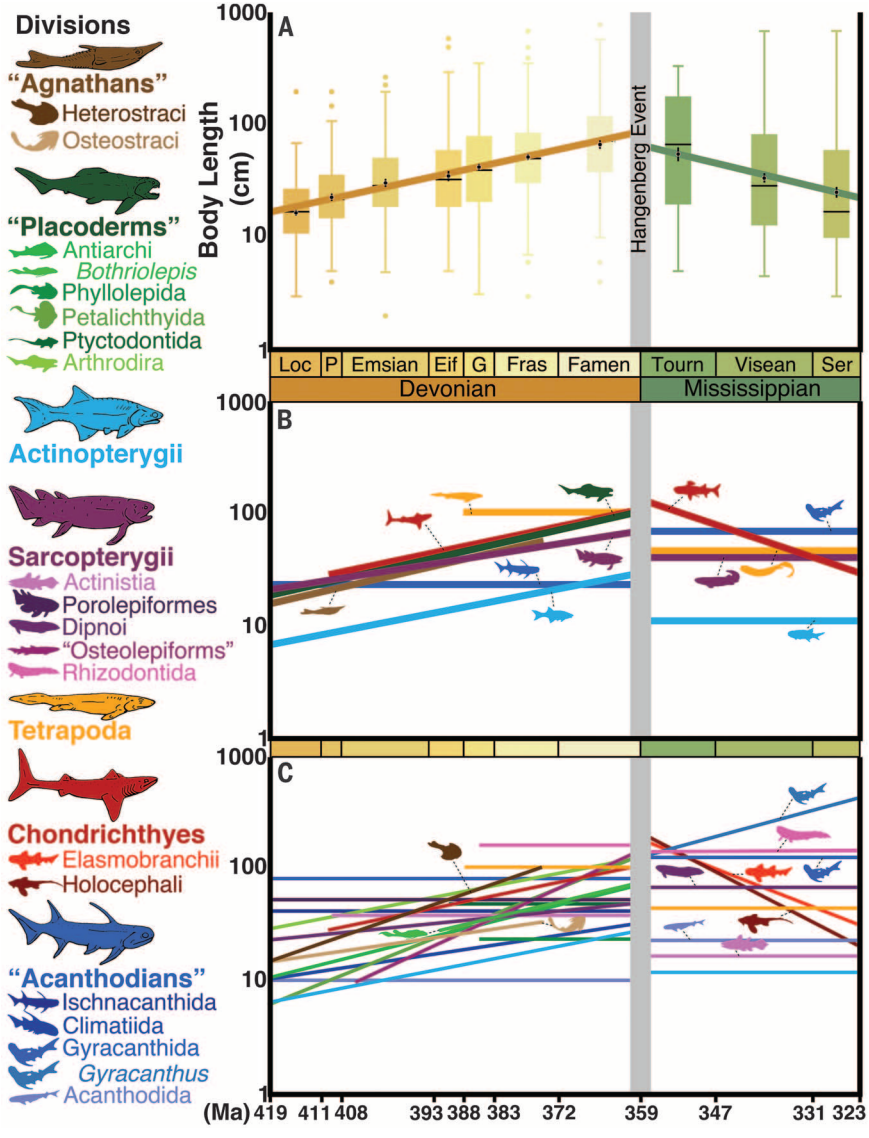

Fig. 1. Vertebrates experienced body-size reduction after the Hangenberg extinction. (**A**) Stage distributions and OLS trend lines for the Devonian and Mississippian. Black dots represent means; lines represent variance. Loc, Lochkovian; P, Pragian; Eif, Eifelian; G, Givetian; Fras, Frasnian; Famen, Famennian; Tourn, Tournaisian; Ser, Serpukhovian. (**B**) Trend lines for major vertebrate divisions. Flat lines represent the mean length for groups with insignificant effect sizes. (**C**) Trend lines for vertebrate subclades.

severe losses among larger size classes, despite similar numbers of species (analysis of similarity, $P = 0.009$) (table S15 and Fig. 2A). The majority of taxa at early Mississippian sites were under 40 cm in length, similar to early Devonian faunas dominated by jawless fishes (tables S16 to S18; Figs. 2, B and C, and 3, B to D; and figs. S14 and S15). Altered size structure is indicative of an ecosystem-wide Lilliput effect.

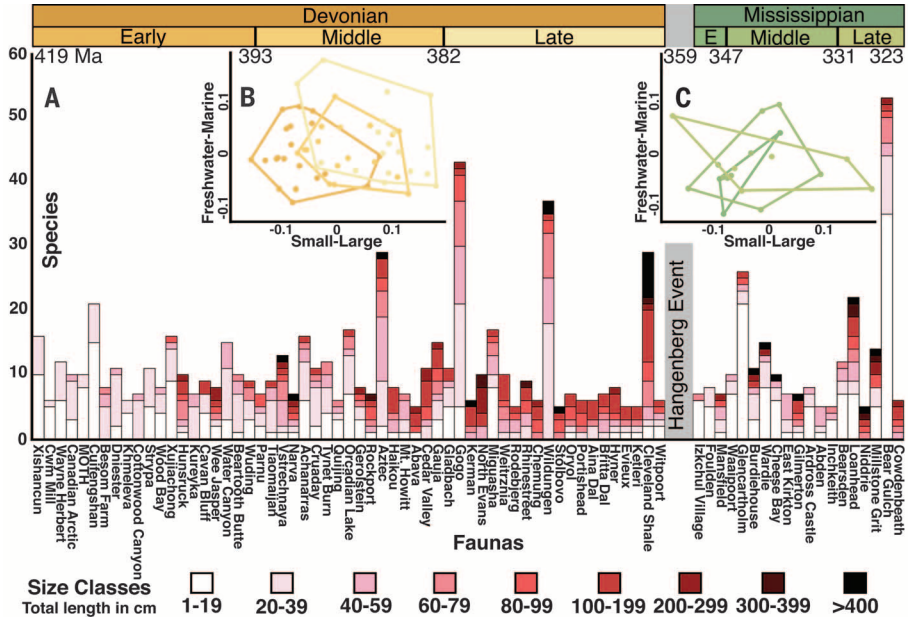

Fig. 2. Small vertebrates were dominant in postextinction faunas. (**A**) Histogram of species per fauna. (**B**) Nonparametric multidimensional (NMDS) ecospace plot of Devonian faunas binned by interval. (**C**) NMDS ecospace plot of Mississippian faunas binned by interval.

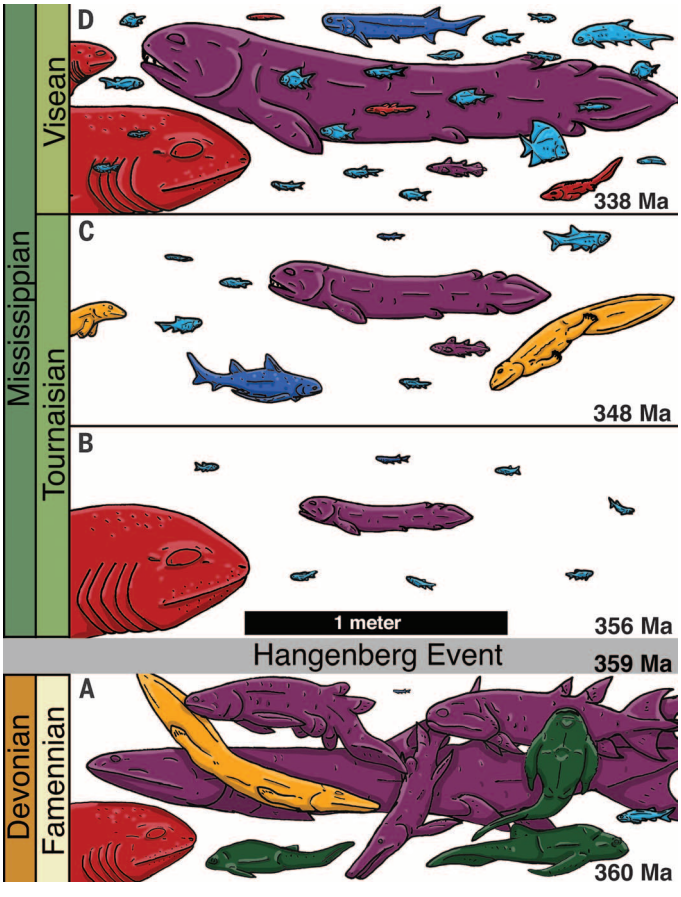

Fig. 3. Small vertebrates were increasingly diverse in postextinction ecosystems. Represented faunas include taxa with known body sizes from elsewhere in the same region and time bin. See Fig. 2A and tables S1 and S14 for sizes and Fig. 1 for taxon key. (**A**) Andreyevka-2, Russia. (**B**) Andreyevka-1/Izkchul Village, Russia. (**C**) Foulden, Scotland. (**D**) Glencartholm, Scotland.

To test the depth of our observed size trends, we analyzed six vertebrate divisions and 22 widespread clades. We aimed to reveal whether the overall pattern resulted from coordinated change, lineage sorting, or taxonomic sampling bias (Fig. 1B) (*2*, *3*). All well-sampled Devonian lineages exhibited significant size increases, including the dominant placoderms and lobe-finned fishes (Sarcopterygii) (tables S19 and S20, Fig. 1B, and figs. S18 to S21) and widespread genera such as *Bothriolepis* (tables S25 and S26, Fig. 1C, and figs. S40 and S41). Multivariate model-fitting strongly supported an active coordinated trend (AW: 0.99) (tables S22 and S31). Therefore, rather than wholly resulting from emerging dominance of novel, already-large-bodied groups (lineage sorting), Devonian vertebrate size increases largely occurred within ecomorphologically stable lineages (*2*, *10*–*12*). This finding supports a traditional Cope's rule phenomenon (*2*–*4*) and validates the signal in our complete data set.

On average, any postextinction lineages started out smaller than their latest Devonian forebears (Fig. 1), a classic Lilliput effect (*4*). However, reduced sizes also characterized newly dominant forms—including cartilaginous and ray-finned fishes and tetrapods (Chondrichthyes, Actinopterygii, and Tetrapoda)—for the next 36 million years (*5*, *13*–*15*) (tables S32 and S33; Fig. 1; and figs. S68 to S70, S74, and S75). This resulted from active trends (e.g., Chondrichthyes), downward shifts in size distribution (e.g., Actinopterygii) (table S21), and/or stasis (e.g., Tetrapoda) (table S19). Newly genus-poor clades (*5*, *15*) exhibited size patterns that conflicted with the overall decline. Some groups (e.g., Rhizodontida) maintained their Devonian body sizes despite diversity losses (*15*) (Fig. 1C, table S1, and figs. S36 and S37). Others, such as the Acanthodida and Dipnoi (Fig. 1C and tables S26 to S30), showed marked length increases across the boundary. The giant acanthodian *Gyracanthus* even exhibited a trend toward larger sizes (Fig. 1C, figs. S80 and S81, and table S27). These forms have previously been dubbed "dead clades walking" (*5*, *15*) to indicate that they are survivors marked by low, declining diversity (*22*).

The existence of large, marginal survivors reduced effect size (tables S4 and S5) by adding long tails to Mississippian size distributions (table S3 and Fig. 1A). Tournaisian mean body length remained similar to that for the Famennian, despite reductions in all other metrics (tables S3 and S6 and Fig. 1A). This masked an immediate Lilliput effect at the faunal level, where small (<40 cm) speciose actinopterygian and chondrichthyan taxa made up an increasing majority of taxa (*15*) (tables S14 to S17). Maximum body lengths were actually greater in the Mississippian than in the Devonian (Fig. 1A and table S3). These values alone would give a false impression of continued Cope's rule trends (*2*, *11*, *12*).

Postextinction global shrinkage was underlain by differential diversification and extinction (*23*),

species selection, and active trends within lineages (*24*). Larger vertebrates comparable to our "dead clades," such as Devonian placoderms and extant sharks (*25*), tend to have low fecundity, high parental investment, and increased energy demands balanced by long life spans, multiple breeding seasons, and wide habitat ranges (*K*-selection) (*1*). Extremes of these traits may confer relative extinction resistance in ecologically depleted times while limiting the potential for speciation (*26*–*28*). Smaller vertebrates, such as holocephalans and ray-finned fishes (*29*), tend to have high reproductive rates, short generation times, and large populations (*r*-selection) (*1*). These traits may increase survival through sheer numbers while promoting diversification via higher variation and population fragmentation (*24*, *26*).

The Mississippian recovery interval favored extreme life histories among survivors, selecting for a bimodal size distribution. In the longer term, larger-bodied but less speciose lineages, such as rhizodonts, remained marginal or went extinct (*5*, *16*). Smaller-bodied, rapidly radiating lineages, such as ray-finned fishes, spread to dominate ecosystems (*13*, *16*). Significant downward shifts in Mississippian chondrichthyan and actinopterygian size distributions suggest that this pattern was mirrored within groups (table S21). The Mississippian approximated a scaled-up ecological succession, in which small, short-lived taxa dominate, whereas larger, longer-lived forms are marginal (*30*).

Scattered observations suggest that this pattern is common during long-term recovery intervals. Gigantic, rare postextinction vertebrates were taken as a sign of ecological restoration (*31*). Shrinkage within postextinction invertebrates (*4*, *6*, *8*) was considered restricted or temporary. The oft-noted tendency for major clades to descend from smaller taxa may be linked to such characteristics of postextinction radiations (*3*, *7*). New, diversifying modern ray-finned fishes were smaller than older, diminished ray-finned fish lineages in the Triassic (*32*). Thus, size-related selection has likely shaped vertebrate biodiversity.

Small, opportunistic taxa eventually give way to larger, longer-lived forms in disturbed ecosystems (*29*). Likewise, Cope's rule trends may be favored during stable, saturated times at some distance from recovery conditions (*2*, *5*, *26*, *27*). This describes the intervals containing Devonian vertebrates, late Mesozoic giants, and later Cenozoic mammals (*2*, *5*, *27*). An overall Phanerozoic Cope's rule (*2*) could result from a greater number and length of stable nonrecovery intervals. Vertebrate size trends appear to result from active selection, probably on life histories, with direction based on long-term conditions and survival.

REFERENCES AND NOTES

1. E. R. Pianka, *Am. Nat.* **104**, 592–597 (1970).
2. N. A. Heim, M. L. Knope, E. K. Schaal, S. C. Wang, J. L. Payne, *Science* **347**, 867–870 (2015).
3. S. M. Stanley, *Evolution* **27**, 1–26 (1973).
4. P. J. Harries, P. O. Knorr, *Palaeogeogr. Palaeoclimatol. Palaeoecol.* **284**, 4–10 (2009).
5. M. Friedman, L. C. Sallan, *Palaeontology* **55**, 707–742 (2012).
6. R. Lockwood, . *Paleobiology* **31**, 578–590 (2005).
7. M. S. Y. Lee, A. Cau, D. Naish, G. J. Dyke, *Science* **345**, 562–566 (2014).
8. J. L. Payne, A. B. Jost, S. C. Wang, J. M. Skotheim, *Evolution* **67**, 816–827 (2013).
9. M. V. Lomolino, *J. Biogeogr.* **32**, 1683–1699 (2005).
10. B. Choo, M. Zhu, W. Zhao, L. Jia, Y. Zhu, *Sci. Rep.* **4**, 5242 (2014).
11. T. W. Dahl *et al.*, *Proc. Natl. Acad. Sci. U.S.A.* **107**, 17911–17915 (2010).
12. J. C. Lamsdell, S. J. Braddy, *Biol. Lett.* **6**, 265–269 (2010).
13. L. C. Sallan, M. Friedman, *Proc. Biol. Sci.* **279**, 2025–2032 (2012).
14. L. C. Sallan, T. W. Kammer, W. I. Ausich, L. A. Cook, *Proc. Natl. Acad. Sci. U.S.A.* **108**, 8335–8338 (2011).
15. L. C. Sallan, M. I. Coates, *Proc. Natl. Acad. Sci. U.S.A.* **107**, 10131–10135 (2010).
16. D. L. Royer, R. A. Berner, I. P. Montañez, N. J. Tabor, D. J. Beerling, *GSA Today* **14**, 4–10 (2004).
17. R. A. Berner, *Am. J. Sci.* **309**, 603–606 (2009).
18. B. Worm, M. Sandow, A. Oschlies, H. K. Lotze, R. A. Myers, *Science* **309**, 1365–1369 (2005).
19. D. M. Raup, *Science* **206**, 217–218 (1979).
20. Materials and methods are available as supplementary materials on *Science* Online.
21. S. M. Stanley, *Proc. Natl. Acad. Sci. U.S.A.* **107**, 19185–19189 (2010).
22. D. Jablonski, *Proc. Natl. Acad. Sci. U.S.A.* **99**, 8139–8144 (2002).
23. P. J. Wagner, G. F. Estabrook, *Proc. Natl. Acad. Sci. U.S.A.* **111**, 16419–16424 (2014).
24. S. M. Stanley, *Proc. Natl. Acad. Sci. U.S.A.* **72**, 646–650 (1975).
25. J. A. Long *et al.*, *Nature* **517**, 196–199 (2015).
26. D. Jablonski, *Science* **231**, 129–133 (1986).
27. J. H. Knouft, L. M. Page, *Am. Nat.* **161**, 413–421 (2003).
28. B. Van Valkenburgh, X. Wang, J. Damuth, *Science* **306**, 101–104 (2004).
29. L. A. K. Barnett, R. L. Earley, D. A. Ebert, G. M. Cailliet, *Mar. Biol.* **156**, 301–316 (2009).
30. J. F. Ponge, *Ecol. Evol.* **3**, 1113–1124 (2013).
31. N. B. Fröbisch, J. Fröbisch, P. M. Sander, L. Schmitz, O. Rieppel, *Proc. Natl. Acad. Sci. U.S.A.* **110**, 1393–1397 (2013).
32. C. Romano *et al.*, *Biol. Rev.* 10.1111/brv.12161 (2014).

ACKNOWLEDGMENTS

We thank G. Hunt for assistance with methods; N. Sheldon for advice on climate models; and T. Kailing, D. Rabosky, M. Friedman, J. Clarke, S. Giles, N. Heim, M. Brazeau, and three anonymous reviewers for discussions. We also thank the University of Pennsylvania, Kalamazoo College, the University of Michigan, and the Michigan Society of Fellows for support. All data are available in the supplementary materials.

SUPPLEMENTARY MATERIALS

www.sciencemag.org/content/350/6262/812/suppl/DC1
Materials and Methods
Supplementary Text
Figs. S1 to S91
Tables S1 to S40
References (*33*–*49*)

4 June 2015; accepted 9 October 2015
10.1126/science.aac7373

SMALL RNAS

MicroRNA-encoded behavior in *Drosophila*

Joao Picao-Osorio,[1] Jamie Johnston,[1] Matthias Landgraf,[2] Jimena Berni,[2] Claudio R. Alonso[1]*

The relationship between microRNA (miRNA) regulation and the specification of behavior is only beginning to be explored. We found that mutation of a single miRNA locus (*miR-iab4/iab8*) in *Drosophila* larvae affects the animal's capacity to correct its orientation if turned upside down (self-righting). One of the miRNA targets involved in this behavior is the *Hox* gene *Ultrabithorax*, whose derepression in two metameric neurons leads to self-righting defects. In vivo neural activity analysis reveals that these neurons, the self-righting node (SRN), have different activity patterns in wild type and miRNA mutants, whereas thermogenetic manipulation of SRN activity results in changes in self-righting behavior. Our work thus reveals a miRNA-encoded behavior and suggests that other miRNAs might also be involved in behavioral control in *Drosophila* and other species.

The regulation of RNA expression and function is emerging as a hub for gene expression control across a variety of cellular and physiological contexts, including neural development and specification. Small RNAs such as microRNAs (miRNAs) (*1*) have been shown to affect neural differentiation (*2*, *3*), but their roles in the control of behavior are only beginning to be explored.

Previous work in our laboratory focused on the mechanisms and impact of RNA regulation on the expression and neural function of the *Drosophila Hox* genes (*4*–*7*). These genes encode a family of evolutionarily conserved transcription factors that control specific programs of neural differentiation along the body axis (*8*–*10*), offering an opportunity to investigate how RNA regulation relates to the formation of complex tissues such as the nervous system.

We used the *Hox* gene system to investigate the roles played by a single miRNA locus (*miR-iab4/iab8*) (*4*, *11*–*16*) on the specification of the nervous system during early *Drosophila* development. This miRNA locus controls the embryonic expression of posterior *Hox* genes (*4*, *11*–*16*). Given that we found no detectable differences in the morphological layout of the main components of the

[1]Sussex Neuroscience, School of Life Science, University of Sussex, Brighton BN1 9QG, UK. [2]Department of Zoology, University of Cambridge, Cambridge CB2 3EJ, UK.
***Corresponding author. E-mail: c.alonso@sussex.ac.uk**

nervous system in late *Drosophila* embryos of wild type and *miR-iab4/iab8*–null mutants [herein Δ*miR* (*14*)] (fig. S3, B to F), we analyzed early larval behavior as a stratagem to probe the functional integrity of the late embryonic nervous system.

Most behaviors in early larva were unaffected by the miRNA mutation (fig. S1 and movies S1 and S2), except self-righting (SR) behavior (Fig. 1, A to C, and movies S3 and S4): miRNA mutant larvae were unable to return to their normal orientation at the same speed as their wild-type counterparts.

By means of selective target overexpression followed by SR phenotype analyses, we identified the *Drosophila Hox* gene *Ultrabithorax* (*Ubx*) (*17*, *18*) as a miRNA target implicated in the genetic control of SR behavior (Fig. 1F). Overexpression of Ubx within its expression domain did not affect any larval behavior tested except SR, which is in agreement with the effects observed in miRNA mutants (Fig. 1, D and E). Analysis of *Ubx* 3′ untranslated region (3′UTR) fluorescent reporter constructs expressed in the *Drosophila* central nervous system (CNS) (fig. S2) indicates that the interaction between *miR-iab4/iab8* and *Ubx* is direct, which is in line with prior observations in other cellular contexts (*11*–*13*).

To identify the cellular basis for SR control, we systematically overexpressed Ubx within subpopulations of neurons (fig. S4). Increased levels of Ubx within the pattern of *Cha(7.4kb)-Gal4*, which largely targets cholinergic sensory and interneurons, phenocopied the miRNA SR anomalies (fig. S4). Further overexpression analysis identified two metameric neurons as the minimal node required for the SR behavior [self-righting node (SRN)] (Fig. 2, A and B).

Several lines of evidence confirm the role of miRNA-dependent *Ubx* regulation within the SRN as a determinant of SR. First, both *Ubx* and miRNA transcripts (*miR-iab4*) derived from the *miR-iab4/iab8* locus were detected within the SRN (Fig. 3, A to C). Second, in the context of miRNA mutation, Ubx protein expression is increased within the SRN (Fig. 3, D to F). Third, reduction of Ubx (*Ubx* RNAi) specifically enforced within SRN cells is able to ameliorate or even rescue the SR phenotype observed in miRNA mutants (Fig. 2C).

Two plausible scenarios arise to explain the effects of *miR-iab4/iab8* in regard to SR behavior.

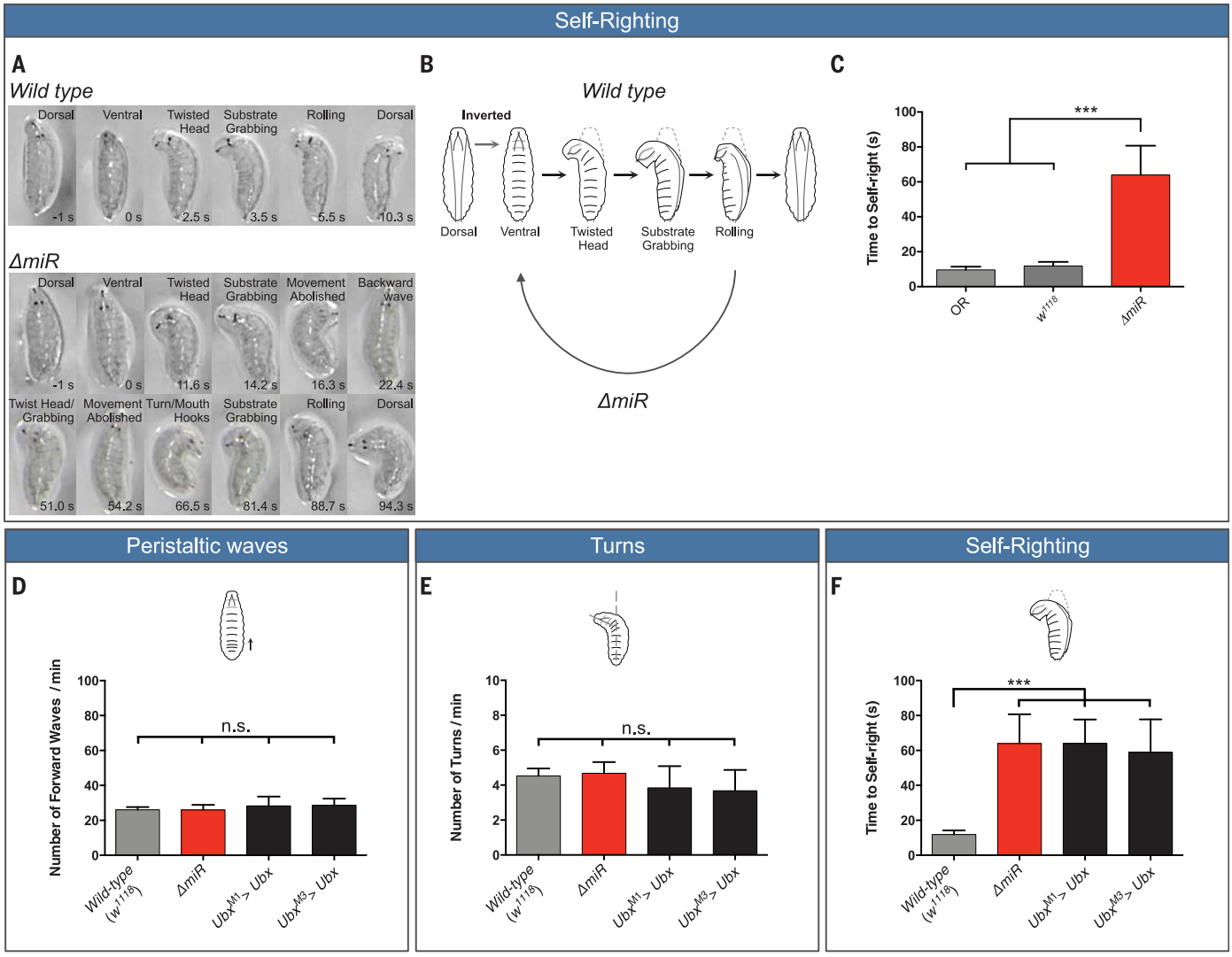

Fig. 1. Both removal of *miR-iab4/iab8* and overexpression of Ubx disrupt a specific larval locomotor behavior: self-righting (SR). (**A** and **B**) Description of larval SR behavior. (A) Time lapses of larval SR behavior. (Top) Wild-type larvae placed in an inverted position (ventral up), twisted their heads, grabbed the substrate with the mouth hooks, and rolled their bodies onto their ventral surface (dorsal up). (Bottom) In contrast, Δ*miR* larvae displayed problems in self-righting their bodies. (B) Diagram of the self-righting behavioral response. (**C**) Quantification of the time required for the successful completion of the SR behavior (mean ± SEM; *n* = 27 to 29 larvae per genotype) in two wild-type controls (*OR* and w^{1118}, light and dark gray, respectively) and Δ*miR* larvae (red). (**D** to **F**) Quantification of larval behavior in Ubx overexpression lines (Ubx^{M1}>*Ubx* and Ubx^{M3}>*Ubx*). Quantification of (D) number of forward peristaltic waves per minute, (E) larval turning per minute, and (F) time to self-right in wild type (w^{1118}, gray), Δ*miR* (red), and Ubx^{M1}>*Ubx* and Ubx^{M3}>*Ubx* (black) (mean ± SEM; *n* = 15 to 29 larvae per genotype). A nonparametric Mann-Whitney *U* test was performed to compare treatments; $P > 0.05$ (nonsignificant; n.s.); $P < 0.001$ (***).

One is that miRNA input is required for the late embryonic development of the neural networks underlying SR, arguing for a "developmental" role of the miRNA; another is that miRNA repression affects normal physiological/behavioral functions largely without disrupting neural development in line with a "behavioral" role. Two independent experiments support that the primary roles of *miR-iab4/8* are behavioral. First, anatomical analysis of SRN cells in wild type (wt), Δ*miR*, and *R54503>Ubx* [SRN-driver line (*19*, *20*)] show no significant differences in total numbers of SRN cells (fig. S5B) or in SRN cell body size (fig. S5C); furthermore, analysis of wt, Δ*miR*, and *R54503>Ubx* show indistinguishable SRN-projection patterns (fig. S5, D and E). Second, Gal-80$_{ts}$–mediated conditional expression experiments show that SRN-specific Ubx overexpression after embryogenesis is sufficient to trigger the SR behavior (Fig. 2, D and E).

The results presented above suggest that miRNA-dependent *Hox* regulation within the SRN must somehow modify the normal physiology of SRN cells so that when the miRNA is mutated, these neurons perform functions different from those in wild-type animals. To test this hypothesis, we used genetically encoded calcium sensors [GCaMP6 (*21*)] specifically expressed in SRN cells and tracked down spontaneous profiles of neural activity. SRN cells in miRNA mutants produce activity traces that are significantly different from those observed in wild-type SRN cells (Fig. 4, B and C, and fig. S6A). Quantification of maximal amplitude and proportion of active cells in each genotype also reveal significant differences (Fig. 4D and fig. S6B) in SRN function across the genotypes, but no change in cell viability is observed (fig. S6C). Neural activity differences across genotypes are significant within regions of expression of *miR-iab4* (Fig. 4E), suggesting that this miRNA (and not *miR-iab8*) might be the main contributor to SR control. Analysis of mutations that selectively affect *miR-iab4* or *miR-iab8* (*14*, *15*, *22*, *23*) strongly suggests that *miR-iab4* is the key regulator of SR (Fig. 3, G and H).

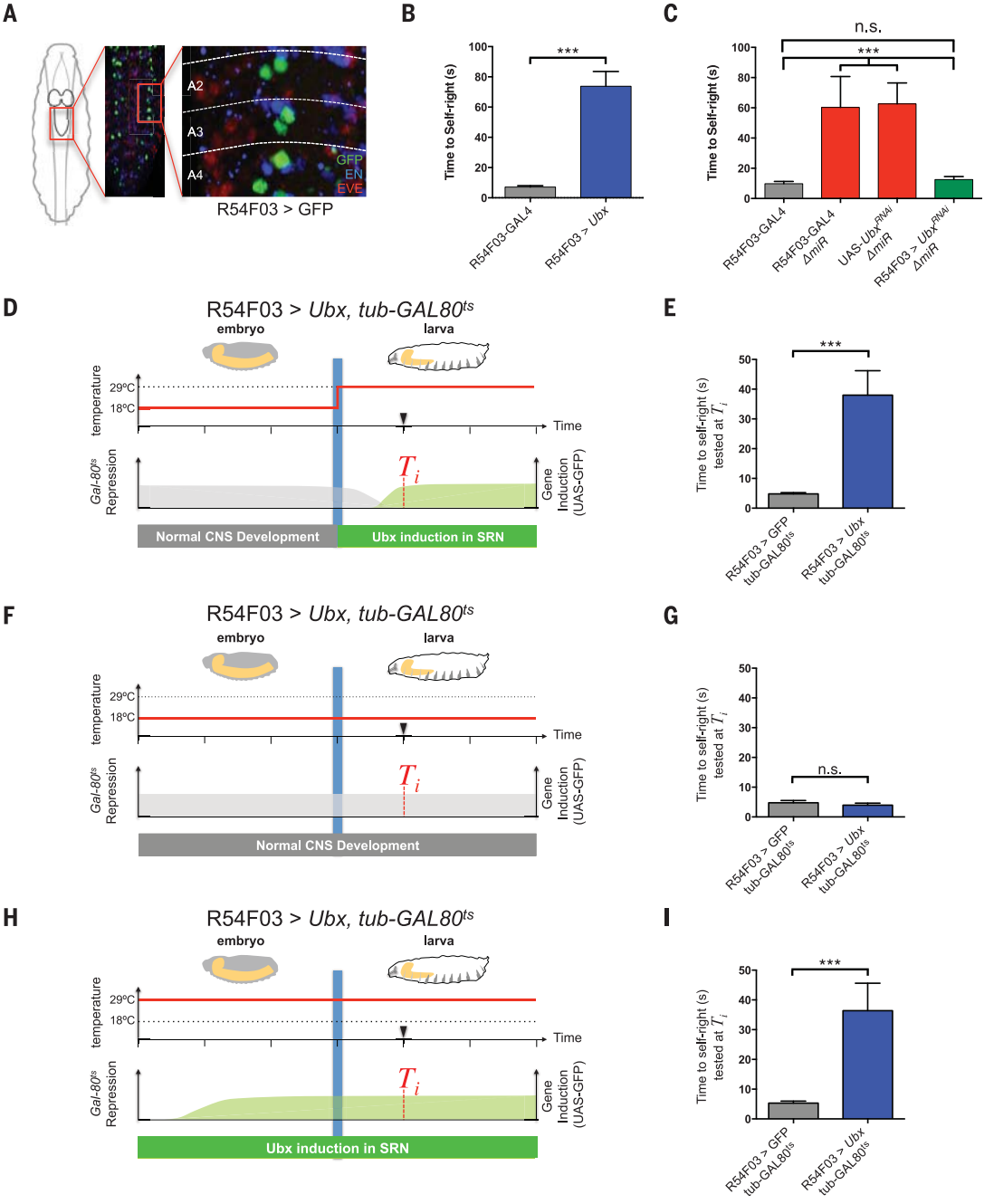

Fig. 2. miRNA-dependent *Ubx* regulation in SRN cells underlies SR behavior. (**A**) *R54F03*-GAL4 expression [green fluoprescent protein (GFP), green] in the larval abdominal CNS. Even-skipped protein is in red; Engrailed protein is in blue; and A2, A3, and A4 refer to abdominal segments 2 to 4, respectively. (**B**) Artificial increase of *Ubx* expression in two metameric neurons driven by the *R54F03* promoter (mean ± SEM; *n* = 60 larvae per genotype). (**C**) Artificial decrease of Ubx expression with Ubx^{RNAi} within SRN cells in Δ*miR* larvae (*R54F03*-GAL4, Δ*miR*/UAS-*Ubx*^{RNAi}, Δ*miR*, green) (mean ± SEM; *n* = 20 to 23 larvae per genotype). (**D** to **I**) Conditional increase of Ubx expression during embryonic and early larval development with *tub*-Gal80^{ts} (Gal80^{ts} represses GAL4 activity at 18°C) within SRN cells: *R54F03* > Ubx, *tub*-GAL80^{ts} (UAS-*Ubx*/+ ; *R54F03*/*tub*-Gal80^{ts}). Controlled increase of Ubx expression in SRN cells in early larvae [(D) and (E); mean ± SEM; *n* = 20 larvae per genotype] and from mid-embryogenesis to early larvae [(H) and (I); mean ± SEM; *n* = 15 larvae per genotype]. [(**F**) and (**G**)] Repressed increase of Ubx expression in SRN cells throughout embryogenesis and early larvae (mean ± SEM; *n* = 15 larvae per genotype). A nonparametric Mann-Whitney *U* test was performed to compare treatments; *P* > 0.05 (nonsignificant, n.s.); ***$P < 0.001$.

To demonstrate that the changes in SRN neural activity were causal to SR behavior, we artificially activated (Fig. 4F) or inhibited (Fig. 4G) SRN cells (*24*, *25*) and showed that this triggered the aberrant SR phenotype. This suggested that activation of SRN cells in larvae placed "right side up" might be sufficient to "evoke" actions reminiscent of a self-righting response. We developed an optogenetic system in which we activated SRN cells by means of *R54F03*-driven *Channelrhodopsin 2 (ChR2)* in trans-retinal fed larvae. Under blue light stimulation, larvae performed

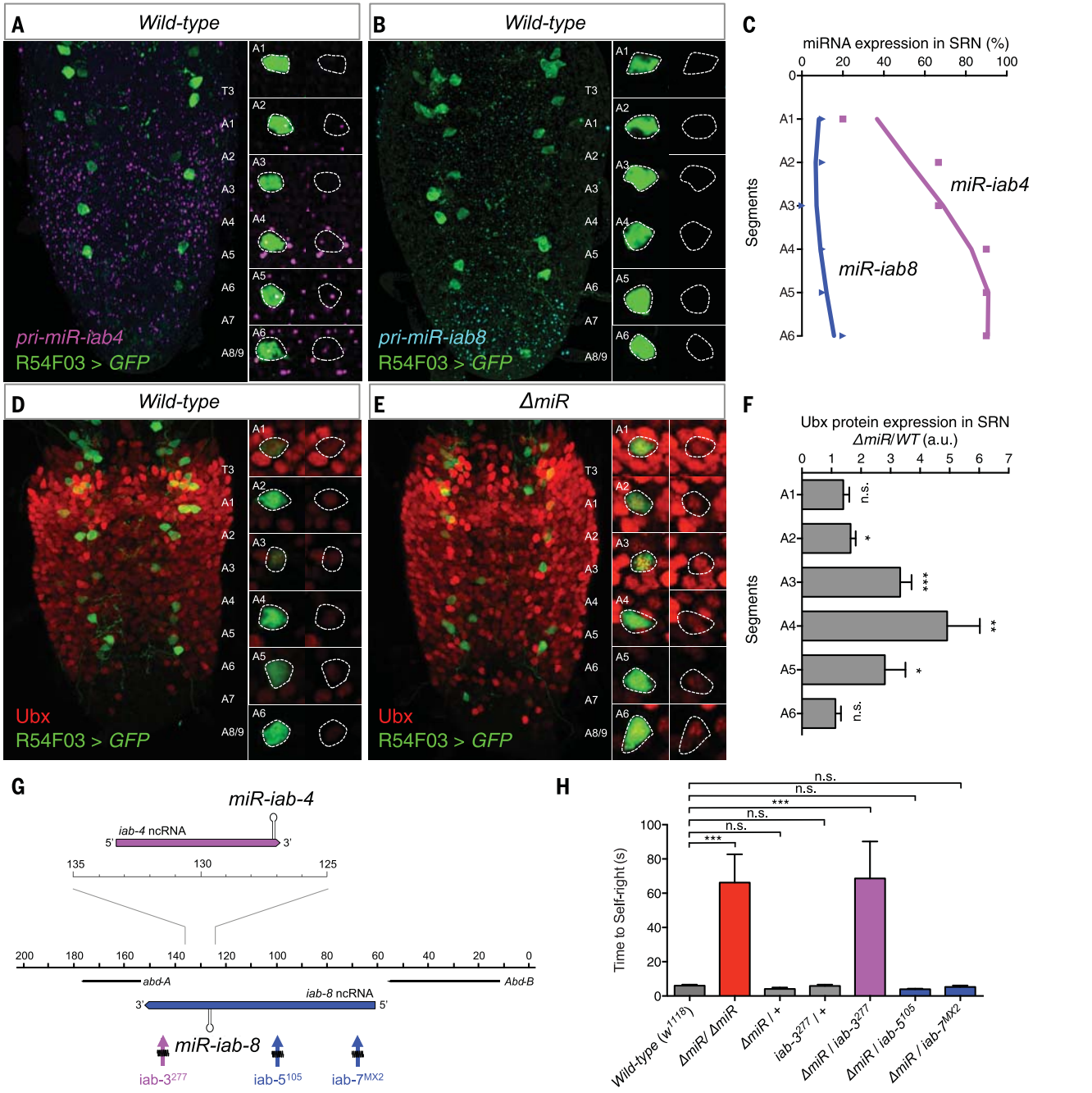

Fig. 3. Regulation of Ubx protein expression in SRN cells by *miR-iab4/iab8*. (**A**) Wild-type expression of precursor *miR-iab4* transcripts [RNA–fluorescence in situ hybridization (RNA-FISH), purple] in SRN cells (*R54F03*>GFP, green) of the ventral nerve cord (VNC) of first-instar *Drosophila* larvae. (**B**) Wild-type expression of precursor *miR-iab8* transcripts (RNA-FISH, blue) in SRN cells (R54F03>GFP, green) of the VNC of first-instar *Drosophila* larvae. (**C**) Percentage of SRN cells expressing *miR-iab4* (purple, square) and *miR-iab8* (blue, triangle) precursors across A1 to A6 ($n = 10$ larvae). (**D** and **E**) Ubx protein expression (red) in SRN cells of wild-type (D) and *ΔmiR* (E) first-instar larvae VNCs. (**F**) Quantification of Ubx protein expression ratio of *ΔmiR* over wild type within the SRN cells (red) by fluorescent intensity ($n = 8$ larvae per genotype; arbitrary units, a.u.). (**G**) Diagram of a subregion of the bithorax complex based on (*14*) showing *iab-4* (purple) and *iab-8* (blue) noncoding RNAs (ncRNAs), and rearrangement breakpoints affecting *miR-iab-4* (iab-3^{277}, purple) and *miR-iab-8* (iab-5^{105} and iab-7^{MX2}, blue). (**H**) Genetic complementation tests to determine the involvement of *miR-iab4* or *miR-iab8* in SR behavior by using trans-heterozygote larvae for *ΔmiR* and different chromosomal rearrangement breakpoints that disrupt the bithorax complex (mean ± SEM; $n = 17$ to 20 larvae per genotype). A nonparametric Mann-Whitney *U* test was performed to compare treatments; $P > 0.05$ (nonsignificant; n.s.); $^*P < 0.05$; $^{**}P < 0.01$; $^{***}P < 0.001$.

an atypical bending movement, frequently adopting a "lunette" position (fig. S7 and movie S5). Neither parental line *R54F03*-Gal4 nor UAS-*ChR2* showed similar reactions to stimulation, confirming the specificity of this effect (fig. S7 and movies S6 and S7).

To study the links between SRN neurons and the SR movement, we labeled SRN projections with *myr-GFP* and discovered that SRN cells

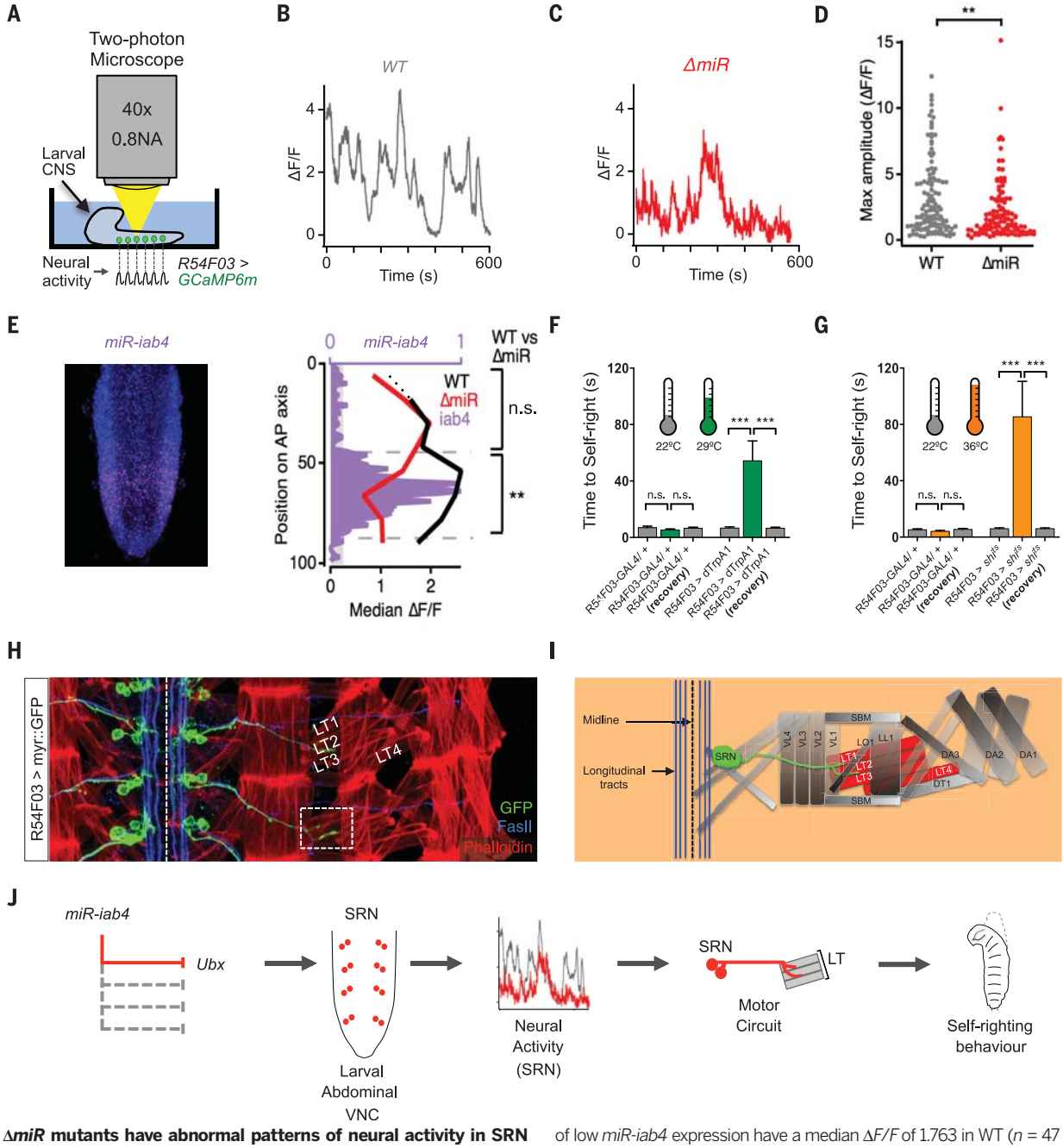

Fig. 4. Δ*miR* mutants have abnormal patterns of neural activity in SRN cells. (**A**) Schematic of the larval CNS expressing GCaMP6m in SRN cells (*R54F03> GCaMP6m*, green) imaged in a two-photon microscope. (**B**) Examples of spontaneous activity recorded over 10 min from wild type (WT: UAS-*GCaMP6m/+*; *R54F03*-GAL4/+) and (**C**) Δ*miR* mutants (UAS-*GCaMP6m/+*; *R54F03*-GAL4, Δ*miR*/Δ*miR*) in SRN cells. (**D**) Maximum amplitude of spontaneous activity in SRN cells: WT (median $\Delta F/F = 1.91$; $n = 120$ SRN cells) and in Δ*miR* mutants (median $\Delta F/F = 1.27$; $n = 115$ SRN cells) (**$P < 0.01$, Mann-Whitney *U* test). (**E**) Expression pattern of *miR-iab4* (purple) and 4′,6-diamidino-2-phenylindole (DAPI, blue) in the VNC of a freshly hatched larva (left). Median $\Delta F/F$ in SRN cells of WT (black line) and Δ*miR* (red line) larval VNCs, and relative expression of *miR-iab4* (purple) along the anterior-posterior (A-P) axis. Median $\Delta F/F$ of WT (median of 2.132, $n = 73$ SRN cells) and Δ*miR* (median of 1.122, $n = 68$ SRN cells) in regions of high *miR-iab4* expression (**$P < 0.01$, Mann-Whitney *U* test). Regions of low *miR-iab4* expression have a median $\Delta F/F$ of 1.763 in WT ($n = 47$ SRN cells) and 1.749 ($n = 47$ SRN cells) in Δ*miR* specimens (n.s., $P > 0.05$; Mann-Whitney *U* test). (**F** and **G**) Thermogenetic manipulation of neural activity in SRN cells. Activation [(F), *R54F03>dTrpA1*] and inhibition [(G), *R54F03>shi^{ts}*] of SRN neural activity (mean ± SEM; $n = 17$ larvae per genotype, ***$P < 0.0001$, Mann-Whitney *U* test) [29°C (green) for activation (H) and 36°C (orange) for inhibition (I)]. (**H**) Wild-type motor axonal projections of SRN cells (UAS-*myr::GFP*/UAS-*myr::GFP*; *R54F03*-GAL4/*R54F03*-GAL4, green) into muscles (phalloidin, red) lateral transverse 1 and 2 (LT1 and LT2) in late embryos (stage 17) (Fasciclin II, FASII, blue). Scale bars, 10 μm. (**I**) Diagram of SRN cells projecting to the LT1 and LT2 muscles. (**J**) A model that summarizes the data reported in this study. Mutation of *miR-iab4* (left) leads to Ubx derepression in the SRN node, affecting SRN neural activity patterns and triggering an anomalous SR behavior (right).

innervate two of the lateral transverse (LT) muscles and that they can be colabeled with antibodies against Fasciclin 2 (Fas2) (Fig. 4H), demonstrating these to be motorneurons. LT muscles are innervated by Bar-H1^{+} motorneurons (fig. S8A), so we used *Bar-H1*-Gal4 as a second driver to demonstrate that appropriate Ubx levels in these cells are required for normal SR behavior (fig. S8B), establishing the SRN cells as the LT-MNs.

We have therefore shown that miRNA-dependent *Hox* gene repression within a distinct group of motorneurons (SRN/LT-MNs) is required for the control of a specific locomotor behavior in the early *Drosophila* larva. Our finding that *Hox* gene posttranscriptional regulation is involved in SR control suggests that other RNA-based regulatory processes affecting *Hox* gene expression might also impinge on specific neural outputs; we are currently investigating this possibility, with special regard to the roles of the *Hox* genes in the specification of neural lineages with axial-specific architectures, and systematically testing the roles of other miRNAs on behavior.

That we could not detect any obvious neuroanatomical changes in miRNA mutant embryos suggests that these are either very subtle or that the role of miRNA regulation may be primarily behavioral, in the sense of affecting the performance of a correctly wired neural system, rather than developmental, contributing to the development of the network (*26*). Given that *miR-iab4/iab8* is involved in adult ovary innervation (*16*), it seems that miRNAs—much like ordinary protein-coding genes—can be involved in several distinct roles within the organism.

The results of this study contribute to the understanding of how complex innate behaviors are represented in the genetic program. Our data lead us to propose that other miRNAs might also be involved in the control of behavior in *Drosophila* and other species.

REFERENCES AND NOTES

1. D. P. Bartel, *Cell* **136**, 215–233 (2009).
2. X. Li, P. Jin, *Nat. Rev. Neurosci.* **11**, 329–338 (2010).
3. A. X. Sun, G. R. Crabtree, A. S. Yoo, *Curr. Opin. Cell Biol.* **25**, 215–221 (2013).
4. S. Thomsen, G. Azzam, R. Kaschula, L. S. Williams, C. R. Alonso, *Development* **137**, 2951–2960 (2010).
5. H. C. Reed *et al.*, *Genetics* **184**, 745–758 (2010).
6. L. F. de Navas *et al.*, *Development* **138**, 107–116 (2011).
7. A. Rogulja-Ortmann *et al.*, *Development* **141**, 2046–2056 (2014).
8. W. McGinnis, R. Krumlauf, *Cell* **68**, 283–302 (1992).
9. R. K. Maeda, F. Karch, *Development* **133**, 1413–1422 (2006).
10. M. Mallo, C. R. Alonso, *Development* **140**, 3951–3963 (2013).
11. M. Ronshaugen, F. Biemar, J. Piel, M. Levine, E. C. Lai, *Genes Dev.* **19**, 2947–2952 (2005).
12. D. M. Tyler *et al.*, *Genes Dev.* **22**, 26–36 (2008).
13. A. Stark *et al.*, *Genes Dev.* **22**, 8–13 (2008).
14. W. Bender, *Genes Dev.* **22**, 14–19 (2008).
15. M. Gummalla *et al.*, *PLOS Genet.* **8**, e1002720 (2012).
16. D. L. Garaulet *et al.*, *Dev. Cell* **29**, 635–648 (2014).
17. C. B. Bridges, T. H. Morgan, *The Third-Chromosome Group of Mutant Characters of* Drosophila melanogaster (Carnegie Institution of Washington, Baltimore, MD, 1923).
18. E. Sánchez-Herrero, I. Vernós, R. Marco, G. Morata, *Nature* **313**, 108–113 (1985).
19. B. D. Pfeiffer *et al.*, *Proc. Natl. Acad. Sci. U.S.A.* **105**, 9715–9720 (2008).
20. L. Manning *et al.*, *Cell Rep.* **2**, 1002–1013 (2012).
21. T.-W. Chen *et al.*, *Nature* **499**, 295–300 (2013).
22. M. Gummalla, S. Galetti, R. K. Maeda, F. Karch, *Front. Cell. Neurosci.* **8**, 96 (2014).
23. F. Karch *et al.*, *Cell* **43**, 81–96 (1985).
24. F. N. Hamada *et al.*, *Nature* **454**, 217–220 (2008).
25. T. Kitamoto, *J. Neurobiol.* **47**, 81–92 (2001).
26. S. Brenner, *Genetics* **77**, 71–94 (1974).

ACKNOWLEDGMENTS

We thank L. Lagnado for his support to this project and S. Pinho and P. Reed for technical assistance. We also thank R. White for antibodies; Welcome Bender, E. Sánchez-Herrero, and the Bloomington Stock Centre for *Drosophila* stocks; and P. Patraquim for bioinformatic support. This paper is dedicated to the memory of Amalia Lamuedra de Alonso for her devoted support to this work. This research was funded by a Wellcome Trust Investigator Award to C.R.A. [WT grant 098410/Z/12/Z] and a Ph.D. studentship to J.P.O. by Fundação para a Ciência e a Tecnologia (Portugal) [FCT grant SFRH/BD/63312/2009]. J.B. is funded by Sir Henry Dale Fellowship (Wellcome Trust and the Royal Society) Grant 105568/Z/14/Z, and M.L. was supported by grants from the Biotechnology and Biological Sciences Research Council (UK) (BB/I022414/1) and the Wellcome Trust (092986/Z).

SUPPLEMENTARY MATERIALS

www.sciencemag.org/content/350/6262/815/suppl/DC1
Materials and Methods
Figs. S1 to S11
References (*27*–*48*)
Movies S1 to S7

24 July 2015; accepted 25 September 2015
Published online 22 October 2015
10.1126/science.aad0217

HUMAN EVOLUTION

Ancient Ethiopian genome reveals extensive Eurasian admixture throughout the African continent

M. Gallego Llorente,[1]*† E. R. Jones,[2]*† A. Eriksson,[1,3] V. Siska,[1] K. W. Arthur,[4] J. W. Arthur,[4] M. C. Curtis,[5,6] J. T. Stock,[7] M. Coltorti,[8] P. Pieruccini,[8] S. Stretton,[9] F. Brock,[10,11] T. Higham,[10] Y. Park,[12] M. Hofreiter,[13,14] D. G. Bradley,[2] J. Bhak,[15] R. Pinhasi,[16]*‡ A. Manica[1]*‡

Characterizing genetic diversity in Africa is a crucial step for most analyses reconstructing the evolutionary history of anatomically modern humans. However, historic migrations from Eurasia into Africa have affected many contemporary populations, confounding inferences. Here, we present a 12.5× coverage ancient genome of an Ethiopian male ("Mota") who lived approximately 4500 years ago. We use this genome to demonstrate that the Eurasian backflow into Africa came from a population closely related to Early Neolithic farmers, who had colonized Europe 4000 years earlier. The extent of this backflow was much greater than previously reported, reaching all the way to Central, West, and Southern Africa, affecting even populations such as Yoruba and Mbuti, previously thought to be relatively unadmixed, who harbor 6 to 7% Eurasian ancestry.

The ability to sequence ancient genomes has revolutionized our understanding of human evolution. However, genetic analyses of ancient material have focused on individuals from temperate and Arctic regions, where ancient DNA is preserved over longer time frames (*1*). Africa has so far failed to yield skeletal remains with much ancient DNA, with the exception of a few poorly preserved specimens from which only mitochondrial DNA could be extracted (*2*). This is particularly unfortunate, as African genetic diversity is crucial to most analyses reconstructing the evolutionary history of anatomically modern humans, by providing the baseline against which other events are defined. In the absence of ancient DNA, geneticists rely on contemporary African populations, but a number of historic events, in particular a genetic backflow from West Eurasia into Eastern Africa (*3*, *4*), act as confounding factors.

Here, we present an ancient human genome from Africa and use it to disentangle the effects of recent population movement into Africa. By sampling the petrous bone (*5*), we sequenced the genome of a male from Mota Cave (herein referred to as "Mota") in the southern Ethiopian highlands, with a mean coverage of 12.5× (*6*). Contamination was estimated to be between 0.29 and 1.26% (*6*). Mota's remains were dated to ~4500 years ago [direct calibrated radiocarbon date (*6*)] and thus predate both the Bantu expansion (*7*) and, more importantly, the 3000-year-old West Eurasian backflow, which has left strong genetic signatures in the whole of Eastern and, to a lesser extent, Southern Africa (*3*, *4*).

We compared Mota to contemporary human populations (*6*). Both principal component analysis (PCA) (Fig. 1A) and outgroup f_3 analysis using Ju|'hoansi (Khoisan) from Southern Africa as the outgroup (Fig. 1, B and C) place this ancient

[1]Department of Zoology, University of Cambridge, Downing Street, Cambridge CB2 3EJ, UK. [2]Smurfit Institute of Genetics, Trinity College Dublin, Dublin, Ireland. [3]Integrative Systems Biology Laboratory, Division of Biological and Environmental Sciences and Engineering, King Abdullah University of Science and Technology (KAUST), Thuwal 23955-6900, Kingdom of Saudi Arabia. [4]Department of Society, Culture, and Language, University of South Florida St. Petersburg, 140 7th Avenue South, St. Petersburg, FL 33701, USA. [5]Department of Anthropology, Ventura College, 4667 Telegraph Road, Ventura, CA 93003, USA. [6]Humanities and Social Sciences Program, UCLA Extension, University of California Los Angeles, 10995 Le Conte Avenue, Los Angeles, CA 90095, USA. [7]Department of Archaeology and Anthropology, University of Cambridge, Pembroke Street, Cambridge CB2 3QG, UK. [8]Department of Physical Sciences, Earth and Environment, University of Siena, Via di Laterina, 8-53100 Siena, Italy. [9]Department of Anthropology, University of Illinois at Urbana-Champaign, Public Service Archaeology and Architecture Program, 109 Davenport Hall, 607 South Mathews Avenue, Urbana, IL 61801, USA. [10]Oxford Radiocarbon Accelerator Unit, Research Laboratory for Archaeology and the History of Art, University of Oxford, Dyson Perrins Building, South Parks Road, Oxford OX1 3QY, UK. [11]Cranfield Forensic Institute, Cranfield University, Defence Academy of the United Kingdom, Shrivenham, Oxon SN6 8LA, UK. [12]Theragen BiO Institute, 2nd Floor B-dong, AICT bldg, Iui-dong, Youngtong-gu, Suwon 443-270, Republic of Korea. [13]Institute for Biochemistry and Biology, Faculty for Mathematics and Natural Sciences, University of Potsdam, Karl-Liebknechtstraße 24–25, 14476 Potsdam Golm, Germany. [14]Department of Biology, University of York, Wentworth Way, Heslington, York YO10 5DD, UK. [15]The Genomics Institute, Ulsan National Institute of Science and Technology, Ulsan 689-798, Republic of Korea. [16]School of Archaeology and Earth Institute, University College Dublin, Dublin 4, Ireland.
***Corresponding author. E-mail: mg632@cam.ac.uk (M.G.L.); joneser@tcd.ie (E.R.J.); ron.pinhasi@ucd.ie (R.P.); am315@cam.ac.uk (A.M.)** †These authors contributed equally to this work. ‡These authors contributed equally to this work.

individual close to contemporary Ethiopian populations, and more specifically to the Ari, a group of Omotic speakers from southern Ethiopia, to the west of the highland region where Mota lived. Our ancient genome confirms the view that the divergence of this language family results from the relative isolation of its speakers (*8*), and indicates population continuity over the last ~4500 years in this region of Eastern Africa.

The age of Mota means that he should predate the West Eurasian backflow, which has been dated to ~3000 years ago (*3*, *4*). We formally tested this proposition by using an f_4 ratio estimating the West Eurasian component (*6*), following the approach adopted by Pickrell *et al.* (*3*). As expected, we failed to find any West Eurasian component in Mota (table S5), thus providing support for previous dating of that event (*3*, *4*).

Given that Mota predates the backflow, we searched for its most likely source by modeling the Ari, the contemporary population closest to our ancient genome, as a mixture of Mota and another West Eurasian population (*6*). We investigated both contemporary sources (*3*) and other Eurasian ancient genomes (*5*, *9*). In this analysis, contemporary Sardinians and the early Neolithic LBK (Stuttgart) genome stand out (Fig. 2A). Previous analyses have shown Sardinians to be the closest modern representatives of early Neolithic farmers (*10*, *11*), implying that the backflow came from the same genetic source that fueled the Neolithic expansion into Europe from the Near East/Anatolia, before recent historic events changed the genetic makeup of populations living in that region. An analysis with haplotype sharing also identified a connection between contemporary Ethiopians and Anatolia (*4*, *12*). Interestingly, archaeological evidence dates the arrival of Near Eastern domesticates (such as wheat, barley, and lentils) to the same time period (~3000 years ago) (*13*, *14*), suggesting that the direct descendants of the farmers that earlier brought agriculture into Europe may have also played a role in the development of new forms of food production in the Horn of Africa.

Using Mota as an unadmixed African reference and the early farmer LBK as the source of the West Eurasian component, it is possible to reassess the magnitude and geographic extent of historical migrations, avoiding the complications of using admixed contemporary populations (*6*). We estimated a substantially higher Eurasian backflow admixture than previously detected (*3*), with an additional 4 to 7% of the genome of most African populations tracing back to a Eurasian source. Moreover, we detected a much broader geographical impact of the backflow, going all the way to West and Southern Africa (Fig. 2B). Even though the West Eurasian component in these regions is smaller than in Eastern Africa, it is still sizable, with Yoruba and Mbuti, who are often used as African reference populations (*15*, *16*), showing 7% and 6%, respectively, of their genomes to be of Eurasian origin (table S5).

Since Mota predates recent demographic events, his genome can act as an ideal African reference

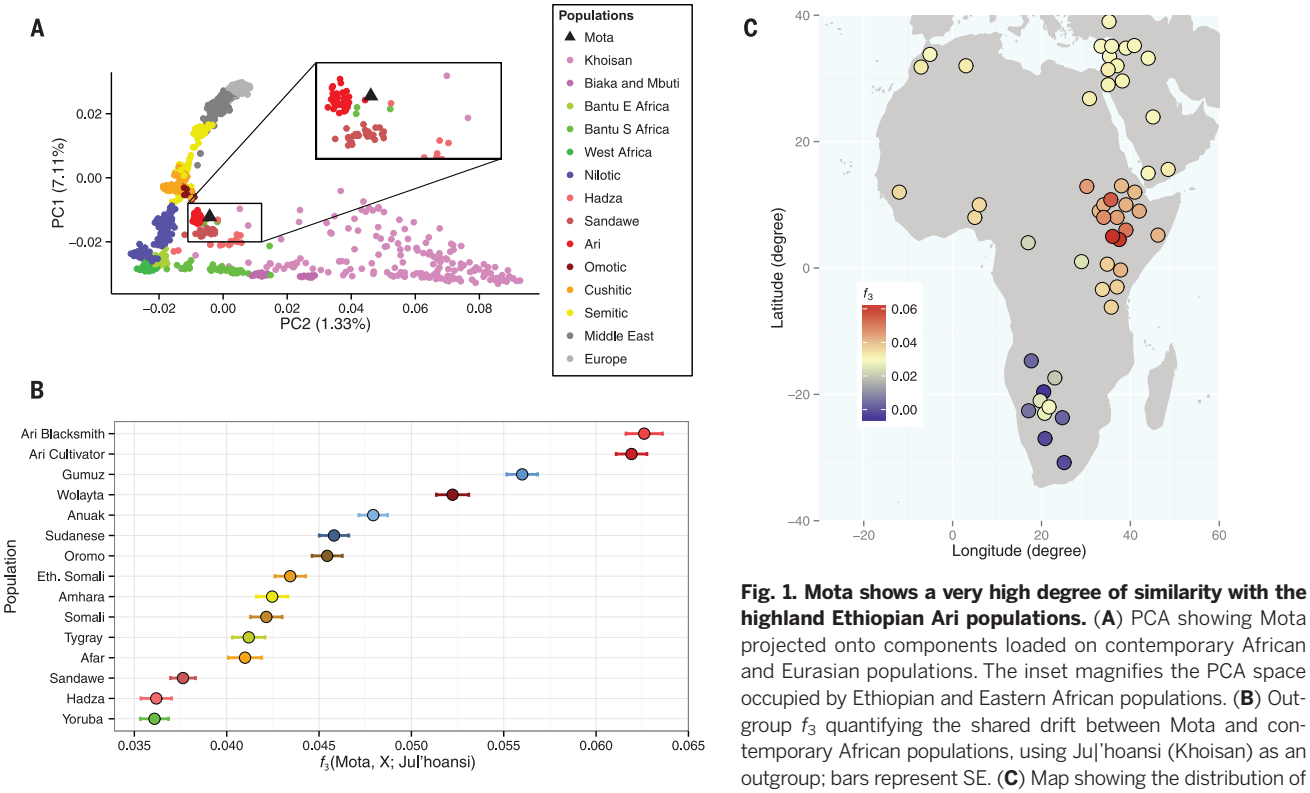

Fig. 1. Mota shows a very high degree of similarity with the highland Ethiopian Ari populations. (**A**) PCA showing Mota projected onto components loaded on contemporary African and Eurasian populations. The inset magnifies the PCA space occupied by Ethiopian and Eastern African populations. (**B**) Outgroup f_3 quantifying the shared drift between Mota and contemporary African populations, using Ju|'hoansi (Khoisan) as an outgroup; bars represent SE. (**C**) Map showing the distribution of outgroup f_3 values across the African continent. In (A) and (B), populations speaking Nilo-Saharan languages are marked with blue shades, Omotic speakers with red, Cushitic with orange, Semitic with yellow, and Bantu with green. Mota is denoted by a black symbol.

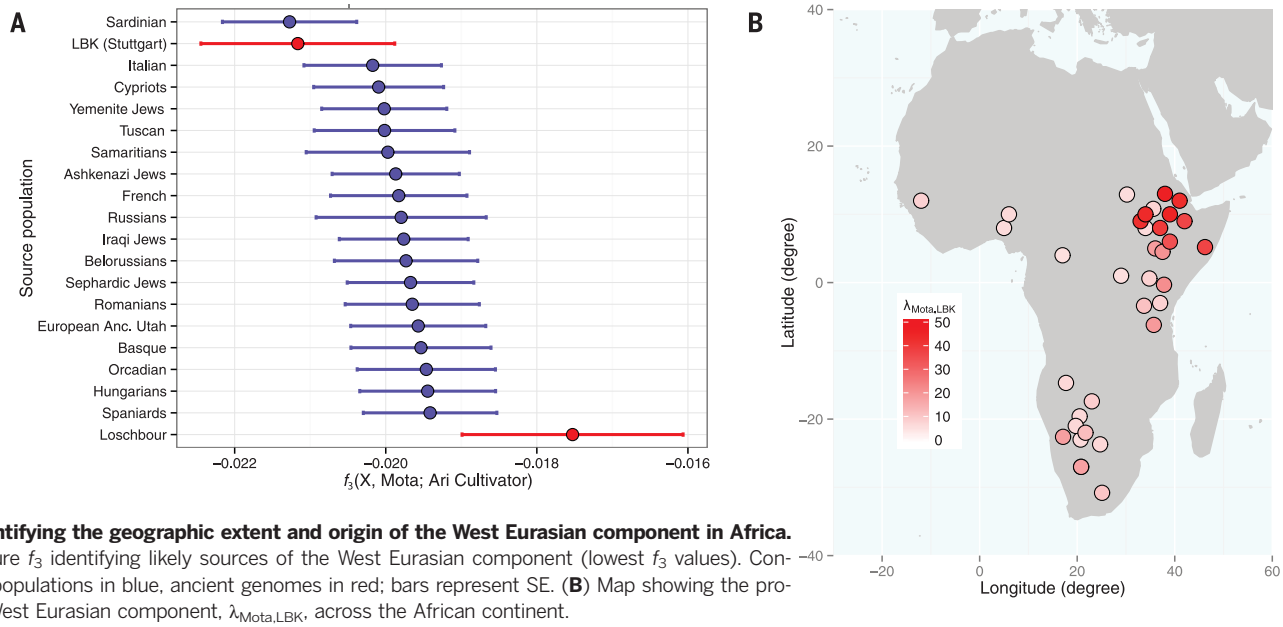

Fig. 2. Quantifying the geographic extent and origin of the West Eurasian component in Africa. (**A**) Admixture f_3 identifying likely sources of the West Eurasian component (lowest f_3 values). Contemporary populations in blue, ancient genomes in red; bars represent SE. (**B**) Map showing the proportion of West Eurasian component, $\lambda_{Mota,LBK}$, across the African continent.

to understand episodes during the out-of-Africa expansion. We used him as the African reference to quantify Neandertal introgression in a number of contemporary genomes (*6*). Both Yoruba and Mbuti, which are routinely used as African references for this type of analysis (*15*, *16*), show a marginally closer affinity with Neandertal than Mota on the basis of *D* statistics, and an f_4 ratio analysis detected a small Neandertal component in these genomes at around 0.2 to 0.7%—greater than previously suggested (*16*) and consistent with our estimates of the magnitude of their Western Eurasian ancestry (*6*). Although the magnitude of Neandertal ancestry in these contemporary African populations is not enough to change conclusions qualitatively (estimates of Neandertal ancestry in French and Han only increased marginally when tested with Mota as a reference), it should be accounted for when looking for specific introgressed haplotypes (*17*) or searching for unknown ancient hominins who might have hybridized with African populations (*18*).

We also investigated the Mota genome for a number of phenotypes of interest (*6*). As expected, Mota lacked any of the derived alleles found in Eurasian populations for eye and skin color, suggesting that he had brown eyes and dark skin. Mota lacked any of the currently known alleles that confer lactose tolerance, which may have implications concerning when pastoralism appeared in southwestern Ethiopia. In addition, Mota did possess all three selected alleles that recently have been shown to play a role in the adaptation to altitude in contemporary highland Ethiopian populations (*19*). The presence of these mutations supports our conclusion that Mota is the descendant of highland dwellers, who have lived in this environment long enough to accumulate adaptations to the altitude (*20*, *21*).

Until now, it has been necessary to use contemporary African populations as the baseline against which events during the worldwide expansion of anatomically modern humans are defined (*16*, *22*–*24*). By obtaining an ancient whole genome from this continent, we have shown that having an unadmixed reference that predates the large number of recent historical migrations can greatly improve our inference. This result stresses the importance of obtaining unadmixed baseline data to reconstruct demographic events, and the limitations of analyses that are solely based on contemporary populations. Even older African genomes will thus be needed to investigate key demographic events that predate Mota, such as earlier instances of backflows into Africa (*25*).

REFERENCES AND NOTES

1. M. Hofreiter *et al.*, *BioEssays* **37**, 284–293 (2015).
2. A. G. Morris, A. Heinze, E. K. F. Chan, A. B. Smith, V. M. Hayes, *Genome Biol. Evol.* **6**, 2647–2653 (2014).
3. J. K. Pickrell *et al.*, *Proc. Natl. Acad. Sci. U.S.A.* **111**, 2632–2637 (2014).
4. L. Pagani *et al.*, *Am. J. Hum. Genet.* **91**, 83–96 (2012).
5. C. Gamba *et al.*, *Nat. Commun.* **5**, 5257 (2014).
6. See supplementary materials on *Science* Online.
7. S. Li, C. Schlebusch, M. Jakobsson, *Proc. Biol. Sci.* **281**, 20141448 (2014).
8. R. Blench, in *SemitoHamitic Festschrift for A.B. Dolgopolsky and H. Jungraithmayr*, G. Takacks, Ed. (Dietich Reimer Verlag, Berlin, 2008), pp. 63–78.
9. I. Lazaridis *et al.*, *Nature* **513**, 409–413 (2014).
10. M. Sikora *et al.*, *PLOS Genet.* **10**, e1004353 (2014).
11. P. Skoglund *et al.*, *Science* **336**, 466–469 (2012).
12. T. Kivisild *et al.*, *Am. J. Hum. Genet.* **75**, 752–770 (2004).
13. M. C. Curtis, in *The Oxford Handbook of African Archaeology*, P. Mitchell, P. J. Lane, Eds. (Oxford Univ. Press, 2013), pp. 571–584.
14. M. Harrower, M. McCorriston, A. D'Andrea, *Am. Antiq.* **75**, 452–472 (2010).
15. Q. Fu *et al.*, *Nature* **524**, 216–219 (2015).
16. K. Prüfer *et al.*, *Nature* **505**, 43–49 (2014).
17. S. Sankararaman *et al.*, *Nature* **507**, 354–357 (2014).
18. M. F. Hammer, A. E. Woerner, F. L. Mendez, J. C. Watkins, J. D. Wall, *Proc. Natl. Acad. Sci. U.S.A.* **108**, 15123–15128 (2011).
19. N. Udpa *et al.*, *Genome Biol.* **15**, R36 (2014).
20. E. Huerta-Sánchez *et al.*, *Mol. Biol. Evol.* **30**, 1877–1888 (2013).
21. G. Alkorta-Aranburu *et al.*, *PLOS Genet.* **8**, e1003110 (2012).
22. A. Eriksson *et al.*, *Proc. Natl. Acad. Sci. U.S.A.* **109**, 16089–16094 (2012).
23. A. Eriksson, A. Manica, *Proc. Natl. Acad. Sci. U.S.A.* **109**, 13956–13960 (2012).
24. L. Pagani *et al.*, *Am. J. Hum. Genet.* **96**, 986–991 (2015).
25. J. A. Hodgson, C. J. Mulligan, A. Al-Meeri, R. L. Raaum, *PLOS Genet.* **10**, e1004393 (2014).

ACKNOWLEDGMENTS

A.M. was supported by European Research Council (ERC) Consolidator Grant 647787 "LocalAdaptation"; R.P by ERC Starting Grant 263441, "ADNABIOARC"; M.H. by ERC Consolidator Grant 310763 "GeneFlow"; J.B. by the 2014 Research Fund (1.140113.01, 1.140064.01) of UNIST (Ulsan National Institute of Science and Technology) and Geromics internal research funding; J.T.S. by ERC Consolidator Grant 617627 "ADaPt"; K.W.A. by NSF award 1027607; D.G.B. by ERC Investigator Grant 295729-CodeX; V.S. by a scholarship from the Gates Cambridge Trust; and M.G.L. by a Biotechnology and Biological Sciences Research Council (BBSRC) DTP studentship. Permission for the archaeology was given by the Ethiopian Authority for Research and Conservation of Cultural Heritage and offices of the Ministry of Culture and Tourism for the Southern Nations, Nationalities, and Peoples Region. Raw reads from Mota are available for download through the National Center for Biotechnology Information, BioProject ID PRJNA295861, and the corresponding BAM and VCF files are available at africangenome.org.

SUPPLEMENTARY MATERIALS

www.sciencemag.org/content/350/6262/820/suppl/DC1
Supplementary Text
Figs. S1 to S8
Tables S1 to S14
References (*26*–*74*)

25 August 2015; accepted 28 September 2015
Published online 8 October 2015
10.1126/science.aad2879

GENOME EDITING

Dynamics of CRISPR-Cas9 genome interrogation in living cells

Spencer C. Knight,[1] Liangqi Xie,[2] Wulan Deng,[3,4] Benjamin Guglielmi,[2] Lea B. Witkowsky,[2] Lana Bosanac,[2] Elisa T. Zhang,[2] Mohamed El Beheiry,[5] Jean-Baptiste Masson,[3] Maxime Dahan,[4,5] Zhe Liu,[3,4]* Jennifer A. Doudna,[1,2,6,7,8]* Robert Tjian[2,3,4,6,9]*

The RNA-guided CRISPR-associated protein Cas9 is used for genome editing, transcriptional modulation, and live-cell imaging. Cas9-guide RNA complexes recognize and cleave double-stranded DNA sequences on the basis of 20-nucleotide RNA-DNA complementarity, but the mechanism of target searching in mammalian cells is unknown. Here, we use single-particle tracking to visualize diffusion and chromatin binding of Cas9 in living cells. We show that three-dimensional diffusion dominates Cas9 searching in vivo, and off-target binding events are, on average, short-lived (<1 second). Searching is dependent on the local chromatin environment, with less sampling and slower movement within heterochromatin. These results reveal how the bacterial Cas9 protein interrogates mammalian genomes and navigates eukaryotic chromatin structure.

The RNA-guided endonuclease Cas9 uses RNA-DNA complementarity to target and cleave double-stranded DNA upstream of a protospacer-adjacent motif (PAM) (*1*, *2*). Cas9 can be programmed with a single-guide RNA (sgRNA) to cleave specific DNA sequences within eukaryotic cells, which facilitates its use as a tool for genome engineering (*3*–*5*). Biochemical and genome occupancy studies have established the PAM and adjacent ~5 to 8 base pairs (the "seed" region) of the DNA target site as the basis for Cas9 DNA interrogation and off-target activity (*1*, *6*–*13*). Nonetheless, how Cas9 explores large eukaryotic genomes and identifies targets within the context of chromatin remains largely unknown. In particular, the in vivo kinetics of on- versus off-target binding and Cas9 dependence on the chromatin environment have not yet been examined in living eukaryotic cells.

To investigate the live-cell dynamics of Cas9 target searching, we tracked single, fluorescently labeled, catalytically inactive *Streptococcus pyogenes* Cas9 (dCas9) molecules to determine their diffusion and chromatin binding properties in live mouse cell nuclei (*14*). dCas9 was fused at its C terminus with a HaloTag domain and stably integrated into the genome of NIH 3T3 cells under an inducible, tetracycline response element (TRE)–tight promoter (Fig. 1A and figs. S1 to S3) (*15*). Guide RNAs were transiently expressed from a blue fluorescent protein (BFP) reporter plasmid. Covalent linkage of a cell-permeable, fluorescent HaloTag ligand (JF549) allowed for visualization of single Cas9-HaloTag molecules under leaky expression (Fig. 1, A and B, and fig. S4) (*16*).

To study dCas9-HaloTag binding dynamics at endogenous genomic loci, we transfected cells with a guide RNA targeted to short interspersed nuclear elements (SINEs) of the B2 type. The B2 elements are repeated ~350,000 times throughout the mouse genome, often in intragenic regions, with a single element per insertion site (*17*, *18*). We reasoned that the abundance of these loci would shift the global equilibrium of Cas9-HaloTag binding and allow us to observe otherwise rare target-binding events. Two-photon fluorescence correlation spectroscopy (FCS) experiments revealed a substantial reduction in global dCas9-HaloTag mobility for B2 sgRNA-transfected cells relative to apo (no sgRNA) protein (Fig. 1C). Both apo and B2-loaded dCas9-HaloTag displayed biphasic kinetic behavior in our FCS measurements, which reflected slowly and rapidly moving populations for both conditions. The magnitude of the slow diffusion coefficient was reduced by >90% in the presence of B2 sgRNA relative to the apo protein (fig. S5).

We conducted two-dimensional (2D) tracking experiments at short (10-ms) exposure times in cells transfected with a plasmid encoding either B2 or a phage-derived "nonsense" guide bearing minimal homology to the 3T3 genome (figs. S6 to S8). A nonsense sgRNA has the potential to direct Cas9 off-target interactions through millions of PAMs and short seed sequences within the genome and thus serves as a proxy for a Cas9 protein in the process of searching (*1*, *6*). The

[1]Department of Chemistry, University of California, Berkeley, CA, USA. [2]Department of Molecular and Cell Biology, University of California, Berkeley, CA, USA. [3]Janelia Research Campus, Howard Hughes Medical Institute, Ashburn, VA, USA. [4]Transcriptional Imaging Consortium, Janelia Research Campus, Howard Hughes Medical Institute, Ashburn, VA, USA. [5]Laboratoire Physico-Chimie Curie, Institut Curie, Centre National de la Recherche Scientifique UMR 168, Paris, France. [6]Howard Hughes Medical Institute, Department of Molecular and Cell Biology, University of California, Berkeley, CA, USA. [7]Physical Biosciences Division, Lawrence Berkeley National Laboratory, Berkeley, CA, USA. [8]Innovative Genomics Initiative, University of California, Berkeley, CA, USA. [9]Li Ka Shing Biomedical and Health Sciences Center, University of California, Berkeley, CA, USA.
*Corresponding author. E-mail: liuz11@janelia.hhmi.org (Z.L.); doudna@berkeley.edu (J.A.D.); jmlim@berkeley.edu (R.T.)

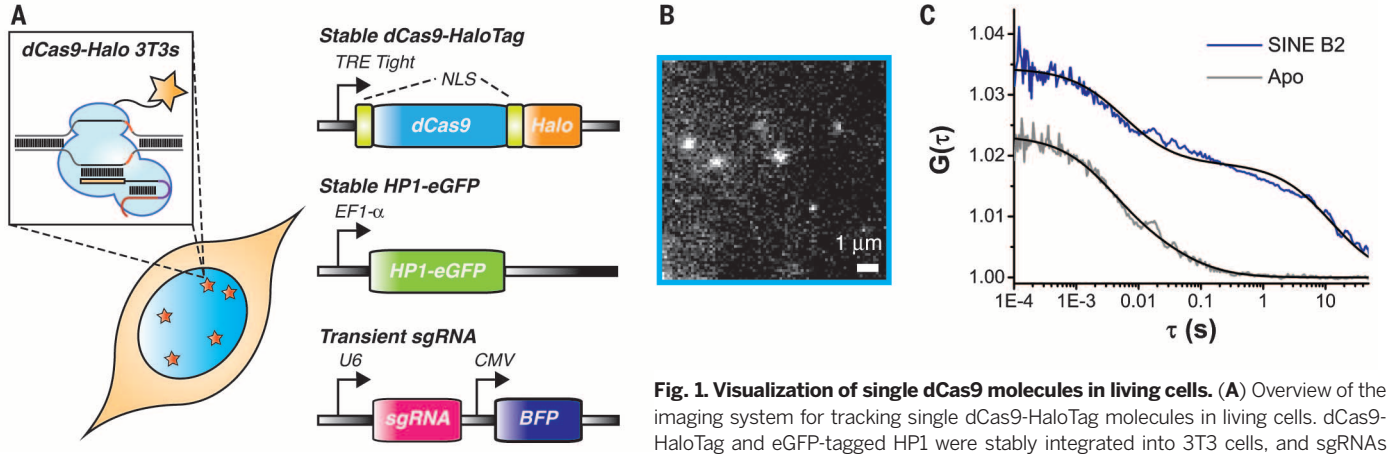

Fig. 1. Visualization of single dCas9 molecules in living cells. (**A**) Overview of the imaging system for tracking single dCas9-HaloTag molecules in living cells. dCas9-HaloTag and eGFP-tagged HP1 were stably integrated into 3T3 cells, and sgRNAs were transiently transfected. (**B**) 2D single-molecule visualization of dCas9-HaloTag molecules within live 3T3 nuclei during a 10-ms exposure. (**C**) Two-photon FCS correlation curves and mathematical fits for dCas9-HaloTag in the absence of sgRNA (apo, gray) or loaded with cognate SINE B2 sgRNA (blue). Fluorescence correlation was measured within diffraction-limited volumes over time at random locations within cell nuclei (N = 11 cells for each condition).

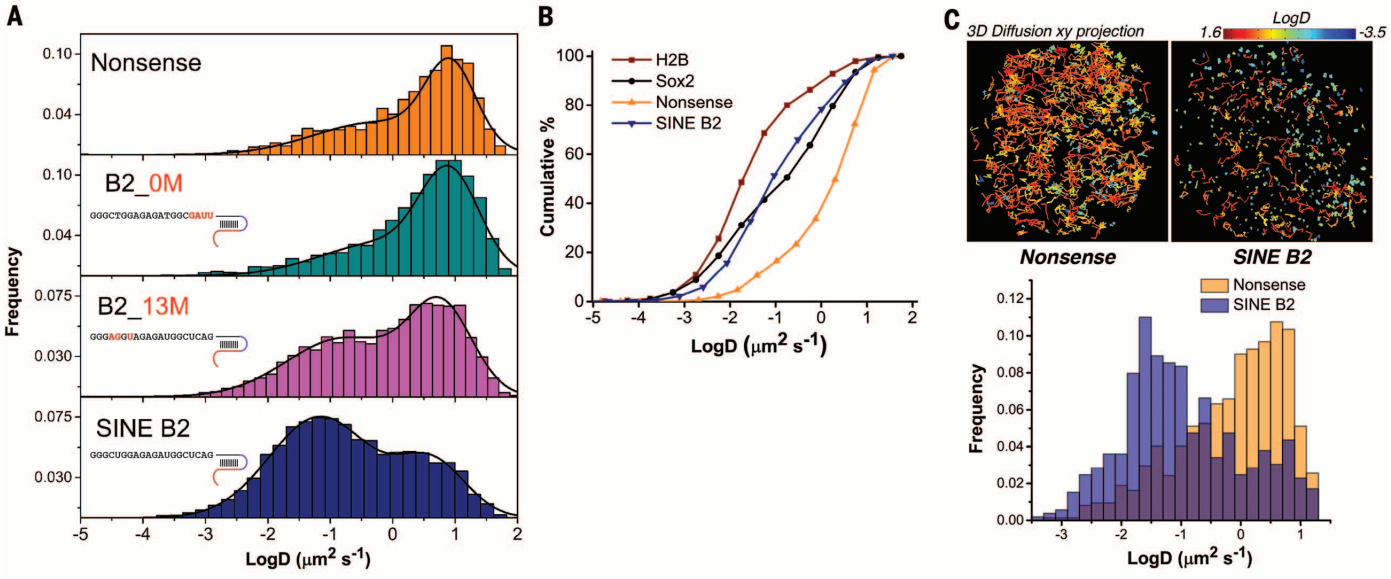

Fig. 2. Cas9 exploration is dominated by 3D diffusion during the search for target sites in vivo. (**A**) Normalized histograms and two-component Gaussian fits illustrating the log diffusion coefficient distributions for dCas9-HaloTag with different sgRNAs ($N \geq 12$ cells for each condition). For reference, chromatin-bound H2B molecules can be fitted with a single Gaussian with log$D \approx 0.1$ $\mu m^2 \cdot s^{-1}$. (**B**) Cumulative distribution plots quantifying the log diffusion coefficient for SINE B2 or nonsense-loaded dCas9-HaloTag relative to histone H2B or Sox2. (**C**) (Top) 2D projections of single-particle trajectories obtained from 3D imaging using a multifocus microscope. (Bottom) Histograms showing the log$D$ distribution of trajectories. The trajectories are color-coded according to diffusion coefficient. The 3D movies were collected at an exposure time of 30 ms, and diffusion coefficients were extracted directly from the mean square displacements of the 3D trajectories (*28*) ($N = 2$ cells for each condition).

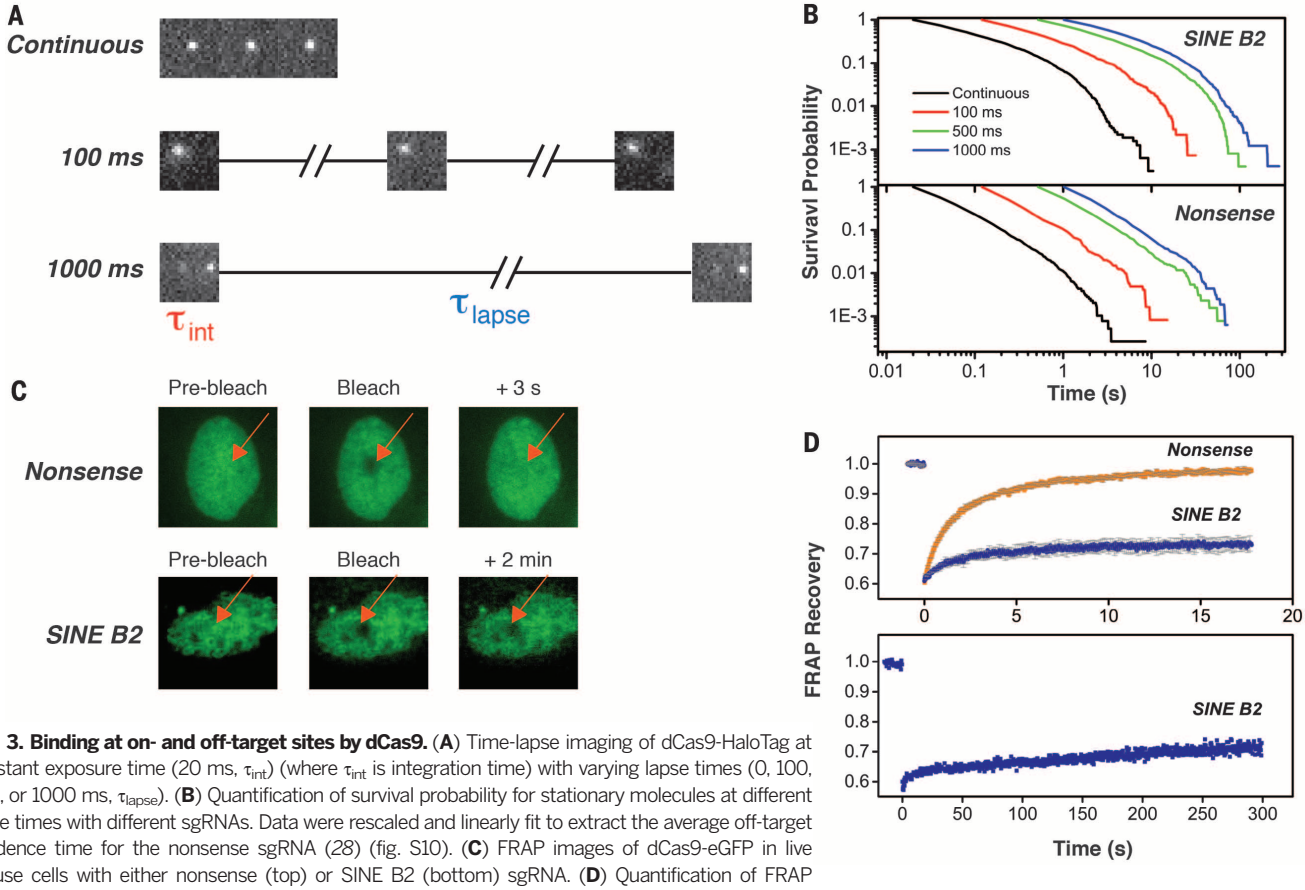

Fig. 3. Binding at on- and off-target sites by dCas9. (**A**) Time-lapse imaging of dCas9-HaloTag at constant exposure time (20 ms, τ_{int}) (where τ_{int} is integration time) with varying lapse times (0, 100, 500, or 1000 ms, τ_{lapse}). (**B**) Quantification of survival probability for stationary molecules at different lapse times with different sgRNAs. Data were rescaled and linearly fit to extract the average off-target residence time for the nonsense sgRNA (*28*) (fig. S10). (**C**) FRAP images of dCas9-eGFP in live mouse cells with either nonsense (top) or SINE B2 (bottom) sgRNA. (**D**) Quantification of FRAP images for dCas9-eGFP using different sgRNAs ($N = 17$ cells for each condition).

resulting log diffusion coefficient histograms showed a large fraction of highly immobile ($D < 0.1\ \mu m^2 \cdot s^{-1}$) Cas9 molecules for B2 sgRNA relative to nonsense sgRNA or no-guide controls, consistent with more chromatin binding for the B2-loaded Cas9 (Fig. 2A and fig. S9). In similar experiments, a B2 guide with mismatches proximal to the target PAM gave rise to Cas9 diffusion histograms similar to those of the nonsense guide; in contrast, a B2 guide with homology mismatches distal to the target PAM gave rise to a distribution more similar to the cognate B2 guide (B2_0M and B2_13M, respectively) (Fig. 2A and fig. S6). These observations are consistent with the noted role of the seed region in driving Cas9's RNA-guided interaction with DNA (*6*, *10*, *11*).

Compared with a binding-dominant protein (e.g., H2B) or a protein that demonstrates a mixture of binding and diffusion (e.g., Sox2), both the nonsense-loaded and apo Cas9 showed considerably more apparent 3D diffusion in cell nuclei (Fig. 2B, fig. S9, and movies S1 to S4). In addition, 3D multifocus tracking experiments with the nonsense guide showed that Cas9–guide RNA complexes use diffusion-dominated target searching throughout the entirety of the cell nucleus (Fig. 2C and movie S5) (*19*). These results underscore the dominance of 3D diffusion over binding during DNA interrogation by Cas9 and demonstrate an in vivo target search mechanism similar to what has been observed in vitro (*6*).

To determine the relative kinetics of on- versus off-target binding, we measured in vivo residence times of dCas9-HaloTag molecules bound to chromatin. We performed time-lapse experiments at a constant exposure time (20 ms, τ_{int}) while varying the lapse time τ_{lapse} between successive frames (Fig. 3A, movies S6 to S9). From these movies, we plotted the probability that a dCas9-HaloTag molecule would remain stationary as a function of time (survival probability) (Fig. 3B). Rescaling and concatenation of these plots allowed us to extract an average off-target residence time of 0.75 ± 0.1 s for Cas9 containing a nonsense guide (τ_{ns}) (fig. S10) (*20*, *21*). We note that a small fraction of the binding events in our concatenated plot were longer than 10 s, which might be attributed to rare genomic sequences with higher homology to the nonsense guide (fig. S10) (*6*, *22*). We also measured the binding of nonsense-loaded protein in dCas9-eGFP stable cell lines using fluorescence recovery after photobleaching (FRAP), a bulk technique for assessing protein mobility based on exchange between bleached and unbleached molecules within a region of interest. We observed nearly full recovery within 10 s, which indicated mostly transient (milliseconds to seconds) chromatin interactions intermixed with diffusion (Fig. 3, C and D) (*23*).

Although nonsense guide–loaded dCas9-eGFP recovered rapidly after photobleaching in our FRAP curves, the B2 guide–loaded protein resulted in a large immobile fraction even when measured out to 5 min (Fig. 3, C and D, and movies S10 to S12). Similarly, survival probability plots of B2 guide–loaded Cas9 showed substantially longer residence times compared with those with the nonsense guide (Fig. 3B). These data suggest that Cas9 binding at bona fide targets (τ_s) could be considerably longer (i.e., minutes or more) in vivo relative to short-lived (milliseconds to seconds) binding typical of PAMs and very short seed sequences (τ_{ns}) (*6*). We refrain from more precisely estimating τ_s here because of (i) a likely mixture of off-target and on-target binding in the immobile fraction, (ii) imaging limitations due to photobleaching in our single-molecule measurements (curved tails) (Fig. 3B), and (iii) known complications with extracting residence times from FRAP data (*24*).

The ability of Cas9 to target heterochromatic regions (HRs) is important for its application to genome editing. To study Cas9 behavior in HRs, we performed tracking experiments in cells with eGFP-labeled heterochromatin protein 1 (HP1) (fig. S11) (*25*–*28*). dCas9-HaloTag molecules with nonsense sgRNA were stochastically excited and tracked in live-cell nuclei, and the trajectories were overlaid onto HP1-labeled nuclear images to visualize searching with respect to heterochromatin. The resulting composite image shows marked depletion of tracks within HRs (30 ± 9% track density reduction) (fig. S11). Diffusion analysis of tracks within HRs revealed that dCas9 diffusion is moderately slower in these regions (Fig. 4A and fig. S12) (*29*). We also performed jumping angle analysis on three-point sliding windows of our Cas9 trajectories to monitor the anisotropy of searching in HRs (*28*, *30*). The resulting angle distributions revealed a slight bias toward reverse (180°) angles, which suggested more compact exploration and a tendency of Cas9 to return to its starting point while interrogating heterochromatin (Fig. 4B and fig. S13). Together, these results show that Cas9 search efficiency is reduced, but not eliminated, in HRs.

To test whether dCas9 can bind to target sites in heterochromatin, we transfected cells expressing dCas9-HaloTag with a plasmid encoding a sgRNA targeted to pericentromeric DNA sequences within heterochromatin. We observed distinct puncta within HRs of fixed cells colocalized with dense Hoechst staining, consistent with successful dCas9 targeting to pericentromeres (Fig. 4C). This result strongly suggests that Cas9 is able to bypass chromatin obstacles and faithfully engage with HR target sites despite reduced sampling efficiency within these regions.

Our data provide a direct visualization of DNA interrogation by Cas9 in mammalian cells. The target search mechanism involves rapid three-dimensional diffusion of Cas9 around the nucleus, with occasional forays into heterochromatic regions. Our imaging approach complements chromatin immunoprecipitation experiments by capturing many of the more transient interactions with DNA that predominate as Cas9 scans vast mammalian genomes in search of its target site. Overall, our results provide a quantitative understanding of

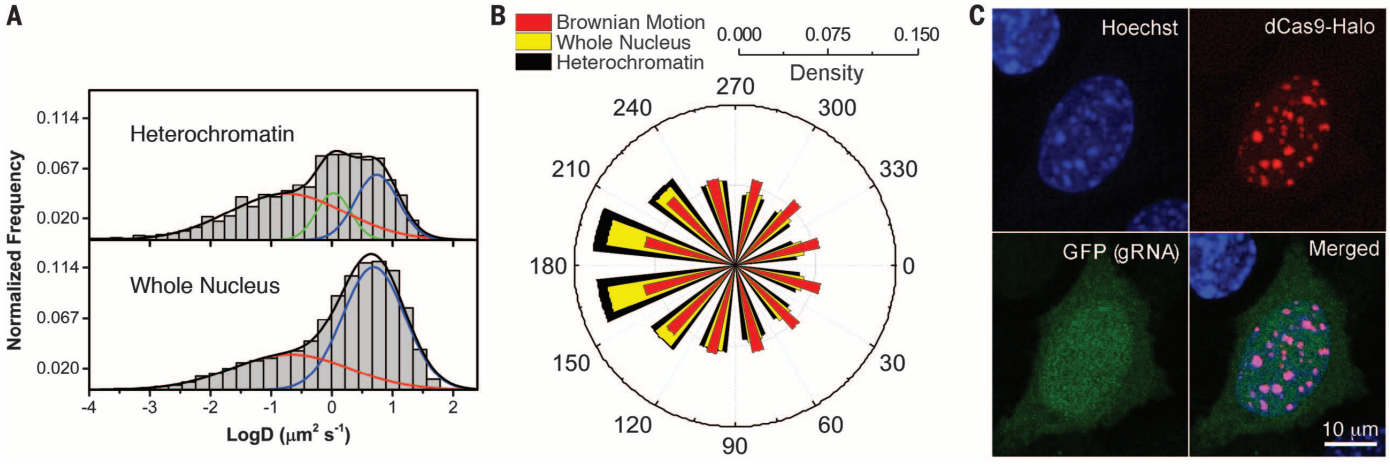

Fig. 4. Cas9 search efficiency is reduced, but not eliminated, in heterochromatic regions. (**A**) Log diffusion coefficient histograms and Gaussian fits for dCas9-HaloTag in HRs versus the entire cell nucleus ($N = 11$ cells). (**B**) Jumping angle analysis of diffusion anisotropy within HRs relative to the entire cell nucleus ($N = 5$ cells). (**C**) Epi-fluorescence image illustrating puncta formation in cells transfected with pericentromere-targeted sgRNA. Cells were fixed and costained with Hoechst 33258 for orthogonal labeling of pericentromeres.

Cas9 dynamics in living cells and offer insight into how Cas9 navigates hierarchical organization of DNA within a eukaryotic nucleus.

REFERENCES AND NOTES

1. M. Jinek *et al.*, *Science* **337**, 816–821 (2012).
2. G. Gasiunas, R. Barrangou, P. Horvath, V. Siksnys, *Proc. Natl. Acad. Sci. U.S.A.* **109**, E2579–E2586 (2012).
3. P. D. Hsu, E. S. Lander, F. Zhang, *Cell* **157**, 1262–1278 (2014).
4. J. A. Doudna, E. Charpentier, *Science* **346**, 1258096 (2014).
5. R. M. Terns, M. P. Terns, *Trends Genet.* **30**, 111–118 (2014).
6. S. H. Sternberg, S. Redding, M. Jinek, E. C. Greene, J. A. Doudna, *Nature* **507**, 62–67 (2014).
7. M. Jinek *et al.*, *Science* **343**, 1247997 (2014).
8. H. Nishimasu *et al.*, *Cell* **156**, 935–949 (2014).
9. C. Anders, O. Niewoehner, A. Duerst, M. Jinek, *Nature* **513**, 569–573 (2014).
10. X. Wu *et al.*, *Nat. Biotechnol.* **32**, 670–676 (2014).
11. C. Kuscu, S. Arslan, R. Singh, J. Thorpe, M. Adli, *Nat. Biotechnol.* **32**, 677–683 (2014).
12. P. D. Hsu *et al.*, *Nat. Biotechnol.* **31**, 827–832 (2013).
13. V. Pattanayak *et al.*, *Nat. Biotechnol.* **31**, 839–843 (2013).
14. B. Chen *et al.*, *Cell* **155**, 1479–1491 (2013).
15. G. V. Los *et al.*, *ACS Chem. Biol.* **3**, 373–382 (2008).
16. J. B. Grimm *et al.*, *Nat. Methods* **12**, 244–250, 3, 250 (2015).
17. J. Jurka, O. Kohany, A. Pavlicek, V. V. Kapitonov, M. V. Jurka, *Cytogenet. Genome Res.* **110**, 117–123 (2005).
18. C. A. Espinoza, J. A. Goodrich, J. F. Kugel, *RNA* **13**, 583–596 (2007).
19. S. Abrahamsson *et al.*, *Nat. Methods* **10**, 60–63 (2013).
20. J. C. M. Gebhardt *et al.*, *Nat. Methods* **10**, 421–426 (2013).
21. D. Normanno *et al.*, *Nat. Commun.* **6**, 7357 (2015).
22. M. D. Szczelkun *et al.*, *Proc. Natl. Acad. Sci. U.S.A.* **111**, 9798–9803 (2014).
23. B. L. Sprague, R. L. Pego, D. A. Stavreva, J. G. McNally, *Biophys. J.* **86**, 3473–3495 (2004).
24. F. Mueller, D. Mazza, T. J. Stasevich, J. G. McNally, *Curr. Opin. Cell Biol.* **22**, 403–411 (2010).
25. J. C. Eissenberg, S. C. R. Elgin, *Curr. Opin. Genet. Dev.* **10**, 204–210 (2000).
26. Z. Liu *et al.*, *eLife* **3**, e04236 (2014).
27. S. Manley *et al.*, *Nat. Methods* **5**, 155–157 (2008).
28. Materials and Methods are available as supplementary materials on *Science* Online.
29. M. El Beheiry, M. Dahan, J. B. Masson, *Nat. Methods* **12**, 594–595 (2015).
30. I. Izeddin *et al.*, *eLife* **3**, e02230 (2014).

ACKNOWLEDGMENTS

We thank L. Lavis for generously providing HaloTag ligands for imaging experiments; J. Macklin for expert assistance with FCS experiments; and X. Darzacq, R. Singer, J. Cate, and members of the Doudna and Tjian labs for helpful discussions and critical reading of the manuscript. S.C.K. acknowledges support from the Janelia Visitor Program, S.C.K. and E.T.Z. acknowledge support from the National Science Foundation Graduate Research Fellowship Program, W.D. acknowledges support from the Helen Hay Whitney Foundation, and Z.L. acknowledges support from the Janelia Fellow Program. Funding was provided by the National Science Foundation (MCB-1244557 to J.A.D.) and the California Institute for Regenerative Medicine (CIRM, RB4-06016 to R.T.). J.A.D. and R.T. are Investigators of the Howard Hughes Medical Institute. This work was performed in part at the University of California Berkeley Cancer Research Laboratory Molecular Imaging Center, supported by the Gordon and Betty Moore Foundation. J.A.D. is a co-founder of Caribou Biosciences, Inc., Editas Medicine and Intellia Therapeutics.

SUPPLEMENTARY MATERIALS

www.sciencemag.org/content/350/6262/823/suppl/DC1
Materials and Methods
Table S1
Figs. S1 to S13
Captions for Movies S1 to S12
References (*31*–*38*)
Movies S1 to S12

27 May 2015; accepted 7 October 2015
10.1126/science.aac6572

ANTIVIRAL IMMUNITY

Nlrp6 regulates intestinal antiviral innate immunity

Penghua Wang,[1,6]* Shu Zhu,[2]* Long Yang,[1,6] Shuang Cui,[1] Wen Pan,[3] Ruaidhri Jackson,[2] Yunjiang Zheng,[2] Anthony Rongvaux,[2] Qiangming Sun,[1]† Guang Yang,[1]‡ Shandian Gao,[1] Rongtuan Lin,[4] Fuping You,[1] Richard Flavell,[2,5]§|| Erol Fikrig[1,5]§||

The nucleotide-binding oligomerization domain–like receptor (Nlrp) 6 maintains gut microbiota homeostasis and regulates antibacterial immunity. We now report a role for Nlrp6 in the control of enteric virus infection. *Nlrp6*$^{-/-}$ and control mice systemically challenged with encephalomyocarditis virus had similar mortality; however, the gastrointestinal tract of *Nlrp6*$^{-/-}$ mice exhibited increased viral loads. *Nlrp6*$^{-/-}$ mice orally infected with encephalomyocarditis virus had increased mortality and viremia compared with controls. Similar results were observed with murine norovirus 1. Nlrp6 bound viral RNA via the RNA helicase Dhx15 and interacted with mitochondrial antiviral signaling protein to induce type I/III interferons (IFNs) and IFN-stimulated genes (ISGs). These data demonstrate that Nlrp6 functions with Dhx15 as a viral RNA sensor to induce ISGs, and this effect is especially important in the intestinal tract.

Nucleotide oligomerization domain (NOD)–like receptors (NLRs) play a central role in the immune response to diverse microorganisms and react to environmental insults and cellular danger signals (*1*, *2*). Some NLRs contribute to antiviral immunity. NOD2 recognizes single-stranded RNA (ssRNA) viruses to induce type I interferons (IFNs) via mitochondrial antiviral-signaling protein (MAVS) (*3*), and the NLRP3 inflammasome is crucial for the control of diverse viral infections in vivo (*4*–*7*). Several NLRs, on the other hand, dampen antiviral immune responses. NLRX1 and NLRC5 negatively regulate type I IFNs and nuclear factor κB (NF-κB) signaling via distinct molecular mechanisms (*8*–*12*); NLRC3 attenuates Toll-like receptor signaling and the stimulator of interferon genes (STING)–mediated anti-DNA virus immune signaling (*13*, *14*). A role for Nlrp6 in the regulation of antibacterial immune responses has recently been documented (*15*–*18*); however, whether Nlrp6 regulates viral infection has not yet been elucidated.

Nlrp6 exhibits a tissue- and cell-type–specific pattern of expression, with the highest level in intestinal epithelial cells (IECs) (*15*) (figs. S1 and S2). We therefore determined whether Nlrp6 plays a prominent role in inhibiting enteric virus infection at the intestinal interface. We used a (+) ssRNA virus, encephalomyocarditis virus (EMCV), which is transmitted via the fecal-oral route in nature. We infected both wild-type (WT) and *Nlrp6*$^{-/-}$ mice with EMCV systemically via intraperitoneal injection and noted that the survival curve of *Nlrp6*$^{-/-}$ mice was similar to that of WT animals (Fig. 1A). Viral dissemination was also the same in the blood, brains, and hearts of *Nlrp6*$^{-/-}$ and WT mice. The intestinal viral burden of *Nlrp6*$^{-/-}$ mice was, however, higher than that of WT animals (Fig. 1B)—suggesting that Nlrp6 plays an important role in limiting EMCV replication at this location. In support of this, *Nlrp6* mRNA expression was much higher in the intestines than other tissues after EMCV infection (Fig. 1C). We therefore reasoned that Nlrp6 prevents systemic infection and mortality when EMCV is delivered orally to its principal site of infection—the intestine. Indeed, *Nlrp6*$^{-/-}$ mice were more susceptible to oral infection with EMCV than WT animals (Fig. 1D and Fig. 3E).

Alterations in microbiota and inflammasome activation are two potential processes that may influence the ability of *Nlrp6*$^{-/-}$ mice to control intestinal EMCV infection. The intestinal microbial ecology of *Nlrp6*$^{-/-}$ mice is different from that of WT mice (*15*), which could affect antiviral immunity. We therefore cohoused mice for 4 weeks before EMCV infection, which we previously showed was sufficient to equilibrate the microbiota between WT and *Nlrp6*$^{-/-}$ mice. WT and *Nlrp6*$^{-/-}$ mice had similar levels of *TM7* and *Prevotellacae* bacteria (*15*) after cohousing (fig. S3A), indicating stabilization of the microbiota. *Nlrp6*$^{-/-}$ mice, however, died of EMCV infection more rapidly than WT and cohoused WT animals (Fig. 1D), and viremia was ~10-fold higher in *Nlrp6*$^{-/-}$ than WT animals (Fig. 1E). When inoculated systemically

[1]Section of Infectious Diseases, Yale University School of Medicine, 300 Cedar Street, New Haven, CT 06510, USA. [2]Department of Immunobiology, Yale University School of Medicine, 300 Cedar Street, New Haven, CT 06510, USA. [3]Department of Genetics, Yale University School of Medicine, 300 Cedar Street, New Haven, CT 06510, USA. [4]Lady Davis Institute, Department of Medicine, McGill University, Montreal, Quebec, Canada. [5]Howard Hughes Medical Institute, Chevy Chase, MD 20815-6789, USA. [6]Department of Microbiology and Immunology, New York Medical College, Valhalla, NY 10595, USA.
*These authors contributed equally to this work. †Present address: Institute of Medical Biology, Chinese Academy of Medical Sciences, and Peking Union Medical College, Kunming, People's Republic of China. ‡Present address: Department of Parasitology, School of Medicine, Jinan University, Guangzhou, China. §The laboratories of these authors contributed equally to this work. **||Corresponding author. E-mail: richard.flavell@yale.edu (R.F.); erol.fikrig@yale.edu (E.F.)**

via intraperitoneal injection, EMCV loads in the intestines of cohoused *Nlrp6*$^{-/-}$ mice were also more than 10-fold higher than those of cohoused WT animals (Fig. 1F). Similar survival results were noted for *Nlrp6*$^{-/-}$ and *Nlrp6*$^{+/+}$ littermates (fig. S3B). These data demonstrate that the increased viral susceptibility of *Nlrp6*$^{-/-}$ mice is not a result of altered intestinal microbial ecology. To extend our finding further, we examined another enteric virus, murine norovirus 1 (MNV-1), a (+) ssRNA virus. MNV-1 was rapidly cleared by the innate immune system in WT mice (*19*) but persisted much longer in *Nlrp6*$^{-/-}$ mice (fig. S3, C to E). Nlrp6 initiates inflammasome signaling via caspase-1. We therefore determined whether Nlrp6 requires caspase-1 to control EMCV at the intestinal epithelia. In agreement with a previous report (*20*), following EMCV challenge, the survival of *Casp1*$^{-/-}$ and WT mice was similar (Fig. 1D). These data suggest that intestinal Nlrp6 controls EMCV infection by an alternative mechanism.

To understand how Nlrp6 contributes to antiviral innate immune responses, we used an Nlrp6 antibody to immunoprecipitate Nlrp6 binding partners from mouse primary IECs and a FLAG-Nlrp6 overexpression system in human embryonic kidney 293 T (HEK293T) cells. We identified DEAH (Asp-Glu-Ala-His) box helicase 15 (Dhx15) by mass spectrometry (fig. S4) and confirmed it using a specific antibody to Dhx15 (Fig. 2A and fig. S5A). Glutathione *S*-transferase–Dhx15 expressed in *Escherichia coli* pulled down FLAG-Nlrp6 expressed using a mammalian in vitro translation system (fig. S5B), suggesting a direct interaction. Nlrp6 is composed of three functional domains: an N-terminal pyrin domain (PYD), a NACHT domain, and a C-terminal leucine-rich repeat domain (LRR). Each individual domain failed to bind Dhx15 when compared with full-length Nlrp6 (fig. S5C). A fragment encompassing the NATCH and NACHT-associated domain (NAD) interacted with Dhx15 (Fig. 2B). NLRP3, a close relative of Nlrp6, did not interact with Dhx15, demonstrating specificity (fig. S5C).

Dhx15 is a putative pre-mRNA-splicing factor and adenosine triphosphate (ATP)–dependent RNA helicase that modulates antiviral immune responses via MAVS, an adaptor protein for retinoic acid inducible gene 1 (RIG-I)–like receptors (RLRs) (*21*, *22*). We reasoned that the Nlrp6-Dhx15 complex might use MAVS to trigger type I IFN responses. Indeed, FLAG-Nlrp6 bound endogenous MAVS, as did Nlrp3 (*(23)*) and RIG-I (*24*–*27*) (Fig. 2C). The negative controls FLAG-NLRC5 (*11*) or Nlrp10 did not coprecipitate with MAVS (fig. S5D), confirming the specificity of the Nlrp6-MAVS interaction. Because Dhx15 is a putative RNA helicase and viral RNA sensor (*22*), we then determined whether Nlrp6-Dhx15 forms a viral RNA-sensing complex. Both Nlrp6 and Dhx15 showed high affinity for viral RNA (Fig. 2D and fig. S6A). The Nlrp6 NACHT domain was sufficient for RNA binding but weaker than full-length Nlrp6 (fig. S6B). To exclude nonspecific binding due to overexpression, we examined endogenous Nlrp6 binding to viral RNA in WT and FLAG-Nlrp6 knock-in mice (fig. S2). Both Nlrp6 and FLAG-Nlrp6 was coimmunoprecipitated with EMCV RNA from infected IECs (Fig. 2E and fig. S6C). Because the RNA binding capacity of Dhx15 was much greater than that of Nlrp6, we reasoned that Nlrp6-RNA binding was dependent on Dhx15. Indeed, the amount of Nlrp6-bound viral RNA was reduced significantly in Dhx15 small interfering RNA (siRNA)–treated cells (Fig. 2F). In contrast, Dhx15-RNA binding was not altered in *Nlrp6*$^{-/-}$ cells (fig. S6D). Like Dhx15 (*22*), Nlrp6 bound only RNA but not DNA viruses (fig. S6E). To assess the nature of viral RNA bound by Nlrp6, we tested several synthetic RNA analogs. Nlrp6 preferably bound the long double-stranded RNA (dsRNA) analog polyinosinic-polycytidylic acid (polyIC) (Fig. 2G). To provide in vivo evidence for a functional interaction between MAVS, Dhx15, and Nlrp6, we examined MAVS-Dhx15 interactions in WT and *Nlrp6*$^{-/-}$IECs. Consistent with a previous report (*22*), MAVS binding to Dhx15 was enhanced by EMCV infection in WT IECs, but the interaction was weaker in *Nlrp6*$^{-/-}$ (Fig. 2H). *Mavs*$^{-/-}$ mice

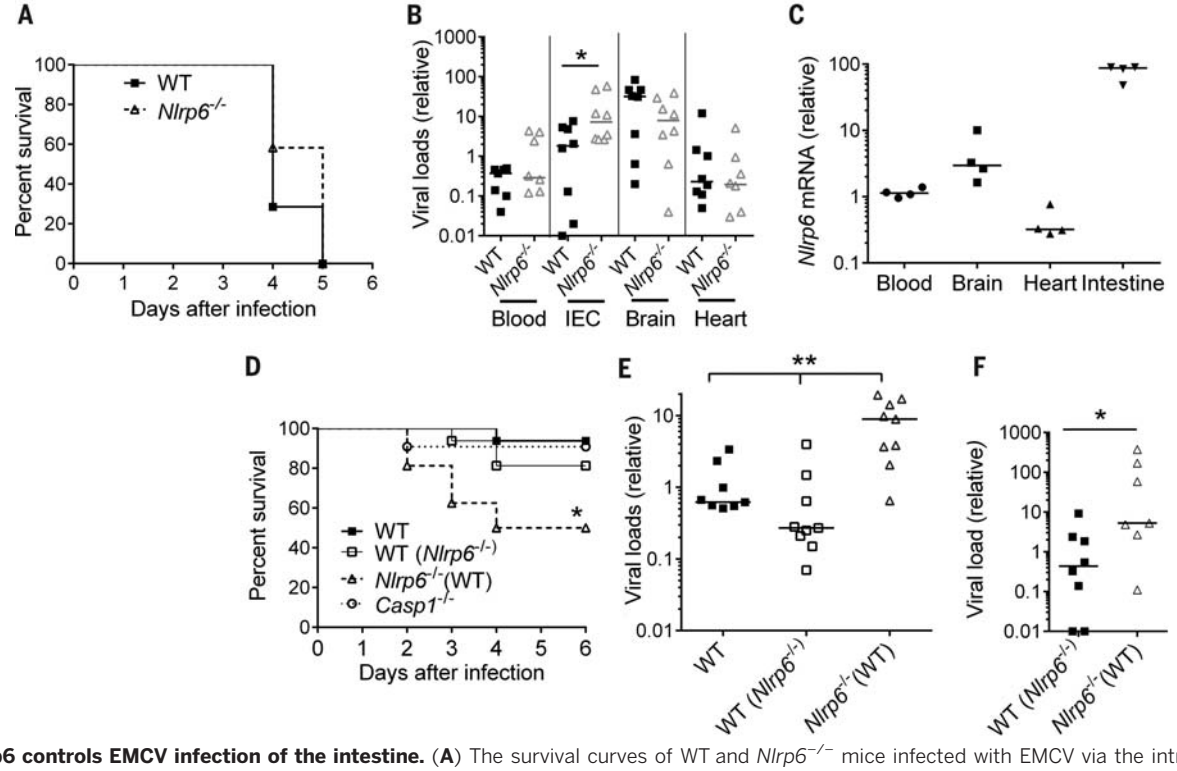

Fig. 1. Nlrp6 controls EMCV infection of the intestine. (**A**) The survival curves of WT and *Nlrp6*$^{-/-}$ mice infected with EMCV via the intraperitoneal route. *N* = 12 mice per group. (**B** and **C**) Quantitative polymerase chain reaction (qPCR) analyses of (B) EMCV viral loads and (C) *Nlrp6* in various tissues 72 hours after infection with EMCV intraperitoneally Intestinal epithelial cells (IEC). (**D**) The survival curves of WT mice, WT mice cohoused with *Nlrp6*$^{-/-}$ [WT (*Nlrp6*$^{-/-}$)], *Nlrp6*$^{-/-}$ mice cohoused with WT [*Nlrp6*$^{-/-}$(WT)], and *Casp1*$^{-/-}$ mice after oral infection with EMCV. *N* = 10 to 16 mice per group. *P < 0.05 (log-rank test). Results were pooled from two independent experiments. (**E** and **F**) qPCR analysis of EMCV loads (E) in the whole blood cells 72 hours after oral infection or (F) in the intestines 72 hours after intraperitoneal infection. Each symbol in (B), (C), (E), and (F) represents one mouse; small horizontal lines indicate the median of the result. *P < 0.05; **P < 0.01 (nonparametric Mann-Whitney analysis). The data are representative of at least two to three independent experiments.

were also much more susceptible to EMCV administered orally when compared with WT mice (Fig. 2I). These data suggest that the Dhx15-Nlrp6-MAVS axis plays an important role in restricting EMCV infection of the intestine.

To validate a role for Nlrp6 in Dhx15-Mavs–mediated antiviral immunity, we examined the expression of type I/III IFN-induced genes (ISGs). The mRNA and protein expression of a number of ISGs was reduced in *Nlrp6*$^{-/-}$ IECs compared with WT (fig. S7A and Fig. 3, A and B). Although both types I and III IFNs can elicit antiviral responses, type III IFNs are particularly critical for controlling viral infection in IECs (*28*–*30*). IFN-λ (also known as IL-28a) protein and mRNA, and *Ifnb* mRNA, were reduced in *Nlrp6*$^{-/-}$ intestines after EMCV infection (fig. S7B). ISG mRNA amounts were, however, similar in other WT and *Nlrp6*$^{-/-}$ tissues (fig. S8).

To assess whether the Nlrp6-caspase-1 inflammasome regulates antiviral immunity in the intestine, we compared ISG expression in *Nlrp6*$^{-/-}$ with *Casp1*$^{-/-}$ and WT mice. The viral loads and ISG expression were similar in the intestines of *Casp1*$^{-/-}$ and WT mice (fig. S9), demonstrating an inflammasome-independent antiviral mechanism for Nlrp6. In support of the in vivo findings, EMCV loads in *Nlrp6*$^{-/-}$ embryonic fibroblasts (MEFs) were sixfold higher than those in *Nlrp6*$^{+/-}$ cells at 16 hours after infection, while antiviral gene expression was significantly lower (Fig. 3, C and D, and fig. S10, A and B). We also observed a decrease in polyIC-induced *Ifnb1* expression in *Nlrp6*$^{-/-}$ compared with *Nlrp6*$^{-/+}$ MEFs (fig. S10C). In agreement with the results from *Nlrp6*$^{-/-}$ cells, overexpression of Nlrp6 enhanced *Ifnb1* and *Il6* expression modestly (fig. S11). All these data demonstrate a pivotal role for Nlrp6 in inducing type I/III IFNs and ISGs. Type III IFNs are particularly critical for control of viral infection of IECs (*28*–*30*). Indeed, exogenous IFN-λ fully protected WT and *Nlrp6*$^{-/-}$ mice against lethal EMCV infection and reduced viremia significantly (Fig. 3E). We next determined whether the antiviral function of Nlrp6 is specific for RNA viruses. Neither herpes simplex virus–1 (HSV-1) titers nor *Ifnb1* expression in *Nlrp6*$^{-/-}$ was different from those in *Nlrp6*$^{-/+}$ cells (fig. S12A). IFN-α, polydAT, or lipopolysaccharide-induced ISGs or cytokine expression in *Nlrp6*$^{-/-}$ was also similar to that in *Nlrp6*$^{-/+}$ MEFs (fig. S12, B to D).

As viral infections and the ligands that can induce robust type I IFN expression also upregulated Nlrp6 expression (Fig. 3C and figs. S10C, S12C, and S13), we reasoned that Nlrp6 per se might be an ISG. Indeed, induction of *Nlrp6* mRNA expression by EMCV or polyIC

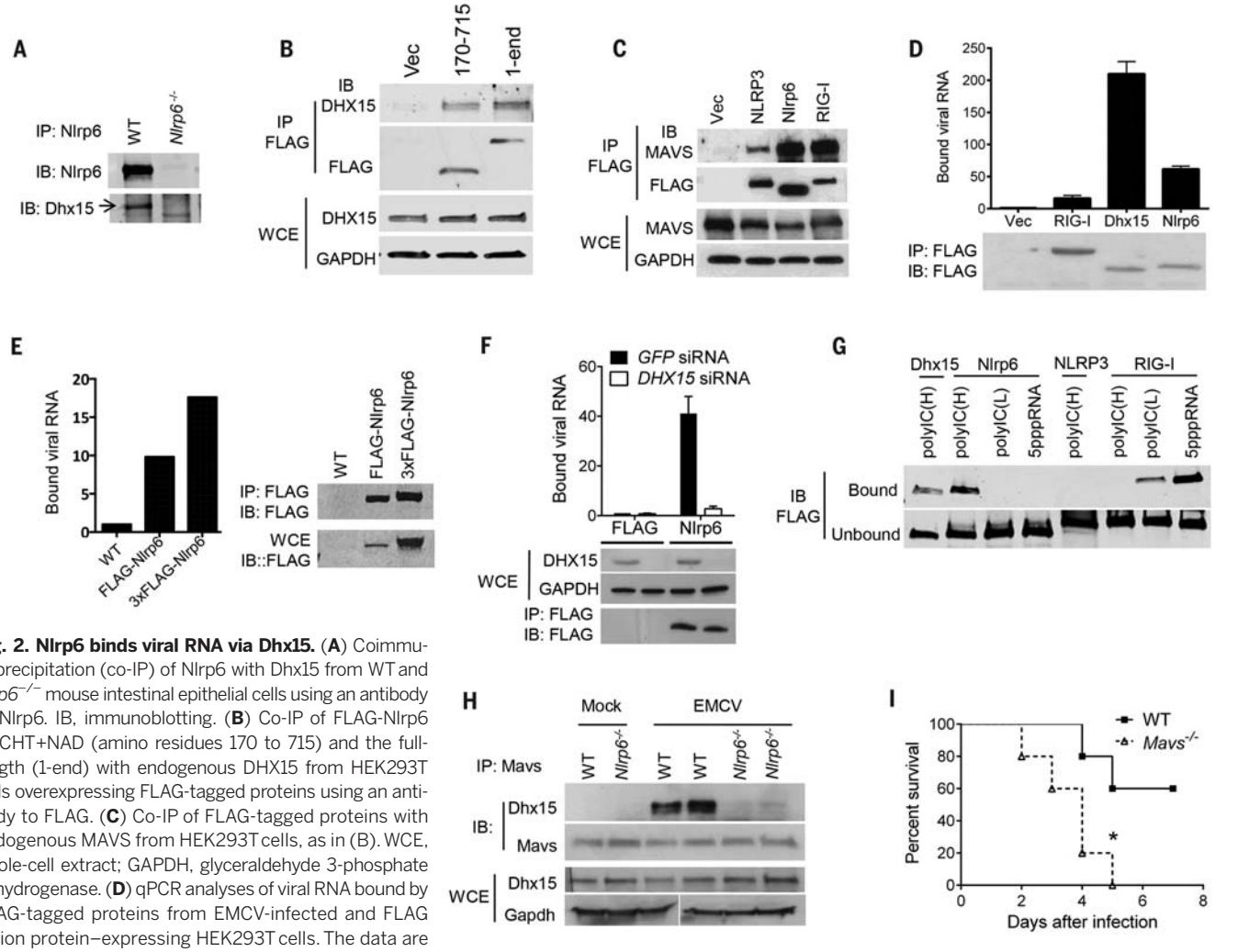

Fig. 2. Nlrp6 binds viral RNA via Dhx15. (**A**) Coimmunoprecipitation (co-IP) of Nlrp6 with Dhx15 from WT and *Nlrp6*$^{-/-}$ mouse intestinal epithelial cells using an antibody to Nlrp6. IB, immunoblotting. (**B**) Co-IP of FLAG-Nlrp6 NACHT+NAD (amino residues 170 to 715) and the full-length (1-end) with endogenous DHX15 from HEK293T cells overexpressing FLAG-tagged proteins using an antibody to FLAG. (**C**) Co-IP of FLAG-tagged proteins with endogenous MAVS from HEK293T cells, as in (B). WCE, whole-cell extract; GAPDH, glyceraldehyde 3-phosphate dehydrogenase. (**D**) qPCR analyses of viral RNA bound by FLAG-tagged proteins from EMCV-infected and FLAG fusion protein–expressing HEK293T cells. The data are presented as relative increase over vector (FLAG). (**E**) Binding of endogenous Nlrp6 to viral RNA. (Left) qPCR analyses of viral RNA bound by endogenous FLAG-Nlrp6 in IECs. (Right) Immunoblots of FLAG-Nlrp6 in WCE and IP. 3xFLAG-Nlrp6 denotes three FLAG motifs tagged to Nlrp6. (**F**) (Top) qPCR analyses of EMCV RNA bound by FLAG-Nlrp6 from *GFP* or *DHX15* siRNA-treated HEK293T cells. (Bottom) Immunoblots of WCE and IP. (**G**) Immunoblots showing FLAG-tagged proteins (purified from HEK293T) bound by biotin-labeled RNA analogs. polyIC(H), high molecular weight (1.5 to 8 kb); polyIC(L), low molecular weight (0.2 to 1 kb). (**H**) Co-IP of Mavs with Dhx15 from IECs of WT and *Nlrp6*$^{-/-}$ mice infected with EMCV using a rabbit polyclonal antibody to Mavs. (**I**) The survival curves of WT and *Mavs*$^{-/-}$ mice after oral infection with EMCV. $N = 5$ mice per group; $^*P < 0.05$ (log-rank test). The data are representative of at least two independent experiments.

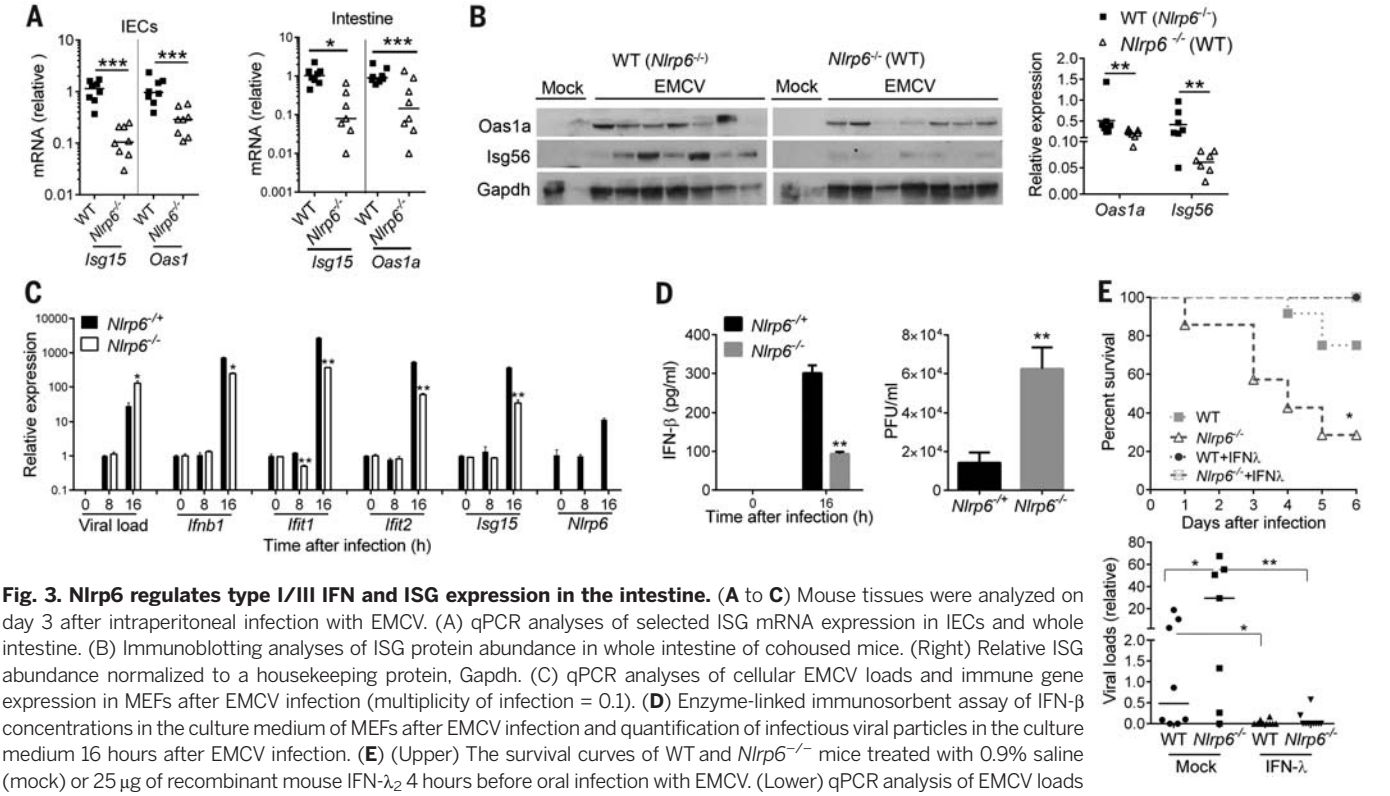

Fig. 3. Nlrp6 regulates type I/III IFN and ISG expression in the intestine. (**A** to **C**) Mouse tissues were analyzed on day 3 after intraperitoneal infection with EMCV. (A) qPCR analyses of selected ISG mRNA expression in IECs and whole intestine. (B) Immunoblotting analyses of ISG protein abundance in whole intestine of cohoused mice. (Right) Relative ISG abundance normalized to a housekeeping protein, Gapdh. (C) qPCR analyses of cellular EMCV loads and immune gene expression in MEFs after EMCV infection (multiplicity of infection = 0.1). (**D**) Enzyme-linked immunosorbent assay of IFN-β concentrations in the culture medium of MEFs after EMCV infection and quantification of infectious viral particles in the culture medium 16 hours after EMCV infection. (**E**) (Upper) The survival curves of WT and *Nlrp6*$^{-/-}$ mice treated with 0.9% saline (mock) or 25 μg of recombinant mouse IFN-λ_2 4 hours before oral infection with EMCV. (Lower) qPCR analysis of EMCV loads in the whole blood cells 72 hours after infection. $N = 7$ to 10 mice per group. *$P < 0.05$ (log-rank test). In (A) and (E), the data are normalized with mouse beta actin and are presented as relative change over the mean of the results of WT [Mock-WT in (E)] mice. Each band/dot represents an animal. The horizontal lines in the figures indicate the median of the results. *$P < 0.05$; **$P < 0.01$; ***$P < 0.001$ (nonparametric Mann-Whitney analysis). In (C) and (D), scale bars show mean + SEM; $n = 3$ mice. *$P < 0.05$; **$P < 0.01$ (unpaired Students' t test). The data are representative of at least two independent experiments.

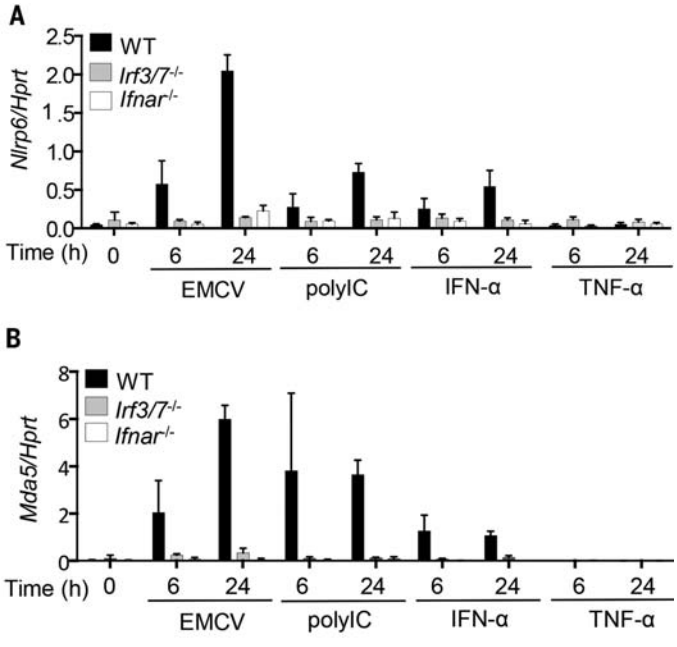

Fig. 4. Nlrp6 is an ISG. qPCR analyses of the transcripts of (**A**) *Nlrp6* and (**B**) *Mda5* in WT, *Irf3/7*$^{-/-}$, and *Ifnar*$^{-/-}$ MEFs treated with EMCV, polyIC, recombinant IFN-α, or TNF-α. The data are expressed as percentage of a housekeeping gene *Hprt*. Scale bars, mean + SD. The data are representative of at least two independent experiments.

treatment was almost abolished in *Irf3/7*$^{-/-}$ or *Ifnar1*$^{-/-}$ MEFs. Consistent with this, recombinant IFN-α, but not tumor necrosis factor–α (TNF-α) was able to induce *Nlrp6* expression vigorously, suggesting that interferon regulatory factor (IRF)/IFN signaling, but not NF-κB signaling controls Nlrp6 expression (Fig. 4 and fig. S14A). *Nlrp6* mRNA expression was also induced by recombinant IFN-λ2 (fig. S14B). These results indicate that *Nlrp6* expression is regulated by type I/III IFNs via IRF3/7.

The above-mentioned data demonstrate that Dhx15-Nlrp6 senses long dsRNA in the cytoplasm (Fig. 2G), a well-established feature for MDA5. We then determined whether Nlrp6-mediated signaling is also dependent on MDA5. siRNA knockdown of Nlrp6 reduced *Ifnb1* and *Isg15* mRNA expression after polyIC stimulation in *Mda5*$^{-/-}$ MEFs (fig. S15A), suggesting an MDA5-independent antiviral role for Nlrp6. Similar results were noted with *Rig-I*$^{-/-}$ MEFs (fig. S15B). Nlrp6-RNA binding was unchanged in *Mda5*$^{-/-}$ or *Rig-I*$^{-/-}$ MEFs compared with WT (fig. S15C), and there was no interaction between Nlrp6 and MDA5 or RIG-I (fig. S15D). We next examined the relative antiviral role for MDA5 in the intestine in comparison with Nlrp6. The viral loads in both *Nrp6*$^{-/-}$ and *Mda5*$^{-/-}$ IECs were similar but were much higher than those in WT mice (fig. S15E). These results, in conjunction with the Nlrp6, Dhx15, and MDA5 expression data (fig. S1), suggest that Dhx15-Nlrp6 constitutes the first line of anti-EMCV defense in the intestinal epithelia, whereas MDA5 is dominant in myeloid cells.

Our results demonstrate that Nlrp6 controls enteric virus infection in the intestine by interacting with an RNA sensor, Dhx15, to trigger MAVS-dependent antiviral responses. This inflammasome-independent response provides a mechanism for Nlrp6 to elicit pleotropic effects in the host and demonstrates its importance against diverse classes of microbes.

REFERENCES AND NOTES

1. K. Schroder, J. Tschopp, *Cell* **140**, 821–832 (2010).
2. T. Strowig, J. Henao-Mejia, E. Elinav, R. Flavell, *Nature* **481**, 278–286 (2012).
3. A. Sabbah *et al.*, *Nat. Immunol.* **10**, 1073–1080 (2009).
4. T. Ichinohe, H. K. Lee, Y. Ogura, R. Flavell, A. Iwasaki, *J. Exp. Med.* **206**, 79–87 (2009).
5. I. C. Allen *et al.*, *Immunity* **30**, 556–565 (2009).
6. T. D. Kanneganti *et al.*, *Nature* **440**, 233–236 (2006).
7. P. G. Thomas *et al.*, *Immunity* **30**, 566–575 (2009).
8. C. B. Moore *et al.*, *Nature* **451**, 573–577 (2008).
9. I. C. Allen *et al.*, *Immunity* **34**, 854–865 (2011).
10. Y. Lei *et al.*, *Immunity* **36**, 933–946 (2012).
11. J. Cui *et al.*, *Cell* **141**, 483–496 (2010).
12. Y. Tong *et al.*, *Cell Res.* **22**, 822–835 (2012).
13. M. Schneider *et al.*, *Nat. Immunol.* **13**, 823–831 (2012).
14. L. Zhang *et al.*, *Immunity* **40**, 329–341 (2014).
15. E. Elinav *et al.*, *Cell* **145**, 745–757 (2011).
16. K. Kersse, M. J. Bertrand, M. Lamkanfi, P. Vandenabeele, *Cytokine Growth Factor Rev.* **22**, 257–276 (2011).
17. M. Wlodarska *et al.*, *Cell* **156**, 1045–1059 (2014).
18. P. K. Anand *et al.*, *Nature* **488**, 389–393 (2012).
19. S. M. Karst, C. E. Wobus, M. Lay, J. Davidson, H. W. Virgin 4th, *Science* **299**, 1575–1578 (2003).
20. J. V. Rajan, D. Rodriguez, E. A. Miao, A. Aderem, *J. Virol.* **85**, 4167–4172 (2011).
21. K. Mosallanejad *et al.*, *Sci. Signal.* **7**, ra40 (2014).
22. H. Lu *et al.*, *J. Immunol.* **193**, 1364–1372 (2014).
23. N. Subramanian, K. Natarajan, M. R. Clatworthy, Z. Wang, R. N. Germain, *Cell* **153**, 348–361 (2013).
24. T. Kawai *et al.*, *Nat. Immunol.* **6**, 981–988 (2005).
25. E. Meylan *et al.*, *Nature* **437**, 1167–1172 (2005).
26. R. B. Seth, L. Sun, C. K. Ea, Z. J. Chen, *Cell* **122**, 669–682 (2005).
27. L. G. Xu *et al.*, *Mol. Cell* **19**, 727–740 (2005).
28. J. Pott *et al.*, *Proc. Natl. Acad. Sci. U.S.A.* **108**, 7944–7949 (2011).
29. A. H. Broquet, Y. Hirata, C. S. McAllister, M. F. Kagnoff, *J. Immunol.* **186**, 1618–1626 (2011).
30. T. J. Nice *et al.*, *Science* **347**, 269–273 (2015).

ACKNOWLEDGMENTS

The data presented in this manuscript are tabulated in the main paper and in the supplementary materials. This work was supported by National Institutes of Health grants N01-HHSN272201100019C, AI099625, and AI103807. E.F. and R.F. are Investigators of the Howard Hughes Medical Institute. S.Z. was supported by a fellowship from Howard Hughes Medical Institute–The Helen Hay Whitney Foundation.

SUPPLEMENTARY MATERIALS

www.sciencemag.org/content/350/6262/826/suppl/DC1
Materials and Methods
Figs. S1 to S15
References (*31*–*37*)

9 April 2015; accepted 2 October 2015
Published online 22 October 2015
10.1126/science.aab3145

MUCOSAL IMMUNITY

A gut-vascular barrier controls the systemic dissemination of bacteria

Ilaria Spadoni,[1] Elena Zagato,[1] Alice Bertocchi,[1] Roberta Paolinelli,[2] Edina Hot,[1] Antonio Di Sabatino,[3] Flavio Caprioli,[4] Luca Bottiglieri,[5] Amanda Oldani,[2] Giuseppe Viale,[5] Giuseppe Penna,[1] Elisabetta Dejana,[2,6,7] Maria Rescigno[1,6]*

In healthy individuals, the intestinal microbiota cannot access the liver, spleen, or other peripheral tissues. Some pathogenic bacteria can reach these sites, however, and can induce a systemic immune response. How such compartmentalization is achieved is unknown. We identify a gut-vascular barrier (GVB) in mice and humans that controls the translocation of antigens into the bloodstream and prohibits entry of the microbiota. *Salmonella typhimurium* can penetrate the GVB in a manner dependent on its pathogenicity island (Spi) 2–encoded type III secretion system and on decreased β-catenin–dependent signaling in gut endothelial cells. The GVB is modified in celiac disease patients with elevated serum transaminases, which indicates that GVB dismantling may be responsible for liver damage in these patients. Understanding the GVB may provide new insights into the regulation of the gut-liver axis.

Upon ingestion, food antigens can access the lymphatics to reach the mesenteric lymph nodes (MLNs) (*1*) and the blood stream (portal vein) to reach the liver (*2*). In contrast, the microbiota cannot access the liver (*3*) and can reach the spleen only when the MLNs are excised (*4*). This suggests that the microbiota are actively excluded from the bloodstream and that the MLNs provide a firewall for the systemic dissemination of the microbiota from the lymphatics (*5*). What determines antigen access to the bloodstream is unknown.

We hypothesized the existence of a gut-vascular barrier (GVB) that might control the type of antigens that are translocated across blood endothelial cells (ECs) to reach the portal vein. To evaluate the presence of such a barrier, we injected mice intravenously with fluorescein isothiocyanate (FITC)–dextran of different molecular sizes and analyzed leakage of the dye into the intestine. We observed that there is an endothelial barrier that discriminates between differently sized particles of the same nature. FITC-dextran of 4 kD freely diffused through the ECs, whereas FITC-dextran of 70 kD could not (Fig. 1A; fig. S1, A and B; and movies S1 and S2). However, after oral infection with *Salmonella enterica* serovar Typhimurium, which disseminates systemically in mice (*6*), 70 kD dextran was readily released from the bloodstream (Fig. 1A, fig. S1, and movies S3 and S4). This was not due to increased blood flow during infection, as 1-μm microspheres were retained within the vessels even after *Salmonella* infection (fig. S1, C and D, and movies S5 and S6). These results suggest the existence of a GVB that prevents the translocation of molecules of around 70 kD and that can be disrupted by *Salmonella*.

Endothelial barriers are characterized by the presence of elaborate junctional complexes that include tight junction (TJ) and adherens junction (AJ), which strictly control paracellular trafficking of solutes and fluids (*7*, *8*). Other cell types, such as pericytes or fibroblasts, can be found associated with the microvasculature and are involved in the maintenance of the vascular barrier, where they form a vascular unit (*9*). To study GVB characteristics, we analyzed the composition of TJ and AJ in gut ECs. We found that enteric ECs have TJ formed by occludin, zonula occludens-1 ZO-1, cingulin, and junctional adhesion molecule-A JAM-A (Fig. 1B and fig. S2) and AJ formed by vascular endothelial cadherin (VE-cadherin) and β-catenin (Fig. 1C and fig. S3). Claudin-5 was expressed primarily in lymphatic endothelial TJ (fig. S4). Claudin-12 was associated with other cell types in the lamina propria (fig. S2), which probably reflects a function in ion transport rather than in sealing (*10*). Finally, we found that gut ECs were surrounded by enteric glial cells expressing the intermediate filament glial fibrillary acidic protein (GFAP) and by pericytes expressing desmin (Fig. 1D and fig. S5). Thus, gut ECs are organized in a gut-vascular unit and express TJ and AJ proteins.

We then analyzed the expression of plasmalemma vesicle–associated protein-1 (PV1) (*11*), a marker of EC permeability (*12*, *13*). We found that gut blood ECs in the lamina propria (but not in the submucosa) did not express PV1 (Fig. 2A). We then hypothesized that PV1 expression could be modulated upon *Salmonella* challenge, which would reflect the increased vessel permeability. We observed a peak of PV1 up-regulation on blood but not lymphatic vessels in the jejunum and ileum 6 hours after *Salmonella* infection (Fig. 2, A and B). This correlated with *Salmonella* dissemination to the liver and spleen (Fig. 2C) and

[1]Department of Experimental Oncology, European Institute of Oncology, Milan, Italy. [2]The Italian Foundation for Cancer Research (FIRC) Institute of Molecular Oncology (IFOM), Milan, Italy. [3]First Department of Medicine, St. Matteo Hospital, University of Pavia, Pavia, Italy. [4]Unità Operativa Gastroenterologia ed Endoscopia, Fondazione IRCCS Cà Granda, Ospedale Maggiore Policlinico di Milano, and Dipartimento di Fisiopatologia Medico-Chirurgica e dei Trapianti, Università degli Studi di Milano, Milan, Italy. [5]Department of Pathology and Laboratory Medicine, European Institute of Oncology, Milan, Italy. [6]Department of Biosciences, Università degli Studi di Milano, Italy. [7]Department of Genetics, Immunology and Pathology, Uppsala University, Uppsala, Sweden.
***Corresponding author. E-mail: maria.rescigno@ieo.eu**

with liver damage (Fig. 2D). In the blood-brain barrier (BBB), which is the most selective vascular barrier, the down-regulation of PV1 during maturation is paralleled by the up-regulation of claudin-3 (*12*) and claudin-5 (*14*). However, expression of claudin-3 and -5 were only marginally detected on vascular ECs, and claudin-3 was modified only in epithelial cells upon infection (fig. S6).

To confirm increased barrier permeability, we injected FITC-dextran in intestinal loops at different time points. We detected the dye in the serum only if mice were infected with *Salmonella* (fig. S7). The kinetics of FITC-dextran translocation into the bloodstream was different throughout the intestinal tract. Maximal leakage was observed in the duodenum and jejunum loops at 4 hours and in the ileum at 24 hours after *Salmonella* infection (fig. S7).

To distinguish between direct gut-liver dissemination via the portal circulation and a systemic dissemination through the lymphatics-thoracic duct, we evaluated the presence of 70 kD FITC-dextran in the liver and spleen after intestinal injection. We found that 60 min after injection, the dye was detected in the liver but not the spleen of mice previously infected with *Salmonella* (fig. S8). We could not detect any dye in either tissue at an earlier time point (20 min), which suggests that the dye reaches the liver before the spleen, using the portal circulation, consistent with a report showing that liver and spleen infections of *Salmonella* originate from a different pool of bacterial colonies compared with those of Peyer's patches (PP) and MLNs (*15*).

To assess whether the capacity to cross the epithelial barrier would be sufficient for a bacterium to reach the endothelial barrier and cross it, we constructed a nonpathogenic strain of *Escherichia coli* with the *Yersinia enterocolitica* Inv protein (*E. coli* pInv), which enabled it to cross the epithelial barrier and penetrate the different segments of the gut (fig. S9). However, *E. coli* pInv was unable to disseminate to the liver and spleen (fig. S9), even if we administered 10 times the dose used for *Salmonella*, which suggested that the ability of *Salmonella* to disseminate systemically is not simply due to its capacity to cross the epithelium and face the endothelial barrier but rather results from an active process.

BBB maturation is controlled by the activation of the canonical Wnt/β-catenin signaling pathway (*12*, *16*). We hypothesized that this pathway might be important also for GVB maturation and that *Salmonella* might interfere with it. We generated primary lung ECs as we were unable to culture primary enteric ECs (*17*) and confirmed that they can be infected by *Salmonella* (fig. S10A). We treated these cells with different *Salmonella* mutants or with Wnt3a to stimulate β-catenin activation (*12*). We found that *Axin2* expression,

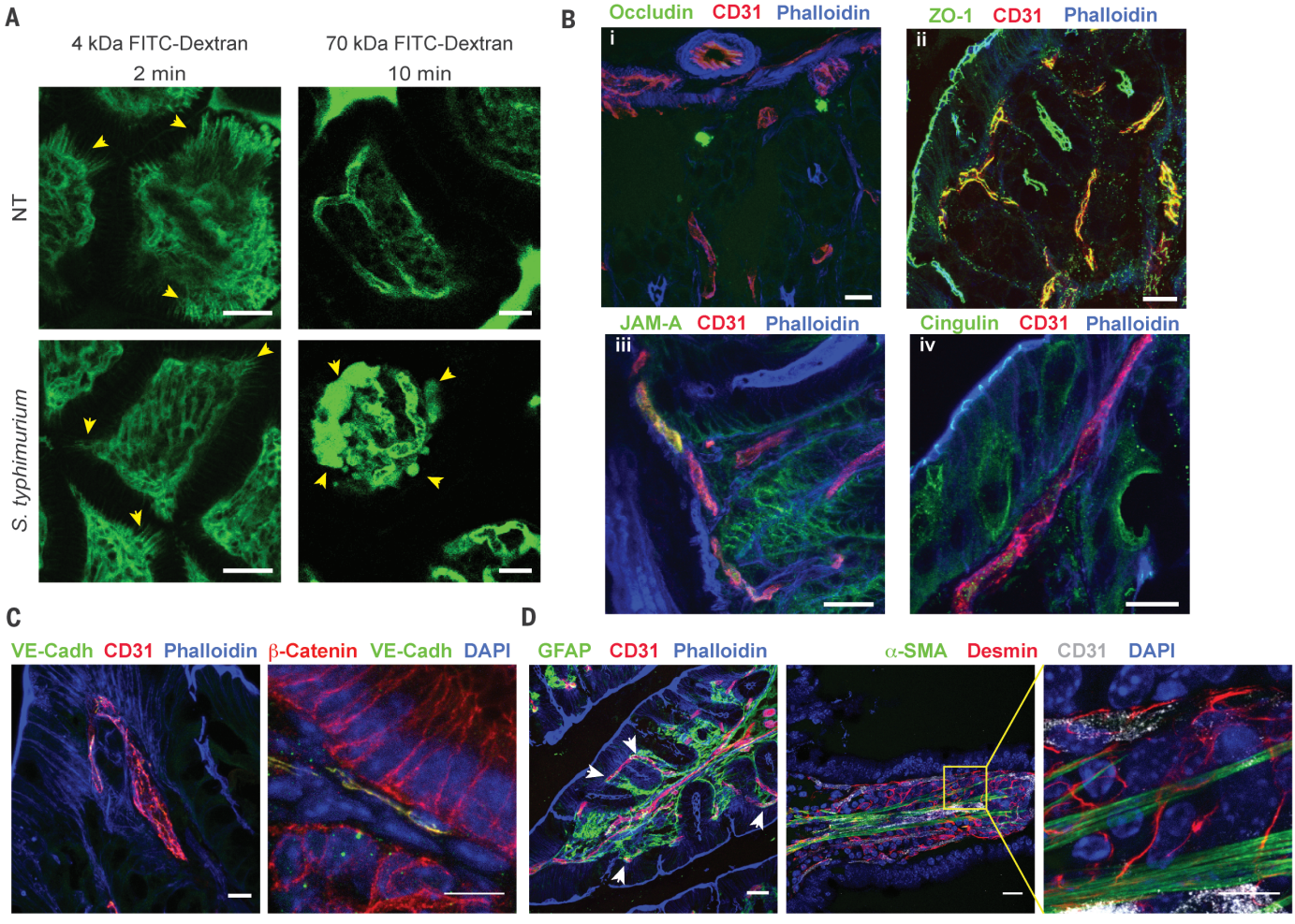

Fig. 1. Characterization of the GVB. (**A**) Intestinal blood vessels permeability to 4 kD and 70 kD FITC-dextran was analyzed by intravital two-photon microscopy in untreated or *Salmonella*-infected mice. Images were acquired every 30 s for 10 min. Arrowheads indicate fluorophore extravasation. Scale bar, 20 μm. Images are representative of three mice per group. (**B**) Localization of indicated TJ proteins (green) on endothelial cells (CD31, red) in the mouse intestine. Scale bars: (i and iv) 10 μm; (ii and iii) 20 μm. (**C**) AJ proteins expression on intestinal vessels. Scale bars, 10 μm. (**D**) Confocal images of C57BL/6J mice intestine stained with CD31 (red) and GFAP (green) (scale bar, 30 μm) or CD31 (gray), α-SMA (green), and desmin (red). Scale bars: (right) 20 μm, (left) 10 μm. In each section, actin filaments or nuclei were stained with phalloidin or 4′,6′-diamidino-2-phenylindole (DAPI) (blue), respectively. For panels (B) to (D), images are representative of six different mice.

a β-catenin target gene (*18*), was reduced upon wild-type (WT) *Salmonella* infection, even after Wnt3a stimulation (Fig. 3A), which suggested that *Salmonella* affects the GVB by inhibiting canonical Wnt signaling. *Salmonella* is equipped with type III secretion systems that are encoded by the *Salmonella* pathogenicity island 1 and 2 (Spi1 and Spi2) (*6*). We found that the *Salmonella* Spi2 mutant (Δ*ssaV*) could not down-regulate *Axin2* expression (Fig. 3A), even though the levels of Spi2-encoding genes were higher in ECs than in epithelial cells (fig. S10B). Together, these results show that *Salmonella* infection interferes with β-catenin activation in ECs via the Spi2.

We then asked whether *Salmonella* could still disseminate if we induced β-catenin transcriptional activation only in ECs in mice carrying an inducible degradation-resistant β-catenin. Cre^+ (with a degradation-resistant form of β-catenin in ECs) and Cre^- (control) mice contained equivalent bacterial burdens in the different intestinal tracts, MLNs, and PPs after infection (fig. S11A). By contrast, in Cre^+ mice, *Salmonella* lost the ability to reach the liver or the spleen (Fig. 3B). Moreover, we could not detect any PV1 up-regulation at 2 or 6 hours and only a slight up-regulation at 24 hours in Cre^+ mice (fig. S12). Gut permeability measured by FITC-dextran leakage was also affected in Cre^+ *Salmonella*-infected mice (fig. S13). We excluded that Cre^+ mice had an impaired ability to initiate inflammation by testing the production of several inflammatory mediators including *S100a9*, *Ccl2*, *Cxcl1*, *Il1*β, and *Il6* in PPs after *Salmonella* infection (fig. S14). We also ensured that liver dissemination of *Salmonella* upon intravenous infection was similar in Cre^+ and Cre^- mice (fig. S15). Together, these results indicate that *Salmonella* cannot penetrate the GVB when we force β-catenin activation. It remains to be established whether modulation of β-catenin signaling is the target of *Salmonella* for its dissemination in vivo.

We next assessed whether the *Salmonella* Spi2 was responsible for conferring GVB-disrupting properties to *Salmonella* in vivo. We challenged the mice with Δ*ssaV Salmonella* and analyzed bacterial dissemination. We used 10 times as many Δ*ssaV* bacterial cells to overcome their reduced

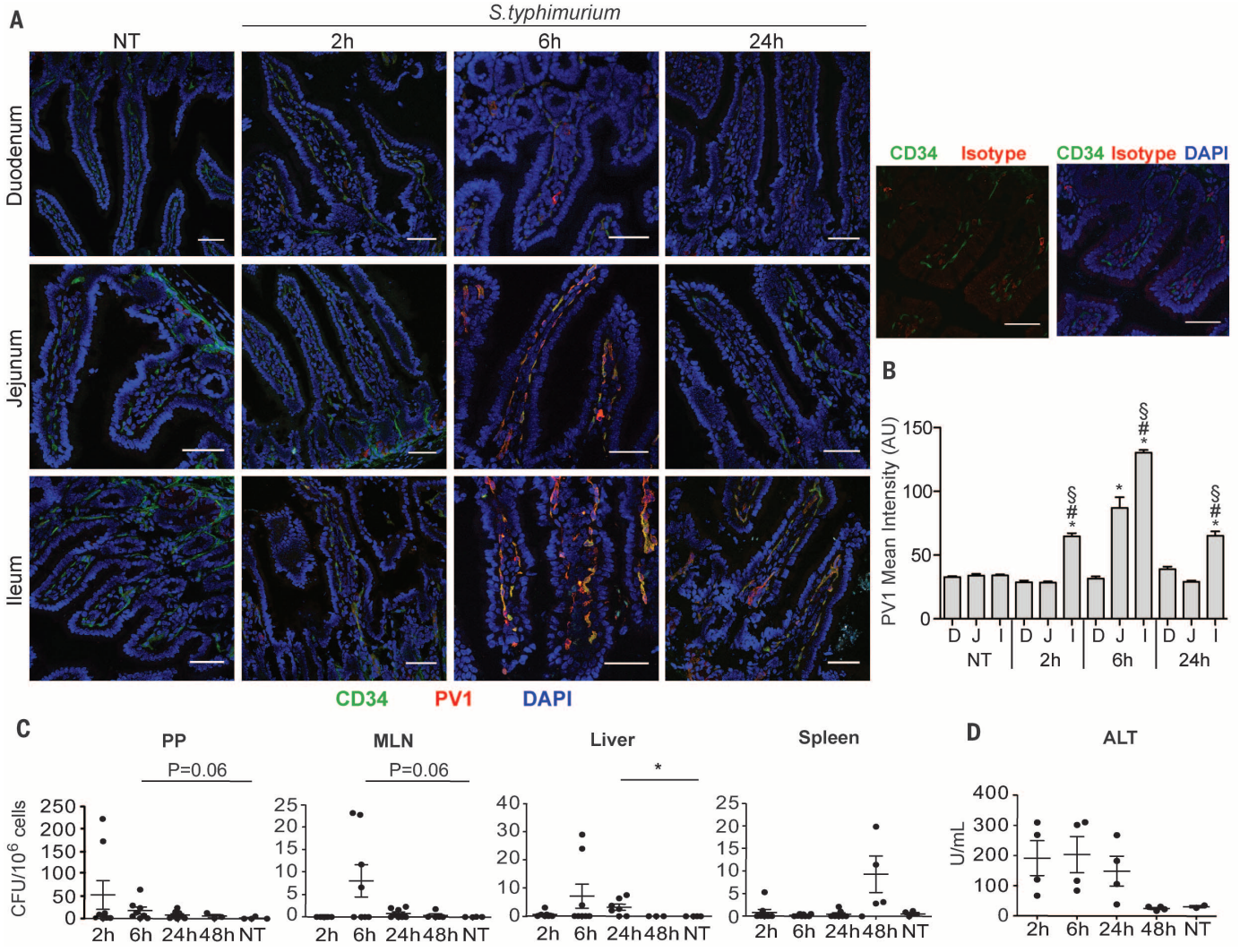

Fig. 2. PV1 expression correlates with *Salmonella* systemic dissemination. (**A**) C57BL/6J mice were orally infected or not with *S. typhimurium* Δ*aroA*, and PV1 (red) expression was evaluated in small intestinal (SI) blood vessels stained with CD34 (green). Cell nuclei were stained with DAPI (blue). Scale bars, 50 μm. (**B**) Mean fluorescence intensity of PV1 was measured to quantify the up-regulation of the protein in the intestinal vessels. AU, arbitrary units. Statistical comparisons were based on one-way analysis of variance (ANOVA). *$P < 0.001$. Each part of the SI was compared with its nontreated counterpart; #,§$P < 0.001$ ileum (I) was compared with duodenum (D) (#) or with jejunum (J) (§) at the same time point. (**C** and **D**) *S. typhimurium* dissemination in PPs, MLNs, spleen, and liver (C) and ALT in the serum (D) were evaluated at the indicated time points after infection. Two independent experiments are shown, each data point representing an individual mouse ($n = 4$ to 8). Error bars represent SEM. Student's unpaired *t* test was used to determine statistical significance. NT, not treated.

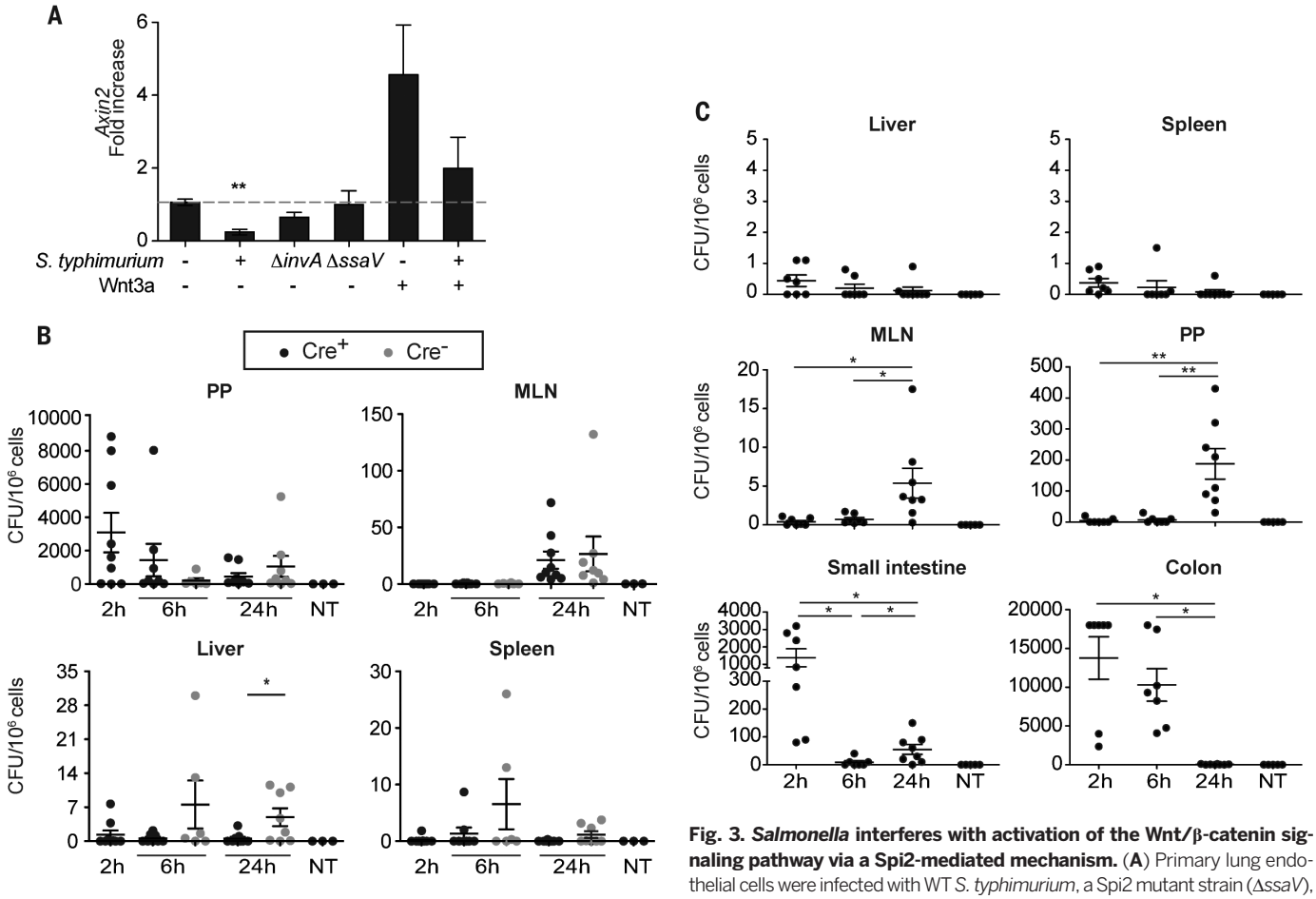

Fig. 3. *Salmonella* interferes with activation of the Wnt/β-catenin signaling pathway via a Spi2-mediated mechanism. (**A**) Primary lung endothelial cells were infected with WT *S. typhimurium*, a Spi2 mutant strain (Δ*ssaV*), or a Spi1 mutant strain (Δ*invA*). Alternatively, cells were treated with recombinant Wnt3a as a positive control. The expression of *Axin2* was assessed by quantitative reverse transcription polymerase chain reaction. Results are pooled from three independent experiments. Error bars represent SEM. Statistical significance between untreated and treated samples was evaluated using one-way ANOVA. Error bars represent SEM. (**B**) β-Catenin gain-of-function mice (black symbols) or β-catenin$^{lox(ex3)/lox(ex3)}$ control mice (gray symbols) were orally infected with *S. typhimurium* Δ*aroA*. Colony-forming units (CFUs) in PPs, MLNs, spleen, and liver were determined at the indicated time points. Two independent experiments are pooled; each data point represents an individual mouse (n = 3 to 9). (**C**) Bacterial counts in PPs, MLNs, liver, spleen, SI, and colon at the indicated time points after C57BL/6J mice infection with 10^{10} *S. typhimurium* Δ*ssaV*. NT, not treated. Each dot represents one mouse (n = 5 to 8). Error bars represent SEM. Statistical significance was evaluated by Student's unpaired t test. *P < 0.05 **P < 0.01.

ability to survive intracellularly. *Salmonella* Δ*ssaV* entered the gut and reached the PPs but not the liver or spleen (Fig. 3C). This correlated with the inability to induce PV1 up-regulation in any of the intestinal tracts (fig. S11, B and C). Hence, *Salmonella* is capable of disseminating systemically through, presumably, the down-modulation of β-catenin activation via a Spi2-mediated mechanism that leads to PV1 up-regulation.

Finally, we evaluated whether we could identify a GVB in the human intestine. We found that human intestinal ECs were ensheathed by GFAP$^+$ enteric glial cells and were in close proximity to α-SMA$^+$ and desmin$^+$ pericytes (Fig. 4A). In addition, blood ECs displayed both AJ and TJ proteins (fig. S16), and similarly to the mouse, claudin-5 was expressed primarily in lymphatic vessels (fig. S16). We detected PV1 up-regulation both in the ileum and in the colon upon apical infection with *Salmonella enterica* serovar Typhi (fig. S17, A and B). These results indicate that the human gut also harbors a GVB and that it can be disrupted by *Salmonella* infection.

To assess whether disruption of the GVB in the human gut may lead to liver damage, we analyzed the tissue of celiac disease patients following a gluten-free diet and displaying increased alanine transaminase (ALT) serum levels, in whom no gut histopathology was observed and other possible causes of liver damage were excluded. Celiac disease patients with high ALT displayed a higher expression of PV1 compared with those with normal serum ALT (Fig. 4, B to D). To address whether liver damage can disrupt the GVB, we intravenously injected WT mice with concanavalin A (Con A) to induce liver inflammation. As expected, we found a strong increase of serum transaminases (fig. S18A); however, we could not detect any significant up-regulation of intestinal PV1, which suggested that GVB impairment is not secondary to liver damage (fig. S18, B and C).

Our results demonstrate the existence of a GVB with morphological and functional characteristics similar to those of the BBB, particularly characteristic of pial vessels in the subarachnoid space, which are prone to damage during infection (*19*) but have some distinct features. Although the BBB has a size exclusion of 500 daltons, in the GVB, molecules as large as 4 kD can easily diffuse. This is probably because the GVB must allow passage of larger molecules for nutrient exploitation and tolerance induction and may be due to differences in EC-TJ composition. Similarly to the BBB, β-catenin signaling in the GVB inhibits vascular permeability and bacterial penetration. Previous work is also consistent with a role of Wnt/β-catenin signaling in controlling the endothelial barrier, as the administration of R-spondin3 during ischemia reperfusion of the gut induced tightening of the endothelium and reduced leakage (*20*).

Our data from celiac disease patients with elevated serum transaminases, independently of an epithelial barrier defect, indicate that endothelial barrier modifications may be responsible for liver damage and that endothelial and epithelial barriers are independent entities.

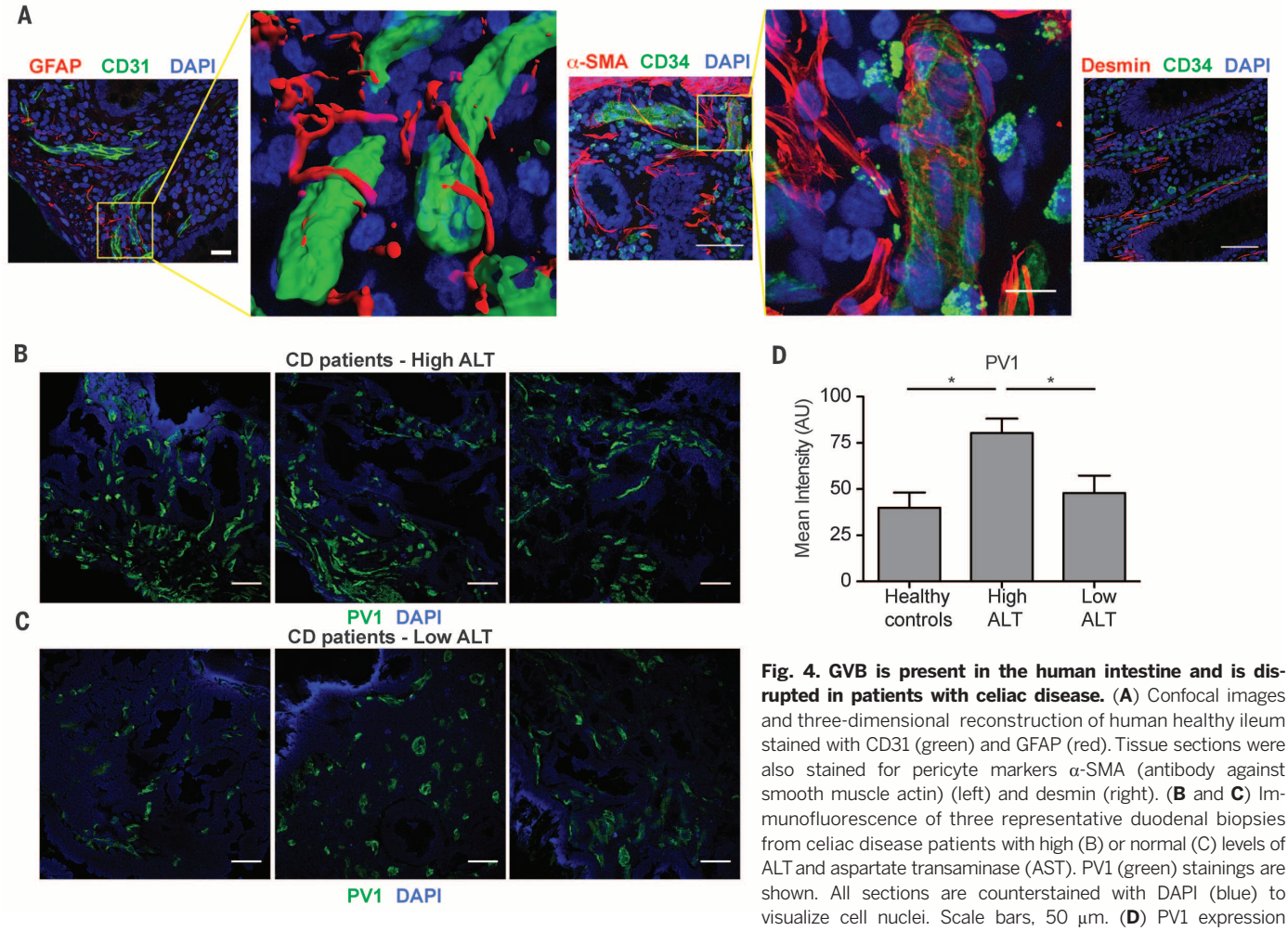

Fig. 4. GVB is present in the human intestine and is disrupted in patients with celiac disease. (**A**) Confocal images and three-dimensional reconstruction of human healthy ileum stained with CD31 (green) and GFAP (red). Tissue sections were also stained for pericyte markers α-SMA (antibody against smooth muscle actin) (left) and desmin (right). (**B** and **C**) Immunofluorescence of three representative duodenal biopsies from celiac disease patients with high (B) or normal (C) levels of ALT and aspartate transaminase (AST). PV1 (green) stainings are shown. All sections are counterstained with DAPI (blue) to visualize cell nuclei. Scale bars, 50 μm. (**D**) PV1 expression quantified in 6 samples from celiac disease patients with high ALT and AST, 9 from patients with low ALT and AST, and 10 from healthy individuals. One-way ANOVA and *t* test were used to determine statistical significance. *$P < 0.05$.

REFERENCES AND NOTES

1. T. Worbs *et al.*, *J. Exp. Med.* **203**, 519–527 (2006).
2. A. Goubier *et al.*, *Immunity* **29**, 464–475 (2008).
3. M. L. Balmer *et al.*, *Sci. Transl. Med.* **6**, 237ra66 (2014).
4. A. J. Macpherson, T. Uhr, *Science* **303**, 1662–1665 (2004).
5. A. J. Macpherson, K. Smith, *J. Exp. Med.* **203**, 497–500 (2006).
6. M. E. Ohl, S. I. Miller, *Annu. Rev. Med.* **52**, 259–274 (2001).
7. H. C. Müller-Redetzky, N. Suttorp, M. Witzenrath, *Cell Tissue Res.* **355**, 657–673 (2014).
8. R. Daneman, M. Rescigno, *Immunity* **31**, 722–735 (2009).
9. S. Y. Yuan, R. R. Rigor, *Regulation of Endothelial Barrier Function* (Morgan & Claypoole Life Sciences, San Rafael, CA, 2010).
10. H. Fujita *et al.*, *Mol. Biol. Cell* **19**, 1912–1921 (2008).
11. R. Hallmann, D. N. Mayer, E. L. Berg, R. Broermann, E. C. Butcher, *Dev. Dyn.* **202**, 325–332 (1995).
12. S. Liebner *et al.*, *J. Cell Biol.* **183**, 409–417 (2008).
13. Y. Wang *et al.*, *Cell* **151**, 1332–1344 (2012).
14. Y. Zhou *et al.*, *J. Clin. Invest.* **124**, 3825–3846 (2014).
15. C. H. Lim *et al.*, *PLOS Pathog.* **10**, e1004270 (2014).
16. B. Engelhardt, S. Liebner, *Cell Tissue Res.* **355**, 687–699 (2014).
17. Q. G. Dong *et al.*, *Arterioscler. Thromb. Vasc. Biol.* **17**, 1599–1604 (1997).
18. E. H. Jho *et al.*, *Mol. Cell. Biol.* **22**, 1172–1183 (2002).
19. P. K. Mishra, J. M. Teale, *PLOS Negl. Trop. Dis.* **7**, e2099 (2013).
20. L. Kannan *et al.*, *Proc. Natl. Acad. Sci. U.S.A.* **110**, 14348–14353 (2013).

ACKNOWLEDGMENTS

This work was funded by the European Research Council (M.R., Dendroworld and HomeoGUT; E.D., Wnt for Brain), the Italian Association for Cancer Research (AIRC) and the Italian Ministry of Health (Ricerca finalizzata). I.S. is the recipient of a FIRC fellowship. The authors declare no competing financial interests.

SUPPLEMENTARY MATERIALS

www.sciencemag.org/content/350/6262/830/suppl/DC1
Materials and Methods
Supplementary Text
Figs. S1 to S18
Tables S1 and S2
References (*21*–*28*)
Movies S1 to S6

13 July 2015; accepted 6 October 2015
10.1126/science.aad0135

NEW ENGLAND BioLabs® Inc.

Even more *from* less.

NEBNext® Ultra™ II DNA Library Prep Kit for NGS

Are you challenged with trying to get higher library yields using ever-decreasing input amounts? Each component in the NEBNext Ultra II DNA Library Prep Kit from NEB® has been reformulated, resulting in a several-fold increase in library yield with as little as 500 picograms of input DNA. These advances deliver unprecedented performance, while enabling lower inputs and fewer PCR cycles. Get even more from less with NEBNext Ultra II.

Visit **NEBNextUltraII.com** to learn more and request a sample.

The NEBNext Ultra II DNA Library Prep Kit for Illumina® produces the highest yield libraries from a broad range of input amounts.

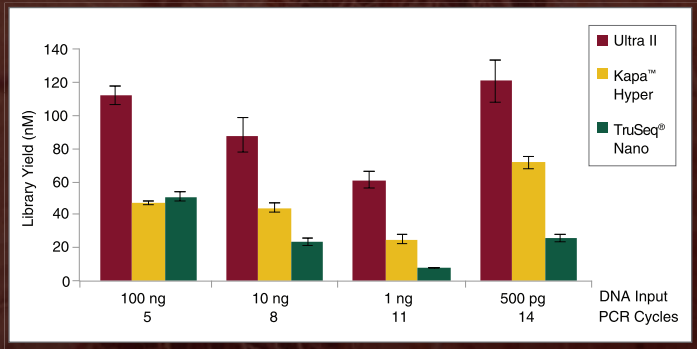

Libraries were prepared from Human NA19240 genomic DNA using the input amounts and numbers of PCR cycles shown. Manufacturers' recommended protocols were followed, with the exception that size selection was omitted.

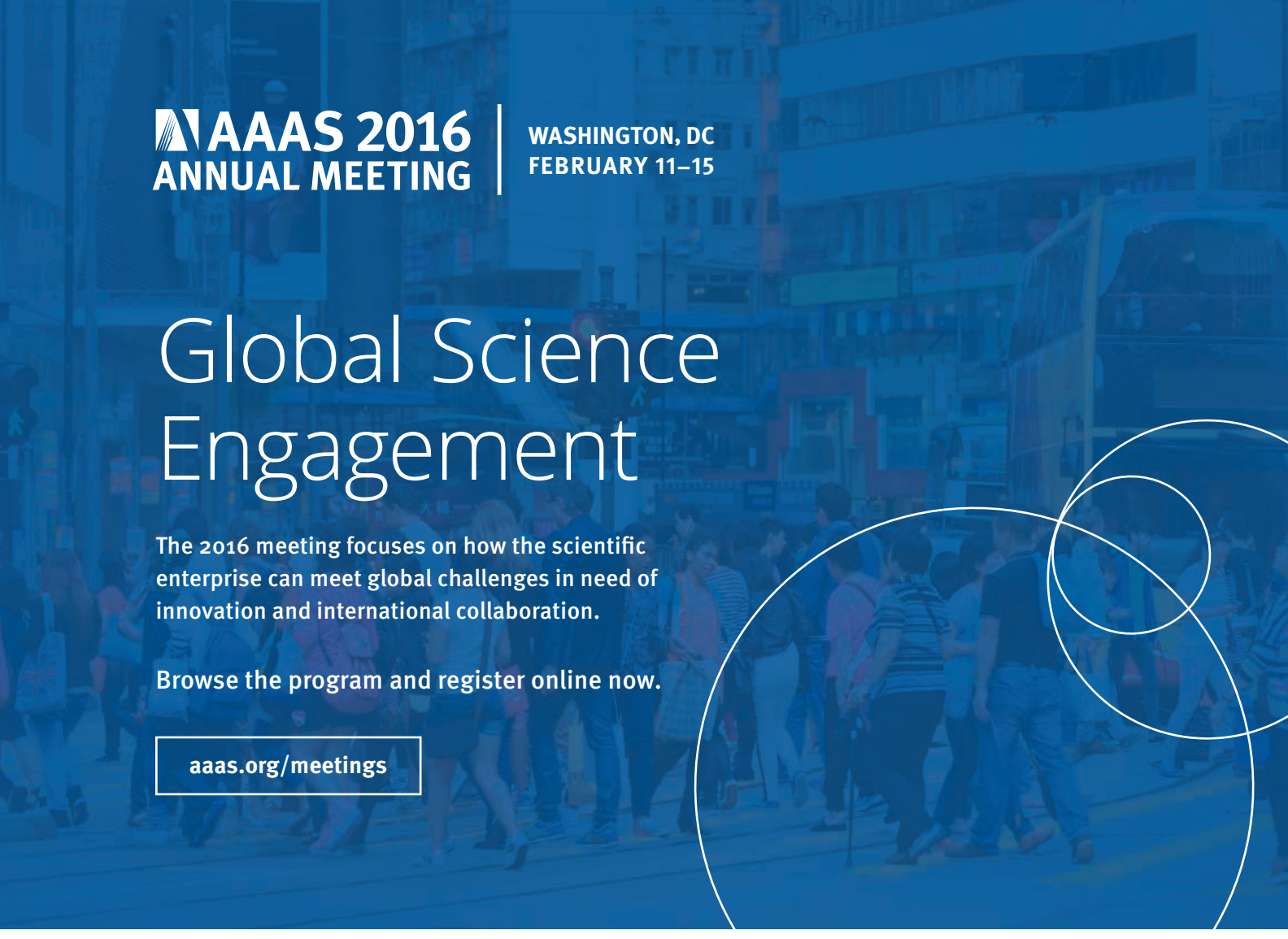

AAAS 2016 ANNUAL MEETING | WASHINGTON, DC FEBRUARY 11–15

Global Science Engagement

The 2016 meeting focuses on how the scientific enterprise can meet global challenges in need of innovation and international collaboration.

Browse the program and register online now.

aaas.org/meetings

AAAS, publisher of *Science*, thanks the sponsors and supporters of the 2016 Annual Meeting

European Commission

SUBARU

RESEARCH COUNCILS UK

HELMHOLTZ ASSOCIATION

THE KAVLI FOUNDATION

NANYANG TECHNOLOGICAL UNIVERSITY

for its generous support of the Science Journalism Awards

As of October 26, 2015

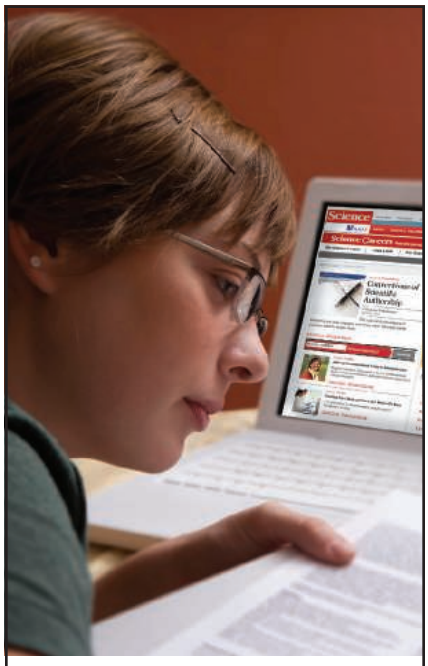

AAAS is here –
helping scientists achieve career success.

Every month, over 400,000 students and scientists visit ScienceCareers.org in search of the information, advice, and opportunities they need to take the next step in their careers.

A complete career resource, free to the public, *Science* Careers offers a suite of tools and services developed specifically for scientists. With hundreds of career development articles, webinars and downloadable booklets filled with practical advice, a community forum providing answers to career questions, and thousands of job listings in academia, government, and industry, *Science* Careers has helped countless individuals prepare themselves for successful careers.

As a AAAS member, your dues help AAAS make this service freely available to the scientific community. If you're not a member, join us. Together we can make a difference.

To learn more, visit
aaas.org/plusyou/sciencecareers

AAAS + U = Δ

Novartis Prizes for Immunology

Discover | Inspire | Transform

Call for nominations

25 years of recognizing breakthroughs in the most challenging areas of immunology and novel therapies

Novartis Prizes for Immunology are calling for nominations for the 2016 awards, held at the International Congress of Immunology.

The prizes honor exceptional scientists that have transformed our understanding of immunology. One prize is awarded for basic research and another for clinical research, each worth CHF 100,000.

Jury: Prof. Hidde L. Ploegh, Prof. Jan E. de Vries, Prof. Charles A. Dinarello, Prof. Tadamitsu Kishimoto, Prof. Bernard Malissen, Prof. Diane Mathis, Prof. Anne O'Garra

Nominations: 16 November 2015 – 8 January 2016

To nominate your peers visit:

novartisimmunologyprizes.com

AAAS Marion Milligan Mason Award for Women in the Chemical Sciences

Marion Milligan Mason was a chemist and a proud AAAS member. Her will provided for the creation of a fund with a $2.2 million bequest to support research by early-career women in the chemical sciences. AAAS is grateful for philanthropic gifts like Dr. Mason's bequest, which make it possible for us to support promising scientists early in their careers.

The online application site will open
November 16, 2015

Proposals are due on or before
March 1, 2016

Awards will be announced on or before
January 2017

Apply today!

www.aaas.org/masonaward

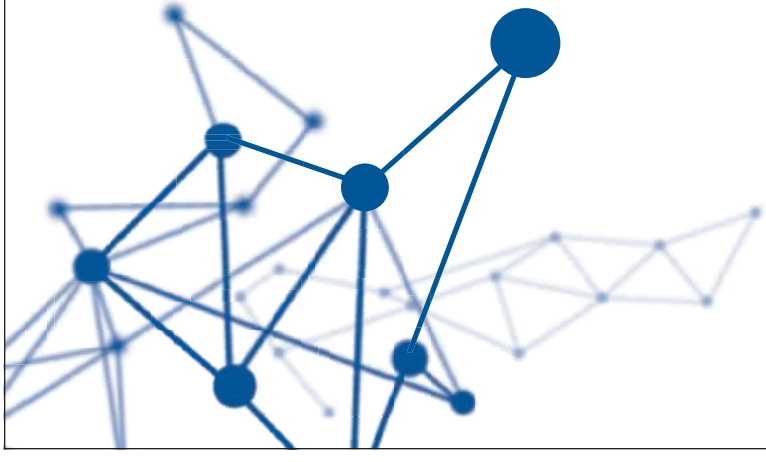

Congratulations to the 2015 Recipients

ALISON FOUT
Assistant Professor of Chemistry
University of Illinois at Urbana-Champaign

Nitrite Reduction in a Non-Heme System: Evidence for an Alternative Mechanism

KATHERINE MACKEY
Assistant Professor, Department of Earth System Science
University of California Irvine

Aerosol Trace Metal Chemistry in a Changing Ocean

KRISTIN PARENT
Assistant Professor of Biochemistry and Molecular Biology
Michigan State University

Cryo-electron tomography of large and challenging biological specimens

LUISA WHITTAKER-BROOKS
Assistant Professor of Chemistry
The University of Utah

Exploration of scalable polymer-metal for thermoelectric applications

AAAS
ADVANCING SCIENCE, SERVING SOCIETY

Produced by the *Science*/AAAS Custom Publishing Office

The Art and Science of Traditional Medicine
Part 3: The Global Impact of Traditional Medicine

Sponsored by

中医药规范研究学会
GP-TCM
Research Association

Join AAAS. Get instant access to *Science*. Support all of the sciences.

When you subscribe to *Science*, you become part of the American Association for the Advancement of Science (AAAS), a nonprofit community of more than 120,000 members worldwide who believe in the power of science to make the world a better place. AAAS is hard at work promoting science in government, schools, and in the public commons around the globe.

AAAS's award-winning journal *Science* offers the top peer-reviewed research across multiple disciplines.With your subscription, you'll get:

- 51 weeks of home delivery of *Science*
- Instant online retrieval of every *Science* article ever published, dating back to 1880
- Full access to the *Science* mobile site and apps
- Career advice, webinars, blogs and fascinating features exclusively for AAAS members
- Members-only newsletters, and much more

With increasing public skepticism about science–and public funding for research more uncertain than ever–our work has never been more important. Join hands with us today!

Visit promo.aaas.org/joinaaas. Together we can make a difference.

Science
AAAS

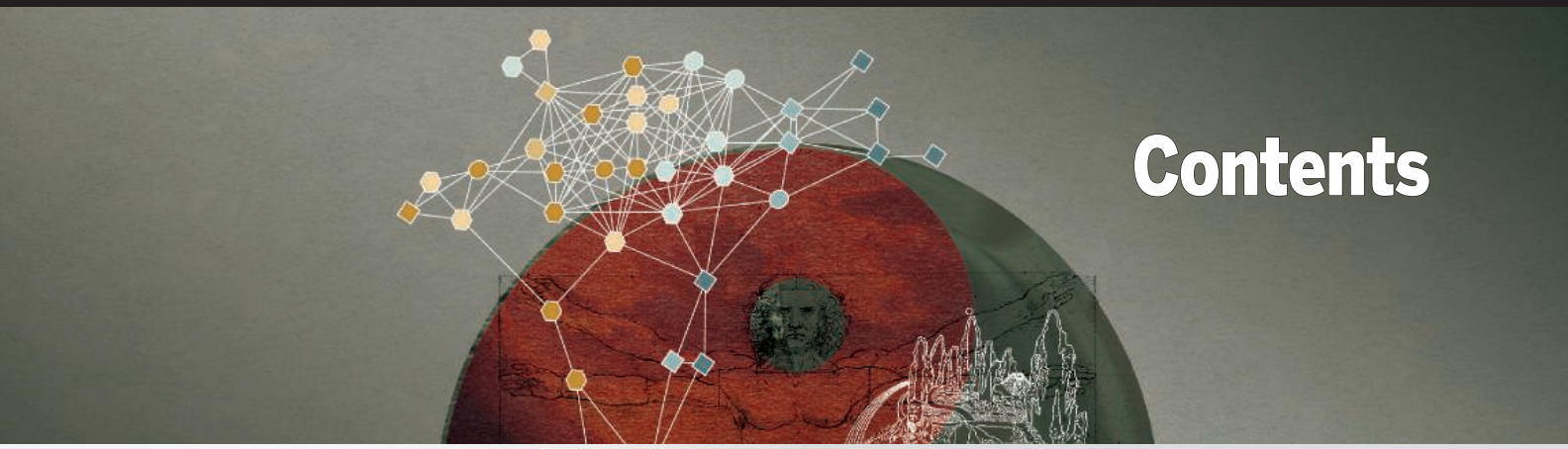

Contents

It is appropriate and timely that Chinese scientist Youyou Tu was awarded half of the 2015 Nobel Prize in Physiology or Medicine in recognition of her pioneering work on the antimalarial artemisinin, extracted from *Artemisia annua*, an ancient herbal remedy used to treat fever. This third issue in the Art and Science of Traditional Medicine series features another time-honored herb, ginseng. Also discussed are the systems and network pharmacology of TCM, pharmacognosy and regulation of traditional medicine in Europe, and how these best practices can be applied globally, but particularly in Africa. Attention garnered by the Nobel award hopefully will generate interest in traditional medicines from other parts of the world, including the Middle East, the Indian sub-continent, and the Americas.

Articles

The content contained in this special, sponsored section was commissioned, edited, and published by the *Science*/AAAS Custom Publishing Office. It was not peer-reviewed or assessed by the Editorial staff of the journal *Science*; however, all manuscripts have been critically evaluated by an international editorial team consisting of experts in traditional medicine research selected by the project editor. The intent of this section is to provide a means for authors from institutions around the world to showcase their state-of-the-art traditional medicine research through review/perspective-type articles that highlight recent progress in this burgeoning area. The editorial team and authors take full responsibility for the accuracy of the scientific content and the facts stated. Articles can be cited using the following format: [Author Name(s)], Sponsored supplement to *Science*, **350** (6262), Sxx-Sxx (2015).

ILLUSTRATION (FRONT) CHARLOTTE LOKIN

Ginseng: A panacea linking East Asia and North America?

Authors:
Ran Joo Choi[1],
Alice S. T. Wong[2],
William Jia[3],
Il-Moo Chang[4],
Ricky N. S. Wong[5],
Tai-Ping Fan[1*],
Yeong Shik Kim[6*]

According to ancient Chinese medical literature and Korean history, ginseng has been used since around 2000 BCE. It has been regarded as a very precious medicinal plant, on par with poppy, aloe, and garlic, the use of which goes back to the same period in other parts of the world. It is not surprising that the name *Panax*—meaning "all healing" in Greek—has been applied to this plant, because it has been used to treat various diseases from ancient times, and is also recognized, especially in Asian countries, as a health supplement that can increase energy and instill a sense of well-being. To date, fourteen species belonging to the *Panax* genus have been identified, and three species are widely circulated on the global market: *Panax ginseng* C.A. Meyer, cultivated mainly in Korea and northeastern China; *Panax quinquefolius* L. (American ginseng), grown mainly in the Canadian provinces of Ontario and British Columbia and the American state of Wisconsin; and *Panax notoginseng* Burkill, found in southern China (*1*).

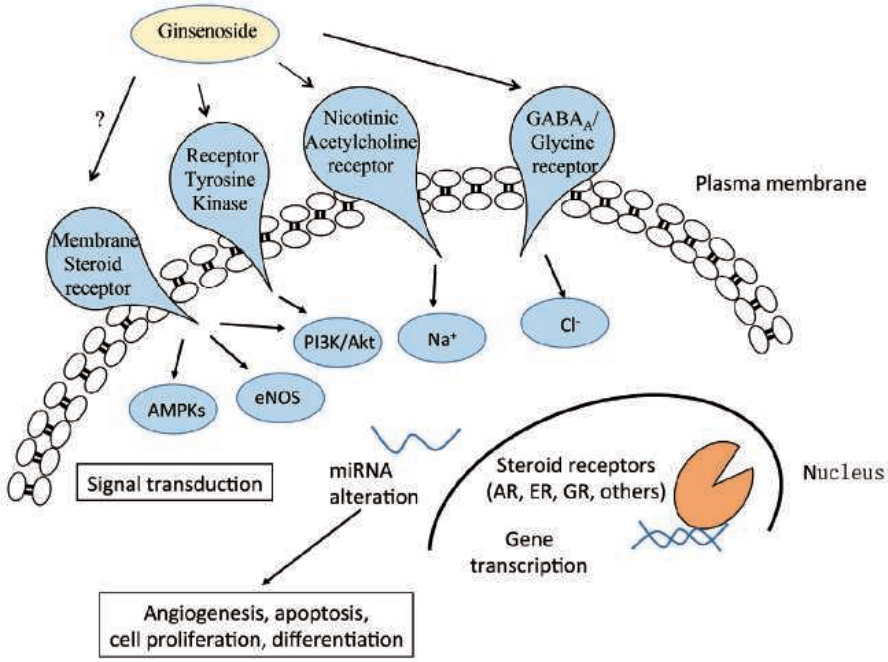

FIGURE 1. Schematic representation of genomic and nongenomic actions by ginsenosides. Ginsenosides can act through genomic effects by binding to steroid hormone receptors, such as androgen receptors (AR), estrogen receptors (ER), and glucocorticoid receptors (GR), to modulate gene expression. On the other hand, nongenomic activities, such as phosphoinositide 3-kinase/Akt (PI3K/Akt), adenosine monophosphate-activated protein kinases (AMPKs), and endothelial nitric oxide synthases (eNOS) that occur outside the nucleus can also be involved in the mechanisms of action (MOAs) of ginsenosides. Ginsenosides are also implicated in ion channel regulation that includes the nicotinic acetylcholine receptor that results in sodium ion (Na^+) influx and the $GABA_A$/glycine receptor that conducts chloride (Cl^-) ions. In addition, ginsenosides can be a regulator of microRNAs (miRNAs) that modulate angiogenesis, apoptosis, cell proliferation, and differentiation.

History and use

P. ginseng is likely to have originated in Manchuria (now the northeast part of China) and in the ancient Three Kingdoms of Korea (*2*). The first description of ginseng in the history of traditional Chinese medicine appeared in the pre-Han era (BCE 33–48), over 2,000 years ago. In 1713, the Royal Society published a letter from Father Jartoux, a Jesuit missionary in China, containing a description of ginseng's botany, habitat, and medicinal uses (*3*). *P. quinquefolius* was discovered by American settlers in the mid-1700's in New England. This plant had long been used by the Native Americans, who valued the root for its curative powers and life-enhancing capabilities. Ginseng has purported use for the treatment of cancer, diabetes, and cardiovascular dysfunctions, as well as for cognitive enhancement with an apparently low rate of adverse effects. In combination with other materia medica, *P. ginseng* and *P. notoginseng* have been used in complex Chinese formulations for treating angina pectoris (*4, 5*).

[1]Department of Pharmacology, University of Cambridge, Cambridge, United Kingdom
[2]School of Biological Sciences, University of Hong Kong, Hong Kong, China
[3]Davad Mowafaghian Centre for Brain Health, University of British Columbia, Vancouver, Canada
[4]R&D Headquarters, Korea Ginseng Corporation, Daejeon, South Korea
[5]Department of Biology, Hong Kong Baptist University, Hong Kong, China
[6]World Health Organization Collaborating Centre for Traditional Medicine, Natural Products Research Institute, Seoul National University, Seoul, South Korea
*Corresponding Authors: tpf1000@cam.ac.uk (T.P.F.), kims@snu.ac.kr (Y.S.K.)

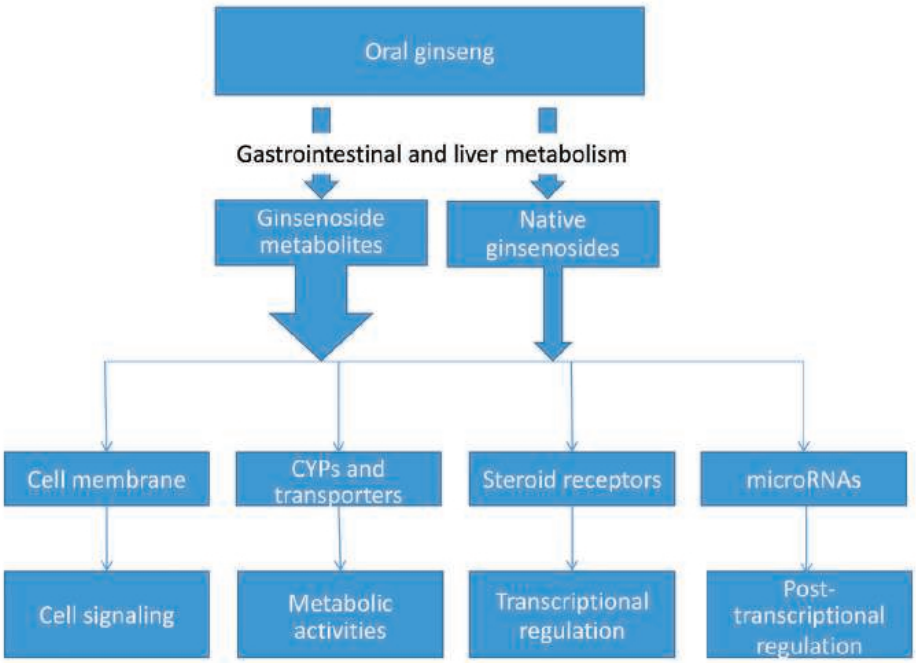

FIGURE 2. Metabolism of ginseng. Ginsenosides can be converted into their metabolites that may contribute the majority of bioactivities by regulating the transportation and metabolism of crucial substances in the human body. Metabolism mainly occurs in the intestine and the liver by adenosine triphosphate (ATP)-binding cassette transporters (ABC transporters), cytochrome P450 enzymes (CYPs), and others.

Processing, chemistry, and metabolism

Most ginseng in today's market is cultivated in the field for 4 to 6 years. Ginseng is classified into three types, depending on how it is processed after harvest: fresh ginseng (can be consumed in its fresh state), white ginseng (dried after peeling), and red ginseng, which requires special preparation skills, such as steaming and drying under specific conditions. Technology for the long-term storage of red ginseng was developed by pioneers in ginseng manufacture, securing the foundation for this form of the root. The process of steaming stabilizes the ginseng with regard to metabolism, and transforms the secondary metabolites into less polar phytosteroids that are thought to be both more active in the body and safer.

The active ingredients in ginseng include ginsenosides and polysaccharides. Ginsenosides belong to the saponin family and are divided into 20(*S*)-panaxadiols and 20(*S*)-panaxatriols, depending on the dammarane skeleton and the number of hydroxyl groups that can be substituted with other groups (*1*). The biological activities of these phytosteroids have been studied intensively with regard to their structure-activity relationships. Asian ginseng typically contains six types of ginsenosides: panaxadiols (Rb_1, Rb_2, Rc, and Rd) and panaxtriols (Re and Rg_1). In contrast, American ginseng contains high levels of Rb_1, Rd, and Re (*6, 7*).

Ginsenosides are extensively metabolized in the gastrointestinal tract after oral administration (*8*), with sugar moieties being removed to generate the aglycones, 20(*S*)-protopanaxadiol (aPPD), and 20(*S*)-protopanaxatriol (aPPT), and the partially deglycosylated ginsenosides. Since most native ginsenosides are either poorly absorbed in the intestines or are quickly metabolized by deglycosylation, oxidation, and esterification in the intestine or the liver, they could be regarded as "pro-drugs." Thus, understanding the pharmacokinetics and pharmacodynamics of native ginsenosides and their metabolites is critical for their clinical application.

Standardization

Currently, there are many ginseng products on the market and the quality control of these commodities is of paramount importance. Quality control of ginseng extracts and finished products is usually based on the determination of specific bioactive ginsenosides. Although the international standard ISO 17217-1:2014 specifies minimum requirements and test methods for ginseng seeds and seedlings (*9*), ginseng extract should also be standardized such that each batch contains an acceptable concentration range of active ingredients to guarantee quality and efficacy from product to product. Distinguishing between *P. ginseng* and *P. quinquefolius*, which have similar chemical and physical properties but seemingly different pharmacological activities, is a challenge. Recently, all known ginsenosides were identified by metabolomics using high-performance chromatography/mass spectrometry analysis, and this large data set was statistically analyzed. In a targeted analysis, ginsenoside Rf was confirmed as a chemical marker present in processed *P. ginseng*, but not in processed *P. quinquefolius* (*10*).

Diverse pharmacological activities via multiple mechanisms

Given the structural similarity between ginsenosides and steroid hormones, we hypothesized that ginsenosides function as receptor agonists, partial agonists, or antagonists depending on the microenvironment. As shown in Figure 1, ginsenosides act by binding to steroid hormone receptors, such as androgen, estrogen, and glucocorticoid receptors, to modulate gene expression (*11–14*). We have previously reported that the dominance of Rg_1 leads to angiogenesis, whereas Rb_1 exerts an opposing effect (*15*) through activation of glucocorticoid (*16*) and estrogen (*17*) receptors. In addition to their classic genomic effects, ginsenosides can also function through transcription-independent, nongenomic activation

of signaling cascades, such as phosphoinositide 3-kinase/Akt, adenosine monophosphate-activated protein kinase, and calcium signaling that occurs outside the nucleus (*18–23*) (Figure 1). Ginsenosides are also implicated in ion channel regulation, including voltage-dependent and ligand-gated ion channels, for the control of cardiovascular function and hypertension (*24–26*). Recent developments have also revealed ginsenosides to be an important regulator of microRNAs (miRNAs) (*27–30*). Moreover, messenger RNA-like, noncoding RNAs were identified in ginseng, suggesting that it might exert a regulatory role through miRNAs and small interfering RNAs (siRNAs) (*31*). Whether these small RNAs could affect our body function awaits further investigation (*32*). A number of studies have demonstrated that ginsenosides, and especially their metabolites, interact with cytochrome P450 enzymes (CYPs) and adenosine triphosphate (ATP)-binding cassette transporters (ABC transporters, including breast cancer resistance protein, BCRP) (*33–36*). Given the fundamental roles of ABC transporters and CYPs in the absorption, transportation, and metabolism of nutrients, hormones, and environmental toxins, it is plausible that ginseng may exert its wide-ranging biological effects and health benefits by modulating the transportation and metabolism of vital substances in the human body (Figure 2). Intriguingly, aPPD and aPPT are BCRP inhibitors and therefore potential chemosensitizers (*37*). Ginseng root also contains acidic polysaccharides that appear to play important roles in immune modulation (*38*). In addition, ginseng polysaccharides have shown antifatigue (*39, 40*) and antidiabetic (*41*) effects. However, although numerous studies have been done in vitro and in vivo, very few clinical studies exist.

Challenges and opportunities

Despite playing an important role as a health supplement and medicine in East Asia for millennia, the clinical efficacy of ginseng remains to be established through stringent evidence-based validation. The synthesis of ginsenosides, including the backbone and its glycosylated derivatives, is extremely challenging. This bottleneck limits the development of ginsenosides as drug candidates. Thus, developing novel techniques for enriching bioactive components in ginseng should be a top priority. For example, selective transformation of ginsenosides by specific intestinal microbes may provide a new opportunity for drug discovery. It is also an exciting prospect to obtain the full genome sequence of ginseng root as a precursor to manipulating the biosynthesis of specific ginsenosides and realizing a "ginsenoside factory" (*42–44*). A high-throughput, multidisciplinary approach should be developed to bring new insights into the molecular actions of ginsenosides and how the multiple, distinct signaling networks that it impacts are interconnected. Finally, more robust clinical trials should be designed and implemented. Only good clinical outcomes can instill faith in patients and the general public with regard to products derived from this time-honored treatment.

References

1. L. P. Christensen, *Adv. Food Nutr. Res.* **55**, 1 (2009).
2. "A History of Ginseng," in *Korean Ginseng,* H. W. Bae, Ed. (Korea Ginseng Research Institute, Republic of Korea, 1978), pp. 12–74.
3. J. H. Appleby, *Notes Rec. Roy. Soc.* **37**, 121 (1983).
4. X. Zhao *et al.*, *Science* **347**, S38 (2015).
5. R. Liu *et al.*, *Science* **347**, S40 (2015).
6. N. Fuzzati, *J. Chromatogr. B Analyt. Technol. Biomed. Life Sci.* **812**, 119 (2004).
7. J. B. Wan *et al.*, *J. Sep. Sci.* **30**, 825 (2007).
8. L. W. Qi *et al.*, *Curr. Drug Metab.* **12**, 818 (2011).
9. International Standards Organization Online Browsing Platform, ISO 17217-1:2014(en), "Traditional Chinese Medicine–Ginseng Seeds and Seedlings–Part I: Panax Ginseng C.A. Meyer"; available at https://www.iso.org/obp/ui/#iso:std:iso:17217:-1:ed-1:v1:en.
10. H. W. Park *et al.*, *J. Ginseng Res.* **38**, 59 (2014).
11. Y. J. Lee *et al.*, *Mol. Cell Endocrinol.* **133**, 135 (1997).
12. Y. N. Lee *et al.*, *J. Steroid Biochem. Mol. Biol.* **67**, 105 (1998).
13. Y. Yu *et al.*, *Cancer* **109**, 2374 (2007).
14. B. Cao *et al.*, *Int. J. Cancer* **132**, 1277 (2013).
15. S. Sengupta *et al.*, *Circulation* **110**, 1219 (2004).
16. K. W. Leung *et al.*, *J. Biol. Chem.* **281**, 36280 (2006).
17. K. W. Leung *et al.*, *Br. J. Pharmacol.* **152**, 207 (2007).
18. K. Shinkai *et al.*, *Jpn. J. Cancer Res.* **87**, 357 (1996).
19. K. W. Leung *et al.*, *FEBS Lett.* **580**, 3211 (2006).
20. K. W. Leung *et al.*, *FEBS Lett.* **581**, 2423 (2007).
21. T. T. Hien *et al.*, *Toxicol. Appl. Pharmacol.* **246**, 171 (2010).
22. K. W. Leung *et al.*, *Angiogenesis* **14**, 515 (2011).
23. Y. Liu *et al.*, *Cell Death Dis.* **2**, e145 (2011).
24. T. Kimura *et al.*, *Gen. Pharmacol.* **25**, 193 (1994).
25. S. Y. Nah, *Front Physiol.* **5**, 98 (2014).
26. C. H. Lee *et al.*, *J. Ginseng Res.* **38**, 161 (2014).
27. K. O. Skaftnesmo *et al.*, *Curr. Pharm. Biotechnol.* **8**, 320 (2007).
28. L. S. Chan *et al.*, *Eur. J. Pharm. Sci.* **38**, 370 (2009).
29. N. Wu *et al.*, *Acta Pharmacol. Sin.* **32**, 345 (2011).
30. I. S. An *et al.*, *Oncol. Rep.* **29**, 523 (2013).
31. M. Wang *et al.*, *J. Integr. Plant Biol.* **57**, 256 (2015).
32. L. Zhang *et al.*, *Cell Res.* **22**, 107 (2012).
33. Y. Zhao *et al.*, *Planta Med.* **75**, 1124 (2009).
34. N. T. Chiu *et al.*, *Biopharm. Drug Dispos.* **35**, 104 (2014).
35. S. Deb *et al.*, *J. Steroid Biochem. Mol. Biol.* **141**, 94 (2014).
36. A. Kawase *et al.*, *J. Nat. Med.* **68**, 395 (2014).
37. J. Jin *et al.*, *Biochem. Biophys. Res. Commun.* **345**, 1308 (2006).
38. S. Kang *et al.*, *J. Ginseng Res.* **36**, 354 (2012).
39. J. Wang *et al.*, *Arch. Pharm. Res.* **37**, 530 (2014).
40. D. L. Barton *et al.*, *J. Natl. Cancer Inst.* **105**, 1230 (2013).
41. C. Sun *et al.*, *Food Funct.* **5**, 845 (2014).
42. K. J. Kim *et al.*, *DNA Res.* **11**, 247 (2004).
43. N. H. Kim *et al.*, *J. Ginseng Res.* **38**, 130 (2014).
44. S. Chen *et al.*, *Science* **347**, S27 (2015).

Acknowledgments

This work was supported by grants from the National Research Foundation of Korea to Y.S.K. (MRC2009-93146) and the Health and Medical Research Fund to A.S.T.W. (11121191)

Pharmacognosy in the United Kingdom: Past, present, and future

Authors: Melanie-Jayne R. Howes and Monique S.J. Simmonds*

For centuries, pharmacognosy has been instrumental in developing both conventional and herbal medicines in Europe. Isolated phytochemicals from natural sources have been the source for new pharmaceutical drugs and provided template chemical structures for drug discovery. In recent years, natural products have played a role in the development of approximately 50% of approved new chemical entities (*1*). Moreover, the majority of new small-molecule drugs of natural origin are derived from terrestrial microbes, with others coming from higher plants, marine organisms, and terrestrial animals (*2*). Juxtaposed with natural product drug discovery is the development of herbal medicines. These mixtures encompass medicinal plants that may contain diverse and biologically active phytochemicals; however, the active constituents of many herbal medicines are unknown and evidence for efficacy is often limited. Therefore, a major challenge for such medicines is quality control and standardization. In the European Union (EU), movements to harmonize the legislation surrounding traditional herbal medicines have aimed to improve their safety and quality. However, there are limitations and, in some respects, herbal medicines are still less well-regulated compared to conventional medicines. Although the use of herbal medicines in the United Kingdom (UK) is popular, detailed knowledge of their pharmacological and clinical effects is often lacking, as are data on their pharmacokinetic and pharmacodynamic properties. While EU legislation now provides standards for the quality and safety of many herbal medicines, research to establish the "science" behind their use is not progressing at the same pace. Moreover, pharmacovigilance reporting practices could be improved to assist practitioners in gaining a better understanding of appropriate uses and safety.

Herbal medicine use in the UK

Although herbal medicines are relatively popular (used by 35% of the population in the UK), there is a general lack of understanding about what herbal medicines are (or are not); however, there is a broad perception amongst the public that they are safe because they are "natural" (*3*). The EU Directive (2004/24/EC) on Traditional Herbal Medicinal Products (HMPs) introduced regulatory standards for herbal medicines in April 2004. The directive requires EU member states to implement regulatory arrangements for HMPs that can be used without medical supervision and that have evidence for traditional use (*4*). In response to this directive, the UK's Medicines and Healthcare products Regulatory Agency (MHRA) launched the Traditional Herbal Medicines Registration Scheme in 2005. Following a transition period to allow HMP manufacturers time to comply with the directive's requirements, all such products intended for sale in the UK require either a full marketing authorization or a traditional herbal registration (THR). These regulations mean that THR HMPs that are intended for minor conditions and are suitable for self-diagnosis must meet the required standards for quality and safety [with respect to European Pharmacopoeia (EP) monographs and community herbal monographs that are evaluated by the Committee on Herbal Medicinal Products]. THR HMPs are required to have been used medicinally for at least 30 years (prior to THR application), with at least 15 years of use relating to the EU.

While these regulations have made advances in improving the safety and quality of registered HMPs, several issues still need to be addressed for the use of herbal medicines. Evidence for "traditional use" currently takes the place of hard scientific data from pharmacological tests and clinical trials. Therefore, evidence for efficacy, the scientific or pharmacological basis to explain the reputed activity, and knowledge of the active constituents and their mechanisms of action are limited for many herbal medicines. There are relatively few robust clinical trials assessing efficacy for the majority of herbal medicines. Clinical evaluation and comparability are major issues for trials that investigate inadequately authenticated or standardized herbal medicines not subject to THR standards. Furthermore, Regulation 3 of The Human Medicines Regulations 2012, commonly referred to as the "herbalist exemption," permits unlicensed herbal remedies to be prepared and supplied by an herbal practitioner to meet the needs of an individual patient following a one-to-one consultation. Although this practice enables herbal practitioners to meet the needs of patients by supplying tailored herbal medicines, a current regulatory loophole allows anyone to practice herbal medicine, regardless of their qualifications or experience. This clearly has implications for public health, from receiving an appropriate diagnosis and treatment to dealing with the safety and quality issues of the remedies that may occur with unlicensed herbal medicines.

Herbal medicines used in the UK include traditional European medicines such as sage (*Salvia officinalis* L.), described in a 16th-century herbal by Gerard, who says it is "singularly good for the head and brain and quickenethe the nerves and memory," and by Culpeper 50 years later, who states that sage "also heals the memory, warming and quickening the senses" (*5*). There are limited clinical trial data to suggest that *S. officinalis* extracts can improve cognitive function for healthy subjects and patients with dementia (*5*). Although traditionally used to aid memory, *S. officinalis* HMPs are unlikely to gain THR status for cognitive disorders such as dementia, because THR HMPs must comply with permitted indications, which entail conditions that are suitable for self-medication without the need for medical supervision. However, *S. officinalis* THR HMPs are available in the UK to

Royal Botanic Gardens Kew, Richmond, Surrey, United Kingdom
*Corresponding Author: m.simmonds@kew.org

relieve some conditions that do not normally require medical intervention, which include menopausal and cold symptoms (based on traditional use). In addition to traditional European herbal medicine, other practices of traditional herbal medicine from a variety of cultures are increasingly being used in the UK, including traditional Chinese medicine (TCM) and those from Ayurvedic, African, and South American traditions. Some of these are supplied under the herbalist exemption and not controlled by THR regulations.

In 1864, the first edition of the British Pharmacopoeia (BP) was introduced, containing the official monographs for medicines in the UK. This collection of standards comprised the required characteristics and tests for numerous herbal medicines, including potentially toxic plants such as aconite, *Digitalis*, and belladonna, as well as other naturally derived remedies, such as purified ox bile and leeches (*6*). Over the last 150 years, the development of conventional pharmaceutical drugs has increased considerably, while the use of herbal medicines in conventional "Western" medicine has declined. This trend is reflected in the current BP, with fewer herbal medicine monographs included than pharmaceutical drug monographs (*7*). However, with the introduction of THR and HMP quality standard requirements, the number of monographs for herbal medicines is now increasing once again in the BP and European Pharmacopoeia. Moreover, a higher number of species monographs are included, reflecting the incorporation of different practices into UK medicine, such as TCM (e.g., *Salvia miltiorrhiza* Bunge root and rhizome) and Ayurvedic medicine (e.g., *Withania somnifera* (L.) Dunal root) (*7*).

Future directions

The introduction of the EU Directive (2004/24/EC) and THR scheme in the UK have enabled progress on the safety and quality control issues of many HMPs; however, the impact of these regulations on safeguarding public health remains to be determined. To evaluate these issues, thorough monitoring of adverse responses to HMPs, either due to intrinsic (i.e., effects inherent in the plant itself) or extrinsic (i.e., effects resulting from quality control issues such as adulteration or substitution of the intended species) are essential. In general, there is an underreporting (via pharmacovigilance schemes) of adverse drug reactions (ADRs) by health care professionals (HPCs) (*8*) as well as much variation between HCPs in the reporting of ADRs (*9*). The importance of this type of reporting is exemplified by St. John's wort (*Hypericum perforatum* L.). In this case, ADR reporting through pharmacovigilance schemes led to the identification of several clinically important drug interactions and potential safety issues (*10*). To promote herbal medicines' safe use, we recommend that HCPs improve their knowledge of such remedies and encourage them to report any ADRs and herb-drug interactions. Moreover, the preparation and supply of unlicensed herbal medicines as permitted under the herbalist exemption should also be further scrutinized to improve the regulation of this practice and address potential quality and safety issues, while maintaining access to trained herbal medicine practitioners, which many patients value.

Finally, the issue of efficacy needs to be addressed far more robustly for many herbal medicines. More research is needed to identify the active constituent(s) and their modes of action, and to determine their polyvalent nature, while understanding more about their pharmacokinetic and pharmacodynamic properties (similar to the process for conventional pharmaceuticals). It is essential to authenticate and standardize HMPs in order to define their safety, quality, and efficacy standards and to enable clinical trial data to be based on phytochemically characterized HMPs containing standardized levels of active constituents. Meanwhile, the fact that plants are incredible synthetic chemists and have already provided numerous lead chemical structures (e.g., paclitaxel and docetaxel) for the development of conventional pharmaceutical drugs, which may not have been discovered via synthetic compound libraries, should not be ignored. Plants have an important role in the future of medicine and, whether they are used as herbal medicines or in drug discovery programs, it is essential that they are cultivated from sustainable sources and that their medicinal products are designed to meet the appropriate standards for quality and public health safety.

References

1. D. J. Newman, G. M. Cragg, *J. Nat. Prod.* **75**, 311 (2012).
2. A. D. Kinghorn, L. Pan, J. N. Fletcher, H. Chai, *Nat. Prod. Rep*. **74**, 1539 (2011).
3. MHRA, "Public Perception of Herbal Medicines"; available at https://www.gov.uk/drug-safety-update/public-perception-of-herbal-medicines.
4. Council Directive 2004/24/EC, *O. J. L.* **136**, 85-90 (2004).
5. M-J. R. Howes, P. J. Houghton, *Curr. Alzheimer Res*. **9**, 67 (2012).
6. *British Pharmacopoeia* (General Council of Medical Education and Registration of the United Kingdom, London, 1864).
7. *British Pharmacopoeia* (The Stationery Office, London, 2014).
8. L. Hazell, V. Cornelius, P. Hannaford, S. Shakir, A. J. Avery, *Drug Saf*. **36**, 199 (2013).
9. G. Yamey, *Br. Med. J.* **319**, 1322 (1999).
10. Committee on Safety of Medicines, Medicines Control Agency, *Current Problems in Pharmacovigilance* **26**, 6 (May 2000).

Traditional herbal medicines in the European Union: Implementing standardization and regulation

Authors:
Werner Knöss[1*] and
Ioanna Chinou[2]

Medicinal plants have been used in Europe since ancient times. A variety of traditions for using herbal preparations have developed throughout the current member states of the European Union (EU), with a diverse set of regulations developing throughout the 20th century. Recently however, common legislation for the regulation of medicinal products in the EU has emerged (*1*, *2*). Providing a complete set of data to satisfy EU regulatory requirements for bringing herbal medicines to market has proven challenging because many products have had a long history of different traditional uses in the different states. A new legislative approach was therefore developed in 2004 to harmonize the assessment of and access to traditional herbal medicinal products (*3*). The new legislation worked to combine scientific evaluation with the large database of accumulated evidence collected over many years of herbal medicine use.

Legal provisions for herbal medicine in the EU

The approval of medicinal products in the EU is linked to the assessment of quality, safety, and efficacy by a regulatory authority. Basic definitions for herbal substances, herbal preparations, herbal medicinal products, and traditional herbal medicinal products have been provided in Community Directive 2001/83/EC, as amended by Directive 2004/24/EC (*1, 2*). The legislation also describes the details of the documentation requirements for market access for the three main categories of herbal medicines: (1) marketing authorization for *new herbal medicinal products* based on a full set of new efficacy and safety data; (2) marketing authorization for *herbal medicinal products* based on well-established use documented in published literature (including clinical trials); and (3) registration for *traditional herbal medicinal products*, for which efficacy is based on plausibility and long-standing use.

In order to harmonize scientific evaluation in the EU, the Committee on Herbal Medicinal Products (HMPC) was established at the European Medicines Agency (EMA) in London in 2004 (*3*, *4*). This scientific committee is composed of 28 members with one scientific expert from each member state. Five co-opted members represent special fields of expertise: pediatrics, general medicine, pharmacology, clinical pharmacology, and toxicology. The core task of the HMPC is to standardize herbal medicinal products and traditional herbal medicine products in the EU by developing monographs and list entries for herbal substances and their preparation. The establishment of monographs and other regulatory documents is a fully transparent process starting with a public "call for data." A rapporteur is nominated by the HMPC and is responsible for the evaluation of information provided from the public call for data, the results of a systematic literature research in the public domain, and market overviews provided by the member states. A draft monograph is established while the scientific evidence is evaluated and documented in an assessment report. Scientific discussions in the Working Party on European Union Monographs and List Entries (MLWP) and HMPC contribute to revision of both documents, which are published for comments together with a list of references. When a monograph is finally adopted by the HMPC, the entire set of documents, including an overview on the comments from the public consultation, is made available on the EMA's website. Since 2013, the agendas and minutes of the plenary meetings of the HMPC have also been published, and any interested party, applicant, or citizen can access the work of the HMPC (*5*).

Developing standards for herbal medicines

When creating monographs for herbal medicines in the EU, all of the available data is scientifically evaluated to create a unified view of the safety and efficacy of herbal substances and their preparations. Monographs may include two variations: well-established use and/or traditional use.

Well-established use is based on approval of a product for medicinal use in the EU market for at least 10 years. Efficacy must be proven by at least one published successful clinical trial together with published data that meet the further requirements for efficacy and safety.

For traditional herbal medicinal product registration, evidence for safety and efficacy are derived from the long-standing use of a traditional medicinal product. The criteria for a product's acceptance includes demonstrating its use as an herbal medicine for 30 years with at least 15 years of such use in the EU. Additional safety data may be requested by a national regulatory authority when deemed necessary. This approach to approving traditional herbal medicines is only appropriate for products that are very safe. Therefore, this avenue is restricted to products that are administered orally, externally, or by inhalation and that treat minor complaints. Ailments that require a medical prescription, diagnosis, or supervision by a medical doctor are excluded and traditional herbal medicines must comply with provisions for over-the-counter medicines.

The application of monograph standards

Within the last 10 years, the HMPC has released approximately 130 monographs (for examples, see Table 1), 12 list entries, 13 public statements, and about 40 guidance documents (*5*). Only 25 monographs have been approved based on well-established use. Public statements have been developed when a monograph could not be drafted for reasons such as

[1]Department of Complementary and Alternative Medicines and Traditional Medicinal Products at the Federal Institute for Drugs and Medical Devices (BfArM), Bonn, Germany
[2]University of Athens, Faculty of Pharmacy, Division of Pharmacognosy and Chemistry of Natural Products, Zografou Campus, Athens, Greece
[*]Corresponding Author: werner.knoess@bfarm.de

a lack of data or substance-specific concerns. The guidance documents address a broad set of issues related to quality, safety, and efficacy to support further harmonization among the member states.

The inventory of herbal substances that the monographs are intended to represent currently has about 180 entries. Creating such support for the safe and effective use of traditional herbal medicinal products in the EU is the primary goal of the HMPC. The committee conducts a review of the monographs every five years in order to provide a sustainable and reliable system that represents the current state of scientific knowledge. More than 1,300 traditional herbal medicinal products have been registered by the national regulatory authorities of the EU member states. The registrations were granted for individual applications that took the standards laid down in the legislation and described by the monographs into account. These registered traditional herbal medicinal products cover a broad spectrum of conditions, including coughs and cold, mood and sleep disorders, gastrointestinal disorders, urinary tract/gynecology disorders, and pain and inflammation. Approximately one-third of the approved products are composed of multiple herbal preparations.

TABLE 1. Selected examples of Committee on Herbal Medicinal Products (HMPC) monographs for herbal substances. TU, traditional use; WEU, well-established use.

Substance	TU	WEU
Harpagophyti radix	✓	
Hyperici herba	✓	✓
Pelargonii radix	✓	
Valerianae radix	✓	✓
Passiflorae herba	✓	
Ginseng radix	✓	
Ginkgo folium	✓	✓

Globalization of traditional medicines

The ongoing globalization of traditional medicines has brought with it a broad diversity of regulatory systems in different countries and regions. For example, there is a lack of internationally accepted definitions and standard requirements for quality, safety, and efficacy. Different concepts have been established to consider the particular characteristics of traditional medicines. Thus, companies face immense obstacles when trying to gain access to different markets for their herbal medicines. An international dialogue about scientific and regulatory issues is necessary to develop reasonable and adequate requirements. Such a conversation should also address topics such as translating indications into another cultural context or therapeutic environment (e. g., an additional diet or a parallel physical treatment), using material of a nonherbal origin, and classifying herbal products.

The European legislation was primarily designed to deal with traditional herbal medicinal products with a well-known origin in Europe. However, the existence of therapeutic systems and products from traditional Chinese medicine (TCM) or Ayurvedic medicine within Europe has prompted the HMPC to address issues related to non-European traditional medicines (*6*). A document was released in the spring of 2014 that explained the European regulatory framework and the options and limitations for traditional products originating from non-European regions (*7*). In addition, the HMPC has started a pilot project to create monographs for the herbal substances used in Asian traditional medicines, such as TCM and Ayurvedic medicine.

Conclusions

Harmonizing the process for evaluating and authorizing traditional herbal medicines in the 28 member states of the EU is an ongoing process. The legislation and practices over the last decade have demonstrated that it is possible to standardize the scientific and regulatory evaluation of traditional medicines. By considering their individual characteristics and long-standing uses, traditional medicines have been made available to citizens in a more regulated environment. HMPC monographs and monographs related to the quality of herbs from the European Pharmacopeia form the basis of the regulation standards (*8*). Admittedly, there are still challenging issues in the EU surrounding specific topics such as assigning well-established uses and classifying certain products. The EU's legislation is not specific regarding how to distinguish between (herbal) medicinal products, food supplements, medical devices, and cosmetics. On the global level, there is a need to discuss different legal frameworks and to develop harmonized solutions, which should take into account the specific indications for traditional medicines; the availability of marketed products with adequate quality, safety, and efficacy; and the means to provide reliable information to consumers and health care experts for the use of herbal medicinal products.

References

1. European Parliament and EU Council, Directive 2001/83/EC; available at http://ec.europa.eu/health/files/eudralex/vol-1/dir_2001_83_cons/dir2001_83_cons_20081230_en.pdf.
2. European Commission Health and Safety Directorate-General, "Marketing Authorisation, Notice to Applicants"; available at http://ec.europa.eu/health/files/eudralex/vol-2/a/vol2a_chap1_201507.pdf.
3. European Parliament and EU Council, Directive 2004/24/EC; available at http://ec.europa.eu/health/files/eudralex/vol-1/dir_2004_27/dir_2004_27_en.pdf.
4. European Parliament and EU Council, Regulation (EC) No. 726/2004; available at http://eur-lex.europa.eu/LexUriServ/LexUriServ.do?uri=OJ:L:2004:136:0001:0033:en:PDF.
5. European Medicines Agency, "HMPC: Agendas, Minutes and Meeting Reports"; available at http://www.ema.europa.eu/ema/index.jsp?curl=pages/news_and_events/document_listing/document_listing_000193.jsp&mid=WC0b01ac0580028e96.
6. Committee on Herbal Medicinal Products, "HMPC Work Programme for 2012–2015"; available at http://www. ema.europa.eu/docs/en_GB/ document_ library/Work_programme/2011/12/WC500119957.pdf.
7. Committee on Herbal Medicinal Products, "Questions & Answers on the EU Framework for (Traditional) Herbal Medicinal Products, Including Those from a 'Non-European' Tradition"; available at http://www.ema.europa.eu/docs/en_GB/ document_library/ Regulatory_and_procedural_guideline/2014/05/WC500166358.pdf.
8. *European Pharmacopeia,* 8th Ed. (European Directorate for the Quality of Medicines, Strasbourg, 2014).

Acknowledgments

The views expressed in this article are the views of the authors and may not be understood or quoted as being made on behalf of or reflecting the position of the European Medicines Agency or any of its Committees or Working Parties. The authors state no conflict of interest. The data and figures provided are based on data available in September 2014.

Traditional African medicine: From ancestral knowledge to a modern integrated future

Authors:
Joseph Kahumba[1],
Tsiry Rasamiravaka[2,3],
Philippe Ndjolo Okusa[4],
Amuri Bakari[1,4],
Léonidas Bizumukama[5],
Jean-Baptiste Kalonji[6],
Martin Kiendrebeogo[7],
Christian Rabemenantsoa[3],
Mondher El Jaziri[2],
Elizabeth M. Williamson[8*],
Pierre Duez[4*]

Traditional African medicine (TAM) is characterized by a belief in the supernatural as a cause of illness, divination as a diagnostic tool, and the ritualized use of a wide variety of plant- and animal-derived agents in its treatment (*1*). These are usually purchased from local markets (Figures 1A and 1B) and remain the primary source of health care for 80% of both rural and urban populations (*2*). In its strategy for 2014–2023, the World Health Organization (WHO) encourages the development and modernization of TAM as an integral part of emerging health care systems (*3*). However, some of the more exotic practices in TAM, which include the use of animal parts, especially in the *vodun* (voodoo) religion in West Africa, generate lurid headlines in the press and reduce the scientific credibility of TAM. Herbs may be used as part of a regimen in which physical characteristics (aroma, shape, color) and attendant rituals (incantation, song) are more important than pharmacological effects. However, effective strategies for using TAM herbal knowledge are available, as exemplified by a study on antimalarial plants used by traditional healers in Nigeria (*4*). The demand for medicinal plants in Africa is increasing dramatically due to population growth, resulting in the risk of extinction of certain species and an increasing likelihood of falsification of herbal materials. National policies need to be developed to protect both patients and endangered species (*3*) while protecting traditional knowledge and conservation policies (*5*).

TAM as a source of therapeutic agents

It is necessary to understand how individual plants are used in TAM in order to provide a context for exploration. Even though they have been the source of new drugs, poisonous species are rarely used for healing, since it is not possible to accurately control the dose. *Physostigma venenosum*, the Calabar bean, produces the alkaloid physostigmine (eserine), and its derivative rivastigmine, used to treat Alzheimer's disease. It has no traditional medical use and was in fact administered as an ordeal poison in Nigeria to those accused of witchcraft (*1*). From an estimated African biodiversity of ~45,000 plant species, only 5,000 have documented medicinal use (*6*). The list of drugs provided by the African flora (Table 1) is short compared with those from other traditional medical systems, suggesting an unrivaled opportunity for the discovery of new drugs. Ethnobotanically directed approaches are more successful than random selection, as demonstrated in studies using South

TABLE 1. Discoveries based on African medicinal plants.

Properties	Plant species	Constituents and therapeutics
Anticancer	*Catharanthus roseus* (L.) G. Don (Apocynaceae);	Vincristine, vinblastine, and others, to treat leukemias, Hodgkin's lymphoma
	Combretum caffrum (Eckl. & Zeyh.) Kuntze (Combretaceae)	Combretastatins – possible anti-angiogenic; induces apoptosis in proliferating endothelial cells
α_2 adrenergic antagonist	*Pausinystalia johimbe* (K.Schum.) Pierre ex Beille (Rubiaceae)	Yohimbine, to treat erectile dysfunction and hypotension
Cholinesterase inhibitor	*Physostigma venenosum* Balf. (Fabaceae)	Physostigmine derivatives, to treat myasthenia gravis (neostigmine) and Alzheimer's disease (rivastigmine)
Antihypertensive/ antipsychotic	*Rauvolfia vomitoria* Afzel. (Apocynaceae)	Reserpine[‡], occasionally used clinically to treat hypertension and experimentally to deplete catecholamines
Anti-HIV	*Sutherlandia frutescens* (L.) R. Br. (Fabaceae)	Antiretroviral effects under investigation
Cardiotonic	*Strophanthus gratus* (Wall. & Hook.) Baill. (Apocynaceae)	Ouabain (formerly for heart failure), used experimentally to block Na-K-ATPase
Hallucinogenic	*Tabernanthe iboga* Baill. (Apocynaceae)	Ibogaine, possible treatment for narcotic addiction

[‡]Reserpine had, however, been isolated 2 years earlier from *Rauvolfia serpentina* (L.) Benth. ex Kurz, found in India.

[1]Laboratoire de Pharmacognosie, Université de Lubumbashi, Lubumbashi, Democratic Republic of the Congo
[2]Laboratoire de Biotechnologie Végétale, Université Libre de Bruxelles, Belgium
[3]Laboratoire de Biodiversité et de Biotechnologie, Institut Malgache de Recherches Appliquées (IMRA), Antananarivo, Madagascar
[4]Department of Therapeutic Chemistry and Pharmacognosy, Université de Mons (UMONS), Mons, Belgium
[5]Department of Chemistry, Université du Burundi, Bujumbura, Burundi
[6]Laboratoire de Pharmacie Galénique et Analyse des Médicaments, Université de Lubumbashi, Lubumbashi, Democratic Republic of the Congo
[7]Laboratoire de Biochimie et Chimie Appliquées, Université de Ouagadougou, Ouagadougou, Burkina Faso
[8]School of Pharmacy, University of Reading, Whiteknights Campus, Reading, United Kingdom
[*]Corresponding Authors: e.m.williamson@reading.ac.uk (E.M.W) and pierre.duez@umons.ac.be (P.D.)

A

FIGURE 1A. A traditional medicine stall in Madagascar. Key: (**1**) *Eucalyptus citriodora* leaves (respiratory antiseptic), (**2**) *Aloe vahombe* leaves (immunostimulant), (**3**) *Cedrelopsis grevei* bark (tonic, aphrodisiac), (**4**) *Zea maïs* (silk) (diuretic), (**5**) *Aphloia theiformis* leaves (antipyretic), (**6**) *Combretum albiflorum* seeds (deworming), (**7**) *Curcuma longa* rhizome powder (against jaundice), (**8**) *Raventsara aromatica* bark (respiratory antiseptic, antibiotic), (**9**) *Mollugo nudicaulis* leaves (antitussive), (**10**) Tallow molded into balls.

B

FIGURE 1B. A traditional medicine stall in Lubumbashi, Democratic Republic of the Congo. Key: (**1**) *Pterocarpus angolensis* D.C. Stem (hemorrhoids, nappy/diaper rash), (**2**) *Solanum incanum* L. fruits (gonorrhea and hernia), (**3**) Shell from Lualaba River (welding fontanel), (**4**) Tortoise shell (burns treatment), (**5**) *Albizia adianthifolia* stem bark (aphrodisiac and perianal swelling treatment), (**6**) *Diplorhynchus condylocarpon* (Müll.Arg.) Pichon stem (abdominal pain, wound healing), (**7**) *Cassia sieberiana* D.C. roots (hemorrhoids, skin irritation), (**8**) *Mucuna poggei* Taub seeds (nappy/diaper rash; analgesic in pelvic pain).

African Cape flora (*7*) and African plants that contain effective antihyperglycaemic agents (*8*).

Parasitic infections are a major cause of death in Africa, and TAM herbs are widely used to treat them. However, like many diseases in developing countries, these diseases remain underresearched as they do not promise a good commercial return on investment. Nevertheless, new lead antiprotozoal compounds have emerged from herbs used in TAM to treat malaria, and include cowaxanthone (from *Garcinia cowa*), which has comparable antiplasmodial activity to pyrimethamine (*9*), and cryptolepine (from *Cryptolepis sanguinolenta*) (*10*). Clinical trials of *Nauclea pobeguinii* extracts have also shown promising results in the treatment of malaria (*11*). There are still no vaccines for leishmaniasis, and the toxicity of antimony- and pentamidine-based drugs means that interest in plant-derived leads for potential antileishmanial drugs remains high. These include chelerythrine derivatives (from *Garcinia lucida*), gibbilimbol B (*Piper malacophyllum*), warifteine (*Cissampelos sympodialis*), and flavonoids from *Baccharis retusa* and *Kalanchoe pinnata* (*12*). African trypanosomiasis (sleeping sickness) is usually fatal if left untreated, but *Momordica balsamina*, *Securidaca longipedunculata*, and *Quassia africana* have yielded compounds with potent activity (*13*). Medicinal plants also contain compounds with activities unrelated to traditional use, which must be borne in mind and may also be exploited. Indeed the antileukemia *Vinca* alkaloids were discovered serendipitously when the Madagascar periwinkle *Catharanthus roseus* was being investigated for its antidiabetic properties.

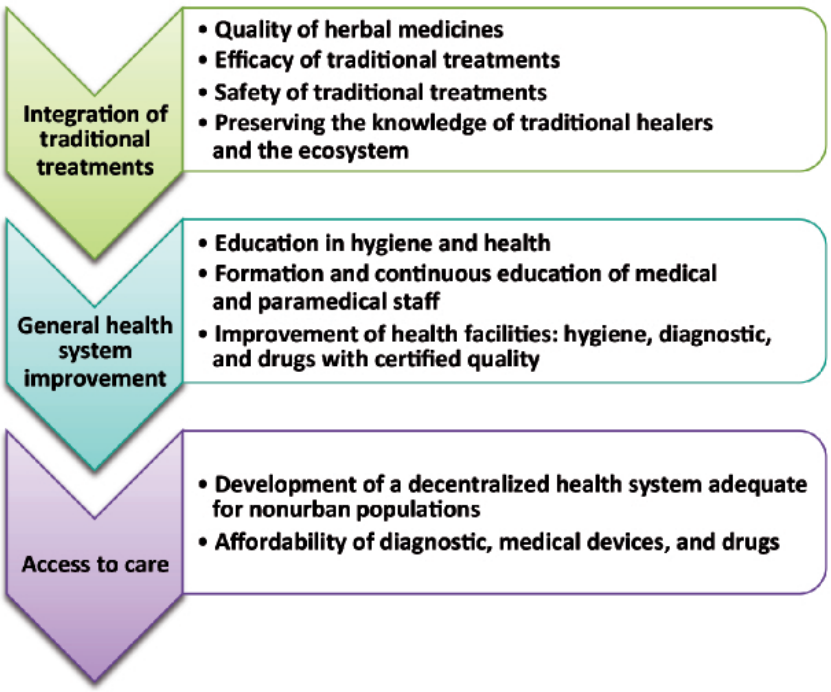

FIGURE 2. Africa's challenge: A future modern health care system integrating traditional medicine.

The alarming incidence of bacterial multidrug resistance to antibiotics requires an urgent search for new antibacterials. The expression of virulence factors in many pathogens requires the full activation of quorum sensing (QS) processes: cell-to-cell bacterial communication mechanisms that detect critical cell numbers by producing and recognizing diffusible signal molecules termed "autoinducers." The compounds coordinate the expression and regulation of virulence factors, biofilm formation, and motility. QS presents a promising series of targets to antagonize virulence in pathogens and/or disturb biofilm formation. For example, catechin and naringenin inhibited the production of virulence factors in *Pseudomonas aeruginosa* PAO1, a consequence of reduced expression of QS- (*lasB* and *rhlA)* and QS-regulatory (*lasI*, *lasR*, *rhlI* and *rhlR)* genes (*14*, *15*). Recently, the Malagasy species *Dalbergia trichocarpa*, traditionally used to treat diarrhea and laryngitis, was shown to inhibit a wide variety of virulence factors in *P. aeruginosa* PAO1; its constituent coumarate esters interfere with the QS system's *rhl* and *las* gene expression (*16*). Extracts of *Kigelia africana*, used topically on wounds and abscesses, have been shown to interfere with the response of bacteria to autoinducers, and to modulate their synthesis in *Chromobacterium violaceum* and *Agrobacterium tumefaciens* (*17*).

Conclusions

TAM currently supports the medical needs of millions of Africans. Based on experience gained from other traditional medicine systems, its modernization and integration with conventional medicine may offer a new and holistic view of health care, contributing to better universal health coverage in Africa, as advocated by the World Health Organization. This remains quite a challenge, as depicted in Figure 2, despite the rich source of new active compounds to be found in African flora. This flora is ripe for exploration, as long as traditional medical uses and methods of administration are interpreted with caution, and the rights of local people and the environment are respected.

References

1. D. T. Okpako, *Trends Pharm. Sci.* **20**, 482 (1999).
2. O. M. J. Kasilo, J. M. Trapsida, C. N. Mwikisa, P. Lusamba-Dikassa, *The African Health Monitor* **14**, 7 (2010).
3. *WHO Traditional Medicine Strategy: 2014–2023* (World Health Organization, Geneva, 2013).
4. I. P. Dike, O. O. Obembe, F. E. Adebiyi, *J. Ethnopharmacol*. **144**, 618 (2012).
5. WHO Regional Office for Africa, "Intellectual Property Approaches to the Protection of Traditional Knowledge in the African Region"; available at http://www.aho.afro.who.int/en/ahm/issue/13/reports/intellectual-property-approaches-sprotection-traditional-knowledge-african.
6. M. F. Mahomoodally, *Evid. Based. Complement. Alternat. Med.* **2013**, 617459 (2013).
7. C. H. Saslis-Lagoudakis *et al*., *Proc. Natl. Acad. Sci. U.S.A.* **109**, 15835 (2012).
8. R. N. Ndip, N. F. Tanih, V. Kuete, in *Medicinal Plants Research in Africa* (Elsevier, London, UK, 2013), pp. 753–776.
9. J. Bero, M. Fréderich, J. Quentin-Leclercq., *J. Pharm. Pharmacol.* **61**, 1401 (2009).
10. L. F. Rocha e Silva *et al*., *Phytomed.* **20**, 71 (2012).
11. K. Mesia *et al*., *Planta. Med*. **78**, 853 (2012).
12. M. Wink., *Molecules* **17**, 12771 (2012).
13. D. Musuyu Muganza *et al., J. Ethnopharmacol.* **141**, 301 (2012).
14. O. M. Vandeputte *et al., Appl. Environ. Microbiol.* **76**, 243 (2010).
15. O. M. Vandeputte *et al*., *Microbiology* **157,** 2120 (2011).
16. T. Rasamiravaka *et al., Microbiology* **159**, 924 (2013).
17. H. Y. Chenia, *Sensors* **13,** 2802 (2013).

Traditional Chinese herbal medicine preparation: Invoking the butterfly effect

Authors:
Helen Sheridan[1],
Brigitte Kopp[2],
Liselotte Krenn[2],
Dean Guo[3],
Jandirk Sendker[4*]

The metaphor of the "butterfly effect"—in which the proverbial butterfly's flapping wings contribute to a tornado across the other side of the globe—is based in chaos theory and encapsulates the concept that a small change at one place in a complex system can have large effects elsewhere (*1*). Such an effect could be construed as contributing to the unique nature of Chinese herbal medicines (CHMs), whereby several specific variables that initially may have minor effects can have a significant downstream impact on the quality, potency, and therapeutic efficacy of the final product (*2*). Two of these factors are the pharmaceutical practices of *paozhi* processing of herbal drugs and the formation of hot-water decoctions from single or multiple herbal drugs (formulae) based on ancient tradition. These two factors act on the chemical composition and biological activity of the resulting *tang* decoction that is finally consumed (*3, 4*).

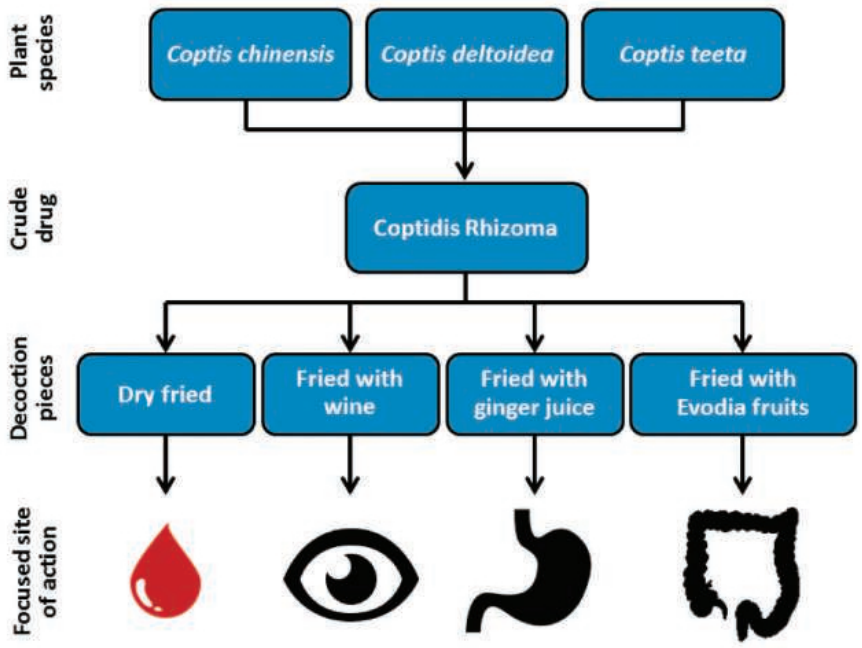

FIGURE 1. According to TCM theory, *paozhi* processing yields decoction pieces with variable therapeutic properties (*3, 7*).

The art of *paozhi*

According to traditional Chinese medicine (TCM) theory, *paozhi* processing transforms raw herbal drugs into "decoction pieces," thus instilling them with the desired properties for their medical application, including improved flavor and detoxification or alteration of their therapeutic efficacy. *Paozhi* encompasses techniques such as cutting, crushing, calcining, or frying with or without liquid adjuvants such as vinegar or honey (*3*). A prominent example is the highly toxic crude root of *Aconitum carmichaelii* (*Fuzi*) which, after detoxification by *paozhi* processing, is incorporated into numerous TCM formulae used to treat joint pain and rheumatic disease (*5, 6*). Also, different kinds of decoction pieces can be derived from the same raw material by processing in different ways. For example, the Chinese pharmacopeia describes four different decoction pieces that may be derived from raw rhizomes of the species *Coptis* (*7*). These pieces, from the same source, have distinct activity and different sites of action within the human body (Figure 1). Despite its long tradition, it is only recently that the effects of *paozhi* have been systematically studied. The current understanding is that *paozhi* processing can alter the qualitative and quantitative chemical composition of herbal materials and can thus impact the final pharmacological or toxicological properties of the decoction pieces (*3*).

Chinese herbal decoctions

TCM formulae are typically composed of two or more processed herbal drugs that are jointly decocted. Traditional decoctions (*tang*) are prepared by repeated boiling of decoction pieces in water for 1 or more hours. The method may also require soaking in cold water before heating, or the introduction of single herbal components later in the process. The composition of the *tang* decoction can be changed by simple actions such as an initial soaking in cold water, which initiates innate enzymatic activity resulting in the alteration of chemical

[1]Trinity College Dublin, School of Pharmacy and Pharmaceutical Sciences, and Trinity International Development Initiative, Trinity Biomedical Sciences Institute, Dublin, Ireland
[2]University of Vienna, Department of Pharmacognosy, Vienna, Austria
[3]Shanghai Research Center for Modernization of Traditional Chinese Medicine, Shanghai Institute of Materia Medica, Chinese Academy of Sciences, Shanghai, China
[4]University of Münster, Institute of Pharmaceutical Biology and Phytochemistry, Münster, Germany
[*]Corresponding Author: jandirk.sendker@uni-muenster.de

composition, as demonstrated by the formula of *Fuzi Xiexin Tang* (FXT) (*8*). In addition, studies of the simple two-herb formula *Danggui Buxue Tang* (DBT), composed of *Astragalus membranaceus* root and *Angelica sinensis* root, demonstrate how multiple parameters like decoction time, initial temperature, *paozhi* processing, or the ratio of the two herbal ingredients may impact the chemical composition and activity of the resulting *tang* decoction (Figure 2) (*4, 9–11*). In particular, in the examples of DBT and FXT, as well as other studies, the practice of joint decoction of herbal materials itself was found to affect the properties of the final product. With DBT, joint decoction showed a significantly improved cardioprotective effect on isolated rat hearts (*12*) and osteoblast differentiation (*13*) when compared to a mixture of individually prepared decoctions of *Angelica* and *Astragalus* roots. Significantly, the concentrations of some of DBT's phytochemicals were found to be increased by 10% to 4,900% in the same studies due to coextraction. It was concluded that the observed synergism results from physicochemical interactions between the chemical constituents of both herbal ingredients. Such interactions have been observed in several studies with other formulae (see *8, 14–16*).

Physicochemical interactions

Physicochemical interactions may affect the solubility of phytochemicals in simpler environments than a Chinese *tang* decoction. It has been observed that ubiquitous herbal constituents like sugars, amino acids, or small organic acids can function singly or in combination as natural deep eutectic solvents, which are able to dissolve phytochemicals and biological macromolecules up to 460,000-fold better than water (*17*). The solubility of phytochemicals in water itself can also be affected by the presence of other small organic molecules, as exemplified by hypericine from St. John's wort, the solubility of which increases 120-fold in the presence of tannins (*18*). In contrast, a reduction in the solubility of different toxic alkaloids was observed in the presence of rhubarb root, a process believed to be linked to the formation of insoluble sediments (*8*).

An exciting new finding is that traditional *paozhi* processing techniques may also augment a decoction's therapeutic efficacy based on physicochemical interactions. Preparing DBT with *Angelica sinensis* root that has been processed with rice wine according to the traditional protocol not only resulted in modified concentrations of *Angelica* phytochemicals, but also significantly increased the concentrations of the observed *Astragalus* phytochemicals; the qualitative phytochemical changes were accompanied by an increase in estrogenic and osteogenic activity (*19*). Some of these physicochemical interactions have been recently modeled using ferulic acid, a constituent of *Angelica sinensis*. The acid increased the concentrations of *Astragalus* phytochemicals and displayed a dose-dependent effect on the estrogenic and osteogenic activity of a decoction from *Astragalus* roots, but only when added before the decoction process. Ferulic acid alone was completely inactive in these models (*20*). This example demonstrates that such complex physicochemical interactions may account for synergistic effects on the biological activity of CHMs and thus contribute to other possible synergisms that may occur due to pharmacokinetic or pharmacodynamic effects (*14*).

Conclusions

Modern scientific study of TCM is leading to an increased understanding of the complex interactions occurring between herbal components during the processing and extraction of these medicines. The examples given here indicate that the evolution of these ancient processes over millennia may actually have improved the therapeutic efficacy and safety of the resulting *tang* decoctions. The increased knowledge of these relationships provides support for the proper use of traditional procedures in the preparation of CHMs.

As discussed above, subtle changes in the complex production chain of CHMs can influence the composition and efficacy of *tang* decoctions through specific interactions between their constituents. The extent of such interactions may be influenced by a single detail like the *paozhi* impact on one ingredient, thus invoking a butterfly effect.

Unlike the proverbial butterfly, however, the application of modern scientific methodologies allows the source of the disruption to be traced by correlating the chemical profile (metabolome) of the herbal preparation with its bioactivity. This approach can also effectively aid the identification of chemical features that indirectly influence an herbal medicine's therapeutic efficacy (*21*). Knowledge about the role of particular herbal ingredients or phytochemicals within a CHM is a prerequisite for the development of meaningful quality control assays, and thus a requirement for the international registration of TCM products. Without fully understanding the subtle contributing factors,

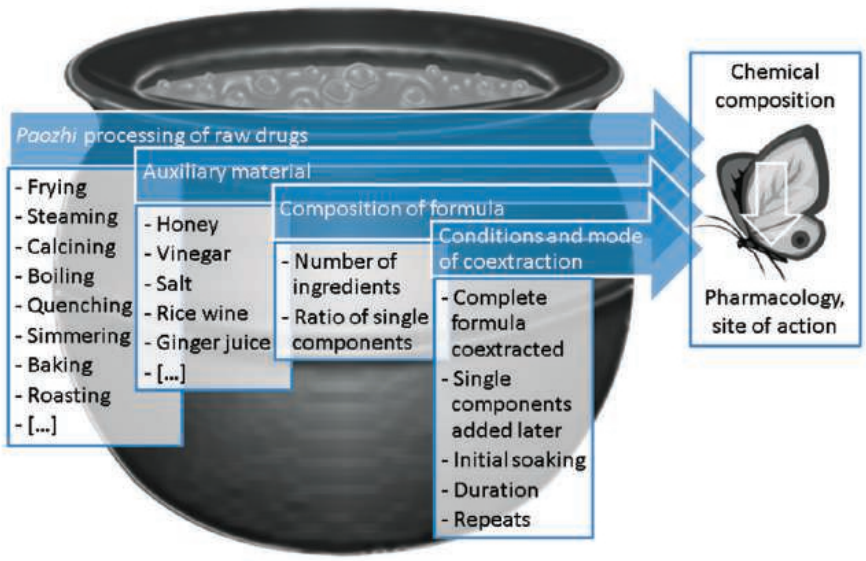

FIGURE 2. Selection of factors affecting the chemical composition of a *tang* decoction.

modernization of TCM could negatively impact the unique properties and therapeutic activity of these medicines. Modern technologies and international collaborations will provide an excellent platform to fully explore and elucidate the complex interactions in herbal medicines in the future and thus aid the development of modernized CHMs that maintain the therapeutic properties of their ancestors.

References

1. K. J. Dooley, *Nonlinear Dynamics Psychol. Life Sci.* **13**, 279 (2009).
2. Q. Xu *et al., J. Altern. Complement. Med.* **13**, 132 (2013).
3. Z. Zhao *et al., Planta Med.* **76**, 1975 (2010).
4. W. L. Zhang *et al., Evid. Based Complement. Alternat. Med.* **2014** (2014), doi: 10.1155/2014/608721.
5. Y. Li, Y. Wang, L. Su, L. Li, Y. Zhang, *Chem. Cent. J.* **7**, 36 (2013).
6. J. Singhuber, M. Zhu, S. Prinz, B. Kopp, *J. Ethnopharmacol.* **126**, 18 (2009).
7. State Pharmacopeia Committee, *Pharmacopoeia of the People's Republic of China* (China Medical Science and Technology Press, Beijing, 2010).
8. Q. Zhang, C. Wang, Y. Ma, E. Zhu, Z. Wang, *Biomed. Chrom.* **27**, 1079 (2013).
9. Z. H. Song *et al., Planta Med.* **70**, 1222 (2004).
10. Q. Gao *et al., Chin. Med.* **2**, 12 (2007).
11. Y. Z. Zheng *et al., Planta Med.* **76**, 439 (2010).
12. D. H. F. Mak, P. Y. Chiu, T. T. X. Dong, K. W. K. Tsim, K. M. Ko, *Phytother. Res.* **20**, 561 (2006).
13. R. C. Y. Choi *et al., Evid. Based Complement. Alternat. Med.* **2011** (2011), doi: 10.1093/ecam/nen085.
14. Y. Yang *et al., Fitoterapia* **92**, 133 (2014).
15. S. S. Zhou *et al., J. Chin. Mass Spec. Soc.* **34**, 88 (2013).
16. M. Xu, G. Wang, H. Xie, Q. Huang, W. Wang, *J. Ethnopharmacol.* **115**, 483 (2008).
17. Y. Dai, J. van Spronsen, G. J. Witkamp, R. Verpoorte, Y. H. Choi, *Anal. Chim. Acta* **766**, 61 (2013).
18. A. Nahrstedt, V. Butterweck, *J. Nat. Prod.* **73**, 1015 (2010).
19. T. T. X. Dong *et al., J. Agric. Food Chem.* **54**, 2767 (2006).
20. K. Y. Z. Zheng *et al., Planta Med.* **80**, 159 (2014).
21. H. Sheridan *et al., J. Ethnopharmacol.* **140**, 482 (2012).

Bridging the seen and the unseen: A systems pharmacology view of herbal medicine

Authors: Yan Schroën[1,2], Mei Wang[1,3], Herman A. van Wietmarschen[1,4], Renger Witkamp[5], Thomas Hankemeier[6], Tai-Ping Fan[7], Jan van der Greef[1,3,4,6*]

The human body functions as a dynamic ecosystem consisting of innumerable interacting systems, creating emerging properties and synergetic effects and extending beyond the physical barriers of the human organism, encompassing interactions with the environment. Understanding the human organism in its full complexity requires consideration of its different levels of organization (Figure 1, left) (*1*).

Medical questions regarding how a disease develops and how to prevent and intervene are amenable to a system-oriented paradigm in which interventions include multitarget pharmacological strategies that can influence processes across systems (*2*, *3*).

Although Western medicine has provided a very successful disease management system based on intervention at a single target, further improvements will rely heavily on new diagnostic tools to differentiate between disease subtypes and individual biological patterns.

Recognition of the uniqueness of each human entails differentiation at higher levels of organization, which requires a systems approach and expanded diagnostic insights (*4*). A better understanding of the biology and the influence of multitarget approaches on regulatory pathways could provide new perspectives for system-level interventions (*5*). Understanding system resilience to a multitude of environmental stressors will shed light on personalized health and prevention options within a biopsychosocial context.

In medical plant research, isolates of single components are primarily used, which does not reveal the synergetic properties and full impact of the natural product. This was elegantly demonstrated in studies of *Berberis fremontii* (Frémont's mahonia), which showed that the antimicrobial effects of the bioactive compound berberine were enhanced >100-fold when combined with an inactive component, 5′-methoxyhydnocarpin, isolated from the same plant (*6*). Reverse pharmacology, wherein a traditional preparation is taken as a starting point, holds promise for studying the synergetic nature of herbal medicine (*5*), especially when combined with subtyping based on modern 'omics technologies. Combining phenomenological descriptions of a system from TCM with experimental data can provide a top-down guide that includes a wealth of information and may even facilitate novel insights.

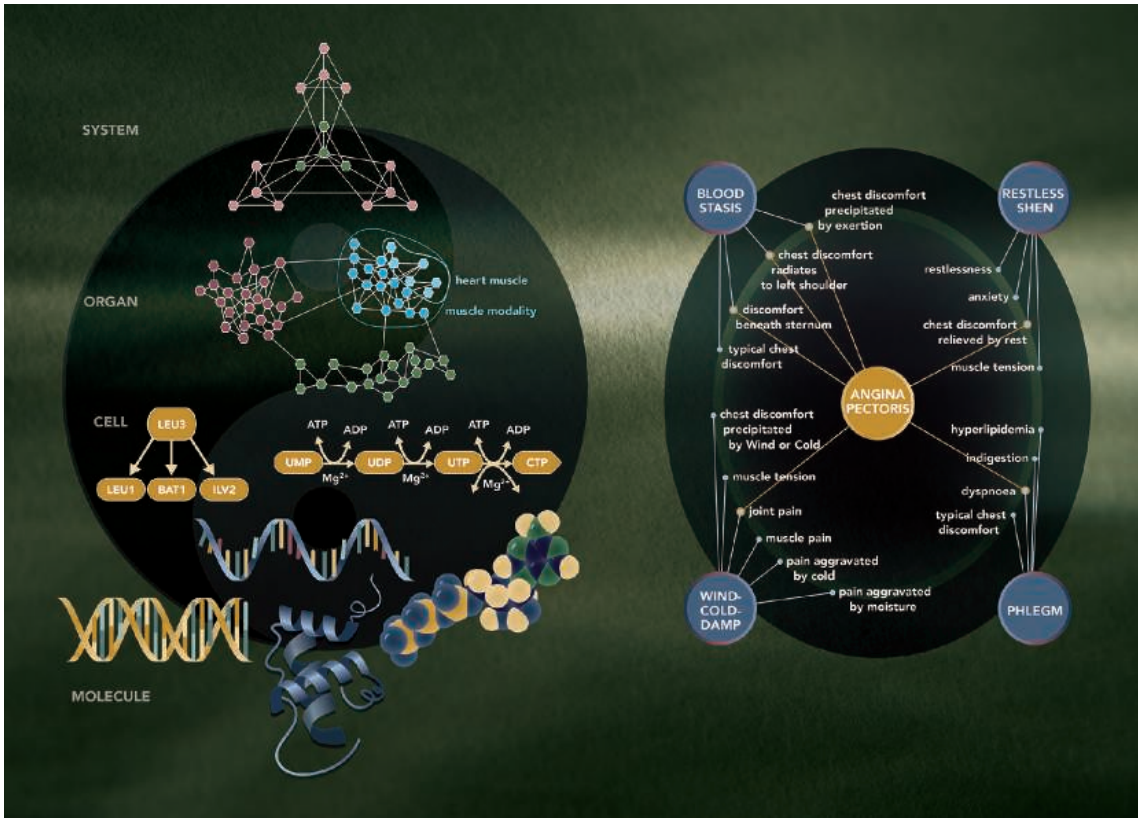

FIGURE 1. An example of systems pharmacology in herbal medicine. Left, a systems view of human biology, with selected effects of *Diao Xin Xue Kang* (DXXK). Right, the four traditional Chinese medicine (TCM) symptom clusters that are the main intervention targets for DXXK in China are illustrated for angina pectoris.

DXXK as an example

An example of the application of a systems pharmacology perspective in multitarget pharmacology research can be illustrated by *Diao Xin Xue Kang* (DXXK), the first traditional Chinese herbal medical product registered in Europe and produced in China according to the European Traditional Herbal Medicinal Products legislation. DXXK is an extract of rhizomes from *Dioscorea nipponica* Mankino, a plant from the Dioscoreaceae (yam) family. Over 300 papers have been published on the extract's pharmacology, safety, and mechanisms of action, and DXXK has been subjected to phase 1, 2, and 3 clinical trials with an estimated 16,000 patients enrolled (*7*). The main focus in these studies has been its use in the treatment of myocardial dysfunction, an indication included in the TCM description of the plant.

To obtain a systems view of the biochemical and functional effects of DXXK, pharmacological studies have examined various biochemical pathways, ranging from molecular to organ-level assessments. Analysis of DXXK's phytopharmacological constituents revealed that its bioactivity could be attributed to a group of steroidal saponins, namely dioscin, diosgenin, prosapogenin A, and prosapogenin C (*8*–*12*). Saponins influence oxidative stress (*12*, *13*), which is a major risk factor for vascular endothelial cell apoptosis, a process that is implicated strongly in the pathogenesis of cardiovascular disorders (*14*, *15*). Steroidal saponins also exhibit vasodilator and protective effects on human vascular endothelial cells (*16*, *17*). Clinical studies have shown that these saponins have protective effects against hyperlipidemia, including inhibition of platelet aggregation and reductions in cholesterol and triglyceride levels (*18*–*20*).

Studies at the cellular level have revealed that DXXK affects the renin-angiotensin-aldosterone system in a manner that is consistent with its antihypertensive effects (*21*). At the organ level, the phytoestrogen diosgenin, which is also found in DXXK, acts as a vasodilator and modulates vascular smooth muscle function by regulating cell viability, migration, and calcium homeostasis (*22*, *23*). Recent studies have revealed that the significant anti-inflammatory effect may be attributed to its inhibitory effect on the NF-κB/COX-2 pathway and relevant inflammatory mediators including prostaglandin 2, nitric oxide, tumor necrosis factor α, interleukin (IL) 1β and IL-6 (*24*).

In TCM, DXXK is used to treat a variety of conditions, including myocardial dysfunction, atherosclerosis, hypertension, migraine, and muscle spasms. From a Western perspective, these disparate applications suggest that there may be

[1]Sino-Dutch Centre for Preventive and Personalized Medicine, Zeist, the Netherlands
[2]Oxrider, Education and Research, Hilvarenbeek, the Netherlands
[3]SU BioMedicine BV, Utrechtseweg, Zeist, the Netherlands
[4]TNO, Department of Microbiology and Systems Biology, Zeist, the Netherlands
[5]Division of Human Nutrition, Wageningen University, Wageningen, the Netherlands
[6]Division of Analytical Biosciences, Leiden Academic Centre for Drug Research, Leiden University, Leiden, the Netherlands
[7]Department of Pharmacology, University of Cambridge, Cambridge, United Kingdom
*Corresponding Author: jan.vandergreef@tno.nl

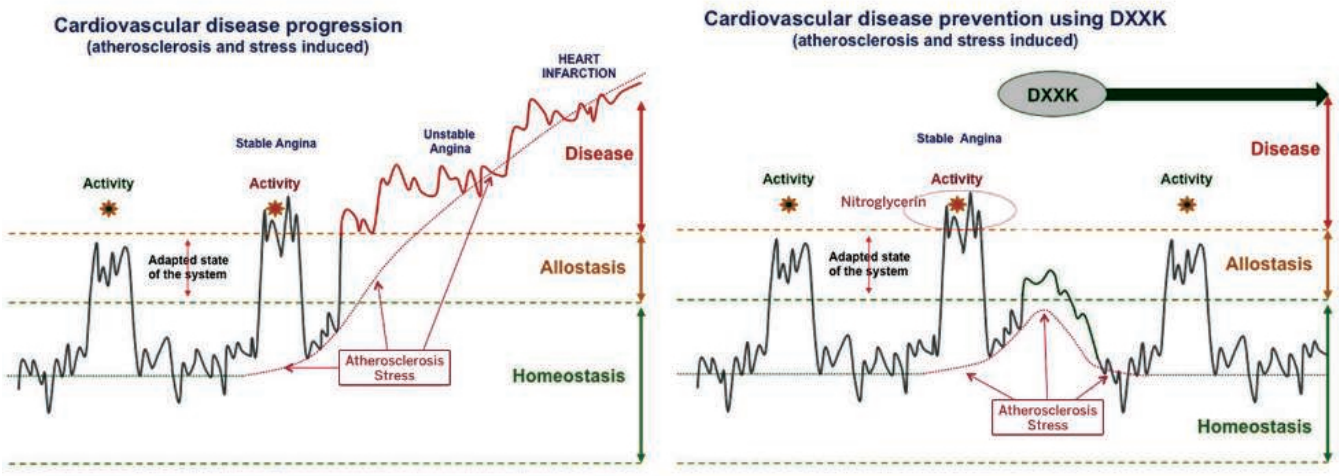

FIGURE 2. Conceptual depiction of the preventive effect of *Diao Xin Xue Kang* (DXXK) on the progression from a healthy to a diseased condition over time. The graph on the left illustrates a loss of resilience and the allostatic response. The graph on the right illustrates how intervention with DXXK can bring the system back to a healthy, resilient state, reducing the long-term influence of stressors.

shared regulatory pathways related to these conditions. In a more general sense, TCM offers attractive ways to generate a systems view on interdisease relationships owing to its unique knowledge of symptom patterns, which can be translated into Western concepts.

However, some important and intrinsic characteristics underlying the complexity of the TCM concepts can be lost in translation. Elucidating this missing information can build a bridge between Western and Chinese medicine, providing insights into large-scale organization (Figure 1, left). In particular, symptom relationships can help to bridge Chinese and Western perspectives on disease states (Figure 1, right) and can point to associations among regulatory pathways, a likely level at which major synergetic effects can be uncovered.

Where East meets West

Closer examination of points of interconnectedness between Chinese disease subtypes and Western pharmacology suggests that key elements in DXXK bioactivity involve the musculature. This is consistent with DXXK's ability to induce relaxation of vascular muscles (*25–28*) and reduce stress-related tension in intestinal, cardiac, and skeletal muscles (the latter involving the neck), as well as to reduce muscle spasms in the lower back and legs (*29*). Interestingly, Leino-Arjas et al. demonstrated a relationship between cardiovascular risk factors such as atherosclerosis and lower back pain (*30*).

A dynamic systems view of the effects of DXXK on cardiovascular disease progression is illustrated schematically in Figure 2. A healthy system can respond to and exchange information with its environment efficiently. Stressors can move a resilient system into a temporary state of allostasis. Systems should return to homeostasis when the offending stressors have been alleviated. The development of an allostatic load leads to the loss of ability to cope with stressors within the boundaries of a healthy condition (*31*), resulting in a stable angina. Eventually, the system may fall into a state in which it is unable to return to normal stasis conditions, even after direct stressors have been alleviated. That is, a person may develop unstable angina and even cardiac infarction (Figure 2, left). Clinical observations and phase 3 clinical study findings suggest that DXXK may prevent the system from progressing toward the diseased state (Figure 2, right) (*32*). The multitude of pharmacological effects related to the relaxation of vascular muscles observed with administration of DXXK can be explained by a putative systems-level organization change wherein an underlining dysfunctional regulatory process may be influenced. If so, then DXXK may be achieving an improvement in the muscle function at a higher system level, resulting in reduction of vascular tension and, thereby, increases in the oxygen flow to active tissues. The effect of DXXK on muscles relates directly to DXXK's TCM symptom treatment pattern, namely muscle cramps in the neck, lower back, and legs as well as dysfunction of cardiac muscle. Moreover, this association is consistent with known manifestations of stress in the musculature, such as lower back pain (*33*) and heart attacks (*34*). The physical manifestations of chronic stress highlight an important aspect of integrating physiological and psychological determinants in both the diagnosis and intervention, a key perspective in psychoneuroendocrinology (*35–37*).

Future perspectives

Looking to the future, further studies are needed to obtain a more detailed accounting of system level actions, particularly with respect to the dynamics of higher organization systems and elucidation of biochemical variations among different clinical subgroups. Furthermore, enhancing our knowledge of biological rhythmicity and dynamics will be important for attaining a fuller understanding of systems biology in medicine (*38, 39*). Indeed, the notion of dynamic system rhythms being reflected in the manifestation of symptoms over time is key in TCM. The TCM view of dynamics resonates with the classical

idea of *Panta rhei*, or "everything flows," credited to the Greek philosopher Heraclitus. Major knowledge gaps remain in our understanding of how psychological and environmental factors influence health and in our discernment of higher system-level organization (*40*). A systems pharmacology approach that connects TCM symptom descriptions with biochemical pathway knowledge has the potential to bridge these gaps.

References

1. I. Prigogine, G. Nicolis, *Ann. N.Y. Acad. Sci*. **231**, 99 (1974).
2. L. Von Bertalanffy, *Acad. Manag. J*. **15**, 407 (1972).
3. J. van der Greef, R. N. McBurney, *Nat. Rev. Drug Discov*. **4,** 961 (2005).
4. J. van der Greef *et al*., *Planta Med*. **76,** 2036 (2010).
5. J. van der Greef *et al*., in *Metabolic Profiling: Its Role in Biomarker Discovery and Gene Function Analysis,* G.C. Harrigan, R. Goodacre, Eds. (Kluwer, Boston, 2003), pp. 171–198.
6. F. R. Stermitz *et al*., *Proc. Natl. Acad. Sci U.S.A.* **97**, 1433 (2000).
7. Z. R. Liu *et al*., *China J. Traditional Chin. Med. Pharmacy* **19**, 620 (2004)
8. S. Du, W. Liu, T. Fu, B. Li, Z. Xia, *Acta Medica Sinica* **37**, 267 (2002).
9. X. G. Liang, Q. X. Pang, *Chin. J. Geriatr. Heart Brain Vessel Dis.* **6**, 129 (2004).
10. L. Ni, P. Xu, X. S. Wu, F. Chen, *Shanghai Journal of Traditional Chinese Medicine* **41** (11), 76 (2007).
11. K. Ning, Y. Li, H. Cao, L. Li, *Trad. Chin. Drug Res. Clin. Pharm.* **19**, 1 (2008).
12. T. Wang *et al*., *J. Ethnopharmacol.* **139**, 214 (2012).
13. J. S. Jaswal *et al*., *Biochim. Biophys. Acta* **1813**, 1333 (2011).
14. C. Cardillo, J. A. Panza., *Vasc. Med*. **3**, 138 (1998).
15. M. Cattaruzza, T. J. Guzik, W. Słodowski, *Circ. Res.* **95**, 841 (2004).
16. K. L. G. Dias *et al*., *Eur. J. Pharm.* **574**, 172 (2007).
17. G. Gong, *Chem. Biol. Interact.* **184**, 366 (2010).
18. Y. Liu, Y. Lin, *Fujian Medical J.* **19**, 65 (1997).
19. Z. Feng *et al*., *New Drugs Clin. Rem.* **13**, 152 (1994).
20. S. Xie, J. Zhang, *New Drugs Clin. Rem*. **13**, 161 (1994).
21. Y. P. Zhu, B. G. Li, in *Diao Xin Xue Kang Jiao Nang* (Science Press, Beijing, 2004), p. 172.
22. A. L. S. Au *et al., Eur. J. Pharm.* **502**,123–133 (2004).
23. M. Esfandiarei *et al*., *J. Pharm. Exp. Therapeutics* **336**, 925 (2011).
24. L. Wang *et al*., *Int. J. Clin. Exp. Pathol.* **8**, 4830 (2015)
25. Y. Y. Guan *et al*., *Acta Pharmacol. Sin.* **15**, 392 (1994).
26. H. B. Arcasoy *et al*., *Boll. Chim. Farm*. **137**, 473 (1998).
27. C. Y. Kwan, *Acta Pharmacol. Sin*. **21**, 1101 (2000).
28. Y. H. Wang *et al*., *J. Natural Products (India)* **2**, 123 (2009).
29. Chinese Pharmacopoeia Commission, *Pharmacopoeia of the People's Republic of China 2010*, ISBN 9780119207798 (2010).
30. P. Leino-Arjas, S. Solovieva, J. Kirjonen, A. Reunanen, H. Riihimaki, *Scand. J. Work Environ. Health* **32**, 12 (2006).
31. P. Sterling, *Physiol. Behav*. **106**, 5 (2011).
32. Z. Zhou, *New Drugs Clin. Rem*. **13**, 84 (1994)
33. L. A. Päivi *et al*., *J. Epidemiol. Community Health* **43**, 293 (1989).
34. E. Mostofsky *et al*., *Heart J*. **35**, 1404 (2014).
35. P. D. Gluckman *et al*., *Lancet* **373**, 1654 (2009).
36. B. S. McEwen, *Proc. Natl. Acad. Sci. U.S.A.* **2012**, 1 (2012).
37. B. L. Fredrickson *et al., Proc. Natl. Acad. Sci. U.S.A.* **110**, 13684 (2013).
38. L. Glass, *Nature* **410**, 277 (2001).
39. J. Bass, J. S. Takahashi, *Science* **330**, 1349 (2010).
40. J. van der Greef, *Nature* **480**, S87 (2011).

Acknowledgments
The authors thank Charlotte Lokin for producing the artwork in Figure 1.

Hypothesis-driven screening of Chinese herbs for compounds that promote neuroprotection

Authors:
Thomas Friedemann[1],
Min Li[2†],
Jian Fei[3†],
Udo Schumacher[4],
Juxian Song[2],
Sven Schröder[1*]

Protection against the loss of neurons or the retardation of disease progression is the major challenge for the treatment of neurodegenerative disorders like Alzheimer's disease (AD) and Parkinson's disease (PD). Current established drug therapies treat mainly symptoms, leading to cognitive enhancement in AD or improved movement in PD. However, neuronal repair or prevention of further degeneration has not been convincingly demonstrated in humans (*1*). Common mechanisms of neuronal damage include, among others: oxidative stress, mitochondrial dysfunction, autophagy dysfunction, excitotoxicity, protein aggregation, and genetic defects (*1–3*). Practically all drugs for AD that were neuroprotective in both in vitro and in vivo preclinical models failed in large clinical trials. Due to this failure, the therapeutic potential of traditional Chinese medicine (TCM) has recently received increased attention. Multiple herbs have been tested in cell cultures or animal models. However, in a situation similar to that of synthetic drugs, the evidence of neuroprotection in clinical studies is still unsatisfactory, most likely due to the fact that the paradigm of treatment with a single chemical entity is not easily applicable to the complexity of TCM prescriptions (*4*).

The screening modality bottleneck

In recent decades the search for novel plant-derived drugs has relied on hypothesis-free, high-throughput screening (HTS) using metabolomic, proteomic, and genomic methodologies (*5*). The professed goal has been to identify isolated single-target small molecular chemicals based on compound libraries. However, even the largest plant compound libraries represent only a small fraction of possible chemical diversity of natural products (*6*). Further, in vitro HTS hits often lack efficacy in vivo (*7*). One instructive example is Huperzine A, an alkaloid isolated from *Huperzia serrata*, which showed multiple beneficial effects in preclinical models, but failed in a phase 2 clinical study for AD (*8*). Research that primarily focuses on monocompounds isolated from plants carries a high risk that the observed effects will not be transferable from in vitro or animal models to clinical practice.

Neurodegeneration is a complex process involving multiple pathophysiological mechanisms; therefore it seems only rational to apply a multitargeted approach to a multifactorial

disease. Accordingly, multicomponent medicines may prove to be more potent by virtue of multiple bioactive components (*9*).

TCM herbal mixtures have long been used to treat AD and PD. Examples include modified *Huanglian-Jiedu-Tang* (*10*) and *Fu-Zhi-San* (*11*) for AD and *Jia-Wei-Liu-Jun-Zi-Tang* (*12*) or *San-Huang-Xie-Xin-Tang* (*13*) for PD. Even if controlled clinical trials show efficacy, elucidating the mechanisms of action is an onerous challenge due to the complex chemical composition of herbal extracts.

Hypothesis-driven screening

The philosophy and practice of physiology and pathology vary significantly between TCM and Western medicine in that similar pathophysiological features are often described using different terminologies. Therefore, the application of traditional clinical knowledge to the Western system requires an interdisciplinary and intercultural validation process to identify effective herbal candidates and develop the optimal experimental design.

Cell and animal models used to validate drug candidates from classical screening processes can mimic human pathophysiology to a limited extent. By contrast, the candidate herbs from a bedside-to-bench-to-bedside approach have already been tested successfully in humans. This latter, hypothesis-driven approach (as opposed to the hit-and-miss high-throughput approach) reduces the risk of running into cost-intensive dead ends due to inefficacy or unexpected side effects discovered during clinical trials. The process begins when candidate herbs are systematically reviewed in the scientific and medical literature for their in vitro, in vivo, and clinical actions, and discussed by an interdisciplinary panel of experts. A substantiated working hypothesis is then established by analyzing and integrating the traditional medicinal usage and current scientific data of individual herbs and their known bioactive compounds. Based on this knowledge, one can carefully select in vivo and in vitro models for the primary screening and efficacy assay steps. After initial screening, transcriptomic, proteomic, and metabolomic analysis can be performed to further substantiate mode-of-action hypotheses (*14*).

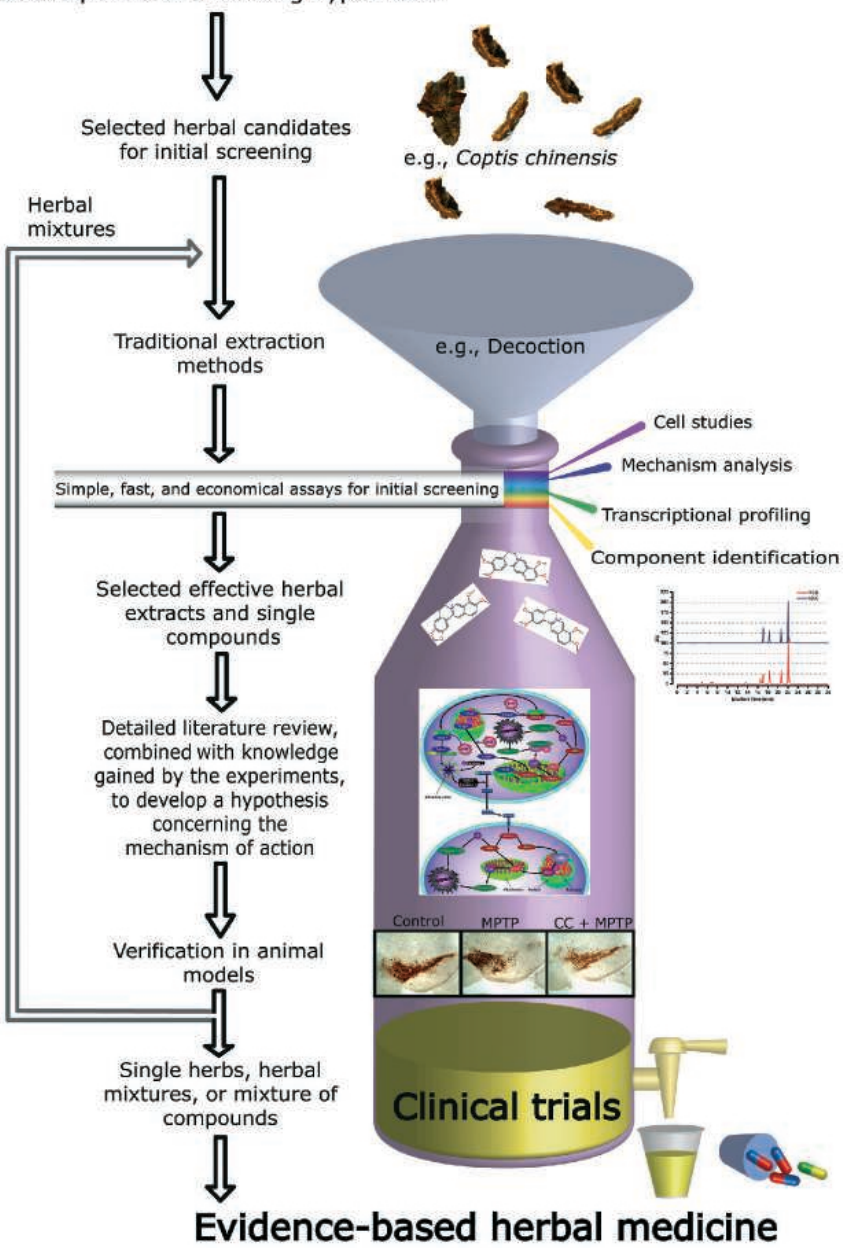

FIGURE 1. Workflow of hypothesis-driven screening with examples from authors' research. MPTP, 1-methyl-4-phenyl-1,2,3,6-tetrahydropyridine; CC, *Coptis chinensis*.

[1]HanseMerkur Center for Traditional Chinese Medicine at the University Medical Center Hamburg-Eppendorf, Hamburg, Germany
[2]Mr. & Mrs. Ko Chi-Ming Centre for Parkinson's Disease Research, School of Chinese Medicine, Hong Kong Baptist University, Hong Kong, China
[3]School of Life Sciences and Technology, Tongji University, Shanghai, and Shanghai Research Center for Model Organisms, Shanghai, China
[4]Institute of Anatomy and Experimental Morphology, University Medical Center Hamburg-Eppendorf, Hamburg, Germany
[†]Contributed equally to this work.
[*]Corresponding Author: schroeder@tcm-am-uke.de

These hypothesis-based screenings should be followed by mechanistic studies to identify the mode of action of the drug as a prerequisite for the preparation of clinical trials. Figure 1 represents a hypothesis-driven screening process for the evidence-based evaluation of a TCM product. The aim is not to find just one single compound for a single pathway, but rather to apply the procedure to combinations of herbs or substances, thus enabling the discovery of additive and synergistic effects, reflecting the current practice of TCM. Substantial optimization of this process is still required, but it provides a potentially valuable alternative to current, suboptimal classical screening methods.

Test case: Finding herbs for PD

Following careful consideration, the traditional formula *Jia-Wei-Liu-Jun-Zi-Tang* was chosen to test our hypothesis-based screening methodology. It has previously been shown to improve symptomatology and communication ability in PD patients (*12*). We screened a series of extracts and compounds from this formula and identified several autophagy enhancers with neuroprotective effects (*15–17*). Two representative compounds isolated from *Uncaria rhynchophylla* (Miq.) Jacks (Gouteng), corynoxine (Cory) and corynoxine B (Cory B), were found to promote the degradation of α-synuclein (the main component of Lewy body fibrils) and protect dopaminergic neurons by enhancing autophagy in cell culture and *Drosophila* models of PD. Cory enhances autophagy by inhibiting the mechanistic target of rapamycin (mTOR) pathway, while Cory B elicits that same effect by targeting HMGB1-Beclin 1 interaction (*18*) and restores autophagy inhibited by α-synuclein (*15*). These two active compounds may exert synergistic effects, accounting for the neuroprotective activity. Proteomic/metabolomic analysis and animal studies are ongoing to clarify the molecular mechanisms of action and potential preclinical efficacy.

In a second study, hypothesis-driven screening guided us to *Coptis chinensis* Franch. (CC) and coptisine (Cop, a component of CC), both of which showed neuroprotective effects against oxidative stress-induced cytotoxicity (*19*). However, a crude extract of CC was more effective than Cop alone (*20*). Subsequently, we extended our research to in vitro and in vivo models for PD, using 1-methyl-4-phenyl-1,2,3,6-tetrahydropyridine (MPTP) in mouse experiments to create a subchronic PD model, and its active metabolite 1-methyl-4-phenylpyridinium (MPP^+) in cell experiments. Furthermore, we found that CC and Cop protected cells from MPP^+-induced cytotoxicity and CC also protected MPTP-treated mice from movement disorders and loss of dopaminergic cells in the substantia nigra. Our data suggested that the neuroprotective effect of CC or Cop might at least in part be caused by transcriptional regulation (*18*). Microarray analyses of the transcriptome of CC-treated cells revealed only two differentially regulated genes, MTND1 and TXNIP, which could possibly explain the neuroprotective effect (*19*, *20*).

It is apparent from our work that combining single compounds or herbs, which act via different modes, has the potential to generate additive or synergistic effects. Comparing the efficacy of the crude herb, its active compounds, and traditional mixtures using the herb as an ingredient, may help us to better understand the scientific principles behind herbal compositions. Validation of this promising approach will not be an easy path, and can only be achieved through the concerned efforts of a collaborative network of scientists and medical professionals.

Conclusions

TCM herbal mixtures have been used successfully for millennia, but their mode of action remains poorly understood. Nevertheless, they may have an enormous potential due to their multitarget mode of action for treating multifactorial complex diseases, including AD and PD, for which satisfactory conventional treatments do not exist. The classical screening approach using shotgun methods has not been as successful as hoped, despite considerable cost and effort. The development of hypothesis-driven screening methods is therefore essential and should result in valuable outcomes.

References

1. C. Holscher, *Neural Regen. Res.* **9**, 1870 (2014).
2. J. L. Cummings *et al.*, *Alzheimers Res. Ther.* **6**, 37 (2014).
3. A. L. Petraglia *et al.*, *Surg. Neurol. Int.* **2**, 146 (2011).
4. D. Normile, *Science* **299**, 188 (2003).
5. A. L. Harvey *et al.*, *Nat. Rev. Drug Discov.* **14**, 111 (2015).
6. D. H. Drewry *et al.*, *Curr. Opin. Chem. Biol.* **14**, 289 (2010).
7. J. L. Medina-Franco *et al.*, *Drug Discov. Today* **18**, 9 (2013).
8. M. S. Rafii *et al.*, *Neurology* **76**, 1389 (2011).
9. B. M. Schmidt *et al.*, *Nat. Chem. Biol.* **3**, 360 (2007).
10. S. S. Durairajan *et al.*, *PLOS ONE* **9**, e92954 (2014).
11. M. Bi *et al.*, *Neurosci. Lett.* **501**, 35 (2011).
12. W. F. Kum *et al.*, *Evid. Based Complement. Alternat. Med.* **2011**, 724353 (2011).
13. Y. C. Lo *et al.*, *Evid. Based Complement. Alternat. Med.* **2012**, 501032 (2012).
14. X. Wang *et al.*, *Mol. Cell. Proteomics* **12**, 1226 (2013).
15. J. X. Song *et al.*, *Autophagy* **10**, 144 (2014).
16. J. H. Lu *et al.*, *Autophagy* **8**, 98 (2012).
17. L. L. Chen *et al.*, *J. Neuroimmune Pharmacol.* **9**, 380 (2014).
18. D. Tang *et al.*, *J. Cell Biol.* **190**, 881 (2010).
19. T. Friedemann *et al.*, *J. Ethnopharmacol.* **155**, 607 (2014).
20. T. Friedemann *et al., Evid. Based Complement. Alternat. Med.* **2015,** 827308 (2015).

Acknowledgments

The authors would like to acknowledge Prof. Wolfgang Schwarz for the founding and establishment of a scientific Sino-German Network on TCM research. Thanks to Sarah Mirza for the illustration. This work was supported by the HanseMerkur Insurance Group and the Innovation Foundation Hamburg (721.230-002), and by grants from the General Research Fund (HKBU 121009/14), the Innovation and Technology Fund (ITS/274/12), and the Health and Medical Research Fund (HMRF 12132091) from the Hong Kong Government (For M. Li).

Mapping ancient remedies: Applying a network approach to traditional Chinese medicine

Author:
Shao Li*

Over the thousands of years that traditional medicine has been practiced, a wealth of clinical experience and a large number of herbal formulae have been accumulated to support the practice of traditional Chinese medicine (TCM). It is challenging to assess TCM therapies that are mechanistically unclear, in particular because many ingredients in an herbal formula may exert their effects on the body through low affinity binding to multiple different targets. This is at odds with the current "one target, one drug" approach most often associated with Western therapies, which is committed to the pursuit of drugs that bind to a single target with high affinity and specificity. At the same time that the single target-based, high-throughput screening assays that are the hallmark of reductionist research are being questioned due to high failure rates (*1*), network pharmacology is evolving as a systematic paradigm for drug discovery and development (*2*, *3*). Network pharmacology adopts a network approach to represent and analyze the complex biological systems underlying diseases and drug actions. It thus aids in drug discovery, drug design, and drug development, sharing a holistic perspective that is characteristic of TCM (*2*–*5*). Today, the integration of TCM and network pharmacology (TCM-NP) provides an innovative research perspective for proponents of both reductionist and holistic medicine.

Treating a network as a therapeutic target

TCM-NP highlights a "network target, multicomponent therapeutics" approach (*6*). The core principle of a network target is to construct a biological network that can be used to decipher complex diseases. The network is then used as the therapeutic target, to which multicomponent remedies, such as herbal formulae, are applied (*5*, *6*). Here, a network-based model incorporating an "effect-on" and "effect-off" switch can be proposed as a means to understand how herbal medicine might work. For the model to be "on," multiple ingredients (or a single ingredient as a special case) in an herb or herbal formula should induce additive or synergistic effects on a set of interacting targets within a given network, such that the final outcome reaches a threshold to produce a measureable pharmacological result by network propagation and integration in both space (spatial extension) and time (temporal duration) (Figure 1A). In this way, multiple low-affinity actions can achieve a significant effect. By contrast, in the "off" scenario, herbal ingredients that exert opposite or antagonistic actions on a target network (Figure 1B), or only weakly affect decentralized targets in a network (Figure 1C), may not produce effects that reach the measureable threshold. This model can help to explain why the actual efficacy of herbal ingredients can be greater than the sum of the effects of individual ingredients (*7*, *8*). For example, a recent study demonstrated that the classic *Liu-Wei-Di-Huang* formula can exert diverse therapeutic actions on metabolic and immune disorders by regulating a set of networked targets through different groups of bioactive ingredients (*9*).

According to the proposed effect-switch model, an optimal combination of herbal ingredients from herbal formulae can be considered worth pursuing if it satisfies the criteria for a network-based effect switch: turning on desirable effects and turning off undesirable effects (including side effects and toxicity).

TCM-NP methodologies

Through the development of computational and experimental methods, TCM-NP aims to map both disease genes (including gene products) and herb targets in a network, and provide information on bioactive compounds, synergistic combinations, mechanisms of action, and modern indications for herbal formulae by measuring the network association (e.g., modularity, connectivity, feedback, and dynamics) between disease genes and herb targets (Figure 2A). Representing complex biological systems as networks provides a foundation for the exchange of scientific and clinical data between modern and traditional forms of medicine. Now, 'omics technologies, knowledge databases, and bioinformatics are providing more actionable data and increasingly sophisticated analysis tools, thus accelerating the understanding of biological networks, a situation that will undoubtedly speed TCM-NP progress. For example, by exploiting the available data pool, a computational method, drugCIPHER, has been developed to predict an herbal compound's target profile by integrating chemical, target, and network information from current FDA-approved drugs (*10*). A sibling method, CIPHER, also performed well in predicting disease genes (*11*). In recent years, the use of systems biology and bioinformatics technologies in TCM has been growing rapidly, as has the generation of TCM-NP data and our understanding of multilayer networks. Through this work, associations have been elucidated between herbs, compounds, molecules, microbes, phenotypes, and diseases and/or TCM syndromes, generating fresh insights into holistic traditional medicine.

Not only does network pharmacology reflect the holistic properties of herbal medicine, but the rich trove of data on the use of TCM as herbal combinations can assist in refining the network. Considering that we still have much to learn regarding biological systems and drug action/interactions, the field of network pharmacology can undoubtedly benefit by combining top-down and bottom-up strategies. Since certain herbal formulae have been shown to be clinically effective, the inclusion of this empirical knowledge

Ministry of Education Key Laboratory of Bioinformatics and Bioinformatics Division, Tsinghua National Laboratory for Information Science and Technology/Department of Automation, Tsinghua University, Beijing, China
*Corresponding Author: shaoli@mail.tsinghua.edu.cn

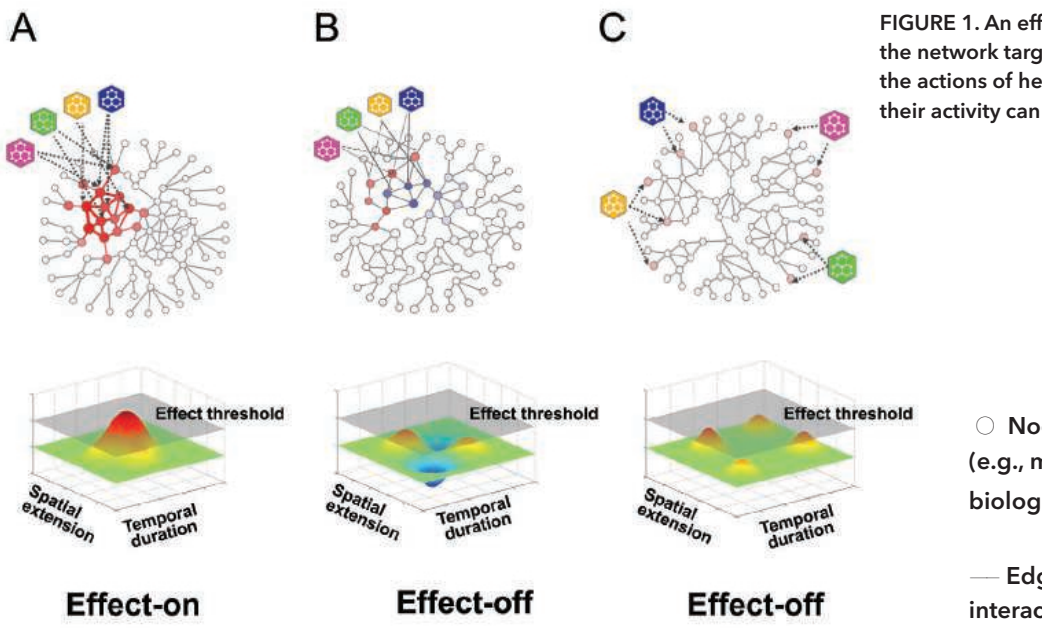

FIGURE 1. An effect-switch model based on the network target can be used to understand the actions of herbal ingredients and how their activity can be modulated.

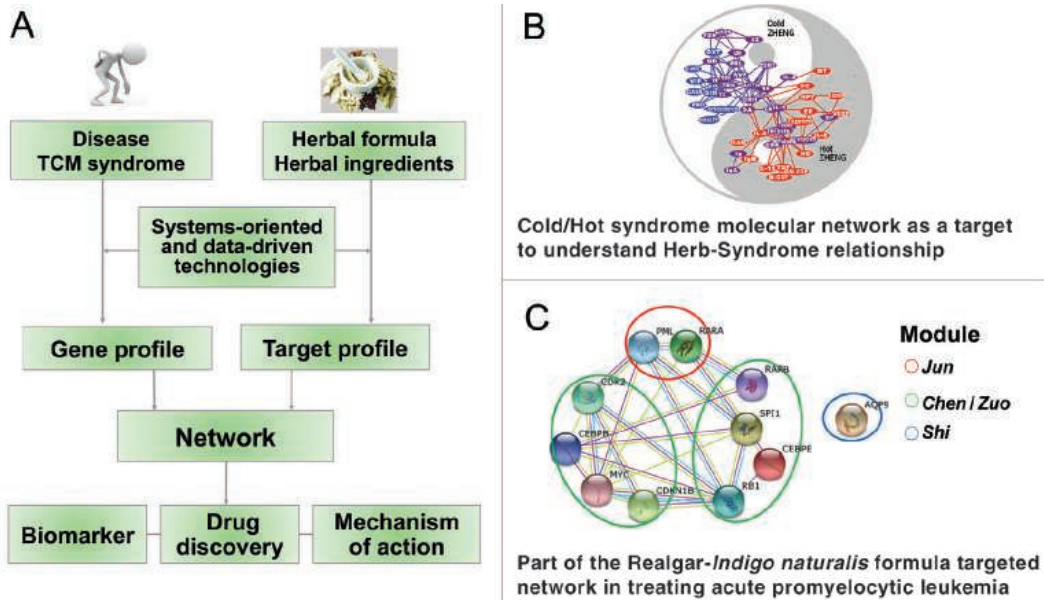

FIGURE 2. (A) Schematic of traditional Chinese medicine-network pharmacology (TCM-NP) methodology. (B) A representation of a Cold/Hot Syndrome molecular network (*12*). **(C)** Part of the Realgar-*Indigo naturalis* components targeted network. PML, promyelocytic leukemia; RARA, retinoic acid receptor, alpha; RB, retinoblastoma; MYC, v-*myc* avian myelocytomatosis viral oncogene homolog; CDK2, cyclin-dependent kinase 2; SPI1, a gene encoding transcription factor PU.1; CDKN1B, cyclin-dependent kinase inhibitor 1B; CEBPB, cytidine-cytidine-adenosine-adenosine-thymidine (CCAAT)/enhancer binding protein, beta; CEBPE, CCAAT/enhancer binding protein, epsilon; RARB, retinoic acid receptor, beta; AQP9, aquaporin 9 (*15*).

of multicomponent therapeutics may permit exciting advancements in network pharmacology.

Application of TCM-NP in traditional medicine

TCM-NP promises to help elucidate the complex molecular mechanisms underlying the actions of traditional therapies as well as explore new indications for their use. Herbal formulae are traditionally used to treat so-called TCM syndromes (*Zheng*). Most medicinal herbs can be categorized as cold, cool, warm, or hot, based on their composition and nature. One of the earliest TCM-NP studies showed that Cold and Hot Syndromes are closely associated with a number of networked

neuroendocrine-immune molecules, indicating a metabolism-immune imbalance. Meanwhile certain so-called cold herbs can target hub nodes in the Hot Syndrome molecular network, and vice versa, to restore the corresponding network balance (*12*) (Figure 2B). It was further found that active compounds in a cold herbal formula, *Qing-Luo-Yin*, could synergistically suppress the cytokine and vascular endothelial growth factor pathways in a hot network to treat disorders involving inflammation and angiogenesis (*13*).

Moreover, TCM-NP may provide a network-based interpretation for the *Jun-Chen-Zuo-Shi* (emperor-minister-assistant-courier) theory of combining herbal formulae. A disease molecular network could accordingly be divided into *Jun-Chen-Zuo-Shi* target modules to aid in the determination of the optimal combination therapy (*14*). For instance, in a Realgar-*Indigo naturalis* formula, tetraarsenic tetrasulfide as a *Jun* can target the promyelocytic leukemia (PML)-retinoic acid receptor alpha (RARA), a fusion protein involved in acute PML. Indirubin and tanshinone IIA can act as *Chen* and *Zuo*, respectively, by targeting the network immediately adjacent to, and interacting with, PML-RARA, while the *Shi* targets the membrane channel transporter, aquaporin-9, to aid arsenic transportation (*15*) (Figure 2C; the target interactions are extracted by using the Search Tool for the Retrieval of Interacting Genes/Proteins, http://string-db.org/). Additional TCM-NP case studies have recently been published (*16*).

Clearly, the merging of TCM and network pharmacology is in its early stages. A more in-depth analysis of TCM-NP will require more powerful computational or experimental methodologies and technologies, together with more comprehensive TCM data. Although the task is challenging, there is much optimism for the future, particularly with the arrival of the big data and precision medicine era. Moving forward, TCM-NP promises to be an innovative way to explore the application and efficacy of TCM, and can contribute to narrowing the gap between Eastern and Western medical practices.

References

1. E. C. Butcher, *Nat. Rev. Drug Discov.* **4**, 461 (2005).
2. A. L. Hopkins, *Nature Chem. Biol.* **4**, 682 (2008).
3. S. Li, *J. Chin. Integrat. Med.* **5**, 489 (2007).
4. A. L. Barabási, N. Gulbahce, J. Loscalzo, *Nat. Rev. Genet.* **12**, 56 (2011).
5. S. Li, B. Zhang, *Chin. J. Nat. Med.* **11**, 110 (2013).
6. S. Li, B. Zhang, N. B. Zhang, *BMC Syst. Biol.* **5**(Suppl. 1), S10 (2011).
7. C. T. Keith *et al.*, *Nat. Rev. Drug Discov.* **4**, 71 (2005).
8. T. Xue, R. Roy, *Science* **300**, 740 (2003).
9. X. Liang *et al.*, *Mol. BioSyst.* **10**, 1014 (2014).
10. S. Zhao, S. Li, *PLOS ONE* **5**, e11764 (2010).
11. X. Wu *et al.*, *Mol. Syst. Biol.* **4**, 189 (2008).
12. S. Li *et al.*, *IET Syst. Biol.* **1**, 51 (2007).
13. B. Zhang *et al.*, *Evid. Based Complement. Alternat. Med.* **2013**, 456747 (2013).
14. S. Li *et al.*, *BMC Bioinformatics* **11**(Suppl. 11), S6 (2010).
15. L. Wang *et al.*, *Proc. Natl. Acad. Sci. U.S.A.* **105**, 4826 (2008).
16. S. Li, T. P. Fan, W. Jia, A. Lu, W. Zhang, *Evid. Based Complement. Alternat. Med.* **2014**, 138460 (2014).

Acknowledgments

The author thanks Dr. Tai-Ping Fan and his colleagues for their review of this work and their valuable comments and suggestions. This work is supported by the National Natural Science Foundation of China (81225025 and 91229201).

Drug discovery in traditional Chinese medicine: From herbal *fufang* to combinatory drugs

Authors: Bing He[†], Cheng Lu[†], Maolin Wang, Guang Zheng, Gao Chen, Miao Jiang, Xiaojuan He, Zhaoxiang Bian, Ge Zhang[*], Aiping Lu[*]

Today, drug discovery is a critical issue in the pharmaceutical industry. Although global spending on drug discovery and development has risen sharply in the last decade, the approval rate for new drugs is declining. This situation is mainly due to drug failure caused by lack of efficacy and/or safety. One important reason for this is that common single-drug therapeutics are rarely able to fully address the complex nature of most human diseases (*1*). Producing combinatory drugs—combinations of multiple drugs against multiple disease targets—is an appropriate approach to address this issue (*2*).

Traditional Chinese medicine (TCM), a medical system based on natural products, has been widely used in East Asia for thousands of years to provide treatments and cures for disease. The long history and extensive documentation of TCM clinical practices have accumulated a considerable number of *fufang* (herbal compound prescriptions) that exhibit in vivo efficacy and safety, and provide a unique resource for combinatory drug discovery.

TCM: Synergy of multiple ingredients

The documented history of TCM dates back more than four thousand years to the times of Shennong (Yan Emperor), while mature TCM theory was established during the Song dynasty (960–1279 CE). TCM theory is based on a holistic, interconnected view of the world. The patient is considered as a system in which the normal balance of Yin/Yang has been disrupted.

The first step in the TCM diagnosis process is to determine the particular *Zheng* (pattern or syndrome) afflicting the patient (*3*). In our studies, we analyzed the molecular networks of *Han Zheng* (cold pattern) and *Re Zheng* (heat pattern) in rheumatoid arthritis patients. The results indicated that *Han Zheng* is related to the Toll-like receptor signaling pathway, while *Re Zheng* impacts the calcium and peroxisome proliferator-activated receptor signaling pathways (*4*). Characteristic molecular signatures for each *Zheng* were also identified (*5*).

Based on the particular *Zheng* and characteristics of the patient, a suitable *fufang* was chosen for treatment. *Fufang* were formulated based on the TCM principle of *Jun-Chen-Zuo-Shi,* with *Jun* (literally "emperor") being the principal ingredient that targets the primary causes and symptoms of

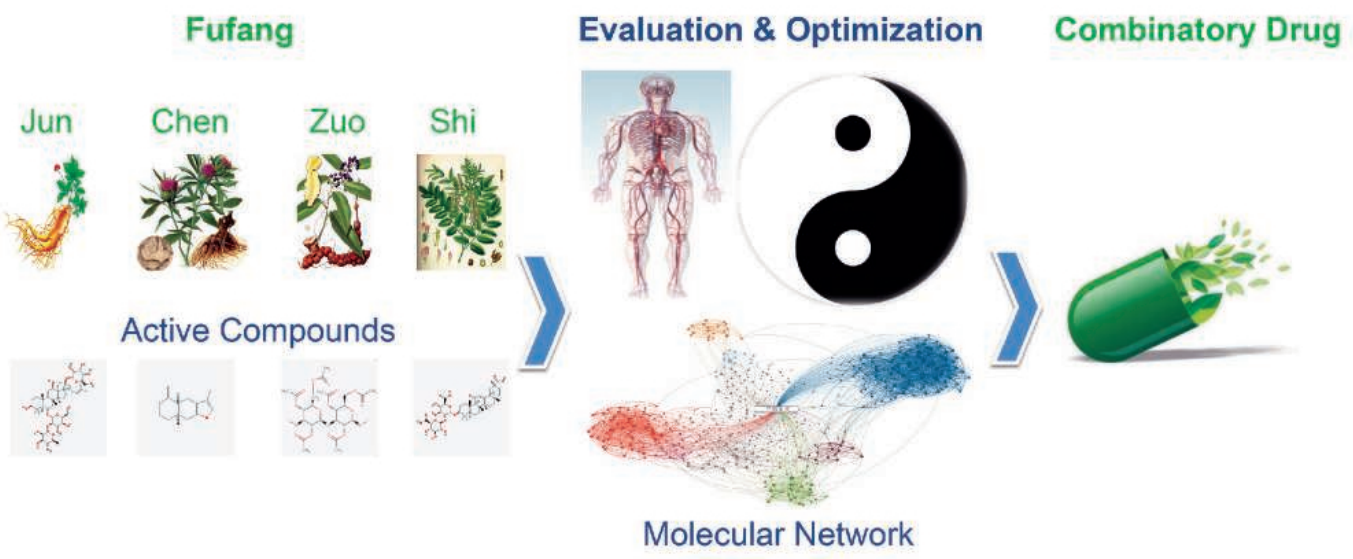

FIGURE 1. Overview: From herbal *fufang* to combinatory drugs.

the disease, *Chen* ("minister") targeting the underlying causes of the disease and potential protective mechanisms, *Zuo* ("assistant") helping the *Jun* and *Chen* ingredients to achieve their optimal curative effects by counteracting any potential adverse side effects and by treating any secondary symptoms of the disease, and finally, *Shi* ("courier") ensuring that all ingredients are properly absorbed and delivered to the target organs.

We will use a well-known and clinically tested *fufang* for leukemia therapy as an example to illustrate this principle. The formula, known as Realgar–Indigo formula (RIF), contains realgar, indigo minerals, and red sage root. Molecular analyses showed that arsenic in realgar works as *Jun* by directly attacking the receptor oncoprotein in leukemia cells. Tanshinone, the active ingredient in red sage root, acts as *Chen* by partially restoring those pathways that stop leukemia spreading. Indirubin, the active ingredient in indigo, works as *Zuo* by antagonizing the toxicity of arsenic and slowing the growth of leukemia cells. Lastly, indirubin and tanshinone work as *Shi*, as these ingredients can enhance the cellular uptake of arsenic by increasing the gene expression and synthesis of carrier pore proteins in the cell membrane (*6*). Such multiple synergetic ingredients in *fufang* offer a unique opportunity to attack multiple disease-causing mechanisms simultaneously, and make it a unique resource for the discovery of new combinatory drugs. Arsenic, the *Jun* ingredient mentioned above, is now the primary drug in a combination therapy for acute promyelocytic leukemia (*7*). Generally, understanding the pharmacology network of *fufang* will be useful in TCM-based combinatory drug discovery. The recent development of 'omics technologies and in silico methods for analyzing signaling pathways provide useful tools for understanding the pharmacology network of various *fufang*.

The application of 'omics and in silico technologies

'Omics technologies such as genomics, transcriptomics, proteomics, and metabonomics are high-throughput technologies used to analyze a variety of molecules simultaneously. These technologies have facilitated the study of the molecular pharmacology of *fufang* at multiple levels (*8*). However, the high cost of such studies has thus far limited the number of *fufang* studies using 'omics technologies. As a lower cost alternative, in silico methods using computational algorithms and cheminformatics can virtual screen large numbers of drug-target interactions in order to construct pharmacology networks of *fufang* activity (*9*). In one example, the active compounds and mechanisms of actions of *Gegen-Qin-Lian-Tang* for the treatment of type 2 diabetes were determined by an in silico approach (*10*).

A network-based evaluation approach

A primary advantage of *fufang* is the ability to simultaneously target multiple points within the complex network of a disease. We established an evaluation approach to examine the interaction between a *fufang* and a human disease network to facilitate the translation of a *fufang* into a combinatory drug (Figure 1).

This approach evaluated three effects of the drug: the major therapeutic effect (MTE), the associated therapeutic effect (ATE), and any ancillary effects (AEs). MTE is the ability of the drug to target the affected disease network and recover normal function, similar to the role of *Jun* ingredients. ATE is the drug's ability to enhance the effects of the MTE and provide protection against negative side effects, as provided by *Chen* and *Zuo*. AEs refer to any additional assistive mechanisms, similar to the role of *Shi* ingredients.

Institute for Advancing Translational Medicine in Bone & Joint Diseases, School of Chinese Medicine, Hong Kong Baptist University, Hong Kong, China
†Contributed equally to this work.
*Corresponding Authors: zhangge@hkbu.edu.hk (G.Z.) and aipinglu@hkbu.edu.hk (A.L.)

The evaluation of ingredients considers three aspects: coverage of the *fufang* target network, the ability of the formula to alter the target's function, and the impact of this alteration on the disease network. Here, we provide an example to illustrate the general evaluation process and its contribution to combinatory drug discovery. *Bizheng-Tang*, the decoction of eight ingredients, could help overcome the low response of leflunomide in rheumatoid arthritis (RA) treatment. To simplify *Bizheng-Tang*, we studied the gene expression profiles of low-response RA mice before and after *Bizheng-Tang* administration, as well as the effect of each separate ingredient in the formula. The results suggested that *Rhizoma Ligustici Chuanxiong* plays an essential role in *Bizheng-Tang*. Further clinical trials confirmed that ligustrazine, the active component of *Rhizoma Ligustici Chuanxiong*, in combination with leflunomide effectively overcame the low response to RA treatment (*11*).

This simplified approach for evaluation of *fufang* ingredients demonstrates a potential way to discover combinatory drugs, although further testing and verification of this process is still required.

Future work

To date, only a small number of *fufang* have been studied using advanced 'omics technologies and in silico methods. Although 'omics technologies are powerful, results are susceptible to variability caused by the use of nonstandardized research materials. Proper standards must therefore be established to better control study-to-study variation. In silico methods used for virtual screening have been developed mainly for Western chemical medicine and a one-drug, one-target system. They are often not sufficiently powerful to handle the complex multidrug, multitarget nature of *fufang*. New algorithms therefore need to be developed specifically for *fufang*. When trying to develop combinatory drugs from *fufang*, one of the most challenging steps is deciding on a short list of effective formulae from the extensive ancient and contemporary literature, as there are over 11,000 plant species used in more than 100,000 *fufang* in China. The future discovery of combinatory drugs from *fufang* will benefit from the development of a research platform that contains biological information on *fufang* herbs and compounds, and on data from standardized 'omics studies, all integrated using TCM-specific in silico tools.

References

1. J. W. Scannell, A. Blanckley, H. Boldon, B. Warrington, *Nature Rev. Drug Dis.* **11**, 191 (2012).
2. J. Woodcock, J. P. Griffin, R. E. Behrman, *New Engl. J. Med.* **364**, 985 (2011).
3. M. Jiang *et al.*, *J. Ethnopharmacol.* **140**, 634 (2012).
4. C. Lu *et al.*, *Rheumatol. Int.* **32**, 61 (2012).
5. C. Lu *et al.*, *Evid. Based Comp. Alternat. Med.* **2012**, 203043 (2012).
6. L. Wang *et al.*, *Proc. Natl. Acad. Sci. U.S.A.* **105**, 4826 (2008).
7. H. H. Zhu, X. J. Huang, *New Engl. J. Med.* **371**, 2239 (2014).
8. X. Cheng *et al.*, *Sci. Reports* **4**, 5147 (2014).
9. S. Li, T. P. Fan, W. Jia, A. Lu, W. Zhang, *Evid. Based Comp. Alternat. Med.* **2014**, 138460 (2014).
10. H. Li *et al.*, *Evid. Based Comp. Alternat. Med.* **2014**, 495840 (2014).
11. M. Jiang *et al.*, *Drug Discovery and Therapy World Congress 2014,* PO-34, 123 (2014); available at http://www.ddtwc.com/pdf/Abstract-Book(2014).pdf.

The polypharmacokinetics of herbal medicines

Authors: Wei Jia[1,2,3]*, Tai-ping Fan[4], Xiaoning Wang[3], Guoxiang Xie[2]

The pharmacokinetics (PK) of multicomponent herbal medicines (HMs) is a long-standing bottleneck for botanical drug and traditional medicine research. There are a number of reasons for this. One is the sheer number of plant-derived molecules that are typically present in HMs, which presents a substantial challenge to chemical and pharmacological evaluation. This is further complicated by the wide concentration range of the components. Another factor is the dynamic nature of chemical interactions between the plant-derived molecules and endogenous molecules. These interactions shape the PK of an HM and, consequently, the treatment outcome for individual patients. Monitoring the chemical components is made still more challenging by a lack of authenticated standards, by the complexity of both botanicals and biological sample matrices, and by the need for cross-disciplinary expertise involving 'omics sciences, biochemistry, pharmacology, bioinformatics, and systems modeling. As a result, current research on the PK of HMs is still in its infancy. It is largely focused on in vivo characterization of one or two key HM components, the results of which may be difficult to link to the holistic treatment effects that result from drug-drug interactions (*1*).

A Poly-PK Approach

The traditional approach to understanding the pharmacology of a multicomponent agent is to study the effects of single active components on well-defined targets, such as specific enzymes or genes. However, it has proven impractical to integrate the results obtained using these reductive approaches to generate a systems understanding of concerted pharmacological interventions (*2*). The attempts to characterize the PK of multicomponent natural products have, however, demonstrated that the PK behavior of a given phytochemical is altered by coexisting constituents (*3–5*).

The advent of comprehensive profiling technologies offers tremendous new opportunities for understanding multicomponent PK. Phytochemical profiling and metabolomics can be coupled to multivariate statistical tools to generate multiparametric assessments. These allow us to create a concentration–time profile of a multicomponent HM, which we call a "Poly-PK," as well as other health determinants associated with the intervention.

We recently proposed an integrated profiling approach. It uses tandem mass spectrometry (MS) to provide quantitative dynamic concentration profiles of bioavailable xenobiotic molecules that result from in vivo absorption, and hepatic and gut bacterial metabolism, of herbal agents (*6, 7*). This Poly-PK approach takes into account both the diversity of the HM's

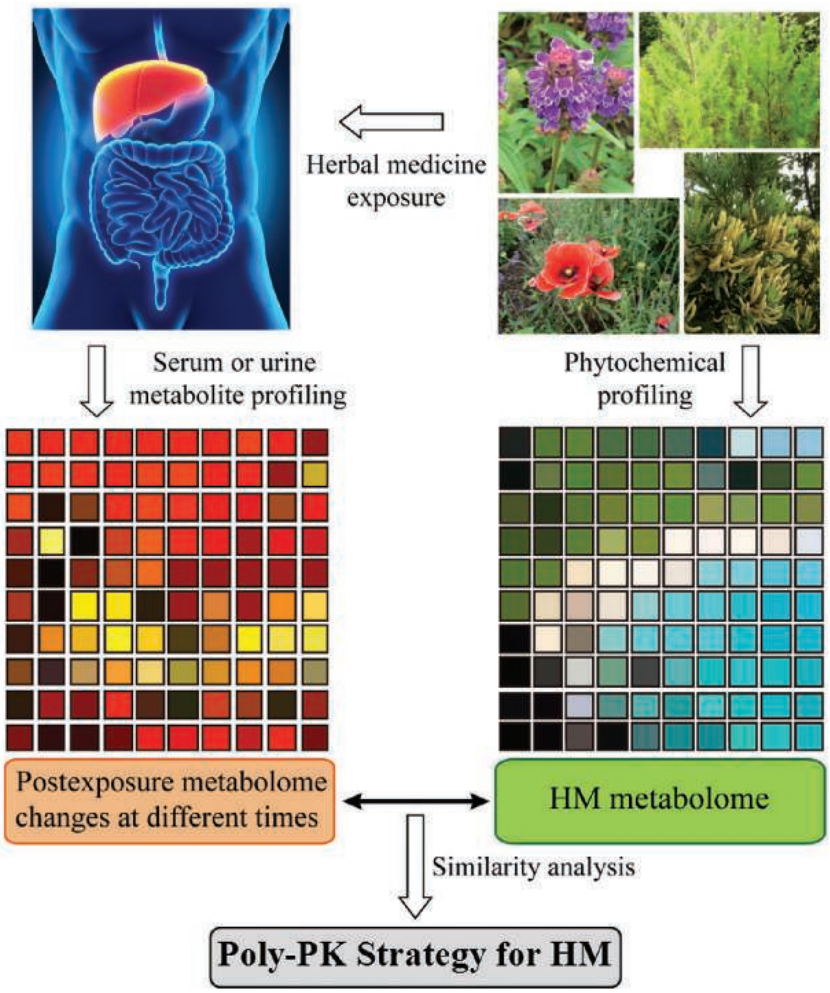

FIGURE 1. A Poly-PK strategy. The pharmacokinetic (PK) study of multicomponent herbal medicines (HMs) that integrates phytochemical and metabolite profiling.

chemical composition and its complex effects on the metabolic pathways of the mammalian system. When HMs enter our body, there are significant metabolite profile changes over time, which fall into three categories as illustrated in Figure 1: (1) HM-derived compounds absorbed into the circulation, (2) new metabolites generated by the chemical transformation of HM compounds by hepatic enzymes and gut microbes, and (3) endogenous metabolites that are altered in response to the HM intervention.

Certain essential PK variables, such as maximum plasma concentration (C_{max}) and the time to reach C_{max} (t_{max}), can be obtained directly from the measured concentration data, while parameters such as the area under the concentration–time curve and the elimination half-life ($t^1/_2$) can be generated using PK modeling software.

Poly-PK in Action

We recently provided proof-of-concept for the above strategy (*8*). The study characterized the in vivo absorption and metabolism in humans of the phytochemicals of Pu-erh, a fermented tea produced in Southwest China. Pu-erh, which contains a large array of polyphenolic constituents, has a range of pharmacological properties, including the ability to reduce blood levels of triacylglycerol and total cholesterol (*9, 10*). Urine samples were collected from volunteers at 0, 1, 3, 6, 9, 12, and 24 hours following consumption of tea, and once a day during a six-week period that included a two-week baseline phase, a two-week daily Pu-erh tea ingestion phase, and a two-week "wash-out" phase. Volunteers were provided with standard meals for six weeks.

The Pu-erh tea water extraction and urine samples collected at the different time points were analyzed using ultraperformance liquid chromatography-quadrupole time-of-flight (TOF) MS and gas chromatography-TOF MS. This analysis generated 1,075 detected features from Pu-erh tea and 6,028 from urine samples (n = 12). The urinary metabolome dataset was subjected to univariate statistical analysis, yielding 2,652 variables that were altered by Pu-erh tea intake ($P < 0.05$). Using multivariate similarity analysis to compare the altered variables to the Pu-erh tea metabolome or the predose urine metabolome, we identified 19 absorbed tea polyphenols, 26 metabolites of the absorbed polyphenols, and 118 endogenous metabolites altered due to tea intake. Subsequent analysis demonstrated, for the first time, a correlation among the dynamic concentration profiles of bioavailable tea components and the human metabolic response profile (Figure 2). This type of approach, in which scientists simultaneously monitor the PK behaviors of multiple phytochemicals in vivo, will lead to the direct elucidation of the pharmacological and molecular mechanisms underlying HMs (*8*).

Perspectives

Over the past two decades HMs have been used increasingly as therapeutic interventions against a number of conditions (*2, 11, 12*). The pharmacology of HMs involves a "network" in which multiple components interact with multiple targets in vivo to exert a holistic treatment effect. The Poly-PK strategy described here uses an integrated phytochemical

[1]Shanghai Key Laboratory of Diabetes Mellitus and Center for Translational Medicine, Department of Endocrinology and Metabolism, Shanghai Jiao Tong University Affiliated Sixth People's Hospital, Shanghai, China
[2]University of Hawaii Cancer Center, Honolulu, Hawaii
[3]E-institute of Shanghai Municipal Education Committee, Shanghai University of Traditional Chinese Medicine, Shanghai, China
[4]Angiogenesis and Traditional Chinese Medicine Laboratory, Department of Pharmacology, University of Cambridge, Cambridge, United Kingdom
*Corresponding Author: wjia@cc.hawaii.edu

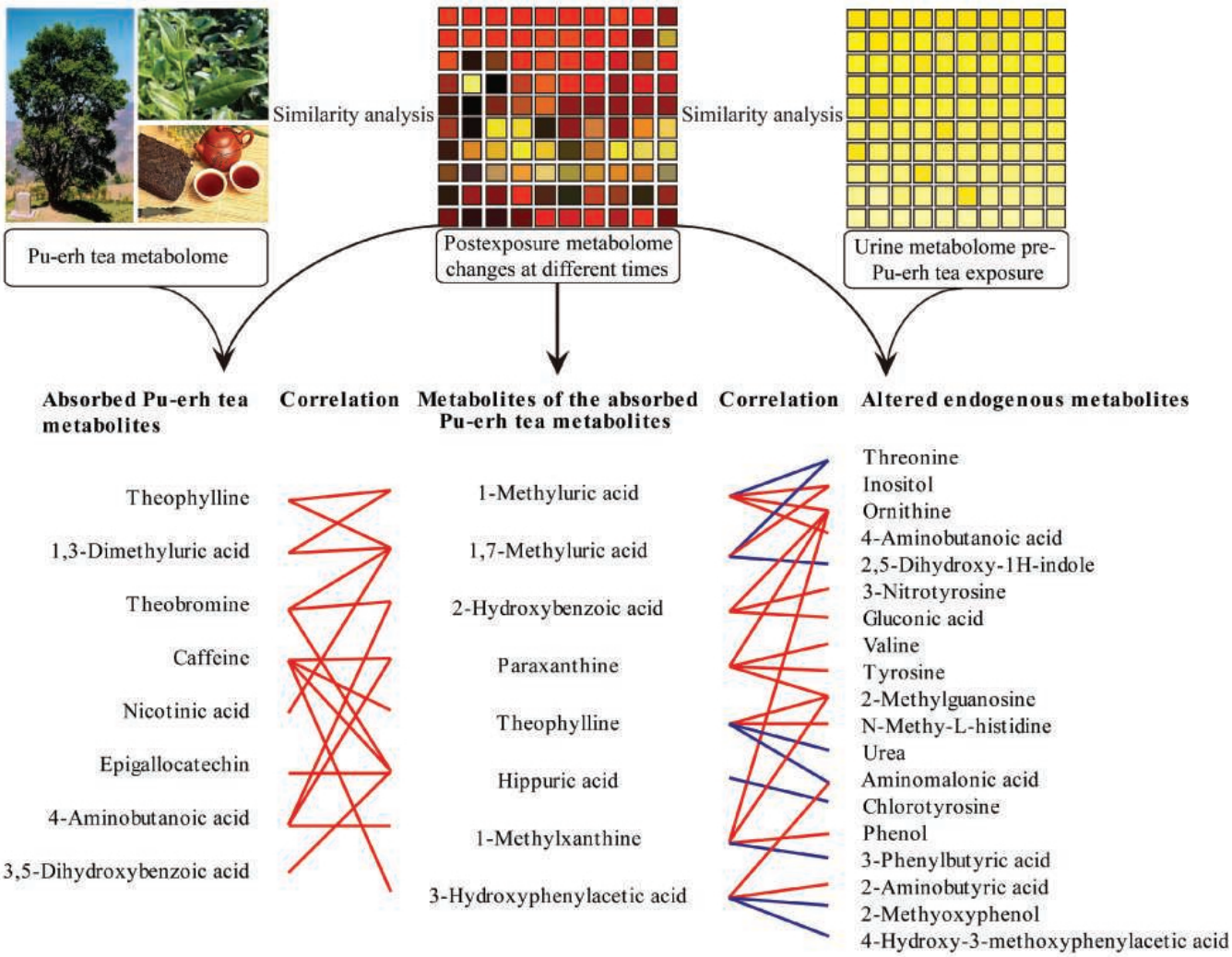

FIGURE 2. Poly-PK metabolomic profiles. The relationships among the three groups of metabolites associated with Pu-erh tea are visualized using correlation maps, as shown by red (positive) or blue (negative) lines.

and metabolomic profiling strategy coupled with multivariate statistical analysis to simultaneously monitor multiple HM components for pharmacological evaluation. This approach reveals the interrelationships between xenobiotics and endobiotics as well as the metabolic impact [using pharmacodynamic (PD) endpoints] of HM agents, providing an unprecedented level of insight into the mechanisms of action for HMs.

Most HMs are administered orally and are therefore exposed to microorganisms in the gut. The symbiotic gut microbiota performs a wide variety of biochemical transformations in which phytochemical compounds are selectively metabolized into active or absorbable components by microbial enzymes. Thus, two sets of genomes—our genome and gut microbiome—comodulate the absorption, distribution, metabolism, and excretion of HM compounds, generating a patient-specific PK profile. Many HM ingredients that were believed to be nonabsorbable and nonactive, such as polysaccharides and lignans, may have significant activities in vivo after oral administration, highlighting the important role that the human gut microbiota plays in HM pharmacology (*13*–*15*). A Poly-PK strategy can facilitate the development of personalized pharmacological evaluation of HMs, linking different patient responses to HM interventions. PK is often studied in conjunction with PD, and the Poly-PK strategy proposed here can simultaneously monitor PD markers through the measurement of multiparametric metabolic changes and other pharmacological endpoints (*6*). To achieve the desired HM therapeutic effect, each of the multiple components of the remedy will require a complete and dynamic panel of PK parameters. This information is essential for minimizing a drug's toxicity, reducing the chances of overdosing a patient or inducing drug complications, and, ultimately, improving patient compliance—and the quality of patients' lives.

We each possess a unique metabolic phenotype, known

as a metabotype, that is characterized by endogenous metabolites and a panel of exogenous metabolites acquired from food consumption and/or drug treatments. This metabotype affects our individual metabolism of, and response to, any given HM. The Poly-PK strategy can unravel the complex interactions between the multiple components in HMs and in mammalian metabolic systems. The advent of the Poly-PK technology will greatly accelerate the holistic pharmacological evaluation of HM candidates and advance novel therapeutic developments. Furthermore, understanding the metabolic fate of a multicomponent drug is also a critical step toward developing the next generation of combinatorial chemical drugs, which will maximize the synergistic effects of certain drug components and help to prevent their undesirable metabolic side effects.

References

1. K. Ito *et al.*, *Pharmacol. Rev.* **50**, 387 (1998).
2. T. Xue, R. Roy, *Science* **300**, 740 (2003).
3. C. Xiang *et al.*, *Drug. Metab. Dispos.* **39**, 1597 (2011).
4. X. Qiao *et al.*, *J. Chromatogr. A* **1258**, 84 (2012).
5. S. M. He, E. Chan, S. F. Zhou, *Curr. Pharm. Des.* **17**, 357 (2011).
6. K. Lan, W. Jia, *Curr. Drug. Metab.* **11**, 105 (2010).
7. K. Lan, G. Xie, W. Jia, *Evid. Based Complement. Alternat. Med.* **2013**, 819147 (2013).
8. G. Xie *et al.*, *J. Proteome Res.* **11**, 3449 (2012).
9. J. K. Lin, S. Y. Lin-Shiau, *Mol. Nutr. Food Res.* **50**, 211 (2006).
10. K. L. Kuo *et al.*, *J. Agric. Food Chem.* **53**, 480 (2005).
11. R. L. Blaylock, *J. Am. Nutraceut. Assoc.* **2**, 19 (1999).
12. J. M. Hollander, J. I. Mechanick, *J. Am. Diet. Assoc.* **108**, 495 (2008).
13. E. D. Sonnenburg *et al.*, *Cell* **141**, 1241 (2010).
14. X. Xu *et al.*, *Biotechnol. Adv.* **31**, 318 (2013).
15. M. Blaut, T. Clavel, *J. Nutr.* **137**, 751S (2007).

The bioavailability barrier and personalized traditional Chinese medicine

Authors:
Lin-Lin Lu[1],
Xiao-Hong Liu[1],
Elaine Lai-Han Leung[3],
Ying Wang[1,2],
Jian Shi[1,2],
Ming Hu[1,4],
Liang Liu[3*],
Zhong-Qiu Liu[1,2*]

Traditional Chinese medicine (TCM) focuses on disease prevention and treatment using personalized therapies. The bioavailability barrier (BB) determines the concentration of drug being taken up by the human body, controlled by efflux transporters (ETs) and drug-metabolizing enzymes (DMEs), which are primarily regulated by nuclear receptors (NRs). Hence, polymorphisms of DMEs, ETs, and NRs can affect the pharmacokinetics of drugs, which ultimately influences the efficacy and/or toxicity of Chinese herbal formulas (CHFs). This paper presents the reconstruction of a BB-based network with new insights that help elucidate the therapeutic mechanisms of CHFs.

Western medicine focuses on molecular target-based therapy; however, there are limitations in transforming genotype-based or disease-oriented medicine into personalized and network-based clinical therapy (*1*). In contrast to Western medicine, CHFs achieve their effect through personalized modulation of a patient's health status. However, CHFs have not been widely accepted because their treatment mechanism has not yet been well defined (*2*). Determining how the components of CHFs will behave in the body is a pivotal aspect in determining treatment mechanisms of TCM. The BB has a key function in controlling absorption, biotransformation, and clearance of drugs in vivo (*3*). Therefore, a BB-based approach together with biological, biochemical, 'omics, and computational technologies is a powerful driver for establishing today's personalized TCM model.

The composition and characteristics of the BB network

The BB can be defined as a physiological defense network, because it plays a central role in preventing xenobiotic interference in the human body (*3*). The network is composed mainly of ETs and DMEs that are distributed in the liver and intestine, responsible for drug distribution and elimination (Figure 1A). ETs and DMEs are regulated by nuclear receptors (NRs) that respond to the endogenous and/or exogenous ligands (*4*). DMEs include cytochrome P450 and conjugating enzymes such as uridine 5′-diphospho-glucuronosyltransferases (UGTs) and sulfotransferases (SULTs). ETs refer to the transmembrane adenosine triphosphate (ATP)-binding cassette

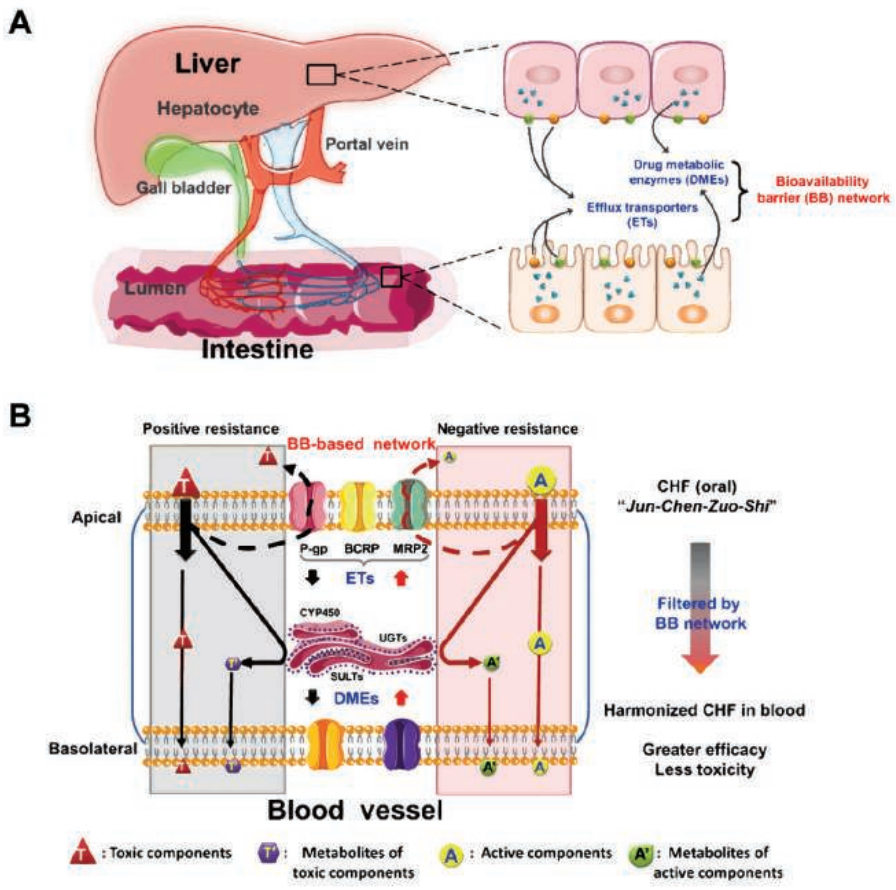

FIGURE 1. Composition of the BB network and its functions. (**A**) The molecular composition of the bioavailability barrier (BB) network in the liver and intestine. (**B**) The bidirectional activity of the BB network during harmonization, indicated by positive (left) and negative (right) resistance to active (yellow circle) and toxic (red triangle) components of Chinese herbal formulas (CHFs). P-gp, p-glycoprotein; BCRP, breast cancer resistance protein; MRP2, multidrug resistance protein 2; UGTs, UDP-glucuronosyltransferases; SULTs, sulfotransferases; ETs, efflux transporters; DMEs, drug-metabolizing enzymes.

efflux transporters (*3*). P-glycoprotein (P-gp), multidrug resistance protein 2 (MRP2), and breast cancer resistance protein (BCRP) on the apical membrane are the most important ETs, delivering or excreting drug metabolites. MRP1 and MRP3 on the basolateral membrane regulate the entry of drugs into the bloodstream. Multiple ETs and DMEs couple to create a complex network regulating disposition of drugs, particularly natural polyphenols abundant in CHFs (*3*).

Drug bioavailability depends not only on the activity of DMEs, but is also influenced by ETs (*3*). Therefore, variations in levels and activity of DMEs and ETs can markedly influence the pattern or pathway coupling in the BB network. For example, genetic variants of CYP2C19 and CYP2D6 are associated with reduced responses to the antiplatelet clopidogrel and the antiestrogen tamoxifen, respectively. The antibiotic doxorubicin exhibits individual differences that maximize therapeutic efficacy and minimize side effects on the basis of genetic variants of the regulatory pregnane X NR receptor (PXR), ETs (ABCB1, ABCG2, ABCC5, ABCB5, and RLIP76), and DMEs (CBR1, CBR3) (*5*). Therefore, the BB network is a critical determinant for implementing personalized medicine.

The BB network and harmonizing CHF efficacy and toxicity

A personalized treatment paradigm is central to the holistic and integrated approach of TCM. CHFs provide a valuable way to study the underlying multitarget mechanisms of personalized TCM treatments. In TCM, the most important principle of formulating CHFs is the *Jun-Chen-Zuo-Shi* (emperor-minister-assistant-courier) principle, which holds that each herb has its own diverse function (*6*). The biological functions of a CHF are harmonized by BB filtration in the body to achieve ideal therapeutic efficacy with minimal toxicity (Figure 1B).

BB filtration can optimize absorption and biotransformation of active and toxic components in CHFs to create a "reharmonized" formulation. The BB mainly exhibits this harmonization effect by bidirectionally driving the bioavailability of active and/or toxic components. Specifically, the bioavailability of active components in CHFs can be enhanced by inhibiting the functions of DMEs and/or ETs in the BB, with consequent improvement in positive

[1]International Institute for Translational Chinese Medicine, Guangzhou University of Chinese Medicine, Guangzhou, China
[2]School of Pharmaceutical Sciences, Southern Medical University, Guangzhou, China
[3]State Key Laboratory of Quality Research in Chinese Medicine, Macau University of Science and Technology, Macau (SAR), China
[4]Department of Pharmacological and Pharmaceutical Sciences, College of Pharmacy, University of Houston, Houston, TX, USA
*Corresponding Authors: lliu@must.edu.mo (L.L) and liuzq@gzucm.edu.cn (Z.L.)

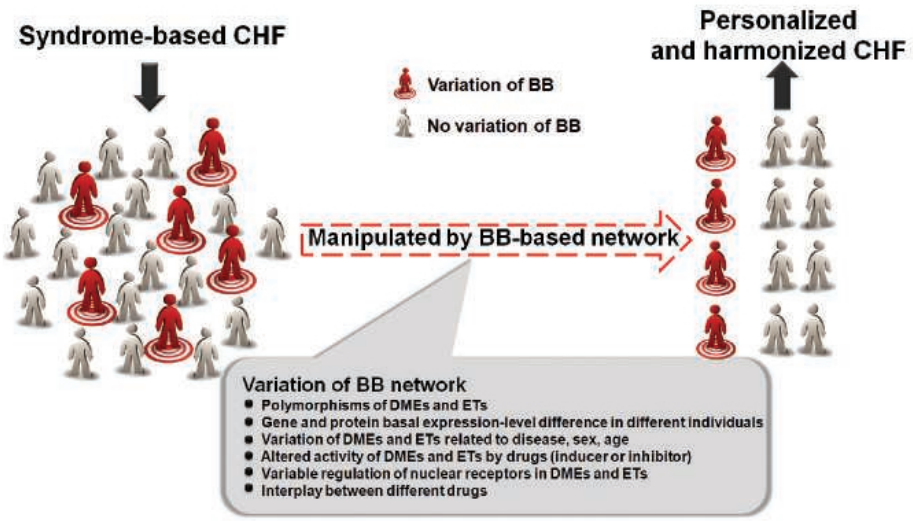

FIGURE 2. Personalized CHF therapy manipulated by the BB network.

pharmacological effects. In contrast, the BB prevents the overabsorption of toxic compounds in CHF (Figure 1B). For example, *Scutellaria baicalensis* contains abundant amounts of diverse polyphenols that possess anticancer and antiaging effects (*3*). MRP2/BCRP and UGTs/SULTs block the bioavailability of polyphenols, resulting in a reduction in pharmacological effects (*7*). However, ETs can act as molecular switches that facilitate the bioavailability of polyphenols (*3*).

Another example is *Radix aconite*, an herb considered to be clinically unsafe. Toxic aconitum alkaloids like aconitine have low bioavailability because of the resistance produced by the BB that limits their toxicity (*8*). In particular, CYP3A4, coupled with P-gp, BCRP, and MRP2 in the BB, blocks the entry of specific toxins into the blood (*9*). Thus, the rational use of such toxic herbs could be controlled by limiting the final dosage to a relatively safe level, not beyond the "resistance" capacity of the BB network. Notably, NRs could interact with the active/toxic components to alter the functions of DMEs and ETs, and consequently affect BB filtration. For example, *Radix glycyrrhizae*, popularly used as a *Shi* herb in CHF, activates PXR (*10*).

In summary, the BB-based network manipulates disposition of the active/toxic components in CHF via dual-directional regulation to achieve the maximal efficacy and minimal side effects of CHF. As such, the BB-based network is able to act as an intelligent, adaptive system for self-defense, while genomic variations of ETs and DMEs result in an individualized BB, which ultimately personalizes TCM treatment by controlling the transport behaviors of CHF (Figure 2).

Perspectives

The BB network is a complex system, largely because of the interplay of its key elements of DMEs, ETs, and NRs. It differs markedly among different individuals due to their unique polymorphisms and genotypes (*11*). The BB can be treated as a personalized system that induces the same drug to produce a variety of actions and toxicities in different individuals. In the future, characterization of personalized BB-based networks will bring a new era in both TCM and conventional medicine.

The essence of TCM is an individualized therapeutic system using CHF (*12*), which is consistent with the principles of personalized BBs. By taking into account BB filtering, CHF can be optimized to produce harmonized, multicomponent, multitarget formulae to achieve optimal effectiveness and low toxicity. We therefore recommend that future CHF research should be implemented together with evidence-based, personalized, and advanced BB research methodologies. The precise molecular mechanisms underlying each personalized BB need to be elucidated. Applying 'omics-related technologies such as metabolomics, proteomics, genomics, and computational prediction to profile individual BB network differences caused by polymorphisms or BB interaction factors could help to assess the unique effects of CHFs in different individuals (Figure 2). In conclusion, the BB network works not only as an indispensable tool for clarifying the mechanisms underlying CHF, but can also be used for characterizing and optimizing personalized TCM therapies.

References

1. E. E. Schadt, *Nature* **461**, 218 (2009).
2. T. P. Fan *et al.*, *J. Ethnopharmacol.* **140**, 568 (2012).
3. M. Hu, *Mol. Pharm.* **4**, 803 (2007).
4. M. Wagner, G. Zollner, M. Trauner, *Hepatology* **53**, 1023 (2011).
5. K. M. Giacomini *et al.*, *Sci. Transl. Med.* **4**, 153ps118 (2012).
6. T. P. Fan *et al.*, *Trends Pharmacol. Sci.* **27**, 297 (2006).
7. E. Wenzel, V. Somoza, *Mol. Nutr. Food Res.* **49**, 472 (2005).
8. L. Ye *et al.*, *Toxicol. Lett.* **216**, 86 (2013).
9. Z. Cai, Y. Wang, L. J. Zhu, Z. Q. Liu, *Curr. Drug Metab.* **11**, 197 (2010).
10. Y. Mu *et al.*, *J. Pharmacol. Exp. Ther.* **316**, 1369 (2006).
11. P. E. Ferreira *et al.*, *Ther. Drug Monit.* **30**, 10 (2008).
12. L. Liu, E. L. Leung, X. Tian, *Nature* **480**, S100 (2011).

Acknowledgments

This work was supported by the National Natural Science Foundation of China (81120108025) and the Macau Science and Technology Development Fund (092/2012/A3).

Transdermal treatment with Chinese herbal medicine: Theory and clinical applications

Authors: Qing Wu[1*], Ling Dong[1], Jianping Liu[2], Dan Jiang[3]

Transdermal treatment with Chinese herbal medicine (CHM) has a long history of clinical application and theory in China. The earliest record of its use can be found in the ancient classic, *Huang Di Nei Jing* (227 BCE). The practice of transdermal treatment continued to evolve, reaching its highest popularity during the Qing dynasty, as elaborated in the book *Li Yue Pian Wen* (Wu Shi-Ji, 1864). It was emphasized in this book that the principles of treatment for both external and internal application of CHM were the same (*1*). This statement was the forerunner of the theory of transdermal administration for CHM, and modern transdermal drug delivery systems (TDDS) use the same concepts, although the precise delivery method is different.

The process of applying transdermal herbal medicine is not as simple as putting it directly on the skin. It should be applied specifically at the relevant acupuncture points (acupoints). According to Wu Shi-Ji, "If a disease is due to an external factor, you should apply herbs to release it on location; however, when the disease has spread into the body, you should apply herbs on the relevant acupuncture points to treat it." (*1*). Thus, transdermal treatments exert their therapeutic actions not only by absorption of active ingredients from herbs, but also the stimulation of acupoints. This concept is one of the distinctive differences between Chinese transdermal herbal treatments and modern TDDS (Figure 1).

Acupoints for treatment

The theory of acupoints and meridians is an important part of traditional Chinese medicine (TCM). The meridian system (or channel network) is believed in TCM theory to be the path along which the "*qi*," or life energy, flows. According to this theory, *qi* and blood fill the meridian system, the channels, and are transported throughout the body via these meridians, feeding the organs. Modern biologists have discovered that there are convergent points of the organs' *qi* and blood along meridians (*2*). Placing an herbal patch directly on the acupuncture point therefore helps to maximize its therapeutic effects, with the aggregate effect being a combination of herbal action plus the acupoint response acting synergistically. The curative effect of an herbal patch placed on an acupoint is commonly regarded as superior to that of a patch placed on a non-acupoint (*3*). Reports on comparing responses of acupoints with non-acupoints indicate noticeable differences (*4*, *5*).

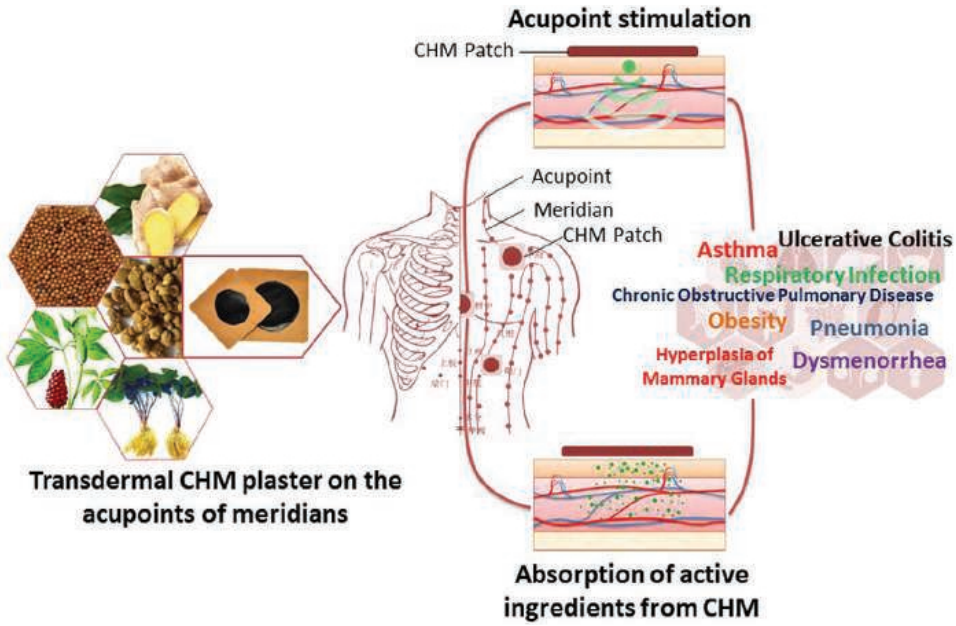

FIGURE 1. A variety of systemic diseases can be treated by application of transdermal Chinese herbal medicine (CHM) patches on meridian acupoints. A combination of acupoint stimulation and the active ingredients in the CHM elicit a healing response.

Materials that appear in this section were not reviewed or assessed by *Science* Editorial staff, but have been evaluated by an international editorial team consisting of experts in traditional medicine research.

[1]School of Chinese Materia Medica, Beijing University of Chinese Medicine, Beijing, China
[2]Centre for Evidence-Based Chinese Medicine, Beijing University of Chinese Medicine, Beijing, China
[3]Hallam Institute of Chinese Medicine, Sheffield, United Kingdom
[*]Corresponding Author: qwu@vip.sina.com

TABLE 1. Diseases and the corresponding acupoints for treatment (*6–18*).

Disease	Acupoints
Asthma in children	FS (BL13); XS (BL15); GS (BL17)
CODP (SP)*	FS (BL13); XS (BL15); GS (BL17)
Allergic rhinitis	DZ (DU14); FS (BL13); PS (BL20); SS (BL23)
Pneumonia in children	FS (BL13); GS (BL17); JL (EX-HN15); GH (BL43); Ashi
Respiratory infection in children	FS (BL13); DC (EX-B01); GH (BL43)
Brady arrhythmia	NG (PC6); XS (BL15)
Insomnia	SQ (RN8); NG (PC6); YQ (KI1)
Dysmenorrhea caused by endometriosis	ZJ (RN3); GY (RN4); ZG (RN19)
Dysmenorrhea	ZJ (RN3); GY (RN4); QH (BL24)
Ulcerative colitis	SJX (ST37); TS (ST25); ZSL (ST36); MM (DU4); GY (RN4)
Chronic renal failure	SQ (RN8)
Simple obesity	ZW (RN12); GY (BL26); QH (RN6); TS (ST25); SD (ST28); DH (SP15)

***Chronic obstructive pulmonary disease (stable phase).** DC, *Ding Chuan*; DH, *Da Heng*; DZ, *Da Zhui*; FS, *Fei Shu*; GH, *Gao Huang;* GS, *Ge Shu*; GY, *Guan Yuan*; GYS, *Guan Yuan Shu*; JBL, *Jing Bai Lao*; MM, *Ming Men*; NG, *Nei Guan*; PS, *Pi Shu*; QH, *Qi Hai*; SD, *Shui Dao*; SJX, *Shang Ju Xu*; SQ, *Shen Que*; SS, *Shen Shu*; TS, *Tian Shu*; XS, *Xin Shu*; YQ, *Yong Quan*; ZG, *Zi Gong*; ZJ, *Zhong Ji*; ZSL, *Zu San Li*; ZW, *Zhong Wan*.

Doctors practicing TCM use their extensive knowledge and experience of syndrome differentiation in clinical practice to diagnose patients before choosing which acupoints to stimulate. How each acupoint relates to a disease is based on both TCM meridian theory and many hundreds of years of empirical knowledge. For example, a transdermal herbal patch could be applied on acupoint *Shen Que* (RN8) for treating diarrhea, menstrual pains, or indigestion; whereas a patch on acupoint *Yong Quan* (KI1) treats high blood pressure, neurasthenia, or the common cold. Some common diseases and the corresponding treatment acupoints are summarized in Table 1 (*6–18*). All have been carefully selected from published clinical research papers using controlled trials and at least 100 cases. Liu and colleagues systematically reviewed the use of an acupoint herbal patch for treating allergic rhinitis and chronic obstructive pulmonary disease (COPD) in the stable phase using a meta-analysis. They included 21 randomized controlled trails (RCTs) involving a total of 2,327 participants (allergic rhinitis) and 20 RCTs involving 2,438 participants (COPD). The authors concluded that an herbal patch alone, or in combination with Western medicine (2011 Global Initiative for Chronic Obstructive Lung Disease guidelines), appeared to be effective for treating these diseases (*19*, *20*).

Recent advances in transdermal herbal preparations

Historically, the most common way to apply transdermal herbal preparations was using a black plaster. To prepare the plaster, herbs were fried in edible oil and red lead oxide (Pb_3O_4) was added to the refined herb oil to form a sticky mass. In recent years, however, since the advent of medicinal polymers, use of a black plaster has gradually given way to adhesive plasters, gel plasters, or patches, which have the significant advantage of reducing skin irritation. The technologies for extraction have also improved, allowing more concentrated extracts of active herbal ingredients to be made, thus facilitating percutaneous absorption of the multiple components of the herbal formula. Inclusion of carrier compounds such as microemulsions (*21*), liposomes (*22*), and cyclodextrin (*23*) can improve the compatibility of complex components and polymer materials. The latest transdermal herbal preparations can be more easily prepared, undergo improved quality control checks, and possess better stability than in the past (*23*). Moreover, pharmaceutical scientists are experimenting with the use of aromatic herbs that can act as natural transdermal uptake enhancers (*24*), which will potentially broaden their clinical application in the future.

References

1. S. Wu, *Li Yue Pian Wen,* 2nd Ed. (China Press of Traditional Chinese Medicine, Beijing, 2007).
2. L. Zheng, *Chin. Acupunct. Moxibustion* **4**, 222 (2003).
3. Y. Sui, *China J. Found. TCM* **9**, 53 2003).
4. X. Guo, X. Liu, *China Journal of Chinese Materia Medica* **37**, 1035 (2012).
5. L. Xu, Z. Cai, *J. TCM External Treat.* **14**, 6 (2005).
6. Y. Liang, *Chin. J. Integr. Tradit. Western Med.* **10**, 1424 (2013).
7. G. Li, L. Wang, Y. Lin, *Chin. J. Integr. Tradit. Western Med. Intens. Crit. Care* **9**, 1187 (2011).
8. M. Zhao, F. Qiao, X. Shen, *J. Tradit. Chin. Med.* **19**, 1661 (2012).
9. Y. Liu, J. Shen, R. Wang, *J. Tradit. Chin. Med.* **10**, 620 (1994).
10. L. Sun, S. Lin, S. Tong, *Chin. Acupunct. Moxibustion* **5**, 21 (1995).
11. L. Xu, Y. Zhang, Y. Zheng, *Chin. Acupunct. Moxibustion* **3**, 192 (2010).
12. J. Hu, F. Yang, *Lishizhen Med. Materia Medica Res.* **6**, 1445 (2013).
13. M. Chen, H. Zhang, J. Li, *Chin. Acupunct. Moxibustion* **9**, 725 (2012).
14. S. Wang, D. Lu, Y. Li, *Chin. Acupunct. Moxibustion* **4**, 265 (2009).
15. L. Hang, Z. Cai, Y. Zhu, *Chin. Acupunct. Moxibustion* **7**, 577 (2013).
16. X. Wu, Z. Liu, X. Zhang, *Chin. J. Integr. Tradit. Western Med. Intens. Crit. Care* **1**, 39 (2004).
17. L. Yin, Y. Li, S. Wang, *Chin. Acupunct. Moxibustion* **6**, 402 (2008).
18. N. Jiao, *Chin. J. Exp. Tradit. Med. Formulae* **12**, 293 (2011).
19. F. Zhou, P. Liu, *Integrative Medicine Research* **4**, 144 (2015).
20. F. Zhou *et al., World Journal of Traditional Chinese Medicine* **1**, 45 (2015).
21. X. Li, Q. Wu, *China Materia Medica* **38**, 37 (2013).
22. Y. Yuan, P. Huang, X. Yang, *Chinese Pharmacist* **7**, 17 (2014).
23. X. Xiong *et al.*, *Chinese Journal of Experimental Traditional Medical Formulae* **17**, 22 (2011).
24. Y. Lan *et al.*, *J. Zhejiang Univ.-Sci. B* **15**, 153 (2014).

Acknowledgments

Thanks to Dr. Yi Lan, Bochen Zhao, and Wenping Wang for their contributions to this article.

Acupuncture as a potential treatment for insomnia

Authors:
Wing-Fai Yeung[1],
Ka-Fai Chung[2],
Stephanie Tjen-A-Looi[3],
John Longhurst[3],
Lixing Lao[1,4*]

Insomnia—difficulty falling and staying asleep—is a frequent complaint, with about one-third of the general population worldwide presenting with symptoms (*1*). Although the neural mechanisms underlying chronic insomnia are poorly understood, substantial evidence has shown that it is a disorder of physiological hyperarousal involving both the central nervous system (CNS) and autonomic nervous system (ANS) (*2*, *3*).

Acupuncture has been widely used for the treatment of insomnia in Asia. According to the theory of traditional Chinese medicine (TCM), the mind (or *shen*) is situated in the heart region; insomnia is considered to be a disorder of the heart, so acupuncture points on the heart and pericardium are often used in treatment (*4*). Recently, several systematic reviews have hinted that acupuncture may be an effective treatment for insomnia. However, deficits in study design and quality have meant that definitive conclusions could not be drawn (*5*).

Other studies have shown that acupuncture may be able to increase β-endorphin production and μ-receptor activity (*6*), both of which are associated with enhanced non-rapid eye movement (NREM) sleep. Acupuncture also appears to regulate various neurotransmitters and hormones involved in sleep regulation, including β-endorphin, serotonin, acetylcholine, nitric oxide, melatonin, dopamine, gamma-aminobutyric acid (GABA), and neuropeptide Y (NPY) (*7*–*9*). Further reports have suggested that acupuncture may be related to a significant increase in secretion of melatonin, a hormone involved in regulation of day-night cycles, in insomnia patients (*10*). In both animal and human clinical studies, evidence indicates that acupuncture inhibits sympathetic nervous system activity and regulates the hypothalamic-pituitary-adrenal (HPA) axis (*11*), which may contribute to its mechanism of counteracting insomnia. This review summarizes the evidence of the possible

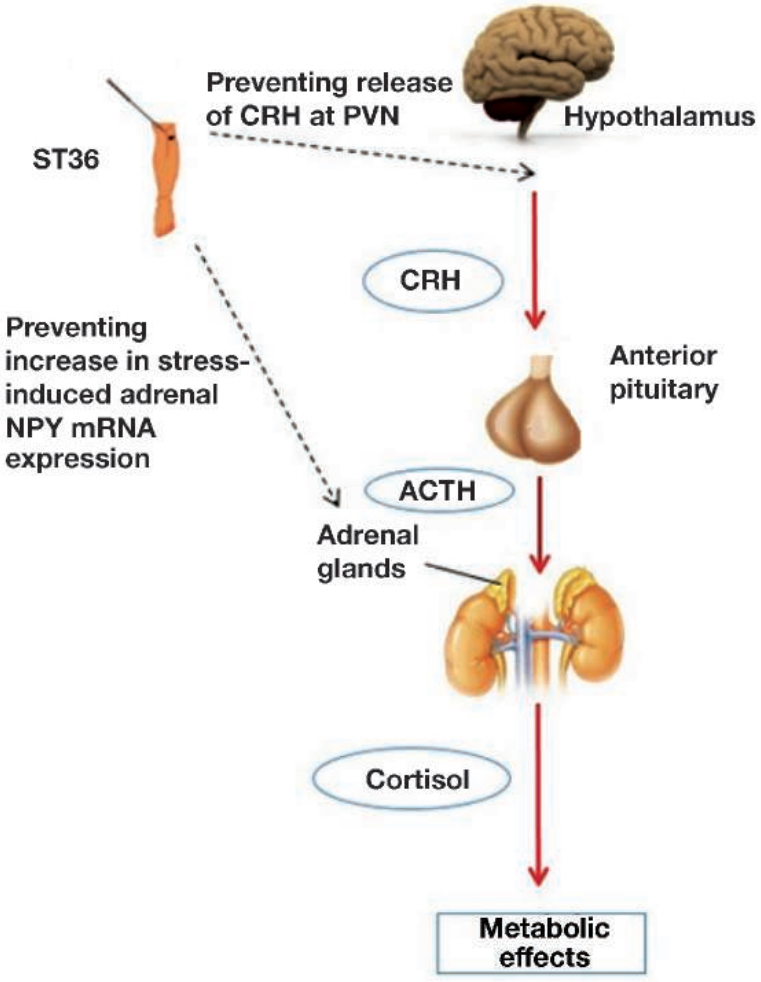

FIGURE 1. The possible pathway describing the effect of acupuncture on hypothalamic-pituitary-adrenal (HPA) activation. The stimulation of Zusanli (ST36) inhibits the HPA axis at or above the level of the paraventricular nucleus (PVN) through corticotropin-releasing hormone (CRH), thereby preventing the stress-induced elevations in circulating adrenocorticotropin hormone (ACTH) and corticosterone levels. It may also prevent increases in stress-induced adrenal neuropeptide Y (NPY) messenger RNA (mRNA) expression.

FIGURE: ADOPTED FROM THE PUBLIC DOMAIN AND FREEDIGITALPHOTOS.NET

[1]School of Chinese Medicine, the University of Hong Kong, Hong Kong, China
[2]Department of Psychiatry, the University of Hong Kong, Hong Kong, China
[3]Susan Samueli Center for Integrative Medicine, School of Medicine, University of California, Irvine, Costa Mesa, California, USA
[4]Center for Integrative Medicine, School of Medicine, University of Maryland, Baltimore, Maryland, USA
*Corresponding Author: lxlao1@hku.hk

mechanisms through which acupuncture may modulate insomnia by acting on hyperarousal of the ANS and regulation of HPA activation.

Possible mechanism of action

Inhibition of sympathetic activity

Acupuncture is believed to modulate sympathetic and parasympathetic activity, as evidenced by its effects on the regulation of cardiovascular function, including lowering blood pressure in patients with hypertension (*12*) and decreasing the heart rate as well as skin blood flow in healthy subjects (*13*). An experimental study in healthy subjects found that needling on the Sishencong (EX-HN1) acupoint, commonly used in the treatment of insomnia, decreases the low-frequency component of the heart rate variability spectrum, which is an indicator of the balance between sympathetic and parasympathetic activities, suggesting that acupuncture enhances cardiac vagal tone and suppresses sympathetic activity (*14*). Acupuncture may alleviate insomnia symptoms and significantly decrease heart rate variability in poststroke patients (*15*), suggesting that improvement in subjective insomnia symptoms results from reducing sympathetic nervous system activity.

The pathophysiological pathway by which acupuncture may facilitate the sleep-wake transition through inhibition of sympathetic activity is not fully understood. Nevertheless, the effects of acupuncture on the excitatory cardiovascular reflexes may provide some hints. A long-loop pathway involving the arcuate nucleus (ARC) and ventrolateral periaqueductal gray (vlPAG), that modulates cardiovascular sympathoexcitatory bulbospinal neurons in the rostral ventrolateral medulla (RVLM) has been suggested as a possible explanation for an acupuncture mechanism. Electroacupuncture stimulation at acupoints Neiguan (PC6), a commonly used acupoint for insomnia, and Jianshi (PC5), activates ARC neurons in the ventral hypothalamus, which, in turn, provides excitatory projections to the midbrain vlPAG. Activation of neurons in the vlPAG stimulates cells in the raphe nuclei, which inhibit activity of cardiovascular premotor sympathoexcitatory neurons in the RVLM via endorphin, enkephalin, GABA, and serotonin (*16*). Since insomniacs apparently show elevated cardiovascular activity associated with ANS hyperarousal, the effects of acupuncture on sleep may involve this long-loop pathway.

Regulation of HPA axis

Acupuncture may improve sleep by regulating the HPA axis. Studies have shown that acupuncture reduces adrenocorticotropin hormone (ACTH), also known as corticotropin, and corticosterone/cortisol levels in animal models of stress (*17*) and in human subjects (*18*). However, precisely where in the HPA pathway acupuncture exerts its effect is not clear. More recently, an experimental study found that electroacupuncture at Zusanli (ST36) prevents chronic stress-induced activation of the HPA axis, as well as elevated sympathetic nervous system-related adrenal NPY (*19*). The study found that corticotropin-releasing hormone (CRH) levels were significantly reduced in acupuncture-treated animals. Findings suggest that acupuncture inhibits the HPA axis activity at or above the level of paraventricular nucleus (PVN) CRH, thereby preventing stress-induced elevations in circulating ACTH and corticosterone levels. Another study demonstrated that electroacupuncture at Zusanli (ST36) prevents an increase in stress-induced adrenal NPY messenger RNA (mRNA) expression (*20*). The increased adrenal NPY expression may result from central signals from either CRH or NPY, which are elevated in the PVN of stressed rats (Figure 1), suggesting that electroacupuncture inhibits the sympathetic NPY pathway by activating neurons in the PVN.

Conclusions

Emerging evidence suggests that acupuncture treatment counteracts insomnia by reducing hyperarousal of the ANS and through regulation of HPA activation. However, the mechanisms underlying acupuncture's actions in insomnia are still far from clear. Further research measuring anatomical location and physiological function are warranted to better understand the mechanisms of acupuncture in the management of insomnia.

References

1. M. M. Ohayon, *Sleep Med. Rev.* **6**, 97 (2002).
2. M. H. Bonnet, D. L. Arand, *Sleep Med. Rev*. **14**, 9 (2010).
3. D. Riemann *et al*., *Sleep Med. Rev*. **14,** 19 (2010).
4. T. J. Kaptchuk, *The Web That Has No Weaver: Understanding Chinese Medicine* (Contemporary Books, Chicago, IL, 2000).
5. E. Ernst, M. S. Lee, T. Y. Choi, *Eur. J. Gen. Pract.* **17**, 116 (2011).
6. C. H. Cheng, P. L. Yi, J. G. Lin, F. C. Chang, *Evid. Based Complement Alternat. Med.* **2011**, 159209 (2011).
7. X. Y. Gao *et al., Zhonggou Zhen Jiu* **27**, 681 (2007).
8. Q. Zhou *et al.*, *Int. J. Clin. Acupunct.* **17**, 79 (2008).
9. N. Samuels, C. Gropp, S. R. Singer, M. Oberbaum, *Behav. Med.* **34**, 55 (2008).
10. D. W. Spence *et al*., *J. Neuropsychiatry Clin. Neurosci.* **16**, 19 (2004).
11. W. Huang, N. Kutner, D. L. Bliwise, *J. Clin. Sleep Med*. **7**, 95 (2011).
12. P. Li *et al., Med. Acupunct.* **27**, 1 (2015).
13. S. Ballegaard *et al*., *Acupunct. Electrother. Res*. **18**, 103 (1993).
14. J. D. Wang, T. B. Kuo, C. C. Yang, *Auton. Neurosci*. **100**, 90 (2002).
15. S. Y. Lee *et al*., *Am. J. Chin. Med*. **37**, 1013 (2009).
16. S. C. Tjen-A-Looi, P. Li, J. C. Longhurst, *J. Appl. Physiol*. **106**, 1793 (2009).
17. H. J. Park *et al*., *Cell. Mol. Neurobiol*. **31**, 1123 (2011).
18. H. Harbach *et al*., *Eur. J. Anaesthesiol*. **24**, 370 (2007).
19. L. Eshkevari, E. Permaul, S. E. Mulroney, *J. Endocrinol*. **217**, 95 (2013).
20. L. Eshkevari *et al*., *Exp. Biol. Med*. **237**, 18 (2012).

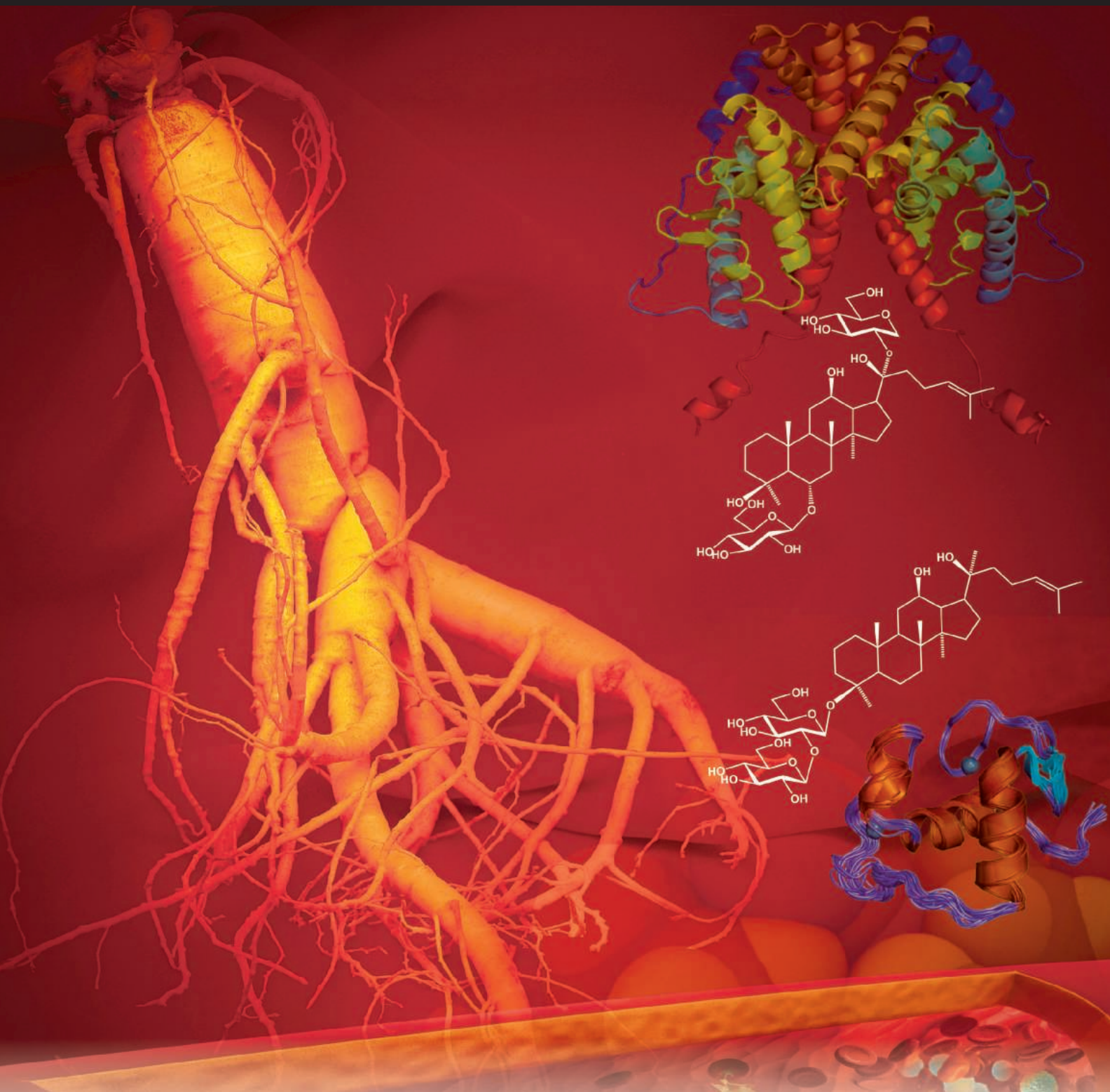

The American Association for the Advancement of Science
1200 New York Avenue NW
Washington, DC 20005

Science
AAAS

The content contained in this special, sponsored section was commissioned, edited, and published by the *Science*/AAAS Custom Publishing Office. It was not peer-reviewed or assessed by the Editorial staff of the journal *Science*; however, all manuscripts have been critically evaluated by an international editorial team consisting of experts in traditional medicine research selected by the project editor. The intent of this section is to provide a means for authors from institutions around the world to showcase their state-of-the-art traditional medicine research through review/perspective-type articles that highlight recent progress in this burgeoning area. The editorial team and authors take full responsibility for the accuracy of the scientific content and the facts stated. Articles can be cited using the following format: [Author Name(s)], *Science* **350** (6262 Suppl), Sxx-Sxx (2015).

UHPLC-MS Instrumentation

New, exceptionally pure mobile phase solvents for ultra-high-performance liquid chromatography-mass spectrometry (UHPLC-MS) instruments have been designed to reduce background signal and minimize chromatographic interferences, facilitating accurate, sensitive, and rapid trace analysis. Fisher Chemical Optima UHPLC-MS solvents are high-quality, ultrapure, and designed to address the trace analysis needs of chromatographers performing state-of-the-art UHPLC. These new solvents are qualified for use with UHPLC/MS instrumentation. UHPLC-MS is becoming the preferred technique to LC-MS in analytical laboratories, as it enables users to perform separations substantially faster due to the innovative sub-2 µm columns. Submicron filtration also reduces clogging of instruments, columns, and check valves. A typical LC-MS gradient run can take up to 60 minutes, whereas UHPLC-MS can reduce this to just 5 minutes while yielding a similar resolution without compromising flow rates. Optima UHPLC-MS solvents are ideal for detecting trace amounts of analyte by tandem mass spectrometry (MS/MS) using either gradient or direct-flow analysis without baseline interference.

Thermo Fisher Scientific
For info: 800-766-7000
www.fishersci.com/fisherchemical

Mass Spectral Database

Scientists conducting research in metabolomics, environmental science, forensics, and food safety can now turn to a globally accessible, web-based fragmentation library for identification of unknown compounds with high-quality, high-resolution accurate-mass (HRAM) data. Developed through a collaboration between Thermo Fisher Scientific and HighChem, mzCloud is a novel, searchable library of HRAM mass spectra, constructed from high-quality data from Thermo Scientific Orbitrap mass spectrometers. The mzCloud offers a tool for researchers who need to identify unknown compounds based on mass spectrometric data. It features a broad diversity of chemical compounds, extensive use of mass spectrometry to reveal substructure information, and a high level of data curation. In addition, production fingerprinting uses extensive mass spectrometry data to identify substructures for truly unknown compounds.

HighChem
For info: +421-2-5263-7868
www.mzcloud.org

Digital Dispenser

The D300e Digital Dispenser is designed for applications that need faster, reliable dispensing down to picoliter volumes. This innovative, easy-to-use device is ideal for the creation of assay plates and can cut setup times from hours or days to just minutes. Users can choose between dispensing aqueous solutions in combination with a surfactant—for the investigation of proteins, antibodies, enzymes, and nucleic acids—and dimethyl sulfoxide (DMSO) for small molecule studies, offering greater flexibility for life sciences workflows. The system's sophisticated yet simple software guides you through every operation, minimizing training times and problem-solving callouts, and providing straightforward setup of enzyme profiles, dose-response curves, and synergy studies. Even the most complex experimental plate layouts can be quickly and easily generated, with optional randomization to reduce the impact of edge effects and increase data integrity. The D300e is compatible with a wide range of microplate formats from 12 to 1,536 wells, including deep-well plates and Society for Biomolecular Screening (SBS)-format tube racks.

Tecan
For info: +41-44-922-81-11
www.tecan.com/d300e

Automation Platform

The MKS Automation Platform is a modular, scalable, and configurable solution for comprehensive control that improves operational and productivity efficiencies. It offers low total cost of ownership and improves utilization of existing tools and assets. The Automation Platform seamlessly integrates with other MKS products, and its library of process routine templates and function blocks facilitates faster implementation. The platform's hardware and software are both scalable and flexible due to its modular, open architecture and its support for many fieldbuses and control networks. It consists of two programmable automation control options; a variety of input/output (IO) modules for interfacing to any type of sensor, actuator, valve, etc.; and the MKS Controls Workbench software for configuration, process monitoring, tuning, and data storage. MKS integration services assist in recipe and logic development, integration, and training. The platform's compact, high-density design reduces the number of modules and controllers required, saving cost and tool real estate.

MKS Instruments
For info: 978-645-5500
www.mksinst.com

Fluorescence Spectroscopy Systems

The new Ultima TCSPC Fluorescence Lifetime system combines the latest in high temporal resolution time-correlated single photon counting (TCSPC) electronics, interchangeable high speed light sources and detector technologies, and Horiba Scientific's FluoroCube, the most flexible dedicated lifetime optical platform, to offer the highest performance photon counting lifetime system available. The Ultima's 400 fs/point time resolution enables it to measure the shortest lifetimes of any comparable commercial system. Its measurement range of 100 ns to seconds, the flexibility of its 16k time channels, and the simplicity of its USB PC connection also make the Ultima easy to use. The Ultima can also be configured for use with microchannel plates (MCPs), femtosecond (fs) lasers, near-infrared (NIR) detectors and excitation and emission monochromators to support virtually any experimental configuration. For those who routinely measure lifetimes below 100 ps, the new Ultima TCSPC offers unprecedented short lifetime performance with exceptional flexibility and ease of use.

Horiba Scientific
For info: 732-494-8660
www.ultimatcspc.com

Electronically submit your new product description or product literature information! Go to www.sciencemag.org/products/newproducts.dtl for more information.

Newly offered instrumentation, apparatus, and laboratory materials of interest to researchers in all disciplines in academic, industrial, and governmental organizations are featured in this space. Emphasis is given to purpose, chief characteristics, and availability of products and materials. Endorsement by *Science* or AAAS of any products or materials mentioned is not implied. Additional information may be obtained from the manufacturer or supplier.

want new technologies?

antibodies
apoptosis
biomarkers
cancer
cytometry
data
diseases
DNA
epigenetics
genomics
immunotherapies
medicine
microbiomics
microfluidics
microscopy
neuroscience
proteomics
sequencing
toxicology
transcriptomics

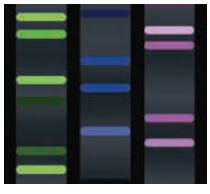

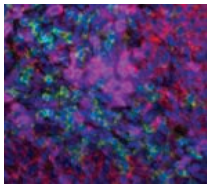

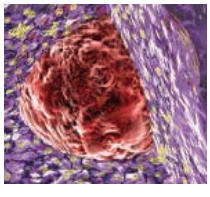

watch our webinars

Learn about the latest breakthroughs, new technologies, and ground-breaking research in a variety of fields. Our expert speakers explain their quality research to you and answer questions submitted by live viewers.

VIEW NOW!
webinar.sciencemag.org

Science
AAAS

Brought to you by the *Science*/AAAS Custom Publishing Office

@SciMagWebinars

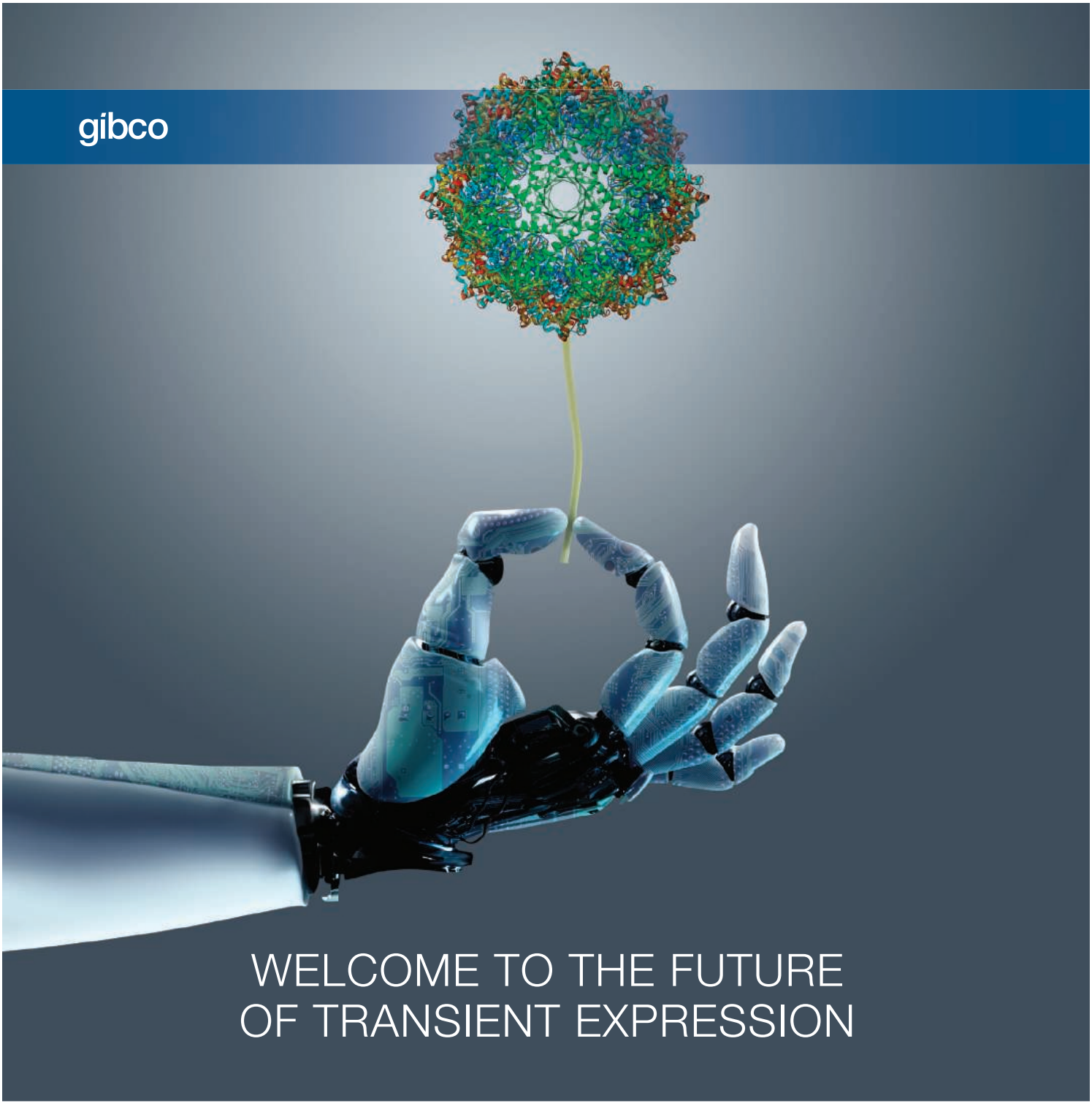

Achieve 3 g/L protein yields in transient CHO with the ExpiCHO™ Expression System

Switching from 293 to CHO cells during drug development may cost you precious time and create uncertainty. Now there's a better way. The new Gibco™ ExpiCHO™ Expression System provides the highest protein yields possible in a transient system. That means you can always work in CHO cells, starting from discovery.

See the future of transient expression at
thermofisher.com/expicho

ThermoFisher SCIENTIFIC

By **Jeremy C. Borniger**

Leaping into the unknown

Passion is not something you can plan for. When I was in elementary school and someone would ask, "What do you want to be when you grow up?" I would shout something along the lines of "a pirate astronaut" or "a *Tyrannosaurus rex*" because those were the things that piqued my interest at the time. As I've aged my passions have changed, and though sometimes I still think it would be fun to be a pirate astronaut, these days I aspire to a career in neuroscience. But it hasn't been a direct path, and changing fields during my training, though challenging, has provided a valuable perspective that has improved my research and, I believe, will continue to serve me well throughout my career.

By the end of my senior year of high school, I knew only that I was more fascinated by the natural world than by business or politics. That was all. But 3 weeks prior to the start of my freshman year of college, I took an elective course in biological anthropology. I became fascinated with human variation; ancient hominid fossils; and the behavior of our closest living relatives, the great apes, and ended up earning a degree in anthropology.

For my undergraduate thesis, I investigated differences in circulating hormones between musicians and nonmusicians and how musical ability might be related to differences in physiology. After this experience, I felt the itch to look deeper into the molecular and cellular mechanisms of behavior. The next step, I decided, was graduate school in neuroscience—a subject in which I had not taken a single course.

Quite a pickle I'd gotten myself into! How was I going to make the jump into this new field? I wrote my graduate school applications to showcase how I had arrived at the decision to pursue neuroscience research without a neuroscience background and my genuine interest in the mechanisms of behavior. I emphasized that I was trained in how to think about complex subjects and use the scientific method—skills I could apply to any topic. To improve my chances, I applied broadly to programs with an emphasis on behavior: anthropology, psychology, and—as a reach—neuroscience. To my relief, it worked! After a gap year spent as the assistant project director for a chimpanzee field site for ecological research in western Uganda, I began graduate school in my first-choice neuroscience program.

Since entering my new field 3 years ago, I've found that a key obstacle to overcome is the lingo. Few things in academia are scarier than walking into a room, listening to a lecture, and having absolutely no idea what just transpired. Early on, I would break out into cold sweats at the thought of having a neuroscience-based conversation. I had to quickly pick up on words like "orthodromic" and "deacetylation" to communicate with my peers. My anthropologist self had to adjust to my new intellectual environment, which I did by reading—a lot.

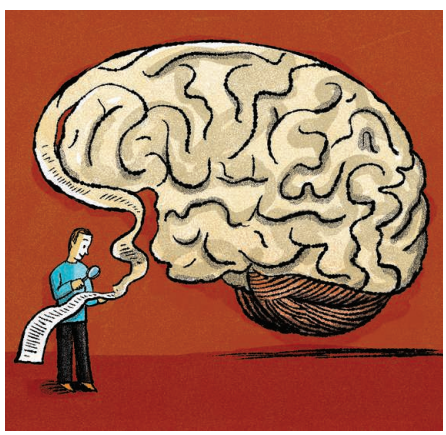

"Being a researcher, no matter the field, is about adaptation."

A cycle emerged: A feeling of severe stupidity would be followed by intense reading, followed by another period of feeling stupid as I realized that, no matter how much I read, new gaps in knowledge would keep popping up. Even now that I feel relatively comfortable identifying myself as a neuroscientist, that cycle continues.

Finding my way in a new discipline helped me realize that being a researcher, no matter the field, is about adaptation. Good scientists need to be able to recognize imminent paradigm shifts and adjust hypotheses accordingly. They should be prepared to explore new experimental approaches when original tactics don't work. And they should be comfortable examining questions from alternative angles, as sometimes the best way to tackle a problem may be hidden in an unfamiliar area. Because of my experience changing fields, I feel equipped to do all of these things, and although it was scary and difficult at times, I believe the experience will make me a better scientist in the long run. I anticipate that my passion will shift again as new discoveries are made. Overcoming the challenge of transitioning fields in graduate school has prepared me for whatever direction my research takes me. ■

Jeremy C. Borniger is a Ph.D. candidate in the neuroscience program at Ohio State University, Columbus. Send your story to SciCareerEditor@aaas.org.

ILLUSTRATION: ROBERT NEUBECKER